DIEGO ALEJANDRO SANZ-BECERRA

DIAMOND PIXEL DETECTORS AND FUTURE 3D DIAMOND DETECTORS

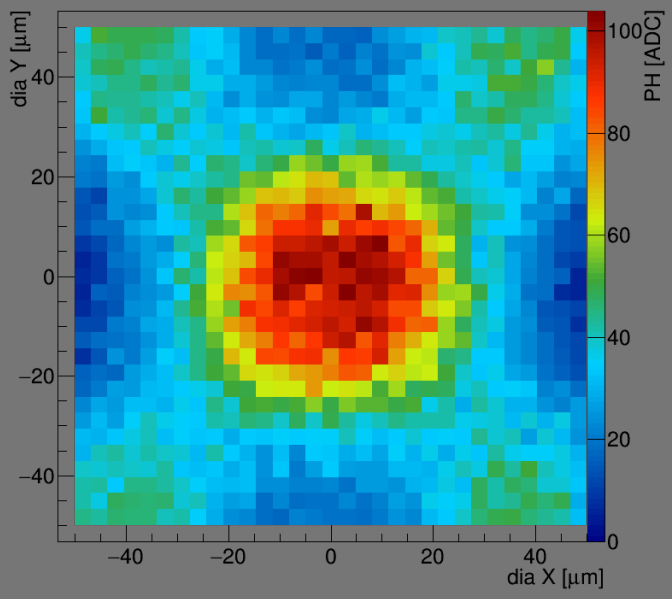

DISS ETH
-29086-

DISS. ETH NO. 29086

DIAMOND PIXEL DETECTORS AND FUTURE 3D DIAMOND DETECTORS

A thesis submitted to attain the degree of

DOCTOR OF SCIENCES

(Dr. sc. ETH Zurich)

presented by

Diego Alejandro Sanz-Becerra

Magíster en Ingeniería, Universidad de los Andes (University of the Andes) - Bogotá

born on 03.09.1986 in Bogotá, Colombia

accepted on the recommendation of

Prof. Dr. Rainer Wallny
Prof. Dr. Stephen Schnetzer

2023

Acknowledgements

I would like to express my sincere gratitude to my supervisor Prof. Dr. Rainer Wallny, and his postdoc Dr. Dmitry Hits, for allowing me to join the diamond detector group and to carry out my Ph.D. at ETH Zurich's Institute for Particle Physics and Astrophysics. I appreciate all the support they gave me, especially during the hard times I encountered during the years I spent in their group.

I am very grateful to Prof. Dr. Stephen Schnetzer and Prof. Dr. Yiwen Chu for agreeing to be my co-examiners and for the corrections and suggestions they gave me to improve this thesis.

I am grateful for having been part of the RD42 collaboration, which allowed me to improve as an experimental physicist by working at test beams at CERN and PSI, and discussing the results in regular meetings. As part of the collaboration, I was able to work with and discuss my work with great scientists such as Prof. Dr. Harris Kagan, Prof. Dr. William Trischuk, and Dr. Alexander Oh, who guided my analysis.

I greatly appreciate the advice and support from the silicon pixel group under the supervision of Dr. Mauro Donegà, Dr. Malte Backhaus, and Dr. Branislav Ristic, who always had an open ear and were glad to lend a helping hand when needed.

I would like to thank the support team at IBM's BRNC, especially Ute Drechsler, for all the unconditional help with the processes required to fabricate a part of the detectors presented in this thesis. In the same way, I would like to thank the CMS group at PSI, especially Dr. Tilman Rohe and Silvan Streuli, for all their support with the bump bonding procedure needed for the pixel prototypes I fabricated.

I sincerely thank the institute's technicians, engineers, and secretaries who constantly make the lives of Ph.D. students easier in the institute. Specifically, I would like to thank Rosa, Caroline, Bettina, Gaby, Jennifer, Diogo, Ulf, Robert, Bruno, and Patrick.

During my years working at HPK's E floor, I was able to meet great friends and colleagues who were also struggling with their Ph.D. Despite the difficulties, they were always a support for me. I am grateful for all the occasions we spent hiking, having after-work drinks, or watching movies with pizza. Especially, I would like to acknowledge Micha for his friendship all these years.

I would like to express my gratitude to the Swiss Government Excellence Scholarship Program for the economic support I was given during the first years of my Ph.D. Without it, I would not have been able to start my Ph.D. at ETH Zurich.

Last but not least, I would like to extend my deepest gratitude to my family, especially to my father, my mother, my brother, and my cousins. Without their unconditional support and endless love, I would not have been able to finish this journey.

Abstract

This thesis aims to push forward the development of diamond particle detectors that could be used in future high-energy experiments where radiation tolerance without cooling is required. The detectors are made with polycrystalline chemical vapor deposition (pCVD) diamonds as the sensor material. This work had two major objectives: The development of a fabrication process that could be scaled up to mass-produce diamond planar pixel detectors and the understanding and modeling of the signal characteristics from 3D diamond detectors.

For the first objective, a fabrication process with yields of up to 99.7 % of the pixels was achieved. All the problems that led to defective pixels were identified and could be solved before scaling up the fabrication process.

As for the second objective, it was determined that hexagonal cells collect more charge than cells with rectangular or square shapes for unirradiated detectors. As for irradiated detectors up to a fluence of 3.5×10^{15} p/cm^2 800 MeV/c protons, efficiencies above 99.6 % were achieved for a threshold similar to the ones available in state-of-the-art readout chips in pixel detectors (i.e. ~ 1500 e) when the cells had a side length of 50 µm. For the irradiated devices with cells of 50 µm and the unirradiated devices with cells of 100 µm, it was found that charge collection efficiencies above 50 % were achieved.

A simulation framework based on the finite element method was used to estimate the capacitance of the measured devices. For most of the devices, the estimated capacitance was within 5 % of the measured capacitance during the test beams. Only one of the simulations underestimated the measured capacitance by 39 %. The reason for this disagreement is unknown.

Extending the simulation framework to model, based on first principles, the movement of the ionized charges inside the diamond, it was possible to reproduce the measure data within 6 % for 3D square cells with a strip readout. The findings support the model proposed by S. Lagomarsino et al., which is based on two mean free paths for the charge carriers that accounts for the movement of the charge carriers parallel to the grain boundaries and perpendicular to the grain boundaries.

Zusammenfassung

Das Ziel dieser Arbeit ist es, die Entwicklung von Teilchendetektoren mit Diamantsensoren voranzutreiben, die in zukünftigen Experimenten der Hochenergiephysik, die Strahlungsbeständigkeit ohne Kühlung erfordern, eingesetzt werden könnten. Die Detektoren haben polykristalline Diamantsensoren, die mit chemischer Gasphasenabscheidung (CVD) synthetisiert werden. Diese Arbeit hatte zwei Schwerpunkte: die Entwicklung eines Herstellungsprozesses, der die Massenproduktion von planaren Diamant-Pixel-Detektoren ermöglicht; und das Verständnis und die Modellierung der Signaleigenschaften von 3D-Diamant-Detektoren.

Für den ersten Schwerpunkt wurde ein Herstellungsprozess mit Pixelausbeuten von bis zu 99.7 % entwickelt. Alle Probleme, die zu fehlerhaften Pixeln führten, wurden identifiziert und konnten gelöst werden, bevor der Fertigungsprozess hochskaliert wurde.

Hinsichtlich des zweiten Schwerpunktes wurde festgestellt, dass unbestrahlte 3D Detektoren mit hexagonalen Zellen mehr Ladung sammeln als Detektoren mit rechteckigen Zellen. Bei Detektoren mit einer Zellengrösse von 50 µm, die mit einer maximalen Fluenz von 3.5×10^{15} p/cm^2 800 MeV/c Protonen bestrahlt wurden, konnten Wirkungsgrade von über 99.6 % erreicht werden, wenn die Auslesechips Schwellenwerte hatten, die vergleichbar mit den Schwellenwerten aktueller Pixeldetektoren sind (d.h. ~ 1500 e). Sowohl für bestrahlte Detektoren mit 50 µm Zellen als auch für unbestrahlte Detektoren mit 100 µm Zellen wurden Ladungssammeleffizienzen von über 50 % erreicht.

Um die Kapazität der untersuchten Detektoren abzuschätzen, wurde ein Simulationsframework verwendet, das auf der Finite-Elemente-Methode basiert. Bei den meisten Detektoren lag die abgeschätzte Kapazität innerhalb von 5 % der während der Teststrahlen gemessenen Kapazität. Nur eine der Schätzungen verfehlte die gemessene Kapazität um 39 %, wobei die Ursache dieser Abweichung nicht gefunden werden konnte.

Die Erweiterung des Simulationsframeworks mit der Modellierung der Bewegung von ionisierten Ladungen im Inneren des Diamanten basierend auf grundlegenden Prinzipien ermöglichte es, die Messdaten von quadratische 3D-Zellen mit einer Streifenauslese mit einer Genauigkeit von 6 % zu reproduzieren. Die Ergebnisse untermauern das von S. Lagomarsino et al. vorgeschlagene Modell, das auf zwei mittleren freien Weglängen für die Ladungsträger basiert, um die Bewegung der Ladungsträger sowohl parallel als auch senkrecht zu den Korngrenzen zu berücksichtigen.

Contents

Acknowledgements iii

Abstract iv

Zusammenfassung v

I Introduction 1

1 Motivation 2

2 Theory 5
2.1 Diamond Characteristics . . . 5
2.2 CVD Diamonds Fabrication . . . 6
2.3 Crystallographic Defects . . . 10
2.4 Radiation Damage . . . 11
2.5 Particle Detection . . . 14
2.5.1 Particle Matter Interactions . . . 14
2.5.2 Charge Collection And Signal Formation . . . 23
2.6 Particle Detector Electronics . . . 29
2.6.1 Signal Preamplifier . . . 30
2.6.2 Signal Shaper . . . 32

II Tested Diamond Devices 35

3 Pixelated Planar Diamond Samples 36
3.1 Readout Chip Characteristics . . . 36
3.2 Pixelated Diamond Detector Characteristics . . . 38
3.3 Sensors Characteristics . . . 39

4 3D Diamond Samples 41
4.1 Charge Sensitive Amplifiers Based On VA ASICs . . . 41
4.1.1 Electronic Noise Sensed By The VA Chip . . . 42
4.2 3D Diamond Strip Detector Characteristics . . . 44

4.3 Diamond Samples . . . 46
4.3.1 Poly-3D . . . 48
4.3.2 Full-3D . . . 49
4.3.3 Multi-3D . . . 50
4.3.4 Irrad-3D . . . 51

III Detectors Fabrication 53

5 Fabrication Of 3D Detectors 54
5.1 Fabrication . . . 54
5.1.1 Samples Preparation . . . 54
5.1.2 3D Wires Formation . . . 54
5.1.3 Surface Metallization . . . 54

6 Fabrication Pixelated Planar Detectors 56
6.1 Sensor's Surface Preparation . . . 58
6.2 Metallization . . . 59
6.2.1 Different Metallization Study . . . 61
6.3 Passivation Layer . . . 63
6.4 Bump Bonds Formation . . . 66
6.5 Bump Bonding . . . 73

IV Strip Detectors Simulations 74

7 Steady State Simulations 75
7.1 Capacitance In Planar Strip Detectors . . . 75
7.2 Capacitance Of Square Cells 3D Strip Detectors . . . 76
7.2.1 Surface Metallization Capacitance . . . 76
7.2.2 Capacitance Of 3D Wires In Square Cells . . . 78
7.2.3 Total Capacitance Of 3D Strips Detectors . . . 81
7.3 Capacitance Of Long Rectangular And Hexagonal 3D Strip Detectors . . . 84
7.4 Electric Field Inside 3D Cells . . . 85

8 Dynamic Simulations 86
8.1 Finite Element Modelling Of Shockley–Ramo Theorem . . . 86
8.1.1 Planar Detector Modelling . . . 86
8.2 Validation Of The Dynamic Simulation With Planar Detectors . . . 89
8.2.1 Hecht Theory Validation . . . 89
8.2.2 Transient Currents Validations . . . 90
8.3 Simulations of Square 3D Strip Detectors . . . 92
8.3.1 Simulation Methodology . . . 92
8.3.2 Charge Collection Definition Discussion . . . 94
8.3.3 Simulated 3D Cell Maps . . . 97

8.3.4 Simulation Without The Sense 3D Wire . . . 99
8.3.5 Simulation Without A HV 3D Wire . . . 101
8.3.6 Summary Of Simulated Square 3D Strip Detectors . . . 102

V Experiments For Testing The Diamond Detectors 103

9 Test Beams At CERN 104
9.1 Beam Characteristics . . . 105
9.2 Experimental Setup With The Strasbourg Telescope For The CERN Test Beams 106
9.2.1 Basic Design . . . 106
9.2.2 Experiments . . . 108
9.2.3 Pumping Procedure . . . 108

10 Test Beams At PSI 110
10.1 Beam Characteristics . . . 111
10.2 Experimental Setup With The ETH High Rate Beam Telescope For The PSI Test Beams . . . 111
10.2.1 ROCs Configuration . . . 115
10.2.2 Experiments . . . 116
10.2.3 Pumping Procedure . . . 116

VI Data Analysis 117

11 Analysis Of Data Taken With The Strasbourg Telescope At CERN Test Beams For Studying The 3D Detectors 118
11.1 Different Digitizer Saturation Values . . . 118
11.2 Raw Signal Decomposition . . . 120
11.3 Pedestal And Common Mode Estimation . . . 121
11.4 Clusters Formation . . . 124
11.5 Hit Prediction Using The Eta Distribution . . . 126
11.5.1 Data-Driven Feed-Across Correction . . . 130
11.6 Data Selection . . . 134
11.7 Alignment . . . 138
11.8 Track Selection For The Transparent Analysis . . . 142
11.9 Transparent Clustering . . . 143
11.10Transparent Grid . . . 144
11.10.1 Vertical Border Identification . . . 145
11.10.2 Grid Superposition . . . 148
11.10.3 Fine Alignment . . . 150
11.10.4 Cells Selection . . . 151

12 Analysis Of Data Taken With The ETH High Rate Beam Telescope At PSI Test Beams For Testing The Fabricated Planar Pixel Detectors 157
12.1 Experimental Data . . . 157
12.1.1 Analog Planes Decoding . . . 157
12.2 Clustering . . . 160
12.3 Alignment . . . 161
12.4 Tracking . . . 166
12.5 Data Selection . . . 166
12.5.1 Beam Interruptions . . . 167
12.5.2 Trigger Phase . . . 167
12.5.3 Angle Distribution . . . 168
12.5.4 χ^2 Of The Linear Fits . . . 169
12.5.5 Pixel Mask . . . 170
12.5.6 Fiducial Region . . . 174
12.5.7 Hit Distance . . . 175
12.6 Pulse Height In ADC Units Vs. Charge In Vcal Units . . . 176
12.6.1 Charge Calibration . . . 178
12.7 Pumping And Rate Scans . . . 179

VII Test Beam Results and Discussions 180

13 Results Of The Fabricated Diamond Pixel Detectors Tested At PSI 181
13.1 Identified Pixel Defects . . . 181
13.1.1 Pixel Defects From Fabrication . . . 182
13.2 Regions Of Study . . . 184
13.3 Data Selection Effects On The Efficiency And The Charge . . . 185
13.4 Charge In Electrons . . . 187
13.5 Complications With The Measured Data . . . 187
13.5.1 Problems With The Detectors' Configuration . . . 188
13.5.2 Problems With The Events Alignment . . . 192
13.6 Voltage Scans . . . 193
13.7 Rate Scans . . . 197

14 Results Of The 3D Diamond Detectors Tested At CERN 201
14.1 Calibration Constants And Equivalent Noise Charge . . . 201
14.2 Regions Of Study . . . 204
14.3 Excess Of Saturated Events In One Of The Digitizers . . . 207
14.4 Comparing Different Geometries With Different Bias Voltages . . . 210
14.5 Test Beam Results For Square Cells . . . 212
14.6 Comparison Of Different 3D Cell Geometries . . . 215
14.7 Simulation Model Comparison With 3D Detectors . . . 218

VIII Conclusions, Outlook And Summary 223

15 Conclusions And Outlook 224

16 Summary 226

IX Appendix 228

A VA Chip Noise Calculations 229

B Chemical cleaning 232

C ICP-RIE 234

D Photolithography 237
D.1 Etch mask . . . 237
D.2 Back-plane, pixel metallization and UBM lift-off masks . . . 238
D.2.1 Positive photoresist . . . 238
D.2.2 Negative photoresist . . . 239
D.3 Indium bumps metallization lift-off mask . . . 240
D.3.1 Positive photoresist . . . 240
D.3.2 Negative photoresist . . . 241

E PECVD SiON Recipe 244

F RIE SiON Recipe 246

G How The η Distribution Works 247

H Efficiencies And Their Uncertainties 249

I Strip 3D Detectors' Efficiency Maps 251
I.1 Poly-3D . . . 251
I.2 Full-3D . . . 252
I.3 Multi-3D . . . 252
I.3.1 Multi-3D Squares . . . 252
I.3.2 Multi-3D Rectangles . . . 253
I.3.3 Multi-3D Hexagons . . . 253
I.4 Irrad-3D . . . 254
I.4.1 Irrad-3D 100 µm . . . 254
I.4.2 Irrad-3D 50 µm . . . 254

J Experiments Performed During The Test Beams At CERN 255

K Experiments Performed During The Test Beams At PSI **258**
K.1 PSI Test Beam 2018 259
K.2 PSI Test Beam 2019 260

List of Figures

2.1 Differences in the crystal configuration of the carbon atoms, as well as the electron orbitals hybridization for graphite (a) and diamond (b). The internuclear distance in diamond is 1.54 Å[37]. 6

2.2 Schematic view of a Microwave-CVD chamber used for growing diamonds[55]. A controlled mixture of gases enters from the left of the chamber, where the pressure is controlled by a vacuum pump and the inlet and outlet speeds of the gases. Using microwaves, the injected gas is ionized to form a plasma which is placed on top of the substrate to grow the synthetic diamond. 8

2.3 Diagram showing the process in which atomic hydrogen captures a hydrogen atom in the deposited hydrocarbon, forming molecular hydrogen and leaving the carbon activated to make an sp^3 bond with another hydrocarbon[36]. 9

2.4 Picture (a) and sketch (b) of the grains in the growth of a pCVD diamond starting from randomly oriented crystals as substrate. 9

2.5 Schematic of some 0D and 1D defects in diamond. (a) represents a self-interstitial defect (0D), (b) is an intrinsic vacancy (0D), (c) is an edge dislocation (1D), (d) are extrinsic substitutional atoms (0D), and (e) is an extrinsic interstitial atom[60]. 10

2.6 Fraction of ionization energy loss as a function of the recoil energy. The displacement energy for carbon is assumed to be 40 eV and 20 eV for silicon[39]. 11

2.7 Charge collection efficiency as a function of the ratio between the schubweg λ and thickness of the sensor Th when the MFP of electrons and holes are equal. 14

2.8 Derived schubweg reciprocals from charge collection measurements for different irradiations fluences of 800 MeV/c protons[64]. The open markers are for the data points measured with a negative bias, while solid markers are for a positive bias. 15

2.9 Mass stopping power for μ^+ in Cu as a function of $\beta\gamma = p/Mc$. The vertical bands delimit different approximation regimes[50]. 16

2.10 Mean energy loss rate for different materials near the minimum[50]. In general, the minimum is reached for $\beta\gamma \sim [3-4]$. For carbon, the minimum is reached for $\beta\gamma \cong 3.9$[68]. 18

2.11 Comparison between the Bethe-Bloch curve with all the corrections, the restricted energy loss cases for twice the MIP energy and 10 times the MIP energy, and the MPV for three different sensor's thicknesses for silicon. The radiative losses are excluded in this plot. The term T_{cut} is the same W_{cut}[50]. 20

2.12 Straggling functions in silicon of different thickness for 500 MeV pions normalized to unity at the MPV Δ/x. The skewness of the functions decreases with the thickness of the material but never approaches a Gaussian. The width w of the functions is the full width at half-maximum[50]. Even though these curves are for silicon, the same behavior of the MPV and the mean shown in the figure apply to carbon. 21
2.13 Diagram showing the small scatterings inside a material of thickness x. The net deflection is shown as θ_{plane}[50]. 22
2.14 Total cross sections as a function of the incident photon energy in carbon. . . . 23
2.15 In (a), the model of an electron in the conduction band inside a diamond. The diamond has a metal electrode at the bottom, connected to the ground, and three metal electrodes on the top connected to a positive bias voltage $+HV$. In (b), the electric field of the model presented in (a) is shown. The color scale in (b) depicts the electric field strength in a logarithmic scale. In (c), the induced charge by the electron at that instant, t_0, is shown in each of the electrodes. As the electron moves upwards due to the electric potential difference across the diamond, the induced charge on the electrodes would change, as is shown an instant later, t_1, in (d). The color scale in (c) and (d) depicts the amount of charge per unit area induced on the electrodes in arbitrary units. The gray lines inside the diamond, depict the electric field lines caused only by the electron. . 27
2.16 Snapshots of the electron inside the diamond sensor at two different times, t_0 in (a) and t_1 in (b). The color maps and the field lines depict the weighting field intensity when the electrode on the top highlighted in bright red is at 1 V, while the other electrodes highlighted in gray are at 0V. The color scale is in logarithmic scale. The colored lines depict the direction of the weighting field. The blue vector pointing upwards from the electron represents its velocity in each instance, while the black vector pointing slightly downwards (always in the direction of the weighting field lines) represents the direction and strength of the weighting field in the electron's position. 29
2.17 Preamplifier in a charge-sensitive configuration. The feedback capacitance integrates the input current. 30
2.18 Preamplified signal from a square pulse with a width of 1 ns 30
2.19 Two pulses piling up with each other. The pileup will continue until the amplifier reaches saturation. 31
2.20 Preamplifier in a charge-sensitive configuration with a feedback resistor to discharge the capacitor between the input current pulses. 31
2.21 Preamplified signal of two current pulses with a small pileup. The capacitor's discharge must be fast enough to avoid large pileups leading to amplifier saturation. 32
2.22 Schematic circuit of a CR-RC shaper which has the same time constant for the CR part as for the RC part. The time constants are set by the capacitors C_s and the resistors R_s. The resistors R_{g1} and R_{g2} set the gain of the shaped signal. . . 32
2.23 Shaped signals for different number of (RC) stages. The more RC stages, the more symmetric the output signal becomes. 34

3.1 The geometry of the psi46digV2.1-respin. The chip consists of 4160 PUCs arranged in 80 rows and 52 columns. Each PUC is 150 µm×100 µm [89] 37

3.2 Simplified schematic of the PUC of the psi46digV2.1-respin ROC. Signals from ionization particles are transferred to the preamplifier by the bump pad. The integrated charge is then transferred to the shaper circuit and later to the sample and hold circuit before being transferred to the periphery.[90] 38

3.3 Diamond detector mounted on a PCB that connects with an adapter plane. The plane communicates with the DTB using a flat cable. 39

3.4 Layouts of the metallization implemented to produce a uniform field through the sensor. A zoom into the top-right corner is shown. 39

3.5 Diagram showing a section of a pixel in a planar detector being transversed by a ionizing particle. In (a), the metallizations on the top and bottom of the sensor are shown in gold and the trajectory of the ionizing particle is represented by the traversing line. In (b), the uniform electric field by applying an electric potential across the top and bottom metallizations is shown with the color pallet and the colored lines depicting the field lines. The red and blue dots and lines, depict the movement of ionized holes and electrons respectively in the detector towards the electrodes (metallization). 40

4.1 Each of the 128 detector strips was wire bonded to a pad just before the preamplifier. As shown in (a), for each channel, the signal was preamplified, shaped, and then sampled and held. An analog multiplexer selected the sampled and held signal one channel at a time, and the analog signal was sent to the outside via a differential analog buffer. In (b), the diagram shows how each of the channels is wire-bonded to the VA chip on one side, while the other side is biased with a HV source through a resistor R_b and a capacitor C_b to filter the noise from the HV source.[93] 42

4.2 Schematic for the noise calculations. Only the noise sources are shown. The preamplifier had a series noise source V_{as} and a parallel noise source I_{ap}. The DUT's noise came from the leakage current, modeled as a parallel current source I_d. The biasing resistor R_b introduced thermal noise, modeled as a series voltage source V_b. Before being shaped, these noise sources would be preamplified through the feedback resistor and capacitor R_f and C_f, respectively. 44

4.3 Diagram showing a section of a square 3D cell of a 3D detector. In (a), the 3D electrodes are depicted in dark gray. The distance between the central electrode and the electrodes in the vertices of the cell is smaller than the thickness of the sensor. The black line depicts the passage of an ionizing particle through the 3D cell. In (b), the non-uniform electric field magnitude is depicted with a color scale for different cross-sections of the 3D cell. The blue and red particles and lines represent the transport of the ionized electron and holes generated by the passage of the ionizing particle through the 3D cell. 45

4.4 A section of 9 square 3D cells shows the conductive HV wires in dark red, the conductive sense wires in gray, and the metallization patterns on the top and bottom surfaces in gold. The bottom metallization is in a grid pattern to deliver the HV to each 3D cell. The top metallization gangs together 3D cells into the read-out channel. This diagram shows three read-out channels, each containing three ganged 3D cells. 46

4.5 In (a), the PCB, where the DUT and the VA2.2 chip are placed, is shown with the passive components for the correct functioning of the VA2.2 chip. In (b), the PCB with the DUT is inside a metallic box that has an opening for the DUT. The opening is covered with black tape to make it light-tight. 47

4.6 Layout of the metallization deposited on the top layer of the Poly-3D after the conductive wires were made. From left to right, the detector consists of three sections: a planar strip detector made with 25 µm strips with a pitch of 50 µm between them, a section with interdigital metallization with a separation between the digits of 75 µm without 3D wires (no 3D cells), and a section with the same interdigital metallization with 3D wires which made 3D square cells of 150 µm side length. 48

4.7 Picture of the Full-3D detector in (a). In (b) and (c), the layouts of the metallization made on each of the faces of the Full-3D, after the conductive wires were made, are shown. One of the sides had a mesh-like pattern to deliver the high voltage, while the other one had strips to read out several 3D sense wires of the 3D cells. 49

4.8 Picture of the Multi-3D in (a). In (b) and (c), the layouts of the metallization on each of the top and bottom sides of the Multi-3D, after the conductive wires were made, are shown. The pitch between the channels of the 3D cells was of 100 µm and the width of the metallization was of 10 µm. This prototype had different geometries for the 3D cells which were square, rectangular, and hexagonal. It also had a planar strip detector with a pitch between channels of 50 µm 50

4.9 Picture of the Irrad-3D in (a). In (b) and (c), the layouts of the metallization made on each of the faces of the Irradiated-3D, after the conductive wires were made, are shown. This prototype was irradiated before the drilling was done to a fluence of 3.5×10^{15} protons 51

5.1 Sketch of the process used to fabricate the conductive 3D wires. The laser was focused on the bottom side of the diamond to start the inscription, and it was raised until it reached the opposite top side of the diamond. This process was done twice. Afterwards, the diamond was flipped, and the laser inscription started on the now top side, lowered until the middle of the diamond, and returned to the top.[99] 55

6.1 Diagrams of four pixels, showing the deposition of metal (dark gray) over the surface of the diamond with a photoresist mask on top (yellow). The photoresist pattern allowed the metallization to be deposited on the desired regions of the diamond. The thickness of the photoresist layer was ~ 1 µm and the metal deposition was made of 10 nm of Ti as the contact metal with the diamond, and 300 nm of Al on top of the Ti. 60
6.2 Resulting metallization pattern after the lift-off process, where the photoresist with metal on top was stripped away. 61
6.3 Microscope photograph showing the Ti/Al pixels left on the surface of the diamond after lift-off. 61
6.4 (a) Layout of the different metallizations on the top side of the diamond. The numbering of the quadrants shows that quadrants 1 and 3 have the same metallization, which is different from the metallization of quadrants 2 and 4. The back side (not shown) has a big square pad that covers the four quadrants. In (b), the picture of the diamond CMS01 with the two different metallizations on the four quadrants is shown. The same amplifier reads all the quadrants. 62
6.5 Comparison of the pulse height distributions for the signal collected by the same metallization but located in different quadrants. The variation of the mean of the distributions was used to estimate the systematic uncertainty caused by the different regions of the diamond. 63
6.6 Ratios of the signals collected by quadrants 1 and 3 (Cr/Au metallization) with respect to the signals collected by quadrants 2 and 4 (Ti/Al/Pt/Au metallization). The red error bars represent the systematic uncertainty from the variations between the quadrants with the same metallization. 63
6.7 The result after the deposition of 600 nm of a passivation layer of SiO_xN_y (light blue). 64
6.8 Four diamonds after the growth of SiO_xN_y via PECVD. The diamonds are on top of a carrier wafer, and pieces of silicon wafer surround the diamonds to prevent them from sliding away inside the PECVD chamber. The colors seen on top of the silicon pieces are caused by thin-film interference from the thin layer of SiO_xN_y. 64
6.9 Photoresist before and after RIE, which covered all the surface except for ⌀10 µm holes on top of each pixel. 65
6.10 Surface of the diamond covered with SiO_xN_y except for the openings. 66
6.11 Images from three different attempts to form the indium bumps. The captions are tags for the variations of the attempts that correspond to the image (see Table 6.2). In (a), the green-pink coloration appeared on the pixels where no bumps were formed. Most bumps in (b) were formed correctly but not in the correct position. There was still the presence of green coloration located where the bumps were not formed correctly. In (c), all the bumps were formed correctly but not in the correct position. 67
6.12 Photoresist mask before and after the evaporation of the UBM (solid golden-brown) covering the opening holes for each pixel. The UBM consisted of 10 nm of Ti, 100 nm of Ni and 10 nm of gold. 68

6.13 Deposited UBM over each pixel's opening hole. 69
6.14 Surface of the diamond after the deposition and lift-off of the UBM. Two concentric circles are appreciated on each pixel. The innermost corresponds to the opening hole, while the outermost corresponds to the UBM covering the hole. 69
6.15 A thick layer of indium was evaporated over the whole surface of the diamond which had a lift-off photoresist mask. The thickness of the photoresist mask was of 3.5 µm and the estimated thickness of the evaporated indium was 2.55 µm. . 70
6.16 Resulting indium "pancakes" on top of each pixel after the lift-off process. . . . 71
6.17 Microscope photograph of the diamond's surface after evaporation and lift-off of the indium. On top of each pixel, the indium "pancakes" can be seen. The inner circles inside each "pancake" correspond to a change in thickness due to the opening holes made through the passivation layer. 71
6.18 Diagram showing the result after the reflow process, where the deposited indium was melted to form bumps. After cooling, the indium solidified keeping the bump shape. 72
6.19 After the reflow, the indium bumps were formed. The size of each bump was $\varnothing \sim 26\,\mu m$. 72
6.20 By pressing the ROC against the sensor, each pixel of the sensor connects with a PUC on the ROC through the indium bumps. The bumps reshaped after a second reflow which homogenized the distance between the sensor and the ROC, and corrected for small misalignments between the ROC and the sensor during the flip-chip process. 73

7.1 Simulation results obtained for strip planar detectors. In (a), a total of 30 strips were simulated and the electric potential inside and outside the diamond is shown with the color scale, while the lines depict the electric field. The detector was biased with 1000 V and was simulated inside an infinite air box. In (b) the total capacitance felt by the middle strip is shown, where the capacitance plateaus at a total of 7 strips (six neighboring strips) where it reaches 99.78 % of the total capacitance. 76
7.2 Model used to simulate the capacitance seen by the middle strip as a function of the number of rows present in the mesh pattern on the bottom of the sensor ((a) and (b)). In (c), the linear relationship for the capacitance as a function of the number of grid rows per strip is shown. 77
7.3 Empirical models that fit the linear parameters shown in Equation 7.2 to the data. 78
7.4 Simulation results for 50 µm square 3D cells. In (a) the color scale depicts the strength of the electric field in decades of V/µm when the sense wires of the middle channel were at 45 V and the rest of the 3D wires were connected to ground. The black curves represent the field lines, and the white circles are the 3D wires. In (b), the relation between the total capacitance and the number of total channels is shown, while (c) shows the relation between the total capacitance and the number of connected 3D cells in a channel. 79
7.5 Empirical model that fits the parameter shown in Equation 7.4 to the data. . . . 80

7.6 In (a) and (b) are shown the top and bottom views respectively of the surface metallization of the modeled detector. Inside the diamond, the 3D wires can be seen. In (c), the linear relationship obtained from the simulation is shown for the 50 µm square 3D cells. 81
7.7 Empirical models that fit the linear parameters shown in Equation 7.6 to the data. 82
7.8 Relative error between the full estimation of the capacitance using Equations 7.5 and the estimation of the capacitance by adding the metallization and the 3D wires capacitance using Equations 7.7. From left to right, the red dots represent the Irrad-3D-50 µm, Full-3D, and Poly-3D detectors. 83
7.9 Simulation result rectangular cells (a) and hexagonal cells (b), when the central strip was biased with 90 V and the rest of the 3D wires were connected to the ground. The color scale shows the magnitude of the electric field in decades of V/µm, and the black curves depict the field lines. 84
7.10 Electric field magnitude inside the square 3D cells with the same 3D wires' radius but different cell length. The color scale represents the electric field magnitude, while the color lines depict the electric field lines. 85

8.1 Theoretic curve for the CCD as a function of the schubweg. The plot is overlaid with the simulation results. The theory curve was introduced in Equation 2.5d in section 2.4. 90
8.2 e-TCT measurements inside the diamond pad detector biased with −1400 V at different heights from the bottom face where the ground was placed.[119] . . . 91
8.3 Comparison between e-TCT data (open red circles) and the simulation (solid blue dots). In (a) the simulated data is shown with only a scaling factor of 24 kΩ. In (b) the simulated data is passed through a band-pass filter from 1 MHz to 1 GHz which is more restrictive than typical for the broadband amplifier used to take the data. 91
8.4 Model used in (a) to simulate the induced charges in square 3D strip detectors. The highlighted square corresponds to the middle cell of the middle strip Ch. M. In (b), the electric field's magnitude in color scale in decades of V/µm is shown when the bias wires are at 90 V, and the sense wires are at 0 V. The middle cell is delimited with a dashed black line. 93
8.5 Weighting fields of the middle channel Ch. M (a) and its channel to the right, Ch. M+1 (b). The magnitude of the fields is shown in the color scale in decades of V/µm. The middle cell in channel Ch. M is delimited with a dashed black line. 94
8.6 Collected charge by each of the channels in the transparent cluster depending on the hit position in the strip of Ch0. For each entry, a total of 10^4 eh-pairs were simulated. 95
8.7 Charge collection for the two and three strips with the highest charge in the transparent cluster as a function of the predicted hit position in the strip of Ch0. For each of the 256 entries, a total of 10^4 eh-pairs were simulated. 96
8.8 Charge maps for the sensor Poly biased with 90 V. 97
8.9 Charge maps for the sensor I-Poly biased with 45 V. 98
8.10 Charge maps for the sensor HI-Poly biased with 45 V. 99

8.11 Charge maps for the sensor Poly biased with 90 V and without the sense 3D wire. 100
8.12 Charge maps for the sensor Poly biased with 90 V and without one HV 3D wire. 101

9.1 CERN's accelerators complex.[122] 104
9.2 Floor plan of building 887 at the North Area of CERN. The four beam lines are painted in red, with beamline H6 wider than the rest. The experimental area, where the experimental setup was placed, is highlighted in green.[123] 105
9.3 Picture of the Wire Chamber and plots of the measured beam profiles 105
9.4 Schematic view to scale of the telescope with the DUT. The beam is aligned with the z-axis. 106
9.5 Schematic view of the telescope with the X-Y coordinates scaled-up. Each plane of the telescope consists of individual X and Y planes. Planes with vertical strips can resolve positions in the x coordinate, while planes with horizontal strips can resolve positions in the y coordinate. 107
9.6 Pumping setup made of plastic and lead bricks to shield the radiation from the source. This measure is needed to protect the people entering the laboratory from radiation exposure. 109

10.1 Section of the Experimental Hall at PSI. The highlighted aquamarine areas show the particles' trajectory through the different acceleration stages until they reach the πM1 experimental area.[130] 110
10.2 Layout of the beamline characteristics for the πM1 area.[131] 111
10.3 Measured particle fluxes for different momenta. The flux for μ particles is not shown, but it is a factor of 100 smaller than the rate of π around 300 MeV/c.[132] 112
10.4 Telescope setup for pad DUTs. Up to two pad detectors could be tested. The pad detectors were read with a DRS4 digitizer. The trigger for each event was given by the TU by processing the coincidence from the FAST-OR from the two planes closest to the DUTs (i.e. Plane 1 and 2) and the scintillator. The waveforms of the pad detectors and of the scintillator were saved along with the telescope planes information from the DTB for each event.[131] 113
10.5 Telescope setup for pixel DUTs. Up to three DUTs could be mounted on the telescope (i.e. planes 4, 5, 6). Planes 4 and 5 were mounted with diamond DUTs, while plane 6 was mounted with a silicon DUT as reference. The coincidence of the FAST-OR signals from the two tracking planes closest to the DUTs (i.e. planes 1 and 2) and the scintillator were processed by the TU, which issued the global trigger signal for the telescope readout and the DUTs readout via DTBs. For each event, the pixel data for each tracking plane of the telescope's DTB and the pixel data from each DUT connected to the DUT's DTB was saved.[136] 114

11.1 Difference between the saturation between Sirocco 4 and 5. The data comes from the same diamond and same VA2.2 ASIC digitized first with Sirocco 4 and then with Sirocco 5 during the same test beam. The histogram of all the PHs from all the channels in the VA2.2 chip is plotted. It can be seen that there is a lower saturation for Sirocco 4 (a) around 3350 ADC while Sirocco 5 (b) the saturation occurs at the maximum PH of 4095 ADC. 119

11.2 Difference between the artificial saturation in two channels of the same VA2.2 chip digitized with Sirocco 4. There is no exact value in ADC units for saturation. Instead, the saturated events follow different distributions on each channel. . . . 119

11.3 PHs without saturated events for an scCVD planar strip detector biased with −500 V and digitized with Sirocco 4 (a) and Sirocco 5 (b). The mean of the distributions agree to within 0.3 % for the same detector connected to different digitizers. . . . 120

11.4 Depiction of the pedestal calculation for the first 500 events for one of the VA2.2 chip's channels connected to a strip on the diamond (aka. diamond channel). The dots are the raw data, while the line represents the calculated mean of the pedestal and the shaded area highlights the 3σ region, which contains the events included in the estimation. . . . 122

11.5 Distribution with the value $r_{ch}(i) - p_{ch}(i-1)$ for the 128 channels of the preamplifier for an event "i." The estimated CM for that event would be −7.84 ADC. . 123

11.6 Distributions used to select the cluster thresholds for the first plane that determines the X position. The red vertical lines depict the values chosen for the threshold-seed t_s (a) and the threshold-hit t_h (b). . . . 125

11.7 Distributions showing the hit, t_h, and seed, t_s, thresholds used for a planar strip DUT. The red lines depict the values for t_s in (a), and for t_h in (b). . . . 125

11.8 Example event on plane 0X of the telescope, which shows a two-channel cluster. The seed was set to the highest channel that exceeds t_s, channel 202. As channel 201 exceeded t_h and was adjacent to the seed channel, it was included in the cluster. As no other adjacent channels to these two exceeded t_h, no more channels were added to this cluster. . . . 126

11.9 Distributions of η for different planes which have different numbers of intermediate floating strips. . . . 127

11.10 The η distribution for a polycrystalline and irradiated single-crystalline diamond sensor has more entries in the values around $\eta = 0.5$ and the peaks are less pronounced than for a non-irradiated single-crystalline diamond sensor. . . . 128

11.11 Example for the position calculation using the η distribution. On the event shown in (a), channels 54 and 55 have signals above the hit threshold t_h and form a cluster. Using the η distribution shown in (b) for the whole run, the cumulative distribution in (c) can be calculated. Using Equation 11.7, the event gives an $\eta = 0.9135$. The resulting CDF for this quantity is $F(\eta = 0.9135) = 0.741$ as shown with the red dot in (c). If the position of channel 54 was $x_L = 1000\,\mu\text{m}$ and the pitch between each channel was $P = 50\,\mu\text{m}$, then the predicted hit position of this event according to Equation 11.8a would be $x = 1037.05\,\mu\text{m}$. . . 129

11.12Example with 10 channels of a VA chip with a two-channel cluster in channels four and five. The readout in this example is from left-to-right. The dotted curve labeled “Charging C" represents the voltage on the readout capacitor as it charges after each transition. The dot-dashed gray line represents the pedestal value of the channel. The dashed red line represents the read value in ADC units taken by the readout sampling from the charging capacitor when there is a mismatch that gives an $\alpha = 0.25$ which is equivalent to $t_0 = 1.39\tau$, where τ is the charging and discharging time constant of the capacitor. The solid blue line is the actual value in ADC units that should have been read. 130

11.13Simulated Monte Carlo distributions. The distribution on the left assumes there is no timing mismatch. The distribution on the right assumes there is a timing mismatch giving an $\alpha = 0.017$. For each case, the mean and the median of the distributions are given. 131

11.14Dependence of the mean and median of the η distribution as a function of the parameter α. The values come from simulation and the fit is a 4th-order polynomial that matches the data points. The fit parameter $p1$, which is the coefficient for the factor α^1, shows the sensitivity of the mean or median as the parameter α deviates from 0. 132

11.15The distributions above show the effects of having a negative α value for correction when the readout is assumed to be from left-to-right (a), and the case when α is positive and the readout is assumed to be from right-to-left (b). 133

11.16Comparison between a correction applying a positive α for the correct readout direction (a) vs. applying a negative α for the wrong readout direction (b). In this plot, saturated values of the ADC are set for 4000 ADC. Channel 5 is read as saturated. It is clear that a negative α would desaturate channel 5. 133

11.17Distributions for η before the data-driven-feed-across-correction, (a) and (b), and after the data-driven-feed-across-correction, (c) and (d). The readout of the detector on the left plots was from left-to-right, while it was from right-to-left for the detector on the right plots. 134

11.18Example of an event with two simultaneous hits. The hit positions of Hit 1 and Hit 2 are identified by an excess of charge across the colored strips. Consequently, there are two possibilities: the hits happened in the locations Hit 1 and Hit 2, or they happened in the “Ghost" positions. Without further information, it is impossible to know the actual position of the hits. 135

11.19Hit map in the telescope’s space. The displayed rectangle corresponds to the shadow of the scintillator, which issues the trigger to save the event. 136

11.20Hit maps in the telescope’s space requiring at least one cluster in the diamond channels (a) and one and only one cluster in the diamond channels (b). The DUT in these hit maps corresponds to the Irradiated-3D biased with −45 V. The shadow of the diamond prototypes can be seen. Features such as the guard rings surrounding the 3D cells can easily be distinguished. Check section 4.3.4 as reference. 137

11.21 Hit map in the telescope's space. A fiducial region for analysis between X : $[110-150]$ and Y : $[45-95]$ is imposed. All events with clusters in the silicon planes outside this rectangular region were not considered further for analysis. The white band around the 3D cells corresponds to the guard ring whose channel was masked. 138

11.22 Example of the plane misalignment with respect to the reference. (a) Shows the reference X-Y plane in gray and the misaligned plane's vertical and horizontal strips. Note that the horizontal and vertical strips in the misaligned plane are not necessarily perpendicular with respect to each other. (b) Shows the angle rotation for the vertical strips ($\phi_x = 15°$) and their horizontal offset ($x_o = 2000\,\mu m$). (c) Shows the angle rotation for the horizontal strips ($\phi_y = 16°$) and their vertical offset ($y_o = 2000\,\mu m$). 139

11.23 Histograms used for alignment. The projection of the 2D histogram in (a) along Delta X, results in the histogram shown in (b). The mean of the histogram of the residuals shown in (b) is used to update the offset x_o^1 in this example. The profile histogram of (a) along the predicted Y position results in (c). The linear dependence can be fitted and the slope $p1$ of the fit is used to update the rotation angle ϕ_x^1. 141

11.24 Histograms after alignment. The projection of the 2D histogram in (a) along Delta X, results in the histogram shown in (b). The mean of the residuals in X is centered around 0 as it can be seen in (b). The profile histogram in (c) is obtained by profiling the histogram of (a) along the predicted Y position. The linear fit is consistent with a horizontal line at 0. 142

11.25 χ^2 distributions from each of the track fits for the X and Y components separately. The blue dashed lines depict the threshold applied to the χ^2 for the fits in the X direction and the Y direction for the tracks selection. The solid red lines depict the theoretical value for a χ^2 distribution with two degrees of freedom. 143

11.26 Collected charge in the transparent cluster of ten strips as a function of the number of strips included for the figure of merit for a highly irradiated scCVD diamond biased with $-1100\,V$ resulting an electric field with a magnitude greater than $2\,V/\mu m$. 144

11.27 Example of the signal in the DUT measured in SNR for different channels in the VA chip connected to the detector. The predicted hit position is marked with a dot, and the Hit Threshold and the Seed Threshold are shown with a blue solid line and a dotted black line respectively. The transparent cluster of 10 channels is built around the predicted hit position, which groups channels 2 to 11 inclusive. The five contiguous to the highest channel are in this example channels 5 to 9 inclusive. 145

11.28 Pulse height maps of two different 3D detectors. It can be seen in (a) that due to the hexagonal tiling, there are two vertical limits for the detector: one for even channels and one for odd channels. 146

11.29 Curve from Equation 11.12 that approximates the detector's projected pulse height onto the y-axis. Three regions are seen, two with lower projected pulse height that surround a higher region corresponding to the region where the 3D cells are located. The transitions are modeled with error functions with different transition lengths determined by the parameters $p1$ and $p4$. The length of y_d, which is the extent of the 3D cells in the Y-direction, is fixed and is known from the detector design. 146

11.30 Examples of the fit of the curve in Equation 11.12 on the pulse height maps for even and odd channels of a detector with square 3D cells. The parameter of interest for the fit is the upper limit of the 3D cells ($p3$). 147

11.31 Example of a rectangular grid. A grid in terms of columns and rows is made such that each grid element can be identified with a column and a row. For rectangular cells, the pitch and the height of the cells must be given to set the tiling. 149

11.32 Example of a hexagonal grid. A grid in terms of columns and rows is made. Note that the number of cells in a column could be different for even or odd channels in the VA chip. 149

11.33 Example of a four-column and two-row grid. The red dots in the corner of the polygons correspond to the biasing 3D wires, while the blue dots in the middle of the polygons represent the sensing 3D wires. The black star represents the predicted hit position by the telescope planes in the 2D space given by the channel of the VA chip and the telescope's Y coordinate prediction. The predicted hit happens in channel position 54.3 and telescope's Y $y_{up} - h/2$. The event is given a coordinate in the grid. In this example, it would be (col, row)=(1,1). Additionally, the event is given a position inside the polygon: $(x_0, y_0) = (0.3, 0)$. 150

11.34 Map of all the cells overlaid together before fine alignment. The lack of symmetry along $x = 0$ and $y = 0$ indicates that fine alignment is required. The color map shows the transparent pulse height for the predicted hit channel. 151

11.35 Profile map of the pulse height of the shifted cells before fine alignment (a) and after fine alignment (b). The projections along the x coordinate in (c) and in (d) show where the minimum of the pulse height, which happens between two cells, is positioned before and after the fine alignment respectively. 152

11.36 Profile map of the cells overlaid after fine alignment. 153

11.37 Example of a selection of cells. The plot on the left (a) shows the pulse height map for the two highest in the transparent cluster. The hexagonal tiling is overlaid in gray to show the different cells. The cells with red boundaries are the ones that are selected for further analysis as shown in the plot on the right (b). 153

11.38 The pulse height of the second closest channel to the predicted hit position is compared with the noise fluctuations of the channels in the selected region (a). A threshold of −170 ADC is used to discriminate normal negative charges from the excess of high negative charges. The position of the events with an excess of negative charges with a measured PH below −170 ADC, is shown in (b). These events surround a 3D HV wire which indicates there could have been a problem with that 3D wire. 154

11.39 Pulse height map of the 100 µm region of the Irrad-3D detector. The single cells selected in red presumably have problems with their 3D sense wires, while the cells selected with the black rectangle are cells that presumably do not have issues with their 3D wires. 154

11.40 Profile histograms of the charge collected by channels Ch0 and Ch1 in the transparent cluster as a function of the hit position in the X direction of the hit 3D cell. For the simulated graphs, (c) and (d), the red selection represents cells without the 3D sense wire, while the black selection represents cells without issues with their 3D wires. For the measured graphs in the Irrad-3D, (a) and (b), the red selection depicts the cells that presumably have problems with their 3D sense wires, while the black selection depicts the cells that presumably do not have issues with their 3D wires. 155

11.41 This is the histogram of the average pulse height for each cell in the Full-3D detector biased with 90V. The red Gaussian curve fits the data for the pulse height of the cells without fabrication problems. The blue dotted line is located five standard deviations away from the mean of the Gaussian distribution and delimits the cells that could have defects with their 3D sense wires. 156

12.1 Oscilloscope image showing the different parts of the data transmitted in analog planes, including the different levels for each address position.[146] 158

12.2 Encoded values for the analog ROC 0. These include Ultra Black, Black, and the address positions. When the timing was correctly set (a) there was a clear separation between the levels. On the other hand, when the timing was not correctly set, the transition between the levels overlapped due to the splitting of the levels and it was not possible to identify accurately the address of the pixel without further steps. 158

12.3 The diagram shown in (a)[145] depicts the splitting effect when the sampling point is set too early. The blue curve in (b) is the histogram of the measured ADC values for the address position CR in ROC 0 when the sampling was early. Only the values for Levels 0, 1, and 2 are shown. The red curve fits the data to the model that replicates the splitting of the levels. The parameters of this model are used to estimate the real separation between the levels and to recover the signals as if they were sampled correctly. 159

12.4 Cluster sizes for all telescope tracking silicon planes in 2019's run 8. Most of the clusters in the tracking planes are one-pixel clusters. 160

12.5 Example of the residual plots used to estimate the translation in the y direction and the rotation angle during the 2nd iteration of the alignment of the 6th plane. The arctan of the slope of the fitted red line gave the correction for the rotation angle $d\phi$. The value of the mean in the histogram for dY, gave the correction dy for the translation of the plane in the y direction. 163

12.6 General curve of a Logistic function. The transition is centered at x_0 and it takes $\sim 10\sigma$ for more than 99 % of the transition to occur. 164

12.7 Curve that describes the parameter n as a function of the iteration. 164

12.8 Data taken into account for alignment in the 2D space of residuals dx and dy for plane 6. 165

12.9 Convergence of the alignment for plane 6. The parameters dR and $d\phi$ converged at the 11th and 2nd iterations, respectively. 165

12.10 Discrete derivative between the events' timestamps with respect to the event number. This result gives an idea of the time taken by the TU between each event. The red line marks the threshold used to identify beam interruptions. . . 167

12.11 Number of entries recorded for each trigger phase in the first DTB. The shaded region in blue represents the three highest contiguous trigger phases which amounted to 73 % of the events. 168

12.12 Angular distribution in the Y direction for the trajectories fitted using the four tracking planes. The violet line in the axis depicts the range of the angles used for the analysis. The fit parameters $p1$ and $p2$ are the center and the standard deviation of the fitted Gaussian distribution, respectively. These fit parameters are typical for the data taken in the 2018 and 2019 test beams. 169

12.13 χ^2 distribution obtained for the linear fit for the X direction for a typical run in 2018. The red line depicts the threshold used to select the 40 % of the tracks with the lowest χ^2, and the dotted black line depicts the theoretical χ^2 distribution for two degrees of freedom. 170

12.14 Example of the two cases where the pulse height calibration failed. In (a) the large χ^2 was caused by the two data points for injected charges above 800 Vcal, where the read pulse heights were 0 ADC. In (b) most of the read values were 0 ADC, such that there were only four data points to fit the curve which gives a total degree of freedom of 0. 171

12.15 Example for the identification of noisy and unresponsive pixels. In (a) the occupancy of plane 4 shows white values for pixels with 0 occupancy which are marked as cold in (b). As for the two pixels circled in red in (a), their occupancy is higher than their neighboring pixels and therefore are marked as hot in (b). Pixels that are not marked as hot or cold in (b) are colored in green, while hot pixels are colored in red and cold pixels are colored in blue. 171

12.16 Profile histogram between the hit column and the predicted X position by the telescope for the DUT in plane 6 (a), and the hit row and the predicted Y position by the telescope for the DUT in plane 4 (b). The linear fit was done in most cases ten pixels away from the borders to ensure the diamond's electric field was uniform and there was less ambiguity with the hit position. The fitted values are shown as $p0$ for the offset term and $p1$ for the proportional term. Ideally, a perfectly perpendicular setup with respect to the beam would give $p1 = 66.67\,\mathrm{col/cm}$ for the column vs. X case, and $p1 = 100\,\mathrm{row/cm}$ for the row vs. Y case. 172
12.17 The extreme cases considered for the resolution in the DUT by the telescope given by the proportionality parameter $p1$. In (a), the tilting by an angle θ of the DUT makes the parameter $p1$ larger. In (b), the tilting of the telescope planes by an angle θ makes the parameter $p1$ smaller. 173
12.18 Distribution of hit columns for a given predicted hit position in x. The σ of the bell-like distribution in (b) was found to be 1.5 columns (parameter p2 in the statistics box). 174
12.19 Incidence of the tracks before and after masking the regions around the unresponsive and noisy pixels shown in Figure 12.15. 174
12.20 Regions showing the fabrication defects that were identified visually before the bump-bonding of sample CMS04. The regions in red enclose the affected regions. The blue rectangle, which is at least three pixels away from the affected areas, was chosen as the planned fiducial region for the studies made on this sample. 175
12.21 Different fits with different functions for the data with 255 calibration values. (a) shows the data fitted with the function *tanh*, (b) shows the case for function *weibull* and (c) shows the χ^2 for all the pixels fitted with *erf*. 177
12.22 Distribution obtained for the calibration of 4864 psi46digV2.1-respin ROCs with a linear regression between Vcal units and electrons.[151] 178
12.23 Complete rate scan for samples CMS04. The red line highlights the first up-scan which disagrees with the rest of the performed scans. 179

13.1 Microscope pictures of sample CMS01 after the development of the mask before the In deposition (a), and after the reflow process to form the In bumps (b). . . . 183
13.2 Example of the identified errors during the bump formation of the bumps on the sample CMS01. The bumps with problems are encircled in each case. 183
13.3 Microscope picture of a section of the affected pixels caused by a problem with metallization in sample CMS02. The leftover metal in the corner of the pixels electrically connected them. 184
13.4 Detection efficiency maps of the silicon DUTs, where the black rectangles depict the selected regions for the studies. 184
13.5 Maps of the detection efficiency (a) and cluster charge (b) of CMS04 biased with $-750\,\mathrm{V}$ and a beam flux of $100\,\mathrm{kHz/cm^2}$. The black box is the selected region for analysis. The microscopy picture showing the fiducial region and the defects can be seen in Figure 12.20. 185

13.6 Detection efficiency maps of the diamond devices. The black polygon encloses the fiducial region chosen for each device. 186

13.7 Effects of the cumulative cuts applied on the efficiency and the collected charge of the sample CMS04 biased with −750 V at an incident particle flux of 100 kHz/cm^2. 186

13.8 Selection effects on the collected charge shown in Figure 13.7b in electrons. The data corresponds to CMS04 biased with −750 V. The black error bars represent the statistical uncertainties, while the red error bars represent the systematic uncertainty of the Vcal-to-electron calibration. 187

13.9 Pulse height calibration for the pixel located at column 26 and row 40 of the DUT CMS01. Around half of the available values of the ADC were not used, which suggests the amplifier gain was not set correctly, and the first injected charge, which was not read as a 0 ADC, had a value of 100 Vcal, which means the detector's threshold was around 4700 e. 188

13.10 Normalized distributions to the MPV around 100 Vcal for the collected charge of DUT CMS04 for a biasing voltage of −100 V, −300 V, and −700 V. 189

13.11 Collected charge in the lower end of the distributions for the silicon DUTs D2 (a) and D8 (b). D2 has a lower MPV than D8 and the cutoff due to the configuration in D2 happened at a higher value (~ 100 Vcal or ~ 4700 e) than in D8 (~ 50 Vcal or ~ 2300 e). 190

13.12 Charge distribution for CMS01 in (a). A large peak with 0 Vcal charge is appreciated. The vertical dashed lines mark the collected charges of 30 Vcal (~ 1400 e) in red and 100 Vcal (~ 4700 e) in black. The events with extrapolated collected charge of 0 Vcal occurred at a constant rate as seen in (b), where the fitted line in red is consistent with a constant rate of 768.5 Hz. The locations of the tracks where these events happened are shown in (c) which correlate with inefficient regions which are shown in (d). 190

13.13 Efficiency measurements for the silicon Si-D2 during a rate scan. There is a drop in efficiency from 97.6 % to 95.7 % between two measurements at a particle flux of 1000 kHz/cm^2. 191

13.14 Plots that indicate that an event misalignment beyond correction was left after the data conversion. The loss of correlation due to this effect causes a random relationship between the predicted hit position and the excited column or row in the silicon DUT. This causes the blue background seen in (b). In (a), the event misalignment causes a drop in efficiency after applying the *rhit* selection criterion. 192

13.15 Efficiencies of the pixel DUTs as a function of the bias voltage in (a). In (b), a closeup around the efficiencies above 90 % is shown. The devices that reached around 90 % efficiency were the ones that were configured correctly with a low threshold, as expected. Note that for the sample II6-750, as its thickness is 50 % larger than the other detectors, the electric field inside it is 66.7 % the electric field of the other detectors at the same bias voltage. 193

13.16 Charge collection in Vcal units for different bias voltages. In (a), all the DUTs, including the silicon DUTs, are shown. In (b), only the diamond DUTs are shown. Except for CMS04 and II6-93, the other diamond DUTs seem not to have reached a plateau in their charge collection. Note that for the sample II6-750, since its thickness is ~ 50 % larger than the other detectors, the electric field inside it is ~ 66.7 % the electric field of the other detectors at the same bias voltage. 194
13.17 Voltage (a) and current (b) vs. time for the voltage scan performed on the DUT II6-750. The vertical lines in the current plot are caused by the ramping of the voltage. It can be seen that the current became erratic during the last applied voltage. 194
13.18 Charge collection distributions for the DUTs CMS01, CMS02, and CMS04. The distributions are normalized to the MPV around 100 Vcal (~ 4700 e). The three DUTs are biased with −600 V for this comparison. 195
13.19 Normalized distributions to the MPV around 100 Vcal (~ 4700 e) for the collected charge of CMS04 for the particle fluxes of 10, 100 and 7700 kHz/cm^2. . 198
13.20 Normalized distributions to the MPV around 100 Vcal (~ 4700 e) for the collected charge of II6-93 for the rates of 100 and 1000 kHz/cm^2. 198
13.21 Ratios of the collected charges with respect to the average value of the data for different particle fluxes. 199

14.1 pedestal fluctuations for the non-connected channels of the VA chip for the Multi-3D device. The red curve is the fitted Gaussian distribution with $\sigma = 7.757(2)$ ADC. 202
14.2 Comparison between the measured noise for each detector and the expected values from the simulations. The cell sizes of the square cells of the Poly-3D were 150 µm, and of the Full-3D and Multi-3D were 100 µm. The uncertainty for the measured noise comes from the uncertainty of the calibration constant presented in Table 14.1. The uncertainty for the expected values of the simulations originates from the variation of 5 % of the sensor's thickness used for the estimations. 203
14.3 Identified fabrication defects of the Full-3D sample. In (a), possible crystallographic defects are shown. In (b), the red circles identify possible breaks in the metallization pattern, causing multiple 3D sense wires to be disconnected in several channels. 205
14.4 Overlaid pictures with the pulse height maps of the Full-3D detector. In (a), The three identified crystallographic defects correspond to cells with low pulse height. In (b), the features marked with A, B, C, D, and E correspond to the identified metallization problems that cause low charge collection to the cells above each feature. The possible identified feature marked with an F did not seem to affect the charge collection of the strip. 205
14.5 Pulse height maps and the fiducial regions enclosed with a black line for the Poly-3D (a), Full-3D (b), and Irrad-3D (c-d). 206
14.6 Average pulse height maps as a function of the predicted hit position and the fiducial regions enclosed with a black line for the Multi-3D detectors. 207

14.7 Pulse height distributions normalized to the total entries (a) and the MPV around 1000 ADC (~ 8200 e) (b) for the 100 µm square 3D cells in the Multi-3D detector measured at the same voltage magnitude of 90 V but different polarities during the same test beam. 208

208subfigure.7.2

14.8 Pulse height distributions normalized to the total entries (a) and to the MPV around 1600 ADC (b) for a ~ 500 µm thick scCVD diamond planar strip detector measured with a voltage magnitude of 500 V with the same digitizer, Sirocco 5. 209

14.9 Pulse height distributions for the square cells in Multi 3D biased with a voltage of 90V with different digitizers and bias polarities. 209

14.10 Efficiency map of the Full-3D detector biased with 60 V. The gray lines depict the location of the 3D cells, and the bright red lines highlight the 3D cells selected for the analysis. 212

14.11 Efficiencies of all the square 3D cells in the 3D detectors. The filled markers represent the 3D cells biased with a positive voltage, while the open markers represent the 3D cells biased with a negative voltage. Along the 3D cells, the efficiencies for the planar strip detector present in the Multi-3D sample are also presented for comparison. 213

14.12 Average charge collection in the selected fiducial regions for the square 3D cells in the Poly-3D, Full-3D, Multi-3D, and Irrad-3D detectors at different bias voltages and hence different cells' average electric field. The results for the charge collection for the planar strip detector present in the Multi-3D are shown for comparison. The black error bars depict the statistical uncertainty of the mean, while the red error bars depict the systematic uncertainty from the charge calibration. 214

14.13 Pulse height distributions, normalized to the peak, of the 3D cells with different geometries of the Multi-3D biased with −90 V and the planar strip part of the Multi-3D with −500 V. These voltages generate an average electric field of 1 V/µm, 0.42 V/µm, 0.62 V/µm, and 0.67 V/µm for the planar strips, rectangular cells, square cells, and hexagonal cells, respectively. 216

14.14 Collected charges of the different 3D cell geometries present in the Multi-3D sample, and the planar strip part of the Multi-3D. 217

14.15 Efficiencies of the different 3D cell geometries present in the Multi-3D sample. 217

14.16 Localization of the pulse heights lower than 500 ADC (~ 4100 e) for square cells (a-b) and hexagonal cells (c-d). The events are localized towards the edges and are not a feature of all the cells. 218

14.17 Simulated collected charges (solid red markers) and the measured collected charges for the Multi-3D (size of 100 µm) and Irrad-3D detectors (open markers). Both regions of the Irrad-3D detector, the 50um and 100um square cells, are shown. The size of the cells for the Poly simulation was 100 µm 219

14.18 Comparison between the charge collected by the 100 µm cells of the Irrad-3D sample biased with 45 V and the simulation of the HI-Poly detector biased with 45 V. The plots represent the amount of charge collected by the three channels in the transparent cluster (Ch0, Ch1, and Ch2 as defined in section 8.3.1) depending on where the ionizing particle hits the 3D cell. In (a) and (b), the charge collected by Ch0 is displayed. In (c) and (d), the charge collected by Ch1 is shown. In (e) and (f), the charge collected by Ch2 is shown. 221
14.19 Simulated collected charges using two life-path constants (solid red markers) and the measured collected charges for the Multi-3D and Irrad-3D detectors (open markers). 222

A.1 Schematic circuit with the different components that affect the noise in the VA. 229

B.1 (a) After a cleaning procedure, a gray-green residue on the surface of the diamond was present, which corresponded to a remnant of the carbide from a previous metallization. After a second cleaning procedure, the residue was gone under optical inspection. (b) Example of an optical inspection of the surface of a diamond done after a cleaning procedure. The white marks on the surface of the diamond were due to scratches during the mechanical polishing after manufacturing the sample. No residue of organic or inorganic nature was found by optical inspection on the surface of this sample. 233

C.1 Diamonds on top of a carrier inside the ICP-RIE chamber. The diamonds were being etched by Ar/Cl_2 plasma. 234

D.1 Diagram showing the effects of UV light exposure on positive and negative photoresists, and the resulting pattern after development.[161] 243

E.1 Different stress of the deposited films. 245
E.2 Reflectometry map of the deposited thickness over the wafer. 245

H.1 Example of the PDF underlying the case of 95 successes out of 100 tries. The MPV shows the measured efficiency, and the shaded area shows the uncertainty that covers the 68 % probability. 250

I.1 Efficiency Poly-3D. 251
I.2 Efficiency Full-3D. 252
I.3 Efficiency Multi-3D squares. 252
I.4 Efficiency Multi-3D rectangles. 253
I.5 Efficiency Multi-3D hexagons. 253
I.6 Efficiency Irrad-3D 100 µm. 254
I.7 Efficiency Irrad-3D 50 µm. 254

List of Tables

2.1 Comparison table of diamond and silicon properties, as found in previous works. The horizontal line between the properties Thermal conductivity and Dielectric constant emphasizes the more relevant properties of using diamond as the sensing material. The Diamond Implications column describes the way these quantities affect the performance of a sensor made with diamond. 7
2.2 Number of fragments of different atomic numbers produced by 10^4 incident protons with a momentum of 10 GeV/c in silicon and diamond. The contribution to the total NIEL for each fragmentation is also shown[39] 12
2.3 Damage constants in terms of $k_{24\,\mathrm{GeV}p} = 0.62 \times 10^{-18}\,\mathrm{cm}^2/(\mathrm{p}\cdot\mu\mathrm{m})$ for different irradiations[65, 64]. 14
2.4 Relevant parameters to calculate the Bethe-Bloch formula for carbon and silicon[68, 71]. 19
2.5 Low field drift mobilities and saturation velocities for diamond. The transition parameter used was $\beta = 1$. 26

3.1 Information of the samples that were made into planar pixel detectors. 40

4.1 Characterized noise of the VA2 chips according to the manufacturer IDEAS.[94] 43
4.2 Characterized noise of the VA2.2 chips according to the manufacturer IDEAS.[93] 43
4.3 Information of the samples that were made into 3D detectors. 47

6.1 Plasmas used for ICP-RIE on the diamond surfaces. 58
6.2 Relevant processes tried and their results. The only process combination that resulted in a correct formation of In bumps (no visible reaction) in the correct place was the one with a pixel metallization of Ti/Al, a passivation layer of SiO_xN_y, and a UBM of Ti/Ni/Au. 67

7.1 Fitted parameters for the data shown in Figure 7.3. 78
7.2 Fitted parameters for the data shown in Figure 7.5 80
7.3 Fitted parameters to the data shown in Figure 7.7. 82

8.1 Low-field drift mobilities and saturation velocities used for the dynamic simulations[44]. 87
8.2 Calculated diffusion coefficients at 300 K, assuming the mobilities in Table 8.1. 87
8.3 Effective conduction masses for charge carriers in CVD diamond. 88

8.4 Discrete time steps for each charge carrier to model the Brownian motion in each direction. . . . 88
8.5 Simulated detectors and their respective parameters for the collected charge (CCD) and for the trapping of the charge carriers (schubweg, MFP, and life-path). The CCD was calculated in a 500 µm diamond under a uniform electric field of 2 V/µm. . . . 92
8.6 Summary of mean and variation for the three definitions of charge collection for 3D strip detectors studied. . . . 96
8.7 Charge collection for the two channels with the highest charge for different simulated square 3D strip detectors. . . . 102

11.1 Major steps for aligning the telescope's tracking planes and the DUT. . . . 139

12.1 Implemented alignment procedure. . . . 162
12.2 Mean value for the χ^2 distributions obtained after fitting the 4160 pixels with the functions *erf*, *tanh* and *weibull*). . . . 177

13.1 Percentages of masked pixels according to their reasons and the expected yield of good pixels for the analysis of the DUTs tested in 2018 and 2019. . . . 182
13.2 Voltage scan results for the tested DUTs. For the average electric field magnitude, an uncertainty of 10 % was assumed on the thickness of the sensors. . . . 196
13.3 Bias voltages applied to the DUTs for the rate scans and their respective estimated average electric field magnitude. . . . 197

14.1 Calculated calibration constants for the non-connected channels for each detector. 202
14.2 Extracted values from Figure 14.9. PH_{4+}, PH_{4-}, and PH_{5-} correspond to the pulse heights digitized by Sirrocco 4 with a positive bias, Sirocco 4 with a negative bias, and Sirocco 5 with a negative bias, respectively. The size of the squares in the Multi-3D detector was 100 µm. The last two columns show the percentage difference between the data taken with both polarities in Sirocco 4, and the percentage difference between the data taken with negative bias in Sirocco 4 and 5. . . . 210
14.3 Average electric field according to simulations for different geometries and different voltages. The 3D wires' diameter for all 3D cells is assumed to be 2.6 µm. The uncertainties in the average electric field correspond to a 6 % variation obtained from a 20 % variation on the 3D wires' diameter. . . . 211
14.4 Average pulse height ratios of the 3D cells for different geometries with respect to the average pulse height of the planar strip detector. The third column is the ratio using the CCE measured during the test beams in this thesis, while the fourth column is the ratio using the previously reported CCE of the sample. The 3D cells were biased with 90 V, while the planar strip detector was biased with 500 V which gives an average electric field of 1 V/µm. . . . 216
14.5 Calculated MFP parameters for electrons and holes for the detectors Multi-3D and Irrad-3D using the data shown in Figure 14.17 in Equations 14.2 and 14.3. 222

E.1 Parameters used to grow the SiO_xN_y layers. 244
E.2 Characterization of film parameters by reflectometry, ellipsometry and stress measurements. 245

F.1 Settings used to etch SiO_xN_y passivation layer. 246

J.1 Relevant runs of the measurements made during the Oct. 2015 Test Beam at CERN. 255
J.2 Relevant runs of the measurements made during the May 2016 Test Beam at CERN. 255
J.3 Relevant runs of the measurements made during the Aug. 2016 Test Beam at CERN. 256
J.4 Relevant runs of the measurements made during the Sep. 2018 Test Beam at CERN. 256
J.5 Relevant runs of the measurements made during the Oct. 2018 test beam at CERN. 257

Part I

Introduction

Chapter 1

Motivation

Since the 1940s, when it was found that silver chloride crystals with an applied voltage could detect radiation particles[1], several crystals have been studied to function as radiation counters. Diamonds were one of such crystals and had advantages over other crystals in that they could work at ambient temperature[2, 3] and were more radiation resistant than other materials [4]. Although there were many improvements in understanding how to use diamonds as particle detectors in the following decades[2, 3, 4, 5], the lack of a process to produce reliable samples and the small yield of good sample candidates[2] hindered the development of radiation detectors made with diamonds.

It wasn't until the development and improvement of the fabrication of artificial diamonds via chemical vapor deposition (CVD) in the 1980s and 90s [6, 7, 8, 9] that samples could be produced with the quality suitable for particle detectors. During the 1990s, various proposals were made to research and implement diamond detectors in large particle accelerator experiments[10, 11]. One of these proposals led to the formation of the RD42 collaboration[12]. The research that arose from the growing interest in using diamonds in large particle accelerator experiments led to improving diamond sensor charge collection distance (CCD) by three orders of magnitude (from $O(0.1\,\mu m)$ to $O(100\,\mu m)$) during the first half of the 1990s[11]. In response to the improvement of diamond detectors in the 1990s, several diamond detectors have been installed as beam monitors for different experiments to detect beam instabilities that could harm the experiments' components and to perform relative luminosity measurements[13, 14, 15, 16, 17]. The Compact Muon Solenoid (CMS)[18] and the A Toroidal LHC ApparatuS (ATLAS)[19] experiments are among the experiments that benefit from the beam monitors fabricated with diamond detectors. These experiments are located in the Large Hadron Collider (LHC) in the Organization Européenne pour la Recherche (CERN)[20] particle accelerator complex.

In the LHC, bunches of particles are accelerated to almost the speed of light in vacuum, and bunches of these particles traveling in opposite directions collide in the center of the main experiments (CMS, ATLAS, LHCb, and ALICE). These collisions led to the discovery of the Higgs boson in 2012 by the CMS and ATLAS collaborations[21, 22]. To attempt to answer the open questions in particle physics, it is required to accumulate a large number of collisions to observe the rare events under study. To achieve this, the number of collisions in the LHC will be increased within this decade by upgrading the accelerator. The project of this upgrade is the High Luminoisity LHC (HL-LHC)[23] which expects to increase the number of interactions

per collision of the bunches by 7.5 times as its nominal luminosity up to a luminosity of 75 Hz/nb[24]. Consequently, the experiments have to be upgraded to cope with the amount of data that will be delivered and to withstand the increased radiation their detectors will face[25].

Different options are under study for upgrading the inner tracker detectors of the LHC experiments, among which 3D silicon sensors are of interest for their high radiation tolerance[25, 26]. A proof of concept on single-crystalline chemical vapor deposition (scCVD) diamond was done by Oh et al.[27], which led to the fabrication and testing of a 3D detector made with scCVD diamond[28]. Ever since, the RD42 Collaboration has been researching the development of 3D diamond detectors to exploit the combination of the high radiation tolerance of diamonds with the high radiation tolerance of the 3D detectors, which could be used in future upgrades beyond the Phase-II upgrade of the HL-LHC's experiments[28]. Several challenges must be met before a tracking detector made out of diamond sensors is suitable for future particle physics experiments. One of the challenges is the absence of a fabrication process to mass produce diamond pixel sensors compatible with current pixel readout chips. In the past, a full module was fabricated[29, 30] with the help of the company IZM[31]. An institute from the RD42 collaboration did the metallization process, but no details were documented for the fabrication process. Another method developed to bond diamond detectors with readout chips, described in the thesis of Michael Reichmann[32], has the problem that the sensors tend to detach from the readout chips, making the process unreliable. Another challenge in making diamond sensors suitable for future particle physics experiments is determining the advantages and weaknesses of 3D diamond detectors with the design constraints needed for the tracking detectors.

This thesis aims to tackle these two challenges by setting the following objectives: The first is to develop a fabrication process that could be scaled up to mass-produce diamond planar pixel detectors, starting by fabricating the sensor to be compatible with the current state-of-the-art pixel readout chips. The second one is to understand and model the signal characteristics from 3D diamond detectors using experimental data collected during this thesis. To achieve the first objective, the equipment and installations of the Binnig and Rohrer Nanotechnology Center (BRNC)[33] were used. Also, the installations and support from the CMS Pixel group at the Paul Scherrer Institute (PSI)[34] were crucial for this first objective. As for the second objective, the samples, detectors and beam time to perform the experiments were provided by the RD42 Collaboration. The experimental tests were performed using the test beam facilities at CERN for the 3D detectors and PSI for the planar pixel detectors.

After this chapter, in chapter 2, an overview of the theory behind the concepts mentioned in the rest of the thesis is given. Afterwards, a description of the used diamond samples is given in chapters 3 and 4, for the pixel and 3D detectors, respectively. The following chapter, chapter 5, briefly describes the fabrication processes employed by the RD42 collaboration to produce the 3D diamond detectors. Chapter 6 describes in detail the fabrication process developed in this thesis to produce the planar pixel detectors as part of one of the main objectives of this thesis, mentioned above. For the other objective of this thesis regarding 3D detectors, a simulation framework was developed, based on first principles, to understand the signals produced by the 3D detectors fabricated by the RD42 collaboration. This simulation framework is described in chapters 7 and 8. Afterwards, the experimental setups using particle beams in test beams made during the progress of this thesis are described in chapter 9, for measuring the 3D detectors, and in chapter 10, for testing the planar pixel detectors fabricated in the scope of this thesis. The

analysis procedures are described in chapter 11 for the data acquired with the 3D detectors, and chapter 12 for the data acquired with the planar pixel detectors. Finally, the results from both analyses are presented in chapters 13 and 14 for the planar pixel detectors and the 3D detectors, respectively.

Chapter 2

Theory

This chapter will present the theory behind the concepts that will be addressed throughout this thesis. The characteristics of diamonds, the material of interest in this thesis, will be given, describing their fabrication and features that make them suitable for the task of particle detection. Then a description of particle detection using solid-state detectors such as the ones studied during this thesis will be done. At the end of the chapter, the basic concepts of the electronics used to process the signals coming from the detector are given.

2.1 Diamond Characteristics

Diamonds are one of the crystal allotropes of carbon among graphite, graphene, or fullerenes, among which the most common ones on Earth are graphite and diamonds. The characteristic that separates diamonds from graphite is the sp^3 and sp^2 hybrid orbitals, respectively. While the sp^2 hybrid orbitals are formed under standard conditions, the sp^3 hybrid orbitals require high pressure and high temperature to form in nature[35]. A diagram showing the splitting and hybridization of the orbitals can be seen in Figure 2.1.

With the sp^3 hybrid orbitals, the carbon atoms arrange in a tetrahedral configuration with covalent bonds with the other carbon atoms. The angle between these bonds is 109.5°. This configuration is referred to as diamond cubic, and it can be reproduced by intersecting two Face Centered Cubic cells of side length a, one of which is displaced by an amount (1/4, 1/4, 1/4)a. The result from the intersection can be seen in Figure 2.1b. Other elements that can form the diamond cubic configuration are silicon and germanium, which are semiconductors[36].

Standard solid-state detectors for particle detection are made of silicon for their low cost and wide technology base[38]. Nevertheless, diamonds are better suited in environments with high radiation and limited cooling capabilities despite their smaller signals[39]. Table 2.1 summarizes the properties of diamond and silicon and emphasizes the implications of using diamond as a sensor.

The large bandgap of diamonds allows their use as ionization chambers without creating a pn-junction as is required with silicon sensors. This property, along with Diamond's high intrinsic resistivity and high breakdown field, limits the sensor's leakage current, allowing the sensor to operate at high voltages and have low electronic noise when coupled with electronic

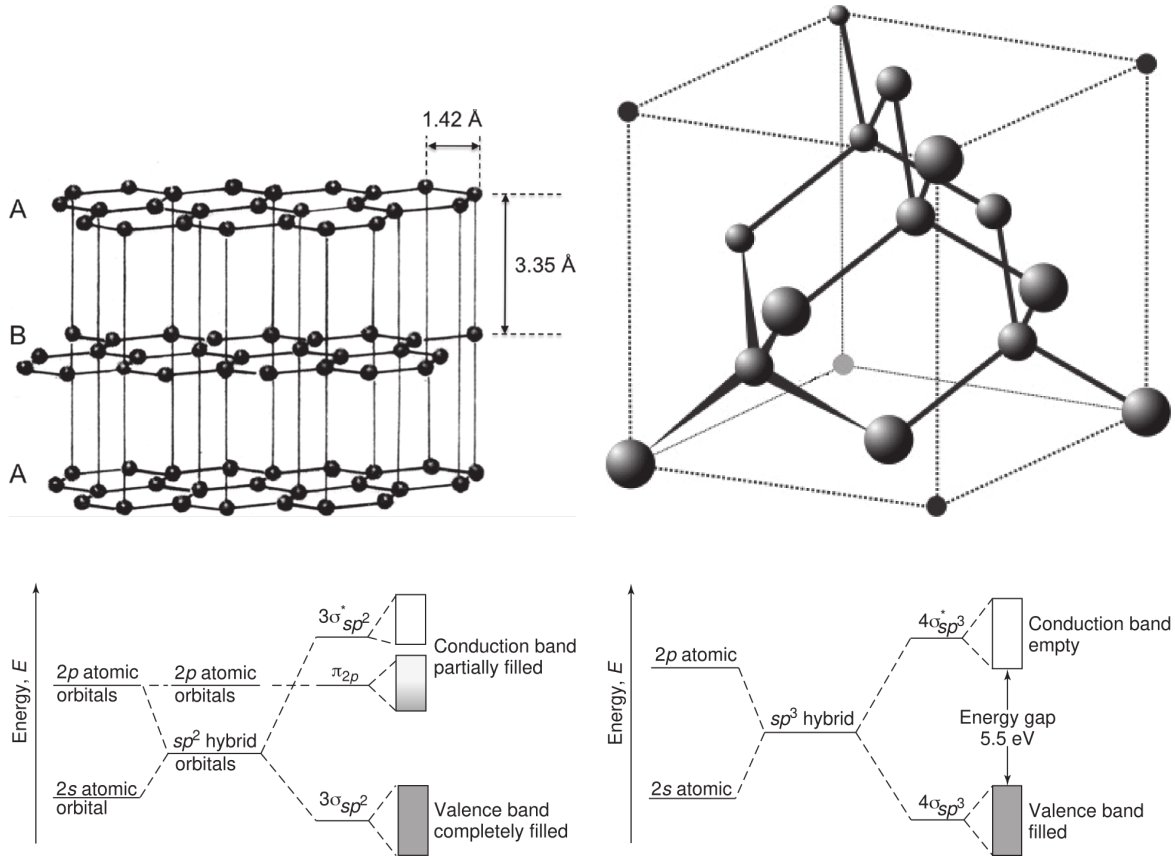

(a) Graphite crystal structure and electron orbitals.

(b) Diamond crystal structure and electron orbitals.

Figure 2.1: Differences in the crystal configuration of the carbon atoms, as well as the electron orbitals hybridization for graphite (a) and diamond (b). The internuclear distance in diamond is 1.54 Å[37].

devices such as amplifiers. Another property that contributes to the low noise of diamond sensors when coupled with electronic devices is their low capacitance due to their low dielectric constant.

The mentioned properties of diamond correspond to top-quality crystals, as imperfections and impurities would affect the mentioned values. For reasons discussed in the following sections, it is desired that the diamonds used as sensors have the least amount of impurities and crystallographic defects. CVD is a method to fabricate synthetic diamonds with the highest purity. For this work, all the samples used were fabricated using this method. The following section will discuss the CVD process to fabricate synthetic diamonds.

2.2 CVD Diamonds Fabrication

Besides the natural growth of diamonds in nature under high temperatures and high pressures, synthetic diamonds can be produced with the High-Pressure High-Temperature (HPHT) process

Property	Diamond	Silicon	Ref.	Diamond Implications
Element	C	Si		
Atomic Number	6	14		
Lattice constant [Å]	3.567	5.431	[40]	
Atomic weight	12.011	28.085	[40]	
Mass density [g/cm^3]	3.515	2.329	[40]	
Thermal conductivity [WK/cm]	22.22	1.3	[41, 40]	Heat spreader
Dielectric constant	5.7	11.7	[42, 40]	Small capacitance
Band gap [eV]	5.47	1.12	[43, 40]	Insulator, high temperatures
Resistivity [Ω m]	10^{14}	3.2×10^3	[36, 40]	Small currents
Electron Mobility [cm^2/Vs]	1714	1440	[44, 45]	Fast carrier velocities
Hole Mobility [cm^2/Vs]	2064	474	[44, 45]	Fast carrier velocities
Electron saturation velocity [cm/s]	9.6×10^6	10.54×10^6	[44, 45]	Fast carrier velocities
Hole saturation velocity [cm/s]	14.1×10^6	9.40×10^6	[44, 45]	Fast carrier velocities
Breakdown field [V/µm]	1000	30	[43, 46, 40]	High electric fields
Displacement energy per atom [eV]	37.5-47.6	12.9-21	[47, 48, 49]	High radiation tolerance
Radiation length [cm]	12.13	9.37	[50]	Thick sensors
eh-pair production energy [eV]	13.3	3.68	[51, 52]	Small signals
eh-pairs per µm for MIP [1/µm]	36	80	[53]	Small signals

Table 2.1: Comparison table of diamond and silicon properties, as found in previous works. The horizontal line between the properties Thermal conductivity and Dielectric constant emphasizes the more relevant properties of using diamond as the sensing material. The Diamond Implications column describes the way these quantities affect the performance of a sensor made with diamond.

or with the CVD process. In the HPHT process, the environmental conditions in nature to transform the sp^2 orbitals of carbon into sp^3 orbitals are replicated using anvils and catalyst metals. The graphite carbon is dissolved by the catalysts, and under pressures of $O(100\,\text{kbar})$ and temperatures of $O(2000\,°\text{C})$, the conversion takes place. [37, 35]. This technique was the first one implemented to produce synthetic diamonds in 1955[54]. The fabricated diamonds with this method have high nitrogen and metal impurities and many crystal defects. For these reasons, they are not suitable for sensor fabrication or other semiconducting applications[36].

On the other hand, growing diamonds via CVD can be achieved at lower pressures. In CVD, each carbon is bonded tetrahedrally, forming the sp^3 orbitals layer by layer. The process consists of the injection of a gas mixture that contains carbon, which is activated to react with a substrate where the diamond layers are grown, followed by the extraction of the by-products[37].

There are many ways to activate the gas mixture, which gives the different processes for CVD growth of diamonds. These techniques can be divided into Thermal decomposition and Plasma-aided deposition. Hot Filament CVD (HFCVD) and Oxy-Acetylene Torch Method are among the Thermal decomposition methods. As for the Plasma-aided deposition techniques, there are methods such as Microwave Plasma-Enhanced CVD (MWCVD), DC Plasma CVD, and RF Plasma CVD[37]. Figure 2.2 shows a diagram of an MWCVD chamber.

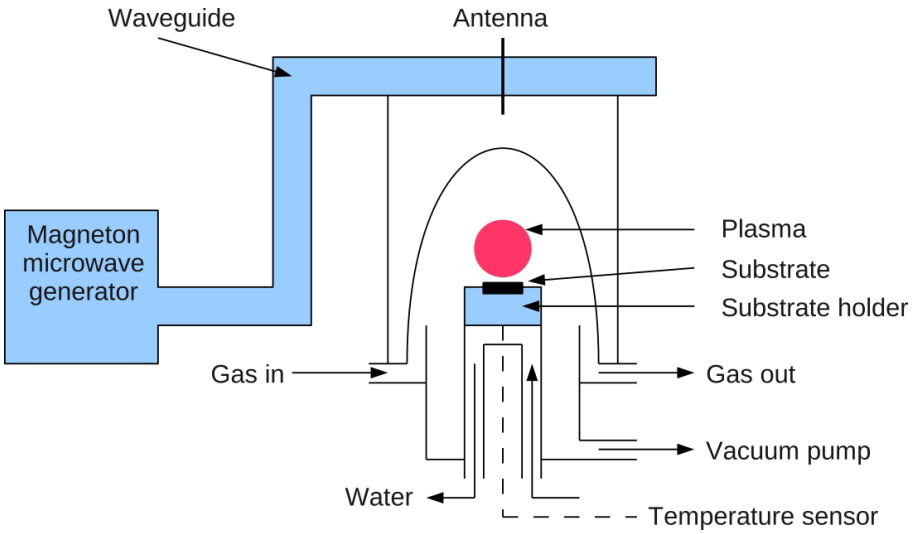

Figure 2.2: Schematic view of a Microwave-CVD chamber used for growing diamonds[55]. A controlled mixture of gases enters from the left of the chamber, where the pressure is controlled by a vacuum pump and the inlet and outlet speeds of the gases. Using microwaves, the injected gas is ionized to form a plasma which is placed on top of the substrate to grow the synthetic diamond.

In CVD growth, the gas mixture is mostly hydrogen (H_2) and a fraction of methane (CH_4). In some cases, oxygen in the form of CO or O_2 is implemented as it lowers the temperature for the formation of the diamond[37]. By any of the techniques mentioned above, the molecular hydrogen is dissociated into atomic hydrogen, while the ionized hydrocarbon is incorporated into the substrate lattice. Afterwards, the atomic hydrogen strips a hydrogen atom from the hydrocarbon by hydrogen abstraction, leaving an activated carbon ready to form an sp^3 bond with another hydrocarbon in the gas[36]. If graphitic bonds are formed in the process, the atomic hydrogen etches the graphite as it is more reactive to graphite than to diamond[37]. A sketch of this process is shown in Figure 2.3.

Among the synthetic diamonds that can be produced, the ones referenced in this thesis are scCVD and pCVD diamonds. The difference between these two types of diamonds starts from the selection of the substrate for the growth of the diamond. If the substrate is another single-crystalline diamond, the lattice of the single-crystal diamond is reproduced throughout the growth of the synthetic diamond, resulting in an scCVD diamond[55]. Although scCVD diamonds have the highest quality among the synthetic diamonds, they are the most expensive, and they also are limited to sizes smaller than 8 mm × 8 mm[56].

On the other hand, pCVD diamonds can be grown on non-diamond substrates like single-

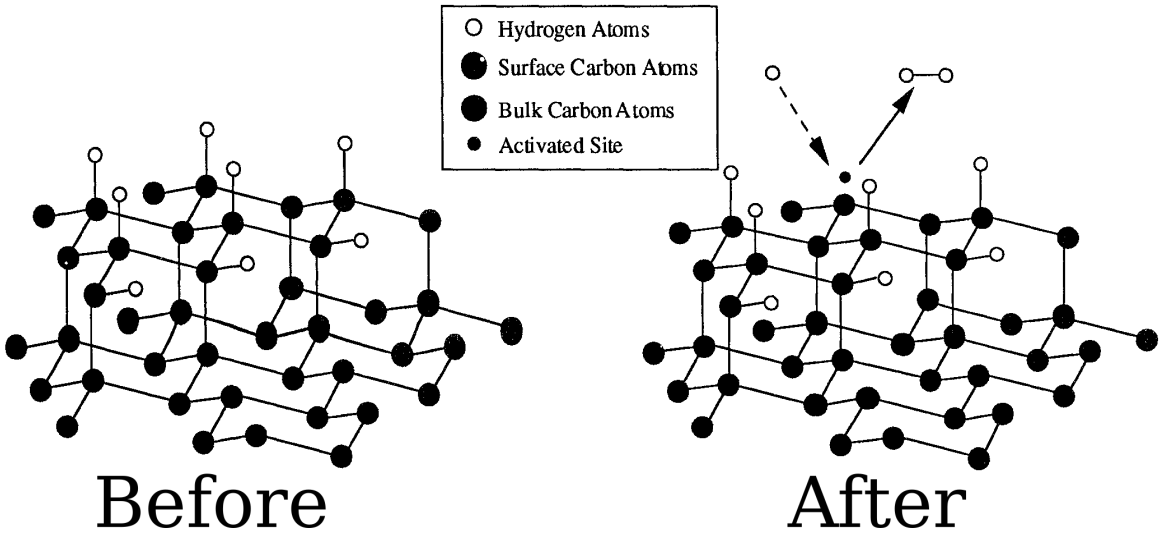

Figure 2.3: Diagram showing the process in which atomic hydrogen captures a hydrogen atom in the deposited hydrocarbon, forming molecular hydrogen and leaving the carbon activated to make an sp^3 bond with another hydrocarbon[36].

crystalline silicon or carbide-forming metals like molybdenum (hetero-epitaxial) or in a non-diamond substrate covered with diamond powder[36]. With each layer of grown diamond, some grains become more prominent, while others disappear[57]. Figure 2.4 depicts the evolution of the grains from the substrate up to the final thickness of the diamond film. Because of their nature, pCVD diamonds have more crystallographic defects than scCVD diamonds, but in contrast, they can be grown to diameters of $O(10\,\text{cm})$[56]. The most common crystallographic defect present in pCVD diamonds is grain boundaries. In the following section, this and other defects will be discussed.

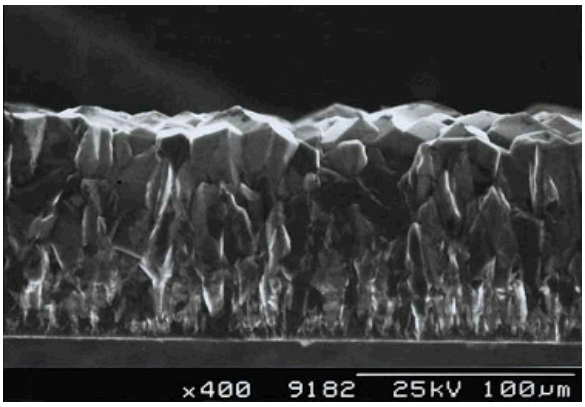

(a) Cross-section of a 100 µm thick pCVD diamond[58].

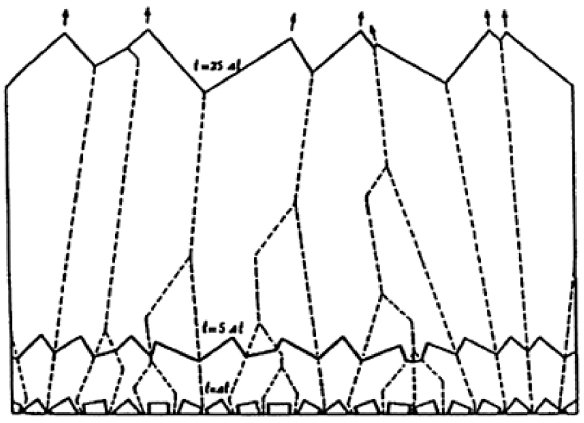

(b) Sketch of a pCVD diamond film growth[59].

Figure 2.4: Picture (a) and sketch (b) of the grains in the growth of a pCVD diamond starting from randomly oriented crystals as substrate.

2.3 Crystallographic Defects

Natural and synthetic diamonds present crystallographic defects during the diamond's fabrication process. These defects can be categorized according to their dimensionality, which are zero-dimensional (0D), one-dimensional (1D), two-dimensional (2D), and three-dimensional (3D). Figure 2.5 depicts in a 2D representation of the lattice some of these defects.

The 0D defects can be split into intrinsic and extrinsic defects. Intrinsic 0D defects are the ones that involve carbon, while extrinsic 0D defects involve other atoms, which are considered impurities. Among the intrinsic 0D defects are interstitial defects, where an atom is not occupying a position valid for the periodicity of the lattice, such as two carbon atoms occupying the same lattice site (self-interstitial), or when an atom from an impurity, like hydrogen, occupies a place between lattice sites (extrinsic interstitial). Other 0D defects are vacancies, an intrinsic defect where a carbon atom is missing from the lattice. When an impurity atom, such as nitrogen, occupies the lattice site instead of a carbon atom, it is an extrinsic substitution[60].

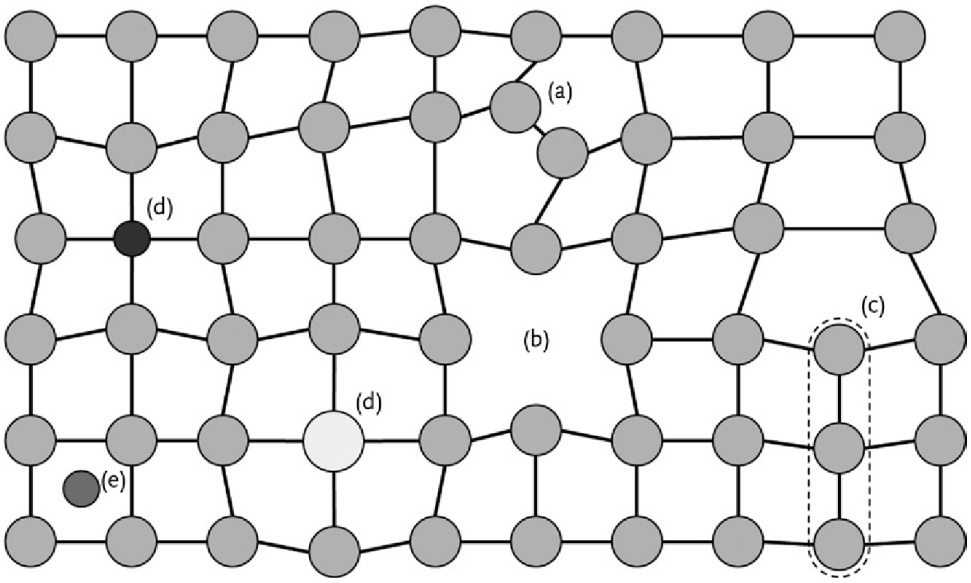

Figure 2.5: Schematic of some 0D and 1D defects in diamond. (a) represents a self-interstitial defect (0D), (b) is an intrinsic vacancy (0D), (c) is an edge dislocation (1D), (d) are extrinsic substitutional atoms (0D), and (e) is an extrinsic interstitial atom[60].

Some of the 0D defects are stable in the lattice (extrinsic substitution), while others are mobile (vacancies, interstitial)[36]. Sometimes mobile defects combine with stable ones to form a new type of defect, such as nitrogen-vacancy (combination of substitutional nitrogen and a vacancy) or Frenkel pair (combination of a self-interstitial and a vacancy)[61]. Frenkel pairs are one of the defects caused by radiation which will be discussed in the next section.

One-dimensional defects include edge and screw dislocations, 2D defects include grain boundaries, stacking faults, and phase boundaries and 3D defects include voidities, cracks, and inclusions. Among these defects, grain boundaries are predominant in pCVD diamonds, as mentioned in the previous section. It has been seen that point defects and strains tend to concentrate at grain boundaries[36].

Defects such as interstitial and substitution introduce deep energy levels in the forbidden energy band between the diamond crystal's valence and conduction band, which serve as recombination centers and radiative transitions. These deep traps affect the charge carriers' lifetime, affecting their mobilities[36].

2.4 Radiation Damage

When particles pass through a material, they deposit energy in the material by ionization, where electrons are ionized, or by Non-ionising energy loss (NIEL) processes. Ionization is a reversible process, while NIEL effects can permanently affect the material causing radiation damage. As seen in Figure 2.6, the fraction of NIEL with respect to the total energy lost in the interaction of an incident particle with the material strongly depends on the incident energy. For energies above 10 MeV, the fraction of energy lost via NIEL in diamond is negligible, although the total amount is not negligible[39].

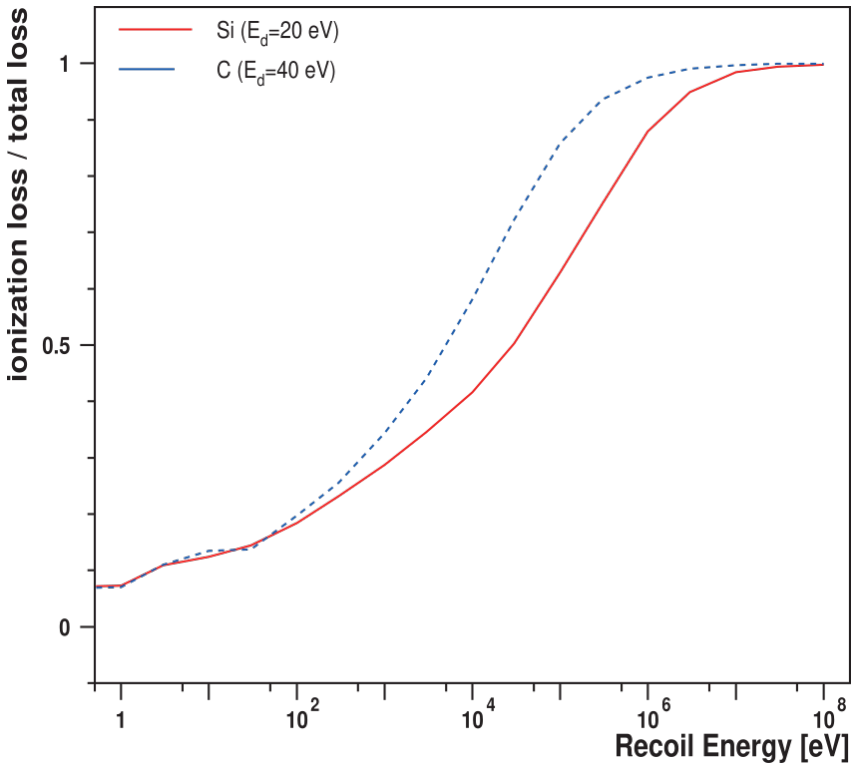

Figure 2.6: Fraction of ionization energy loss as a function of the recoil energy. The displacement energy for carbon is assumed to be 40 eV and 20 eV for silicon[39].

NIEL scatterings can create dislocations if the transfer energy is larger than the displacement energy of the material (see Table 2.1), which can create a domino effect and knock out of position other carbon atoms, leaving behind vacancies and self-interstitial defects. As mentioned before, Frenkel pairs are a common defect created by radiation damage which are formed by the combination of a self-interstitial and a vacancy when the knocked carbon atom assumes

an interstitial position in the lattice leaving a vacancy behind. Another NIEL effect is the fragmentation of the carbon into a lighter nucleus, creating extrinsic interstitials or substitutions.

Table 2.2[39], estimates the number of fragments created and the percentage of the total NIEL caused by inelastic collisions from 10^4 incident protons with a momentum of 10 GeV/c in silicon and diamond. As silicon has a higher atomic number, it can produce a larger variety of fragments than diamond, and more than half of its NIEL produces fragmentations. On the other hand, for diamonds, only a small fraction of the NIEL creates fragments, and most of the NIEL creates displacements in the diamond lattice.

Z_{fr}	$\#Si_{fr}$	$NIEL_{Si}\%$	$\#C_{fr}$	$NIEL_{C}\%$
14	417	4.2	0	0
13	910	9.1	0	0
12	1384	12.5	0	0
11	1021	8.9	0	0
10	1225	8.5	0	0
9	265	1.4	0	0
8	493	2.1	0	0
7	398	1.3	0	0
6	909	2.4	698	0.8
5	270	0.6	869	0.8
4	383	0.7	584	0.4
3	662	0.7	1133	0.6
2	11152	4.4	10625	2.0
1	46107	0.9	30465	0.24
Total	65590	57.4	44374	4.8

Table 2.2: Number of fragments of different atomic numbers produced by 10^4 incident protons with a momentum of 10 GeV/c in silicon and diamond. The contribution to the total NIEL for each fragmentation is also shown[39]

As previously stated, the crystal lattice defects affect the charge carriers' mean free time and, therefore, the mean free path (MFP). The RD42 collaboration has modeled the effects of the radiation damage on the MFP of the charge carriers[62]. In this model, the number of defects N_d is inversely proportional to the MFP of electrons and holes $\lambda_{e,h}$:

$$\lambda_{e,h} \propto \frac{1}{N_d} \equiv \frac{1}{N_0 + k \cdot \phi} \tag{2.1}$$

, where the parameter N_d includes the number of defects N_0 from the growth of the diamond sample and a component proportional to the total fluence ϕ the samples have been irradiated with. The proportionality constant k depends on the irradiation type and momentum.

Following the work from Hecht[63], the average separation distance between electrons and holes under a uniform electric field, the schubweg λ, would be equal under these circumstances to the sum of the MFP of the electrons λ_e with the MFP of the holes λ_h.

The model from the RD42 collaboration assumes a linear relationship between the reciprocal of the schubweg with the radiation fluence ϕ:

$$\frac{1}{\lambda} = \frac{1}{\lambda_0} + k \cdot \phi \tag{2.2}$$

, where the parameter λ_0 represents the initial schubweg in the sensor before irradiation, which is inversely proportional to the initial defects N_0 from the sample's fabrication process. The proportionality constant k is referred to as the "damage constant" for a specific irradiation type and its momentum.

In practice, the radiation effects on the sensor are measured by the amount of charge they collect after different irradiations. Using ionizing particles, a certain amount of ionized charge Q_{ion} is produced in the sensor, and employing a uniform electric field, a charge Q_{coll} is collected. In the following sections, the process in which the charge is ionized in the diamond and the process of collecting the charge will be discussed in detail. The ratio between the collected charge Q_{coll} and the ionized charge Q_{ion} gives the charge collection efficiency (CCE):

$$CCE = \frac{Q_{coll}}{Q_{ion}} \tag{2.3}$$

The RD42 collaboration uses an equivalent measure called the CCD, which, in sensors that are homogeneous across their thickness Th, has the following relatioship with the CCE:

$$CCD \cong \mathrm{Th} \cdot \mathrm{CCE} \tag{2.4}$$

Based on the work from Hecht[63] on the CCE as a function of the schubweg λ, the following relationship is obtained:

$$\mathrm{CCE}(\lambda_\mathrm{e}, \lambda_\mathrm{h}) = \frac{\mathrm{CCD}}{\mathrm{Th}} = \sum_{\mathrm{i=e,h}} \frac{\lambda_\mathrm{i}}{\mathrm{Th}} \left(1 - \frac{\lambda_\mathrm{i}}{\mathrm{Th}} \left(1 - \mathrm{e}^{-\frac{\mathrm{Th}}{\lambda_\mathrm{i}}}\right)\right) \tag{2.5a}$$

$$r \equiv \frac{\lambda_h}{\lambda_e} \tag{2.5b}$$

$$\lambda \equiv \lambda_e + \lambda_h \tag{2.5c}$$

$$\mathrm{CCE}(\lambda, \mathrm{r}) = \frac{\lambda}{\mathrm{Th}} \left(1 - \frac{\lambda}{\mathrm{Th}} \left(\frac{\mathrm{r}^2 \left(1 - \mathrm{e}^{-\left(\frac{\mathrm{Th}}{\lambda} \frac{1+\mathrm{r}}{\mathrm{r}}\right)}\right) + 1 - \mathrm{e}^{-\left(\frac{\mathrm{Th}}{\lambda}(1+\mathrm{r})\right)}}{(\mathrm{r}+1)^2}\right)\right) \tag{2.5d}$$

, where the parameter r is the ratio between the MFP of the holes λ_h and the MFP of the electrons λ_e, and, as mentioned before, the schubweg λ is the sum of the electrons' MFP and the holes' MFP. Figure 2.7 shows the plot for the relation in Equation 2.5d when $r = 1$.

From the relation in Equation 2.5d, the schubweg can be derived from a measurement of the CCD. Figure 2.8 shows the results obtained by the RD42 collaboration for scCVD and pCVD diamonds under 800 MeV/c proton irradiation at different fluences. Except for the scCVD point at the highest irradiation, the linearity supports the model introduced in Equation 2.2. In Table 2.3, the different damage constants for different types of irradiations are shown in terms of the damage constant for 24 GeV/c protons.

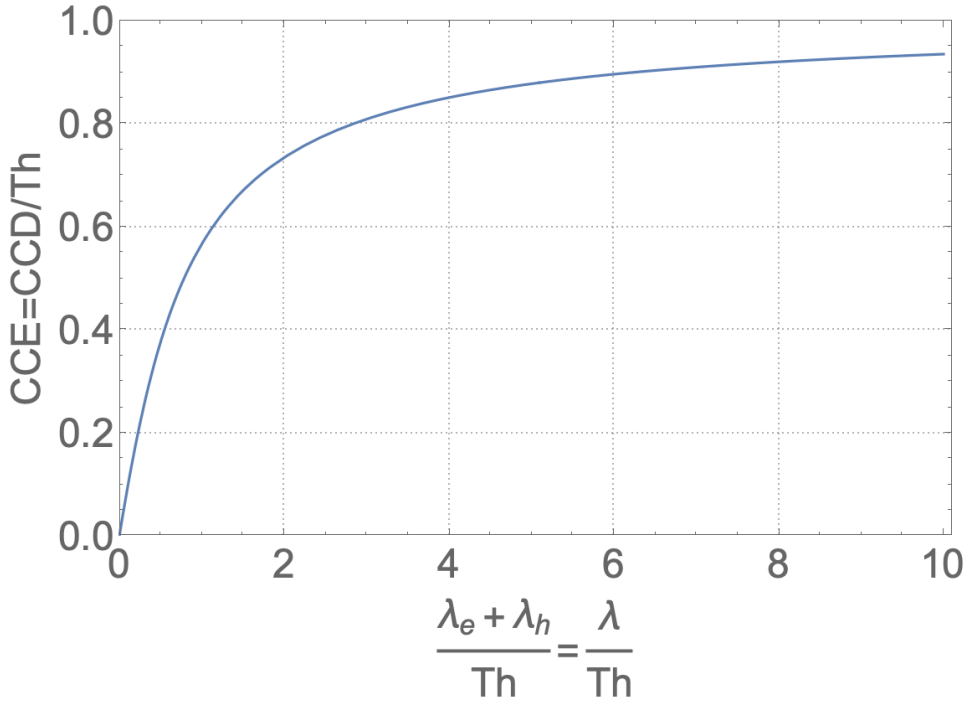

Figure 2.7: Charge collection efficiency as a function of the ratio between the schubweg λ and thickness of the sensor Th when the MFP of electrons and holes are equal.

Particle species	k
24 GeV/c protons	$k_{24\,\mathrm{GeV}p}$
800 MeV/c protons	$1.67(9)\,k_{24\,\mathrm{GeV}p}$
70 MeV/c protons	$2.60(29)\,k_{24\,\mathrm{GeV}p}$
25 MeV/c protons	$4.4(12)\,k_{24\,\mathrm{GeV}p}$
Fast neutrons	$4.3(4)\,k_{24\,\mathrm{GeV}p}$
200 MeV/c pions	$3.2(8)\,k_{24\,\mathrm{GeV}p}$

Table 2.3: Damage constants in terms of $k_{24\,\mathrm{GeV}p} = 0.62 \times 10^{-18}\,\mathrm{cm}^2/(\mathrm{p}\cdot\mu\mathrm{m})$ for different irradiations[65, 64].

2.5 Particle Detection

In the previous sections, diamonds were discussed as a suitable material for particle detection based on the mobilities of its charge carriers and other characteristics shown in Table 2.1 and the effect of radiation on their performance as a sensor. This section will discuss the processes by which a sensor senses the passage of particles.

2.5.1 Particle Matter Interactions

The interaction between the incident particle and the sensor material depends on the characteristics of the incident particle. Each interaction that results in energy loss occurs in single

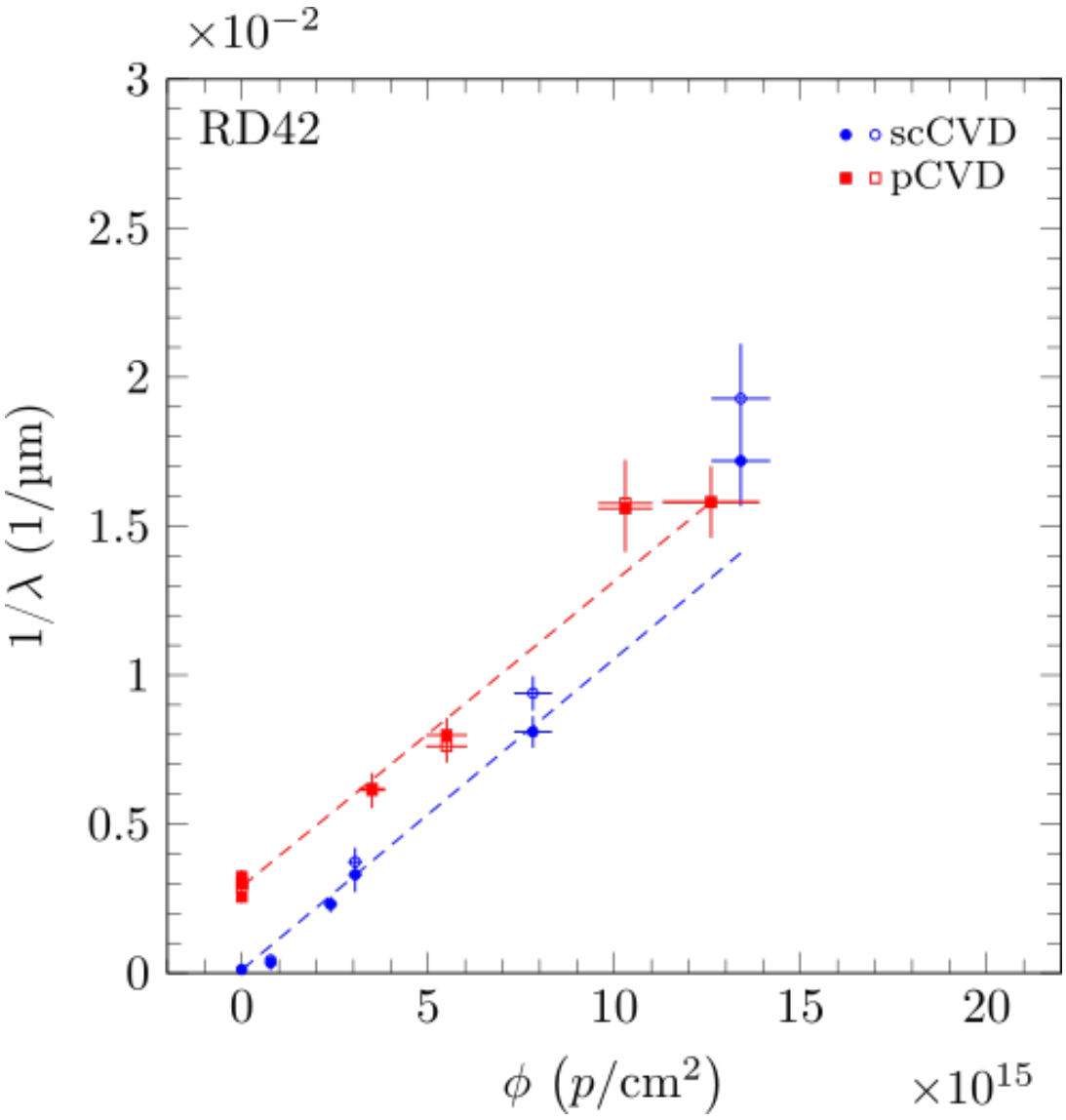

Figure 2.8: Derived schubweg reciprocals from charge collection measurements for different irradiations fluences of 800 MeV/c protons[64]. The open markers are for the data points measured with a negative bias, while solid markers are for a positive bias.

collisions. Charged and neutral particles can scatter via close-range elastic scattering, while only charged particles can scatter through the electromagnetic fields at long ranges. In this section, the interaction of charged particles (excluding electrons and positrons) will be discussed, followed by the corrections needed for the cases of electrons and positrons. Then the effects of multiple scattering of the particles while traversing the material will be addressed, followed by a discussion of the interaction between photons and matter.

Interactions By Charged Particles

As mentioned before, charged particles can interact through electromagnetic fields by exchanging photons with the electrons in the sensor's atoms. If the imparted energy is large enough, the atom's affected electron can become ionized, creating an electron-hole pair (eh-pair). If the energy is large enough, then the ionized electron can ionize more electrons until its energy is below the ionization energy. These electrons are referred to as delta rays. Each interaction is a stochastic process that, over the total path length of the sensor, contributes to quantities that can be measured. Although Bohr tried to calculate the energy loss due to ionization classically, it wasn't until Bethe and Bloch considered the necessary quantum mechanical effects that the energy loss through ionization at medium energies was accurately described[66]. This regime is seen in Figure 2.9, where the mass stopping power over nine orders of magnitude for incident μ^+ in copper is shown.

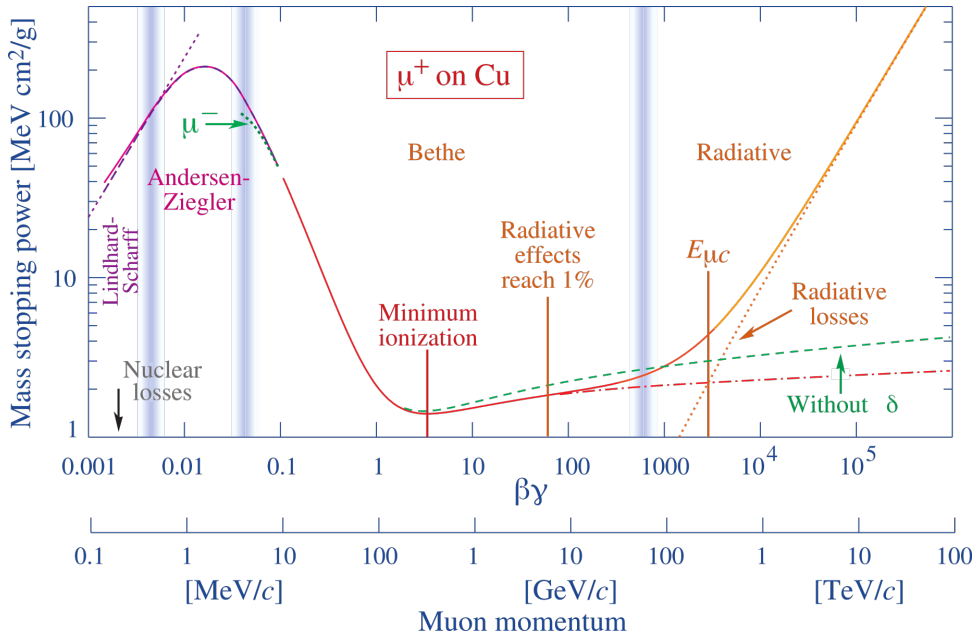

Figure 2.9: Mass stopping power for μ^+ in Cu as a function of $\beta\gamma = p/Mc$. The vertical bands delimit different approximation regimes[50].

The formula that describes the regime denoted as "Bethe" in Figure 2.9 is the following[50]:

$$\langle -\frac{dE}{dx} \rangle = Kz^2 \frac{Z}{A} \frac{1}{\beta^2} \left(\frac{1}{2} \ln \left(\frac{2m_e c^2 \beta^2 \gamma^2 W_{max}}{I^2} \right) - \beta^2 - \frac{\delta(\beta\gamma)}{2} - \left(\frac{C}{Z} \right) \right) \tag{2.6}$$

, where:

m_e is the electron's mass

ρ is the density

x is the mass per unit area (distance in the absorber times the absorber's density)

M is the incident particle mass

E is the incident particle energy

W_{max} is the maximum kinetic energy that can be transferred to a free electron per collision (see Equation 2.7)

z is the charge number of the incident particle

Z is the atomic number of the absorber

A is the atomic mass of the absorber

K is the constant coefficient: $4\pi N_A r_e^2 m_e c^2$

I is the mean excitation energy

$\delta(\beta\gamma)$ is the density effect correction to ionization energy loss

C is the shell correction only applicable for $\beta\gamma \leq 0.1$ in the Bethe regime.

$$W_{max} = \frac{2m_e c^2 \beta^2 \gamma^2}{1 + 2\gamma\frac{m_e}{M} + \left(\frac{m_e}{M}\right)^2} \tag{2.7}$$

The mean excitation energies, I, can be estimated using the empirical formula by Barkas and Berger[67]. The value of I for carbon has been measured to be 78 eV[68].

The curve described by Equation 2.6 fails to describe the energy losses by electrons and positrons traversing a material. For electrons, there are considerable interactions between the incident electron and the electrons in the material's atoms via the Møller effect. In the case of positrons, the scattering between the incident positron and the electrons in the material's atoms, described by the Bhabha scattering, must be included. These results are shown in Equation 2.8 for electrons and Equation 2.9 for positrons.

$$\begin{aligned}\left\langle -\frac{dE}{dx}\right\rangle = \frac{Kz^2}{2}\frac{Z}{A}\frac{1}{\beta^2}\Bigg(\ln\left(\frac{m_e c^2\beta^2\gamma^2(m_e c^2(\gamma-1))}{2I^2}\right) + (1-\beta^2) \\ - \frac{2\gamma-1}{\gamma^2}\ln 2 + \frac{1}{8} - \left(\frac{\gamma-1}{\gamma}\right)^2 - \delta(\beta\gamma) - \left(\frac{2C}{Z}\right)\Bigg)\end{aligned} \tag{2.8}$$

$$\begin{aligned}\left\langle -\frac{dE}{dx}\right\rangle = \frac{Kz^2}{2}\frac{Z}{A}\frac{1}{\beta^2}\Bigg(\ln\left(\frac{m_e c^2\beta^2\gamma^2(m_e c^2(\gamma-1))}{2I^2}\right) + 2\ln 2 \\ - \frac{\beta^2}{12}\left(23 + \frac{14}{\gamma+1} + \frac{10}{(\gamma+1)^2} + \frac{4}{(\gamma+1)^3}\right) - \delta(\beta\gamma) - \left(\frac{2C}{Z}\right)\Bigg)\end{aligned} \tag{2.9}$$

The Bethe-Bloch formula calculates accurately within a few percent in the ranges between $0.1 \leq \beta\gamma \leq 1000$. For $\beta\gamma \leq 0.05$, the curve in Figure 2.9 relies on the phenomenological fitting

formula developed by Andersen and Ziegler[69]. As for $\beta\gamma \leq 0.01$, the theory of Lindhard, where the stopping power is proportional to β, has been successful to describe the mass stopping power of charged particles[70].

For the correction for low energies ($0.05 \leq \beta\gamma \leq 0.1$), the term C/Z in Equation 2.6 is included to account for the case in which the speed of the incident particle is comparable to the speed of the electrons in the orbitals of the absorber.

For $\beta\gamma \leq 1$, the term $1/\beta^2$ is most significant and causes the curve to decrease. At $\beta\gamma \sim 1$, the term $\ln\beta^2$ starts to be meaningful, and the curve begins to flatten. At $\beta\gamma \sim [3-4]$, the curve reaches its minimum. Particles with a $\beta\gamma$ close to this minimum are called minimum-ionizing particle (MIP). Figure 2.10 shows the region around the minimum for different absorbers, where it is clear that the minimum value depends on the material (it decreases with Z). The minimum for carbon occurs at $\beta\gamma \cong 3.9$[68].

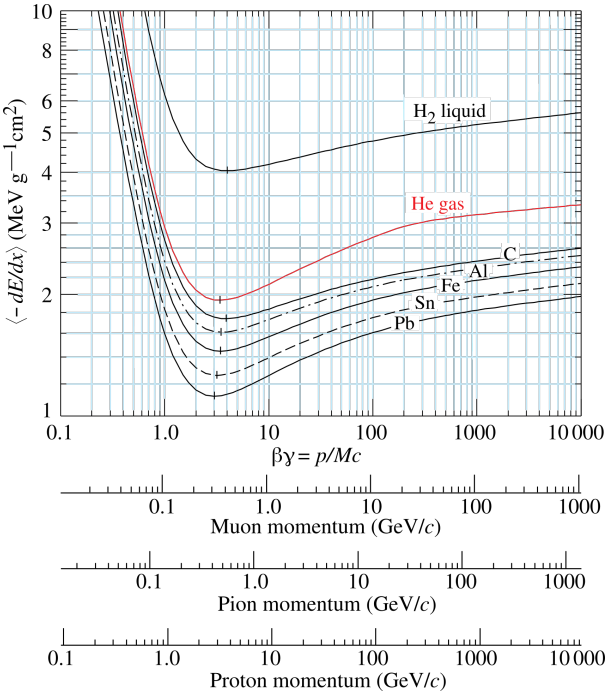

Figure 2.10: Mean energy loss rate for different materials near the minimum[50]. In general, the minimum is reached for $\beta\gamma \sim [3-4]$. For carbon, the minimum is reached for $\beta\gamma \cong 3.9$[68].

At $\beta\gamma$ larger than 4, β is almost constant, with a range between (0.97, 1); therefore, the curve starts to increase by the logarithm of γ. In this region of the logarithmic increase, the density effect correction by the parameter δ becomes important. Figure 2.9 shows the effect of not applying the δ correction to the curve, which makes the mass stopping power grow faster than when the δ correction is applied. The density effect correction accounts for the fact that the media becomes polarized and limits the extension of the electric field contributions to distant collisions[50].

$$\delta(\beta\gamma) = \begin{cases} 2(\ln 10)\log_{10}(\beta\gamma) - \overline{C} & \text{if } \log_{10}(\beta\gamma) \geq x_1 \\ 2(\ln 10)\log_{10}(\beta\gamma) - \overline{C} + a(x1 - \log_{10}(\beta\gamma))^k & \text{if } x_0 \leq \log_{10}(\beta\gamma) < x_1 \\ 0 & \text{if } \log_{10}(\beta\gamma) < x_0 \text{ (nonconductors)} \\ \delta_0 10^{2(\log_{10}(\beta\gamma) - x_0)} & \text{if } \log_{10}(\beta\gamma) < x_0 \text{ (conductors)} \end{cases} \tag{2.10}$$

Table 2.4 shows the values for the parameters in Equation 2.10 for diamond and silicon.

Material	I(eV)	a	k	x_0	x_1	$\overline{C}$	δ_0
C	78	0.26142	2.8697	-0.1135	2.2458	2.4271	0.12
Si	173	0.14921	3.2546	0.2015	2.8716	4.4355	0.14

Table 2.4: Relevant parameters to calculate the Bethe-Bloch formula for carbon and silicon[68, 71].

Equation 2.6 and the curve shown in Figure 2.9 suppose that the target material is infinitely thick, far from real sensors, usually of $O(100\,\mu m)$ in thickness. Infinitely thick materials allow the energy deposition of rare high energetic electrons (delta rays) that would escape the material in thin sensors. A method to limit the energy deposition of rare delta rays is to restrict the energy transfer with the parameter W_{cut}, such that $T \leq W_{cut} \leq W_{max}$. With this change, Equation 2.6 becomes:

$$\langle -\frac{dE}{dx} \rangle \Big|_{T<W_{cut}} = Kz^2 \frac{Z}{A} \frac{1}{\beta^2} \left(\frac{1}{2} \ln \left(\frac{2m_e c^2 \beta^2 \gamma^2 W_{cut}}{I^2} \right) - \frac{\beta^2}{2} \left(1 + \frac{W_{cut}}{W_{max}} \right) - \frac{\delta(\beta\gamma)}{2} - \left(\frac{C}{Z} \right) \right) \tag{2.11}$$

In the limit when W_{cut} approaches W_{max}, the standard Bethe-Bloch formula is recovered. Figure 2.11 shows different cases, including the ones when W_{cut} is equal to twice the kinetic energy for MIP (546 MeV) and to ten times the kinetic energy for MIP in silicon (2730 MeV)[71].

The restricted formula is useful for studying ionization behavior at high kinetic energies. As shown in Figure 2.11, the curve approaches a constant value referred to as the "Fermi plateau". As the most probable vlaue (MPV) and the average energy loss for thin absorbers (modeled with Wcut) reach the Fermi plateau, all particles within the plateau are treated as MIPs. A $W_{cut} = 7.5\,keV$ has been estimated for $500\,\mu m$ diamonds[53], which predicts 36 eh – pair production for MIPs[72, 73].

Another useful approach is given by Landau-Vavilov-Bichsel, where the MPV of the energy loss probability distributions is the center of study instead of the mean. The formula for the MPV of the distribution is the following:

$$\Delta_p = \xi \left(\ln \left(\frac{2m_e c^2 \beta^2 \gamma^2}{I} \right) + \ln \left(\frac{\xi}{I} \right) + j - \beta^2 - \delta(\beta\gamma) \right) \tag{2.12}$$

, where:

Δ_p is the MPV of the energy loss probability distribution

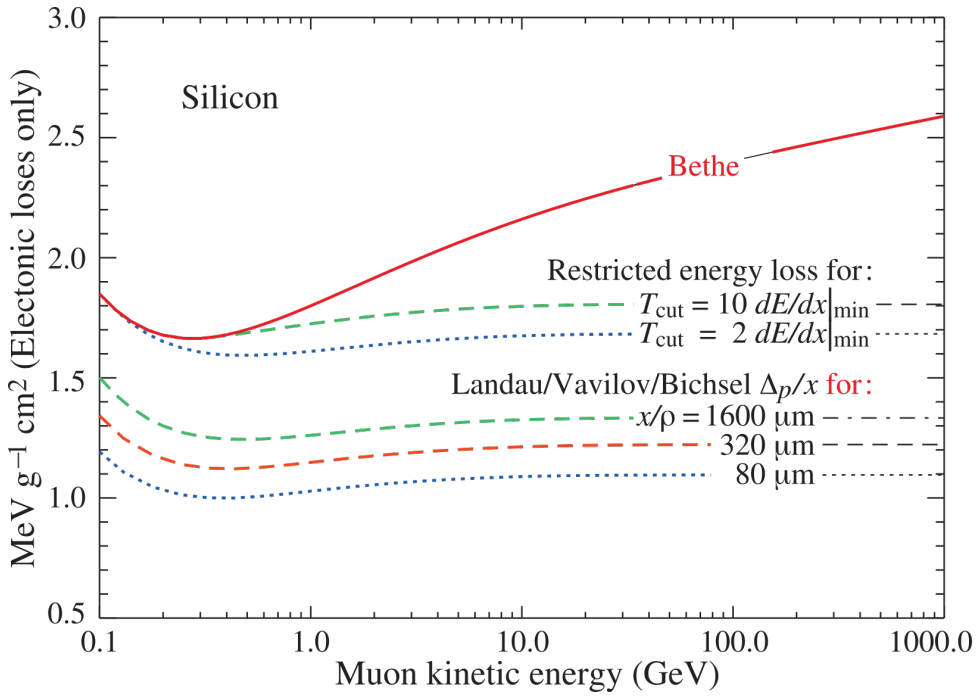

Figure 2.11: Comparison between the Bethe-Bloch curve with all the corrections, the restricted energy loss cases for twice the MIP energy and 10 times the MIP energy, and the MPV for three different sensor's thicknesses for silicon. The radiative losses are excluded in this plot. The term T_{cut} is the same W_{cut}[50].

ξ is the Landau parameter: $\xi = (K/2)\langle Z/A\rangle z^2(x/\beta^2)$MeV

x is the thickness of the material times the material's density in g/cm^2

j is a constant which Bichsel estimates to 0.2[52]

The results for different values of thickness of silicon sensors are shown in Figure 2.11. As in the case of the restricted energy loss with the parameter W_{cut}, the MPV Δ_p also reaches a Fermi plateau at high values of $\beta\gamma$.

The distributions for the energy losses of fast-charged particles in a material with a finite thickness are called straggling functions. Figure 2.12 shows the straggling functions for different thicknesses of silicon.

Although the straggling functions given by Landau and Vavilov correctly estimate the MPV, they fail to estimate the width, usually provided by the full width at half-maximum (*FWHM*), giving an estimate that is smaller than experimental data. Bichsel studied this issue and introduced a better approximation to the straggling functions[74, 52].

Another approximation to the empirical straggling functions is given by the convolution of the theoretical Landau function with a Gaussian distribution. This method, which has been widely used for analysis by the RD42 collaboration and in this work, can be traced back to the work of Blunck and Leisegang in 1950[75].

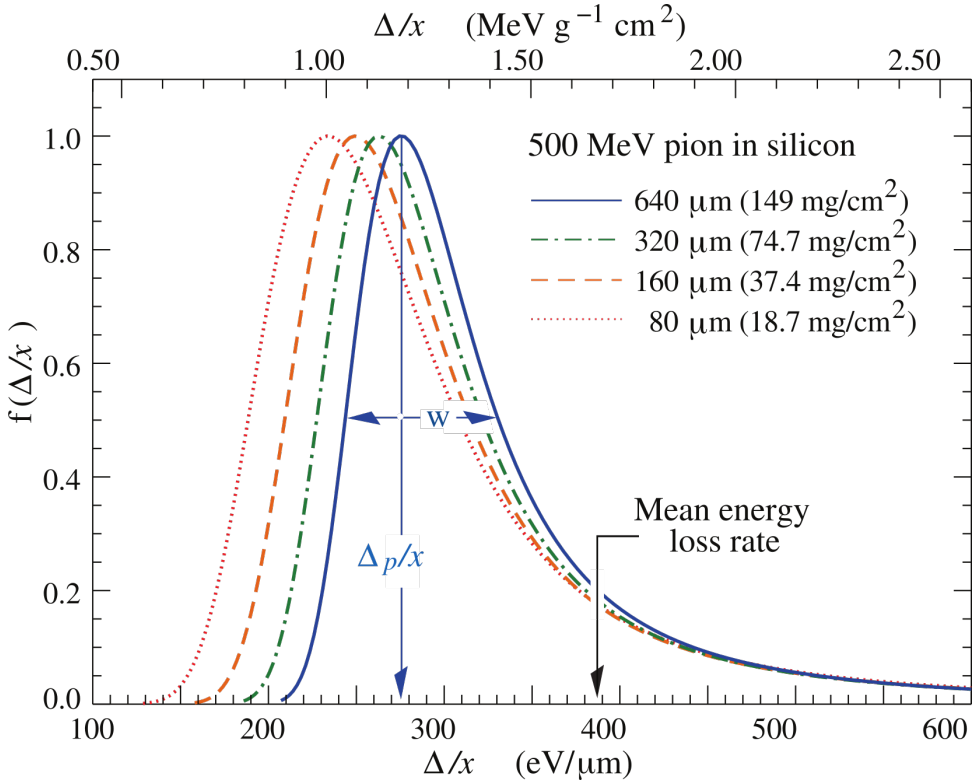

Figure 2.12: Straggling functions in silicon of different thickness for 500 MeV pions normalized to unity at the MPV Δ/x. The skewness of the functions decreases with the thickness of the material but never approaches a Gaussian. The width w of the functions is the full width at half-maximum[50]. Even though these curves are for silicon, the same behavior of the MPV and the mean shown in the figure apply to carbon.

Scattering of Incident Particles

One way in which incident particles deposit energy in the material is by multiple scattering by small angles. These scatterings are primarily due to Coulomb scattering described by the Rutherford cross-section, but they can include contributions from strong interactions if the incident particle has a color charge. Consequently, as a charged particle traverses a material, it will be deflected by small angles. When the particle exits the material, as depicted in Figure 2.13, the 98.9 % of the net deflection and displacement caused by many small-angle scatters follow Gaussian distributions due to the central limit theorem[50].

The theory of Molière describes the scattering angle distributions caused by Coulomb scattering[76]. Using experimental data from Bichsel[77] and Shen et al.[78], Lynch and Dahl approximated the root mean square (RMS) for the central 98 % of the angular distribution of the particles scattering with the following formula[79]:

$$\theta_{plane}^{RMS} = \frac{13.6\,\text{MeV}}{\beta c p} z \sqrt{\frac{x}{X_0}} \left(1 + 0.088 \log_{10}\left(\frac{x z^2}{X_0 \beta^2}\right)\right) \tag{2.13}$$

, where:

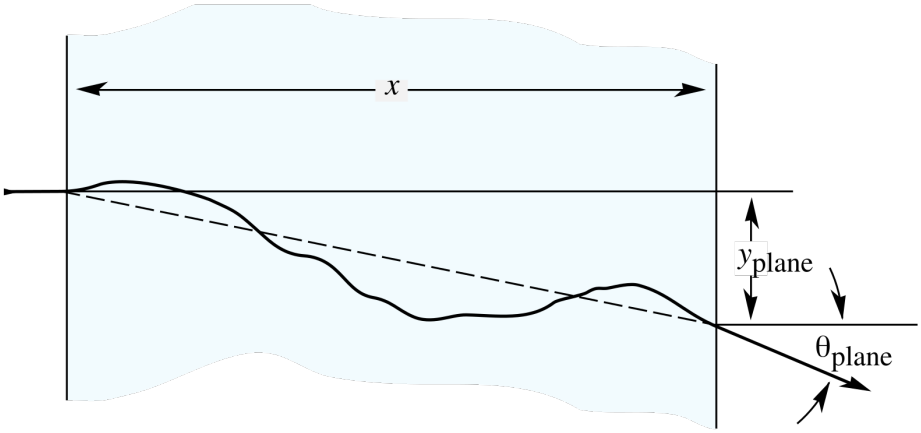

Figure 2.13: Diagram showing the small scatterings inside a material of thickness x. The net deflection is shown as θ_{plane}[50].

z is the charge number of the incident particle

p is the momentum of the incident particle

x/X_0 is the thickness of the scattering medium in radiation lengths

Interactions By Photons

Besides charged particles, photons also deposit energy in diamonds; therefore, diamonds can also be used to detect the passage of photons through them. There are different mechanisms by which photons interact with matter: Through coherent scattering (Rayleigh scattering), atomic photoelectric effect, incoherent scattering (Compton scattering), and pair production. Figure 2.14 shows the cross sections for different energies of the incident photons with diamond.

Rayleigh scattering is the predominant elastic scattering mechanism in which light scatters with particles smaller than the photon's wavelength. As seen in Figure 2.14, the contribution of Rayleigh scattering in the energy ranges shown is negligible, as the atomic photoelectric effect cross section is larger in the low energy ranges.

In the atomic photoelectric effect, the incident photon is absorbed by a core electron which is excited into the conduction band. This excited electron would return to the unexcited state by emitting X-rays or by an Auger electron (which is the process in which the excess energy that would have been released as an X-ray is absorbed by an electron, releasing it from the atom) with lower energy[61].

At medium energies (above $\sim 10\,\text{keV}$), such as X-rays from the K-alpha lines of metals such as Sn (25.7 keV), the main cross section is due to the Compton scattering, where the incident photon is scattered by a valence band electron. In the scattering process, the photon's energy is lowered, deflected from its original trajectory, and the valence band electron is ejected. If enough energy is transferred to the ejected electron, the electron can ionize more electrons or even cause lattice damage[61].

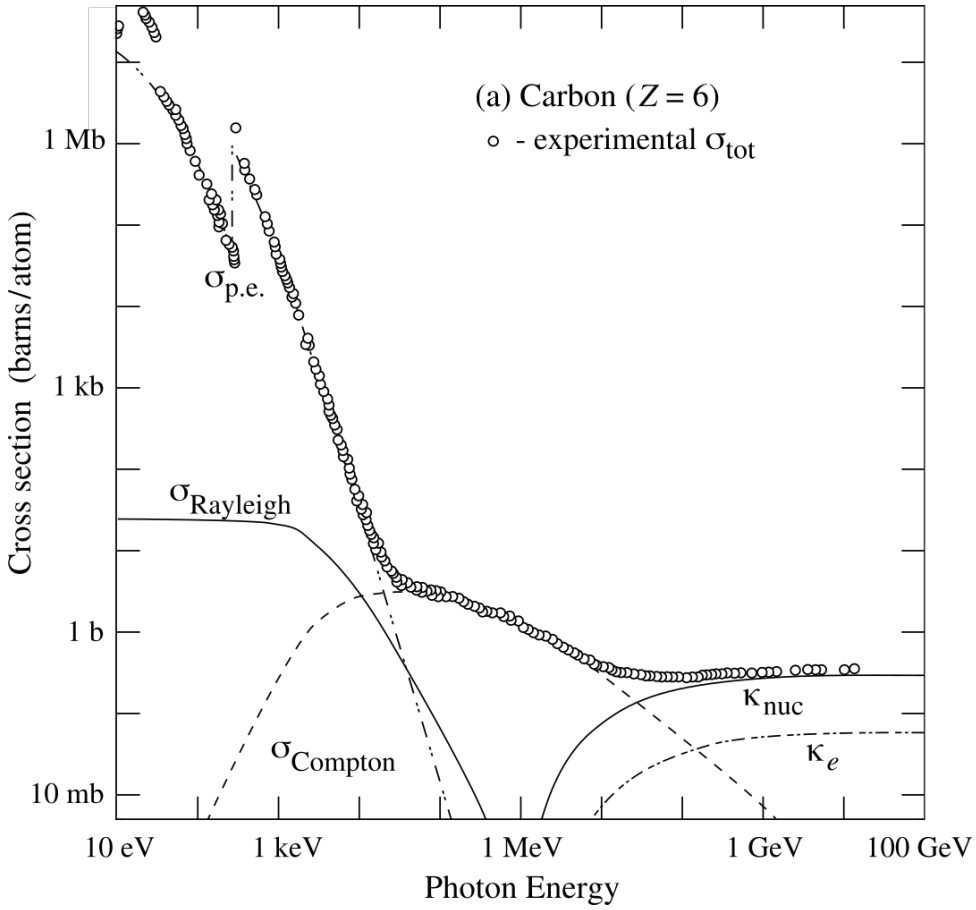

Figure 2.14: Total cross sections as a function of the incident photon energy in carbon.

At energies higher than a couple of MeV (at least twice the electron's mass), the predominant interaction of the photon is the pair production of an electron and a positron. This process occurs mainly through the interaction of the photon with the atom's nucleus and, to a lesser extent, with the atom's electrons. The created electron can ionize more electrons in the material or cause lattice damage in the crystal. The created positrons can ionize electrons in the material and annihilate with an electron to produce lower energy photons[61].

2.5.2 Charge Collection And Signal Formation

The previous section discussed how radiation interacts with a material to generate ionized charges. This section will discuss how these ionized charges inside the sensor generate a signal representing the charge collected by a detector using the sensor.

Diamonds At Room Temperature

Signal formation inside the diamond can be described from a semiconductor perspective. In a semiconductor, the charge transport is carried by electrons in the conduction band and holes in the valence band. These charge carriers are subject to diffusion caused by thermal effects and

are susceptible to electromagnetic fields. As they are not free charge carriers but bound to the crystal's energy bands, effective masses can be attributed to electrons and holes for calculating their transport inside the crystal due to thermal and electromagnetic effects.

Even without the creation of electron holes through ionization, semiconductors have charge carriers thermally excited at room temperature. For this reason, detectors made from silicon must be depleted of the thermally generated charges by creating a pn-junction and reverse-biasing the junction. Thermally generated charge carriers are not a problem in diamond sensors because of their large band gap. The density of electrons thermally excited at room temperature in the conduction band is[80]

$$n_0 \cong N_c e^{-\frac{E_g}{2k_B T}} = 2\left(\frac{2\pi m_n^{DOS} k_B T}{h^2}\right)^{3/2} e^{-\frac{E_g}{2k_B T}} \tag{2.14}$$

, where N_c is the effective density of states available in the conduction band, m_n^{DOS} is the effective density-of-states mass for electrons (which in diamonds is $0.52\,\mathrm{m_e}$[36]), k_B is Boltzmann's constant, T is the temperature, h is Planck's constant, and E_g is the bandgap (5.47 eV in diamonds).

In the case of holes, the density of thermally excited holes at room temperature in the valence band is[80]

$$p_0 \cong N_v e^{-\frac{E_g}{2k_B T}} = 2\left(\frac{2\pi m_p^{DOS} k_B T}{h^2}\right)^{3/2} e^{-\frac{E_g}{2k_B T}} \tag{2.15}$$

, where N_v is the effective density of states available in the valence band, and m_p^{DOS} is the effective density-of-states mass for holes ($0.69\,\mathrm{m_e}$[36] in diamonds).

In intrinsic materials (without dopants), as is the case of the CVD diamonds used as sensors for particle detection, n_0 and p_0 are created in pairs such that the amount of electrons and holes is the same. The intrinsic concentration n_i is defined as shown in Equation 2.16.

$$n_i = \sqrt{n_0 p_0} = \sqrt{N_v \cdot N_c} e^{-\frac{E_g}{2k_B T}} \approx 10^{-27}\,/\mathrm{cm}^3 \tag{2.16}$$

Equation 2.16 shows that at room temperature, essentially, no electrons or holes are expected to be in the conduction band or the valence band, respectively. Therefore, any electron in the conduction band or hole in the valence band is likely to come from the interaction of charged particles or photons with the diamond sensor. For this reason, diamond particle detectors are considered solid-state ionization chambers.

Excited Charge Carriers In An Electric Field

Excited charge carriers (electrons in the conduction band or holes in the valence band) accelerate in the presence of an external electric field until they scatter with other charge carriers or impurities in the lattice. The scattering occurs in random directions, but overall, the charge carriers move parallel to the external electric field at a constant drift velocity. At low electric fields, the speed of the drift velocity is proportional to the electric field's magnitude and the

average time between collisions, and is inversely proportional to the charge carrier's effective transport mass[80]:

$$v_d\left(\vec{r}\right) = \frac{q\tau}{m^*} E\left(\vec{r}\right) \tag{2.17}$$

, where v_d is the speed of the drift velocity, $\vec{r}$ is the spatial position of the charge carrier inside the lattice, q is the elementary charge, τ is the average time between collisions of the charge carrier, m^* is the charge carrier's effective transport mass and E is the magnitude of the external electric field. The quantity proportional to the magnitude of the electric field in Equation 2.17 is called the mobility:

$$\mu \equiv \frac{q\tau}{m^*} \tag{2.18}$$

The net movement of charges inside the crystal gives, as a result, a current that is proportional to the number of charge carriers, their charge, and their speed[80]:

$$\vec{J}_{\text{drift}}\left(\vec{r}\right) = q\left(n\left(\vec{r}\right)\mu_n + p\left(\vec{r}\right)\mu_p\right)\vec{E}\left(\vec{r}\right) = \sigma\vec{E}\left(\vec{r}\right) \tag{2.19a}$$

$$\sigma \equiv q\left(n\left(\vec{r}\right)\mu_n + p\left(\vec{r}\right)\mu_p\right) \tag{2.19b}$$

, where $\vec{J}_{\text{drift}}$ is the current density produced by the movement of the charge carriers, n is the density of the electrons in the conduction band, μ_n is the electrons' mobility in the crystal, p is the density of holes in the valence band, μ_p is the holes' mobility in the crystal and σ is the conductivity of the crystal. This relation is also known as Ohm's law, where a current is proportional to the applied electric field.

At higher electric fields, the drift speed becomes comparable to the thermal velocity of the charge carriers in the lattice. When this happens, an increase in the electric field's magnitude transfers energy thermally into the lattice instead of increasing the drift speed of the charge carrier[80]. This process is not abrupt and has been modeled empirically by Caughey and Thomas[81]:

$$v_d = \frac{E\mu_0}{\left(1 + \left(\frac{E\mu_0}{v_{sat}}\right)^{\beta}\right)^{\frac{1}{\beta}}} \tag{2.20}$$

, where μ_0 is the mobility at low electric fields, v_{sat} is the saturation velocity, and β is the transition parameter which is fitted from empirical data. For scCVD diamond, Pernegger et al.[44] found the above-mentioned parameters which are shown in Table 2.5. These parameters are used as reference in this thesis, although other authors have found other values for other samples[82].

Charge carriers are produced in a localized region near where the ionizing particle passes. Even without an electric field, thermal effects would move the excited charge carriers in the lattice, diffusing them. For this reason, a complete picture of the transport of excited charges must include the diffusion effects caused by random thermal motions in the crystal. This process creates a current from regions with a larger concentration of carriers to regions with a lower concentration of carriers according to Fick's law of diffusion:

Charge carrier	$\mu_0(\mathrm{cm}^2/\mathrm{Vs})$	$v_{sat}(\mathrm{cm/s})$	β
e	1714	9.6×10^6	1
h	2064	14.1	1

Table 2.5: Low field drift mobilities and saturation velocities for diamond. The transition parameter used was $\beta = 1$.

$$\vec{J}_{\text{diff}}\left(\vec{r}\right) = -\left(D_n \vec{\nabla} n\left(\vec{r}\right) + D_p \vec{\nabla} p\left(\vec{r}\right)\right) \tag{2.21}$$

, where D_n and D_p are the electrons' and holes' diffusion constants, respectively. These constants are related to the mobilities by the Einstein relation:

$$D = \frac{\mu k_B T}{q} \tag{2.22}$$

Combining Equations 2.19a and 2.21, gives the total current density of the excited charge carriers inside the sensor:

$$\vec{J}\left(\vec{r}\right) = \vec{J}_{\text{drift}}\left(\vec{r}\right) + \vec{J}_{\text{diff}}\left(\vec{r}\right) \tag{2.23}$$

Induced Current And Shockley-Ramo Theorem

The previous section discussed how excited charge carriers move inside a sensor due to an electric field in the sensor and by thermal diffusion. This section discusses the effects the excited charge carriers have on the space charge near the electrodes.

The electric field generated by a charge inside the sensor will generate a surface charge on each of the electrodes on the sensor. Assuming the electrodes on the sensor's surface are perfect conductors, then the parallel component to the conductor's surface of the electric field on each of the conductors must be zero, which means that all the field lines are perpendicular to the conductors' surfaces. Any Gaussian surface containing any of the conductors would contain a net charge inside their volume. The total sum of the induced charges on all conductors equals the charge inside the sensor with the opposite sign. Figure 2.15 shows an example of this effect.

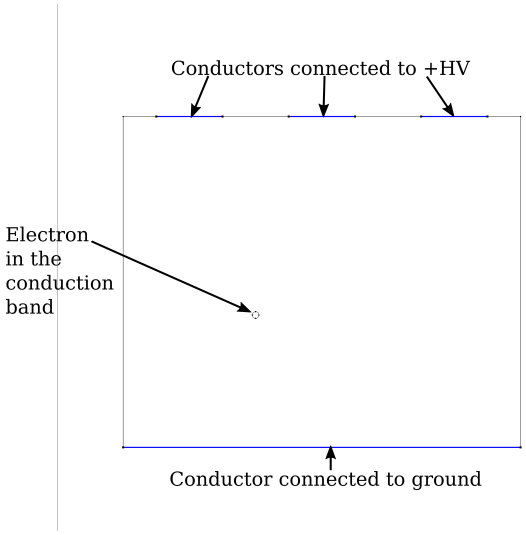

(a) Diagram of an electron inside a diamond.

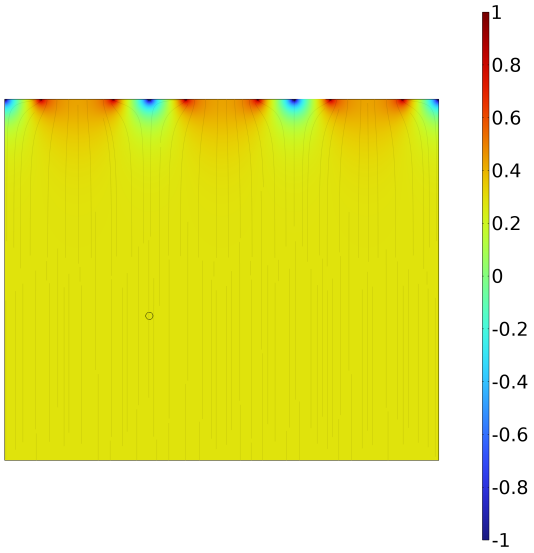

(b) Electric field inside the diamond sensor.

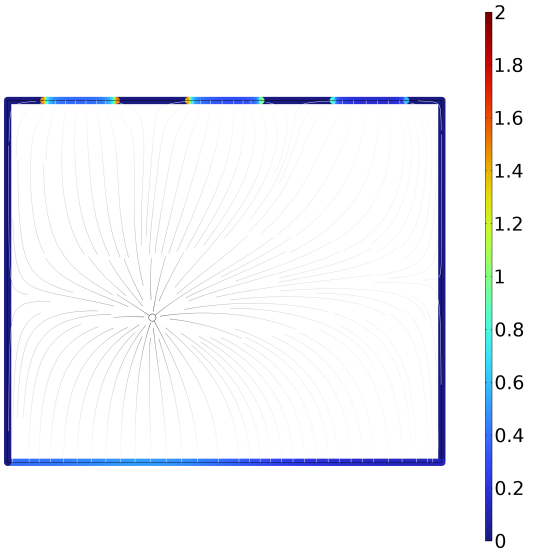

(c) Induced charge by the electron on the conductors at t_0.

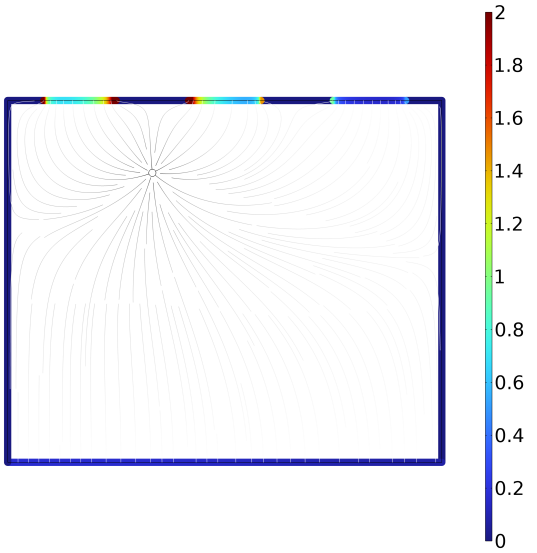

(d) Induced charge by the electron on the conductors at t_1.

Figure 2.15: In (a), the model of an electron in the conduction band inside a diamond. The diamond has a metal electrode at the bottom, connected to the ground, and three metal electrodes on the top connected to a positive bias voltage $+HV$. In (b), the electric field of the model presented in (a) is shown. The color scale in (b) depicts the electric field strength in a logarithmic scale. In (c), the induced charge by the electron at that instant, t_0, is shown in each of the electrodes. As the electron moves upwards due to the electric potential difference across the diamond, the induced charge on the electrodes would change, as is shown an instant later, t_1, in (d). The color scale in (c) and (d) depicts the amount of charge per unit area induced on the electrodes in arbitrary units. The gray lines inside the diamond, depict the electric field lines caused only by the electron.

In the example, a diamond sensor has biased electrodes on the top and bottom, generating an electric field across the sensor. An excited electron inside the sensor at a time t_0 generates surface charges on each of the electrodes on the sensor by means of its electric field. At a later time, t_1, the excited electron will be in a different position, changing the electric field and the induced charge on each sensor's electrodes. The change in time of the surface charge on each of the electrodes generates a current.

Instead of calculating the electric field of each charge carrier and the induced charge on each electrode for every instant of the trajectory of the charge carrier's motion, Shockley[83] and Ramo[84] independently developed a simpler method to calculate the induced charge on each of the electrodes. Although the method was initially applied to vacuum tubes, it was later proven that it could also be used for semiconductor detectors[85, 86]. Nowadays, the method is known as the Shockley-Ramo theorem.

The method splits the problem into two parts. The first one treats the kinematics of the charge carrier due to the transport mechanisms discussed in the previous section. The second part treats the coupling of the charge carrier with the electrode under study. In the example in Figure 2.15, the kinematics of the electron is determined by the electrodes' configuration. With the biasing shown in Figure 2.15a, the electrodes would generate an almost uniform vertical electric field in the sensor, as shown in Figure 2.15b. Then, ignoring the diffusion effects for simplicity, the electron in the example would move upwards with a constant velocity determined by the electric field's strength.

The second part, which is the coupling of one of the electrodes with the charge carrier, is mostly a geometric problem and is determined by calculating the "weighting field" of the electrode in question. This field is generated by setting the electrode of interest at a potential of 1 V, grounding the rest of the electrodes, and removing any charge carriers from the sensor[87]. A detailed demonstration of this method can be found in the reference [87].

Continuing with the example introduced above in Figure 2.15, selecting the upper-left electrode as the electrode of interest, the weighting field of the electrode is calculated as shown in Figure 2.16. In these figures, the instantaneous velocity of the electron is depicted with a blue arrow, and the weighting field vector at the electron's position is depicted with a black arrow.

Knowing the weighting field of the electrode and the velocity of the particle, the induced current in the electrode can be calculated following Equation 2.24[87]:

$$i_j(t) = -\frac{q}{1\,\mathrm{V}}\vec{v}\left(\vec{E}\left(\vec{r}\,(t)\right)\right)\cdot\vec{E}_j\left(\vec{r}\,(t)\right) \tag{2.24}$$

, where at a time t, i_j is the instantaneous current induced in the electrode j, q is the charge of the particle, $\vec{r}$ is the position of the particle, $\vec{v}$ is the velocity of the particle due to the sensor's electric field, $\vec{E}$ is the electric field inside the sensor at the particle's position, and $\vec{E}_j$ is the weighting field of electrode j at the particle's position.

For each electrode, integrating the induced charge over time gives the charge collected by that electrode:

$$Q_{coll_j} = \int i_j(t)\mathrm{d}t \tag{2.25}$$

The charge collection was previously mentioned in the definition of the CCE in Equation 2.3.

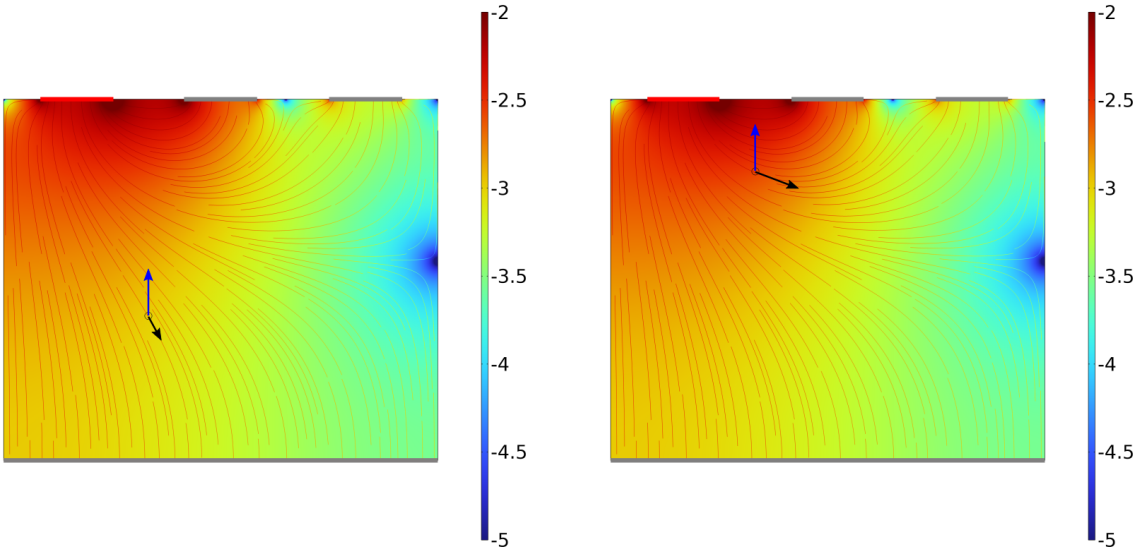

(a) Electron inside the weighting field at instant t_0.

(b) Electron inside the weighting field at instant t_1.

Figure 2.16: Snapshots of the electron inside the diamond sensor at two different times, t_0 in (a) and t_1 in (b). The color maps and the field lines depict the weighting field intensity when the electrode on the top highlighted in bright red is at 1 V, while the other electrodes highlighted in gray are at 0V. The color scale is in logarithmic scale. The colored lines depict the direction of the weighting field. The blue vector pointing upwards from the electron represents its velocity in each instance, while the black vector pointing slightly downwards (always in the direction of the weighting field lines) represents the direction and strength of the weighting field in the electron's position.

Applying the Shockley-Ramo theorem on a parallel plate particle detector, where the sensor's charge carriers have MFPs λ_e and λ_h for electrons and holes, respectively, gives:

$$Q_{coll} = Q_{ion} \sum_{\mathrm{i=e,h}} \frac{\lambda_\mathrm{i}}{\mathrm{Th}} \left(1 - \frac{\lambda_\mathrm{i}}{\mathrm{Th}} \left(1 - \mathrm{e}^{-\frac{\mathrm{Th}}{\lambda_\mathrm{i}}}\right)\right) \tag{2.26}$$

, where "Q_{ion}" is the number of ionized eh-pairs multiplied by the elementary charge, and "Th" is the thickness of the sensor which is also the distance between the electrode plates. In the limit, when $\lambda_{\{e,h\}} \to \infty$, $Q_{coll} \to Q_{ion}$

2.6 Particle Detector Electronics

In the previous section, it was seen that the induced current on an electrode must be integrated to collect the total induced charge on the electrode. For this, a preamplifier in a charge-sensitive configuration can be used.

2.6.1 Signal Preamplifier

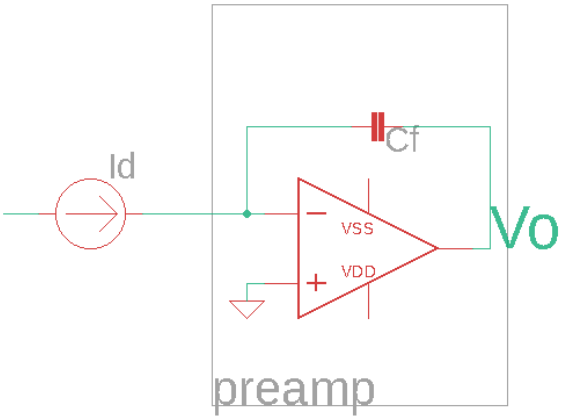

Figure 2.17: Preamplifier in a charge-sensitive configuration. The feedback capacitance integrates the input current.

Figure 2.17 shows a preamplifier in a charge-sensitive configuration. In this configuration, in an ideal operational amplifier with an infinite gain, the input current I_d is integrated through the feedback capacitor C_f.

The output voltage from the amplifier, Vo, is equal to:

$$Vo(t) = -\frac{1}{C_f}\int_0^t I_d(\tau)\mathrm{d}\tau \tag{2.27}$$

For example, suppose the input current I_d is a square pulse with a width of 1 ns. Then, the resulting output voltage from the preamplifier Vo would behave like the one shown in Figure 2.18.

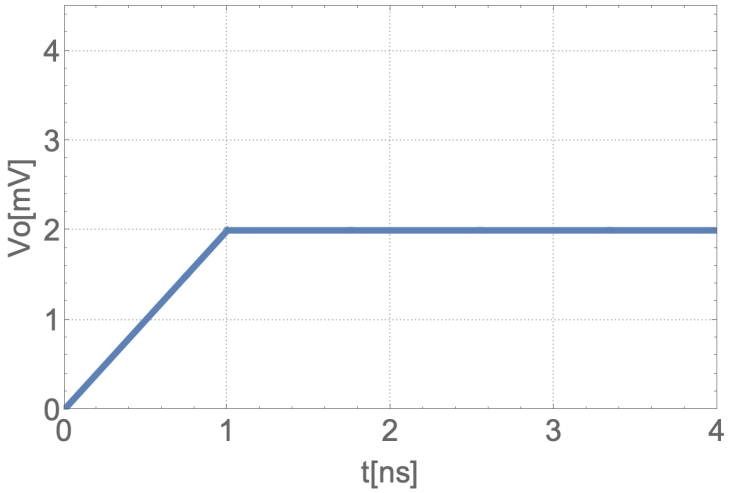

Figure 2.18: Preamplified signal from a square pulse with a width of 1 ns

A problem arises with the configuration shown in Figure 2.17 when more than one particle is incident on the detector. When this happens, a pileup effect, as shown in Figure 2.19, occurs. After several particles, the amplifier would reach saturation.

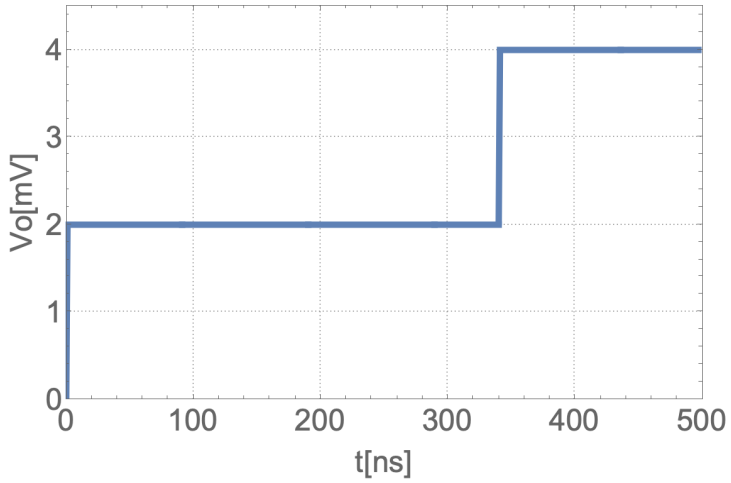

Figure 2.19: Two pulses piling up with each other. The pileup will continue until the amplifier reaches saturation.

A solution to this problem is to discharge the capacitor before the expected time of arrival of a second particle. This can be achieved by placing a large resistor R_f in parallel to the feedback capacitor C_f as shown in Figure 2.20, such that the capacitor discharges with a time constant given by $R_f C_f$. This constant has to be large enough to allow the next stage, the shaping circuit, to process the signal.

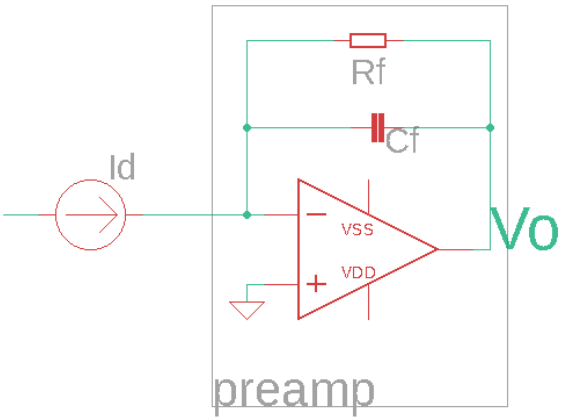

Figure 2.20: Preamplifier in a charge-sensitive configuration with a feedback resistor to discharge the capacitor between the input current pulses.

With the addition of the resistor, the resulting output voltage would be:

$$Vo(t) = -\frac{1}{C_f}\int_0^t I_d(\tau) e^{-\frac{t-\tau}{R_f C_f}} U(t-\tau)\mathrm{d}\tau \tag{2.28}$$

, where U is the step function. For large $R_f C_f$ values, the current integration is unaffected, and the capacitor would discharge after the current pulse has finished, as shown in Figure 2.21.

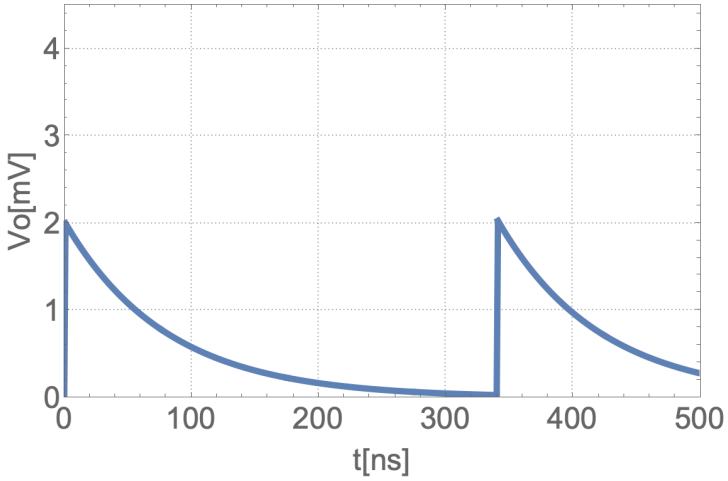

Figure 2.21: Preamplified signal of two current pulses with a small pileup. The capacitor's discharge must be fast enough to avoid large pileups leading to amplifier saturation.

2.6.2 Signal Shaper

The main objective of the shaping circuit is to limit noise by reducing the bandwidth. A common way to achieve this is by applying a high-pass filter, followed by one or several stages of low-pass filters. This shaper configuration is known as a CR-$(RC)^n$ shaper, where n is the number of consecutive RC stages. Another objective of the shaping circuit is to establish the signal gain and to define the signal's peaking time, which is essential to set a predictable sampling time to measure the amplitude of the shaped signal[87]. Figure 2.22 shows a schematic of a CR-RC shaping circuit.

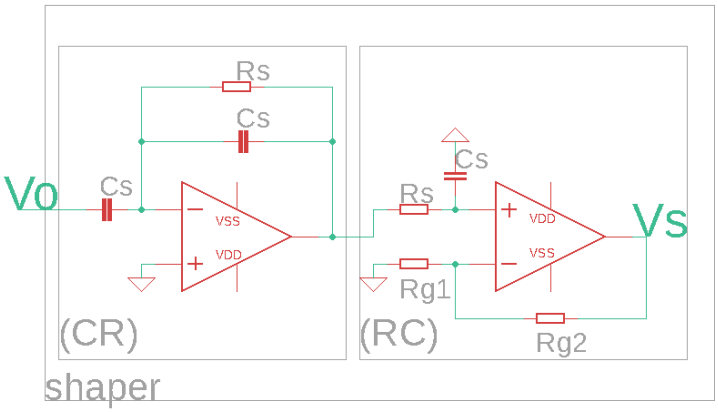

Figure 2.22: Schematic circuit of a CR-RC shaper which has the same time constant for the CR part as for the RC part. The time constants are set by the capacitors C_s and the resistors R_s. The resistors R_{g1} and R_{g2} set the gain of the shaped signal.

Each part of the shaping circuit could have different values for the cutoff frequencies, but the one that reduces the noise the most is when the cutoff frequency for the high-pass filter is the same as for the low-pass filters[87, 88]. The transfer function in the s-plane of a shaper circuit of the form CR-$(RC)^n$ with the same cutoff frequencies for the high-pass and low-pass filters is the following:

$$H(s) = \frac{s\tau_0}{1+s\tau_0} \cdot \left(\frac{A}{1+s\tau_0}\right)^n \tag{2.29a}$$

$$A \equiv \frac{R_{g2}}{R_{g1}} + 1 \tag{2.29b}$$

$$\tau_0 \equiv R_s C_s \tag{2.29c}$$

, where τ_0 is the time constant that determines the cutoff frequency of the filters, A is the gain of the shaping circuit set by the resistors R_{g1} and R_{g2}, and n is the number of (RC) stages in the circuit.

Ideally, the output from the preamplifier is a step function with an amplitude equal to the collected charge Q_{coll} divided by the feedback capacitor of the preamplifier C_f. Using the transfer function of the shaper, the shaped signal can be calculated:

$$Vs(s) = Vo(s) \cdot H(s) \tag{2.30a}$$

$$Vs(s) \cong \frac{Q_{coll}}{C_f} \cdot \frac{1}{s} \cdot H(s) \tag{2.30b}$$

$$Vs(t) = \frac{Q_{coll}}{C_f} \cdot \frac{A^n e^{-\frac{t}{\tau_0}}}{n!} \cdot \left(\frac{t}{\tau_0}\right)^n \tag{2.30c}$$

$$VsMax \equiv Vs(t = n\tau_0) = \frac{Q_{coll}}{C_f} \cdot \frac{A^n n^n}{e^n n!} \tag{2.30d}$$

The shaped signal reaches its maximum value at time $T_p \equiv n\tau_0$, which is the peaking time of the shaper. The peak value of the shaped signal at time T_p is $VsMax$ which is proportional to the collected charge Q_{coll}. Figure 2.23 shows different shaped signals scaled to their maximum value.

The duration of the shaped signal (which is the time it takes for the signal to be less than 0.1 % of the amplitude $VsMax$) is $\sim 10\sqrt{n}\tau_0$. The duration of the shaped pulse has to be shorter than the estimated time of arrival between particles; otherwise, the shaped signals would pile up. Also, in practice, the input signal is not a step function, as it has a rise time that depends on the duration of the current pulse from the detector. To avoid "ballistic deficit" (when the shaping time is comparable to the integration time of the current) which leads to a deficit in the shaped signal, the peaking time T_p must be at least three times the current pulse duration from the detector. These and power limitations are the considerations that need to be taken into account when choosing or designing the electronics to read out the detector's signals.

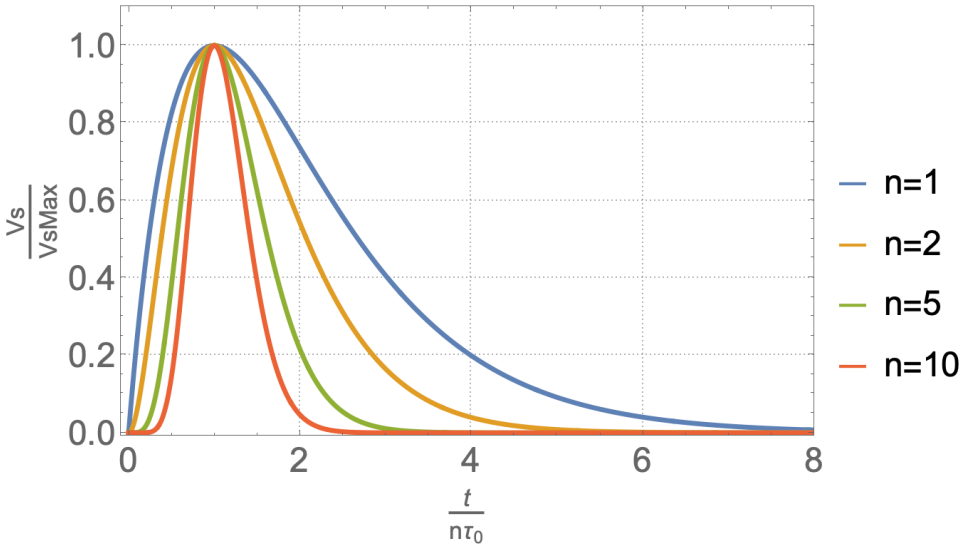

Figure 2.23: Shaped signals for different number of (RC) stages. The more RC stages, the more symmetric the output signal becomes.

Part II

Tested Diamond Devices

Chapter 3

Pixelated Planar Diamond Samples

The following section describes the electronics used to read out the diamond sensors, as well as a description of the geometry used for the sensors' pixels and the characteristics of the diamonds used for the sensors, which were tested during test beams at the PSI in 2018 and 2019.

The readout chip (ROC) used to couple with the sensors was the psi46digV2.1-respin, which could be tuned to a low threshold, which is convenient to read the small signals produced by 500 µm thick pCVD diamond sensors. Additionally, there was abundant familiarity with the ROC as the institute participated in the phase I commissioning of the CMS experiment, which included handling and testing the psi46digV2.1-respin ROC.

3.1 Readout Chip Characteristics

As mentioned above, the ROC used for the hybrid detectors was the psi46digV2.1-respin developed at the PSI. This chip consists of a two-dimensional array of pixel unit cells (PUC) distributed in 80 rows and 52 columns (see Figure 3.1). Each PUC is 150 µm×100 µm and has analog and digital domains. The total active area for the 4160 PUCs in the ROC is 7.8 mm×8 mm. At the bottom of the ROC lies the periphery, which contains the buffers, analog-to-digital converter (ADC), and the wire bond connections used to communicate with the ROC.

Figure 3.2 shows a diagram of a PUC in the ROC. The analog domain of the PUC consists of a bump pad, a charge-sensitive preamplifier, a shaper, a threshold comparator, and a sample and hold circuit. The bump pad is the interface between the sensor and the rest of the PUC that transmits the signal created by the sensor when an ionizing particle passes through it. This signal is integrated by a charge-sensitive preamplifier. The preamplified signal is then shaped by the shaper circuit such that the peak of the shaped signal is proportional to the charge integrated by the preamplifier.

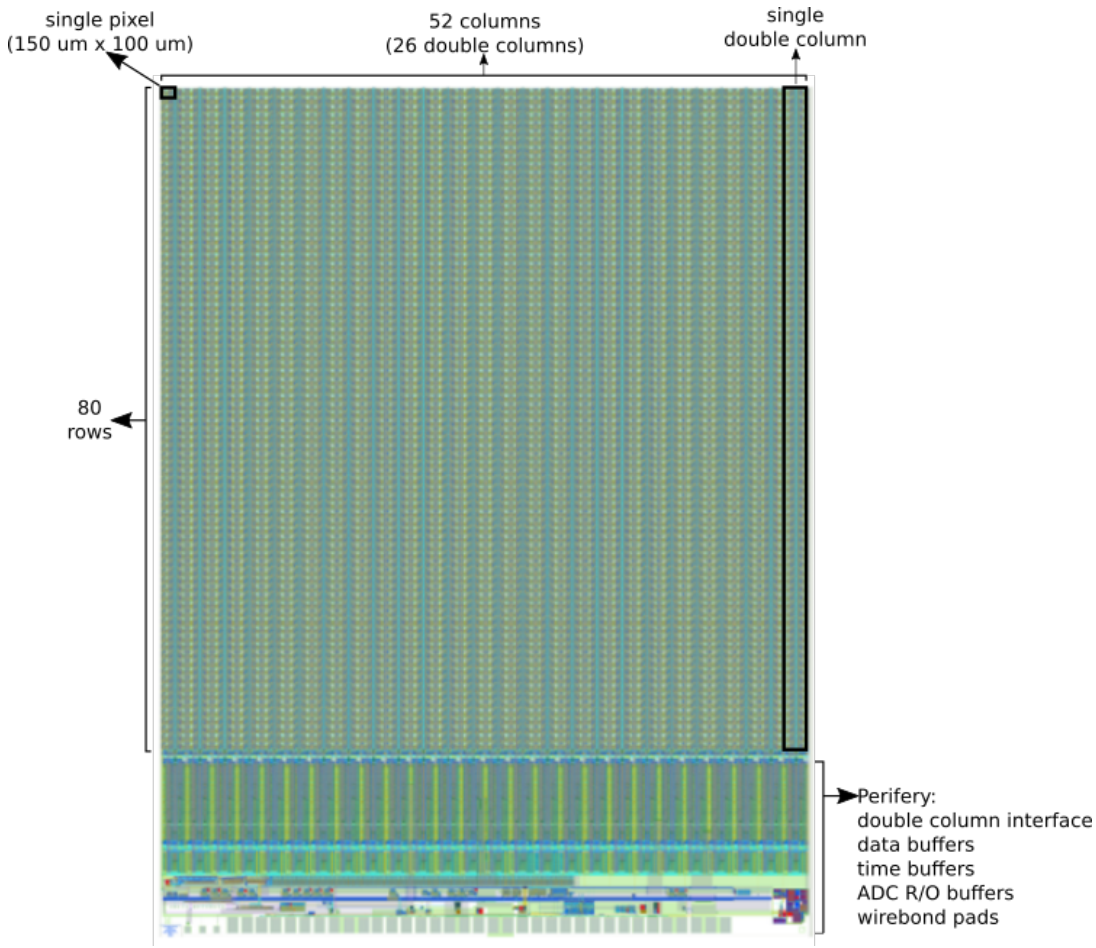

Figure 3.1: The geometry of the psi46digV2.1-respin. The chip consists of 4160 PUCs arranged in 80 rows and 52 columns. Each PUC is 150 µm×100 µm [89]

To limit the amount of transmitted data, a comparator is used to discriminate the signals from the noise through an adjustable threshold which is adjusted using the digital-to-analog converters (DAC) *VTHRCOMP*, *trim bits*, and *VTRIM*. Signals that surpass the threshold are stored by the Sample and Hold circuit, which is activated after a delay to store the peak of the signal coming from the shaper in the Sample and Hold capacitor.

The digital domain is responsible for communicating with the periphery to notify when a signal is above the threshold. When this happens, the PUC is set to a state where it cannot receive further hits before the periphery reads out the signal's pulse height stored in the Sample and Hold capacitor. Up to this point, the signal processing has been asynchronous, and it is the task of the digital domain of the PUC to synchronize the data with the periphery that operates at 40 MHz. The last task of the digital domain before releasing the PUC for further data-taking is to transfer the pixel address and the pulse height to the periphery, where the pulse height is digitized.

To read out individual ROCs, the samples were mounted on a printed circuit board (PCB) that interfaced with an adapter plane that communicated with the digital test board (DTB). The DTB was designed at PSI to provide the ROC with a 40 MHz clock signal, configuration

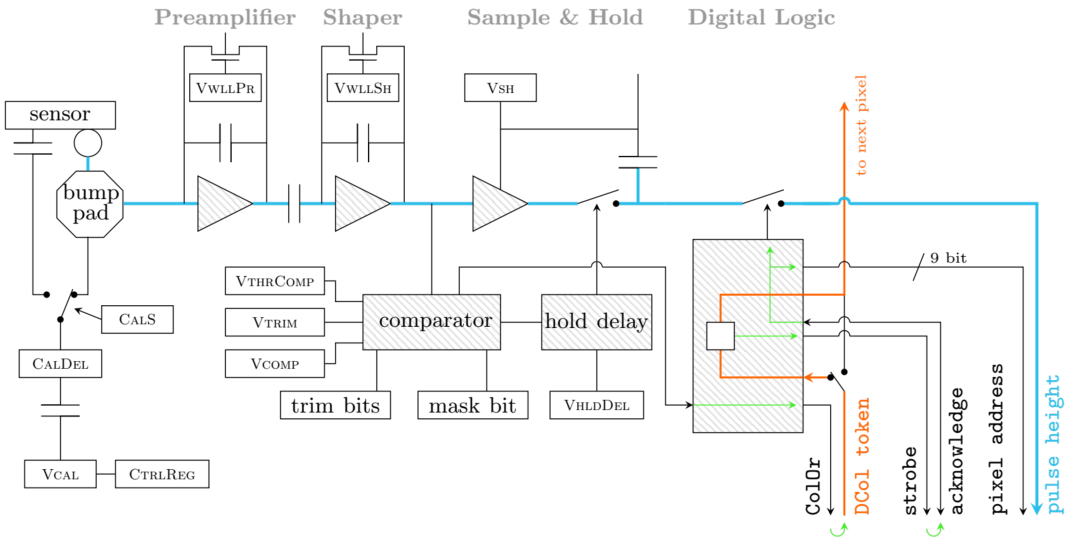

Figure 3.2: Simplified schematic of the PUC of the psi46digV2.1-respin ROC. Signals from ionization particles are transferred to the preamplifier by the bump pad. The integrated charge is then transferred to the shaper circuit and later to the sample and hold circuit before being transferred to the periphery.[90]

commands, and to supply high voltage (HV) if it was not delivered directly to the sensor. The DTB communicated with a computer via USB to store the data read from the ROC and to send the configuration commands to configure the ROC. Figure 3.3 shows how the ROC mounted on the PCB interfaces with the adapter plane and the DTB.

3.2 Pixelated Diamond Detector Characteristics

To make the diamond sensor compatible with the ROC, it was required to process the diamond to have a pixelated structure that matched the two-dimensional array of PUCs of the ROC. For this task, metal pads with a size 10 µm smaller than the size of the PUC (i.e., metal pads of 140 µm×90 µm) were placed on the top surface of the sensor, while a square back-plane of 8.1 mm was placed on the bottom surface of the sensor. The side that was defined as top or bottom depended on the characteristics of the diamond when they were first tested, such that the best IV-relation and charge collection were obtained from the diamond.

This arrangement achieved a uniform electric field across most of the sensor, except in the regions between the pixels and the sensor edges. The designs for the metallization patterns for the top and the bottom of the sensor can be seen in Figure 3.4. A section surrounding one pixel traversed by an ionizing particle is shown in Figure 3.5, showing how the ionized charge carriers drift due to the almost uniform electric field generated by the metalized electrodes.

To couple the sensor with the psi46digV2.1-respin ROC, it was necessary to place conductive bumps on each pixel that could connect the pixelated metallization pattern on the top surface of the sensor with the bonding pads present on the surface of the ROC's PUCs. Chapter 6 will discuss the fabrication process developed to achieve this and the conditioning of the diamond to

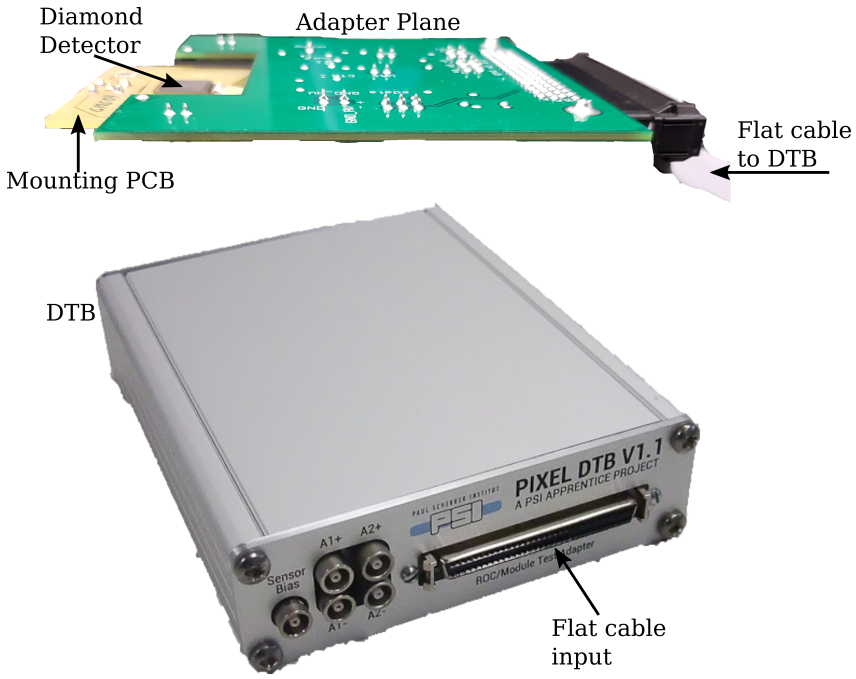

Figure 3.3: Diamond detector mounted on a PCB that connects with an adapter plane. The plane communicates with the DTB using a flat cable.

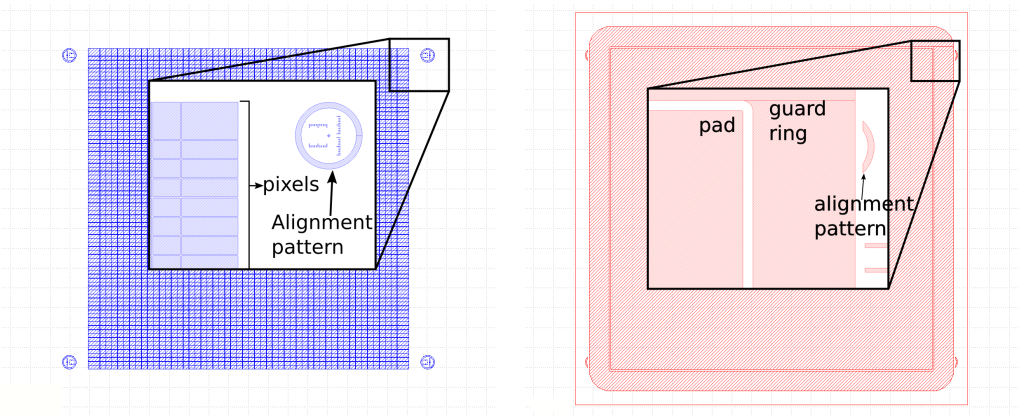

(a) Top side - pixels side.

(b) Back side - HV side.

Figure 3.4: Layouts of the metallization implemented to produce a uniform field through the sensor. A zoom into the top-right corner is shown.

make it a suitable sensor.

3.3 Sensors Characteristics

The samples used to make the pixelated sensors had already been processed by the manufacturer[91]. The samples had a size of $\sim 1\,\text{cm} \times 1\,\text{cm}$ and a thickness of $\sim 500\,\mu\text{m}$, except for one

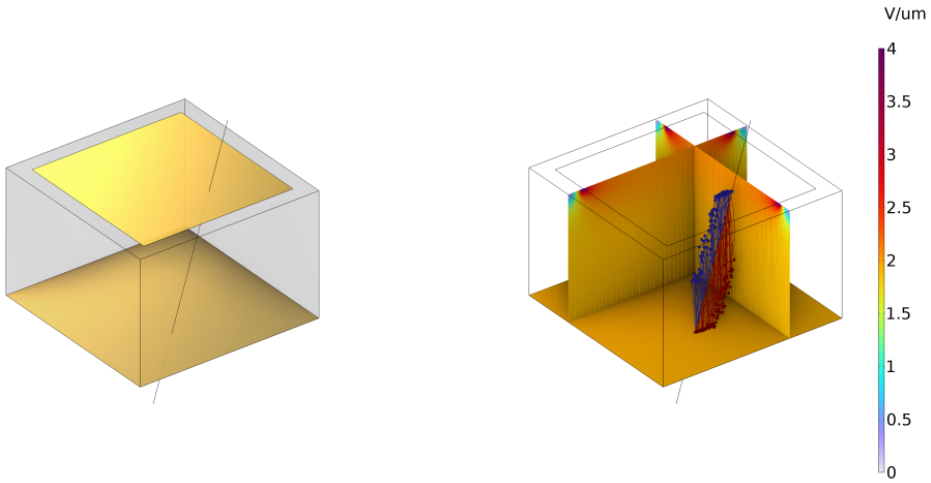

(a) Section of a pixel in a pixelated planar detector.

(b) Electric field inside the detector and the transport of ionized charges.

Figure 3.5: Diagram showing a section of a pixel in a planar detector being transversed by a ionizing particle. In (a), the metallizations on the top and bottom of the sensor are shown in gold and the trajectory of the ionizing particle is represented by the traversing line. In (b), the uniform electric field by applying an electric potential across the top and bottom metallizations is shown with the color pallet and the colored lines depicting the field lines. The red and blue dots and lines, depict the movement of ionized holes and electrons respectively in the detector towards the electrodes (metallization).

sample that was ~ 750 µm thick. The larger faces of the sample were mechanically polished by the manufacturer[91] to homogenize the surfaces and facilitate the fabrication processes.

Table 3.1 summarizes the characteristics of the diamond samples that were processed to make planar pixelated sensors with the fabrication process developed, which will be discussed in Chapter 6. The samples were tested and characterized at Ohio State University by Harris Kagan.

Sample	Identification	Irradiation Type	Fluence	Thickness (µm)	CCD (µm)
CMS04	02A08725	None	None	540*	229*
CMS01	02A08722	None	None	530*	206*
CMS02	02A08723	None	None	540*	201*
II6-93	02A09273	None	None	460*	248*
II6-750	02A09220	None	None	695*	232*

Notes:
* Measured by the RD42 collaboration

Table 3.1: Information of the samples that were made into planar pixel detectors.

Chapter 4

3D Diamond Samples

The following section describes the electronics used to read the information from the diamond sensors, as well as a description of the geometry used for the sensors strips and the characteristics of the diamonds used for the sensors, which were tested during test beams at CERN in 2016, 2017 and 2018. These detectors were part of the effort of the RD42 collaboration to research 3D detectors made with diamonds.

The detectors tested at CERN were strip detectors coupled to the experimental setup for data taking used by the RD42 collaboration. The setup will be described in more detail in section 9.2. The following section describes the chip used to read out the strips on the sensors. Afterwards, a description of the sensors will be given.

4.1 Charge Sensitive Amplifiers Based On VA ASICs

The electronics used to read each strip of the sensors were the VA2.2 Application-specific integrated circuits (ASIC) from IDEAS[92]. The VA2 and VA2.2 ASICs consist of 128 low-noise and low-power channels with charge-sensitive preamplifier, shaper, and sample and hold circuits. The sample and hold (S&H) circuit's analog output is multiplexed with a maximum read-out speed of 10 MHz. The clock signals to each VA chip are supplied by the VME's[1] data acquisition (DAQ) system. Figure 4.1 shows the internal architecture of the VA chip and the connection via wire bonds of the strips on the detector with the channels in the VA chip. The detectors were biased with a DC HV source through a series resistor and a parallel capacitor to the ground to limit the current delivered to the VA chip and shunt the noise from the source, respectively.

[1] Versa Module Europa bus standard

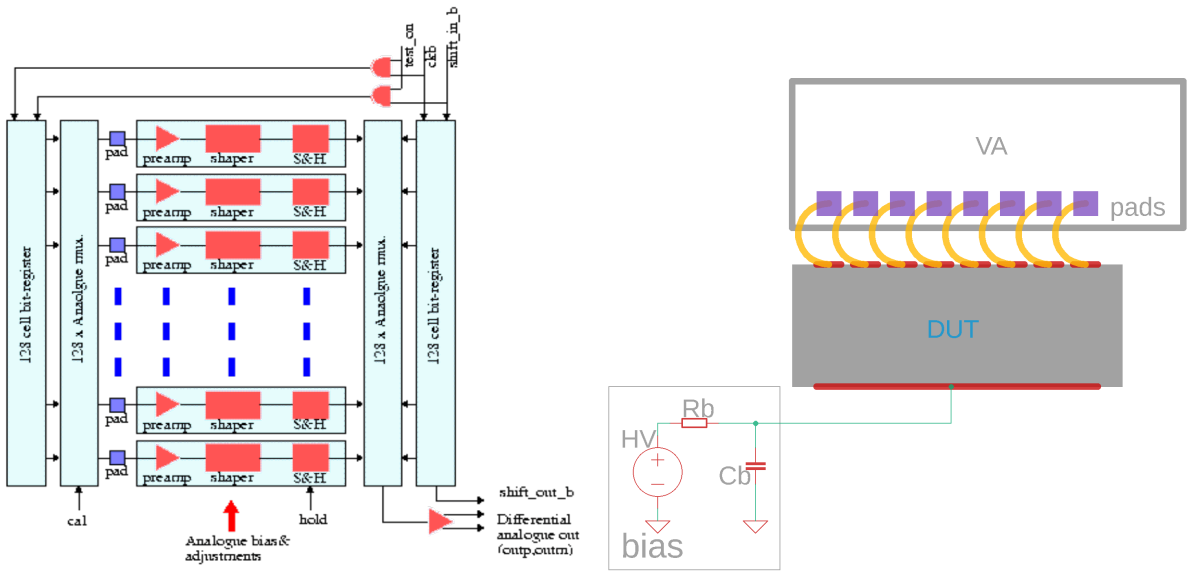

(a) VA2 and VA2.2 architecture

(b) DUT connection to the bias and to the VA2.2 chip

Figure 4.1: Each of the 128 detector strips was wire bonded to a pad just before the preamplifier. As shown in (a), for each channel, the signal was preamplified, shaped, and then sampled and held. An analog multiplexer selected the sampled and held signal one channel at a time, and the analog signal was sent to the outside via a differential analog buffer. In (b), the diagram shows how each of the channels is wire-bonded to the VA chip on one side, while the other side is biased with a HV source through a resistor R_b and a capacitor C_b to filter the noise from the HV source.[93]

4.1.1 Electronic Noise Sensed By The VA Chip

The Equivalent Noise Charges (ENC) for each channel of the VA chip results from the preamplifier's internal series and parallel noise, plus other noise sources due to the components connected to the VA chip's channel. The noise from the VA was modeled as a series noise voltage source (V_{as}) connected to one of the amplifier's inputs and as a parallel current noise source (I_{ap}) connected between the amplifier's inputs. Figure 4.2 shows the schematic representation of the setup with the mentioned noise sources and their representations as voltage sources for series noise or current sources for parallel noise. In general, most of the series noise of the preamplifier comes from the internal input field-effect transistor (FET)[87], whose noise is proportional to the total capacitance connected to the preamplifier's input. In contrast, the parallel noise of the preamplifier is driven by the leakage current flowing into the amplifier[94]. These quantities were characterized by the manufacturer IDEAS[92] and are given as the intrinsic noise of the VA chip for different peaking times (T_p).

In terms of the electron charge q, the internal noise of the VA2 chips used for the telescope's silicon planes is shown in Table 4.1, and the noise for the VA2.2 chips used for the devices under test (DUT) is shown in Table 4.2 as specified by the manufacturer IDEAS[92]. The RD42 collaboration set the peaking time for the VA2.2 chip to 1.8 µs for all measurements presented in this work[95]. This peaking time gives an interpolating noise to first order of 64 q + 11.8 q/pF.

Peaking Time (µs)	VA2 Noise
1.5	125 q + 14.4 q/pF
2	135 q + 12.3 q/pF

Table 4.1: Characterized noise of the VA2 chips according to the manufacturer IDEAS.[94]

Peaking Time (µs)	VA2.2 Noise
1	80 q + 15 q/pF
2	60 q + 11 q/pF
1.8*	64 q + 11.8 q/pF
Notes: * Interpolated value using the values given by the manufacturer for 1 µs and 2 µs peaking times.	

Table 4.2: Characterized noise of the VA2.2 chips according to the manufacturer IDEAS.[93]

The other sources of ENC for each channel of the VA2.2 chip, besides the internal ENC of the preamplifier, were the leakage current contribution (parallel noise) and the biasing resistor contribution (series noise). The following equations show the three main noise contributions: (See Appendix A for a detailed explanation of how these results were obtained.)

$$ENC_{VA} \cong 64\,\mathrm{q} + \frac{11.8\,\mathrm{q}}{\mathrm{pF}} C_d \tag{4.1a}$$

$$ENC_{I_d} \cong \frac{e}{2}\sqrt{\mathrm{q} I_d T_p} \tag{4.1b}$$

$$ENC_{R_b} \cong e\frac{C_d}{C_b}\sqrt{\frac{k_B T T_p}{2R_b}} \tag{4.1c}$$

, where "q" is the charge of the electron, "C_d" is the total capacitance from the sensor strip connected to the preamplifier input, "e" is Euler's number, "I_d" is the leakage current from the sensor strip, "T_p" is the peaking time of the preamplifier, "R_b" is the biasing resistor, "C_b" is the shunting capacitance for the HV, "k_B" is Boltzmann's constant and "T" is the temperature. As the ENC assumed the 1.8 µs interpolation for the peaking time mentioned above, then $T_p = 1.8\,\mu\mathrm{s}$. A typical value used for the HV shunting capacitor during the test beams was $C_b = 2.2\,\mathrm{nF}$. Assuming the values mentioned above, a temperature of 20 °C, the leakage current in nA, the load capacitance in pF, and the bias resistor in MΩ, the noise from Equations 4.1 can be expressed as:

$$ENC_{VA} \cong 64\,\mathrm{q} + 11.8\,\mathrm{q} C_d[\mathrm{pF}] \tag{4.2a}$$

$$ENC_{I_d} \cong 144.1\,\mathrm{q}\sqrt{I_d[\mathrm{nA}]} \tag{4.2b}$$

$$ENC_{R_b} \cong 0.5\,\mathrm{q}\frac{C_d[\mathrm{pF}]}{\sqrt{R_b[\mathrm{M\Omega}]}} \tag{4.2c}$$

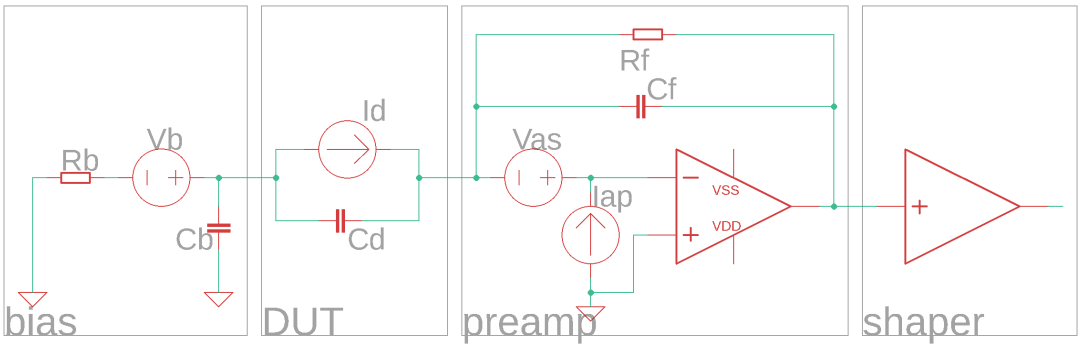

Figure 4.2: Schematic for the noise calculations. Only the noise sources are shown. The preamplifier had a series noise source V_{as} and a parallel noise source I_{ap}. The DUT's noise came from the leakage current, modeled as a parallel current source I_d. The biasing resistor R_b introduced thermal noise, modeled as a series voltage source V_b. Before being shaped, these noise sources would be preamplified through the feedback resistor and capacitor R_f and C_f, respectively.

The total noise, which manifested itself as fluctuations of the channel's baseline voltage (*pedestal*), is then:

$$ENC_{Total} = \sqrt{(ENC_{VA})^2 + (ENC_{I_d})^2 + (ENC_{R_b})^2} \tag{4.3}$$

To illustrate the different ENC expected while measuring diamond strip detectors, two examples were considered: a planar strip detector and a 3D strip detector. For the planar strip detector, if the total leakage current for 64 channels is 2.5 nA (a current per channel of ~0.04 nA per channel), a strip capacitance of ~0.27 pF, and a biasing resistor of 100 MΩ, the expected noise is $ENC = 73.1q$. For the 3D strip detector, if the total leakage current for 36 strips is 14 nA (a current per channel of ~0.39 nA), a strip capacitance of ~1.3 pF, and a bias resistor of 100 MΩ, the expected noise is $ENC = 120.0q$.

4.2 3D Diamond Strip Detector Characteristics

To reduce the drift distances between the generated charges by ionization, in 1997, Parker et al.[96] proposed the fabrication of electrodes that penetrated the bulk of the detector. This measure reduces the collection distances and times by one order of magnitude compared with the equivalent planar counterpart.

A 3D detector consists of 3D cells, which have a central electrode referred to as the sense electrode. It is surrounded by other electrodes that set the geometry of the 3D cell and are referred to as the bias or HV electrodes. The distances between the central electrode and the surrounding electrodes are smaller than the thickness of the sensor. In 3D diamond detectors, as will be seen in chapter 5, the electrodes are made of 3D graphitic conductors ("3D wires") generated by a femtosecond laser. Figure 4.3 shows a 3D cell in a square pattern traversed by an ionizing particle. The central electrode in the Figure is connected to ground, while the four surrounding electrodes that give the square shape are held at a HV potential, creating a

non-uniform electric field inside the sensor. The non-uniform electric field has regions with a low electric field strength, where the main mechanism of transport is diffusion, and regions with high electric field strength. As seen in Figure 4.3, the particles would drift to the nearest electrode, following, in general, the electric field lines. By reducing the distance between the electrodes, more charges would be collected before being trapped by crystal defects.

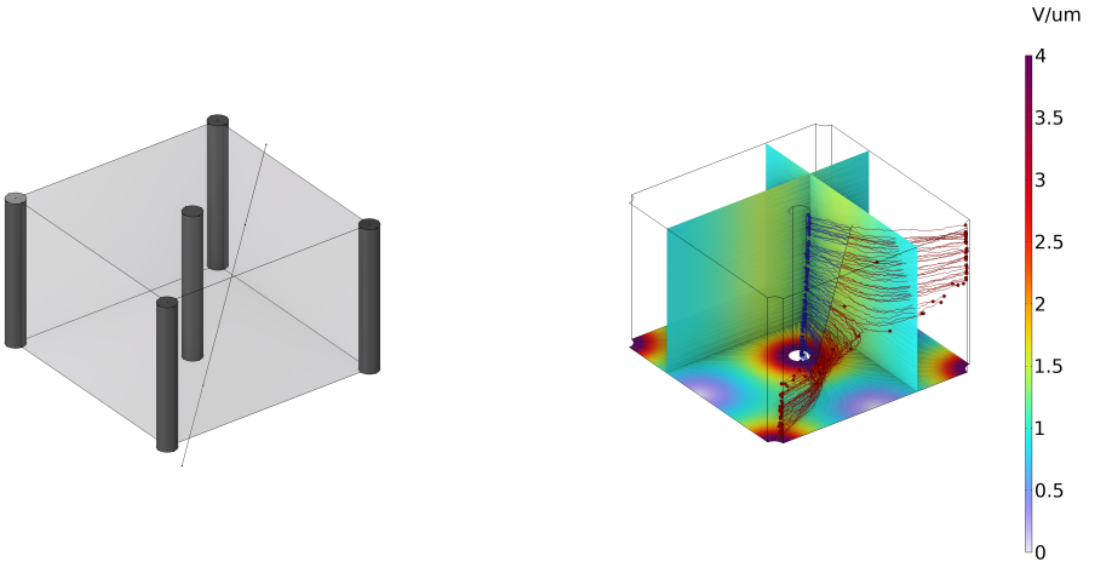

(a) Section of a 3D detector showing one 3D square cell. (b) Electric field inside the 3D square cell and the transport of ionized charges.

Figure 4.3: Diagram showing a section of a square 3D cell of a 3D detector. In (a), the 3D electrodes are depicted in dark gray. The distance between the central electrode and the electrodes in the vertices of the cell is smaller than the thickness of the sensor. The black line depicts the passage of an ionizing particle through the 3D cell. In (b), the non-uniform electric field magnitude is depicted with a color scale for different cross-sections of the 3D cell. The blue and red particles and lines represent the transport of the ionized electron and holes generated by the passage of the ionizing particle through the 3D cell.

The 3D diamond samples studied in this thesis were configured with a strip readout to be compatible with the VA2.2 chip. The readout electrodes of several 3D cells were interconnected by strips. Each of the strips is connected to a channel of the VA chip to read out the signals from the 3D cells. Figure 4.4 depicts a section of nine square 3D cells. The mesh pattern on the bottom of the sensor (used to avoid the readout electrodes in the center of the 3D cells) distributes the bias voltage to the biasing electrodes in the corners of each of the 3D cells. The mesh pattern follows the geometry of the cell, which means that for hexagonal 3D cells, the pattern would be hexagonal instead of square.

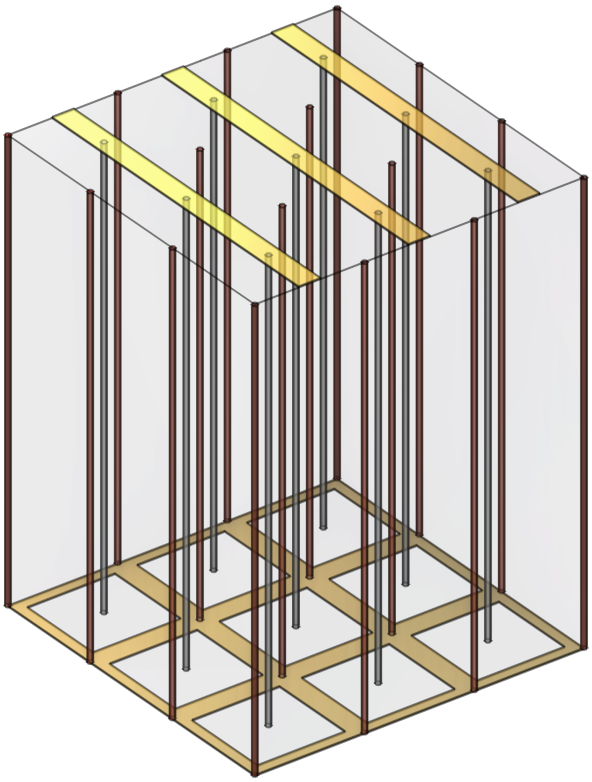

Figure 4.4: A section of 9 square 3D cells shows the conductive HV wires in dark red, the conductive sense wires in gray, and the metallization patterns on the top and bottom surfaces in gold. The bottom metallization is in a grid pattern to deliver the HV to each 3D cell. The top metallization gangs together 3D cells into the read-out channel. This diagram shows three read-out channels, each containing three ganged 3D cells.

4.3 Diamond Samples

The diamond samples with the VA2.2 chips were mounted on a PCB card with passive components to adjust the voltages in the VA2.2 for its correct functioning. The card was placed inside a metallic casing that had a $\varnothing \sim 2\,\text{cm}$ opening for the DUT, which was covered with aluminum foil and black tape to make it light-tight, as can be seen in Figure 4.5.

Table 4.3 shows the four samples made into 3D strip detectors and studied at CERN during test beams in 2015, 2016, and 2018.

Sample	Irradiation Type	Fluence (10^{15} p/cm^2)	Thickness (µm)	CCD (µm)
Poly-3D[97]	None	None	525	234
Full-3D	None	None	500*	275
Multi-3D	None	None	500*	245
Irrad-3D[98]	800 MeV/c protons	3.5(4)	510	136.7(106)

Notes:
* Estimated values

Table 4.3: Information of the samples that were made into 3D detectors.

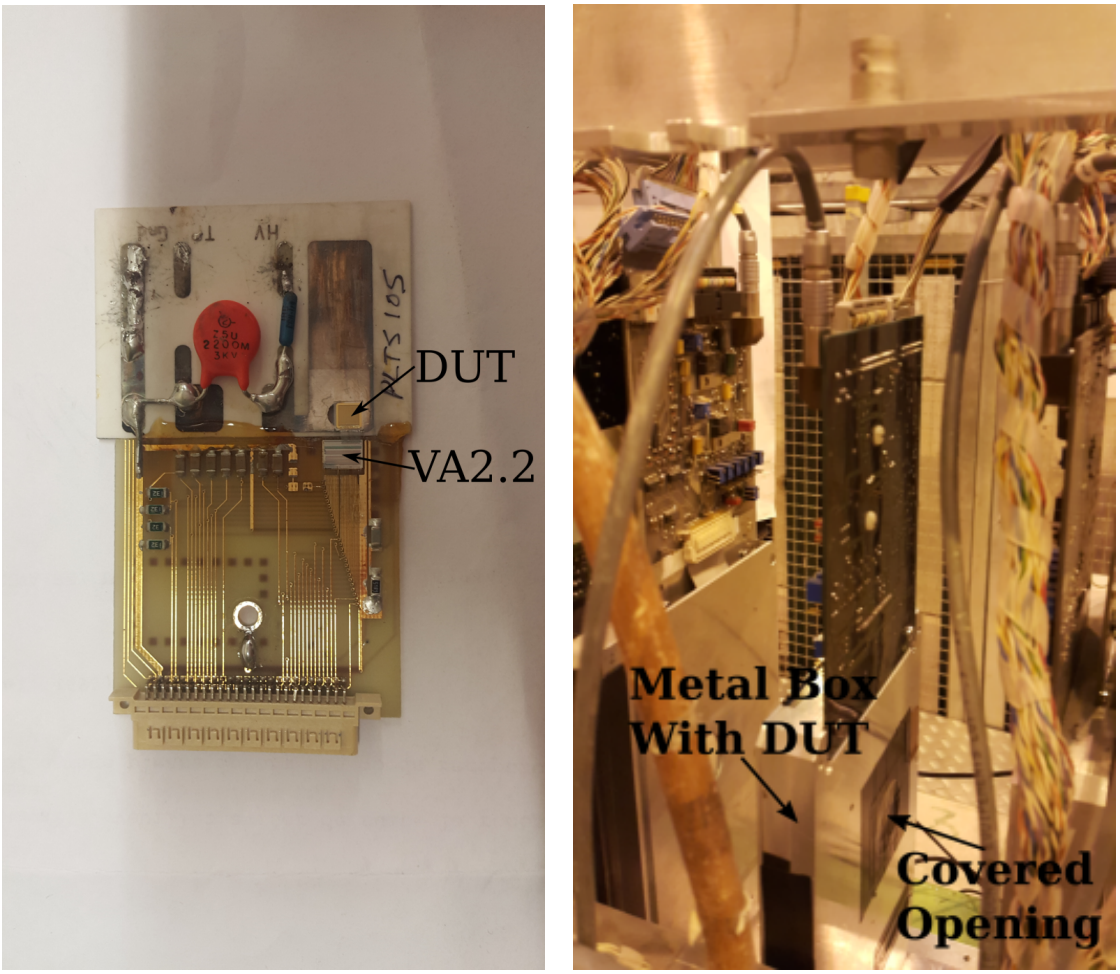

(a) DUT wirebonded to a VA2.2 on a hybrid PCB. (b) DUT inside metal box mounted in the telescope.

Figure 4.5: In (a), the PCB, where the DUT and the VA2.2 chip are placed, is shown with the passive components for the correct functioning of the VA2.2 chip. In (b), the PCB with the DUT is inside a metallic box that has an opening for the DUT. The opening is covered with black tape to make it light-tight.

4.3.1 Poly-3D

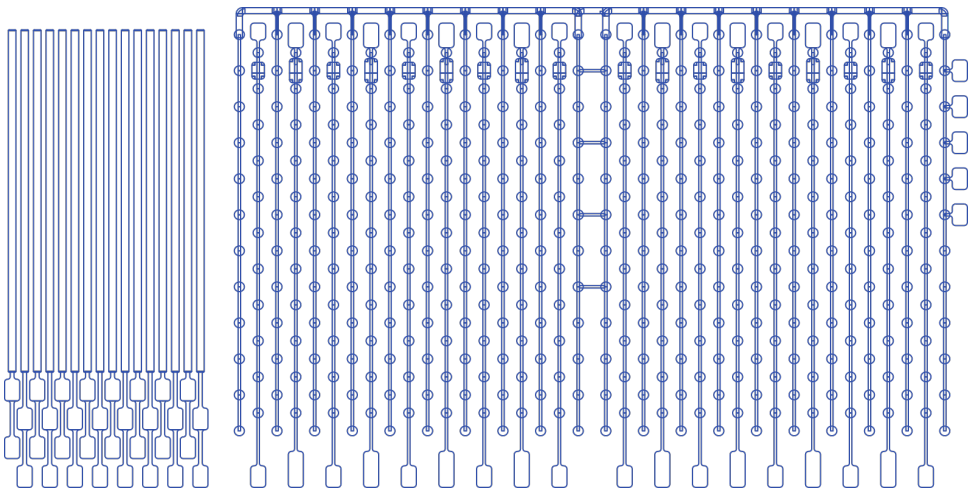

Figure 4.6: Layout of the metallization deposited on the top layer of the Poly-3D after the conductive wires were made. From left to right, the detector consists of three sections: a planar strip detector made with 25 µm strips with a pitch of 50 µm between them, a section with interdigital metallization with a separation between the digits of 75 µm without 3D wires (no 3D cells), and a section with the same interdigital metallization with 3D wires which made 3D square cells of 150 µm side length.

Poly-3D was a detector made with a ~ 5 mm × 5 mm non-irradiated pCVD diamond that had a different metallization pattern than the other devices in the sense that for the 3D cells, the metallization pattern ganging together the sensing 3D wires of each cell and the metallization to deliver the HV to the biasing 3D wires were on the same side (see Figure 4.6), although the metallization was duplicated on the opposite side for redundancy. The 3D cells in this device were square and had a side length of 150 µm, which made the pitch between the strips equal 150 µm.

4.3.2 Full-3D

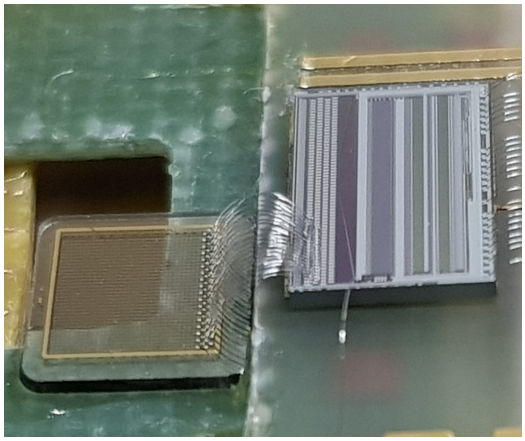

(a) Photograph of the Full-3D detector wire bonded to a VA2.2 chip.

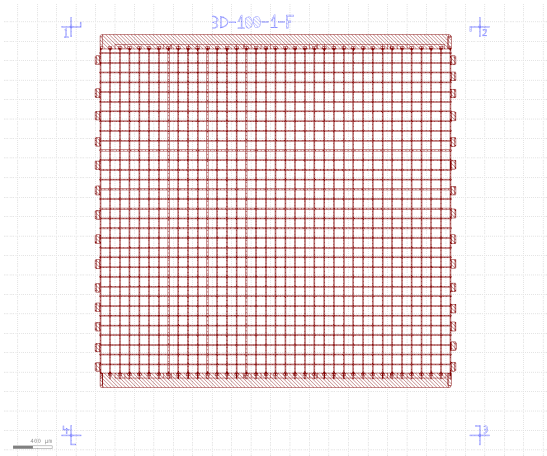

(b) Layout for the HV metallization on the bottom side of the sensor.

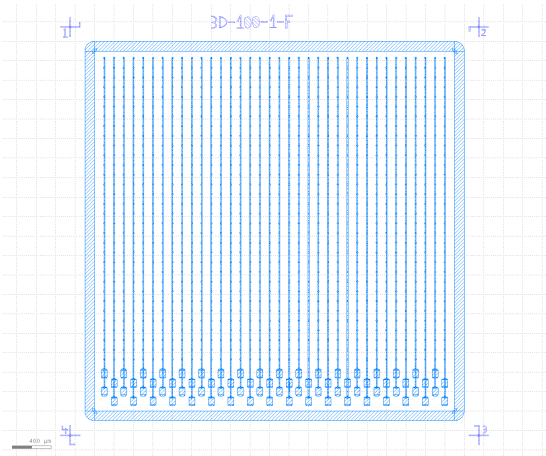

(c) Layout for the readout metallization on the top side of the sensor.

Figure 4.7: Picture of the Full-3D detector in (a). In (b) and (c), the layouts of the metallization made on each of the faces of the Full-3D, after the conductive wires were made, are shown. One of the sides had a mesh-like pattern to deliver the high voltage, while the other one had strips to read out several 3D sense wires of the 3D cells.

The Full-3D device was the first attempt by RD42 to fabricate a 3D detector with more than 1000 3D cells. Since then, more devices with more than 1000 3D cells have been fabricated. An approximately square non-irradiated pCVD diamond of 5 mm side was used for this device. A total of 36 strip channels and 32 rows of square 3D cells, each with a size of 100 µm, were fabricated, which gave a total of 1152 3D cells. Each strip connecting 32 3D cells had a width of 10 µm of chrome-gold metallization. A photograph from the device connected via wire bonds to the VA2.2 chip, along with the metallization layouts for both sides of the diamond, is shown in Figure 4.7.

4.3.3 Multi-3D

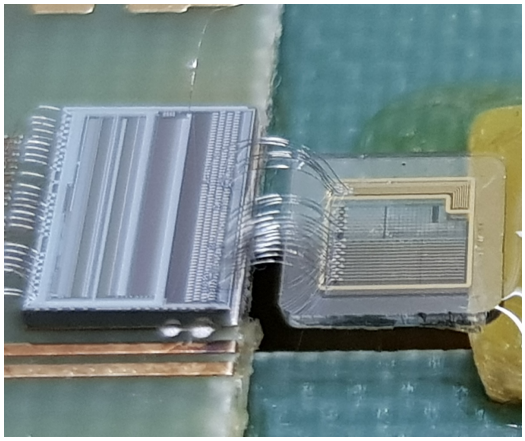

(a) Photograph of the Multi-3D device wire bonded with a VA2.2 chip.

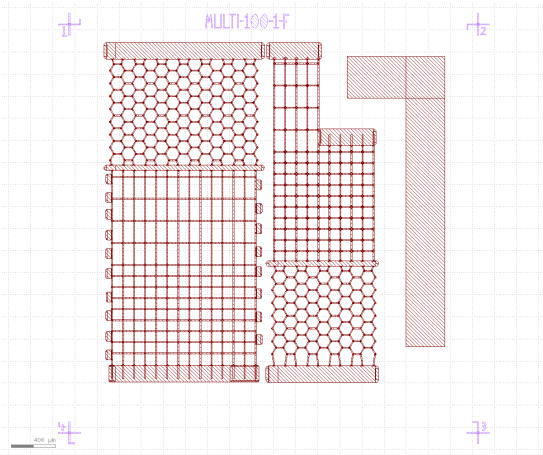

(b) Layout of the HV metallization on the bottom side of the sensor.

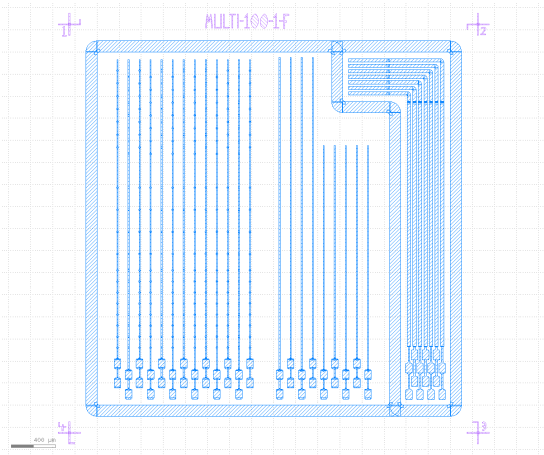

(c) Layout of the readout metallization on the top side of the sensor.

Figure 4.8: Picture of the Multi-3D in (a). In (b) and (c), the layouts of the metallization on each of the top and bottom sides of the Multi-3D, after the conductive wires were made, are shown. The pitch between the channels of the 3D cells was of 100 µm and the width of the metallization was of 10 µm. This prototype had different geometries for the 3D cells which were square, rectangular, and hexagonal. It also had a planar strip detector with a pitch between channels of 50 µm

.

The Multi-3D device was fabricated to study the performances of 3D cells fabricated with different geometries and compare them with a planar detector. It had three sections, as shown in Figure 4.8. From left to right, the first one was where the 3D cells with different geometries were fabricated, the second one had the same metallization pattern as the first one but without the fabrication of the 3D wires, which made it a planar detector, and the last one was an strip planar detector.

The pitch between the channels of the first and second sections was 100 µm, while for the third section, a planar strip detector, it was 50 µm. The metallization width for the first and second sections was 10 µm, and for the third section, it was 25 µm.

The first and second sections were biased with the same voltage, while the third required a different biasing voltage. A picture of the device wire bonded to a VA2.2 chip, along with the layouts for the metallization on both sides of the diamond, can be seen in Figure 4.8.

4.3.4 Irrad-3D

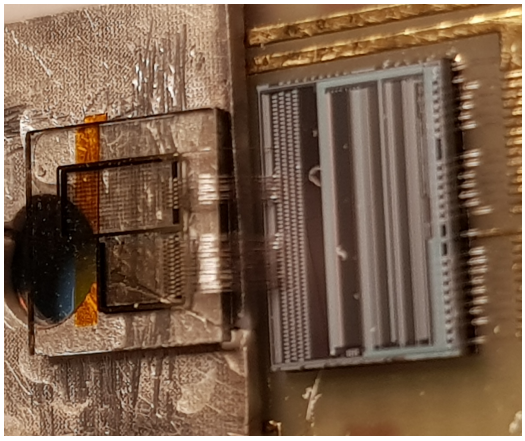

(a) Photograph of the Irrad-3D device wire bonded with a VA2.2 chip.

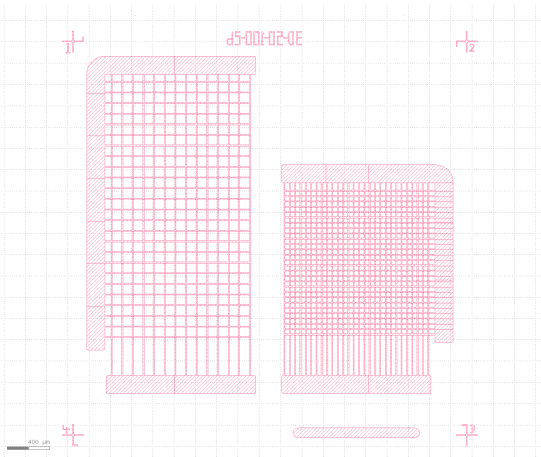

(b) Layout for the HV metallization in the bottom side of the sensor.

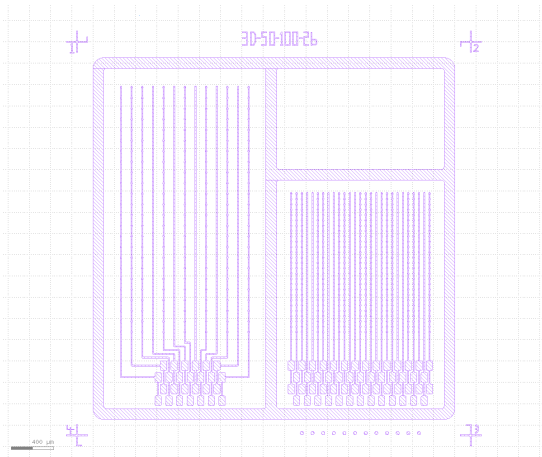

(c) Layout for the readout metallization in the top side of the sensor.

Figure 4.9: Picture of the Irrad-3D in (a). In (b) and (c), the layouts of the metallization made on each of the faces of the Irradiated-3D, after the conductive wires were made, are shown. This prototype was irradiated before the drilling was done to a fluence of 3.5×10^{15} protons

The pCVD diamond sensor for the Irrad-3D was irradiated with 800 MeV/c protons to a fluence of 3.5×10^{15} p/cm^2[64] before the 3D wires were fabricated. This device aimed to test the

advantages of 3D cells in highly irradiated sensors. As seen in Figure 4.9, there were two sections in this device. From left to right, the first section consisted of 13 channels, each with 24 3D square cells with a pitch between channels of 100 µm, and the second section had 27 channels, each with 27 3D square cells with a pitch between channels of 50 µm. Both sections operated in the test beams at the same biasing voltages. A picture of the device wire bonded to a VA2.2 chip is shown in Figure 4.9

Part III

Detectors Fabrication

Chapter 5

Fabrication Of 3D Detectors

The following sections describe the fabrication process used by the RD42 collaboration to make the 3D samples described in section 4.3.

5.1 Fabrication

5.1.1 Samples Preparation

Diamonds that had shown good performance as planar detectors during previous test beams or bench tests, i.e., good charge collection and good current response for different biasing voltages, were selected as substrates for the 3D detector prototypes. The diamonds were first cleaned with hot acids to remove any surface impurities and later dry etched using reactive ion etching (RIE) to remove 1-2 µm of material from the surface removing any contamination present in the top layers of the diamond during its processing. The acids and dry etching process were similar to the ones that will be discussed in section 6.1.

5.1.2 3D Wires Formation

Conductive wires were formed using a 100 fs pulsed laser with 790 nm wavelength and a repetition rate of 1 kHz[100], which converted the crystalline structure of the diamond in the focal point into resistive carbon phases, with a resistivity of $O(0.5\,\Omega\,\text{cm})$[99, 100], which were several orders of magnitude more electrically conductive than the bulk of the diamond (see Figure 5.1). The laser processing was done by the University of Oxford's scientist Patrick Salter. Measurements showed an average diameter of $O(2\,\mu\text{m})$ for the conductive wires[100].

5.1.3 Surface Metallization

After the conductive wires had been formed, metallization was deposited to create readout channels by ganging together 3D cells on one side of the sensor. On the other side, the metallization was deposited in a mesh-like pattern to distribute the HV. The metallization deposition was achieved with electron beam evaporation and lift-off photolithography. Figure 4.4 depicts the metallization patterns used for square 3D cells in all the prototypes. The metals

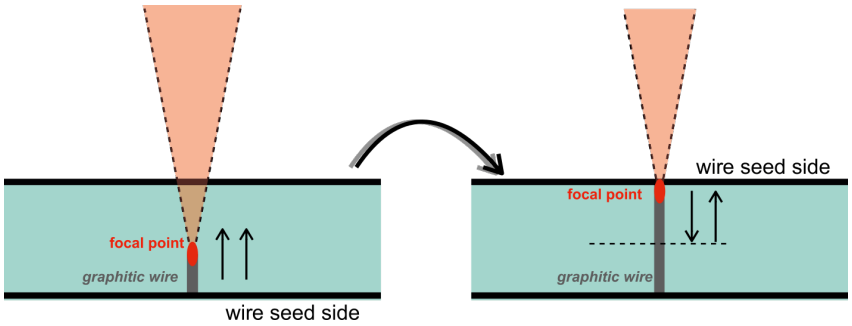

Figure 5.1: Sketch of the process used to fabricate the conductive 3D wires. The laser was focused on the bottom side of the diamond to start the inscription, and it was raised until it reached the opposite top side of the diamond. This process was done twice. Afterwards, the diamond was flipped, and the laser inscription started on the now top side, lowered until the middle of the diamond, and returned to the top.[99]

used for the deposition were Cr for the contact layer, followed by Au for oxidation protection and compatibility with the wire-bonding process. The samples were then annealed at 400 °C for 4 min in an N_2 to promote the Cr-carbide formation for good ohmic contacts[36].

Chapter 6

Fabrication Pixelated Planar Detectors

Unlike pixelated silicon detectors that can be fabricated in many Very large-scale integration (VLSI) foundries, the fabrication of diamond detectors has been more craftmanship work than a scalable industrial process. This motivated the development of a fabrication process that could be scaled to mass-produce pixelated diamond detectors.

Producing a planar pixelated sensor involved various steps in different laboratories. Before developing a successful procedure, other attempts were tried that won't be covered in this work for brevity. The following are the steps from the successful procedure required to produce a functional planar pixelated detector. Most of the processes were performed at IBM's BRNC cleanroom. Processes performed in other labs are shown in parentheses. The "*" means that a solvent-clean procedure was performed before the process. In the following sections, these processes will be discussed in more detail.

- Surface preparation
  - Boiling acid cleaning (Lab: Toxlab)
  - *Surface removal via ICP-RIE
- *Sample gluing onto a carrier wafer
- Back-plane contact metallization
  - Lift-off contact metal photolithography
  - Contact metallization deposition
  - Lift-off - sample removal from the carrier wafer
- *Carbide formation via annealing
- *Sample gluing onto a carrier wafer
- Front-plane contact metallization
  - Lift-off contact metal photolighography
  - Contact metallization deposition

  - Lift-off - sample removal from the carrier wafer
- *Carbide formation via annealing
- *Passivation layer growth via PECVD
- *Sample gluing onto a carrier wafer
- Passivation layer etching via RIE
  - RIE photolithography
  - RIE through the passivation layer
  - Strip remaining photoresist
- *Sample gluing onto a carrier wafer
- under-bump-metallization (UBM)
  - Lift-off UBM photolithography
  - UBM deposition
  - Lift-off - sample removal from the carrier wafer
- *Sample gluing onto a carrier wafer
- Indium bumps metallization
  - Lift-off In bumps metallization
  - In bumps deposition (Lab: PSI)
  - Lift-off - sample removal from carrier wafer (Lab: PSI)
- In bumps formation via reflow (Lab: PSI)
- Flip-chip between the sensor and the psi46digV2.1-respin ROC
- Homogenization via 2nd reflow (Lab: PSI)

As mentioned, processes with a preceding * had a solvent-clean procedure which is the following:

- Acetone clean in an ultrasound (u.s.) bath
- Isopropanol clean in u.s. bath
- Deionized water clean in u.s. bath
- Dehydration on hotplate @ 150 °C

6.1 Sensor's Surface Preparation

In the processing of the samples to have adequate mechanical characteristics for the fabrication of the sensors, it is possible that contamination was involuntarily introduced into the samples during the processing. Moreover, some of the samples had already been processed as sensors and the previously fabricated metallizations needed to be removed. For these reasons, the first step was to prepare the surfaces of the samples to remove any contamination that would interfere with the successful fabrication of sensors.

The diamond substrates were first cleaned using a series of hot acids to remove different types of impurities on the surface of the diamond. The following boiling acids were used several times. Between each acid treatment, deionized (DI) water was used to rinse the samples. (See Appendix B for more details on the acid cleaning procedure)

- To remove carbides from the surface of the diamond:
  - Chromium(III) acid ($Cr_2O_3 \cdot H_2SO_4$)
- To remove other non-carbide contaminants:
  - Aqua Regia
  - Nitrating acid
  - Piranha solution (especially carbohydrates)

After the acid treatment, the removal of $\sim O(1\,\mu m)$ from the top and bottom surfaces of the diamond using inductively coupled plasma reactive ion etching (ICP-RIE) was found to improve the voltage-current characteristics of the diamond sensors.[101]

For this task, a recipe was developed using different plasma mixtures, which would etch the diamond at different rates and have different effects on the surface. Table 6.1 shows the different plasma mixtures used to etch the diamond, the etch rates, and the different reasons for its usage. For more details on the ICP-RIE process, see Appendix C.

Plasma	Estimated rate (nm/min)	time (min)	Reason
SF_6/O_2	100[102]	1	Remove leftover contaminants
Ar/Cl_2	90[103]	3	Smoothen the diamond's surface
O_2	150[104]	7	Deep etch the diamond

Table 6.1: Plasmas used for ICP-RIE on the diamond surfaces.

With the removal of $\sim O(1\,\mu m)$ from the surfaces of the diamond, the surface preparation of the diamond samples was finalized. Since the samples were placed under highly oxidizing acids and then under oxygen plasma, the surface of the diamond was oxygen-terminated, which was desired to have electrically insulating surfaces, unlike hydrogen-terminated diamonds, which would have electrically conductive surfaces.[35]

A process often performed during the fabrication was gluing the diamond onto a carrier wafer. A carrier wafer allowed the indirect manipulation of the diamond, which was convenient

due to the size of the diamond, and also to avoid contamination of the diamond's surface caused by direct manipulation.

For this process, Crystalbond 509 mounting adhesive from SPI Supplies[105] was used. The carrier was placed on top of a hot plate at 90 °C. Then, a small amount of Crystalbond was placed on top of the approximate center of the carrier, such that a thin layer with an area of $\sim O(7\,\mathrm{mm}^2)$ of the Crystalbond melted over the carrier wafer. Finally, the diamond was placed with plastic tweezers on top of the melted Crystalbond on the carrier wafer, so that the surface where the processing would be applied would be opposite to the surface against the carrier wafer. In the end, the corners of the sample were pressed with plastic tweezers to spread the adhesive under the diamond, and the carrier wafer was removed from the hotplate to let the Crystalbond solidify.

6.2 Metallization

In this and the following sections, the figures will have the thickness of the layers on top of the diamond scaled up by a factor of 10 to emphasize the details that would otherwise be difficult to notice. At the end of the process, the vertical scaling on the images will be set to 1 for the processes involving the formation of the bumps.

The metallization patterns were deposited in the desired regions shown in Figure 3.4 using the lift-off technique, in which a layer of photoresist was used to mask the regions where no metal was desired. This technique allowed the patterning of multi-layer metallization with only one process, which would otherwise require several steps of etching techniques. For more information regarding photoresists and photolithography, refer to Appendix D. Then, metal was deposited over all of the sample's surface, followed by the photoresist removal. This cleared the metal from the unwanted regions on the sample's surface. Figures 6.1, 6.2, and 6.3 show the application of this process on a section of four pixels.

Two methods of physical metal deposition were tested: Electron beam evaporation, and Sputtering. Both methods are physical vapor deposition methods with different means of generating the material to be deposited.

In electron beam evaporation, an electron beam is used to heat and melt the metal to be deposited. The chamber where the process is done is kept in a vacuum. The vapors from the metal rise where the samples are held and condense over the samples at thermal energies of $O(\mathrm{meV})$.

On the other hand, sputtering uses the phenomenon where a plasma, typically made of Ar, impacts energetically the metal to be deposited, and particles from the metal are ejected with higher energies than in the evaporation method ($O(\mathrm{eV})$). The ejected particles condense over the samples covering the sample with a layer of the desired material.

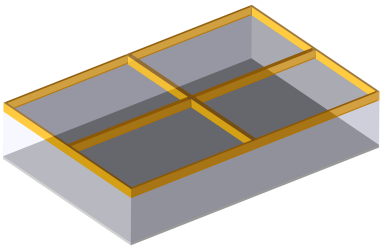

(a) Four pixels with photoresist mask (translucent yellow).

(b) Side view of the cross-section of (a).

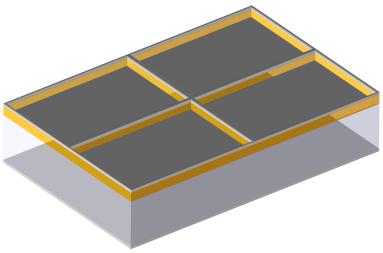

(c) Four pixels with photoresist mask after metal deposition (dark gray).

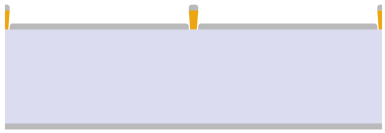

(d) Side view of the cross-section of (c).

Figure 6.1: Diagrams of four pixels, showing the deposition of metal (dark gray) over the surface of the diamond with a photoresist mask on top (yellow). The photoresist pattern allowed the metallization to be deposited on the desired regions of the diamond. The thickness of the photoresist layer was ~ 1 µm and the metal deposition was made of 10 nm of Ti as the contact metal with the diamond, and 300 nm of Al on top of the Ti.

In both methods, the metals stuck to the sample's surfaces and were successfully patterned via lift-off. Ultimately, the evaporation method was chosen over the sputtering method due to its simplicity and fast processing times which saved a couple of hours per process.

The chosen metallization on the diamond was a two-layer metallization, where the contact metal was Ti. The requisite for the contact metal in radiation detectors is that it should form good ohmic contacts[35]. It has been shown that Ti contacts on diamond form good ohmic contacts when carbide is produced after annealing[36, 106, 107]. The second metallic layer was Al for its good conductivity and compatibility with aluminum wire-bonding machines. Another metallization that was tried was Cr/Ni/Au, based on the standard metallization used in the RD42 collaboration (Cr/Au) for prototype devices. In this attempt, the Cr layer would serve as the contact layer[107], the Ni layer would perform as a barrier between the Cr and the Au, and the Au layer would prevent oxidation besides being a good conductor and being compatible with

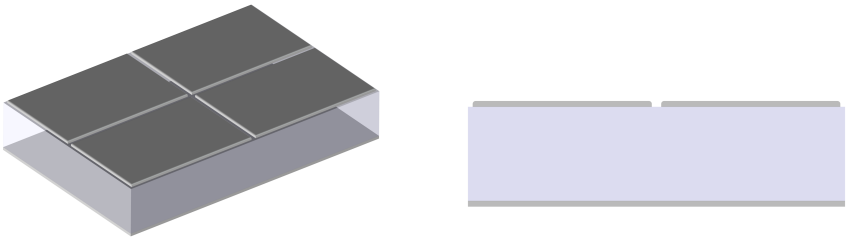

(a) Four pixels with the desired metallization pattern after lift-off.

(b) Side view of the cross-section of (a).

Figure 6.2: Resulting metallization pattern after the lift-off process, where the photoresist with metal on top was stripped away.

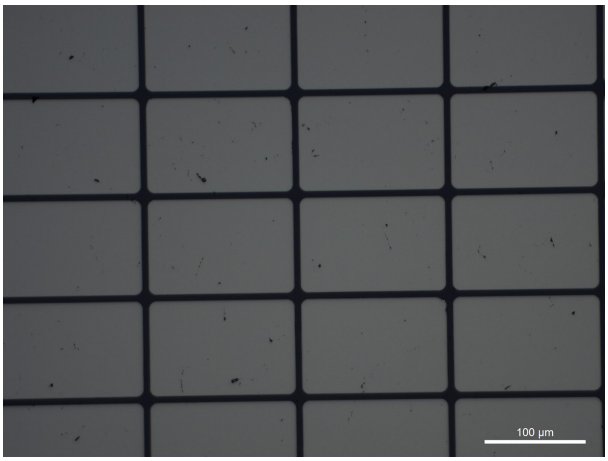

Figure 6.3: Microscope photograph showing the Ti/Al pixels left on the surface of the diamond after lift-off.

aluminum wire-bonding machines. For reasons discussed in section 6.4, the Ti/Al metallization was chosen over the Cr/Ni/Au metallization. The amount of the Ti layer deposited over the samples was 10 nm, followed by the deposition of 300 nm of Al.

6.2.1 Different Metallization Study

To compare the compatibility of the RD42 traditional Cr/Au metallization with the implemented Ti/Al layer, a diamond pad detector was made with the two metallizations in a checkered pattern to study if one of the metallizations was consistently better than the other. The metallization pattern can be seen in Figure 6.4. The metallization deposited over quadrants 1 and 3 was the Cr/Au metallization. In contrast, the metallization deposited over quadrants 2 and 4 was based on the Ti/Al metallization with the addition of Pt/Au layers on top so that the four quadrants

were protected from oxidation. In this case, the Pt layer worked as a diffusion barrier between the Al and Au layers[108]. The sample was connected to a Cividec[109] C6 fast charge amplifier and tested at a test beam at PSI, as will be described in section 10.2.

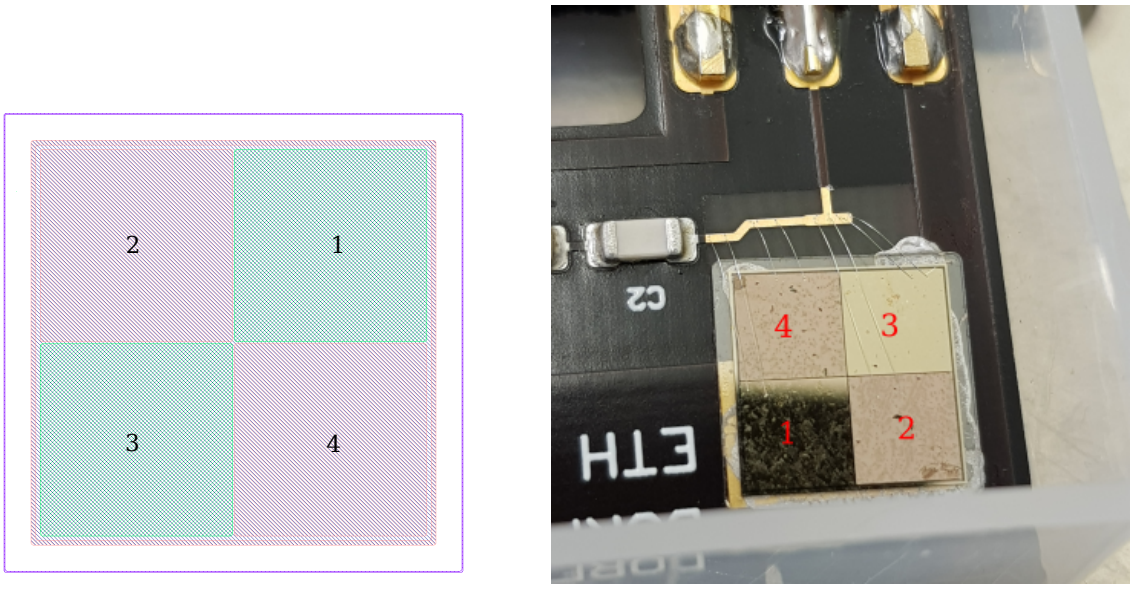

(a) Layout for the top metallization.

(b) Picture of CMS01 with two different metallizations.

Figure 6.4: (a) Layout of the different metallizations on the top side of the diamond. The numbering of the quadrants shows that quadrants 1 and 3 have the same metallization, which is different from the metallization of quadrants 2 and 4. The back side (not shown) has a big square pad that covers the four quadrants. In (b), the picture of the diamond CMS01 with the two different metallizations on the four quadrants is shown. The same amplifier reads all the quadrants.

The sample was measured at different rates and different voltages. More details regarding these tests will be discussed in section 10.2.2. For each measurement, the difference between the signals in different quadrants with the same type of metallization was used as a systematic uncertainty. An example of this is shown in Figure 6.5, where the two signal distributions for quadrants 1 and 3 are compared.

Figure 6.6 shows the ratio between the signal obtained with quadrants 1 and 3 with respect to quadrants 2 and 4 for different voltages and rates, respectively. As seen in Figure 6.6, either metallization has no consistent superiority in the collected signal (the ratios are not always consistently above or below unity). The variations from unity among the tests lie mostly within the systematic uncertainties or not far from them. These variations could be caused by intrinsic differences in the diamond, which were not accounted for. As no clear, consistent superiority of the signal collected with either metallization was seen in the performed experiments, it was concluded that either metallization would produce comparable signals.

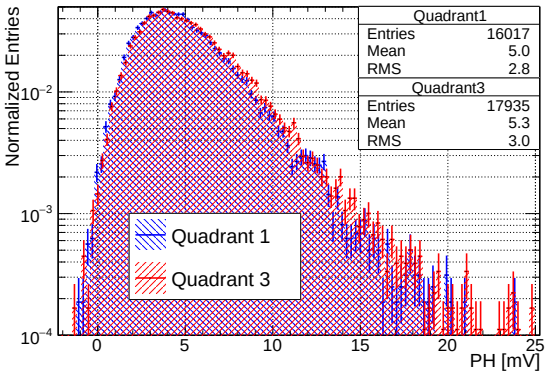

Figure 6.5: Comparison of the pulse height distributions for the signal collected by the same metallization but located in different quadrants. The variation of the mean of the distributions was used to estimate the systematic uncertainty caused by the different regions of the diamond.

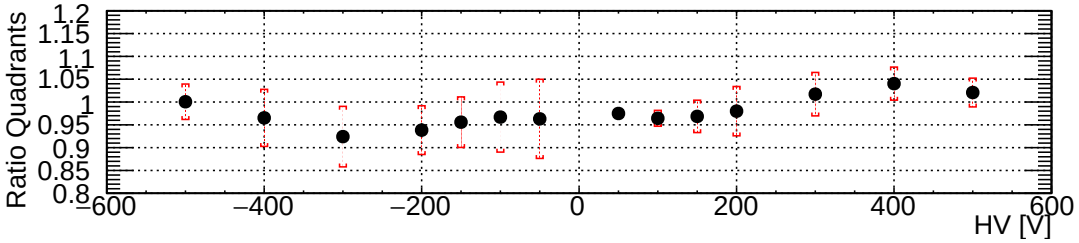

(a) Ratio of the signals with different metallizations for different bias voltages.

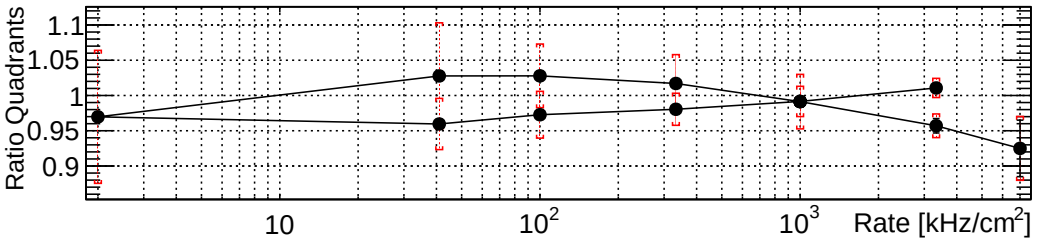

(b) Ratio of the signals with different metallizations for different rates of incident particles.

Figure 6.6: Ratios of the signals collected by quadrants 1 and 3 (Cr/Au metallization) with respect to the signals collected by quadrants 2 and 4 (Ti/Al/Pt/Au metallization). The red error bars represent the systematic uncertainty from the variations between the quadrants with the same metallization.

6.3 Passivation Layer

To separate the pixel metallization from the indium used to form the bump bonding spheroids, different passivation layers with a thickness of 600 nm were tested. The passivation layer was deposited over the whole surface of the diamond such that it covered both metal and diamond (see Figures 6.7 and 6.8). The first passivation layer tested was silicon nitride (SiN_x), and the second was silicon oxynitride (SiO_xN_y). Afterwards, dry etching with RIE was used to create an

opening between pixel metallization and the indium bumps. In the end, silicon oxynitride was preferred over silicon nitride, as discussed in section 6.4.

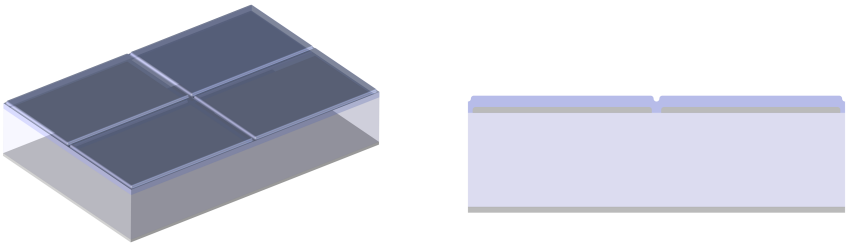

(a) Four pixels covered with the passivation layer.

(b) Side view of the cross-section of (a).

Figure 6.7: The result after the deposition of 600 nm of a passivation layer of SiO_xN_y (light blue).

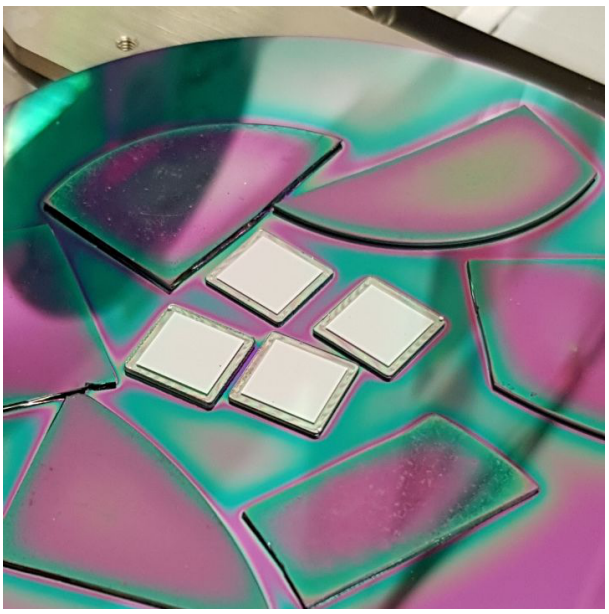

Figure 6.8: Four diamonds after the growth of SiO_xN_y via PECVD. The diamonds are on top of a carrier wafer, and pieces of silicon wafer surround the diamonds to prevent them from sliding away inside the PECVD chamber. The colors seen on top of the silicon pieces are caused by thin-film interference from the thin layer of SiO_xN_y.

The deposition of either passivation layer was done by plasma-enhanced chemical vapor deposition (PECVD). Chemical vapor deposition methods require a mixture of different gases

that react under certain conditions, such as temperature and pressure, to form a layer of the desired substance. With PECVD, as the gases are ionized in a plasma, the temperature for the reaction can be lowered, which is convenient when working with metals as the reaction can happen at temperatures below the melting point of the metals.[110] A PECVD recipe for SiO_xN_y was developed to form the passivation layer. Details of the developed recipe can be found in Appendix E.

As mentioned above, to make a direct connection between the metallic layers below the passivation layer and the indium bumps, openings had to be made through the passivation layer. RIE was performed to etch holes of ⌀10 µm for each pixel. The position of the holes was such that it matched the bump pads of the PUCs on the ROC. A positive photoresist with a thickness of 1.2 µm was placed over the passivation layer and developed with the pattern for the RIE process, as shown in Figure 6.9. For more information about the photolithography process used before the RIE process, see Appendix D.1.

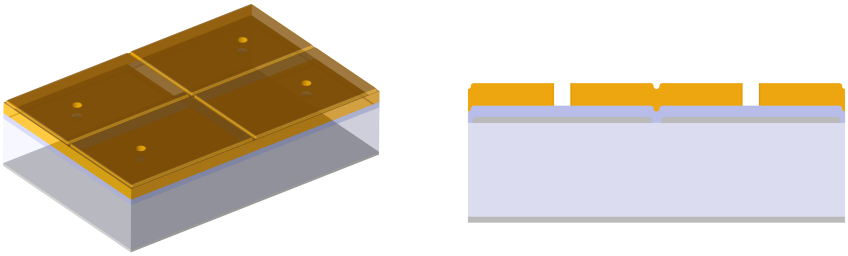

(a) Four pixels with photoresist mask (translucent yellow) before RIE.

(b) Side view of the cross-section of (a).

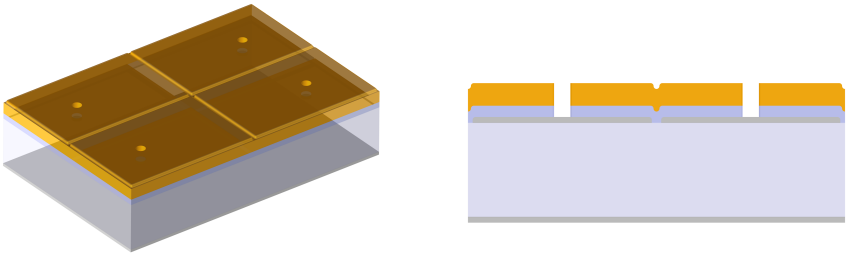

(c) Four pixels with photoresist mask after RIE.

(d) Side view of the cross-section of (c).

Figure 6.9: Photoresist before and after RIE, which covered all the surface except for ⌀10 µm holes on top of each pixel.

RIE based on CHF_3 was used to etch through the SiO_xN_y 600 nm layer. As the layer below

the SiO_xN_y was Al (and Al_2O_3 due to the presence of air after evaporation), over-etching was not a problem, because CHF_3 is a good etchant for silicon oxides and silicon nitrides but not a good etchant for aluminum or aluminum alloys[111]. See Appendix F for more details on the RIE recipe. After the etching, stripping away the remnant photoresist with solvents revealed the structure shown in Figure 6.10.

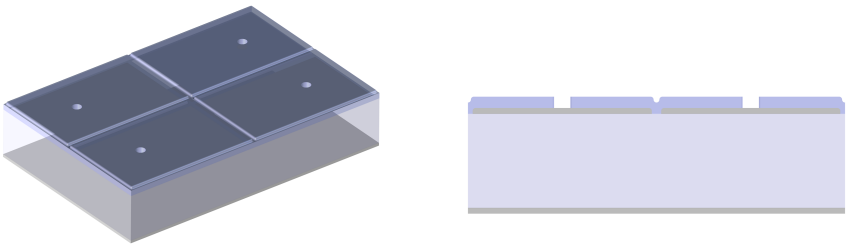

(a) Four pixels after the stripping of the photoresist.

(b) Side view of the cross-section of (a).

Figure 6.10: Surface of the diamond covered with SiO_xN_y except for the openings.

6.4 Bump Bonds Formation

The general process to form indium bumps consists of depositing a thick layer of In, followed by a reflow process to form the bumps. The correct formation of the In bumps on top of the holes made by RIE through the passivation layer became challenging. The formation of In bumps failed in most attempts in two ways: No bump formation or the formation in the wrong position of the bumps. Figure 6.11 shows pictures of these features for different attempts.

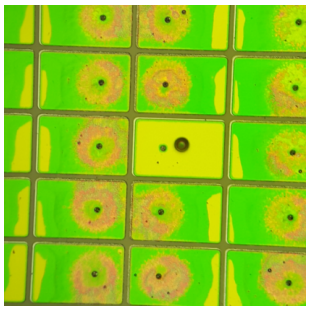

(a) Cr/Ni/Au with SiN_x and no UBM

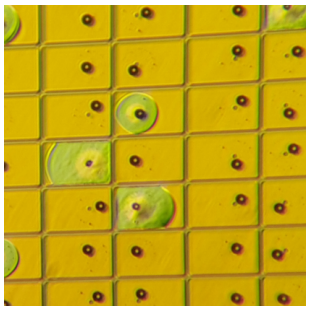

(b) Ti/Al with SiN_x and Ti/Ni/Au UBM

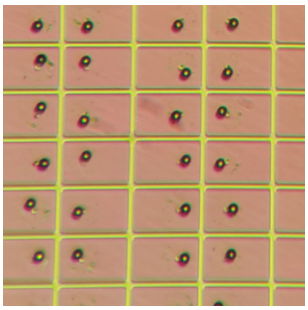

(c) Cr/Ni/Au with SiO_xN_y and Cr/Ni/Au UBM

Figure 6.11: Images from three different attempts to form the indium bumps. The captions are tags for the variations of the attempts that correspond to the image (see Table 6.2). In (a), the green-pink coloration appeared on the pixels where no bumps were formed. Most bumps in (b) were formed correctly but not in the correct position. There was still the presence of green coloration located where the bumps were not formed correctly. In (c), all the bumps were formed correctly but not in the correct position.

When no bumps were formed, there was a change of coloration on the surface of the pixel. This suggested that a reaction of the indium during the bump formation had taken place. To control the bump formation process, a silicon sensor designed for the pixel tracker detector of the CMS experiment was placed alongside the diamond prototypes inside the reflow chamber for every attempt. All the attempts were successful in the In bump formation for the silicon sensors, which meant that the problem was in the diamond fabrication process. Table 6.2 summarizes the relevant procedures tried and the bump formation results.

Processes			Bump results	
Pixel	Passivation	UBM	Visible reaction	Correct position
None	SiN_x	None	Yes	No
None	SiO_xN_y	None	Yes	No
Cr/Ni/Au*	SiN_x	None	No	No
Cr/Ni/Au	SiO_xN_y	None	No	No
Cr/Ni/Au*	SiO_xN_y	Cr/Ni/Au	Yes	No
Ti/Al*	SiN_x	Ti/Ni/Au	Yes	No
Ti/Al	SiO_xN_y	Ti/Ni/Au	No	Yes

* The images from these attempts can be seen in Figure 6.11.

Table 6.2: Relevant processes tried and their results. The only process combination that resulted in a correct formation of In bumps (no visible reaction) in the correct place was the one with a pixel metallization of Ti/Al, a passivation layer of SiO_xN_y, and a UBM of Ti/Ni/Au.

As shown in the successful result in Table 6.2, for the correct formation of the In bumps, it was necessary to deposit a layer of under-bump-metallization (UBM). For this task, a lift-off mask of 1 µm thick photoresist was deposited, such that a circular area with a diameter of 20 µm

was left open on top of the openings through the SiO_xN_y, as seen in Figure 6.12. For more information on the photolithography process used, see Appendix D.2. Afterwards, a multi-layer metallization of 10 nm of Ti, 100 nm of Ni, and 10 nm of Au was evaporated to form the UBM over the openings for each pixel. In this three-layer metallization, the Ti acts as the contact layer with the Al, the Ni is the barrier metal between Ti and Au, and Au is the wetting metal that would stick with the In bump.

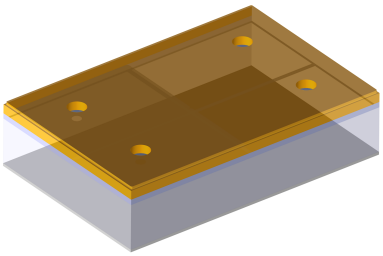

(a) Four pixels with photoresist mask (translucent yellow) before the UBM deposition.

(b) Side view of the cross-section of (a).

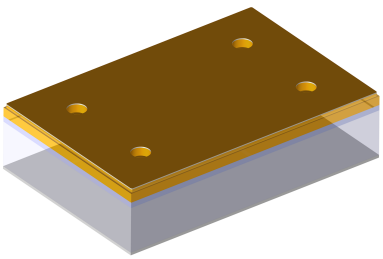

(c) Four pixels with photoresist mask after the UBM deposition (solid golden-brown).

(d) Side view of the cross-section of (c).

Figure 6.12: Photoresist mask before and after the evaporation of the UBM (solid golden-brown) covering the opening holes for each pixel. The UBM consisted of 10 nm of Ti, 100 nm of Ni and 10 nm of gold.

Using solvents to remove the excess metallization deposited on top of the lift-off photoresist mask, the structure seen in Figures 6.13 and 6.14 was revealed, where UBM was placed on top of each of the opening holes, which promoted the sticking of the In bumps in the correct place for each pixel.

To form the In bumps, a thick layer of In was deposited. Each bump was designed to have

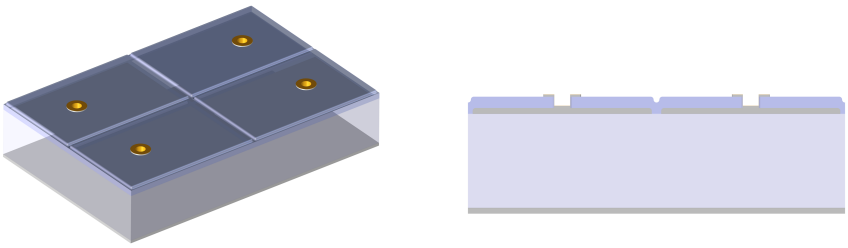

(a) Four pixels with UBM after (solid golden-brown) lift-off with solvents.

(b) Side view of the cross-section of (a).

Figure 6.13: Deposited UBM over each pixel's opening hole.

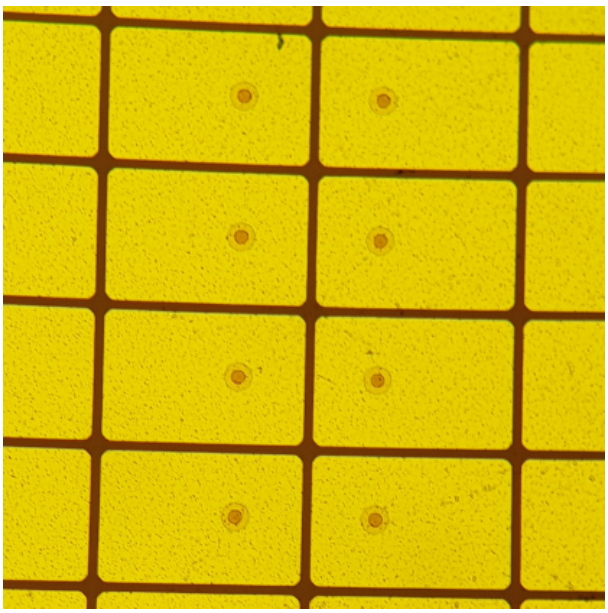

Figure 6.14: Surface of the diamond after the deposition and lift-off of the UBM. Two concentric circles are appreciated on each pixel. The innermost corresponds to the opening hole, while the outermost corresponds to the UBM covering the hole.

$\varnothing \sim 25\,\mu m$, which meant that a volume of $\sim 8200\,\mu m^3$ of In was required for each bump on each pixel. This volume was achieved by depositing $\sim 2.55\,\mu m$ of In over a circular area of $\varnothing 70\,\mu m$ on top of each of the pixel's UBM. The mask for the lift-off needed to be thicker than the deposited indium; therefore, a $\sim 3.5\,\mu m$ layer of photoresist was used (see Appendix D.3 for more information on the photolithography process). Figure 6.15 depicts the photoresist mask before and after the deposition.

The deposition of the indium was achieved with a thermal evaporator at PSI: Inside a vacuum chamber, a resistive container held the indium to evaporate. A high current was passed through

the resistive container, heating it and melting the material to evaporate. The vapors from the material rose where the samples were held upside down to receive the evaporated indium. The amount of indium to evaporate was previously calibrated by the CMS Pixel group at PSI, and it was estimated that a quantity of 3 g of indium would deposit a ~ 2.55 µm layer of indium over the samples' surface.

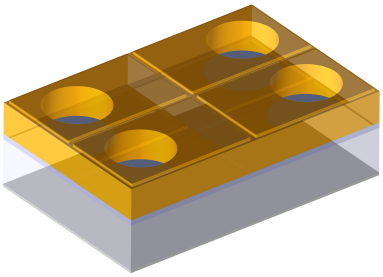

(a) Four pixels with the photoresist mask (translucent yellow) before the indium evaporation.

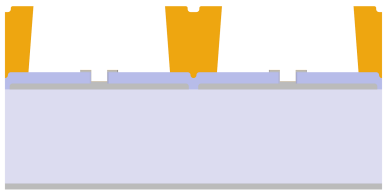

(b) Side view of the cross-section of (a).

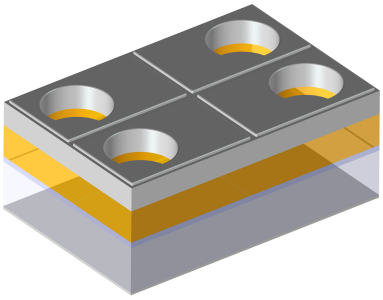

(c) Four pixels with the photoresist mask and the evaporated layer of indium (dark gray).

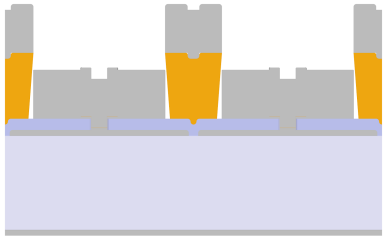

(d) Side view of the cross-section of (c).

Figure 6.15: A thick layer of indium was evaporated over the whole surface of the diamond which had a lift-off photoresist mask. The thickness of the photoresist mask was of 3.5 µm and the estimated thickness of the evaporated indium was 2.55 µm.

After evaporation, the excess of the evaporated indium was removed using solvents to strip away the photoresist mask. Figures 6.16 and 6.17 show the resulting indium "pancakes" left over each pixel.

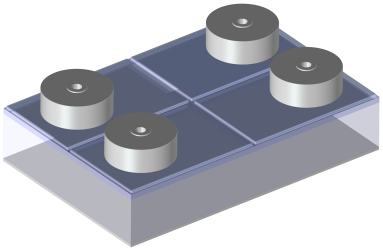

(a) Four pixels with the In “pancakes”.

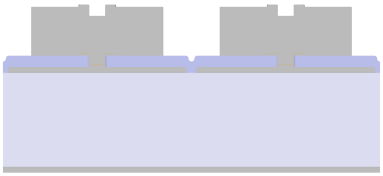

(b) Side view of the cross-section of (a).

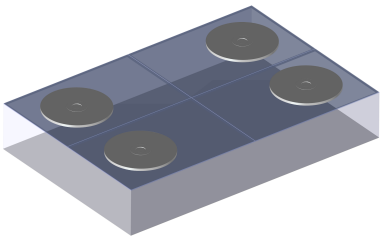

(c) Four pixels with the In “pancakes” with the actual thickness (vertical scaling set to 1).

(d) Side view of the cross-section of (c).

Figure 6.16: Resulting indium “pancakes” on top of each pixel after the lift-off process.

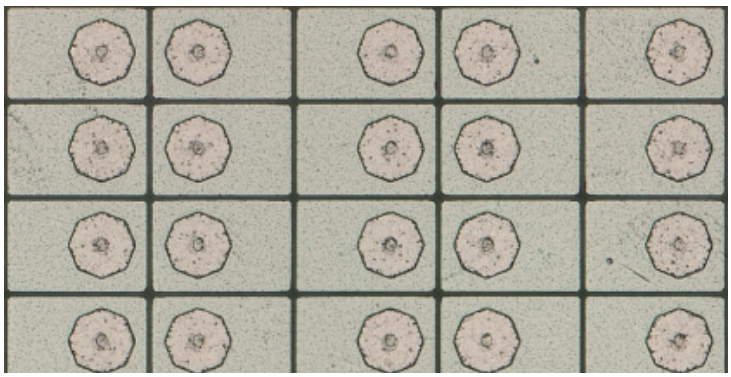

Figure 6.17: Microscope photograph of the diamond’s surface after evaporation and lift-off of the indium. On top of each pixel, the indium “pancakes” can be seen. The inner circles inside each “pancake” correspond to a change in thickness due to the opening holes made through the passivation layer.

For the flat indium "pancakes" to take the form of bumps, the samples were placed inside a chamber for reflow. During the reflow process, the chamber's temperature and atmosphere were controlled, such that the samples were heated in an atmosphere without any free oxygen. Under these conditions, the indium melted without oxidizing, and due to surface tension, the In "pancakes" formed bumps. The chamber then cooled down, and the indium solidified, keeping the shape of the bumps (see Figures 6.18 and 6.19).

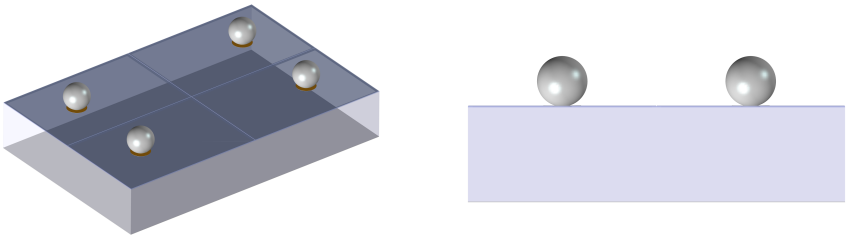

(a) Four pixels with the indium bumps after reflow.

(b) Side view of the cross-section of (a).

Figure 6.18: Diagram showing the result after the reflow process, where the deposited indium was melted to form bumps. After cooling, the indium solidified keeping the bump shape.

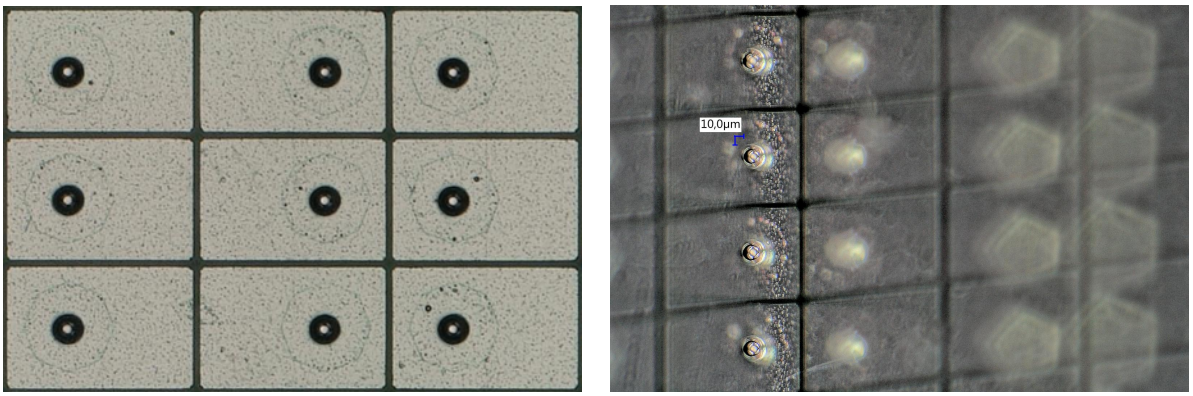

(a) Surface after reflow.

(b) Surface after reflow viewd at 50° with a column of bumps on focus.

Figure 6.19: After the reflow, the indium bumps were formed. The size of each bump was $\varnothing \sim 26\,\mu m$.

6.5 Bump Bonding

Using the position of the bumps, a flip-chip machine located at PSI aligned each ROC with the bump pattern on the sensor. The device exerted a force equivalent to $\sim 4\,\mathrm{kg} \times 9.8\,\mathrm{m/s^2}$ which pressed on each bump with a force of $\sim 9.4\,\mathrm{mN}$. As seen in Figure 6.20, this caused the bumps to deform. The sensor and chip were placed again inside the reflow chamber, where a second reflow process was performed to reshape the bumps according to surface tension and homogenize the distance between the sensor and the ROC.

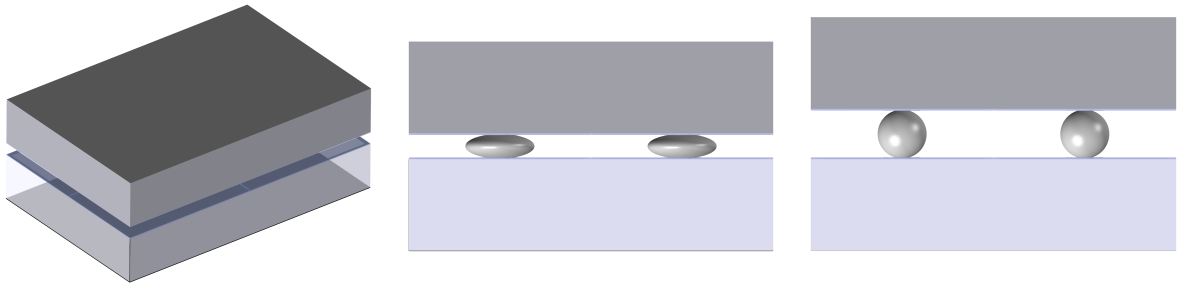

(a) Chip pressed against the sensor. (b) Side view of (a). (c) Side view after second reflow.

Figure 6.20: By pressing the ROC against the sensor, each pixel of the sensor connects with a PUC on the ROC through the indium bumps. The bumps reshaped after a second reflow which homogenized the distance between the sensor and the ROC, and corrected for small misalignments between the ROC and the sensor during the flip-chip process.

Part IV

Strip Detectors Simulations

Chapter 7

Steady State Simulations

When dealing with 3D sensors, design features such as the internal electric field inside the sensor become more complex than for planar sensors. For this reason, accurate methods to predict the electrical characteristics are needed. The use of Finite Elements Method (FEM) allows to estimate the electrical characteristics such as the capacitance in the complex geometries of the 3D sensors, as well as to model the charge transport needed to understand the charge collection of the detectors.

As seen in section 4.1.1, the electronic noise registered by the VA chip's electronics depends on the amount of capacitance connected to the readout channel. There were several sources of capacitance in the detector: The first was the capacitance due to the metallization mentioned in section 5.1.3, the second was caused by the 3D conductive wires inside the sensor, and the third one is the stray capacitance from the wire bonds. In this chapter, the first two sources are estimated using FEM available in the software COMSOL Multiphysics V6.0[112].

7.1 Capacitance In Planar Strip Detectors

Due to computing resources constraints, it was desired to know how much of the detector needed to be modeled and how much could be approximated to make accurate estimations for the capacitance. In planar strip detectors, most of the capacitance comes from the neighboring strips. Instead of simulating all the strips and calculating individual capacitances, the first task was to find how many neighboring strips significantly affected the capacitance of the central strip in the model.

For this task, the capacitance of a middle strip surrounded by a variable number of conductive strips was simulated in a 500 µm thick diamond inside an infinite air box, which had a pad metallization on the bottom side of the diamond which was opposite to the side that contained the strips as it is shown in Figure 7.1a. The width of the strips was 25 µm, the pitch of the strips was 50 µm, and the strips were 4 mm long.

From the results shown in Figure 7.1b, it was found that for a high number of strips (of the order of at least ten or more total strips), the six closest neighboring strips and the backplane contributed to 99.78 % of the total capacitance seen by the middle strip. Considering this, the following simulations containing surface metallization only included seven strips.

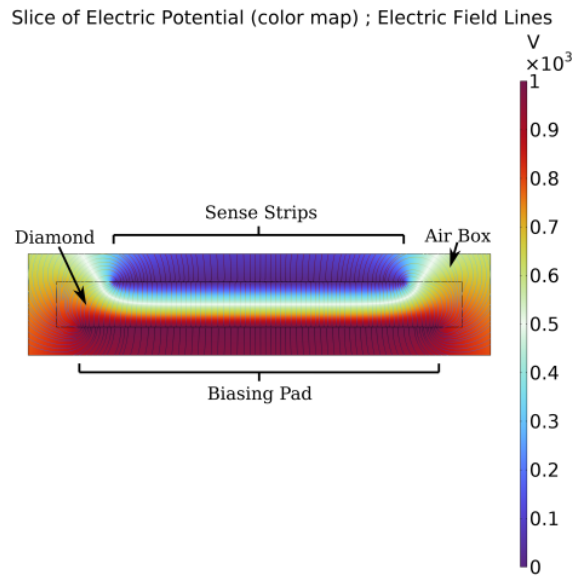

(a) Electric potential in a planar detector.

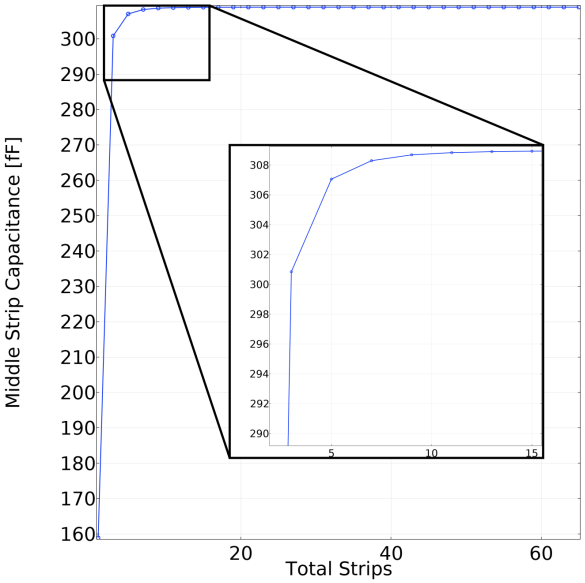

(b) Capacitance of the middle strip as a function of the total number of sensing strips (middle and neighboring strips).

Figure 7.1: Simulation results obtained for strip planar detectors. In (a), a total of 30 strips were simulated and the electric potential inside and outside the diamond is shown with the color scale, while the lines depict the electric field. The detector was biased with 1000 V and was simulated inside an infinite air box. In (b) the total capacitance felt by the middle strip is shown, where the capacitance plateaus at a total of 7 strips (six neighboring strips) where it reaches 99.78 % of the total capacitance.

7.2 Capacitance Of Square Cells 3D Strip Detectors

7.2.1 Surface Metallization Capacitance

As shown in Figure 4.4, the metallizations for 3D square detectors have two features: On the top side of the sensor, the 3D sensing wires of the cells are ganged together by strip metallization to form a sensing strip that would be connected to a channel of the VA chip. On the bottom side, the HV 3D wires are ganged together by a mesh pattern of surface metallization to deliver the HV to all of the HV wires of all the 3D cells in the sensor.

To estimate the capacitance of the surface metallization in the 3D detectors, a 3D model with seven channels was built that included the planar strips on the top, the mesh pattern on the bottom, the bonding pads, and other surface metallization such as the guard ring (which was present in the measured 3D strip detectors) as it is shown in Figure 7.2. As the objective of this model was to estimate the capacitance due to the metallization, no 3D wires were present in the model. The length of the strips was the same as the mesh pattern on the bottom of the sensor, which depended on the number of simulated rows in the grid, and the width of the strips was 10 µm. A linear relation was obtained for the total capacitance seen by the central channel as a function of the number of rows of square cells in the mesh pattern on the bottom side of the

sensor. This relationship, which is linear, is shown in Equations 7.1 for cells with a side length of 50 µm, 100 µm, and 150 µm. The crossing of the lines in Figure 7.2 is a consequence of the initial capacitance for one row of 3D cells, which is larger for smaller cells, and the proportional factor with the number of rows of 3D cells, which is larger for larger 3D cells.

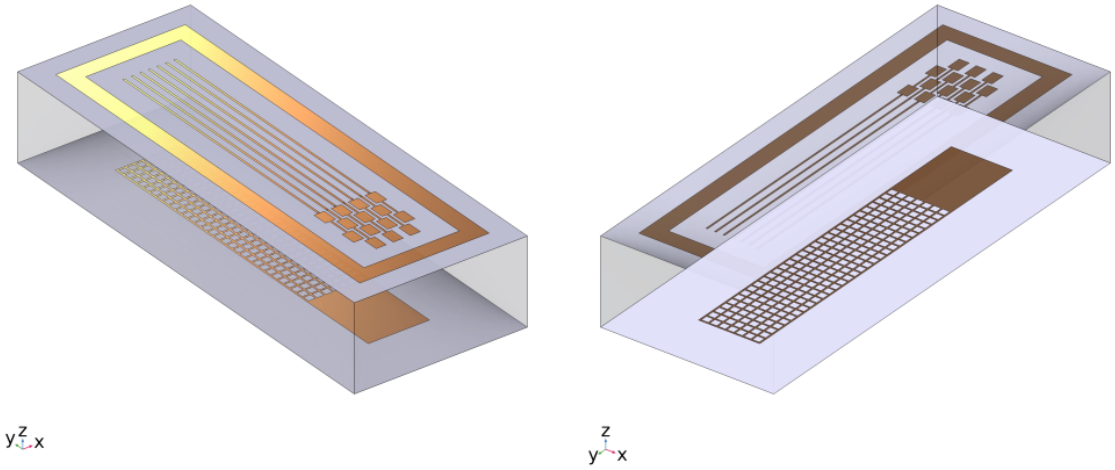

(a) Top view of the model with the surface metallization.

(b) Bottom view of the model with the surface metallization.

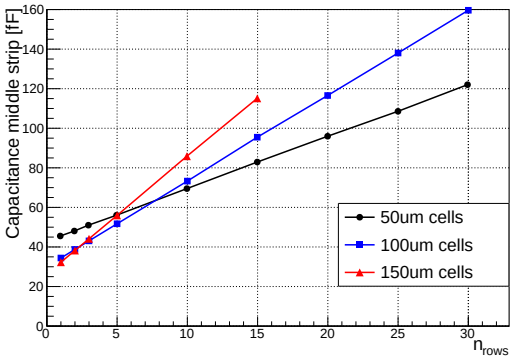

(c) Middle strip capacitance vs. number of rows for 150 µm square cells grid.

Figure 7.2: Model used to simulate the capacitance seen by the middle strip as a function of the number of rows present in the mesh pattern on the bottom of the sensor ((a) and (b)). In (c), the linear relationship for the capacitance as a function of the number of grid rows per strip is shown.

$$C_{M_{50\mu m}}(n_{rows}) = 42.69\,\text{fF} + n_{rows} \cdot 2.63\,\text{fF} \tag{7.1a}$$
$$C_{M_{100\mu m}}(n_{rows}) = 30.10\,\text{fF} + n_{rows} \cdot 4.32\,\text{fF} \tag{7.1b}$$
$$C_{M_{150\mu m}}(n_{rows}) = 25.90\,\text{fF} + n_{rows} \cdot 6.01\,\text{fF} \tag{7.1c}$$

The general form for the expressions in Equations 7.1 is a first-order polynomial, as seen in Equation 7.2. Each polynomial factor can be parametrized according to the pitch between the strips, "pitch," equal to the side of the 3D squares. The parametrization and the empirical models that fit the parameters are shown in Figure 7.3, and the fitted parameters are shown in Table 7.1. From the parametrization, it is clear that the constant independent term C_{M_0} decreases with increasing pitch down to the value given by $C_{M_{00}}$ when the pitch tends to infinity. On the other hand, the term proportional to the number of rows C_{M_n} increases linearly with the pitch.

$$C_{M_p}(p, n_{rows}) = C_{M_0}(p) + C_{M_n}(p) \cdot n_{rows} \tag{7.2}$$

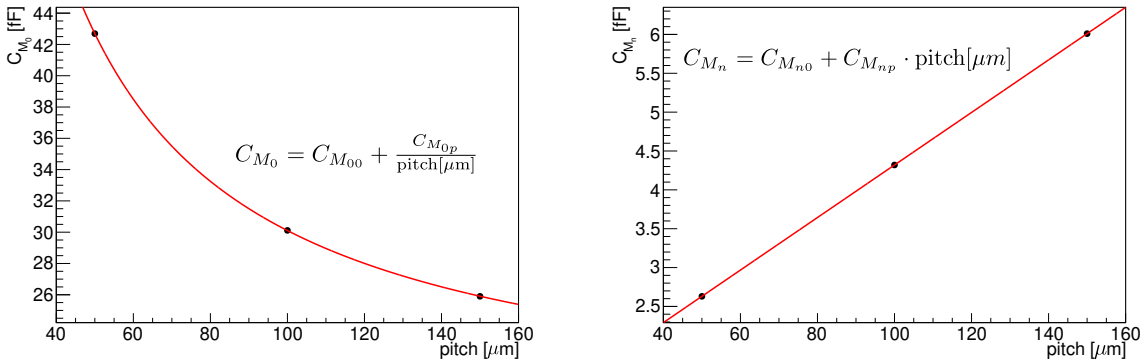

(a) Offset parameter.

(b) Proportional parameter to n_{rows}.

Figure 7.3: Empirical models that fit the linear parameters shown in Equation 7.2 to the data.

$C_{M_{00}}$	$C_{M_{0p}}$	$C_{M_{n0}}$	$C_{M_{np}}$
17.6 fF	1255.8 fF	0.94 fF	0.04 fF

Table 7.1: Fitted parameters for the data shown in Figure 7.3.

7.2.2 Capacitance Of 3D Wires In Square Cells

To estimate the capacitance caused by the conductive 3D wires traversing the sensor, models similar to the one shown in Figure 7.4a were simulated.

Inside the diamond, when considering the electric field due to the 3D electrodes, the electric field component parallel to the 3D electrodes is negligible in most of the volume and can be

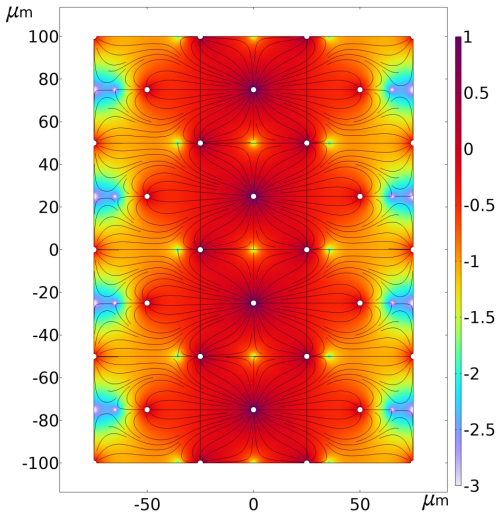

(a) Electric field simulation for 50 µm square 3D cells.

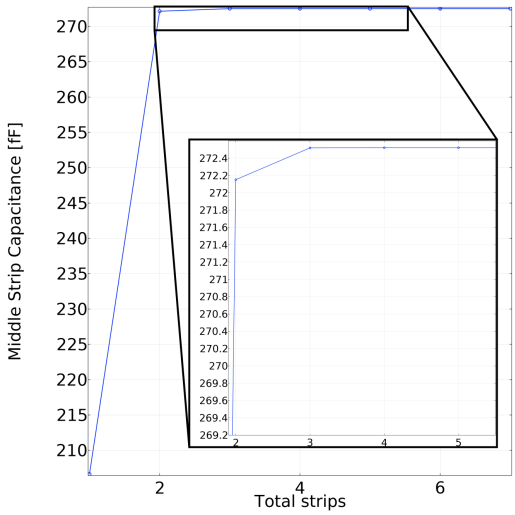

(b) Middle channel capacitance as a function of the total number of strips.

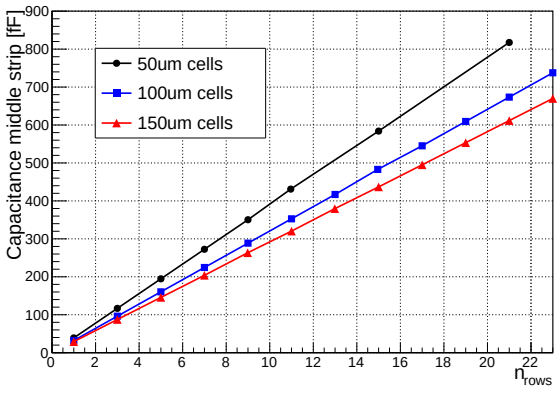

(c) Middle channel capacitance as a function of the number of rows.

Figure 7.4: Simulation results for 50 µm square 3D cells. In (a) the color scale depicts the strength of the electric field in decades of V/µm when the sense wires of the middle channel were at 45 V and the rest of the 3D wires were connected to ground. The black curves represent the field lines, and the white circles are the 3D wires. In (b), the relation between the total capacitance and the number of total channels is shown, while (c) shows the relation between the total capacitance and the number of connected 3D cells in a channel.

ignored for simplicity. As a result, a 2D model can be used. The 2D model consisted of a grid of 3D cells arranged in columns and rows. The 3D wires had a length of 500 µm and 2.6 µm diameter[113]. The sense 3D wires for each of the rows in the same strip were connected such that they were all connected to the same electrical terminal for the simulation.

As before, due to computing resources constraints, before determining the relationship

between the capacitance of the central strip as a function of the number of connected rows in each strip, it was desired to determine how many strips should be modeled to account for more than 99 % of the total capacitance seen by the central strip.

The results for this simulation can be seen in Figure 7.4b. Unlike with the planar strips, where most of the capacitance came from the six closest neighboring strips, for the 3D cells, the wires of the nearest two adjacent strips already contributed to more than 99 % of the total capacitance seen by the central channel (which includes the central strip).

The obtained linear relationship for 50 µm square 3D cells can be seen in Figure 7.4c. Equations 7.3 show the capacitance of a strip as a function of the ganged rows per strip for 50 µm, 100 µm, and 150 µm 3D square cells. As expected, the 3D wires introduce more capacitance to the detector channel than the surface metallization.

$$C_{3DCols_{50\,\mu m}}(n_{rows}) = n_{rows} \cdot 38.93\,\text{fF} \tag{7.3a}$$

$$C_{3DCols_{100\,\mu m}}(n_{rows}) = n_{rows} \cdot 32.07\,\text{fF} \tag{7.3b}$$

$$C_{3DCols_{150\,\mu m}}(n_{rows}) = n_{rows} \cdot 29.12\,\text{fF} \tag{7.3c}$$

As above, the linear parameters can be parameterized as a function of the "pitch", as shown in Equation 7.4. In this case, an empirical model that fits the data for the parameter C_{3D} is shown in Figure 7.5, and the fitted parameters of the model are shown in Table 7.2. From the fit, it is seen that the proportional term C_{3D} decreases with increasing pitch, and in the limit when the cells are infinitely large, the term C_{3D} tends to 0. At the same time, the model suggests, as expected, that the proportionality term C_{3D} blows to infinity when the logarithm of the pitch in µm approaches 0.65 (for a pitch of $\sim 2\,\mu$m), which is comparable to the size of the 3D wires.

$$C_{3DCols_p}(p, n_{rows}) = C_{3D}(p) \cdot n_{rows} \tag{7.4}$$

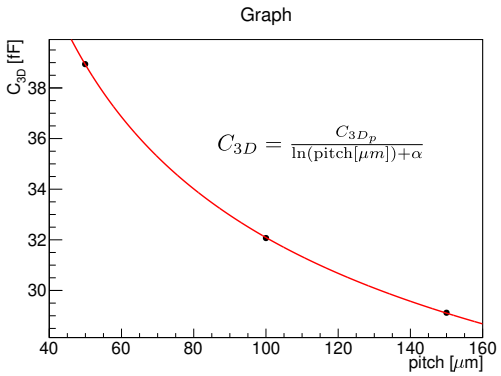

Figure 7.5: Empirical model that fits the parameter shown in Equation 7.4 to the data.

α	C_{3D_p}
−0.65	126.8 fF

Table 7.2: Fitted parameters for the data shown in Figure 7.5

7.2.3 Total Capacitance Of 3D Strips Detectors

The full 3D model shown in Figures 7.6a and 7.6b was simulated to calculate the total capacitance that the VA chip's channel connected to the central strip would see as a consequence of the surface metallization present on both sides of the sensor, as well as the 3D wires of each of the 3D cells that traverse the sensor.

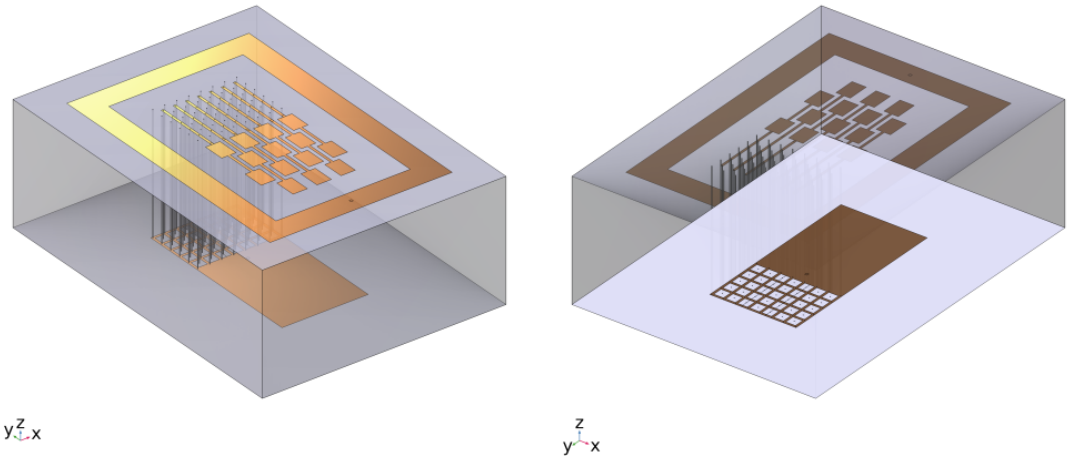

(a) Top view of the model with the strip metallization for each channel.

(b) Bottom view of the model with the mesh metallization.

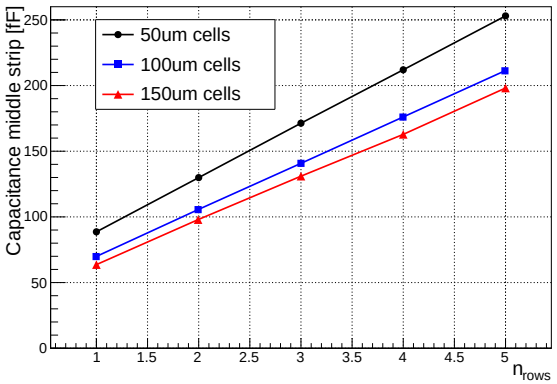

(c) Relationship between the total capacitance and the number of 3D cells per channel.

Figure 7.6: In (a) and (b) are shown the top and bottom views respectively of the surface metallization of the modeled detector. Inside the diamond, the 3D wires can be seen. In (c), the linear relationship obtained from the simulation is shown for the 50 µm square 3D cells.

The simulation results showed that the total capacitance, seen by a channel in the VA chip connected to the central strip, scales linearly with the number of 3D cells connected in each strip. The obtained linear relation for the 50 µm, 100 µm, and 150 µm are displayed in Equation 7.5.

Variations of the resistivity of the 3D wires, within the range $[0.1 - 10]\,\Omega\,\text{cm}$ (which includes the measurements reported in[99]), did not affect the simulated electric fields for the capacitance calculations, as the resistivities of air and diamond are orders of magnitude larger than the resistivity of the 3D wires.

$$C_{3DStrips_{50\,\mu\text{m}}}(n_{rows}) = 48.8\,\text{fF} + n_{rows} \cdot 40.8\,\text{fF} \tag{7.5a}$$

$$C_{3DStrips_{100\,\mu\text{m}}}(n_{rows}) = 34.4\,\text{fF} + n_{rows} \cdot 35.4\,\text{fF} \tag{7.5b}$$

$$C_{3DStrips_{150\,\mu\text{m}}}(n_{rows}) = 30.7\,\text{fF} + n_{rows} \cdot 33.4\,\text{fF} \tag{7.5c}$$

The empirical models that describe the linear parameters in Equation 7.6 can be seen in Figure 7.7. Unlike the metallization capacitance, in which one of the parameters increased with the pitch, both parameters decrease. The fitted parameters of the empirical models can be seen in Table 7.3.

$$C_{3DStrips_p}(p, n_{rows}) = C_{3DSt_0}(p) + C_{3DSt_n}(p) \cdot n_{rows} \tag{7.6}$$

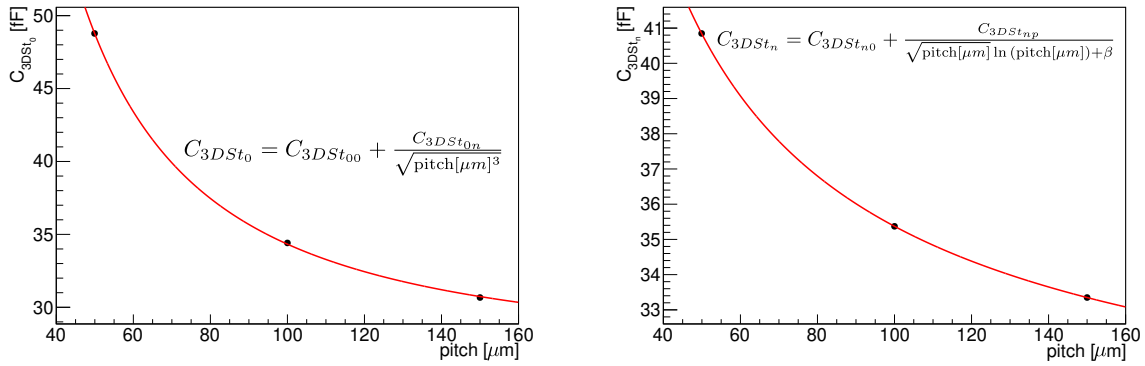

(a) Offset parameter.

(b) Proportional parameter to n_{rows}.

Figure 7.7: Empirical models that fit the linear parameters shown in Equation 7.6 to the data.

$C_{3DSt_{00}}$	$C_{3DSt_{0n}}$	$C_{3DSt_{n0}}$	$C_{3DSt_{np}}$	β
24.1 fF	4808.0 fF	27.4 fF	363.3 fF	-0.69

Table 7.3: Fitted parameters to the data shown in Figure 7.7.

The results from Equation 7.5 were compared with the approach of adding arithmetically the contributions from the surface metallization shown in Equation 7.1a with the contribution from the 3D wires shown in Equation 7.3a. This approach of adding the metallization and the 3D wires' capacitance contributions was needed for estimating the capacitance of a channel in the Multi-3D device because the computing resources did not allow the full detector simulation

with its different parts. The resulting estimated capacitances, following the approach of adding the metallization and the capacitance of the 3D wires, are shown in Equation 7.7.

$$C_{3DStrips_{50\,\mu m}}(n_{rows}) \approx 42.69\,\text{fF} + n_{rows} \cdot 41.56\,\text{fF} \tag{7.7a}$$

$$C_{3DStrips_{100\,\mu m}}(n_{rows}) \approx 30.10\,\text{fF} + n_{rows} \cdot 36.39\,\text{fF} \tag{7.7b}$$

$$C_{3DStrips_{150\,\mu m}}(n_{rows}) \approx 25.90\,\text{fF} + n_{rows} \cdot 35.13\,\text{fF} \tag{7.7c}$$

Figure 7.8 shows the relative error between estimating the capacitance using Equations 7.7 instead of Equations 7.5. The relative error for the approach of estimating the capacitance by adding the metallization capacitance with the 3D wires capacitances is an overestimation of the total capacitance. The red dots in Figure 7.8 correspond to the relevant pitches and number of rows per strip from Irrad-3D, Full-3D, and Poly-3D detectors. A maximum error of 4.7 % was obtained for the Poly-3D. With this in mind, the estimation of the capacitance for the Multi-3D detector, which consists of square, rectangular, and hexagonal cells, was estimated using the approach of adding the metallization capacitance with the capacitance of the 3D wires due to the complexity of the detector. An error of less than 5 % was expected for the capacitance in the Multi-3D estimated in this way.

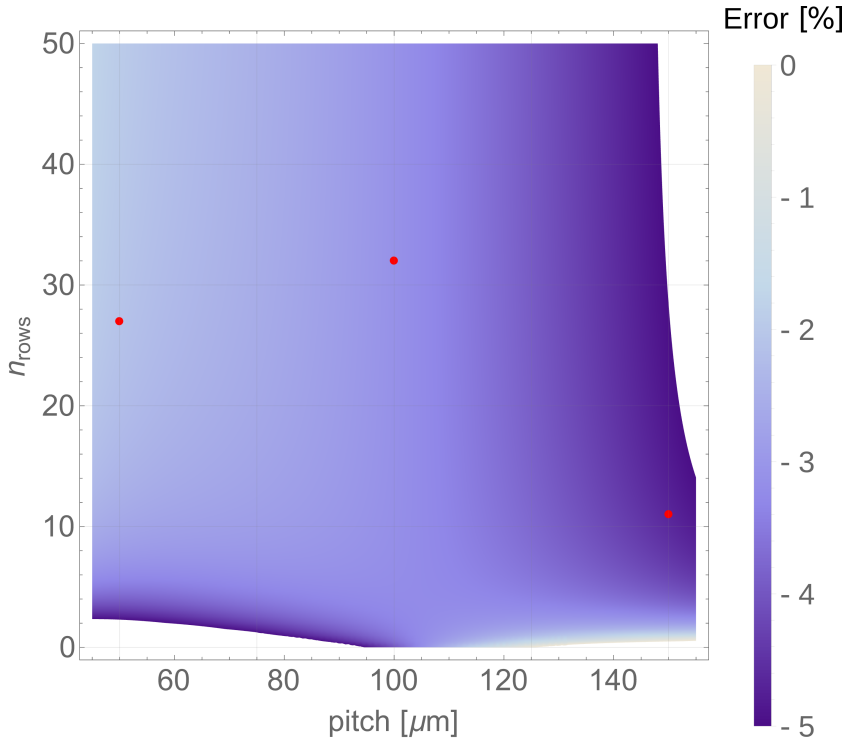

Figure 7.8: Relative error between the full estimation of the capacitance using Equations 7.5 and the estimation of the capacitance by adding the metallization and the 3D wires capacitance using Equations 7.7. From left to right, the red dots represent the Irrad-3D-50 µm, Full-3D, and Poly-3D detectors.

7.3 Capacitance Of Long Rectangular And Hexagonal 3D Strip Detectors

The Multi-3D device had a section that consisted of long rectangular 3D cells with dimensions of 100 µm×200 µm, and another section with regular hexagonal cells with a pitch between the strips of 100 µm, which gave them a side length of 66.67 µm. The 3D wires had a length of 500 µm and 2.6 µm diameter. The simulation of the electric field for the capacitance calculations in these types of 3D detectors can be seen in Figure 7.9. The obtained estimations for the total capacitance for the long rectangular and hexagonal cells are shown in Equations 7.8a and 7.8b, respectively.

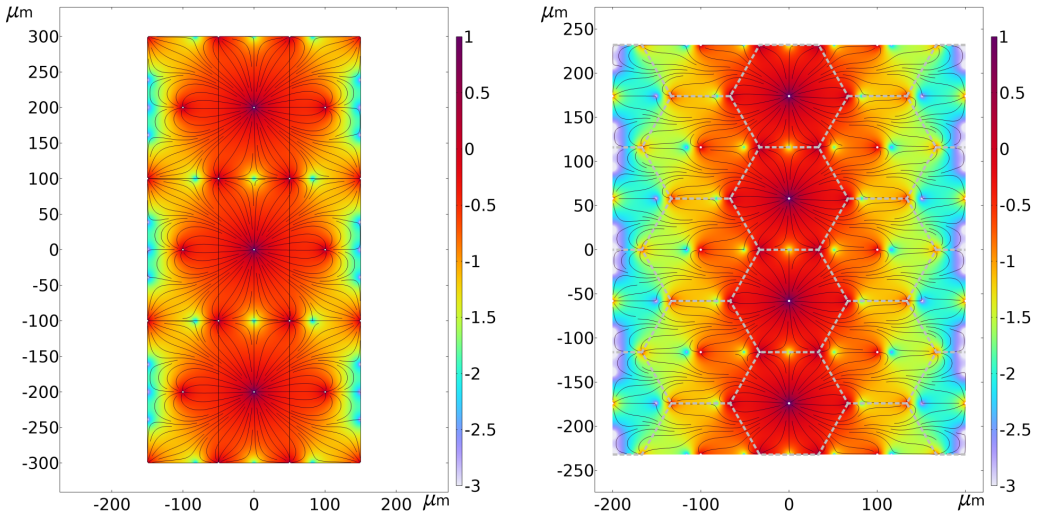

(a) Long rectangular cells. (b) Hexagonal cells.

Figure 7.9: Simulation result rectangular cells (a) and hexagonal cells (b), when the central strip was biased with 90 V and the rest of the 3D wires were connected to the ground. The color scale shows the magnitude of the electric field in decades of V/µm, and the black curves depict the field lines.

$$C_{3DStrip_{rect}}(n_{rows}) \approx 29.84\,\text{fF} + n_{rows} \cdot 39.52\,\text{fF} \tag{7.8a}$$

$$C_{3DStrip_{hex}}(n_{rows}) \approx 32.31\,\text{fF} + n_{rows} \cdot 34.53\,\text{fF} \tag{7.8b}$$

In the Multi-3D, where the square, rectangular and hexagonal cells were present in each detector channel, the capacitance per row of cells was largest for the rectangles, while it was smallest for the hexagons. The simulations in this section will be used to estimate the expected noise measured by the different detectors tested during the test beams at CERN.

7.4 Electric Field Inside 3D Cells

The final use of steady-state simulations for this thesis was to calculate the average electric field inside a 3D cell in a 3D detector (the 3D cell would be surrounded by other 3D cells, as is the case for most 3D cells in a 3D detector). For this task, the bias 3D wires in the corners of the 3D cell were held at a constant voltage potential, while the middle sense 3D wire was set to ground. The simulations calculated the electric field inside the 3D cell, and the field magnitude average was calculated. Figure 7.10 shows the simulation results for 100 µm square 3D cell biased with 90 V and 50 µm square 3D cell biased with 45 V. The average electric field magnitude for the 100 µm cell biased with 90 V was 0.62 V/µm, while the 50 µm cell biased with 45 V was 0.76 V/µm. Even though the applied potential scaled proportionally with the distance between the 3D wires in the cell, it can be seen that for a larger ratio between the square cell length and the 3D wire's radius, the electric field near the wires is larger, but the average electric field magnitude over the whole cell is smaller.

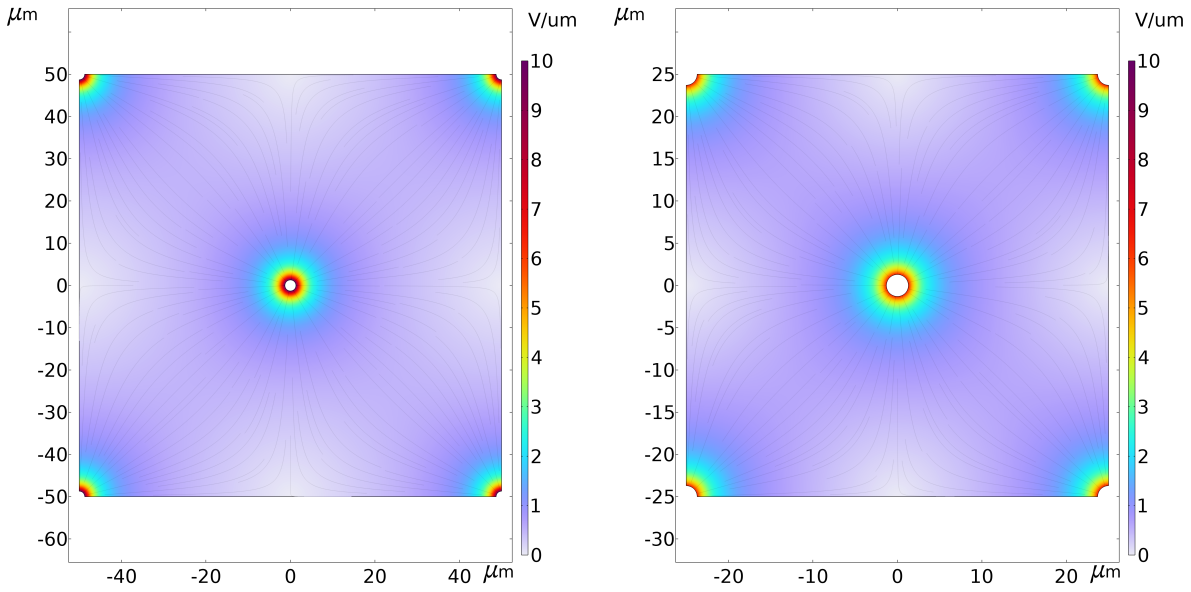

(a) Electric field magnitude for 100 µm square cell biased with 90 V.

(b) Electric field magnitude for 50 µm square cell biased with 45 V.

Figure 7.10: Electric field magnitude inside the square 3D cells with the same 3D wires' radius but different cell length. The color scale represents the electric field magnitude, while the color lines depict the electric field lines.

Chapter 8

Dynamic Simulations

To estimate the effects of different geometries and the impact of fabrication defects in the 3D wires on the performance of the detectors in terms of collected charge, a dynamic model that would predict the charge collected by a channel and its adjacent channels was elaborated from first principles. The model was implemented using COMSOL Multiphysics V6.0[112].

8.1 Finite Element Modelling Of Shockley–Ramo Theorem

As the number of electron-hole pairs generated by the passage of MIP in diamond is usually below O(10^5 eh-pairs) for 500 µm thick sensors, which is low enough so that the generated charges do not significantly affect the fields[1], it was decided to divide the modeling into two parts to increase the speed of the simulations. The first would be a stationary model to calculate the electric and weighting fields[2] in the sensing strip and its neighbors without the effects of the ionized charges. The second would use the resulting electric and weighting fields to make a transient Monte Carlo simulation that incorporated the drift and the diffusion of the carriers to calculate in each time step the induced currents $i_{ch}(t)$ in each of the strips. The integral of the induced current on a strip until a certain time would give the induced charge q_{ch} for the strip at that time (as shown in Equation 8.1). In practice, this is achieved by the use of a charge-sensitive amplifier.

$$q_{ch}(t) = \int_0^t i_{ch}(\tau)\mathrm{d}\tau \tag{8.1}$$

8.1.1 Planar Detector Modelling

The transport of the charge carriers inside the detectors is driven mainly by diffusion and drift due to an electric field. Studies have been performed in characterizing these parameters for scCVD diamonds[44, 82] but not for pCVD diamonds. One of the reasons why this is the case is the inhomogeneity of pCVD diamonds. Unlike good quality scCVD diamonds that show

[1] The generated charge carriers are three orders of magnitude smaller than the charge stored in the capacitance of a 3D cell or of a pixel in a planar detector.

[2] See section 2.5.2 for a description of the weighting fields.

low variability in parameters such as their CCD or the low field mobility for electrons and holes, the variability is much more significant in pCVD diamonds, making it difficult to make generalizations[114, 115].

As an approach to set the pCVD parameters for the simulations, the measured parameters on a scCVD diamond by Pernegger et al.[44] were used unless specified otherwise. These parameters are shown in Table 8.1.

Carrier	μ_0 (cm^2/Vs)	v_{sat}(cm/s)
e	1714	9.6×10^6
h	2064	14.1×10^6

Table 8.1: Low-field drift mobilities and saturation velocities used for the dynamic simulations[44].

Characterization Of Diffusion Parameters

The diffusion was modeled as a Brownian motion with discrete time steps that followed the Maxwell-Boltzmann distribution for the velocity in each of the three spatial directions. To find the diffusion coefficients, the Einstein relation was used:

$$D_{\begin{Bmatrix} e \\ h \end{Bmatrix}} = \frac{\mu_{\begin{Bmatrix} e \\ h \end{Bmatrix}} k_B T}{q} \tag{8.2}$$

, where "k_B" is Boltzmann's constant, "T" is the temperature in K, and "q" is the elementary charge. Using the mobilities in Table 8.1, the diffusion coefficients for electrons and holes shown in Table 8.2 were obtained. These coefficients are in agreement with experimental measurements for CVD diamonds that are in the range $(10, 100)\,\mathrm{cm}^2/\mathrm{s}$[116].

Carrier	D (cm^2/s)
e	44.3
h	53.4

Table 8.2: Calculated diffusion coefficients at 300 K, assuming the mobilities in Table 8.1.

To correctly model the Brownian motion so that the particles diffused according to the diffusion coefficients in Table 8.2, it was necessary to find the length of the time steps in which the particles have a certain velocity determined by Monte Carlo methods.

For a given direction (e.g. x), due to diffusion, the charge carriers spread obeying the following relation:

$$\langle x(t)^2 \rangle = 2Dt \tag{8.3}$$

The mathematical second moment of the position shown in Equation 8.3 can be estimated to first order by dividing the total time t into N discrete time steps τ. Within these steps, the particle is assumed to move with a constant random velocity v_i that follows the Maxwell-Boltzmann

distribution for a given temperature, which is determined using Monte Carlo methods. The temperature used for all calculations was 300 K. The process is shown in Equations 8.4:

$$x(t = N\tau) = \sum_{i=1}^{N} v_i \tau \tag{8.4a}$$

$$\langle x^2 \rangle = \tau^2 \sum_{i=1}^{N} \langle v_i^2 \rangle \tag{8.4b}$$

$$\langle v_i^2 \rangle = \frac{k_B T}{m_{eff}} \tag{8.4c}$$

$$\langle x^2 \rangle = \tau^2 N \frac{k_B T}{m_{eff}} \tag{8.4d}$$

Equating Equations 8.3 and 8.4, an equation for the time step τ is obtained in terms of the temperature T, the diffusion coefficient D, and the effective mass m_{eff}:

$$\tau = \frac{2 D m_{eff}}{k_B T} \tag{8.5}$$

The effective mass (m_{eff}) considers the characteristics of the energy bands of the crystallographic lattice to model the inertia of the charge carriers in the valence and conduction bands. To calculate m_{eff}, the parameters obtained by Naka et al.[117] were used. The calculated effective conduction masses for electrons and holes in terms of the electron mass m_0 are shown in Table 8.3:

Carrier	m_{eff}
e	0.386 m_0
h	0.520 m_0

Table 8.3: Effective conduction masses for charge carriers in CVD diamond.

Using these masses in Equation 8.5, the discrete time steps needed for the Brownian motion for the charge carriers used in the simulations are shown in Table 8.4.

Carrier	τ (ps)
e	0.75
h	1.20

Table 8.4: Discrete time steps for each charge carrier to model the Brownian motion in each direction.

The model was tested with 10 000 eh – pairs, and the simulated Brownian motion of the charge carriers spread according to the diffusion coefficients in Table 8.2.

Charge Carriers Trapping Modelling

In this modeling, the effects of charge carrier traps due to crystallographic defects or NIEL radiation defects in the sensor were represented as charge carrier traps with lifetimes much larger than the simulations' time scales (>$O(10\,\text{ns})$). In previous works, trapping effects in the simulation of diamond detectors with crystallographic defects have been modeled based on the lifetime $\tau_{\{e,h\}}$ of the charge carriers before being trapped[118, 119]. This approach of modeling with the lifetime follows the relationship between the MFP before trapping $\lambda_{\{e,h\}}$ and the drift velocity $v_{d_{\{e,h\}}}$:

$$\lambda_{\{e,h\}} = v_{d_{\{e,h\}}} \tau_{\{e,h\}} \tag{8.6}$$

In uniform electric fields and attributing the charge transport mainly to drift and not diffusion, the "schubweg" can be defined as $\lambda = \lambda_e + \lambda_h$, which would be the mean separation of electrons and holes inside a uniform electric field before being trapped. In 3D cells, the electric field is non-uniform throughout the cell, and there are low-field regions where diffusion is the leading cause of charge carrier transport. For this reason, it was decided to model a *life-path* variable "λ_p" that takes into account the total distance traveled by the charge carriers by means of the electric field and diffusion. It was assumed that electrons and holes in diamonds had the same value of λ_p. If the electric field was uniform, diffusion was ignored and the MFP before trapping of electrons and holes were equal, which means that the schubweg was equivalent to twice the MFP before trapping, then the life-path would be equal to the MFP before trapping.

The idea behind the life-path variable was that crystallographic defects in pCVD diamonds are uniformly distributed throughout the sensor. When irradiated, the radiation damage has no preference and introduces charge traps uniformly in the bulk of the sensor. Therefore the trapping probability for a charge carrier moving through the lattice through drift and diffusion would follow an exponential distribution with the following probability density function:

$$f_{trap}(l;\lambda_p) = \frac{e^{-l/\lambda_p}}{\lambda_p} \tag{8.7}$$

, where l is the total length of the distance traveled by a particle inside the bulk of the sensor.

8.2 Validation Of The Dynamic Simulation With Planar Detectors

8.2.1 Hecht Theory Validation

To validate the equivalence of the modeling with life-path λ_p and the schubweg, the Hecht relation[63] for charge carriers in a uniform field without diffusion was tested. The test was on a planar 500 µm thick diamond detector with a potential difference of 1000 V. A perpendicular line of 10^4 eh-pairs traversing the sensor was generated (simulating the passage of an ionizing particle), and the charge carriers were allowed to drift until they were trapped. This procedure was repeated for different life-paths. The results of the simulation against the Hecht theory are shown in Figure 8.1.

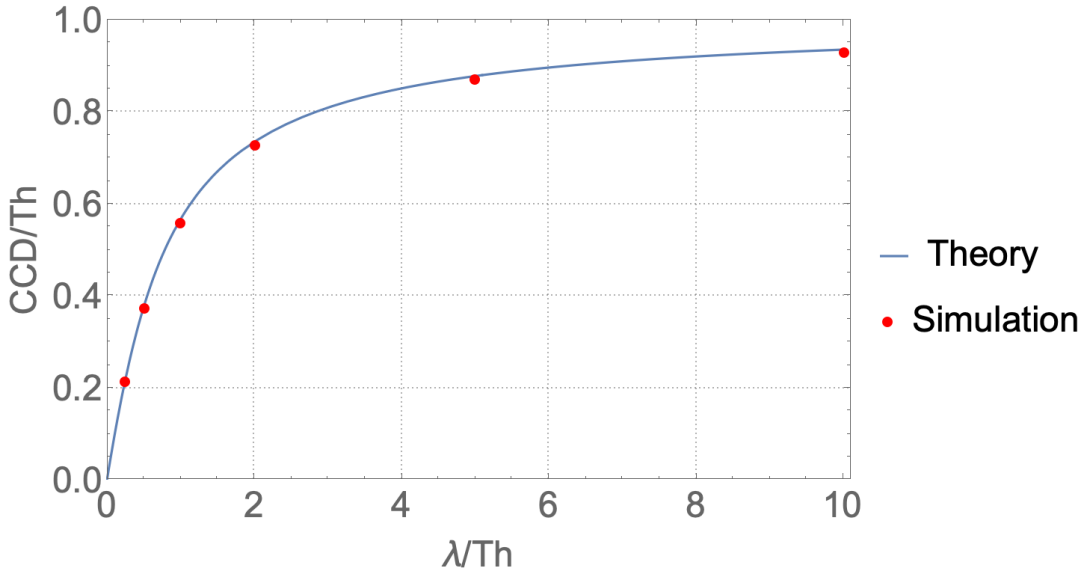

Figure 8.1: Theoretic curve for the CCD as a function of the schubweg. The plot is overlaid with the simulation results. The theory curve was introduced in Equation 2.5d in section 2.4.

8.2.2 Transient Currents Validations

To corroborate the transient capabilities of the simulation, data from Edge transient-current technique (e-TCT) was used. Christian Dorfer, in his Ph.D. thesis, developed an e-TCT setup based on a 25 fs laser pulse from the Ultrafast Laser Physics group at ETH Zurich[120] to focus the laser pulses with a wavelength of 400 nm inside diamond pad detectors generating via 2-photon absorption $O(10^5\,\text{eh}-\text{pairs})$. The eh-pairs drifted to the pad electrodes, and the transient current generated by the transport of the charge carriers was amplified with a broadband amplifier[119]. Figure 8.2 shows results shared by Christian Dorfer for different measurements at different positions in the Y-direction.

The data from the measurement labeled as "340 µm" in Figure 8.2 was used to test the simulation. For the simulation, the parameters for the diamond obtained by Christian Dorfer were used[82], and $10^5\,\text{eh}-\text{pairs}$[3] were generated at the same position as the measurement[4]. The measurement system of the e-TCT used for the data is based on a broadband amplifier with a 40 dB gain and a 50 Ω termination. To compare the simulation results in µA with the data in mV, the induced current had to be multiplied by the 50 Ω of the termination and then multiplied by 100 to account for the 40 dB gain of the amplifier. As only 10^5 eh-pairs were simulated instead of the $\sim 4.8 \times 10^5$ eh-pairs generated in the measurement, the previous result was multiplied by 4.8. This gives a total scaling of the simulated current by 24 kΩ. Additionally, the broadband amplifier frequency range of operation is from 1 MHz to 2 GHz. Passing the simulated data through that band-pass filter did not accurately reproduce the measured data. Instead, the simulated data were required to pass through a band-pass filter with cutoff frequencies from

[3] Simulating 10^5 eh-pairs was the limit in terms of computational resources in the machine used for that simulation.

[4] At 340 µm in the Y direction from the GND plane in Figure 8.2.

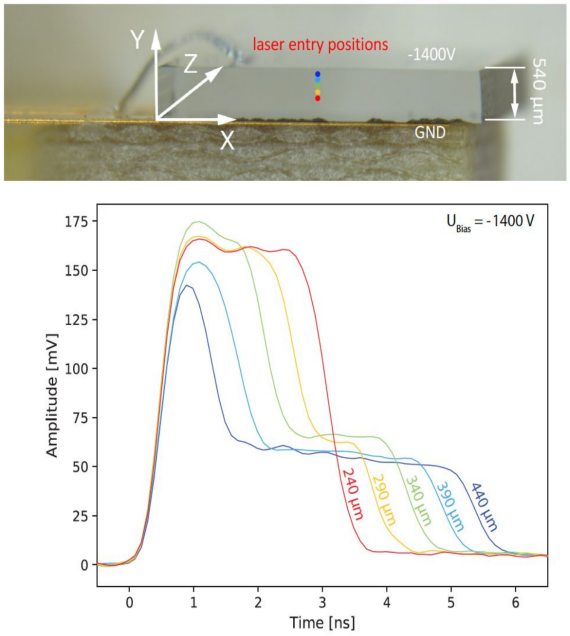

Figure 8.2: e-TCT measurements inside the diamond pad detector biased with −1400 V at different heights from the bottom face where the ground was placed.[119]

1 MHz to 1 GHz to reproduce the measured data accurately. This suggests that a parasitic effective electronic filter was present in the setup, which narrowed the frequency range to ~ 1 GHz. The simulation results compared with the measurement data can be seen in Figure 8.3.

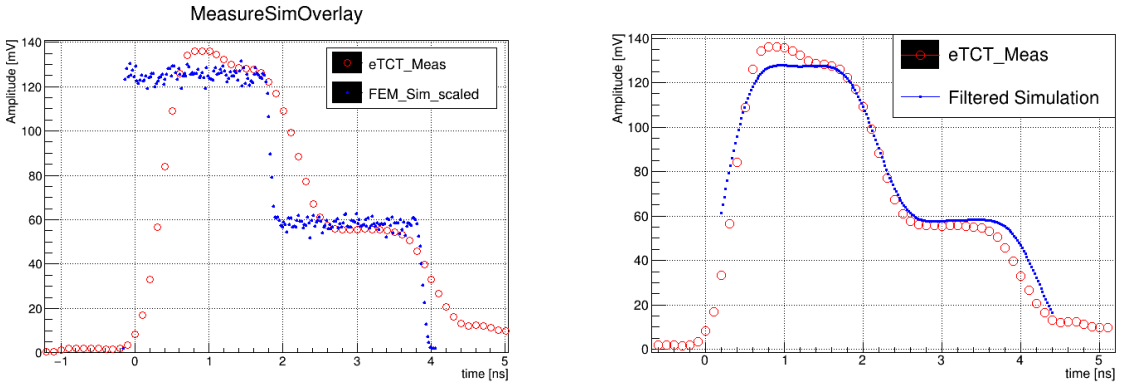

(a) Data and simulation.

(b) Data and filtered simulation.

Figure 8.3: Comparison between e-TCT data (open red circles) and the simulation (solid blue dots). In (a) the simulated data is shown with only a scaling factor of 24 kΩ. In (b) the simulated data is passed through a band-pass filter from 1 MHz to 1 GHz which is more restrictive than typical for the broadband amplifier used to take the data.

The qualitative agreement between the simulation and the measured data in terms of the

signal amplitudes and the time between the signal transitions corroborate the transient capabilities of the simulation model for planar devices.

8.3 Simulations of Square 3D Strip Detectors

For the simulations of square 3D strip detectors, three 500 µm thick samples were chosen as follows: A non-irradiated pCVD diamond (Poly), an irradiated sample with a fluence of $O(3 \times 10^{15}\,\mathrm{p/cm^2})$ with 800 MeV/c protons, and a highly irradiated sample with a fluence of $O(10^{16}\,\mathrm{p/cm^2})$ with 800 MeV/c protons. The damage curve shown in Figure 2.8 for pCVD diamonds in section 2.4 was used to obtain the schubweg, which was used to estimate the CCD from Hecht's theory. The characteristics of the samples in terms of their CCD and their schubweg can be seen in Table 8.5, where the fifth column is the MFP before trapping of the charge carriers, $\lambda_{\{e,h\}}$ (assuming that the ratio between the MFP before trapping of electrons and holes is 1), and the last column is the life-path of the charge carriers. These were tuned in the simulations for agreement with the target CCD. The obtained life-paths are expected to be larger than the MFP before trapping because they include the distance traveled by diffusion. The similarity between the life-paths and the schubweg[5] suggests that at 300 K and electric fields of 2 V/µm, the charge carriers travel a similar distance by diffusion as they travel by drift due to the electric field.

Sensor type	Alias	CCD	Schubweg	$\lambda_{\{e,h\}}$	Life-path (λ_p)
Non-irradiated pCVD	Poly	230 µm	339 µm	169.5 µm	350 µm
Irradiated pCVD	I-Poly	124 µm	145 µm	72.5 µm	145 µm
Highly irradiated pCVD	HI-Poly	50 µm	53 µm	26.5 µm	55 µm

Table 8.5: Simulated detectors and their respective parameters for the collected charge (CCD) and for the trapping of the charge carriers (schubweg, MFP, and life-path). The CCD was calculated in a 500 µm diamond under a uniform electric field of 2 V/µm.

8.3.1 Simulation Methodology

A total of nine strips, each with seven cells ganged together by having the same potential in the sense 3D wire, were simulated, as shown in Figure 8.4. The same transport of the charges used to model the planar detectors in section 8.1 was used for the 3D detectors. As the transport of the charge carriers occurs inside the bulk of the sensor, where the 3D wires' contribution to the internal electric field overshadows the contribution of the surface metallization to the internal electric field, no surface metallization was included in the simulations. As no metallization is present, and no strips are visible in any of the following images, from now on the strips are referred to as channels as if they were the channels of the preamplifier connected to the strips. This will be useful to compare the simulation results with the data of the 3D detectors that will be analyzed in the chapters 11 and 14.

[5]The schubweg is the addition of λ_e and λ_h. In this case, the schubweg is twice the distance traveled by a charge carrier by means of the electric field before being trapped (i.e. neglecting the distance traveled by diffusion).

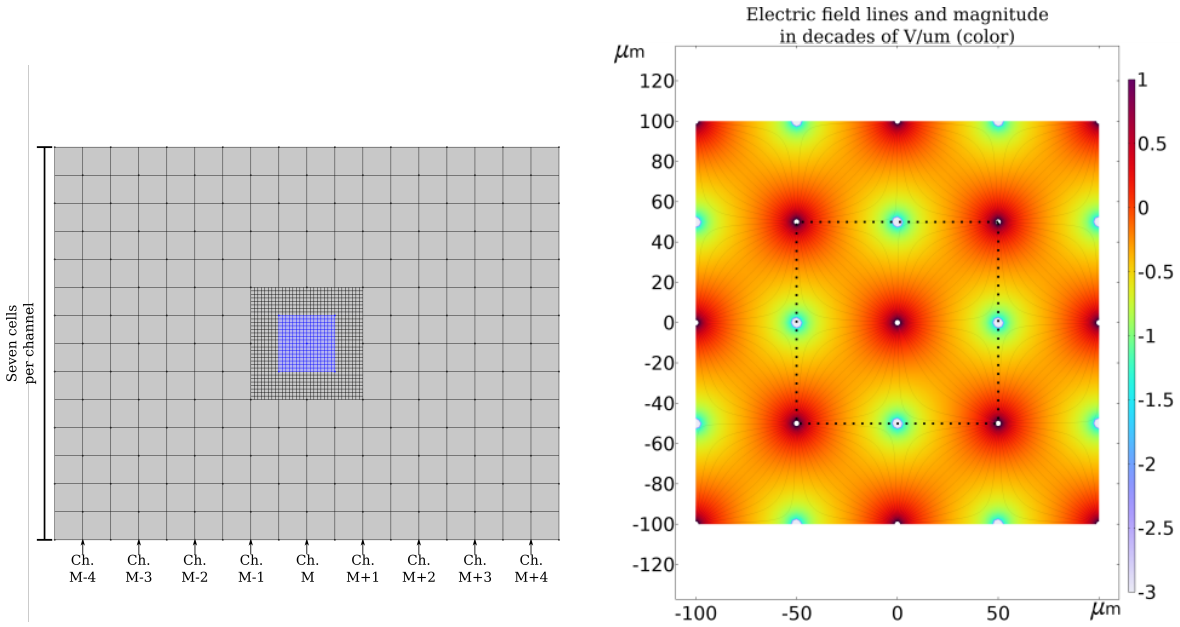

(a) Model geometry. (b) Electric field.

Figure 8.4: Model used in (a) to simulate the induced charges in square 3D strip detectors. The highlighted square corresponds to the middle cell of the middle strip Ch. M. In (b), the electric field's magnitude in color scale in decades of V/µm is shown when the bias wires are at 90 V, and the sense wires are at 0 V. The middle cell is delimited with a dashed black line.

The middle cell in the model was divided into 256 units in a square grid. The electric field and the weighting field for the channels Ch. M, M-1, and M+1 were calculated (see Figures 8.4 and 8.5). These channels would be equivalent to the channel strips in a transparent cluster predicted by the telescope (three channels for 3D strip detectors). As will be seen in chapter 11, a transparent cluster is made by a fixed number of channels around the predicted hit position in the detector under study. For each of the units in the grid of the middle cell, 10^4 eh-pairs were generated at random positions inside the grid unit. For each particle, a maximum distance of travel was randomly assigned from the exponential distribution defined by the life-path (λ_p), as shown in Equation 8.7.

The generated electrons and holes moved according to their drift velocity set by the simulated electric field and the diffusion in the three spatial directions. With the velocity of each particle and the calculated weighting fields, the induced currents in channels Ch. M, M-1, and M+1 were calculated.

In the three-channel transparent cluster for 3D strip detectors, for a convention, the channels were named according to their distance to the predicted hit position. The channel where the ionizing particle was predicted to hit is called Ch0. The next channel closest to the predicted hit position is Ch1. The remaining channel in contact with Ch0 that was not Ch1 is called Ch2.

For each time step, the total distance traveled by each particle was updated. When a particle reached its maximum travel distance, which was set at the beginning, the particle was trapped and stopped moving. The particles would continue to move with each time step, as described in

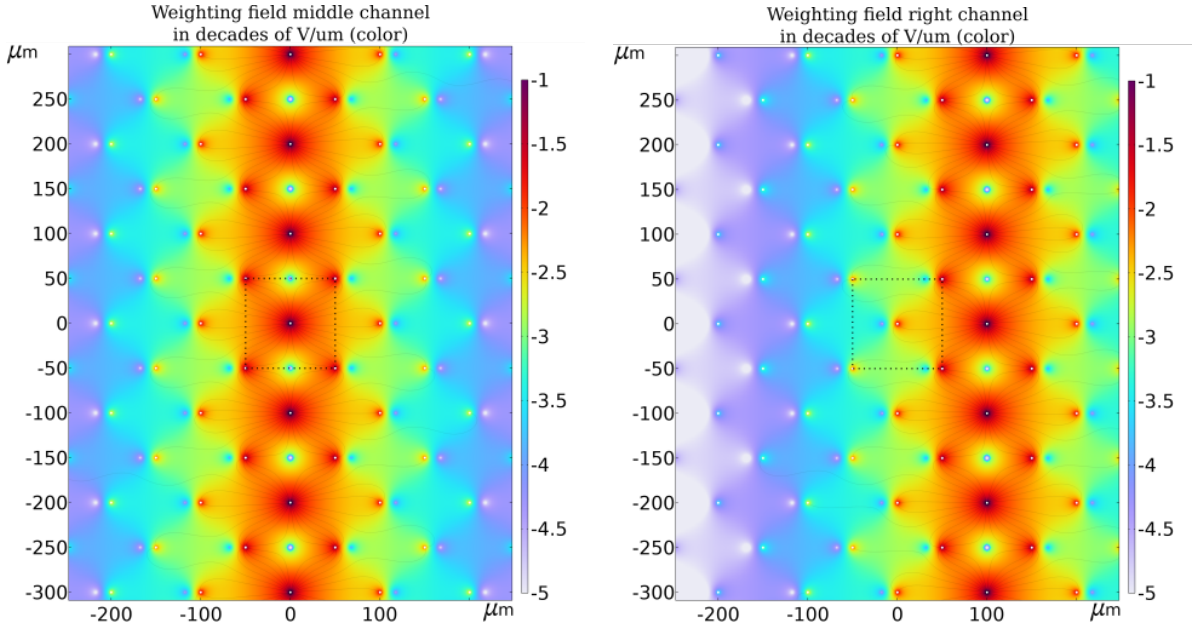

(a) Weighting field for channel Ch. M.

(b) Weighting field for channel Ch. M+1

Figure 8.5: Weighting fields of the middle channel Ch. M (a) and its channel to the right, Ch. M+1 (b). The magnitude of the fields is shown in the color scale in decades of V/µm. The middle cell in channel Ch. M is delimited with a dashed black line.

section 8.1, until they were trapped or reached a 3D wire where they would be collected. The simulation would stop when all the particles stopped moving.

8.3.2 Charge Collection Definition Discussion

Unlike planar strip detectors, in which the charge sharing among channels is always positive (i.e. an excess of charge from their baseline), in 3D detectors, this is not always the case due to the complex weighting field, as seen in Figure 8.5. While Ch0 always presents an excess of charge, Ch1 and Ch2 sometimes present a deficit of charge (read out as a negative charge) depending on the position inside the cell where the ionization occurred. In the simulations, this can be seen in Figure 8.6, where the collected charge by each channel in the transparent cluster is plotted against the hit position in the "hit" channel. It can be seen in Figure 8.6 that the induced charges in Ch1 and Ch2 are negative when the ionizing particle hits near the center of the strip and slightly positive near the edges. The collected charge by Ch0 (the "hit" channel) is always the highest collected charge from the three channels in the transparent cluster, as expected.

In the case of 3D pixel detectors, if the ROC[6] attached to the 3D sensor has zero-suppression[7] and the dimensions of the 3D cells match precisely the dimensions of the pixels in the ROC, then the detector would only sense the excess charge and not the deficit of charge of the surrounding 3D cells. On the other hand, if the 3D cells in the sensor are small enough, such that multiple

[6]Readout chip.

[7]It only registers signals above a threshold.

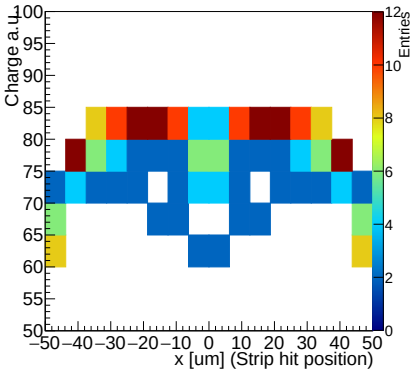

(a) Collected charge Ch0.

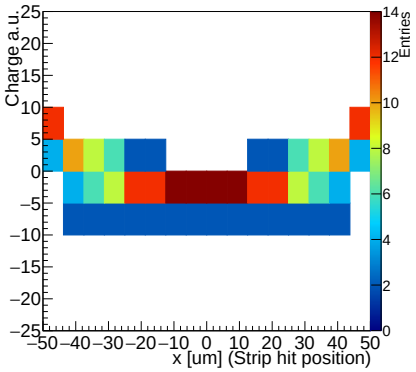

(b) Collected charge Ch1.

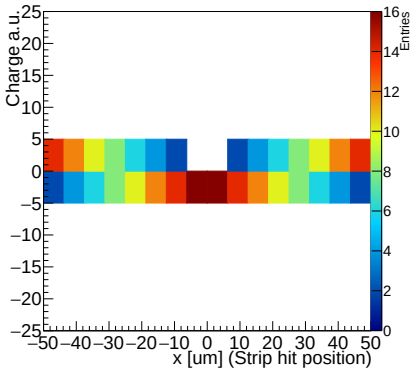

(c) Collected charge Ch2.

Figure 8.6: Collected charge by each of the channels in the transparent cluster depending on the hit position in the strip of Ch0. For each entry, a total of 10^4 eh-pairs were simulated.

3D cells are ganged together for each pixel in the ROC, then the detector would sense the excess and deficit of charge.

In the case of 3D strip detectors, if only the charge from the channel with the highest charge is considered, there would be a drop in the collected charge close to the edge with the adjacent channels due to charge sharing. On the other hand, if the charge collection is considered as the addition of the two highest charges of the channels in the transparent cluster, then the charge sharing near the edge of adjacent channels would be taken into account in the charge collection. Note that for most of the hit positions in the 3D cell, Ch1 would be the second-highest channel, and Ch2 would be the third-highest channel.

Figure 8.6a shows the case where the charge collection is defined as the highest charge in the transparent cluster, which would correspond to the charge in Ch0. The cases where the charge collection is defined as adding the two and three highest channels in the transparent cluster are shown in Figures 8.7a and 8.7b, respectively. Table 8.6 summarizes the expected spatial mean of the collected charge and their spatial standard deviation for each of the cases mentioned above for 3D strip detectors. A low spatial standard deviation would correspond to a better spatial uniformity of the collected charge.

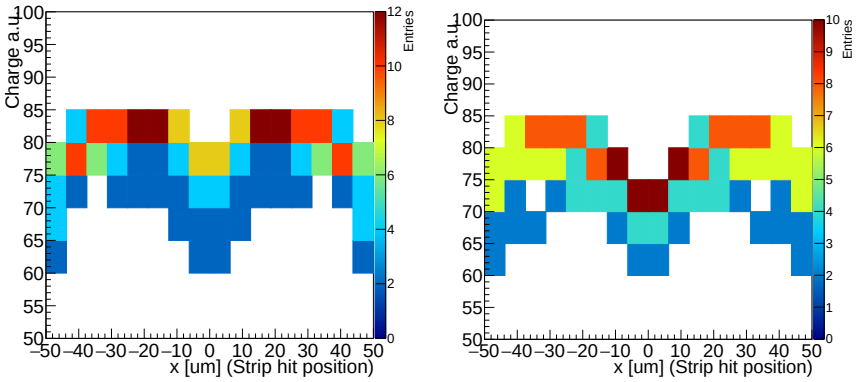

(a) Charge collection for the two channels with the highest charge.

(b) Charge collection for the three channels with the highest charge.

Figure 8.7: Charge collection for the two and three strips with the highest charge in the transparent cluster as a function of the predicted hit position in the strip of Ch0. For each of the 256 entries, a total of 10^4 eh-pairs were simulated.

Charge collection definition	$\langle q \rangle$ (a.u.)	σ_q (a.u.)
1 Highest	77.25	6.34
2 Highest	77.91	5.12
3 Highest	76.06	5.14

Table 8.6: Summary of mean and variation for the three definitions of charge collection for 3D strip detectors studied.

Based on the simulation results in Table 8.6, for the analysis of the data measured on 3D strip detectors, the definition for the collected charge was chosen to be the two channels with the highest charge as they include the charge sharing in the edges when the ionizing particle hits the region between two strips (which gives as a consequence on average the highest charge collection) and also the smallest spatial variation.

8.3.3 Simulated 3D Cell Maps

In this section, the simulated conditions, in terms of temperature and biasing voltage, are similar to those of the test beam data acquired for the 3D strip detectors. Only the simulations for 100 µm 3D cells will be shown, as these cells will be studied in more detail in chapter 14. Figure 8.8 shows the charge maps for the Poly simulations, Figure 8.9 for the I-Poly simulations, and Figure 8.10 for the HI-Poly simulations.

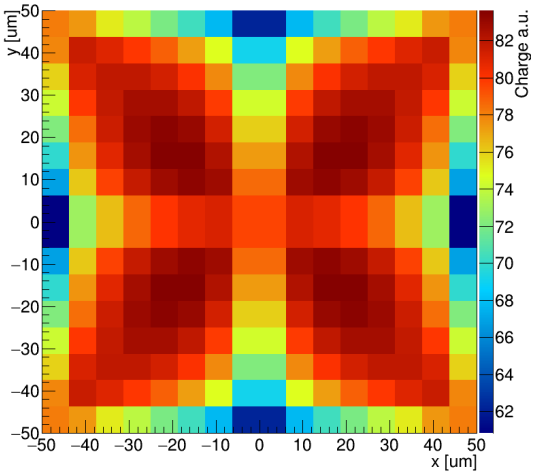

(a) Charge map collection 2 highest channels for Poly.

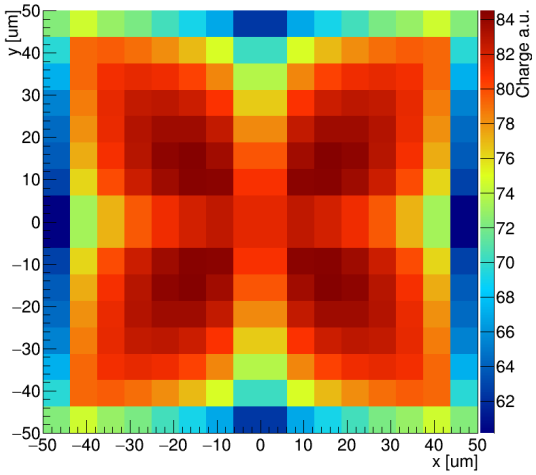

(b) Charge map Ch0 for Poly.

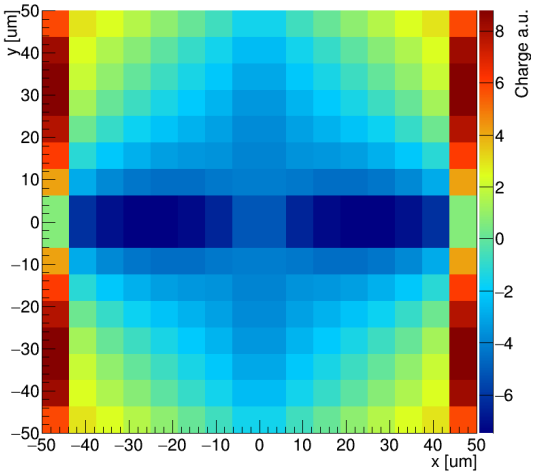

(c) Charge map Ch1 for Poly.

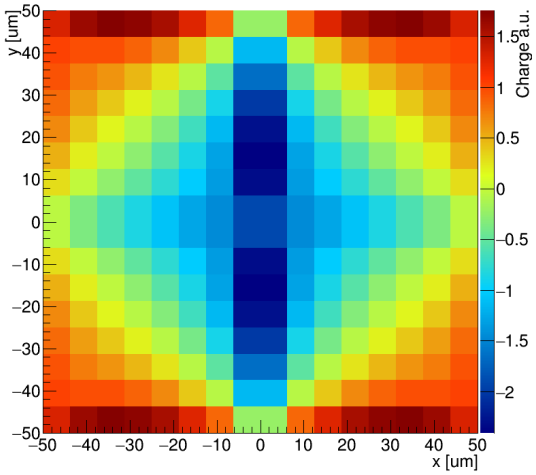

(d) Charge map Ch2 for Poly.

Figure 8.8: Charge maps for the sensor Poly biased with 90 V.

From the collected charge maps in Figure 8.8, it is expected that an unirradiated pCVD diamond 3D strip detector would collect, on average, around 80 % of the ionized charge. The low field regions, in the middle of the cell's edges, collect around 20 % less charge than the rest.

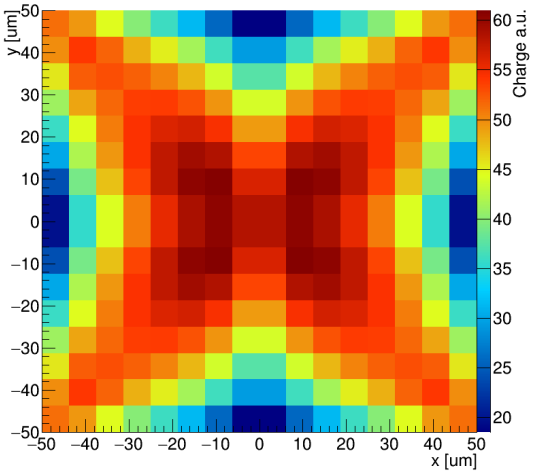

(a) Charge map collection 2 highest channels for I-Poly.

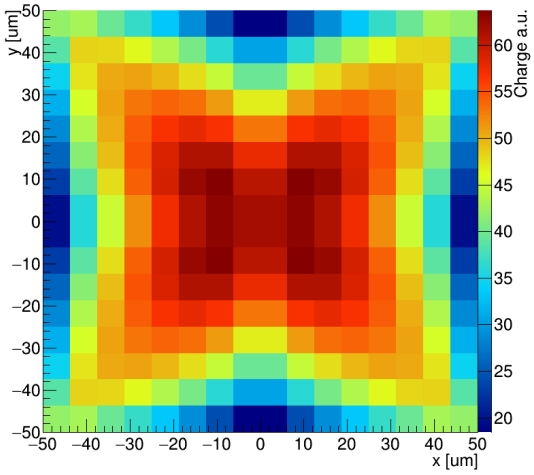

(b) Charge map Ch0 for I-Poly.

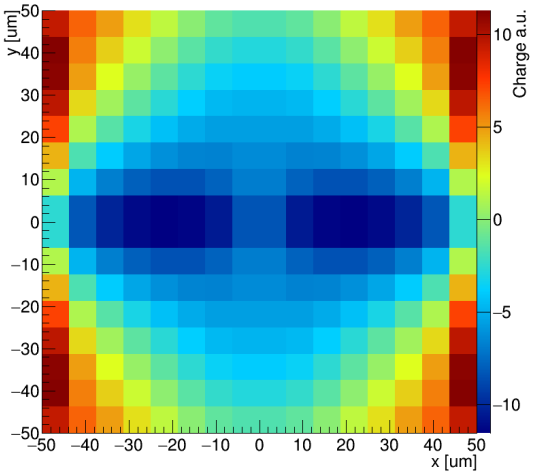

(c) Charge map Ch1 for I-Poly.

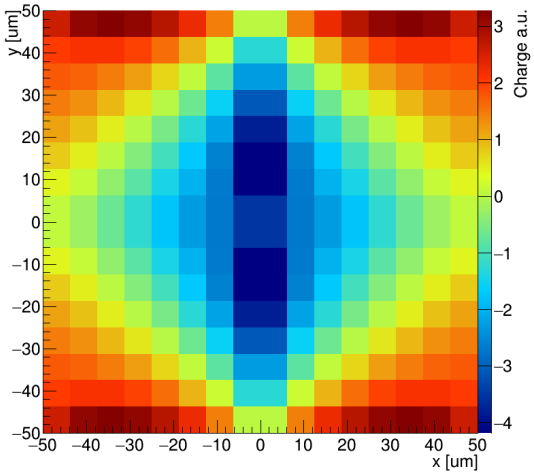

(d) Charge map Ch2 for I-Poly.

Figure 8.9: Charge maps for the sensor I-Poly biased with 45 V.

In the case of the I-Poly simulations shown in Figure 8.9, it is seen that the low charge collection regions are larger than the case of Poly. Also, the negative charges in the charge maps for Ch1 and Ch2 are more negative than the equivalent for Poly.

For the HI-Poly simulation results shown in Figure 8.10, the low charge collection regions are larger in size than in the I-Poly case. This feature is seen in the Ch0 charge map, where the highest charge collection region is reduced to the center of the cell. Although the magnitude of the most negative collected charges is similar in this case to the I-Poly one, the negative region is larger in the HI-Poly compared to the I-Poly simulation.

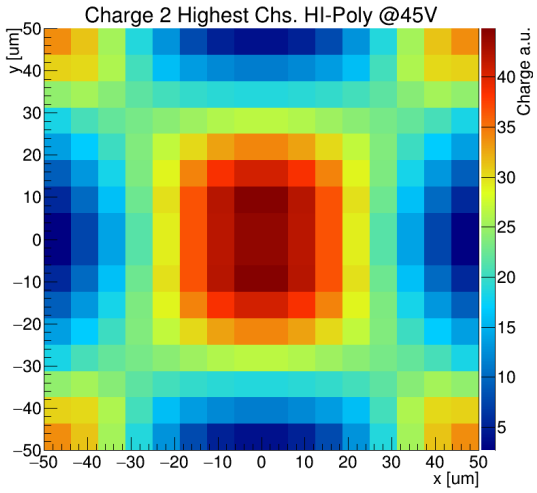

(a) Charge map collection 2 highest channels for HI-Poly.

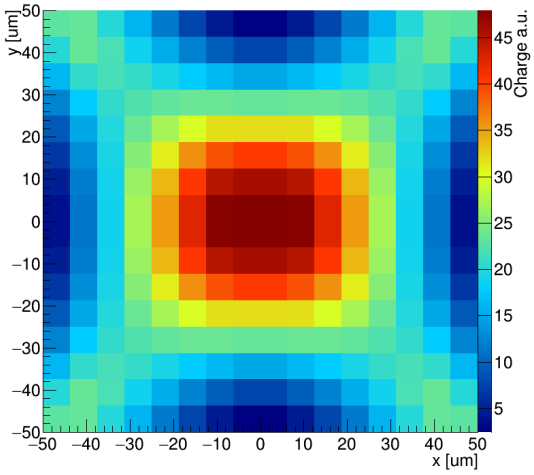

(b) Charge map Ch0 for HI-Poly.

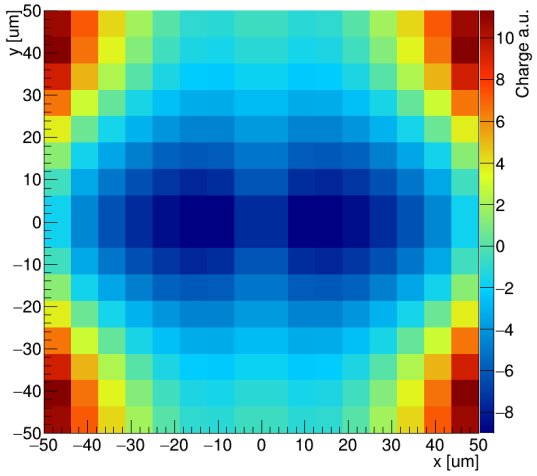

(c) Charge map Ch1 for HI-Poly.

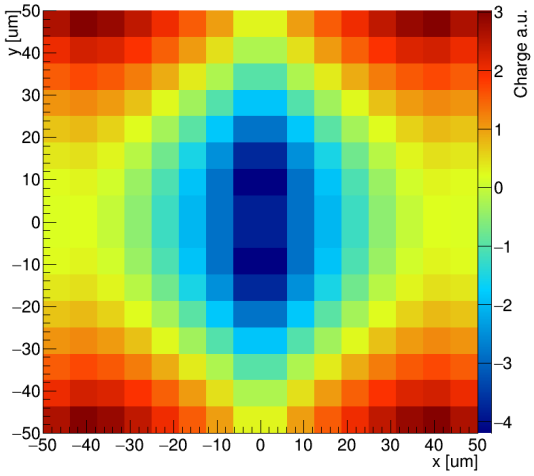

(d) Charge map Ch2 for HI-Poly.

Figure 8.10: Charge maps for the sensor HI-Poly biased with 45 V.

8.3.4 Simulation Without The Sense 3D Wire

To study the effects of a faulty 3D sense wire in one of the cells, a simulation was made in which the only difference from the previous was that the middle 3D sense wire was left floating, such that no net DC current flowed in the wire.

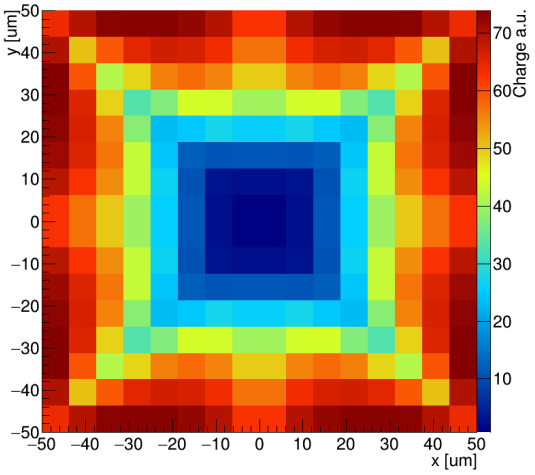

(a) Charge map collection 2 highest for Poly without the sense 3D wire.

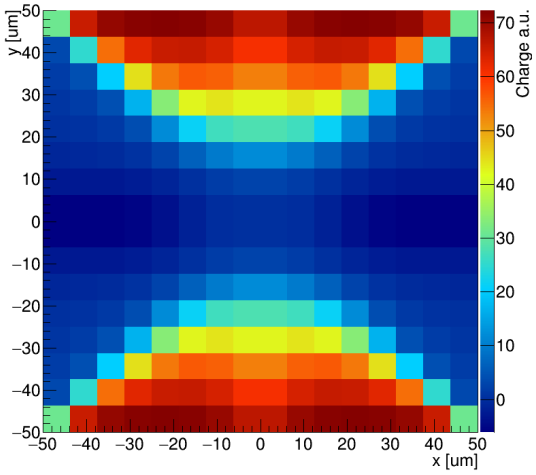

(b) Charge map Ch0 for Poly without the sense 3D wire.

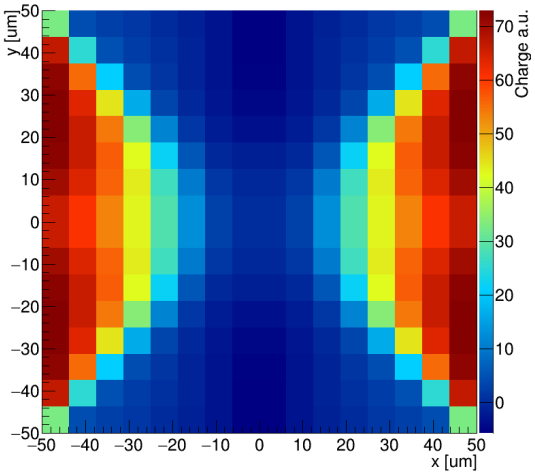

(c) Charge map Ch1 for Poly without the sense 3D wire.

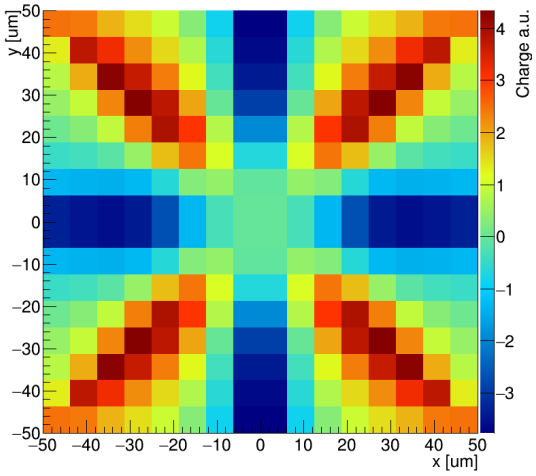

(d) Charge map Ch2 for Poly without the sense 3D wire.

Figure 8.11: Charge maps for the sensor Poly biased with 90 V and without the sense 3D wire.

The simulation results in Figure 8.11 show that when the 3D sense wire is missing, the charge collection from the two channels with the highest charge gives a low value in the region close to the broken 3D sense wire. Compared to a normal working cell, as shown in Figure 8.8, when there is a missing 3D sense wire, the center of the cell is the region that collects the least amount of charge compared to the rest of the cell. As consequence, for both Ch0 and Ch1, the center of the cell has a low charge collection.

8.3.5 Simulation Without A HV 3D Wire

Another possible defect in the 3D cells could arise from a defect in the 3D bias wire. As in the case of the faulty 3D sense wire discussed above, the faulty 3D wire was simulated as if it was disconnected, which meant that no net DC current flowed into the wire. In this case, the defective wire was located in the bottom left corner of the cell.

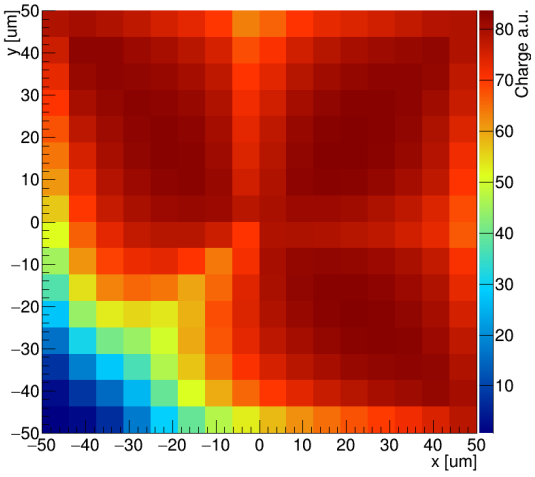

(a) Charge map collection 2 highest for Poly without one HV 3D wire.

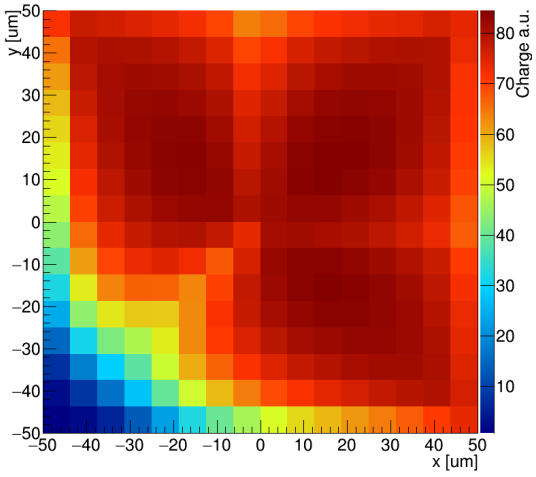

(b) Charge map Ch0 for Poly without one HV 3D wire.

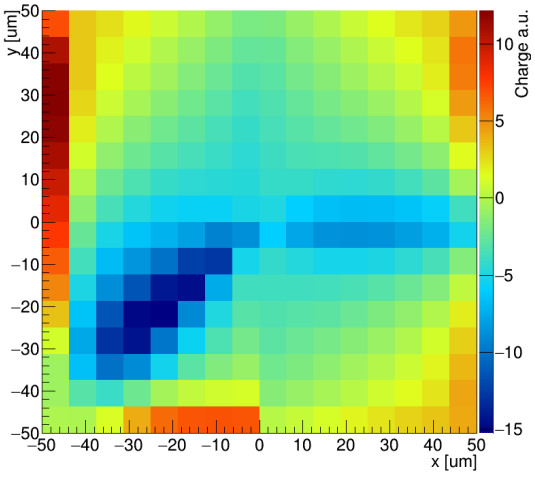

(c) Charge map Ch1 for Poly without one HV 3D wire.

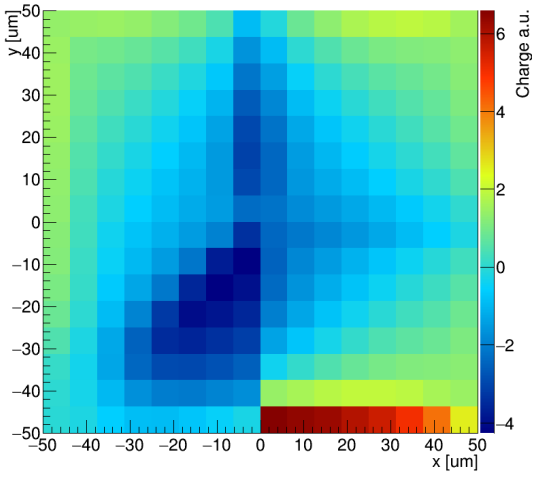

(d) Charge map Ch2 for Poly without one HV 3D wire.

Figure 8.12: Charge maps for the sensor Poly biased with 90 V and without one HV 3D wire.

As seen in the simulation results shown in Figure 8.12, the charge maps for Ch0, Ch1 and Ch2 show the lowest charge towards the defective 3D bias wire. In the case of Ch1 and Ch2, the

charge is negative, with the most negative charge present in Ch1.

8.3.6 Summary Of Simulated Square 3D Strip Detectors

A summary of the relevant simulations made with square 3D strip detectors is shown in Table 8.7. The simulations marked with an * indicate that they can be compared with experimental data from the samples described in section 4.3. In chapter 14, a comparison between the experimental data and the simulation results will be made. Note that not all the possible combinations and bias voltages were simulated due to time constraints.

Sensor			CCE (%)		
Type	Cell Size (µm)	HV (V)	Good 3D wires	No Sense 3D wire	No HV 3D wire
Poly*	100	90	77.9	47.5	71.0
Poly	50	45	88.9	-	-
Poly	25	22.5	95.3	-	-
I-Poly*	100	45	47.2	-	-
I-Poly*	50	45	77.3	-	-
HI-Poly	100	45	23.0	5.1	20.0
HI-Poly	50	45	54.9	-	-
HI-Poly	25	22.5	75.9	-	-

Notes:
- Simulation not available.
* Modeled according to real detectors that were measured.

Table 8.7: Charge collection for the two channels with the highest charge for different simulated square 3D strip detectors.

These simulations based on the life-path parameter (λ_p), indicate that non-irradiated pCVD diamond 3D strip detectors with square 3D cells would collect about 90 % of the generated charge when the size of the 3D cells is 50 µm and the HV is 45 V. This CCE is close to the measured CCE above 90 % for scCVD diamond 3D strip detectors with 3D square cells of 150 µm[28, 97] and 100 µm[100] that were measured in the past. For the case of highly irradiated sensors, 50 µm cells would only collect about 50 % of the ionized charge, and it would be required to shrink the size down to 25 µm cells to collect about 75 % of the charge at an HV of 22.5 V.

Part V

Experiments For Testing The Diamond Detectors

Chapter 9

Test Beams At CERN

The 3D detectors Poly-3D, Full-3D, Multi-3D, and Irrad-3D, presented in section 4.3, were tested during test beams at CERN, using the H6A beamline located in the North Area of the Super Proton Synchrotron (SPS) (Figure 9.1)[121]. The characteristics of this beamline and the available telescope were ideal for the high-resolution studies performed on the 3D detectors.

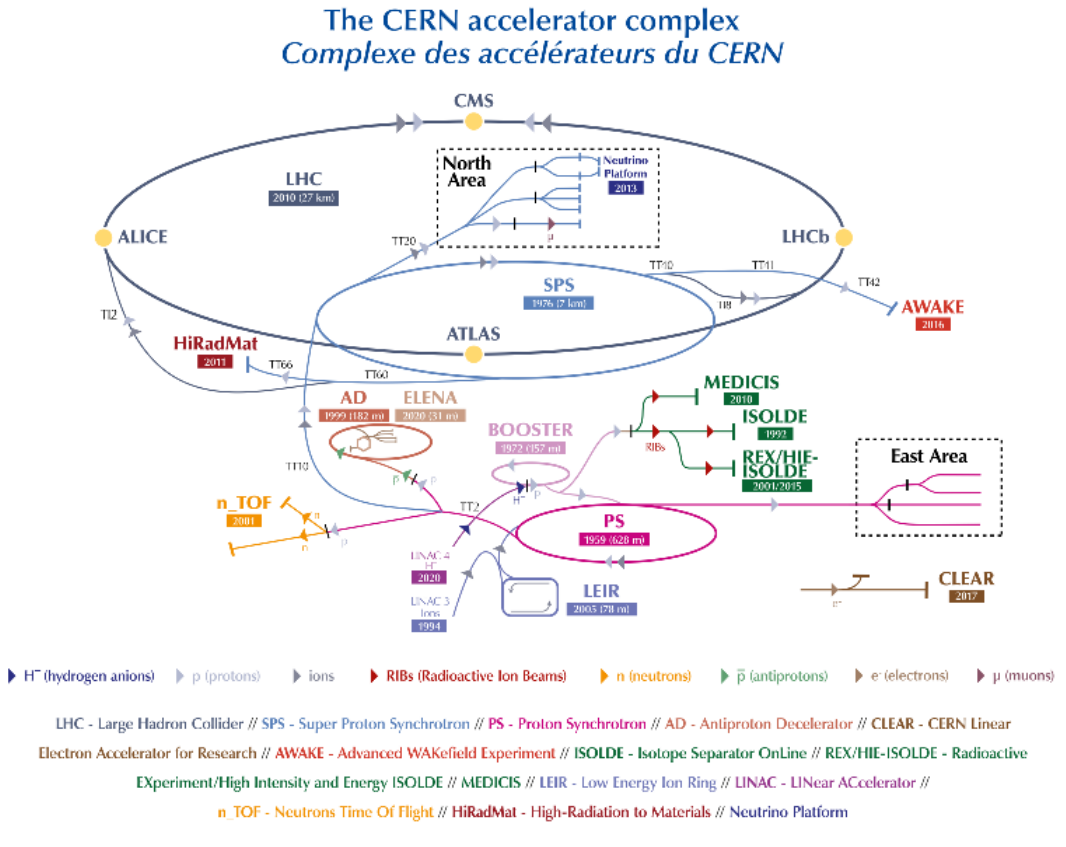

Figure 9.1: CERN's accelerators complex.[122]

9.1 Beam Characteristics

Protons with a momentum of 450 GeV/c from the SPS are extracted to the North Area. They are directed at different targets to produce secondary beams used for various scientific purposes. The RD42 Collaboration uses the H6A beamline (Figure 9.2) tuned to deliver primarily positive hadrons with a momentum of 120 GeV/c. At this momentum, the NIEL effects are expected to be negligible[39], such that most of the energy deposited in the sensors is ionization energy, which is suitable for the RD42 radiation studies. Additionally, the trajectories of the hadrons with this momentum passing through the detectors are expected to be straight, as discussed in the following section.

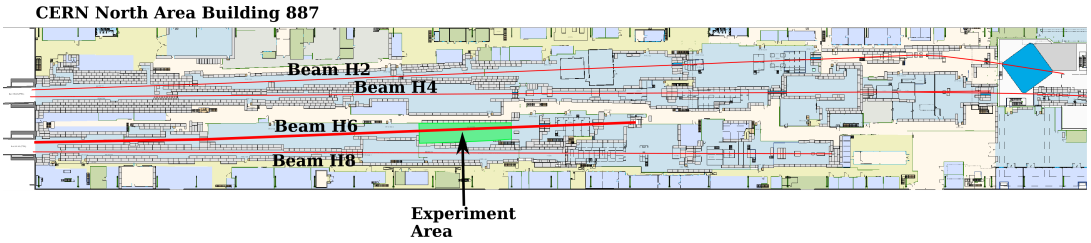

Figure 9.2: Floor plan of building 887 at the North Area of CERN. The four beam lines are painted in red, with beamline H6 wider than the rest. The experimental area, where the experimental setup was placed, is highlighted in green.[123]

The beam optics were tuned so that the beam profile at the telescope covered most of the tested detectors. The beam profiles were monitored through wire chambers located upstream from the telescope. Figure 9.3 shows the wire chamber and a typical beam profile used during the test beams.

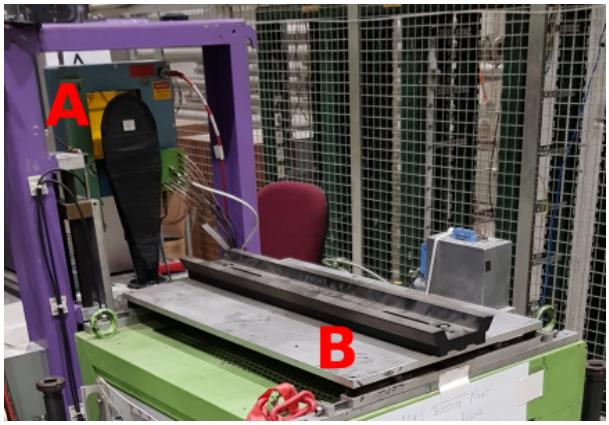

(a) Wire Chamber (A) and Telescope mount (B).

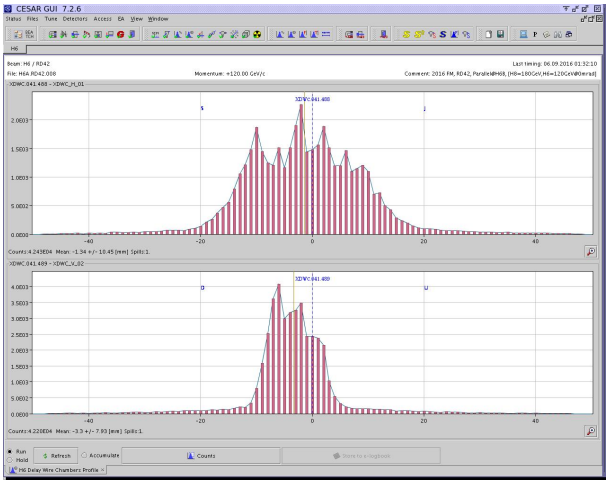

(b) Beam Profile according to Wire Chamber. Top: Horizontal profile. Bottom: Vertical profile.

Figure 9.3: Picture of the Wire Chamber and plots of the measured beam profiles

The test beam telescope was used to resolve the position of the tracks of the ionizing particles that passed through the detectors. For the RD42 test beams, the so-called "Strasbourg Telescope,"[124] which can resolve tracks positions down to the order of 5 µm on the DUT, was used.

9.2 Experimental Setup With The Strasbourg Telescope For The CERN Test Beams

9.2.1 Basic Design

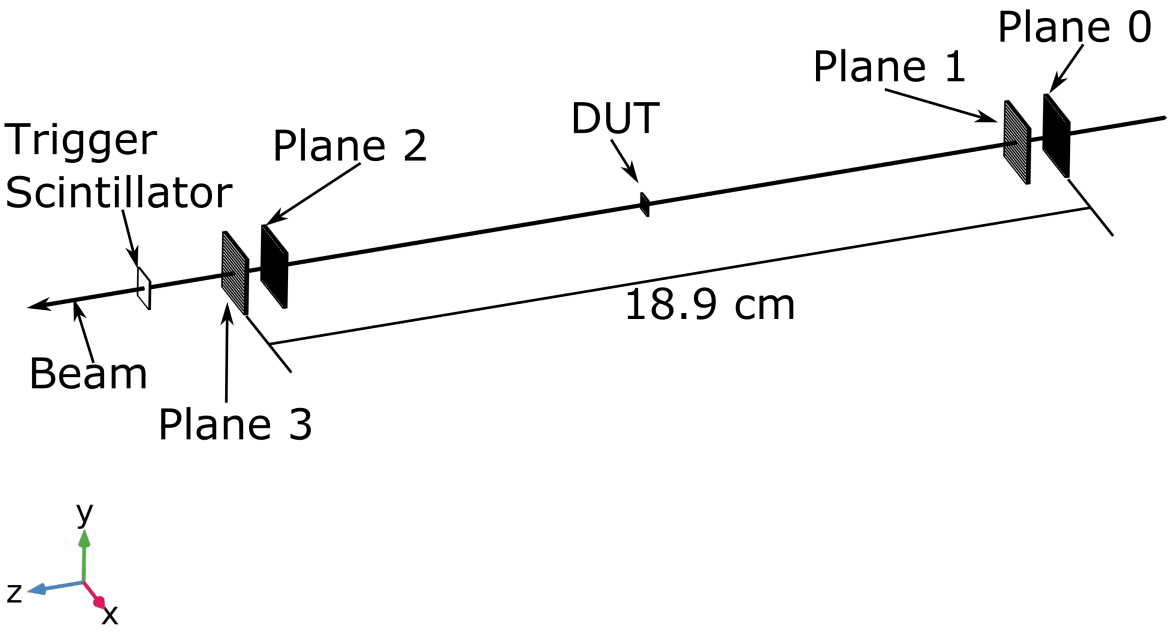

Figure 9.4: Schematic view to scale of the telescope with the DUT. The beam is aligned with the z-axis.

The Strasbourg Telescope consists of eight strip silicon planes that are arranged perpendicular to the hadron beam; four planes have the strips aligned horizontally (to resolve positions in the Y direction), and the other four have the strips aligned vertically (to resolve positions in the X direction) (see Figures 9.4 and 9.5). Each strip silicon plane consists of 256 readout strips

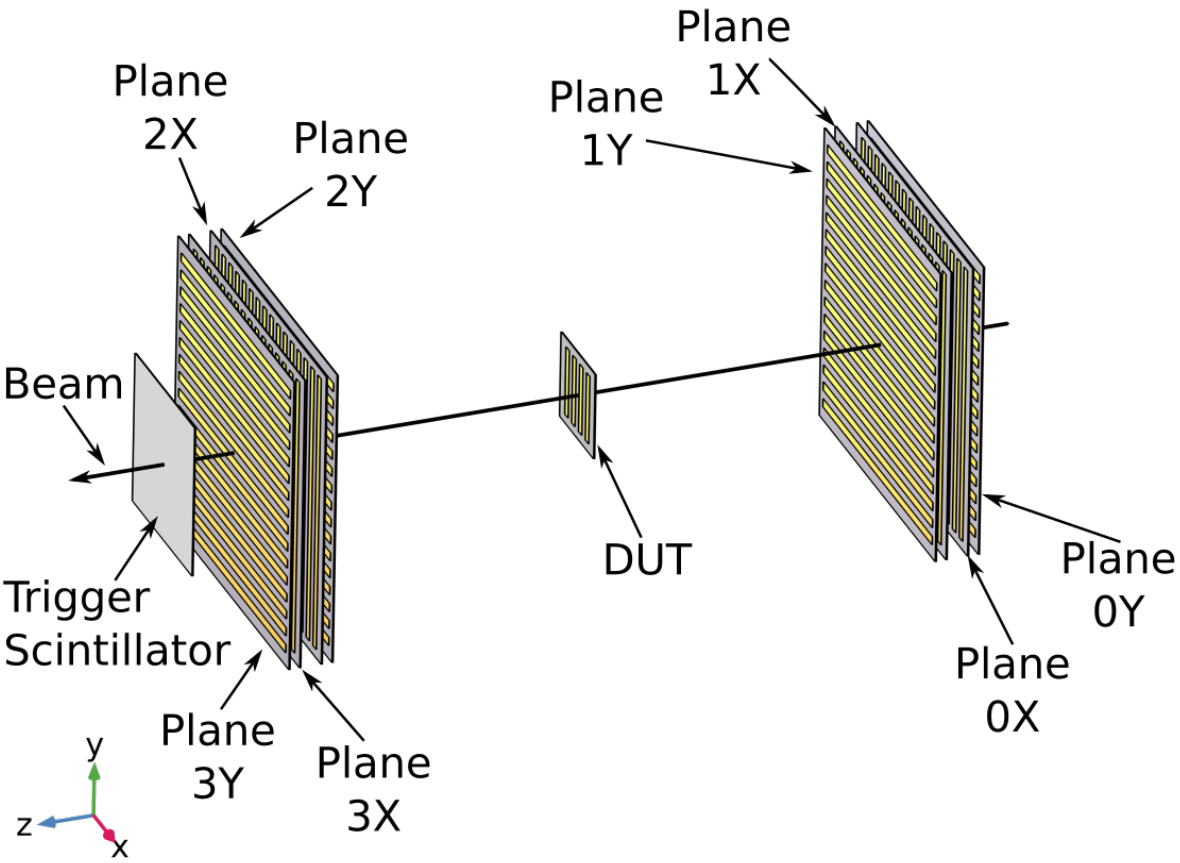

Figure 9.5: Schematic view of the telescope with the X-Y coordinates scaled-up. Each plane of the telescope consists of individual X and Y planes. Planes with vertical strips can resolve positions in the x coordinate, while planes with horizontal strips can resolve positions in the y coordinate.

with a pitch of 50 µm between the readout strips and covers an area of approximately 13 mm × 13 mm.

The strip silicon planes are placed in the following order with respect to the spatial position they resolve: (Y-X)–(X-Y)–(Y-X)–(X-Y). Neighboring planes that resolve positions in different directions are grouped together to make an X-Y plane, identified as planes 0, 1, 2, and 3 from upstream of the beam. Planes 0 and 1 have one intermediate floating strip, while planes 2 and 3 have two intermediate floating strips. These intermediate floating strips help to improve the tracking spatial resolution via charge sharing. The diamond detector prototypes (DUTs) are placed in the middle of the telescope parallel to the silicon planes, such that the strips on the diamond sensor are vertical, as seen in Figure 9.5.

Each strip of the telescope's silicon planes is connected to a channel of a VA2 Charge Sensitive Amplifier ASIC from IDEAS[92]. The VA2 ASIC is based on the Viking chip and can read up to 128 input channels. For this reason, two VA2 ASICs are needed for each silicon plane. For the DUTs, the VA2.2 Charge Sensitive Amplifier ASICs are used instead of the VA2

chip. Each plane is read out via a VME Silicon strip read-out CAMAC controller (Sirocco) ADC[125, 126], controlled by a VME DAQ that runs a real-time Operating System OS-9[127]. This system runs the data acquisition program OS9DAS. It has a predefined scheduler to read the data from the Siroccos, write it, and send a small sample of data for online monitoring. An 8-bit Sirocco ADC was used for the silicon planes, while for the DUTs, a 12-bit ADC was used for better signal resolution. The telescope gives the possibility of measuring two DUTs at the same time. Therefore, two 12-bit Sirocco channels are available for the DUTs, identified as Sirocco 4 and 5. The wire-bonding of the silicon planes to the VA2 chips was mainly done in the same order for all the planes except for plane 1X and plane 3X, which were physically flipped. As a consequence, the readout of the channels in most planes happens from “lower channels" to “higher channels" (left-to-right), while planes 1X and 3X happen from “higher channels" to “lower channels" (right-to-left). The implications of this feature will be discussed later in section 11.5.1.

The trigger of the telescope is achieved using a plastic scintillator of 7 mm × 7 mm with two photomultipliers on opposite sides. A trigger event happens when there is a coincidence of both photomultipliers. For every trigger, the raw data from the ADCs for each strip of each plane is saved in a local computer inside the test beam control cabin for later offline analysis.

Due to the high momentum of the beam used for the test beams, it was estimated that the RMS for small angles due to multiple scattering within the planes of the telescope was $\sim O(10\,\mu\text{rad})$ before the beam interacted with the last X-Y planes of the telescope. Therefore, all the small deviations were negligible and were neglected, implying that all the tracks were assumed to be straight and perpendicular to the planes.

9.2.2 Experiments

The main experiments performed during the CERN test beams were voltage scans, where the samples were biased with a low voltage of ~ 10 V, and the voltage was raised until the maximum voltage the sample could handle before the current spiked or reached $O(100\,\text{nA})$. For this reason, the current was monitored during the data taking. This procedure was performed with both bias voltage polarities, with pumping procedures before each voltage scan. The pumping procedure will be discussed in the next section. The amount of data taken at each voltage was not constant. For the runs at the maximum voltage, around $\sim 10^6$ events were saved, while for the other voltages, around $\sim 10^5$ events were saved. For reference, Appendix J has tables with the measurements performed on the 3D strip detectors tested at CERN test beams during 2015, 2016, and 2018.

9.2.3 Pumping Procedure

The diamond DUTs were inside a light-proof box with a 2 cm diameter opening covered with black tape. Before installing them in the telescope setup, the samples needed to be “pumped.”

Pumping is the passivation of charge carrier traps through ionizing radiation. Deep traps in the sensor can be passivated for months at room temperature and in the dark after exposing the sensor to fluences of the order of 10^{10} MIPS/cm^2[128]. The passivation of deep traps increases the charge collection in diamond detectors, after which shallow and intermediate traps with

lifetimes smaller than $O(1\,\mathrm{s})$ remain at room temperature, which affect the detector's charge collection.

The procedure to pump the diamond samples implemented for the CERN test beams consisted of placing a high activity Sr90 source of $\sim O(54\,\mathrm{MBq})$ with a $\sim 5\,\mathrm{mm}$ diameter opening on top of the black tape covering the opening to the diamond, such that the β particles from the source passivated the deep traps present in the diamond (see Figure 9.6). The source was left for $\sim 8\,\mathrm{h}$, resulting in an exposure equivalent to at least 10^{10} MIPS/cm^2.

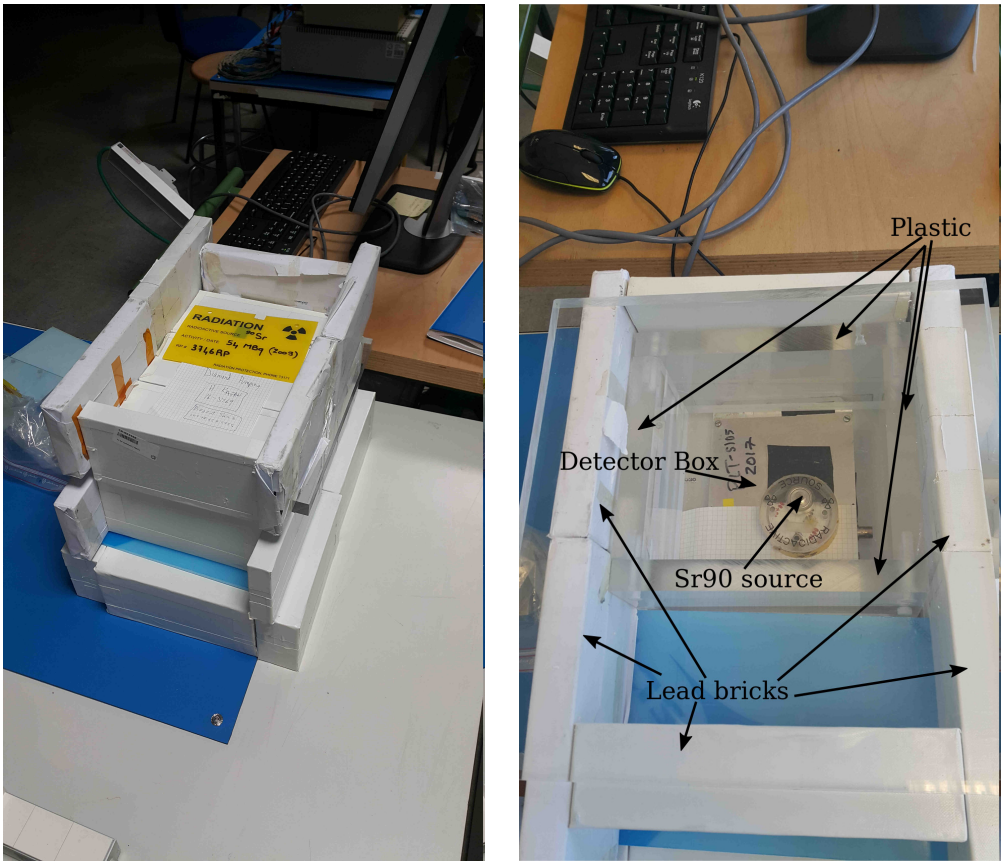

(a) Pumping setup.

(b) Inside the pumping setup.

Figure 9.6: Pumping setup made of plastic and lead bricks to shield the radiation from the source. This measure is needed to protect the people entering the laboratory from radiation exposure.

Chapter 10

Test Beams At PSI

The pixel detectors fabricated with the diamond samples CMS04, CMS01, CMS02, II6-93, and II6-750, previously described in section 3.3, were tested at the PSI Experimental Hall, in the PiM1 ($\pi M1$)[129] beam line. The intense beam of particles delivered to this area allowed rate studies of the detectors. As previous diamond detectors had been tested with this beam, it was desired to use the same beam to compare the performance of the pixel detectors fabricated with the fabrication process given in this thesis and the previous diamond detectors. Figure 10.1 shows the different stages of the acceleration of the protons at the Experimental Hall. A layout of the last stages of the beamline directed to the Pim1 area can be seen in Figure 10.2.

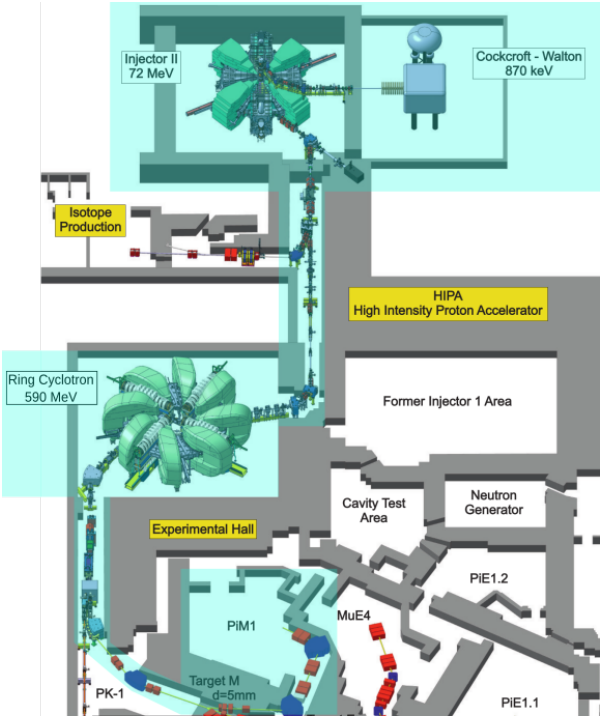

Figure 10.1: Section of the Experimental Hall at PSI. The highlighted aquamarine areas show the particles' trajectory through the different acceleration stages until they reach the πM1 experimental area.[130]

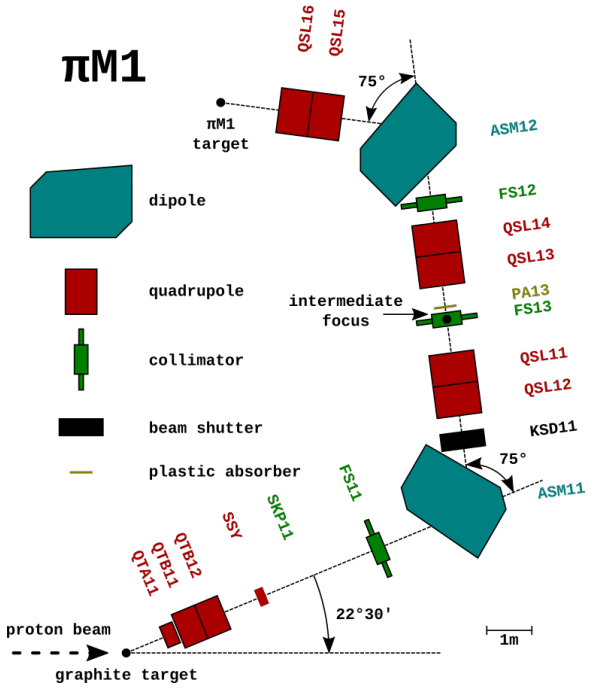

Figure 10.2: Layout of the beamline characteristics for the πM1 area.[131]

10.1 Beam Characteristics

In the Experimental Hall, 72 MeV/c protons are accelerated in a Ring Cyclotron to a momentum of 590 MeV/c before extraction. The protons that go to the πM1 collide with a thin $\sim O(5\,\text{mm})$ carbon target to produce secondary beams split into three. One of these beams ends up in the πM1 area, where the beam's momentum can be tuned between 100 MeV/c and 500 MeV/c using dipole magnets that guide the beam to the πM1 area. The particle composition of the beam has been measured and is shown in Figure 10.3. For the test beams, a momentum of 260 MeV/c was chosen, and a plastic plate was placed before the last dipole magnet to deflect the protons, such that the beam consisted mainly of π^+ particles, had high intensity, and avoided the Δ resonance.

Utilizing the collimators FS11 and FS13 in the beamline shown in Figure 10.2, the flux of the beam could be set between $O(1\,\text{kHz/cm}^2)$ and $O(10\,\text{MHz/cm}^2)$ around the focus point of the beam, where the DUTs were placed. This beamline was ideal for rate studies.

10.2 Experimental Setup With The ETH High Rate Beam Telescope For The PSI Test Beams

The ETH high rate beam telescope was used to resolve the trajectory of the particles passing through the DUTs. The telescope was configured to have four tracking silicon pixel planes: two upstream and two downstream of the DUTs. The four tracking planes were connected to the same DTB[133] to have the same clock signal and share the same datastream. Each

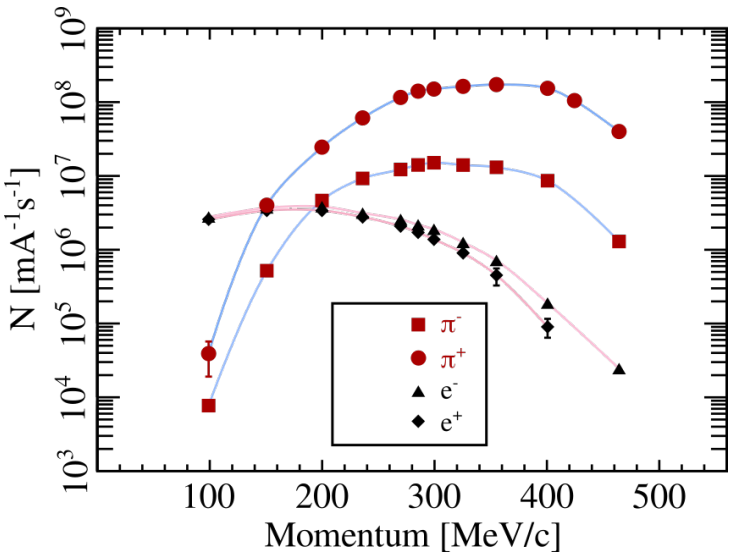

Figure 10.3: Measured particle fluxes for different momenta. The flux for μ particles is not shown, but it is a factor of 100 smaller than the rate of π around 300 MeV/c.[132]

tracking plane had the analog psi46v2 ROC with a pixel size of 100 µm×150 µm, which could handle particle fluxes up to 120 MHz/cm^2 and had a FAST-OR trigger signal synchronized to the 40 MHz clock signal from the DTB. Behind the last tracking plane, a 1 cm×1 cm scintillator was placed as part of the triggering system. The scintillator could handle the particle fluxes that were used to test the DUTs.

The DUTs were placed in the middle of the telescope. For the DUTs, the readout system could be configured in one of two ways. One was to read the analog signal from pad detectors using a charge-sensitive amplifier and a DRS4 digitizer[134, 135] (see Figure 10.4). The other way was to read the digitized signals of pixel detectors fabricated with the psi46digV2.1-respin ROC and using a DTB, different from the one used for the tracking planes (see Figure 10.5). In the case of the pixel setup, the diamond DUTs were placed in planes 4 and 5, and a silicon DUT was placed as a reference in plane 6, according to the diagram in Figure 10.5.

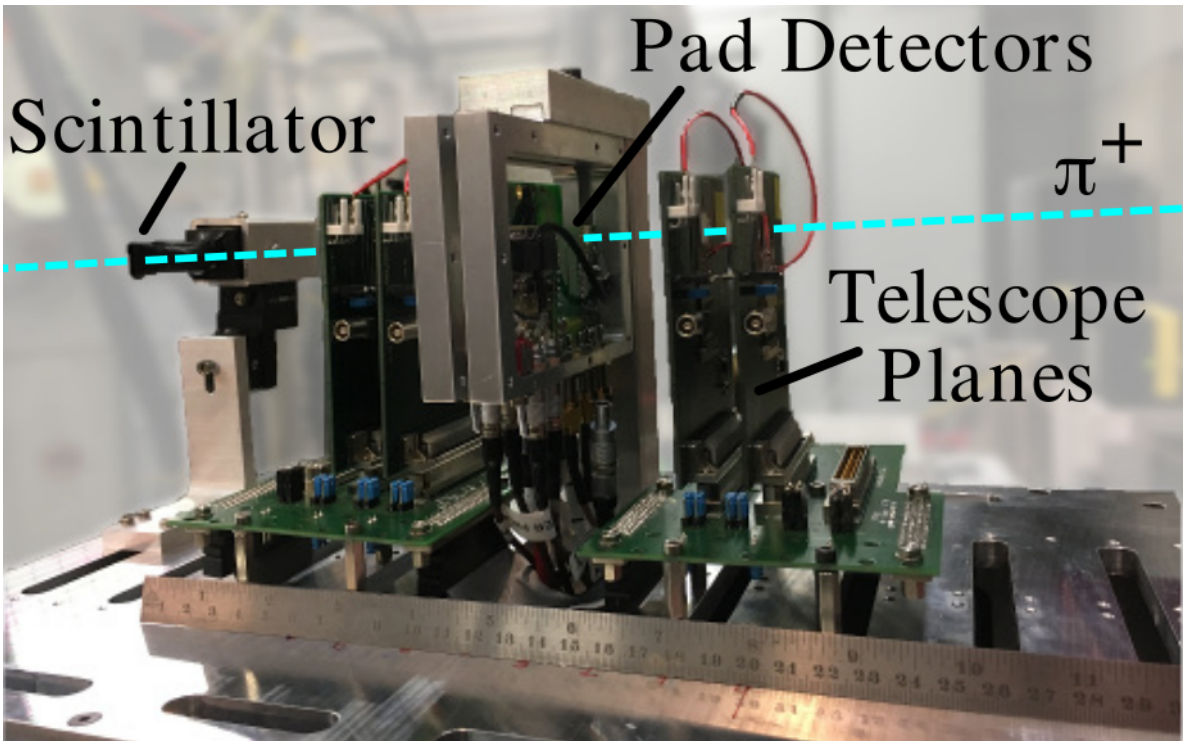

(a) Picture of the telescope with two pad DUTs.

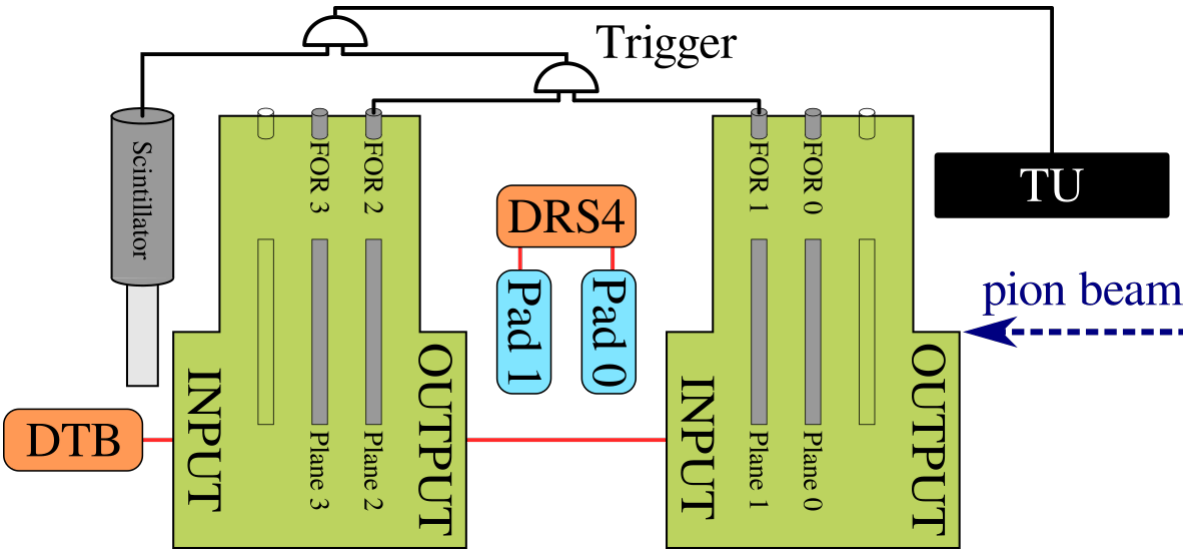

(b) Diagram of the telescope and the trigger logic for pad DUTs.

Figure 10.4: Telescope setup for pad DUTs. Up to two pad detectors could be tested. The pad detectors were read with a DRS4 digitizer. The trigger for each event was given by the TU by processing the coincidence from the FAST-OR from the two planes closest to the DUTs (i.e. Plane 1 and 2) and the scintillator. The waveforms of the pad detectors and of the scintillator were saved along with the telescope planes information from the DTB for each event.[131]

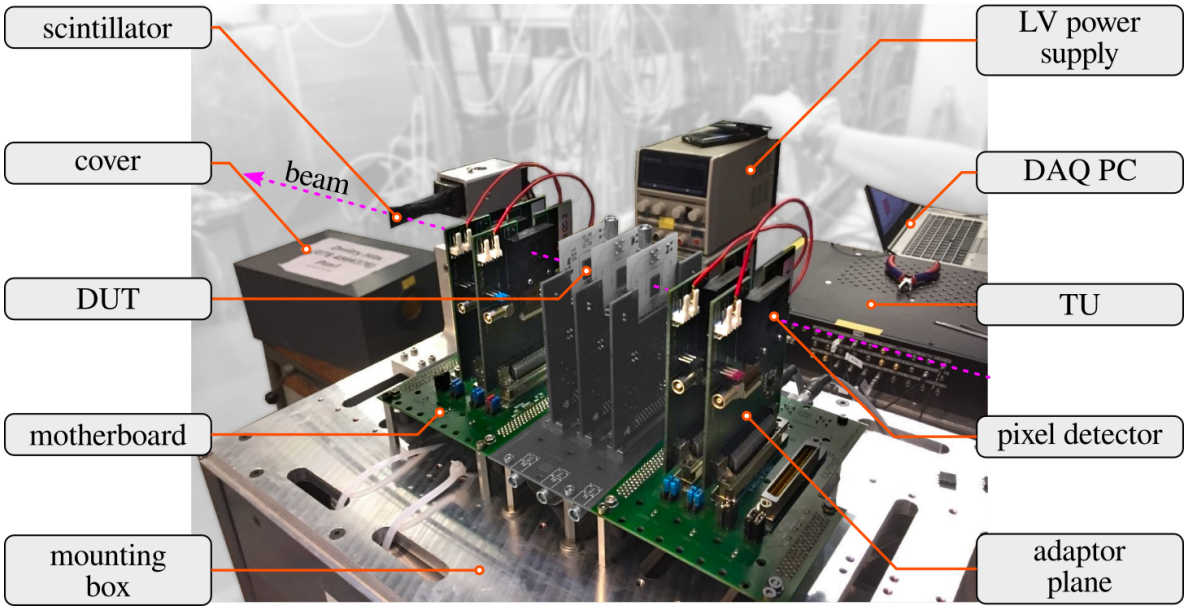

(a) Picture of the telescope with three pixel DUTs.

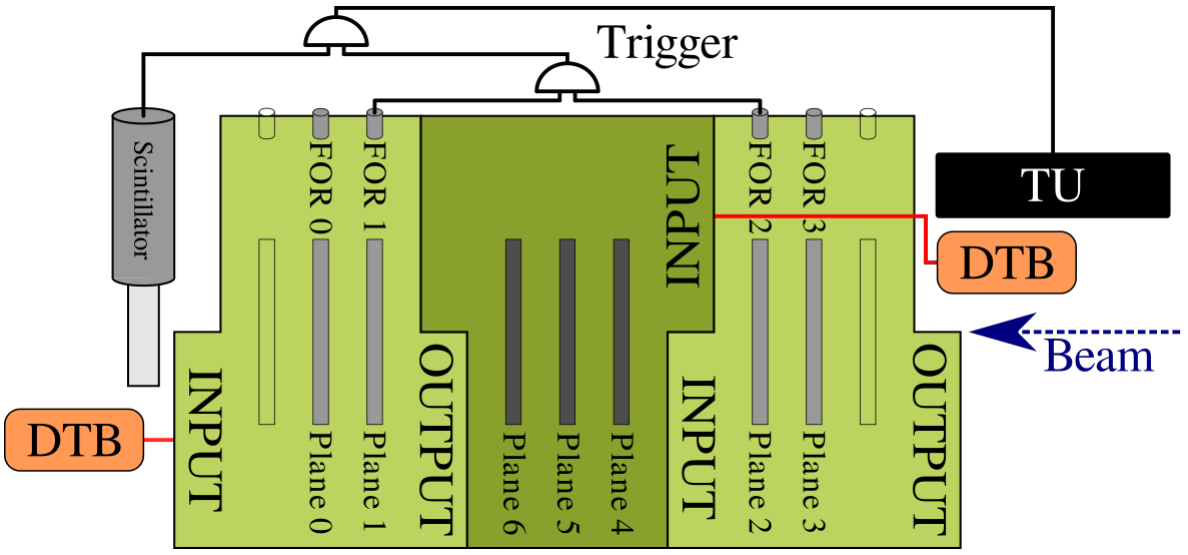

(b) Diagram of the telescope and the trigger unit set for pixel DUTs.

Figure 10.5: Telescope setup for pixel DUTs. Up to three DUTs could be mounted on the telescope (i.e. planes 4, 5, 6). Planes 4 and 5 were mounted with diamond DUTs, while plane 6 was mounted with a silicon DUT as reference. The coincidence of the FAST-OR signals from the two tracking planes closest to the DUTs (i.e. planes 1 and 2) and the scintillator were processed by the TU, which issued the global trigger signal for the telescope readout and the DUTs readout via DTBs. For each event, the pixel data for each tracking plane of the telescope's DTB and the pixel data from each DUT connected to the DUT's DTB was saved.[136]

With a particle beam consisting mainly of pions with a momentum of 260 MeV/c, the deflections of the particle within each plane of the telescope were not negligible. To estimate the small angle due to multiple scattering, the following materials and their thicknesses had to be taken into account for the calculations: Each pixel DUT was placed over a PCB made of FR4 material with a thickness of 1.55 mm, and each tracking detector was placed over a PCB of FR4 with a thickness of 0.65 mm. The tracking silicon detectors had a ~ 285 µm thickness for the sensor and ~ 700 µm for the ROC[137]. As for the DUTs, the thickness of the diamond sensors was of the order of ~ 500 µm. A thickness of ~ 700 µm for the silicon ROC connected to the diamond sensor had also to be taken into account. It was estimated that the RMS of the small angle scattering (θ_0) after passing through the first two tracking planes before interacting with the DUT was ~ 9 mrad or ~ 0.5°. For the case of two pad DUTs, θ_0 after passing through three tracking planes and the DUTs, but before interacting with the last tracking plane, was estimated to be ~ 14 mrad or ~ 0.8°. For three pixel DUTs, θ_0, before interacting with the last tracking plane, was estimated to be ~ 18 mrad or ~ 1.0°[50]. In other words, 98 % of perpendicular incident trajectories could be deflected with an RMS of up to 2.9 mm in the horizontal or vertical direction at a distance of 16.26 cm from the first tracking plane, where the last tracking plane was located.

All pixels in the triggering planes 1 and 2 were masked (i.e., turned off) except for a rectangular region that contained the trajectories that interacted with the DUTs to increase the fraction of triggered events for which a particle transversed the DUTs. With this measure, there was a high possibility that a particle that passed through both unmasked regions in triggering planes 1 and 2 also interacted with the DUTs. As for the triggering scintillator, whose dimensions were larger than the active area of the detectors (i.e., 1 cm × 1 cm), it was manually aligned such that particles that passed through the unmasked regions of the triggering planes 1 and 2 also passed through the scintillator. The signals from the FAST-ORs of planes 1 and 2 and the scintillator were sent to the trigger unit (TU), which issued the trigger signal to the DTBs and, in the case of testing pad detectors, to the DRS4.

To read the data from the pixel ROCs connected to the DTBs, the software Pixel eXpert Analysis & Readout (pXar)[138] was used, which was developed to test the psi46 series ROCs. In the case that the DRS4 was used to read out the data from pad detectors, the DRS4 software that comes with the DRS4 evaluation board was used. A modified version of the *EUDAQ*[139, 140] framework was used to save the data, which was able to manage different producers tuned to use the pXar and the DRS4 readouts. For each trigger event issued by the TU, the EUDAQ framework saved the pixel's column, row, and pulse height information of all the pixels above the tuned threshold for each plane, and in the case of testing pad detectors, the waveforms of the four channels of the DRS4 digitizer. A raw file containing the described data and information from the TU was saved for offline analysis for each run.

10.2.1 ROCs Configuration

Before the data taking, the tracking pixel detectors were configured using pXar to have the thresholds at ~ 5×10^3 electrons. This value is below the expected ~ 22 800 electrons for MIPs in a 285 µm thick silicon detector such as the ones used for tracking in the telescope[38]. As for the DUT ROCs, they were configured to have thresholds at ~ 1.5×10^3 electrons, which is the

minimum threshold that the ROCs can be operated at[141]. The reason for calibrating close to the minimum threshold was to detect the smallest amount of ionized charges in diamonds due to their smaller signals, as mentioned in section 2.1. Pulse height calibration measurements were performed for each pixel to extract from the measured pulse height in the ADCs the charge in terms of the calibration voltages injected to each pixel represented by the DAC *Vcal* (see Figure 3.2).

For the data taking, as each internal clock signal from each DTB was independent, an external clock signal was used to synchronize the DTBs. The external clock 40 MHz signals were issued by the TU. The trigger delay and the clock phases (i.e., the internal delay of the clock signal inside the DTB) for each of the DTBs were optimized before the data taking. Besides the DTB's timing settings, the programmable registers in the PUC that control the delays for calibration signals and for the thresholds were optimized for pulse height calibration and to set the threshold of each pixel.

10.2.2 Experiments

Two main experiments were performed during the PSI test beams on the diamond detectors mentioned at the beginning of this chapter:

The first one was a voltage scan, performed at beam fluxes of $O(100\,\mathrm{kHz/cm^2})$. For each run, the bias voltage of the detector was increased until the detector could not hold the voltage, that is when the leakage current without a beam reached $\sim 100\,\mathrm{nA}$ and became erratic.

The second was a rate scan, where the detectors were held at the maximum voltage they could withstand with leakage currents below $\sim 100\,\mathrm{nA}$, and the beam fluxes were changed from $O(10\,\mathrm{kHz/cm^2})$ up to $O(10\,\mathrm{MHz/cm^2})$ utilizing collimators in the beamline. As the area of the detector was constant, an increase in flux is equivalent to an increase in the rate. A single scan consisted of raising the rate from the lowest rate to the highest and then lowering it down to the lowest again. That was referred to as an up-down scan. A complete rate scan consisted of two of these, which meant an up-down scan followed by another up-down scan.

For reference, a complete list of the experiments held at PSI during 2018 and 2019 for the detectors fabricated in the scope of this thesis is available in Appendix K.

10.2.3 Pumping Procedure

The pumping procedure performed at PSI used the high-intensity beam to passivate the deep traps in the diamonds instead of a source, as done during CERN test beams (section 9.2.3). The particle beam was used at a high rate of particles of $\sim O(1\,\mathrm{MHz/cm^2})$ to pump the diamond sensors. This procedure was done at 0 V before the voltage scan for $\sim 60\,\mathrm{min}$. Before the rate scans, with the DUTs biased with the voltage determined for the rate scans, the DUTs were pumped with the beam for $\sim 25\,\mathrm{min}$. The pumping would stop when the monitored pulse height signals in the DUTs were believed to have reached a stable value.

Part VI

Data Analysis

Chapter 11

Analysis Of Data Taken With The Strasbourg Telescope At CERN Test Beams For Studying The 3D Detectors

As mentioned in section 9.2.1, for every trigger event determined by the scintillator, the pulse height in ADC units of each of the channels of the VA ASICs connected to the telescopes planes and the DUT were saved. For each run, several raw files containing the binary data of 10^4 events were created. For each event, besides the pulse height values for each plane, other information like timestamps and event counts were saved. The first step of the analysis was to read the binary file, extract the pulse height in ADC units, and organize the data in a tree structure ordered primarily by events and secondarily by planes. Each plane is represented by a 1D array with the pulse height in ADC units for each of the channels of the plane.

11.1 Different Digitizer Saturation Values

It was found in 2018 that depending on the Sirocco used to digitize the data of the pulse height (PH) of the DUT, either Sirocco 4 or Sirocco 5, as mentioned in section 9.2.1, the saturation value in the ADCs were different for the data taken since 2012. Figure 11.1 shows data from a test beam in 2018, where different runs on the same diamond planar detector were made using Sirocco 4 or Sirocco 5. These graphs show the histograms of all the PH measured from the 128 channels of the VA2.2 chip for a whole run.

It is clear from Figure 11.1a that for the data taken with Sirocco 4, there were almost no events with PHs between 3350 ADC and 4095 ADC (the maximum value for 12 bits), and there was a spike of events around a PH of 3350 ADC. This resulted in an artificial saturation for Sirocco 4 below the real saturation of the digitizer. In contrast, the histogram in Figure 11.1b of the PH from the 128 channels of the same VA2.2 chip connected to Sirocco 5 populates up to 4095 ADC as expected for a digitizer with 12 bits.

For the digitizer Sirocco 4, the region in ADC units where the saturation happened was not precisely defined, and each channel had a different distribution for saturation, as shown in Figure 11.2.

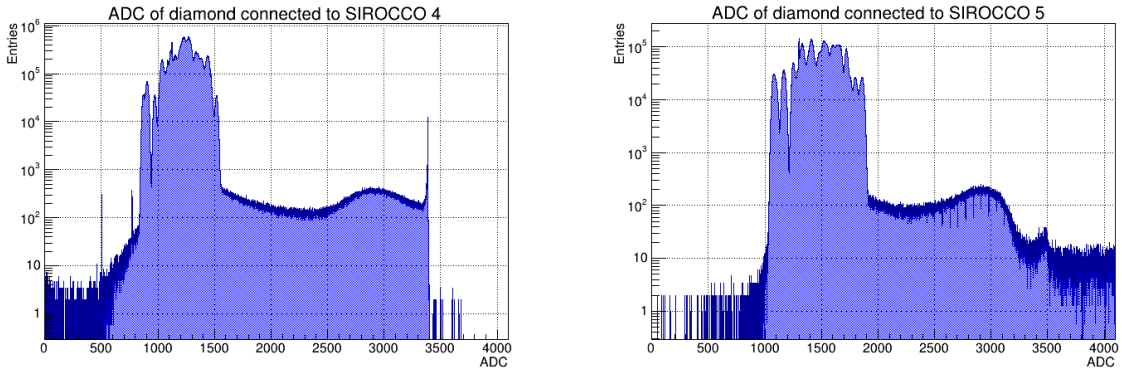

(a) All PHs from all the channels connected to Sirocco 4 (b) All PHs from all the channels connected to Sirocco 5

Figure 11.1: Difference between the saturation between Sirocco 4 and 5. The data comes from the same diamond and same VA2.2 ASIC digitized first with Sirocco 4 and then with Sirocco 5 during the same test beam. The histogram of all the PHs from all the channels in the VA2.2 chip is plotted. It can be seen that there is a lower saturation for Sirocco 4 (a) around 3350 ADC while Sirocco 5 (b) the saturation occurs at the maximum PH of 4095 ADC.

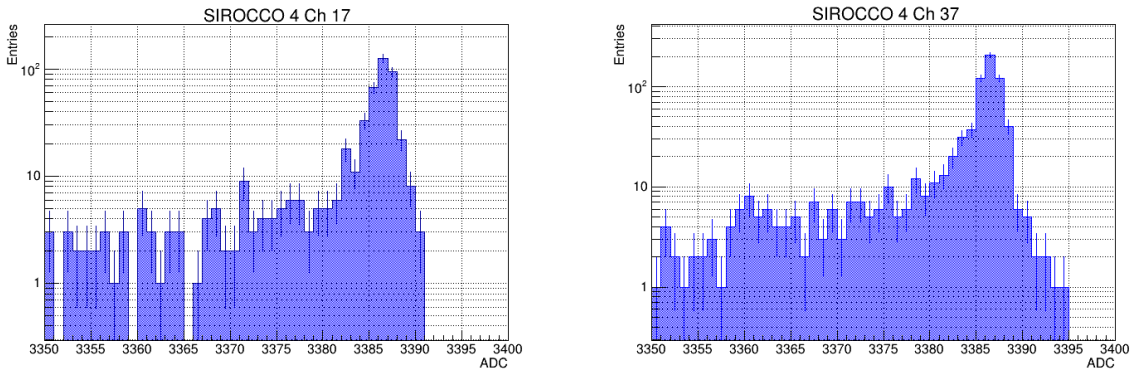

(a) PHs of Ch. 17 connected to Sirocco 4 near artificial saturation (b) PHs of Ch. 37 connected to Sirocco 4 near artificial saturation

Figure 11.2: Difference between the artificial saturation in two channels of the same VA2.2 chip digitized with Sirocco 4. There is no exact value in ADC units for saturation. Instead, the saturated events follow different distributions on each channel.

The Sirocco modules have two settings that can be adjusted: One is the baseline, which can be set through a potentiometer, and the other one is the gain, which is selected with jumpers to have a gain of 1.25 or 5[125]. The output always has the same range of 5 V; therefore, the gain limits the dynamic input range to either 1 V or 4 V. Most likely, the offset in the digitizer Sirocco 4 was not set correctly, such that the maximum signals coming from the VA2.2 chip did not fill completely the ADC registers in digitizer Sirocco 4.

A saturation value for all the channels digitized by Sirocco 4 was imposed to be 3100 ADC,

while it was left unchanged to 4095 ADC for the channels digitized by Sirocco 5. This was done such that the statistical measurements over the pulse height distributions without saturation events (i.e., mean and RMS) of the same DUT with the same VA2.2 chip under the same conditions were the most similar. An example of this is shown in Figure 11.3.

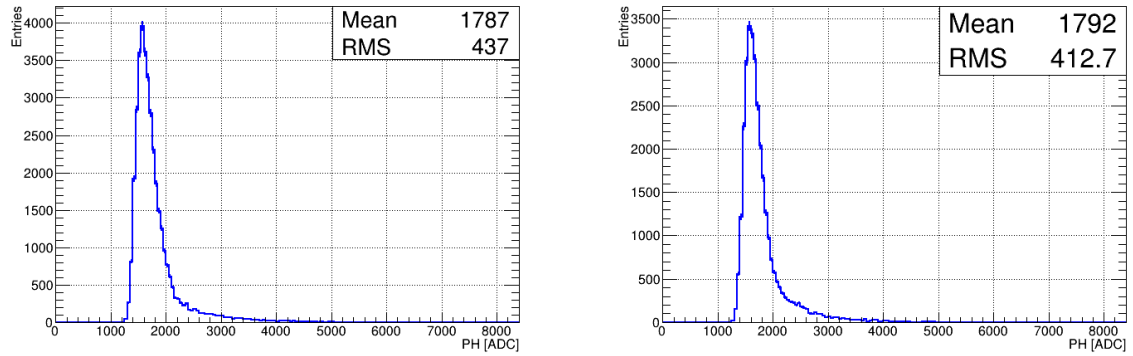

(a) Digitizer Sirocco 4.

(b) Digitizer Sirocco 5.

Figure 11.3: PHs without saturated events for an scCVD planar strip detector biased with −500 V and digitized with Sirocco 4 (a) and Sirocco 5 (b). The mean of the distributions agree to within 0.3 % for the same detector connected to different digitizers.

11.2 Raw Signal Decomposition

The raw data could be decomposed into a pedestal value, which was the value measured from the DC voltage on the channel, plus the pick-up electrical noise from the environment represented as a common mode for all the channels, plus the signal generated by the moving charges ionized in the sensor by a particle, plus random noise fluctuations around the pedestal value. Equation 11.1 shows this relation for a channel ch in the VA chip during event i, where "r" is the raw measured value by the Sirocco ADC, "p" is the pedestal value, "n" is the random fluctuations coming from the noise sources mentioned in section 4.1.1, "CM" is the fluctuation that affects all channels simultaneously, mainly coming from pick-up noise on the detector bias voltage, and q is the signal caused by the moving charges generated in the sensor by an ionizing particle passing through the sensor.

$$r_{ch}(i) = p_{ch}(i) + n_{ch}(i) + CM(i) + q_{ch}(i) \tag{11.1}$$

In order to extract the signal q for each channel and each event, it was necessary to estimate the pedestal p, the common mode CM and the fluctuations of the noise n described as the RMS value of the noise. The following sections describe the standard analysis procedure for the pedestal and common mode estimation for this type of detector, the description of which can be traced back to Weilhammer et al.[142], and has been used for various research projects with diamond detectors[143, 97, 98]. The analysis steps for this type of strip detectors are the following:

- Pedestal and common mode estimation
- Clusters formation
- Hit prediction using the Eta distribution
- Track selection for alignment
- Alignment of planes
- Track selection for transparent clustering
- Transparent cluster formation

11.3 Pedestal And Common Mode Estimation

For this part of the analysis, a buffer of 500 events was used for the pedestal estimation of the data. In the general case, M channels of the detector were connected to the readout chip, and a buffer of size N events was used for the pedestal estimation. For a particular channel ch, the events with an extra charge from ionization (i.e., the ionized charge from the passage of a particle) formed a subset $\mathscr{H}$ with size $N_{\mathscr{H}}$. As for a particular event i, the channels with an extra charge from an ionization event formed a subset $\mathscr{K}$ with size $M_{\mathscr{K}}$. If a channel for a particular event presents a raw value that deviated by more than three standard deviations away from the estimated pedestal, it was considered to contain an extra charge from ionization. Therefore, the event would make part of the subset $\mathscr{H}$ for that channel, and the channel would make part of the subset $\mathscr{K}$ for that event. The channel for that particular event would not be considered for the pedestal, common mode, or noise estimations.

To estimate the pedestal value for each channel, the method used for this task was based on a sliding-window buffer estimation with a size of N events, as mentioned above. If no particle passed through the detector, then no ionized charge was generated in the sensor, and Equation 11.1 would have the q term equal to 0, indicating that the raw value would be centered at the pedestal with random fluctuations coming from the noise sources and the common mode pick-up.

To estimate the first pedestals and noise fluctuations, for each channel ch for the first N events, all of the N values of raw data were assumed to only have contributions from the pedestal with noise fluctuations. The mean value and standard deviation of the N readings were calculated. This result gave a first estimation of the pedestal p for each channel (from the mean value) and the magnitude of the noise fluctuations σ (from the standard deviation). Afterwards, to improve this first estimation, the events with signals within this buffer of the first N events that were more than three standard deviations (3σ) away from the estimated mean were assumed to contain extra charge q from ionization and were excluded from the pedestal mean and standard deviation estimation.

This process was repeated for seven iterations, after which convergence on the pedestal mean and its standard deviation was achieved, updating the values of the estimated pedestal $\hat{p}$ and estimated noise fluctuations $\hat{\sigma}$. The resulting mean value and standard deviation were

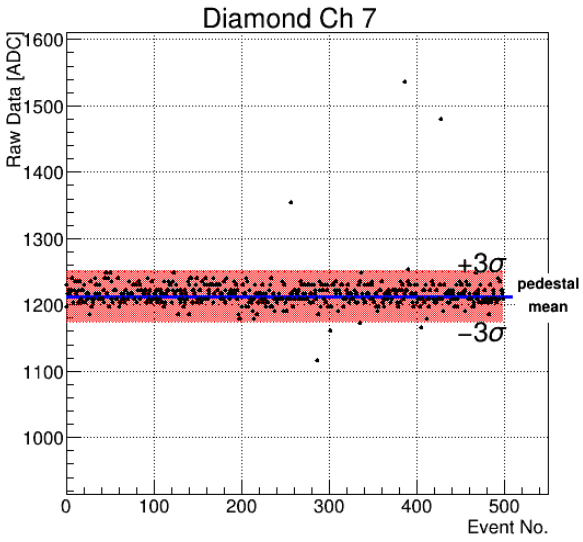

Figure 11.4: Depiction of the pedestal calculation for the first 500 events for one of the VA2.2 chip's channels connected to a strip on the diamond (aka. diamond channel). The dots are the raw data, while the line represents the calculated mean of the pedestal and the shaded area highlights the 3σ region, which contains the events included in the estimation.

assumed to be the initial estimators for each channel's pedestal and the noise's RMS, respectively. Equations 11.2 summarize this procedure. Figure 11.4 illustrates an example for the first pedestal calculation using a buffer size of $N = 500$ events for a single channel in the VA chip.

$$\hat{p}_{ch} = \frac{1}{N - N_{\mathcal{H}}} \sum_{\substack{i=1 \\ i \notin \mathcal{H}}}^{N} r_{ch}(i) \tag{11.2a}$$

$$\hat{\sigma}_{ch} = \sqrt{\frac{1}{N - N_{\mathcal{H}} - 1} \sum_{\substack{i=1 \\ i \notin \mathcal{H}}}^{N} \left(r_{ch}(i) - \hat{p}_{ch}\right)^2} \tag{11.2b}$$

In practice, the value of the pedestal was very stable and was expected to change by less than 1 % between events. With this assumption, if for an event i there was no extra charge q in most of the channels, such that out of the M channels, only $M_{\mathcal{K}}$ channels were excluded from the pedestal and noise fluctuation calculations, and the pedestal p had been estimated for all the channels for the previous event, it was possible to estimate the CM contribution as shown in Equations 11.3. In practice, the number of channels excluded ($M_{\mathcal{K}}$) was small, usually below five out of 128, which allowed the implementation of the mentioned assumption and this method. Figure 11.5 shows the distribution of all the values used to estimate the CM for an event where all 128 channels were considered for the CM estimation. If the sample size were small, the error in the estimation would be significant, and the noise estimation procedure would fail.

$$n_{ch}(i) + CM(i) = r_{ch}(i) - p_{ch}(i) \tag{11.3a}$$

$$\langle n_{ch}(i) + CM(i)\rangle = \langle n_{ch}(i)\rangle + \langle CM(i)\rangle = \langle CM(i)\rangle = \langle r_{ch}(i) - p_{ch}(i)\rangle \tag{11.3b}$$

$$\hat{CM}(i) = \frac{1}{M - M_{\mathcal{K}}} \sum_{\substack{ch=1 \\ ch \notin \mathcal{K}}}^{M} \left(r_{ch}(i) - p_{ch}(i)\right) \cong \frac{1}{M - M_{\mathcal{K}}} \sum_{\substack{ch=1 \\ ch \notin \mathcal{K}}}^{M} \left(r_{ch}(i) - p_{ch}(i-1)\right) \tag{11.3c}$$

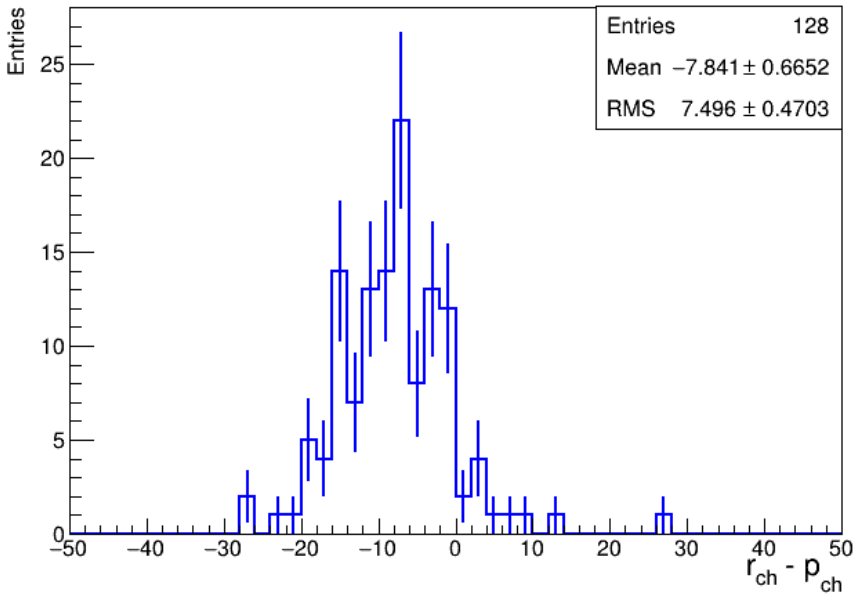

Figure 11.5: Distribution with the value $r_{ch}(i) - p_{ch}(i-1)$ for the 128 channels of the preamplifier for an event "i." The estimated CM for that event would be -7.84 ADC.

For each of the following events, the buffer window slid to include a new event and dropped the first event in the buffer such that the size of the buffer N was maintained. If the new event's $r - CM$ were within 3σ from the estimated pedestal, it would be included in the new event estimation of the pedestal and the noise as shown in Equations 11.4:

$$p_{ch}(i) + n_{ch}(i) = r_{ch}(i) - CM(i) \tag{11.4a}$$

$$\hat{p}_{ch}(i) = \frac{1}{N - N_{\mathcal{H}}} \sum_{\substack{j=i-N-1 \\ j \notin \mathcal{H}}}^{i} \left(r_{ch}(j) - \hat{CM}(j)\right) \tag{11.4b}$$

$$\hat{\sigma}_{ch}(i) \equiv \sqrt{\frac{1}{N - N_{\mathcal{H}}} \sum_{\substack{j=i-N-1 \\ j \notin \mathcal{H}}}^{i} \left(r_{ch}(j) - \hat{CM}(j)\right)^2 - \hat{p}_{ch}^2(i)} \tag{11.4c}$$

Following the procedures mentioned above, for each channel and each event, there would be an estimation of the pedestal $\hat{p}$, the common mode $\hat{CM}$, and the RMS of the noise $\hat{\sigma}$, which accounted for the random fluctuations of the noise n. With these parameters, selecting possible candidates of events with charge q generated from ionization was possible. The resulting ionization charge $\hat{q}$ for each channel ch and event i would be:

$$\hat{q}_{ch}(i) = r_{ch}(i) - \hat{p}_{ch}(i) - \hat{CM}(i) \tag{11.5}$$

11.4 Clusters Formation

As a particle passed through the sensors, a charge was induced on the strips, forming a strip cluster, each of which could be represented by the quantity q in Equation 11.1. Usually, a cluster consists of several adjacent channels with ionization charge $q > 0$, which surround the channel with the largest value of q. Two thresholds were selected: one to determine the seed of the cluster (the largest signal q) and another one to determine if a signal was far enough from noise fluctuations to be considered part of the cluster. These thresholds were respectively t_s (*threshold-seed*) and t_h (*threshold-hit*).

For the silicon tracking planes of the telescope, it was desired to have clean signals and to promote the events that consisted of mainly two-channel clusters to get a better resolution through charge sharing. Thus, it was desired to have a value of t_s as far from noise fluctuations as possible. As for the value of t_h, it was desired that it excluded clusters with sizes larger than two strips.

It was helpful to use a quantity normalized by the width of the noise fluctuations (the one defined in Equation 11.4c) to define the thresholds for the seeds and the hits. This quantity was the signal-to-noise-ratio (SNR), as shown in Equation 11.6.

$$SNR \equiv \frac{\hat{q}}{\hat{\sigma}} = \frac{r - \hat{p} - \hat{CM}}{\hat{\sigma}} \tag{11.6}$$

Figure 11.6a shows the distribution of the SNR of the strip with the largest charge q for all the events for plane 0X of the telescope. As can be seen, there is a clear gap that separates noise fluctuations from signal events. A value of $t_s = 15\,\text{SNR}$ was chosen in this example to select the seeds of the clusters.

As for choosing the value of t_h, distributions such as the one shown in Figure 11.6b, which depict the second largest signal adjacent to the largest signal in terms of SNR, were used. In this distribution, two peaks can be seen. The last one from left to right, which peaks at about 20 SNR, contains most of the two-channel clusters, while the left peak corresponds to noise fluctuations mixed with signals from three-or-more channel clusters. A value in the valley between these two peaks selects most of the two-channel clusters without throwing away many events. In this example, t_h was chosen to be 12 SNR.

For the DUT, it was desired to use the most amount of data possible, which would be used to align the DUT. For this reason, the values of t_s and t_h were chosen to be 4 SNR and 3 SNR, respectively (see Figure 11.7). With the lowest threshold set at 3 SNR, the selected data would contain less than 1 % of noise events. It can be noted that the same value for t_h was also used

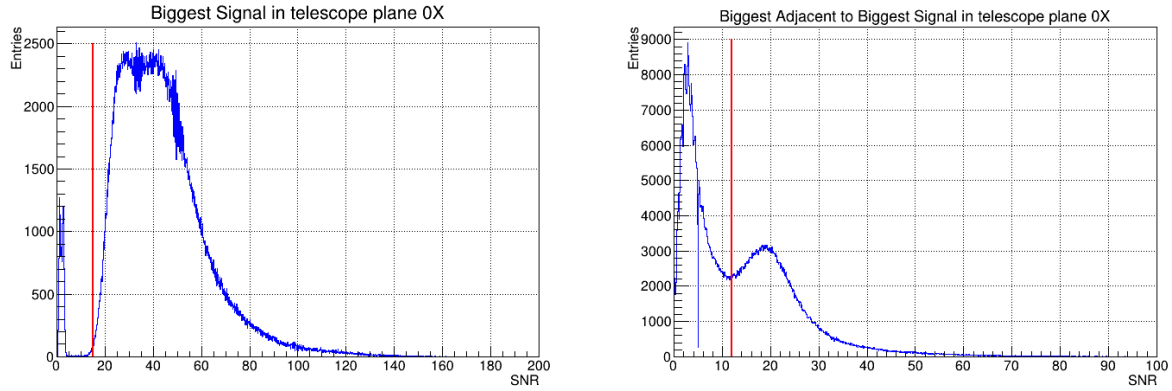

(a) Largest signal distribution in SNR.

(b) Second largest signal adjacent to the largest signal distribution in SNR.

Figure 11.6: Distributions used to select the cluster thresholds for the first plane that determines the X position. The red vertical lines depict the values chosen for the threshold-seed t_s (a) and the threshold-hit t_h (b).

for the threshold to determine if an event was used for the pedestal and noise estimations, as mentioned previously.

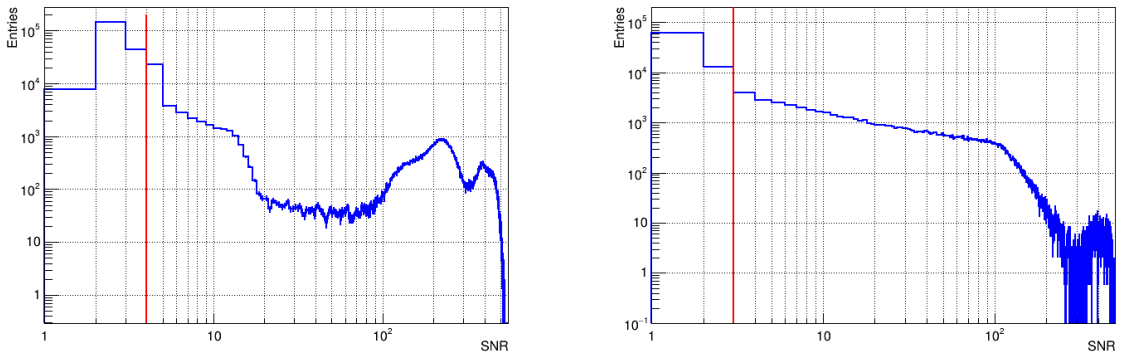

(a) Largest signal distribution in SNR.

(b) Second largest signal adjacent to the largest signal distribution in SNR.

Figure 11.7: Distributions showing the hit, t_h, and seed, t_s, thresholds used for a planar strip DUT. The red lines depict the values for t_s in (a), and for t_h in (b).

It's worth remembering that in Figure 11.7a, the distribution of the channel's signal within the 128 channels of the VA chip with the largest SNR is shown. Ideally, the probability that all the 128 channels have signals within 1 SNR in an event without ionization charge is negligible. Therefore, the bin with $SNR = 1$ is disfavored in this histogram. On the other hand, events with an ionization charge with large clusters would increase the events in the lower bins of the distribution.

On an event-by-event basis for each plane, one or more seed channels were selected if their SNR was above t_s. Afterwards, their adjacent channels were tested to see if they surpassed the threshold t_h. If they did, they were included in the cluster. If two or more adjacent channels surpassed t_s, the highest one was selected as the cluster's seed. By construction, most clusters in the telescope's silicon tracking planes were one-channel or two-channel clusters due to the chosen thresholds. On the other hand, it was possible to have three or more channel clusters in the DUT because its thresholds t_s and t_h were just above 99.9% of the noise fluctuations. Depending on the rate of the incident particles, it was also possible to have events with more than one cluster in a plane. These cases will be addressed later in the analysis. Figure 11.8 shows an event on the telescope's plane 0X.

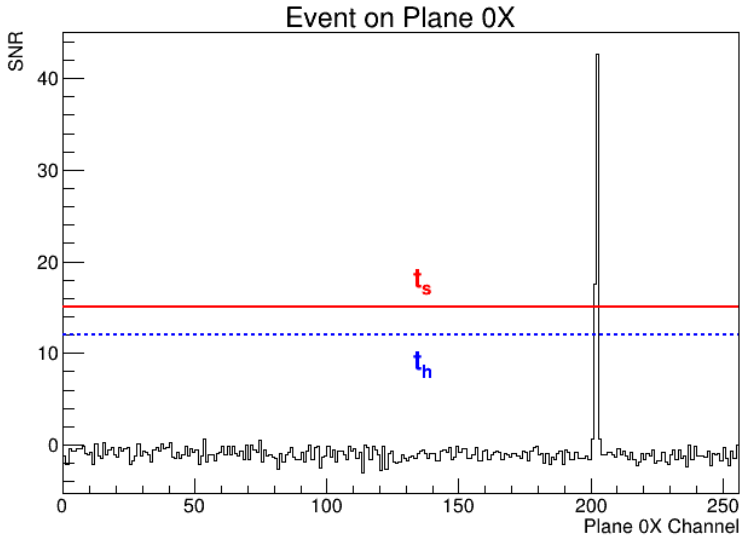

Figure 11.8: Example event on plane 0X of the telescope, which shows a two-channel cluster. The seed was set to the highest channel that exceeds t_s, channel 202. As channel 201 exceeded t_h and was adjacent to the seed channel, it was included in the cluster. As no other adjacent channels to these two exceeded t_h, no more channels were added to this cluster.

11.5 Hit Prediction Using The Eta Distribution

In each event and for each plane, the η value was calculated with the two highest adjacent channels (i.e. the seed channel and its highest signal neighbor) if the signal cluster was made of two or more channels. In this pair, the right-most channel's charge was labeled as q_R and the other as q_L. These quantities were anti-correlated depending on the position where the particle passed. If the particle passed near the middle of the left channel, it was expected that q_L was large while q_R was small. If, on the contrary, the particle passed near the middle of the right channel, then q_L was expected to be small, while q_R was expected to be large. The quantity η, defined in Equation 11.7, contains this information. An η value close to 0 means the particle

passed near the center of the left channel, while an η value close to 1 indicates that the particle passed near the center of the right channel.

$$\eta = \frac{q_R}{q_R + q_L} \tag{11.7a}$$

$$0 \leq \eta \leq 1 \tag{11.7b}$$

The distribution of this quantity should be symmetric about $\eta = 0.5$. The amount of peaks in the distribution depends on the amount of intermediate floating strips between the channels. With no intermediate floating strips, two peaks are expected (one peak close to 0 and another one close to 1); with one intermediate floating strip, three peaks are expected (the middle one at $\eta = 0.5$); and with two intermediate floating strips, four peaks are expected. Figure 11.9 shows these three cases.

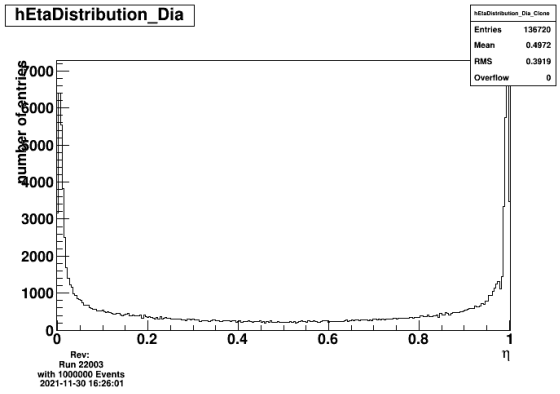

(a) Detector with no intermediate floating strips.

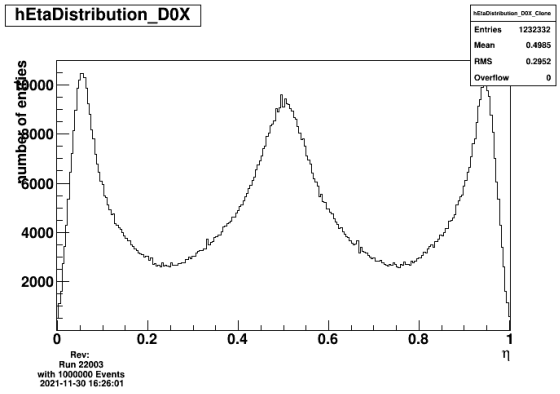

(b) Detector with one intermediate floating strip.

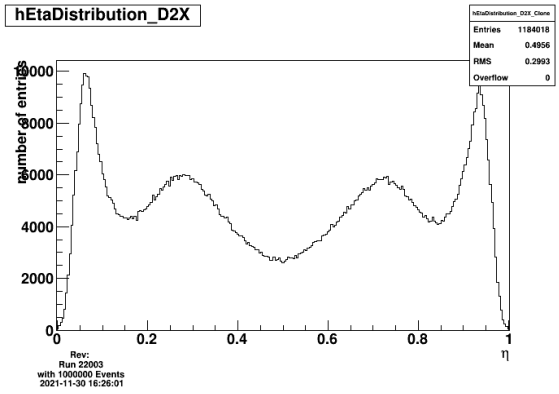

(c) Detector wit two intermediate floating strips.

Figure 11.9: Distributions of η for different planes which have different numbers of intermediate floating strips.

The shape of the distribution is not only defined by the geometry of the detector but also by the crystal defects present in the sensor as it occurs in polycrystalline diamonds (with grain boundaries among other crystal defects) or irradiated diamonds (with impurities and

displacement defects due to radiation damage). Figure 11.10 shows examples from strip detectors made on a single-crystalline diamond, polycrystalline diamond, and irradiated single-crystalline diamond. As shown in Figure 11.10, crystal defects present in polycrystalline and irradiated diamonds improve the charge sharing, as seen in the higher population of Eta values around 0.5.

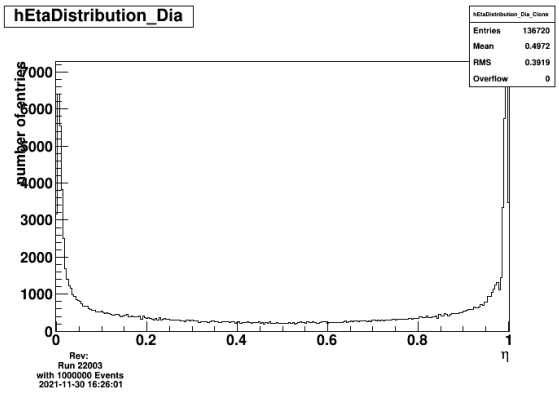

(a) η distribution for single-crystalline CVD diamond strip detector

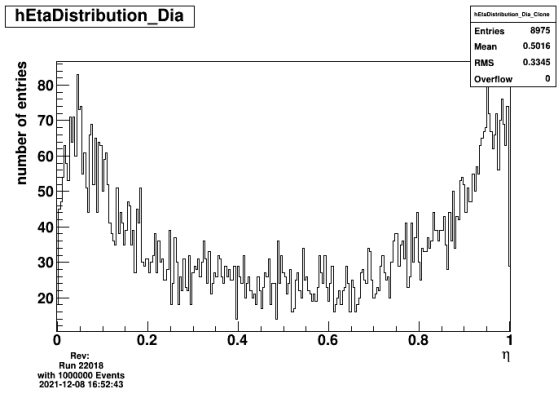

(b) η distribution for polycrystalline CVD diamond strip detector

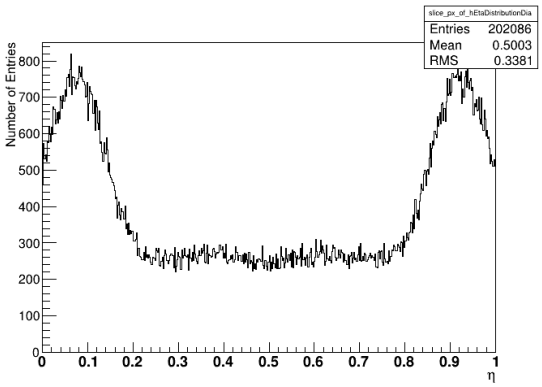

(c) η distribution for irradiated single-crystalline CVD diamond strip detector

Figure 11.10: The η distribution for a polycrystalline and irradiated single-crystalline diamond sensor has more entries in the values around $\eta = 0.5$ and the peaks are less pronounced than for a non-irradiated single-crystalline diamond sensor.

With a beam with a uniform incidence profile across the strips of the detector, the distribution of the hit position between two adjacent strips was expected to be uniform. The data sampled with this uniform distribution produced the non-uniform distribution $f(\eta)$ as shown in Figures 11.9 and 11.10. It was possible to use the Cumulative Distribution Function (CDF) of the distribution $f(\eta)$ to recover the information about the hit position. For a more detailed explanation of how the CDF of the distribution $f(\eta)$ works, see Appendix G.

By applying the CDF F to the random variable η, a variable uniformly distributed between [0, 1] was obtained. Scaling this by the pitch P between the strips, the predicted hit position was

obtained as shown in Equations 11.8a.

$$F(\eta) = \frac{\int_{-\infty}^{\eta} f(\lambda)\mathrm{d}\lambda}{\int_{-\infty}^{\infty} f(\lambda)\mathrm{d}\lambda} = \frac{\int_{0}^{\eta} f(\lambda)\mathrm{d}\lambda}{\int_{0}^{1} f(\lambda)\mathrm{d}\lambda} \tag{11.8a}$$

$$x(\eta) = x_L + P \cdot F(\eta) = x_L + P \cdot \frac{\int_{0}^{\eta} f(\lambda)\mathrm{d}\lambda}{\int_{0}^{1} f(\lambda)\mathrm{d}\lambda} \tag{11.8b}$$

Figure 11.11 gives an example of the application of Equation 11.8a on an event of a diamond detector measured in 2016.

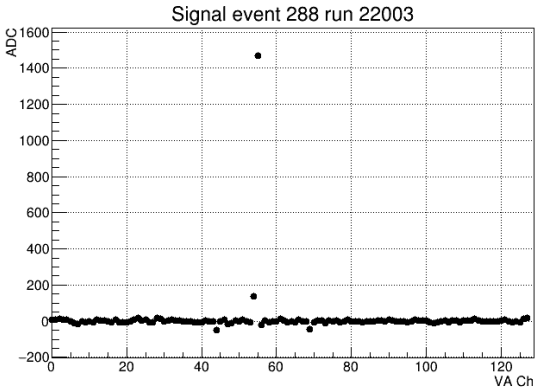

(a) Signal for each channel in the VA chip in ADC units for event 288 of run 22003.

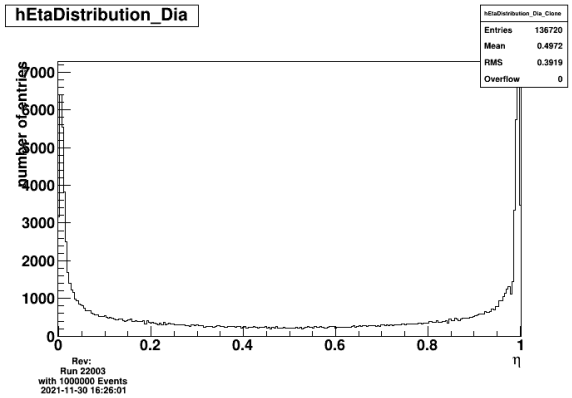

(b) Eta distribution for run 22003 of the detector in (a).

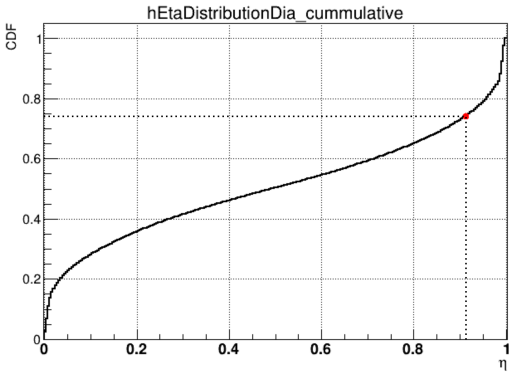

(c) CDF of the distribution in (b).

Figure 11.11: Example for the position calculation using the η distribution. On the event shown in (a), channels 54 and 55 have signals above the hit threshold t_h and form a cluster. Using the η distribution shown in (b) for the whole run, the cumulative distribution in (c) can be calculated. Using Equation 11.7, the event gives an $\eta = 0.9135$. The resulting CDF for this quantity is $F(\eta = 0.9135) = 0.741$ as shown with the red dot in (c). If the position of channel 54 was $x_L = 1000\,\mu\mathrm{m}$ and the pitch between each channel was $P = 50\,\mu\mathrm{m}$, then the predicted hit position of this event according to Equation 11.8a would be $x = 1037.05\,\mu\mathrm{m}$.

11.5.1 Data-Driven Feed-Across Correction

It was seen in the data taken since the 2012 test beams that the η distributions were no longer symmetric. The hypothesis for this effect is that there is a timing mismatch between the sample-and-hold circuit and the readout of the multiplexed signal (see Figure 4.1). This issue is a known problem in sampling analog signals, and an estimation of the miss-match timing would allow the correction of this effect. This affects each VA chip independently, so in theory, it was necessary to calculate 16 compensation factors for the telescope's silicon planes and one for the DUT. For simplicity, a compensation factor was estimated for each plane direction (i.e., X or Y), giving nine compensation factors that needed to be calculated: eight for the telescope's silicon planes and one for the DUT.

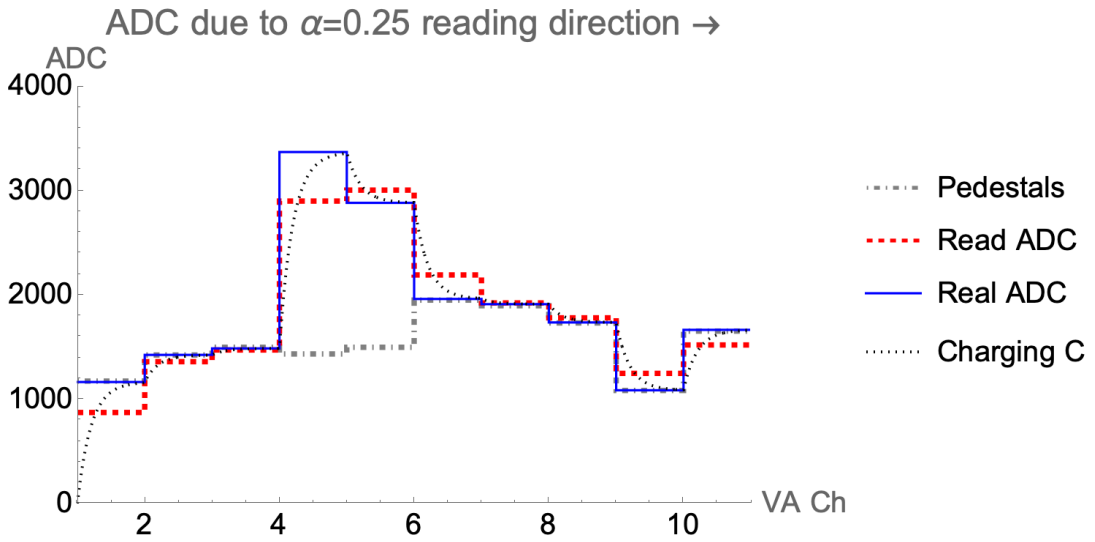

Figure 11.12: Example with 10 channels of a VA chip with a two-channel cluster in channels four and five. The readout in this example is from left-to-right. The dotted curve labeled "Charging C" represents the voltage on the readout capacitor as it charges after each transition. The dot-dashed gray line represents the pedestal value of the channel. The dashed red line represents the read value in ADC units taken by the readout sampling from the charging capacitor when there is a mismatch that gives an $\alpha = 0.25$ which is equivalent to $t_0 = 1.39\tau$, where τ is the charging and discharging time constant of the capacitor. The solid blue line is the actual value in ADC units that should have been read.

Figure 11.12 depicts the problem when there is a timing mismatch with an early readout such that the readout capacitor of the sample-and-hold circuit has not reached saturation after each transition when the chip reads its value. Equations 11.9 describe the problem for each channel transition. Usually, a good readout happens when the reading time t_0 happens at least 9.5τ after the capacitor starts to charge, where τ is the charging and discharging time constant of the capacitor as seen in Equations 11.9. When this happens, the readout error $\left(\frac{|V_{read}-V_{real}|}{V_{real}}\right)$ for each transition is below 0.01% of the transition jump between the previous state (V_{prev}) and the current one (V_{real}). As the readout time t_0 with respect to the capacitor's charging time τ is constant throughout the run, this exponential value can be expressed as a constant α.

$$V_{read} = V_{real} - \left(V_{real} - V_{prev}\right) e^{-t_0/\tau} \tag{11.9a}$$

$$\alpha \equiv e^{-t_0/\tau} \tag{11.9b}$$

$$V_{read} = V_{real} - \left(V_{real} - V_{prev}\right) \alpha \tag{11.9c}$$

$$V_{real} = \frac{V_{read} - \alpha V_{prev}}{1 - \alpha} \tag{11.9d}$$

As shown in Figure 11.13, if there is a timing mismatch (i.e., $\alpha \neq 0$), the distribution for η is asymmetric, its mean and median become smaller than 0.5, and its skewness becomes positive. Figure 11.14 shows how the mean and median of the η distribution change as a function of the parameter α.

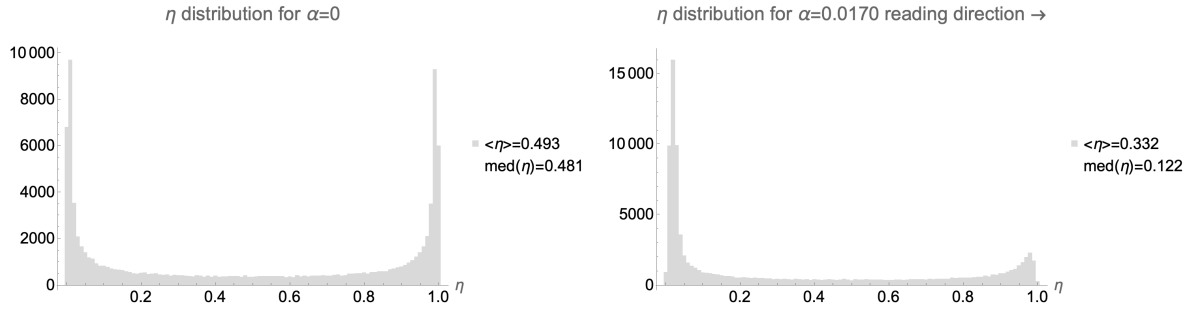

(a) (b)

Figure 11.13: Simulated Monte Carlo distributions. The distribution on the left assumes there is no timing mismatch. The distribution on the right assumes there is a timing mismatch giving an $\alpha = 0.017$. For each case, the mean and the median of the distributions are given.

Felix Bachmair, in his doctoral thesis, implemented an algorithm to correct the data by following the correction shown in Equation 11.9d[97]. It is an iterative process of guessing and updating the value of α to compensate the readout value in ADC units into the "real" value in ADC units for each channel. The algorithm corrects each channel sequentially from "left-to-right," meaning from a lower channel number to a higher channel number. This iterative process uses the mean of the η distribution as the figure of merit. The iterative process stops when the figure of merit is within a small distance from 0.5 or if a fixed number of iterations is reached (usually 100 iterations). On each iteration, if the distribution has a mean value still smaller than 0.5, it means that α should be larger than predicted and has to be updated with a larger value. If the mean value is larger than 0.5, the assumed value of α is too large and should be updated with a smaller value. For each step, the value of the compensation value α is saved with its respective figure of merit (the mean of the distribution). In the end, the α with the best figure of merit is used to correct the readout mismatch for that plane.

Most of the time, the algorithm worked, especially for the DUT, but it always had problems with some of the telescope's silicon tracking planes. Two problems were seen from the implementation of this correction method:

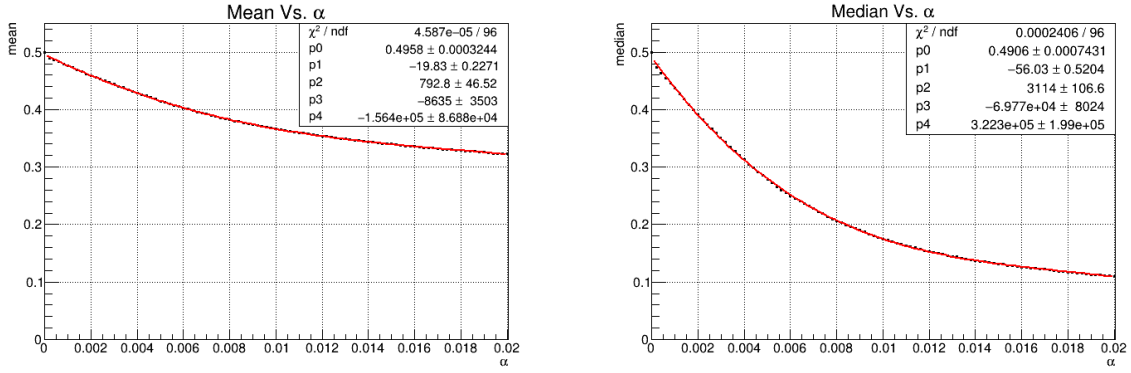

(a) (b)

Figure 11.14: Dependence of the mean and median of the η distribution as a function of the parameter α. The values come from simulation and the fit is a 4th-order polynomial that matches the data points. The fit parameter $p1$, which is the coefficient for the factor α^1, shows the sensitivity of the mean or median as the parameter α deviates from 0.

- Firstly, it did not restrict the values calculated for α, making it possible to assign negative values which should be impossible, as seen in the definition of α in Equation 11.9b. The values of α should be constrained between (0,1). This problem mainly affected two silicon planes (the ones mentioned to have right-to-left readout), which failed to compensate correctly for the asymmetry and affected the telescope's tracking performance.

- Secondly, if the value of α was negative, channels that were initially saturated were corrected such that they were no longer in saturation after the correction.

As it can be seen in Figure 11.15, a negative value of alpha in Equation 11.9d with a readout from left-to-right gives the distribution for η the same statistical characteristics in terms of skewness, mean, and median as a positive alpha with a readout from right-to-left. Figure 11.16 shows how the compensation works when applying a correction with a positive α with a readout from right-to-left and how it works when applying the wrong correction with a negative α with a readout from left-to-right. Negative α corrections assume that more charge was read; therefore, it corrects by reducing the transition between each channel. It can be seen from this plot that saturated channels are corrected to lower values, setting them as not saturated after the correction.

The affected planes were tracking planes 1X and 3X, which had a readout from right-to-left as mentioned previously in section 9.2.1. Consequently, the charge was wrongly compensated for these planes, resulting in a wrong predicted position based on the η distribution, which affected the alignment of the planes, which was critical for the analysis of small 3D cells. This issue had been overlooked as the 3D cells before 2016 had side lengths of 150 µm, unlike the 50 µm cells presented in this thesis which were tested in 2018.

An update to the correction was done by considering the readout direction. At first, it assumed that the readout was from left-to-right. Instead of the mean of the distribution, the

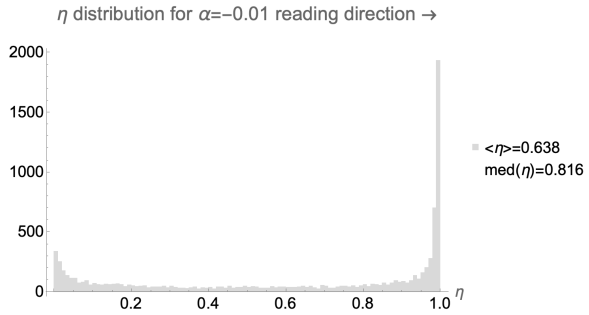

(a) Simulated distribution of η with a negative α with a readout from left-to-right.

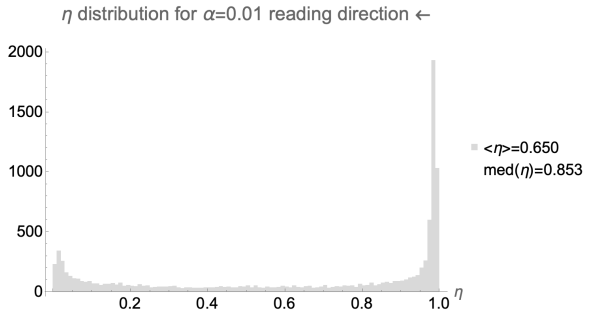

(b) Simulated distribution of η with a positive α with a readout from right-to-left

Figure 11.15: The distributions above show the effects of having a negative α value for correction when the readout is assumed to be from left-to-right (a), and the case when α is positive and the readout is assumed to be from right-to-left (b).

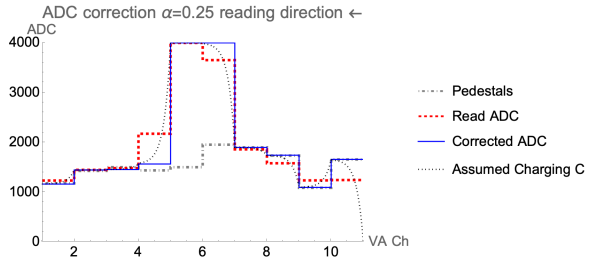

(a) Corrected ADCs for $\alpha = 0.25$ for a readout from right-to-left

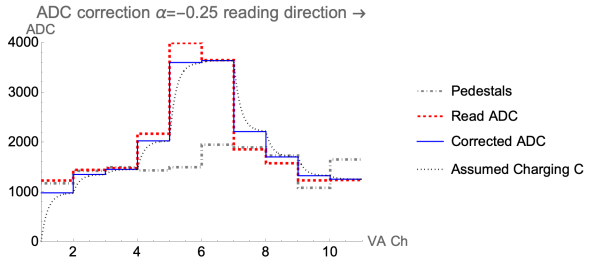

(b) Corrected ADCs for $\alpha = -0.25$ for a readout from left-to-right

Figure 11.16: Comparison between a correction applying a positive α for the correct readout direction (a) vs. applying a negative α for the wrong readout direction (b). In this plot, saturated values of the ADC are set for 4000 ADC. Channel 5 is read as saturated. It is clear that a negative α would desaturate channel 5.

median was selected as the figure of merit. This measure was more sensitive to the parameter α, as shown in Figure 11.14. For corrected distributions, a median close to 0.5 is equivalent to having a mean close to 0.5 or a skewness close to 0. If the median of the initial distribution was smaller than 0.5, then the readout was assumed to be from left-to-right, and the value of α was increased. If otherwise, the median was larger than 0.5, then the readout was assumed to be from right-to-left, and the value of α was increased. The iterative algorithm continued as described above, guaranteeing that saturated channels always remained saturated.

The effect of the procedure is demonstrated in Figure 11.17 for detectors with both readout directions. After applying the correction, the η distributions recover their symmetry as can be seen in Figures 11.17c and 11.17d.

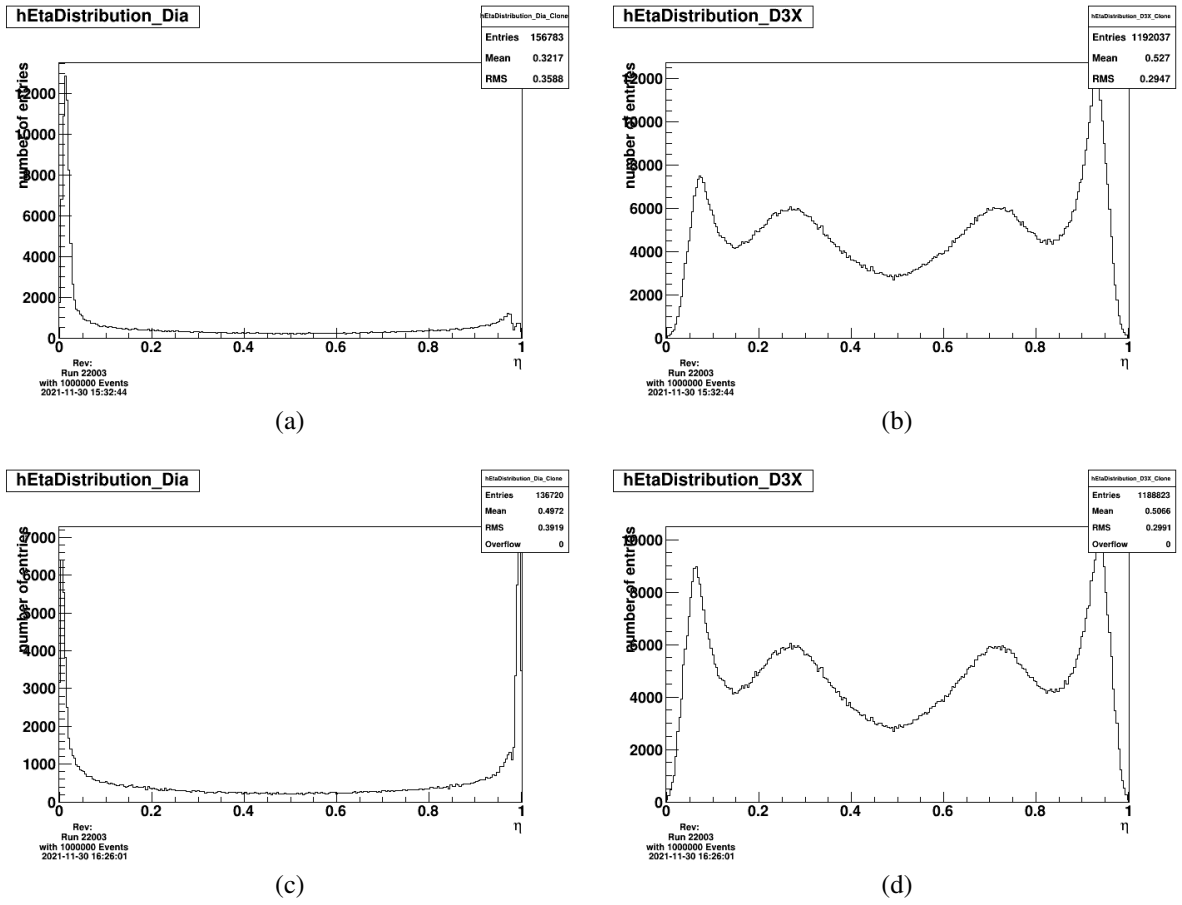

Figure 11.17: Distributions for η before the data-driven-feed-across-correction, (a) and (b), and after the data-driven-feed-across-correction, (c) and (d). The readout of the detector on the left plots was from left-to-right, while it was from right-to-left for the detector on the right plots.

11.6 Data Selection

Two data selections were performed: One for the alignment of the planes and the other for the transparent analysis. The following paragraphs will explain these selection criteria. The selection performed for the alignment was:

- Events within the first 10 % of the data
- One and only one cluster in each silicon plane
- One and only one cluster in the DUT
- Hit position inside the telescope's fiducial region

As for the transparent analysis, the selection performed was the following:

- Events within the last 90 % of the data

- One and only one cluster in each silicon plane
- Hit position inside the telescope's fiducial region
- Tracks with small χ^2
- Transparent clusters in the DUT do not contain masked or invalid channels of the VA chip

As the tracking telescope was made with strip detectors, it was required to use events with only one cluster for each plane. This measure avoided the ambiguity that would arise if two or more clusters were present in a plane, as there was no direct one-to-one correspondence between a hit in an X plane and a hit in a Y plane. An example of the ambiguity can be seen in Figure 11.18, where "Ghost" positions can arise from the ambiguity.

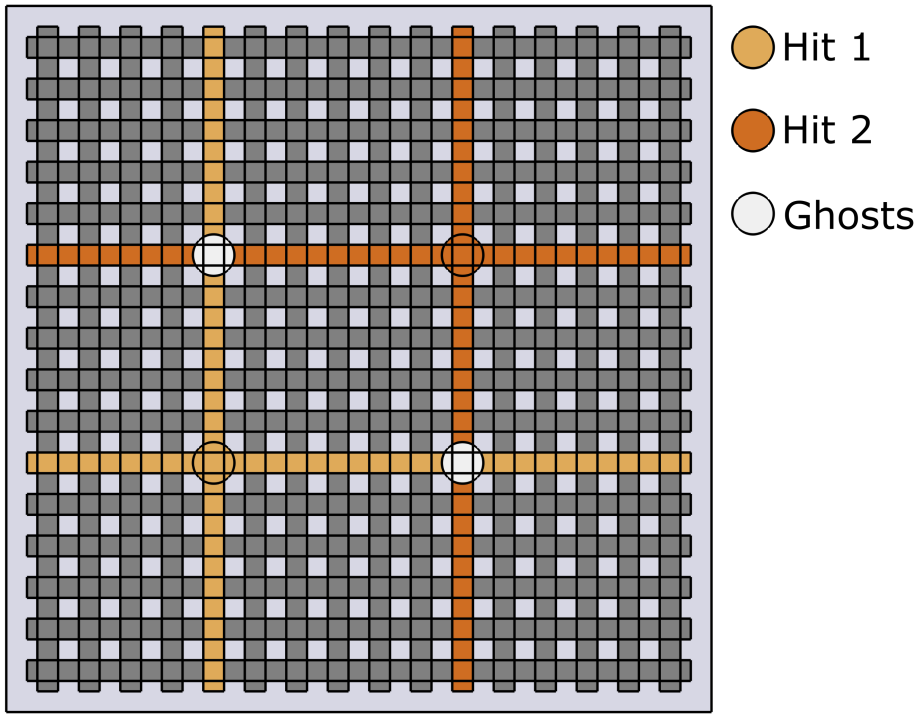

Figure 11.18: Example of an event with two simultaneous hits. The hit positions of Hit 1 and Hit 2 are identified by an excess of charge across the colored strips. Consequently, there are two possibilities: the hits happened in the locations Hit 1 and Hit 2, or they happened in the "Ghost" positions. Without further information, it is impossible to know the actual position of the hits.

As the momentum of the particles in the beam was of the order of $O(100\,\mathrm{GeV/c})$, the width of the angle distribution from small angle multiple scattering was negligible, and particles were assumed to pass straight through the detector without scattering as mentioned previously in section 9.2.1. Additionally, the beam has an imperceptible divergence.

The average of the position in each plane of the tracking planes was set as the position of each cluster for selecting a fiducial region, as shown in Equations 11.10, where X_t and Y_t are defined as the horizontal and vertical coordinates respectively in the local telescope coordinates, and X_{p_i} and Y_{p_i} are the horizontal and vertical coordinates respectively of the telescope's X-Y plane i. By requiring one and only one cluster in each of the silicon tracking planes of the telescope, the "shadow" of the scintillator on the telescope coordinates could be seen as shown in Figure 11.19.

$$X_t = \frac{1}{4}\sum_{i=0}^{3} X_{p_i} \tag{11.10a}$$

$$Y_t = \frac{1}{4}\sum_{i=0}^{3} Y_{p_i} \tag{11.10b}$$

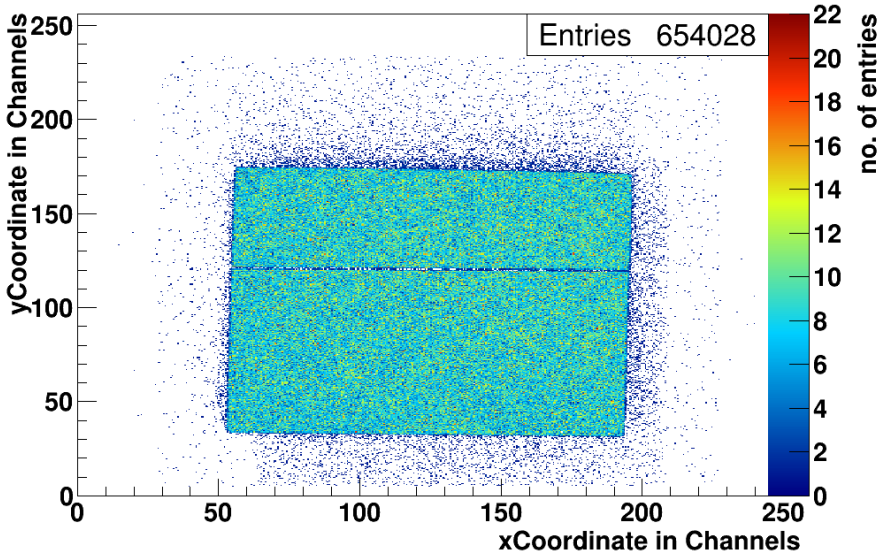

Figure 11.19: Hit map in the telescope's space. The displayed rectangle corresponds to the shadow of the scintillator, which issues the trigger to save the event.

A "shadow" of the DUTs connected to the VA2.2 chip could be seen by requiring at least one cluster event in the diamond's channels. Figure 11.20a shows the "shadows" of the detectors on the Irrad-3D sample (see section 4.3.4).

Doing this was useful for identifying the position of the DUT with respect to the telescope and defining a fiducial region. Even though one and only one cluster were required by the telescope's tracking planes, the DUT could detect more than one cluster as its thresholds t_s and t_h were much lower than for the telescope's tracking planes. Two scenarios could give more

than one cluster in the DUT: Two particles passed through the telescope planes, but only one passed the clustering thresholds, giving as a consequence only one event in the tracking planes, but as the DUT had lower clustering thresholds, the DUT detected the two particles. The other possibility was that noise fluctuations surpassed the thresholds and were considered an extra event. This would happen ~ 0.4 % of the time in the 128 channels of the DUT.

By requiring one and only one cluster in the DUT, the odds that the cluster corresponded to the same particle passing through the telescope planes were higher, making it possible to create tracks using the hit position in each of the planes (including the DUT) to then align the planes. Figure 11.20b shows the event reduction of around 4500 events after applying the requirement of only one cluster in the diamond, corresponding to ≈ 11.5 % of the events.

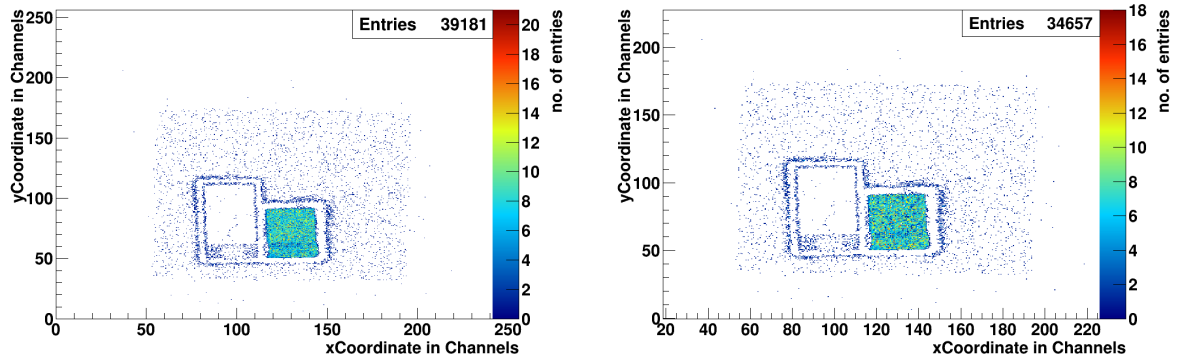

(a) (b)

Figure 11.20: Hit maps in the telescope's space requiring at least one cluster in the diamond channels (a) and one and only one cluster in the diamond channels (b). The DUT in these hit maps corresponds to the Irradiated-3D biased with −45 V. The shadow of the diamond prototypes can be seen. Features such as the guard rings surrounding the 3D cells can easily be distinguished. Check section 4.3.4 as reference.

To take advantage of the limited opportunities to test detectors, in some cases, more than one diamond sensor was wire-bonded to the same VA chip. In other cases, different detector types were present in the same diamond sensor (as is the case for Multi-3D and Irrad-3D). These different detector types could have differences in the geometry used for the 3D cells (e.g., hexagonal cells with a pitch between channels of 100 µm) or even in the type of detector (e.g., a planar strip detector alongside 3D cells). For this reason, the final steps in the analysis were to avoid results from different detector types.

An easy way to achieve this was by defining the fiducial region that selected only a specific detector type or geometry for the next steps of the analysis. Figure 11.21 shows the selected fiducial region, comprised only of events passing through the strips on the diamond with a pitch of 50 µm between the strips and excluded the events passing through the 100 µm pitch strips on the same DUT. As mentioned above, the first 10 % of the total number of events from this region was used for the alignment of the telescope and the DUT.

The last 90 % of the data was used for the transparent analysis. The requirements imposed for the tracks were that there was a well-defined track by the telescope's planes, which meant that there was one and only one cluster in each of the silicon planes and that the χ^2s of the fitted tracks were below a defined threshold. It was also required that the event hit position in the telescope's local coordinates was within the defined fiducial region to target the region of interest in the DUT. The last selection criteria for the transparent analysis will be discussed in the transparent analysis section.

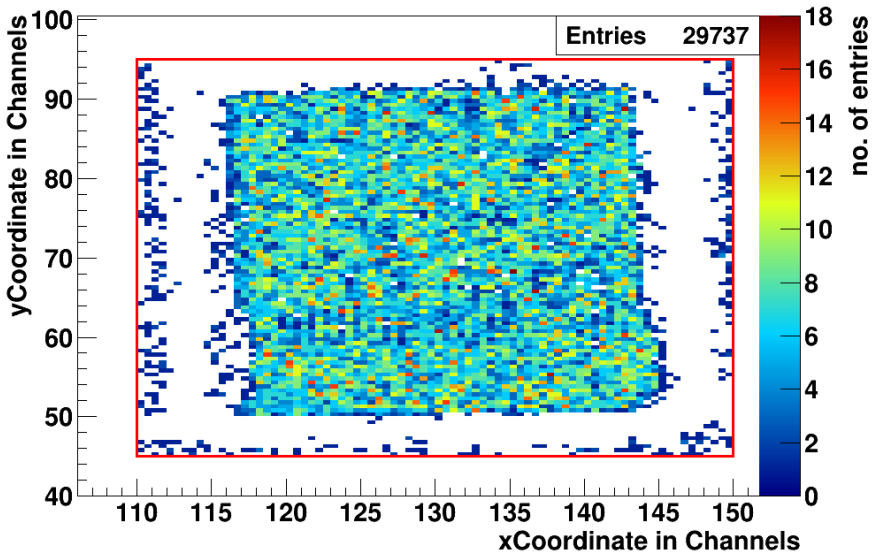

Figure 11.21: Hit map in the telescope's space. A fiducial region for analysis between X : [110 – 150] and Y : [45 – 95] is imposed. All events with clusters in the silicon planes outside this rectangular region were not considered further for analysis. The white band around the 3D cells corresponds to the guard ring whose channel was masked.

11.7 Alignment

The main goal of the alignment procedure was to predict with good spatial accuracy the hit position of the particles that triggered the event on the DUT. Table 11.1 shows the major steps used for the alignment process. In the following paragraphs, the details of the alignment will be given.

It was necessary to set a plane of reference to align the planes of the telescope and the DUT. This was achieved by assuming that the strips in the two detectors that comprised plane 0 (i.e., planes 0X and 0Y) were perpendicular. This measure sets an orthogonal basis and correspondence between channels in the X-Y plane 0 and the spatial position in the plane in microns. With respect to these reference planes, the rest of the X-Y planes were aligned, which means that the relative displacements and rotations were found. For this, it was possible to

Step	Tracking XY-planes	XY-planes to align
1	0	3
2	0, 3	1
3	0, 1, 3	2
4	0, 1, 2, 3	DUT

Table 11.1: Major steps for aligning the telescope's tracking planes and the DUT.

independently align each plane's horizontal and vertical channels. Figures 11.22b and 11.22c depict the parameters estimated in the alignment for each plane X and Y, respectively.

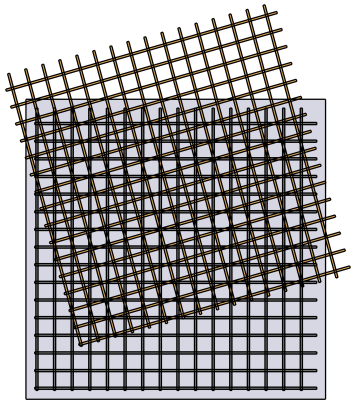

(a) Misaligned plane with respect to the reference.

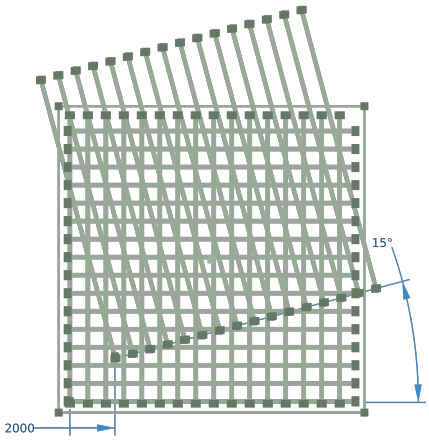

(b) Misaligned plane X with respect to the reference.

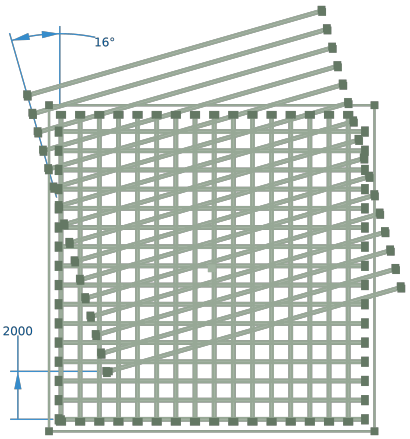

(c) Misaligned plane Y with respect to the reference.

Figure 11.22: Example of the plane misalignment with respect to the reference. (a) Shows the reference X-Y plane in gray and the misaligned plane's vertical and horizontal strips. Note that the horizontal and vertical strips in the misaligned plane are not necessarily perpendicular with respect to each other. (b) Shows the angle rotation for the vertical strips ($\phi_x = 15°$) and their horizontal offset ($x_o = 2000\,\mu m$). (c) Shows the angle rotation for the horizontal strips ($\phi_y = 16°$) and their vertical offset ($y_o = 2000\,\mu m$).

Equation 11.11 describes a rotation and a translation of the form $\vec{r} = R^i \cdot \vec{r}^{\,i} + \vec{r_o}^{\,i}$ for a plane i with respect to the reference, where "$\vec{r}$" is the position vector in the reference coordinates, "R^i" is a rotation matrix associated to plane i, "$\vec{r}^{\,i}$" is the position vector in the local coordinates of the plane i and "$\vec{r_o}^{\,i}$" is the translation offset vector of the plane i with respect to the reference coordinates.

$$\begin{pmatrix} x \\ y \\ z \end{pmatrix} = \frac{1}{\cos\left(\phi_y^i - \phi_x^i\right)} \begin{pmatrix} \cos\phi_y^i & -\sin\phi_x^i & 0 \\ \sin\phi_y^i & \cos\phi_x^i & 0 \\ 0 & 0 & 1 \end{pmatrix} \begin{pmatrix} x^i \\ y^i \\ 0 \end{pmatrix} + \begin{pmatrix} x_o^i \\ y_o^i \\ z_o^i \end{pmatrix} \tag{11.11}$$

The known quantities in Equation 11.11 are the local position vectors given by the planes' $\vec{r}^{\,i}$ and the offsets of the planes "z_o^i" along the beam, which have been measured and are mechanically fixed by design. The unknowns that have to be found in the alignment for each plane are thus: x_o^i, ϕ_x^i, y_o^i, and ϕ_y^i. In the case of the DUT that only has a resolution in the X direction, the predicted position in the Y coordinate by the telescope planes is used for future steps. As mentioned before, the first X-Y plane (plane 0) was set as the reference, the same as having $\phi_x^0 = \phi_y^0 = x_o^0 = y_o^0 = z_o^0 = 0$ in Equation 11.11.

The next step was the alignment of plane 3 with respect to the reference using an iterative method. The iterative process will be discussed in more detail in the following paragraphs. The trajectories of the particles were always assumed to be perpendicular to the planes for these steps. Once plane 3 was aligned with respect to the reference, the first and last planes (i.e., the reference plane 0 and plane 3) were used to produce tracks and predict the hit position on plane 1 via interpolation. Plane 1 was then aligned with respect to the interpolated predictions. The now aligned planes 0, 1, and 3 were then used to predict the hit position on plane 2, which was aligned with respect to the reference. With this step, the telescope alignment was finished, and it was possible to use the four planes of the telescope to predict the hit position in the DUT within a 5 µm margin from the actual position, which was located in the center of the telescope as seen in Figure 9.5, via interpolation. The resolution of the hit positions on the DUT was below 5 µm, according to the measurements[64]. This resolution was verified by looking at the width of the residual distributions for each plane.

The iterative process to align each plane started by looking at the residual distributions of each plane. The residuals, by definition, are the difference between the predicted hit positions and the measured hit positions by the plane under alignment. For simplicity, the alignment process will be described in the X direction of plane 1. Initially, the two-dimensional histogram between the residuals in X vs. the predicted hit position in Y (see Figure 11.23a) was created.

Projecting this histogram along the residuals in X (Delta X in Figure 11.23a) resulted in the distribution of the residuals along the X direction as shown in Figure 11.23b. The mean of this distribution was used to update the value for x_o^1.

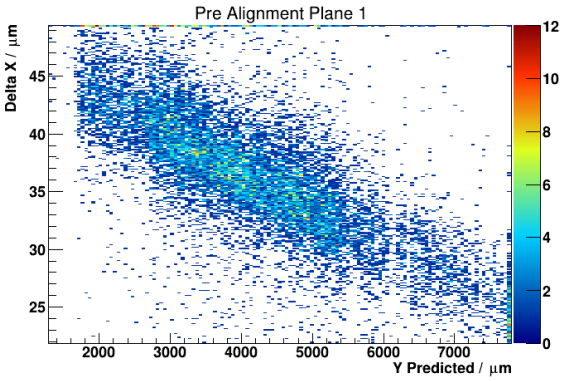

(a) Residuals in X vs. predicted position in Y on plane 1 before alignment.

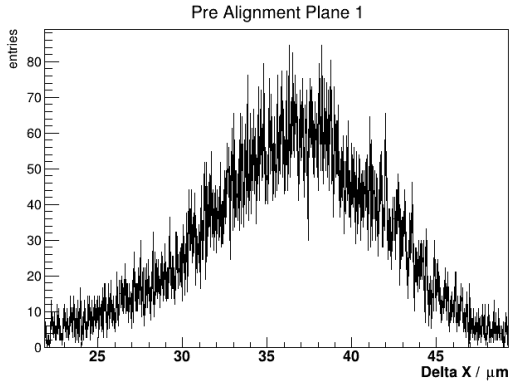

(b) Residuals in X on plane 1 before alignment.

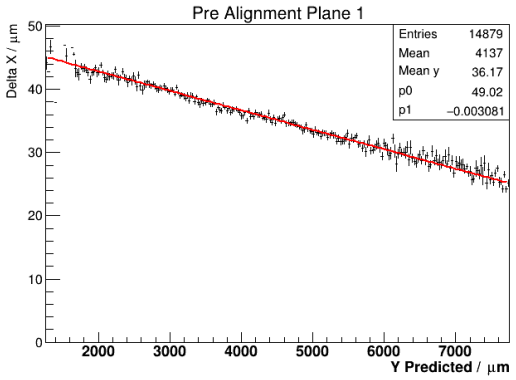

(c) Profile histogram of Residuals in X vs. predicted position in Y on plane 1 before alignment.

Figure 11.23: Histograms used for alignment. The projection of the 2D histogram in (a) along Delta X, results in the histogram shown in (b). The mean of the histogram of the residuals shown in (b) is used to update the offset x_o^1 in this example. The profile histogram of (a) along the predicted Y position results in (c). The linear dependence can be fitted and the slope $p1$ of the fit is used to update the rotation angle ϕ_x^1.

Profiling the histogram in Figure 11.23a along the predicted hit position in Y, which means that for every bin in the predicted hit position in Y, the mean and the RMS of the entries in Delta X are shown, it was possible to perform a linear fit to the resulting 1D profile histogram as shown in Figure 11.23c. The arctan of the slope of the fitted line (i.e., $\arctan(p1)$ in Figure 11.23c) was used to update the rotation angle ϕ_x^1.

The process mentioned above was iterated five times, after which further corrections to the alignment parameters were negligible before considering a plane as aligned. After the fifth iteration of corrections to x_o^1 and ϕ_x^1, the resulting distributions mentioned above can be seen in Figure 11.24. As a result, the residuals are centered at 0, and the fit of the profile histograms gives a horizontal line at 0.

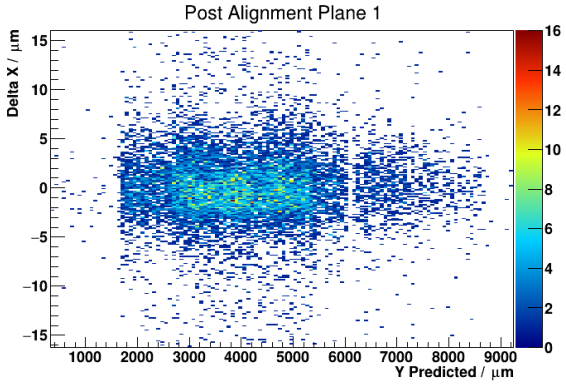

(a) Residuals in X Vs. predicted position in Y on plane 1 after alignment.

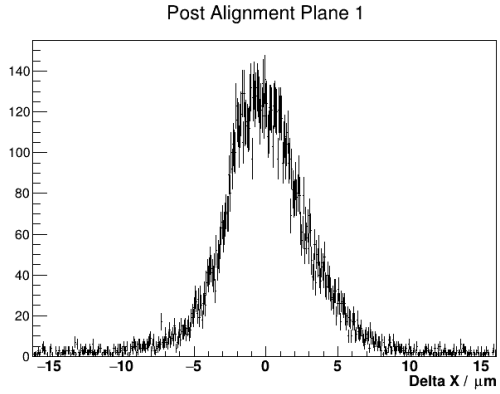

(b) Residuals in X on plane 1 after alignment.

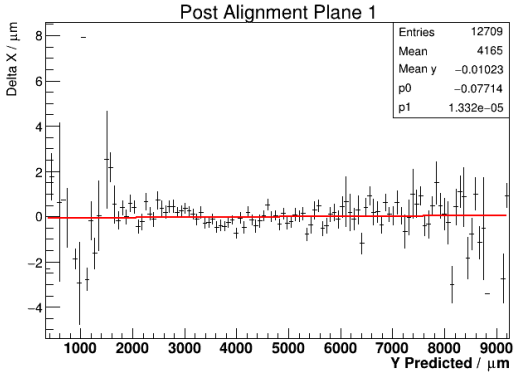

(c) Profile histogram of Residuals in X Vs. predicted position in Y on plane 1 after alignment.

Figure 11.24: Histograms after alignment. The projection of the 2D histogram in (a) along Delta X, results in the histogram shown in (b). The mean of the residuals in X is centered around 0 as it can be seen in (b). The profile histogram in (c) is obtained by profiling the histogram of (a) along the predicted Y position. The linear fit is consistent with a horizontal line at 0.

In Figure 11.24c, the data for values of Y below 1700 µm and above 8500 µm correspond to false triggers from the scintillator (e.g. noise). As a consequence, the residuals are random in these regions.

11.8 Track Selection For The Transparent Analysis

With the planes aligned, for each event that fulfilled the first three selection criteria for the transparent analysis mentioned in section 11.6, a linear fit was performed, and the χ^2 in the X and Y directions were calculated. It was expected that the resulting χ^2 values obtained from the fits followed a χ^2 distribution with two degrees of freedom. An example of the resulting distributions for the obtained χ^2 in the X and Y direction can be seen in Figure 11.25.

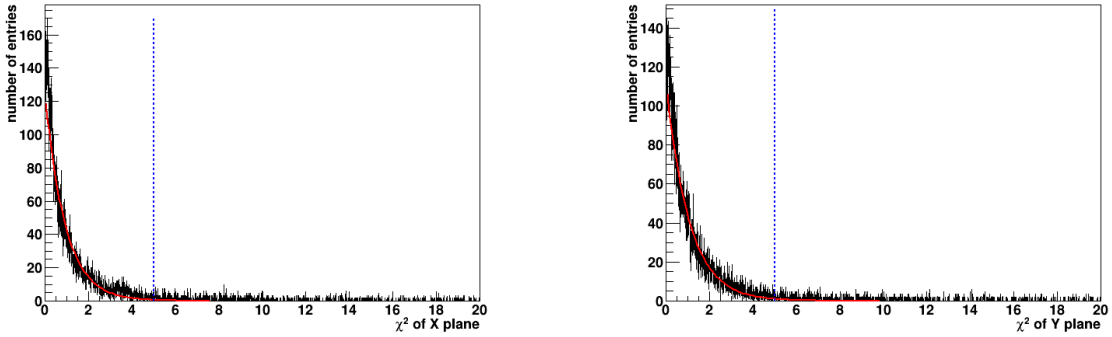

(a) χ^2 distribution in the X direction of the tracks' fit (b) χ^2 distribution in the Y direction of the tracks' fit

Figure 11.25: χ^2 distributions from each of the track fits for the X and Y components separately. The blue dashed lines depict the threshold applied to the χ^2 for the fits in the X direction and the Y direction for the tracks selection. The solid red lines depict the theoretical value for a χ^2 distribution with two degrees of freedom.

A χ^2 cut of 5 on each of the χ^2 distributions was applied, which meant that any track with a χ^2 greater than 5 in the X or Y directions would not be considered for further analysis. This cut was a good compromise between tracks with a good hit position prediction without sacrificing too many events. With these measures, around 8 % of the tracks would be excluded, and a consistent sample of straight tracks through the telescope perpendicular to the telescope's planes was left for the next steps in the analysis.

11.9 Transparent Clustering

The final step for analyzing DUTs with strip readout was to use the predicted hit position by the telescope to evaluate the charge induced by the particle in the vicinity of the hit position. In this way, the induced charge in the DUT could be studied without making any cut on the signal of the DUT.

For the case of planar strip detectors, a transparent cluster of ten strips around the predicted hit position was made. Ten strips were found to cover the cases where charge sharing was present and where fabrication processes mistakes encouraged the charge to be collected away from the predicted hit position. Extra strips that do not have a charge due to ionization should average to 0 over the whole run as they only contain noise fluctuations. Five adjacent channels centered around the channel with the largest signal were taken out of the ten strips. The sum of these five signals was used as the figure of merit for the collected charge. Five channels showed that more than 90 % of the total charge in the ten strips was collected as shown in Figure 11.26.

In the case of strips with 3D cells, due to the arrangement of the electrodes, which reduced the amount of charge sharing between neighboring cells, a transparent cluster of only three strips was found to be required. As discussed in section 8.3.2, out of the three channels in the transparent cluster, the two channels with the largest signal were taken as the figure of merit for the collected charge.

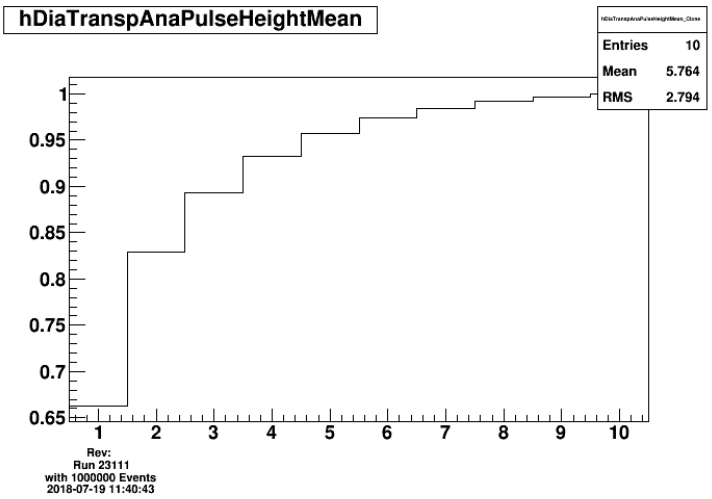

Figure 11.26: Collected charge in the transparent cluster of ten strips as a function of the number of strips included for the figure of merit for a highly irradiated scCVD diamond biased with −1100 V resulting an electric field with a magnitude greater than 2 V/µm.

With the transparent clustering, besides the unbiased studies of the charge collected by the detector, efficiency studies based on a given threshold could be made.

Figure 11.27 shows how a transparent cluster of ten strips is formed using the predicted hit position. Note that channels below the hit threshold t_h would be considered in the transparent analysis. Channels with signals within the range of noise fluctuations average out to zero when considering all the events. In this example, from the ten strips surrounding the predicted hit position, the five contiguous channels centered around the channel with the highest SNR (defined in Equation 11.6) were considered to calculate the charge.

11.10 Transparent Grid

For 3D detectors, it is possible to use the predicted hit position to study the pulse height response of individual cells. This helps distinguish the effects of the detector design, the quality of the sensor, and the effects of fabrication defects on the collected charge. For this purpose, the Transparent Grid was implemented.

During alignment, the DUT plane was aligned such that the spatial X coordinate of the DUT was parallel to the spatial X coordinate of the telescope's planes and perpendicular to the spatial Y coordinate of the telescope's planes. For this reason, for every hit, it was possible to correlate the predicted hit position in terms of the telescope's spatial horizontal position in microns with the predicted channel of the VA chip connected to the strip where the particle hit. As for the Y coordinate, the only knowledge of the event position in this direction came from the predicted hit position of the telescope.

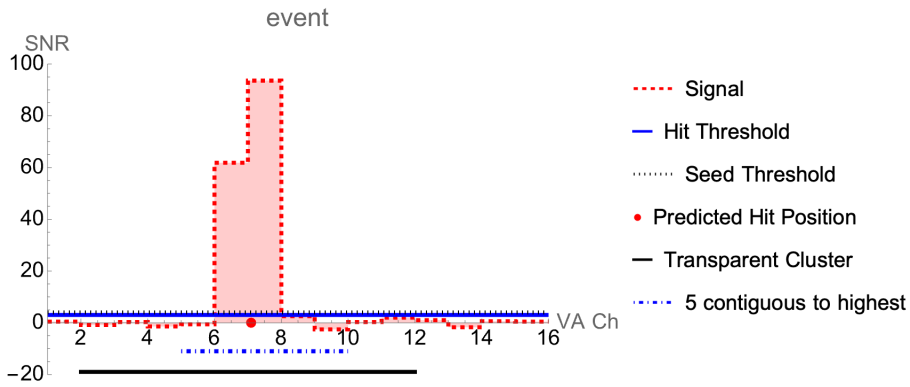

(a) SNR of an event for a set of 15 channels of the VA chip.

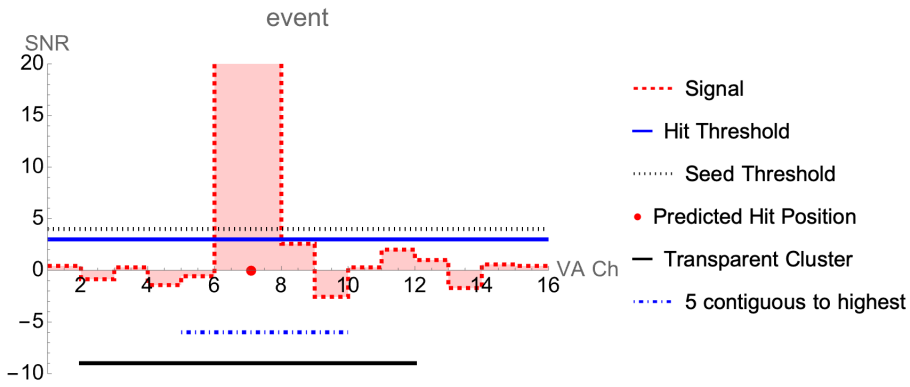

(b) Zoom around 0 SNR of an event for a set of 15 channels of the VA chip.

Figure 11.27: Example of the signal in the DUT measured in SNR for different channels in the VA chip connected to the detector. The predicted hit position is marked with a dot, and the Hit Threshold and the Seed Threshold are shown with a blue solid line and a dotted black line respectively. The transparent cluster of 10 channels is built around the predicted hit position, which groups channels 2 to 11 inclusive. The five contiguous to the highest channel are in this example channels 5 to 9 inclusive.

11.10.1 Vertical Border Identification

The first task to set the grid was to identify the vertical borders of the detector. For this task, it was helpful to plot the pulse height map of the detector as a function of the predicted hit channel in the VA chip for the X-axis and the predicted hit position on the Y-axis. Figure 11.28 shows that the region where the 3D cells are located can be identified from this plot as the pulse height is larger in the region of the 3D cells than outside the 3D cells.

For example, in the 3D cells shown in Figure 11.28b, if the plot is projected onto the Y axis, the resulting plot has the shape described by the curve in Figure 11.29. Equation 11.12 shows an equation that parametrizes this curve. In this equation, the parameter $p3$ marks the uppermost vertical border of the 3D cells (y_{up}); $p1$ and $p4$ represent the width of the pulse height transition between the lower and upper limits of the 3D cells; "y_d" is the length of the region with 3D cells in the Y-direction; and "$p0$," "$p2$," and "$p5$" are free parameters for the projected pulse

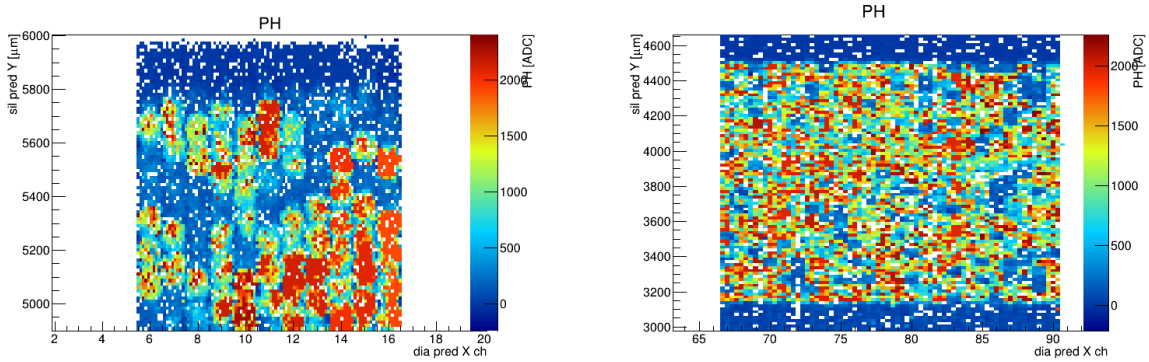

(a) Pulse height map of hexagonal 3D cells in the Multi-3D detector at 90 V

(b) Pulse height map of square 3D cells in the Full-3D detector at 90 V

Figure 11.28: Pulse height maps of two different 3D detectors. It can be seen in (a) that due to the hexagonal tiling, there are two vertical limits for the detector: one for even channels and one for odd channels.

heights which characterize three regions: pulse height of the region above the selected 3D cells, pulse height in the selected 3D cells and pulse height below the region of the selected 3D cells.

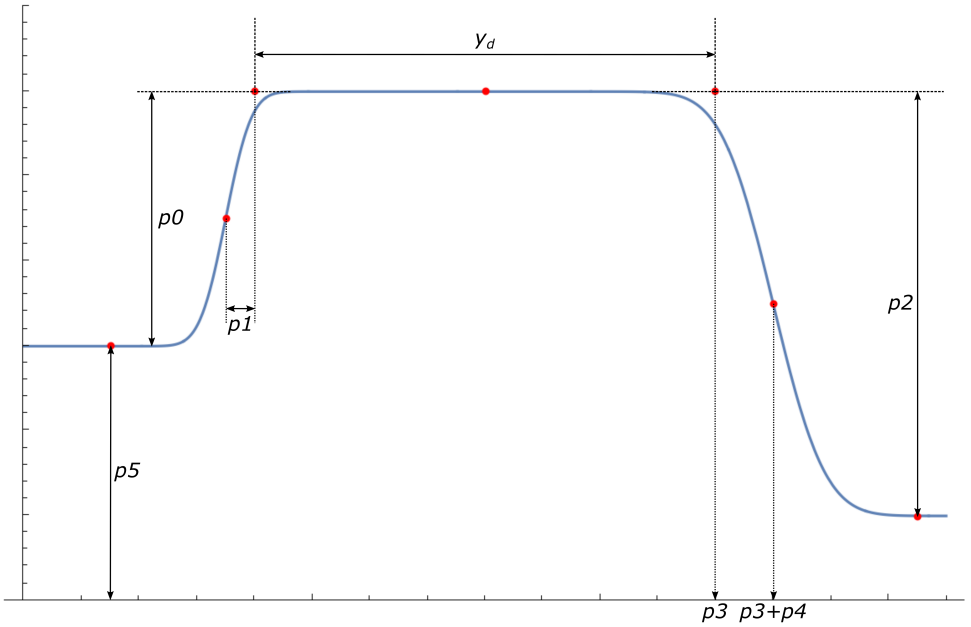

Figure 11.29: Curve from Equation 11.12 that approximates the detector's projected pulse height onto the y-axis. Three regions are seen, two with lower projected pulse height that surround a higher region corresponding to the region where the 3D cells are located. The transitions are modeled with error functions with different transition lengths determined by the parameters $p1$ and $p4$. The length of y_d, which is the extent of the 3D cells in the Y-direction, is fixed and is known from the detector design.

The transition regions are due to a combination of the electric fields in the borders that leak out from the 3D cells, collecting the charge deposited outside the 3D cells, combined with the telescope's resolution. The length of the region with 3D cells y_d is, by definition, the number of cells ganged together in each channel of the DUT (n_c) times the height of each 3D cell (h_{cell}).

$$g(y) = \frac{p0}{2}\left(\text{erf}\left(\frac{y-(p3-y_d-p1)}{p1}\right)+1\right) - \frac{p2}{2}\left(\text{erf}\left(\frac{y-(p3+p4)}{p4}\right)+1\right)+p5 \tag{11.12a}$$

$$y_d \equiv n_c \cdot h_{cell} \tag{11.12b}$$

A fit of the function $g(y)$ shown in Equation 11.12 was done separately for even and odd channels. This measure accounted for the fact that the upper limits for odd channels and even channels are different in hexagonal tiling. This procedure was also done for rectangular cells. An example of these fits for square 3D cells is shown in Figure 11.30.

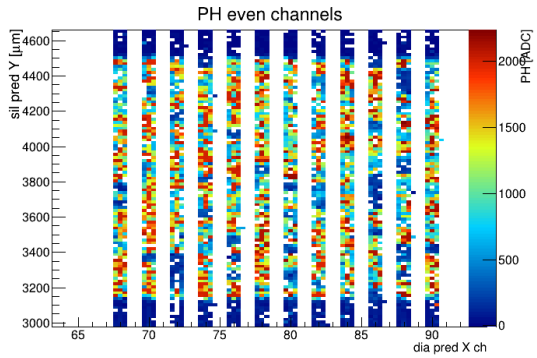

(a) Pulse height map for even channels.

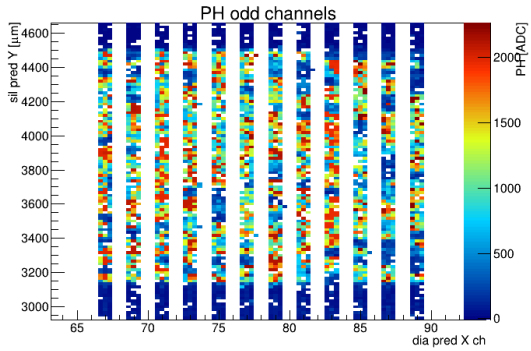

(b) Pulse height map for odd channels.

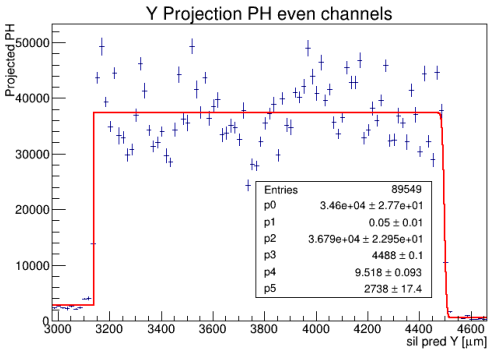

(c) Y projection of the pulse height map for even channels.

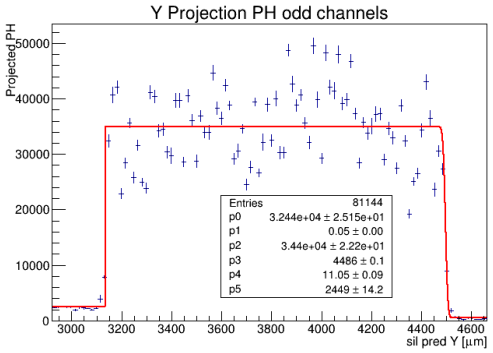

(d) Y projection of the pulse height map for odd channels.

Figure 11.30: Examples of the fit of the curve in Equation 11.12 on the pulse height maps for even and odd channels of a detector with square 3D cells. The parameter of interest for the fit is the upper limit of the 3D cells ($p3$).

For rectangular 3D cells, an average of the parameter $p3$ obtained from the fit of even

($y_{up_{even_{fit}}}$) and of odd ($y_{up_{odd_{fit}}}$) DUT channels was used as the first estimate of the uppermost limit of the 3D cells in the detector as it can be seen in Equation 11.13.

$$y_{up} = \frac{y_{up_{odd_{fit}}} + y_{up_{even_{fit}}}}{2} \tag{11.13}$$

For hexagonal 3D cells, the difference between the uppermost limit of the 3D cells between even and odd channels needed to be $h_{cell}/2$, where "h_{cell}" is the height of the hexagonal cell (see Figure 11.32). For this reason, Equation 11.14 was used to calculate the first estimate for the uppermost limit of the 3D cells.

$$y_{up_{\{odd\}_{even}}} = \begin{cases} \frac{y_{up_{odd_{fit}}} + y_{up_{even_{fit}}}}{2} \pm \frac{h_{cell}}{4} & , \quad y_{up_{odd_{fit}}} > y_{up_{even_{fit}}} \\ \frac{y_{up_{odd_{fit}}} + y_{up_{even_{fit}}}}{2} \mp \frac{h_{cell}}{4} & , \quad y_{up_{odd_{fit}}} < y_{up_{even_{fit}}} \end{cases} \tag{11.14}$$

11.10.2 Grid Superposition

Once the upper limit of the cells was estimated, a grid pattern was placed on the predicted hit in the DUT's channel and the telescope predicted Y position space, such that any coordinate in this space would correspond to a cell of the tiling.

For the rectangular cells, the essential parameters for the tiling are shown in Figure 11.31. The tiling is specified by the height of the cells h_{cell} and the pitch between the strips on the detector, which was the same as the width of the 3D cells. The columns were numbered starting from 0, and the first column was assigned to the first channel of the DUT that can have a transparent event. As for the rows, they were also numbered starting from 0 and incremented vertically. In the example of Figure 11.31, the first channel of the DUT that could have a transparent event is Ch 53 which is assigned "Column 0". In the example, the grid consists of only four columns and two rows. As can be seen, the 3D cells are not necessarily square.

For the hexagonal cells, the cell's width must be given along with the cell's height and the channel's pitch. Even channels and odd channels could have a different number of cells ganged together, as shown in Figure 11.32, which means that there was a different row numbering for even and odd channels.

Each polygon of the tiling could determine if a coordinate in the plane, defined by the channel in the VA chip connected to the hit cell and the predicted Y position in the telescope, was inside the polygon. Consequently, it was possible to assign a specific cell (a row and a column in the grid) for each transparent event, as well as the internal coordinates inside the cell with respect to the cell's center. Figure 11.33 shows an example of a rectangular tiling. In this example, the predicted hit position has coordinates of 54.3 in the DUT's channel and $y_{up} - h/2$ in the Y position, where "h" is the cell's height, and "y_{up}" is the uppermost limit of the 3D cells. In this example, the transparent grid assigns the event row 1, column 1, and internal cell coordinates $(x_0, y_0) = (0.3, 0)$.

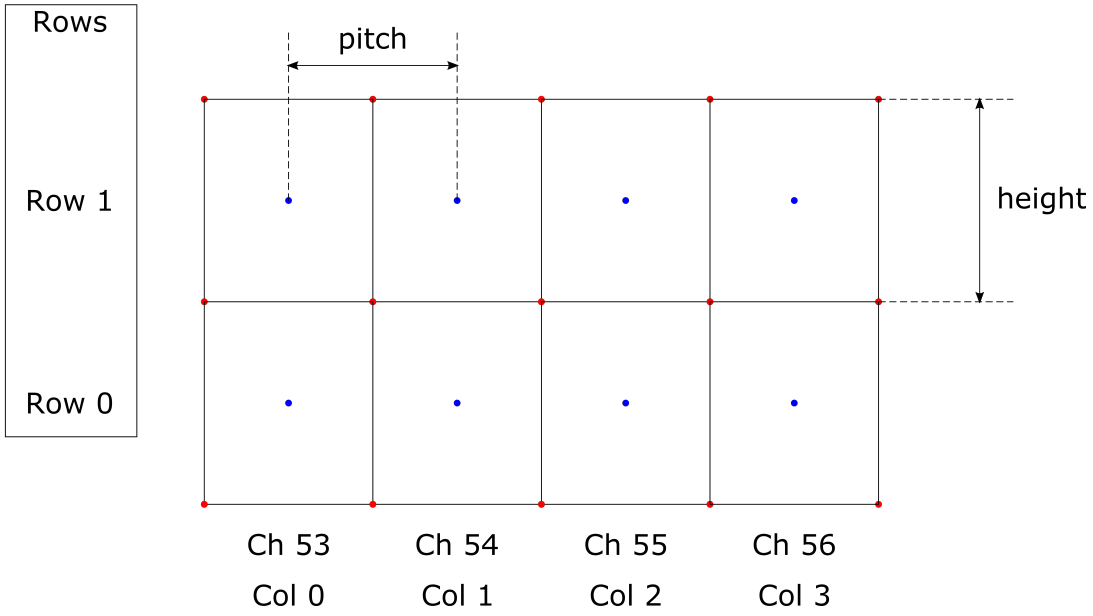

Figure 11.31: Example of a rectangular grid. A grid in terms of columns and rows is made such that each grid element can be identified with a column and a row. For rectangular cells, the pitch and the height of the cells must be given to set the tiling.

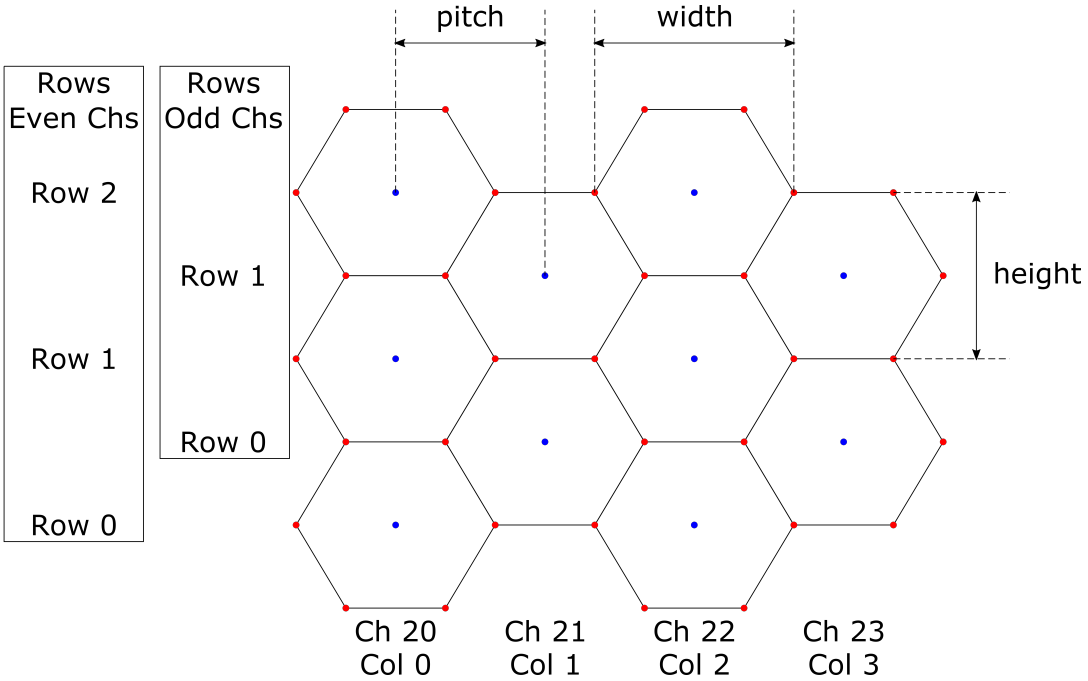

Figure 11.32: Example of a hexagonal grid. A grid in terms of columns and rows is made. Note that the number of cells in a column could be different for even or odd channels in the VA chip.

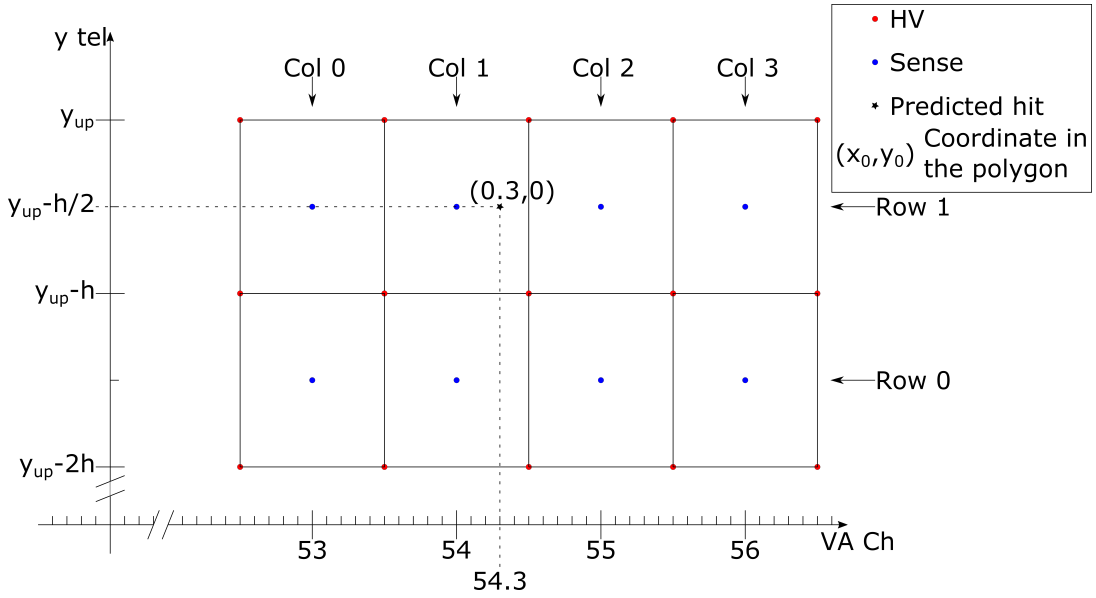

Figure 11.33: Example of a four-column and two-row grid. The red dots in the corner of the polygons correspond to the biasing 3D wires, while the blue dots in the middle of the polygons represent the sensing 3D wires. The black star represents the predicted hit position by the telescope planes in the 2D space given by the channel of the VA chip and the telescope's Y coordinate prediction. The predicted hit happens in channel position 54.3 and telescope's Y $y_{up} - h/2$. The event is given a coordinate in the grid. In this example, it would be (col, row)=(1,1). Additionally, the event is given a position inside the polygon: $(x_0, y_0) = (0.3, 0)$.

11.10.3 Fine Alignment

Using the internal coordinates of each event inside its corresponding polygon, it was possible to overlay the charge in ADC units for a selection of cells. Making the mapping in Equations 11.15b and 11.15c, where the definition for rounding to the closest integer was defined as shown in Equation 11.15a, it was possible to adjust the offsets x_{off} and y_{off} for fine alignment.

$$\lceil f \rfloor \equiv \lfloor f + 0.5 \rfloor \tag{11.15a}$$

$$x_0 \mapsto w \cdot \left(\frac{x_0 - x_{off}}{w/p} - \left\lceil \frac{x_0 - x_{off}}{w/p} \right\rfloor \right) \tag{11.15b}$$

$$y_0 \mapsto h \cdot \left(\frac{y_0 - y_{off}}{h} - \left\lceil \frac{y_0 - y_{off}}{h} \right\rfloor \right) \tag{11.15c}$$

, where w, h, and p are the width, height, and pitch of the 3D cells, respectively, and x_0 and y_0 are the center coordinates of the polygons.

The mapping in Equations 11.15b and 11.15c allows overlaying all the cells into a window of dimensions $w \times h$ wrapping around in both directions. Figure 11.34 shows the effect of such mapping on a 150 µm square 3D cell.

As shown in Figure 11.34, there was no symmetry along $x = 0$ or $y = 0$. This feature suggests

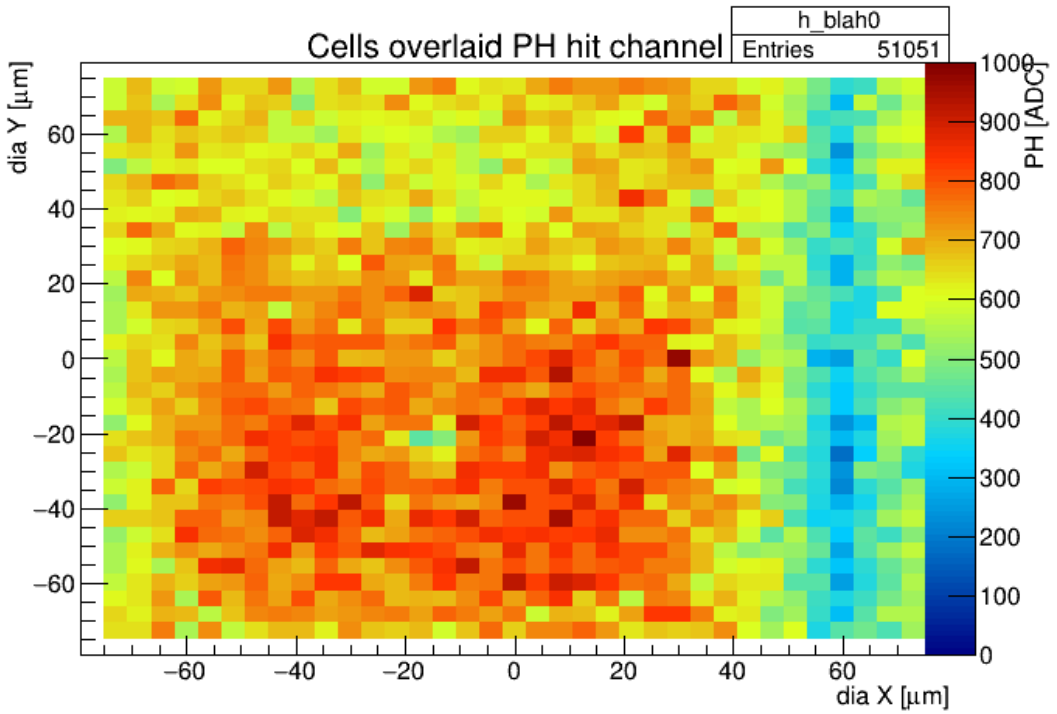

Figure 11.34: Map of all the cells overlaid together before fine alignment. The lack of symmetry along $x = 0$ and $y = 0$ indicates that fine alignment is required. The color map shows the transparent pulse height for the predicted hit channel.

that a fine alignment could be performed. By shifting the cell by half its width w and half its height h, the attention could be focused on the boundaries between the cells, which should have lower pulse height due to the charge sharing with the neighboring cells. This shift can be seen in Figure 11.35a. It was possible to find the necessary shift in each direction by projecting this pulse height profile histogram along each of the x and y coordinates and adjusting the offsets such that the minimums were located at $x = 0$ and $y = 0$. An example of the projection along the x-axis is shown in Figure 11.35c. After applying the fine alignment corrections in both coordinates, a symmetric pulse height map of the shifted cell with minimums along $x = 0$ and $y = 0$ was obtained as shown in Figures 11.35b and its projection 11.35d.

Shifting back by half a cell in the x coordinate and the y coordinate to restore the focus in the whole cell with the sense 3D wire in the center, the final effects of the fine alignment can be seen (Figure 11.36). The shifts necessary were updated in the grid, and the cell information for each event was modified accordingly.

11.10.4 Cells Selection

After the fine alignment, it was possible to make a selection of cells in the grid for further analysis. This possibility was useful if it was known that some of the cells had problems during the fabrication process, such as metallization scratches, or cells that were made on regions of the diamond with crystallographic defects, such as voids[144]. Figure 11.37 shows an example

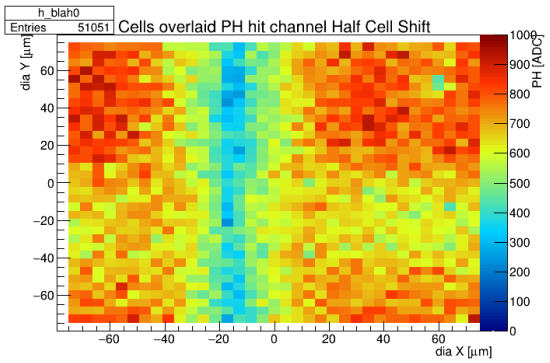

(a) Before fine alignment. Cells overlaid together after shifting half the width horizontally and half the height vertically.

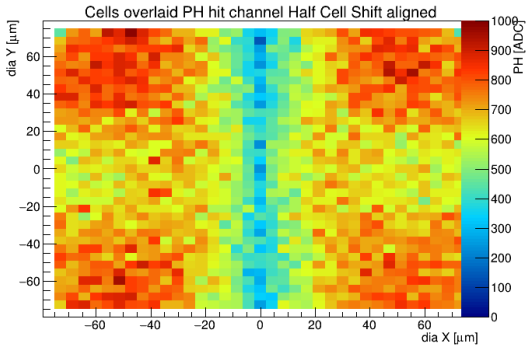

(b) After fine alignment. Cells overlaid together after shifting half the width horizontally and half the height vertically.

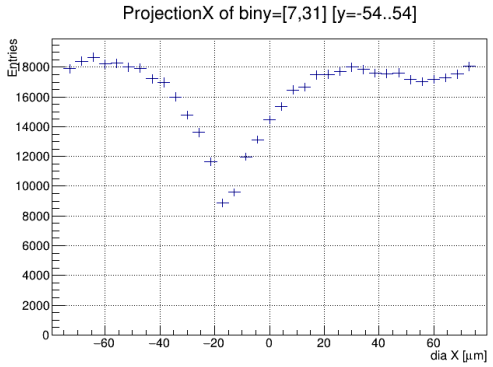

(c) Projection along x of Figure 11.35a.

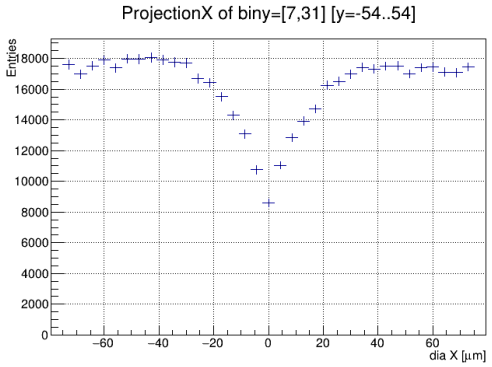

(d) Projection along x of Figure 11.35b.

Figure 11.35: Profile map of the pulse height of the shifted cells before fine alignment (a) and after fine alignment (b). The projections along the x coordinate in (c) and in (d) show where the minimum of the pulse height, which happens between two cells, is positioned before and after the fine alignment respectively.

of a selection on the hexagonal tiling of the Multi-3D device.

Within the selected cells, the pulse height of the second channel closest to the predicted hit position (i.e., Ch1 in the simulations of section 8.3) shows negative and positive charges, as shown in Figure 11.38. These charges were beyond the fluctuations from the noise and came from the non-uniform electric field of the 3D cells, as was seen in the simulations in Figure 8.8c in section 8.3.3. Nevertheless, as seen in Figure 8.12c in section 8.3.5, an excess of large negative charges was an indicator of HV 3D wires not working correctly, as it could happen when there was bad contact with the metallization or there was a problem in the fabrication of the 3D wire. Figure 11.38b shows the excess of very negative charges were localized around a HV 3D wire, as predicted from the simulations in section 8.3.5 which suggests that there could have been a problem with that HV 3D wire. These events were labeled as "Negative Events" and the cells containing them were avoided from the final cell selection region for further analysis.

Other cells that were avoided were those that showed a low charge collection for the predicted

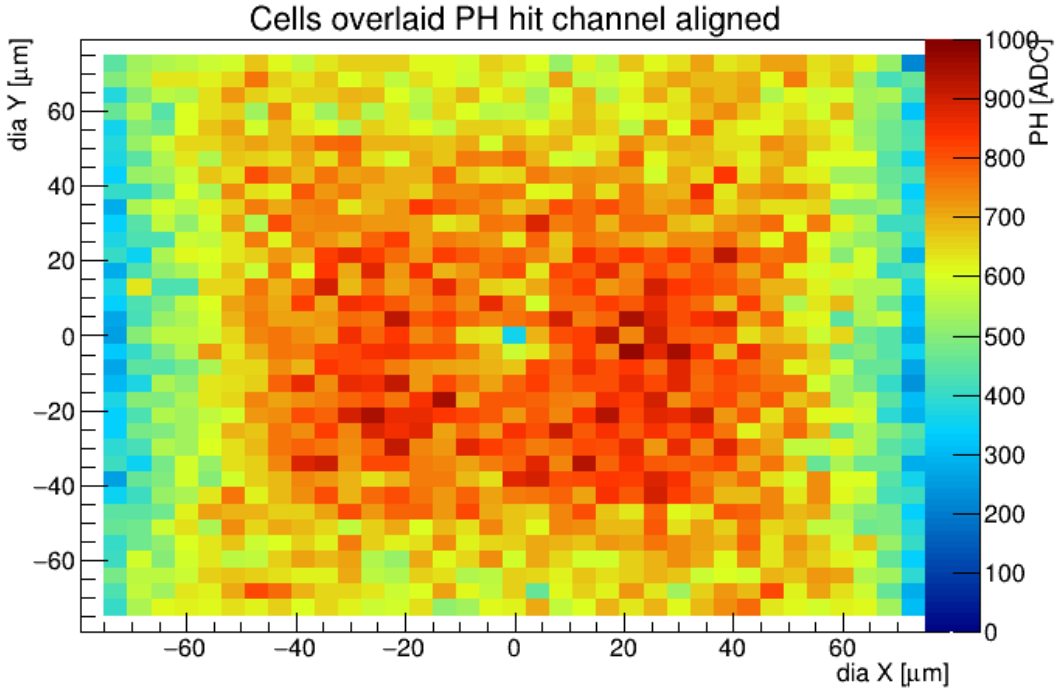

Figure 11.36: Profile map of the cells overlaid after fine alignment.

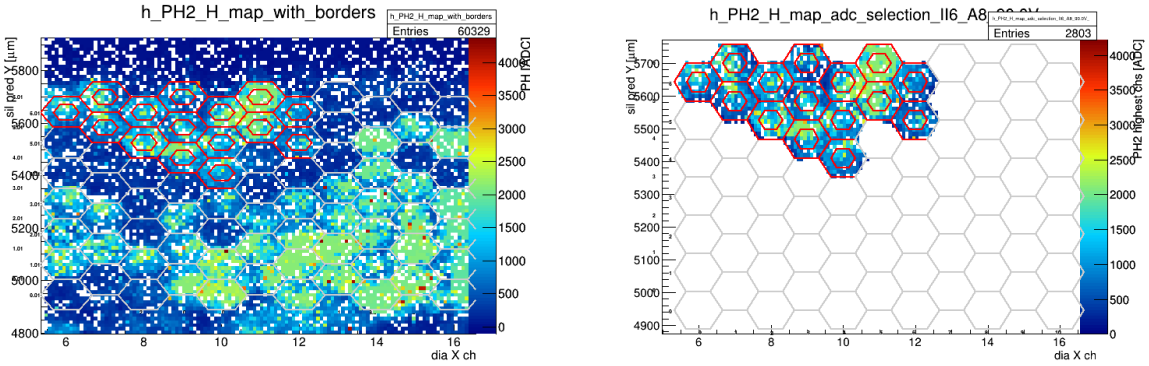

(a) Pulse height map of a region of the diamond.

(b) Pulse height map of the selected cells in the hexagonal tiling of the detector Multi-3D.

Figure 11.37: Example of a selection of cells. The plot on the left (a) shows the pulse height map for the two highest in the transparent cluster. The hexagonal tiling is overlaid in gray to show the different cells. The cells with red boundaries are the ones that are selected for further analysis as shown in the plot on the right (b).

hit cell (i.e., Ch0 in the simulations of section 8.3). As seen in section 8.3.4, cells with a defective 3D sense wire, due to the fabrication of the 3D wire or from a bad contact with the metallization, present a significantly reduced charge collection for the predicted hit channel.

To illustrate the last-mentioned effect, an example of different regions in the 100 µm section

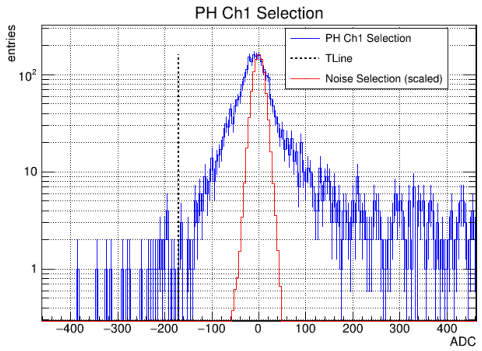

(a) Pulse height of the second channel closest to the predicted hit position (blue), with the noise fluctuations of the channels in the selected region (red). The dotted line at −170 ADC is the threshold used to discriminate excess of negative events in this example.

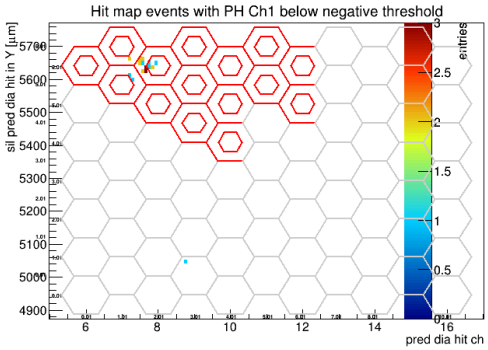

(b) Hit map of the events that have a pulse height lower than the threshold at −170 ADC in the selected region.

Figure 11.38: The pulse height of the second closest channel to the predicted hit position is compared with the noise fluctuations of the channels in the selected region (a). A threshold of −170 ADC is used to discriminate normal negative charges from the excess of high negative charges. The position of the events with an excess of negative charges with a measured PH below −170 ADC, is shown in (b). These events surround a 3D HV wire which indicates there could have been a problem with that 3D wire.

of the Irrad-3D detector are considered (depicted in Figure 11.39). The regions selected in red are regions that presumably have a problem with their 3D sense wire. On the other hand, the regions inside the black rectangle are regions that are assumed to not have issues with their 3D wires.

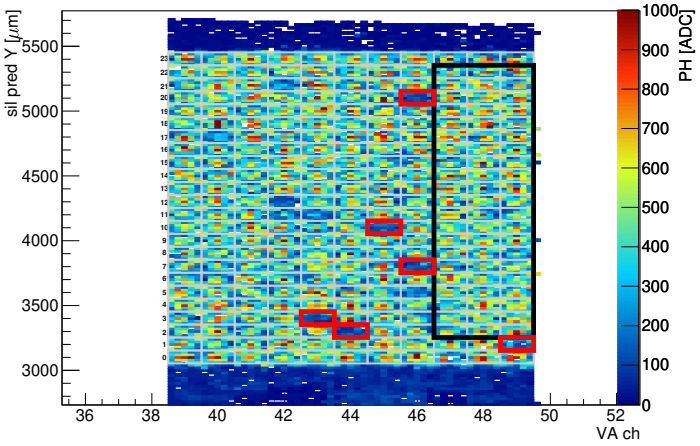

Figure 11.39: Pulse height map of the 100 µm region of the Irrad-3D detector. The single cells selected in red presumably have problems with their 3D sense wires, while the cells selected with the black rectangle are cells that presumably do not have issues with their 3D wires.

Using the simulation results of the charge collected by channels Ch0 and Ch1 in the 100 µm cells in the Irrad-3D detector as a function of the predicted hit positions in the cell, such as the ones shown in Figure 8.11, a relation between the collected charge by channels Ch0 and Ch1 as a function of the predicted hit position in the X axis was produced. These simulation predictions can be compared with the measured results, shown in Figure 11.40.

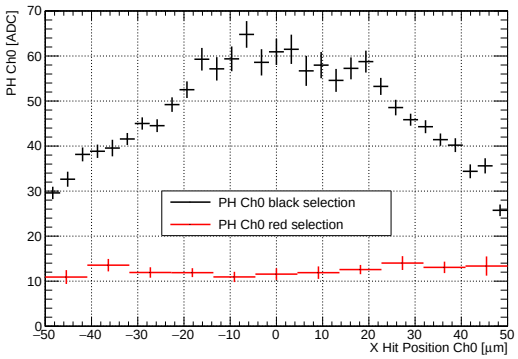

(a) Measured PH in Ch0 as a function of the predicted hit position in the X axis.

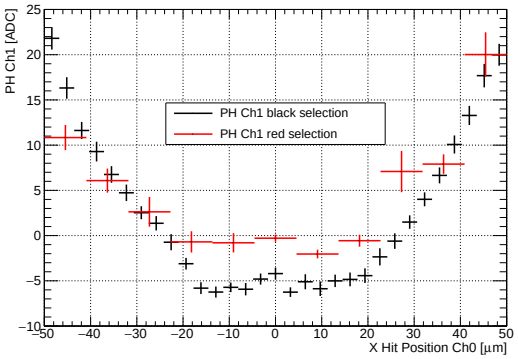

(b) Measured PH in Ch1 as a function of the predicted hit position in the X axis.

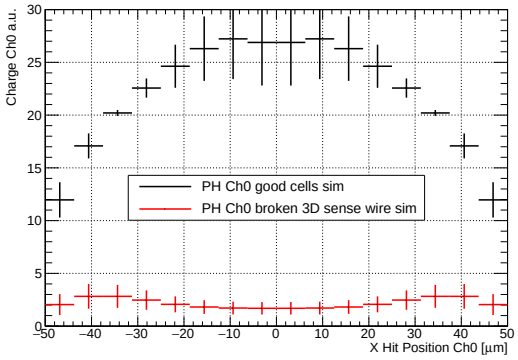

(c) Simulated charge collected by Ch0 as a function of the predicted hit position in the X axis.

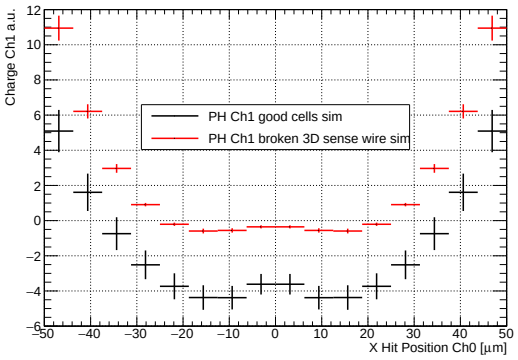

(d) Simulated charge collected by Ch1 as a function of the predicted hit position in the X axis.

Figure 11.40: Profile histograms of the charge collected by channels Ch0 and Ch1 in the transparent cluster as a function of the hit position in the X direction of the hit 3D cell. For the simulated graphs, (c) and (d), the red selection represents cells without the 3D sense wire, while the black selection represents cells without issues with their 3D wires. For the measured graphs in the Irrad-3D, (a) and (b), the red selection depicts the cells that presumably have problems with their 3D sense wires, while the black selection depicts the cells that presumably do not have issues with their 3D wires.

As seen in the simulated profiles shown in Figure 11.40, the charge collected by Ch0 in the transparent cluster for all the hit positions along the X-axis is lower for cells with an issue with their 3D sense wire compared with cells that do not have problems with their 3D wires. At the same time, the charge collected by Ch1 in the transparent cluster around the center

of the cell (x=0) is almost 0 for the cells with an issue with their 3D sense wire, while it is consistently negative for the cells without problems with their 3D wires. For the positions close to the boundaries of the cells, both types of cells have a positive charge collection in Ch1 of the transparent cluster. As seen in Figure 11.40, the measured cells in the different regions match the predictions from the simulation, which suggest that the selected cells in red have problems with their sense 3D wires and that the selected cells inside the black rectangle do not have problems with their 3D wires.

Figure 11.41 shows the histogram of the mean charge collection for all the 3D cells in the Full-3D detector, where the Gaussian distribution show the charge collection of the cells that are not expected to be defective. The dotted vertical line is located at a distance of five standard deviations from the mean of the Gaussian distribution marked in red. This delimitation was used to discriminate the possible cells with defective 3D sense wires. Cells with a pulse height lower than the delimitation value were excluded from the final selection of cells for further analysis.

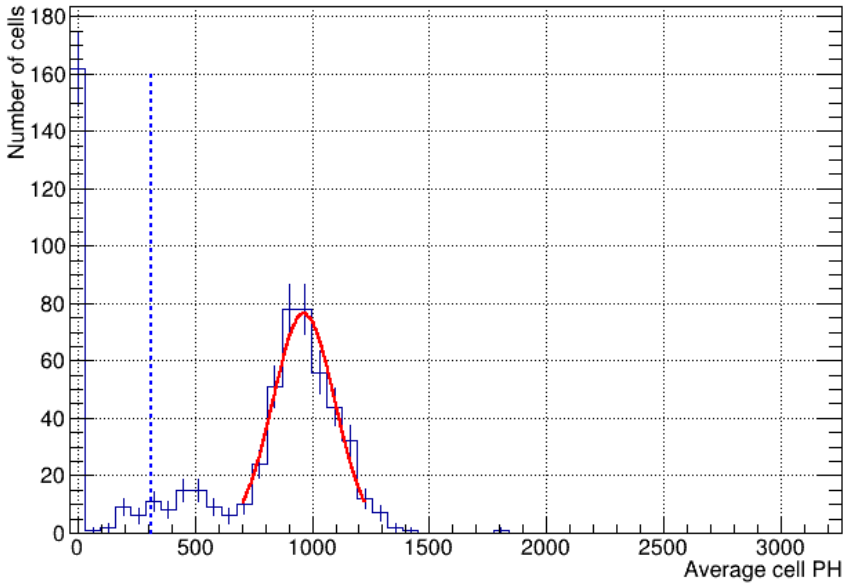

Figure 11.41: This is the histogram of the average pulse height for each cell in the Full-3D detector biased with 90V. The red Gaussian curve fits the data for the pulse height of the cells without fabrication problems. The blue dotted line is located five standard deviations away from the mean of the Gaussian distribution and delimits the cells that could have defects with their 3D sense wires.

For the final cell selection, charge collection and efficiency studies were performed. These studies were used to determine which cell geometry had better charge collection and to compare the 3D detectors with respect to standard planar strip detectors. The results will be shown in chapter 14.

Chapter 12

Analysis Of Data Taken With The ETH High Rate Beam Telescope At PSI Test Beams For Testing The Fabricated Planar Pixel Detectors

As mentioned in section 10.2, on every trigger event from the TU, an event was saved with the data from the tracking planes of the telescope, and information of the DUTs. The following explains the necessary steps required to analyze the data.

12.1 Experimental Data

The first step of the analysis was to read the raw files and convert them to an event-based ROOT Tree file. For this task, the EUDAQ Converter was used.

12.1.1 Analog Planes Decoding

As mentioned before in section 10.2, the silicon tracking planes in the telescope had analog ROC information, and therefore the position of the pixels in a hit needed to be decoded. If the planes were configured correctly, this task was done automatically by the software pXar[145].

During the test beam held in September 2019, there was a problem while setting the parameters of the analog planes, and as a result, the sampling point of the ADC within a clock cycle was not set correctly, which made the address levels split depending on the previous level.

Figure 12.1[146] shows how the data is encoded to identify the address of the pixel and its pulse height when the ROC has been setup correctly. The first two levels, Ultra Black and Black, define the spacing needed to identify the levels for the address positions C0, C1, R0, R1, and CR. The specific combination of levels of these address levels determines the position of the pixel that was triggered. When the timing to sample the data is wrong (i.e., too early), splitting of the levels occurs. Figure 12.2 shows a comparison between the encoded values when the

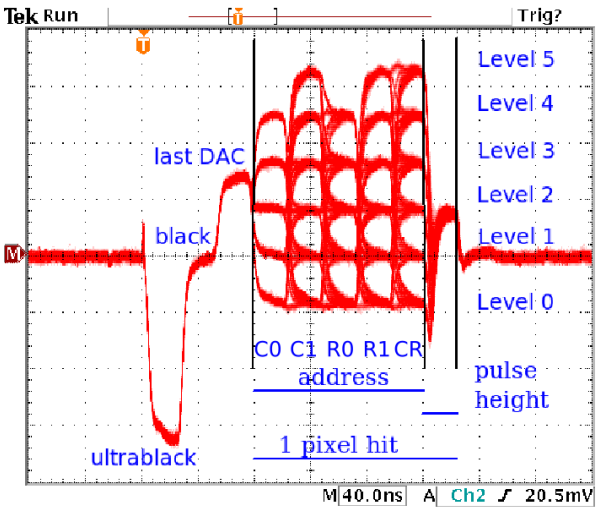

Figure 12.1: Oscilloscope image showing the different parts of the data transmitted in analog planes, including the different levels for each address position.[146]

timing was set correctly (i.e., no level splitting) versus the case where the timing was not set correctly (i.e., level splitting).

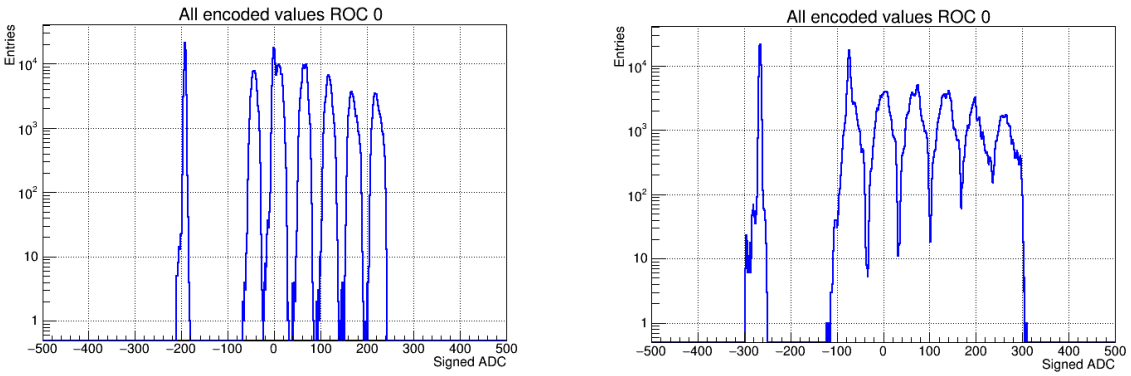

(a) Timing correctly set.

(b) Timing incorrectly set.

Figure 12.2: Encoded values for the analog ROC 0. These include Ultra Black, Black, and the address positions. When the timing was correctly set (a) there was a clear separation between the levels. On the other hand, when the timing was not correctly set, the transition between the levels overlapped due to the splitting of the levels and it was not possible to identify accurately the address of the pixel without further steps.

The splitting of the levels is depicted in Figure 12.3a. In Pulse 2, the transitions from five of the six levels to Level 2 are shown. If Pulse 2 is sampled where the blue arrow is pointing, one value is obtained for Level 2. On the other hand, if it is sampled where the red arrow is pointing (early sampling), different values are obtained for Level 2. Figure 12.3b shows an example of data taken in 2019 where the sampling was not done correctly. The histogram in blue shows the

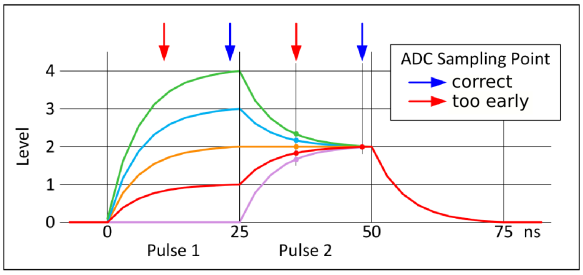

(a) Effects of different sampling points.

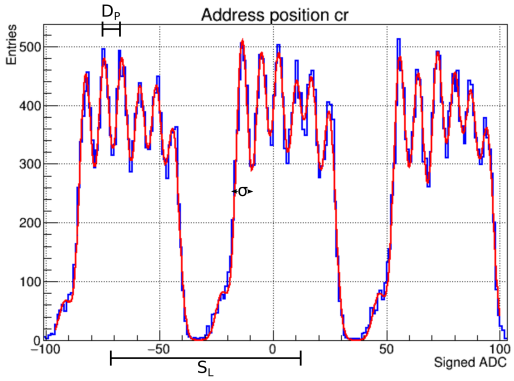

(b) ADC values for address position CR in ROC 0 with splitting due to an early sampling.

Figure 12.3: The diagram shown in (a)[145] depicts the splitting effect when the sampling point is set too early. The blue curve in (b) is the histogram of the measured ADC values for the address position CR in ROC 0 when the sampling was early. Only the values for Levels 0, 1, and 2 are shown. The red curve fits the data to the model that replicates the splitting of the levels. The parameters of this model are used to estimate the real separation between the levels and to recover the signals as if they were sampled correctly.

levels 0, 1, and 2 sampled in the address position CR. Instead of showing three distinct peaks, three clusters of six peaks are obtained due to the splitting of the levels.

To solve this issue, the converter in EUDAQ and the decoding procedure in pXar were modified to add the parameters required to recover the correct levels on an event-by-event basis. The Ultra Black, the Black, and the address position CR were chosen for this task. The CR position was designed to distinguish between left and right pixels in a row of a double-column. This feature gave it a similar number of entries for each possible level, which made easier the recovery process.

The first step to correct the levels was to estimate the values of the positions in Ultra Black and Black by using the mean of all the Ultra Black and Black values in the data. The second step was to fit the first three levels of the address position CR with 18 Gaussian distributions (one for each peak as the ones shown in Figure 12.3b). The separation between consecutive Gaussian distributions in a Level is set by the parameter D_p, and the separation between each of the three levels (clusters of peaks) is modeled by the parameter S_L (see Figure 12.3b). The first estimate for the width of each of these Gaussian distributions (σ) was the standard deviation of the values in the position Black of the encoded analog data. The amplitude of each Gaussian was left as a free parameter. The result of this fit is shown in red in Figure 12.3b.

A better estimation of the Ultra Black and Black values was calculated with the fitted parameters. From the fitted model, the corrected value for the Black position, the offset between the value in Level 1 and the value in the Black position, the spacing between the Levels 0-5, and the compensation parameter to recover the signal (as if it was sampled correctly) were passed to pXar to decode the addresses of the pixels and to correctly extract the pulse height of the signal for each event.

12.2 Clustering

With the correct decoding, the EUDAQ[139, 140] Converter created a ROOT[147] file with the data organized on an event-by-event basis. For each event, the column (*col*), row (*row*), and pulse height (q) of each pixel that had a hit from an ionizing particle for each plane were stored. Additional information from the TU as the time in ms was also saved.

When an ionizing particle generated enough charge above the threshold in more than one pixel, a cluster would form. As shown in Figure 12.4, in ~ 85 % of the time, the ionizing particles just excited a single pixel in the detectors above the threshold, and in ~ 13 % of the time, they excited two pixels. The remaining ~ 2 % corresponded to three or more pixel clusters.

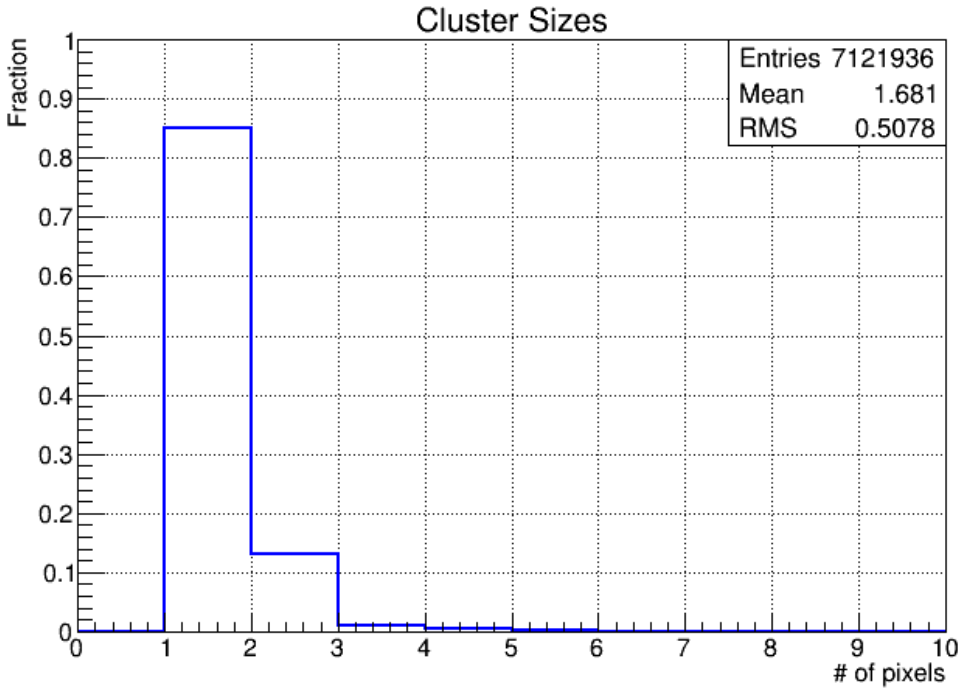

Figure 12.4: Cluster sizes for all telescope tracking silicon planes in 2019's run 8. Most of the clusters in the tracking planes are one-pixel clusters.

The positioning of the cluster was done by taking into account the amount of charge in each of the pixels in the cluster. The following is a generalized description of the positioning: If for an event i the plane p had a cluster consisting of N contiguous pixels which formed a set $\mathscr{H}$, and the pulse height of the h-th pixel in the set $\mathscr{H}$ was q_h, then the local position of the cluster

was calculated as shown in Equation 12.1.

$$col_{p_{local}}(i) = \frac{\sum_{\substack{h=1 \\ h\in\mathscr{H}}}^{N} col_h(i)\cdot q_h(i)}{\sum_{\substack{h=1 \\ h\in\mathscr{H}}}^{N} q_h(i)} \tag{12.1a}$$

$$row_{p_{local}}(i) = \frac{\sum_{\substack{h=1 \\ h\in\mathscr{H}}}^{N} row_h(i)\cdot q_h(i)}{\sum_{\substack{h=1 \\ h\in\mathscr{H}}}^{N} q_h(i)} \tag{12.1b}$$

As mentioned in section 3.1, each pixel had a width of 150 µm and a height of 100 µm. To convert the local col-row coordinates into local spatial coordinates, the following transformation was done:

$$x_{p_{local}} = 150\,\mu\text{m}\cdot\left(col_{p_{local}} - \frac{52}{2}\right) \tag{12.2a}$$

$$y_{p_{local}} = 100\,\mu\text{m}\cdot\left(row_{p_{local}} - \frac{80}{2}\right) \tag{12.2b}$$

The constants that were subtracted in Equations 12.2 made the center of the plane have the local spatial position (0,0).

The charge of the cluster would be calculated afterwards using the pulse height calibration for each pixel.

12.3 Alignment

For each arrangement of the telescope, ~ 10 % of the events of a run were used for alignment. The selected run for alignment had a low particle rate of the order of $O(100\,\text{kHz/cm}^2)$ or less, and the DUTs' voltages were set close to the maximum voltage obtained during a voltage scan to maximize their efficiency. The rest of the runs were used for analysis and relied on the alignment parameters found with the alignment run.

A global spatial reference should be set to align the planes to have good spatial accuracy for the hit position of the particles that passed through tracking planes 1 and 2 and the triggering scintillator. This reference was set to the local spatial coordinates of the first plane upstream of the DUTs (i.e., plane 3).

The representation of any point in the plane i with respect to the reference has been shown in Equation 11.11. In this case, by construction, the local coordinates x^i and y^i were perpendicular for these pixelated detectors; therefore, the two rotation angles in a plane should be equal, and

only one rotation angle had to be found: $\phi_y^i = \phi_x^i \equiv \phi^i$. The resulting rotation and translation for this telescope are shown in Equation 12.3. The initial values for the alignment parameters for each plane were assumed to be 0 (i.e. $\phi^i = x_0^i = y_0^i = 0$).

$$\begin{pmatrix} x \\ y \\ z \end{pmatrix} = \begin{pmatrix} \cos\phi^i & -\sin\phi^i & 0 \\ \sin\phi^i & \cos\phi^i & 0 \\ 0 & 0 & 1 \end{pmatrix} \begin{pmatrix} x^i \\ y^i \\ 0 \end{pmatrix} + \begin{pmatrix} x_o^i \\ y_o^i \\ z_o^i \end{pmatrix} \tag{12.3}$$

Different procedures regarding the order and the tracking planes were tested. Table 12.1 shows the procedure implemented for the analysis.

Step	Tracking planes	Planes to align
1	3*	2, 1, 0
2	3, 0	2, 1
3**	3, 2, 1, 0	Si-DUT
4	3, 2, 1, 0, (Si-DUT)**	Diamond DUTs

Notes:
* Assumes perpendicular trajectories
** If there was a Silicon DUT (Si-DUT)

Table 12.1: Implemented alignment procedure.

In each step, a similar approach to the iterative alignment procedure described in section 11.7 was implemented. The differences were in the number of iterations, the selection of data for each step, and the termination criteria. The termination criteria of each step were determined by a maximum number of iterations set to 20 or by the convergence of the residuals between each iteration. All of the alignment steps converged before the maximum number of iterations.

For each iteration and each plane under alignment, the profile histogram of the residuals in x (dX) vs. the predicted position in y, and vice versa (dY vs. x), were plotted. A linear fit of each of these plots gave information on the rotation angle ϕ for each plane using the arctan on the slope of each fitted line. As mentioned above, there was only one rotation angle per plane, so the average of both results was taken as the estimator for the rotation angle. The obtained value gave the correction $d\phi$ that should be added to the parameter ϕ to align the plane. A projection of each of these profile histograms along the residual axis gave a distribution for the residual (i.e., dX or dY), which should have a mean value of zero. The offset of these quantities from zero, namely dx and dy, were used to update the corresponding translations along the x and y axes. Figure 12.5 shows an example of the residual plots used for an iteration of one of the planes. It can be seen in Figure 12.5 that after the 2nd iteration, the corrections needed for the rotations and translations are negligible.

The events taken into account for each iteration of each step of the alignment were those with only one cluster in each of the planes to reduce the ambiguity of the trajectories of particles exacerbated by multiple scattering. All the data points that met this criterion were considered for the first step of the iteration. For the next iterations, outliers in the residual plane of dX and dY were excluded. One identified explanation for these outliers was noisy pixels that were not masked while configuring the planes before the runs. Including these outliers in the alignment would affect the convergence of the alignment.

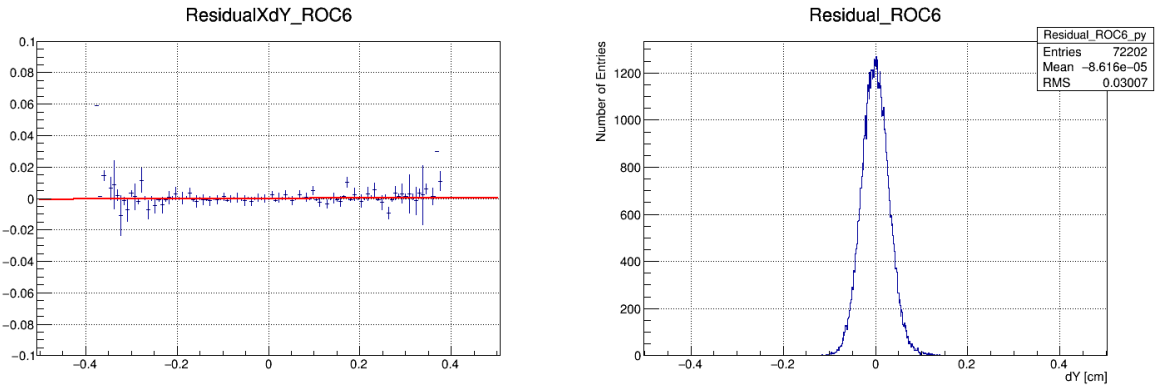

(a) Residuals dY vs. predicted hit position in x.

(b) Residuals dY.

Figure 12.5: Example of the residual plots used to estimate the translation in the y direction and the rotation angle during the 2nd iteration of the alignment of the 6th plane. The arctan of the slope of the fitted red line gave the correction for the rotation angle $d\phi$. The value of the mean in the histogram for dY, gave the correction dy for the translation of the plane in the y direction.

An ellipse around the residuals centered at 0 was chosen, and with each step of the iteration, the ellipse size would be reduced to exclude the outliers. Equation 12.4 shows the region that would be included for each iteration step, where the parameter "$n(i)$" is the number of standard deviations away from the origin for the iteration i. Events outside this region were not included in updating the alignment parameters.

$$\left(\frac{dX}{n(i)\cdot\sigma_{dX}}\right)^2+\left(\frac{dY}{n(i)\cdot\sigma_{dY}}\right)^2\leq 1 \tag{12.4}$$

It was desired that for the first iteration ($i=0$), all the data points were included and that the size of the region decreased such that $\sim 99\,\%$ of the data was taken into account at all times. This meant that if the data behaved as a two-dimensional normal distribution, a starting value of $n\sim 5$ would include almost all the data, and a final value of $n=3$ would include $\sim 99\,\%$ of the data. Different functions were tested to model the parameter n. The one that was the most stable and that allowed a quick convergence was a sigmoid-like transition described by a Logistic function. Equation 12.5 shows the general case for a Logistic function, where the parameter "A" describes the amplitude of the transition, the parameter "x_0" is the point where the curve reaches 50 % of the transition, and the parameter "σ" indicates the width of the transition as shown in Figure 12.6.

$$f(x)=\frac{A}{1+\exp\left(-\frac{x-x_0}{\sigma}\right)} \tag{12.5}$$

Equation 12.6 shows the implemented function to model the parameter n for each iteration i and the maximum number of iterations set by the parameter $MaxIt$ (in practice, it was set to 20). The values 7 and 25 in the equation were set such that the transition from the initial value of $n\sim 5$ and the final value of $n\sim 3$ happened during the first 40 % of the maximum

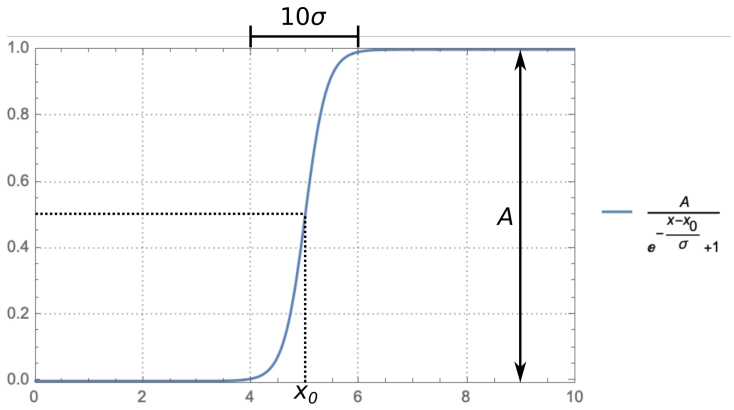

Figure 12.6: General curve of a Logistic function. The transition is centered at x_0 and it takes $\sim 10\sigma$ for more than 99 % of the transition to occur.

number of iterations, and that the value $n = 4$ happened at $\sim 14\,\%$ of the maximum number of iterations. These values were found empirically to obtain reliable results for a maximum number of iterations greater than 9. The curve in Equation 12.6 is shown in Figure 12.7. The effects on the data taken into account for the alignment can be seen in Figure 12.8.

$$n(i) = 3 + \frac{2}{1 + \exp\left(\frac{i - \frac{MaxIt}{7}}{\frac{MaxIt}{25}}\right)} \tag{12.6}$$

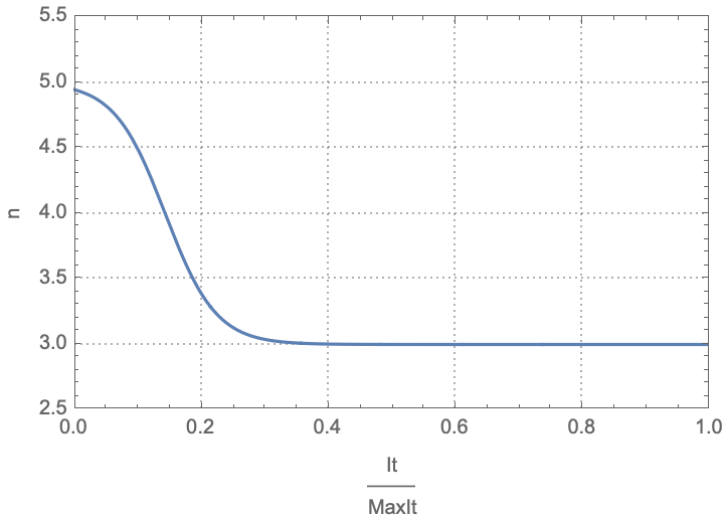

Figure 12.7: Curve that describes the parameter n as a function of the iteration.

To test the convergence of the alignment between each iteration step for termination, one of two conditions had to be met for all the planes under alignment: the quantities $dR \equiv \sqrt{dx^2 + dy^2}$ and $d\phi$ were less than the specified thresholds, or the changes in dR and $d\phi$, namely ΔdR and $\Delta d\phi$, were less than 10 % of the given thresholds. Equations 12.7 show the termination criteria for the alignment.

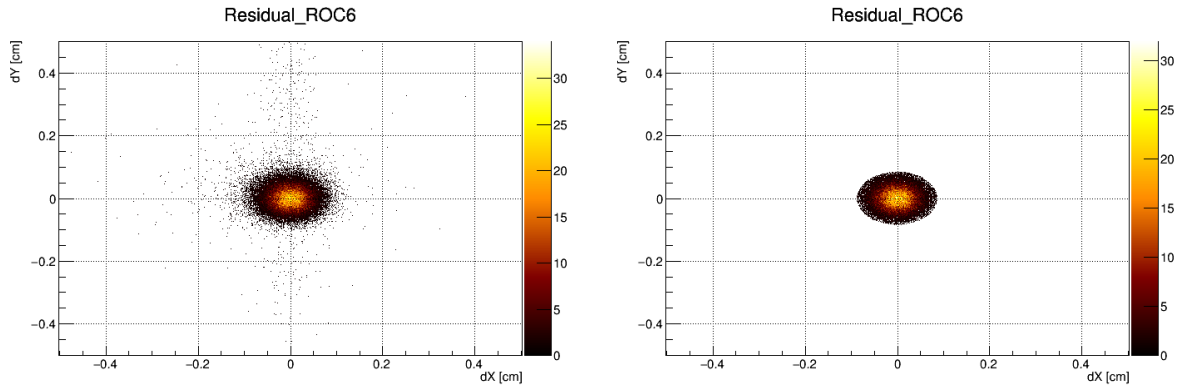

(a) Data taken into account for the second iteration

(b) Data taken into account for the last iteration

Figure 12.8: Data taken into account for alignment in the 2D space of residuals dx and dy for plane 6.

$$dR < 10^{-4}\,\text{mm} \tag{12.7a}$$
$$d\phi < 10^{-3}\,\text{rad} \tag{12.7b}$$
$$\Delta dR < 10^{-5}\,\text{mm} \tag{12.7c}$$
$$\Delta d\phi < 10^{-4}\,\text{rad} \tag{12.7d}$$

Figure 12.9 shows the convergence for alignment step 4, where the silicon DUT was in plane 6 (see Figure 10.5). The criteria for dR were reached at the 11th iteration, while the convergence for the parameter $d\phi$ was reached in the second iteration.

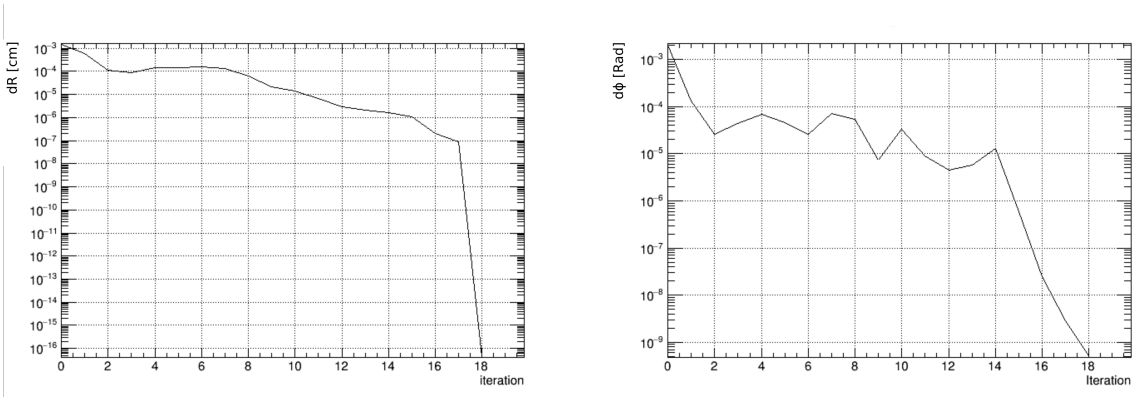

(a) Convergence of parameter dR.

(b) Convergence of parameter $d\phi$.

Figure 12.9: Convergence of the alignment for plane 6. The parameters dR and $d\phi$ converged at the 11th and 2nd iterations, respectively.

12.4 Tracking

With the alignment parameters x_0^i, y_0^i, and ϕ^i for each plane in the telescope, it was possible to generate tracks for the rest of the runs. For each run, the events considered for analysis were the ones with one cluster for each tracking plane, as more clusters would create ambiguity in creating the trajectories of the incident particles. The trajectories were assumed to be straight lines, and the effects of this assumption would be observed in the χ^2 of the linear fits.

With a cluster in each silicon plane, a linear fit was performed in the x-z plane and another one in the y-z plane. The χ^2 of the linear fit was used as the goodness of fit for the fitted trajectory of the incident particle. The uncertainties used for the position in each plane were extracted from the residuals in each plane from previous runs. For the first plane upstream (i.e., plane 3), the digital resolution of $pix_{size}/\sqrt{12}$ was used for the uncertainties as it was set as the reference. These fits were used to predict the hit position of the particles in the DUTs.

If the DUT had a cluster, the residuals in the X and Y directions between the predicted hit position and the DUTs cluster position were calculated.

12.5 Data Selection

The following subsections describe the selections made on the data for the analysis. The data selection was performed after the alignment and tracking were performed. The following is a list of the different selection criteria applied to the data for the final analysis:

- Reconstructed trajectory (referred to as *track*)
- Beam interruptions (referred to as *beam*)
- Trigger phase (referred to as *phase*)
- Angle distribution (referred to as *angle*)
- χ^2 of the linear fits (referred to as *chi2*)
- Pixel mask (referred to as *mask*)
- Fiducial region (referred to as *fiducial*)
- Hit distance (referred to as *rhit*)

The first criterion, reconstructed track, is the starting point, where a track is reconstructed using all the tracking planes of the telescope.

12.5.1 Beam Interruptions

As rate studies were performed during the test beams at PSI, it was important to have a constant rate for each run. Periodically the beam was diverted to other experimental areas, which made the rate at the πM1 area drop for a couple of seconds before rising again to the nominal point that had been set. Besides the planned beam diversions, the rate of the beam also dropped if there were problems with the stability of the beam.

The time stamps for the event generated by the TU were used to identify the beam interruptions. The resolution of these timestamps was 100 ms. For this task, the derivative of the timestamps of the events with respect to the events was estimated. With a stable beam, this derivative was expected to be zero in most cases, with values in the order of $O(\sim 100\,\text{ms/event})$ between each step in the resolution of the timestamps. Values larger than 1500 ms were expected to correspond to beam interruptions. Events that came within 5 s before and 20 s after the beam interruption were discarded from the analysis. An example of the derivative of the timestamps and the threshold to determine the beam interruptions is shown in Figure 12.10.

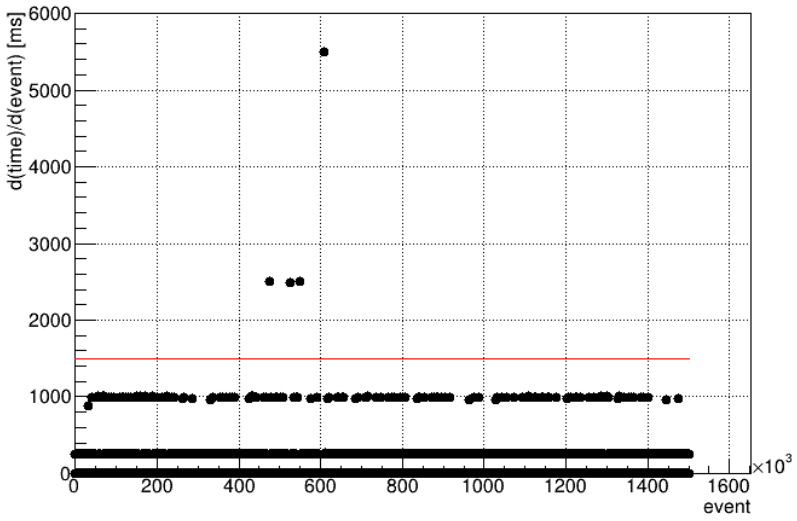

Figure 12.10: Discrete derivative between the events' timestamps with respect to the event number. This result gives an idea of the time taken by the TU between each event. The red line marks the threshold used to identify beam interruptions.

12.5.2 Trigger Phase

As mentioned in section 10.2.1, the clock signal sent by the TU to the DTBs was a 40 MHz signal. The DTB generated a 400 MHz signal with the received clock signal to determine the "time" when the trigger arrived within the 40 MHz clock cycle. This is called the trigger phase and is given a number between 0 and 9. A trigger phase of 0 means the trigger arrived at the beginning of the 40 MHz clock cycle, while a trigger phase of 9 implies the trigger came at the end of the 40 MHz clock cycle.

It was expected that events coming from particles not responsible for the trigger signal would have a different trigger phase that deviated from the ones optimized during the setup. For this reason, only events that fell within the three trigger phases for each DTB with the largest number of events, which correspond to 65 %-75 % of the data, were chosen for the analysis. Figure 12.11 shows the amount of data for each trigger phase for a run made in 2018. The selected trigger phases are shaded in blue and correspond to 73 % of all the data for that run. The reason for choosing three trigger phases instead of five was to minimize the fraction of events that did not correspond to the particle that triggered the event, which compromised the number of events used in the analysis.

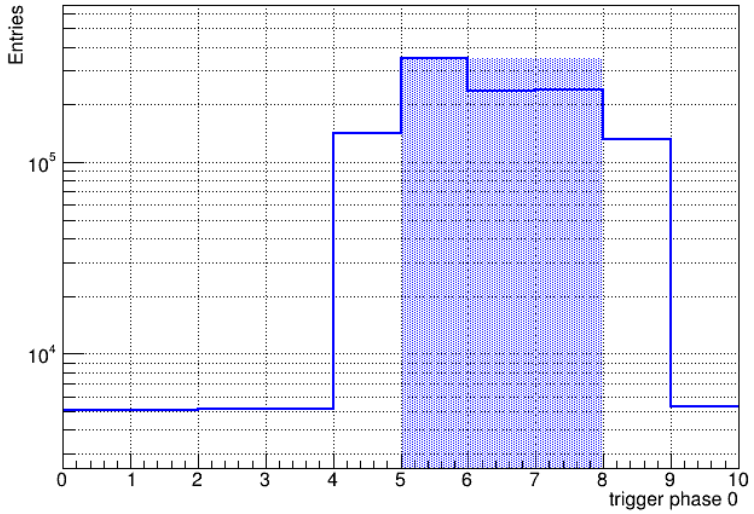

Figure 12.11: Number of entries recorded for each trigger phase in the first DTB. The shaded region in blue represents the three highest contiguous trigger phases which amounted to 73 % of the events.

12.5.3 Angle Distribution

An example of the angular distributions of the inclinations of the tracks in the x-z plane (i.e., angle in x) and the y-z plane (i.e., angle in y) can be seen in Figure 12.12. The distributions are Gaussian-like according to the beam divergence at the point where the setup was placed. Around the tails of the angular distribution, it was expected to have particles with momentum slightly different from the one set by the collimators and the dipole magnets. These particles would deposit a different charge than the expected for particles with a momentum of 260 MeV/c. Additionally, particles that did not traverse the sensor perpendicularly would deposit more charge

as they would travel a larger distance through the sensor.

$$E_Q < \frac{1}{\cos\theta} - 1 \tag{12.8a}$$

$$\theta < \arccos\left(\frac{1}{1+E_Q}\right) \tag{12.8b}$$

Equation 12.8 shows the relative error on the deposited charge E_Q for a given particle with an incident angle $\theta \neq 0$. A selection of the tracks with incident angles smaller than 1.5°, which accounted for ~ 95 % of the data, was set such that all the selected tracks deposited the same charge with an error E_Q smaller than 0.1 %. The criterion was applied for angles in the Y and X directions. Figure 12.12 shows the angular distribution in the Y direction for the tracks of a run taken in 2018.

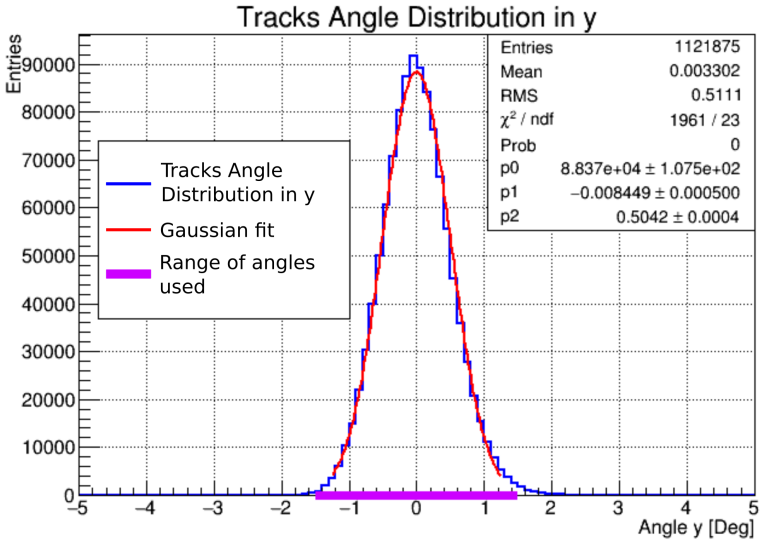

Figure 12.12: Angular distribution in the Y direction for the trajectories fitted using the four tracking planes. The violet line in the axis depicts the range of the angles used for the analysis. The fit parameters $p1$ and $p2$ are the center and the standard deviation of the fitted Gaussian distribution, respectively. These fit parameters are typical for the data taken in the 2018 and 2019 test beams.

12.5.4 χ^2 Of The Linear Fits

In the ideal case, a χ^2 distribution with two degrees of freedom was expected for fitting a straight trajectory with four data points as was the case for the setup. Multiple scattering could cause the distribution to deviate from the ideal case. Selecting the 40 % of the tracks with the lowest χ^2 in the "X" and "Y" direction was a good compromise between selecting the tracks with a small amount of scattering within the planes and having enough data for the efficiency and charge

studies performed. Figure 12.13 shows the threshold set in the χ^2 distribution for the tracks fitted in the X direction for a run in 2018.

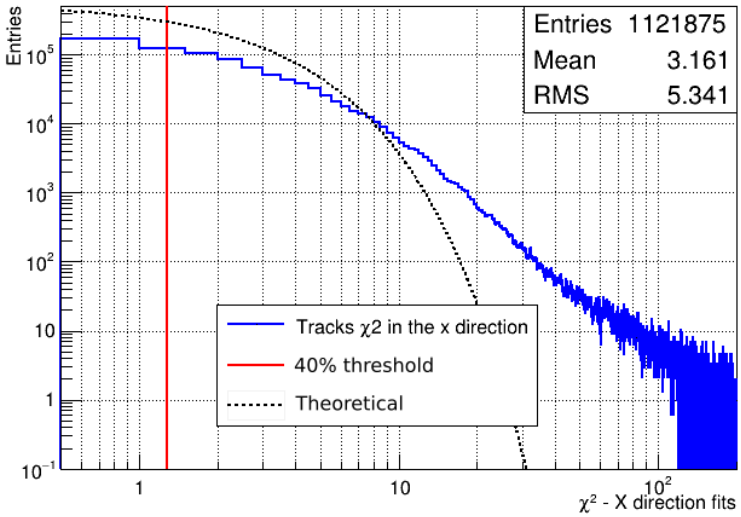

Figure 12.13: χ^2 distribution obtained for the linear fit for the X direction for a typical run in 2018. The red line depicts the threshold used to select the 40 % of the tracks with the lowest χ^2, and the dotted black line depicts the theoretical χ^2 distribution for two degrees of freedom.

12.5.5 Pixel Mask

Two types of pixel defects were found in the tested detectors. The first type was caused by the manipulation of the sensor during fabrication. The other type was related to the ROC and was independent of the sensor. The problems caused during the fabrication process, such as scratches on one of the fabrication layers mentioned in chapter 6, made the pixels unresponsive to charges injected into the sensor's damaged pixel by the ROC. These problems could be identified by visual inspection using a microscope. In the case of the issues related to the ROC, the pixels were noisy or failed the pulse height calibration. Including these known problems would affect the charge and efficiency studies. Therefore these pixels were masked from the charge and efficiency studies.

To identify the pixels that failed the pulse height calibration, the χ^2 and the degrees of freedom obtained for the fitted curves between the injected charge in Vcal units and the measured pulse height in ADC units for each pixel were used. Pixels with a large χ^2 with respect to the degrees of freedom and pixels with a small number of degrees of freedom did not have a reliable pulse height calibration and therefore were masked. The two cases are shown in Figure 12.14. Besides the pixels that failed the pulse height calibration, pixels that were calibrated successfully but that were only responsive to injected charges (i.e., they responded only to charges with high Vcal units, above ~ 1000 e from the set threshold) were also masked.

The unresponsive pixels were identified before the data taking and were saved in a mask file. As for the noisy pixels, the occupancy of the run was used. A pixel was identified as noisy and

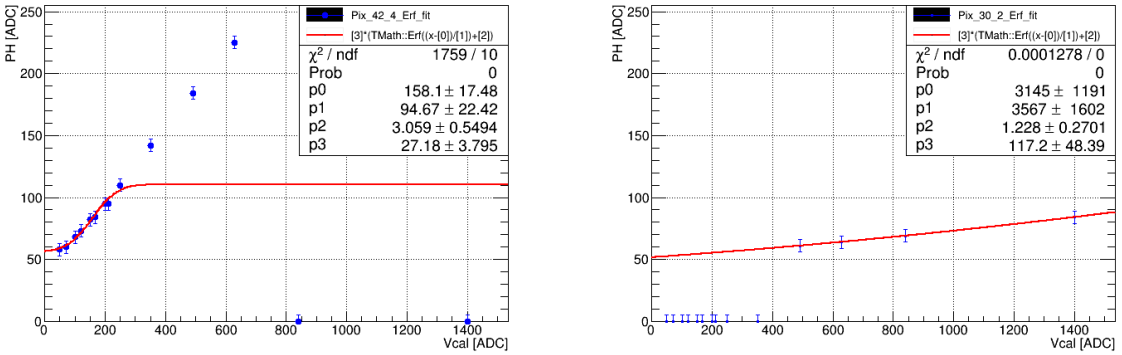

(a) Example of a pixel with a high χ^2.

(b) Example of a pixel with low degrees of freedom.

Figure 12.14: Example of the two cases where the pulse height calibration failed. In (a) the large χ^2 was caused by the two data points for injected charges above 800 Vcal, where the read pulse heights were 0 ADC. In (b) most of the read values were 0 ADC, such that there were only four data points to fit the curve which gives a total degree of freedom of 0.

masked if it had an occupancy larger than eight standard deviations above the average of its 24 closest neighboring pixels. Figure 12.15 shows an example of the identified unresponsive and noisy pixels.

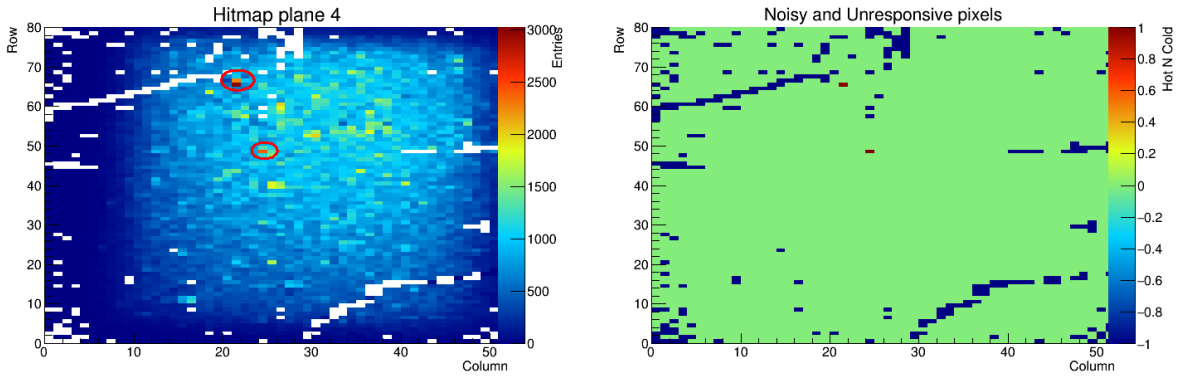

(a) Occupancy of plane 4 during a test beam run.

(b) Identification of masked pixels.

Figure 12.15: Example for the identification of noisy and unresponsive pixels. In (a) the occupancy of plane 4 shows white values for pixels with 0 occupancy which are marked as cold in (b). As for the two pixels circled in red in (a), their occupancy is higher than their neighboring pixels and therefore are marked as hot in (b). Pixels that are not marked as hot or cold in (b) are colored in green, while hot pixels are colored in red and cold pixels are colored in blue.

Problematic pixels would affect the charge and efficiency studies by misrepresenting the rest of the pixels in the detector. For example, if a particle passes through an unresponsive pixel, then the efficiency and the collected charge would drop. Therefore, the predicted hit

positions of the tracks in the DUT were used to select only the trajectories that did not pass through identified defective pixels. Using the predicted hit position and the column and row positions for single pixel clusters in the DUT, a linear relation was found between the predicted hit position and the local pixel position in terms of columns and rows. Figure 12.16 shows the linear relationship between the predicted hit position in the X coordinate and the pixel column in the DUT located in plane 6, and the linear relationship between the predicted hit position in the Y coordinate and the pixel row in the DUT located in plane 4. In theory, if the planes were completely perpendicular to the beam, the proportionality term of the linear fit should be $p1 = 66.67\,\text{col/cm}$ for the columns vs. the X-positions, and $p1 = 100\,\text{row/cm}$ for the rows vs. Y-positions.

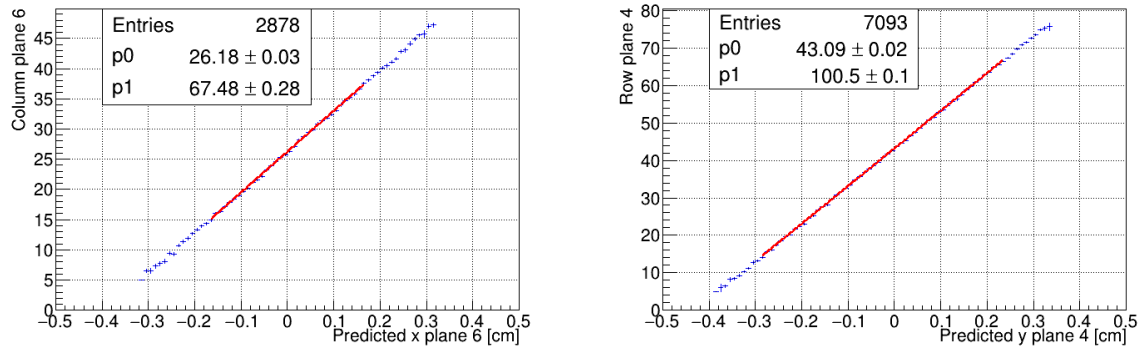

(a) Column vs. X.

(b) Row vs. Y.

Figure 12.16: Profile histogram between the hit column and the predicted X position by the telescope for the DUT in plane 6 (a), and the hit row and the predicted Y position by the telescope for the DUT in plane 4 (b). The linear fit was done in most cases ten pixels away from the borders to ensure the diamond's electric field was uniform and there was less ambiguity with the hit position. The fitted values are shown as $p0$ for the offset term and $p1$ for the proportional term. Ideally, a perfectly perpendicular setup with respect to the beam would give $p1 = 66.67\,\text{col/cm}$ for the column vs. X case, and $p1 = 100\,\text{row/cm}$ for the row vs. Y case.

In practice, the plane would not be perfectly perpendicular to the beam and would have a small inclination θ. The two extreme cases were considered, such that all cases were between these two extremes: The first one was when the telescope's planes were perpendicular to the beam, but the DUT plane was not and had small inclinations $\theta_{\{x,y\}}$ (see Figure 12.17a). The other case was when the telescope's planes had a small inclination $\theta_{\{x,y\}}$ with respect to the beam, and the DUT did not (see Figure 12.17b). In the first case, the proportionality term would be larger than the ideal case by the amounts shown in Equation 12.9 for small angles θ_x and θ_y. In the second case, the proportionality term would be smaller than the ideal case by the amounts shown in Equation 12.10.

The small angle inclinations were estimated to be less than 10° which bounded the proportionality constants to be: $65.65\,\text{col/cm} \leq p1_{col,x} \leq 67.69\,\text{col/cm}$, and $98.48\,\text{row/cm} \leq p1_{row,y} \leq$

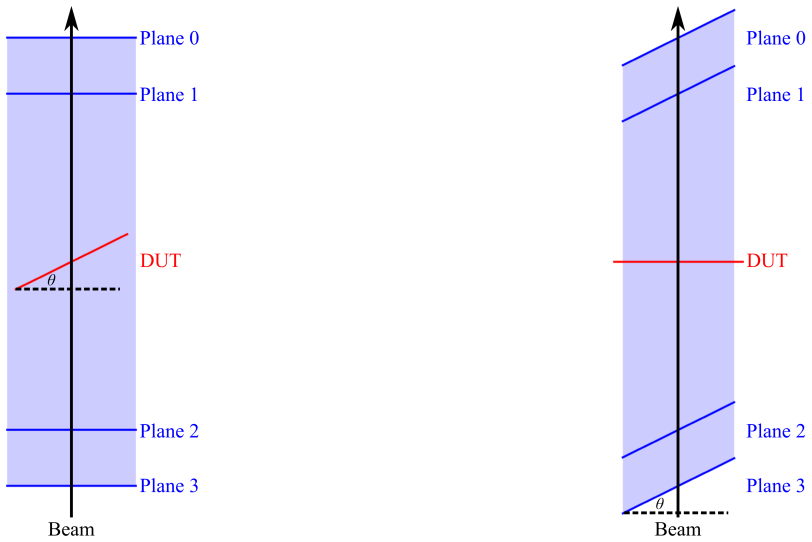

(a) Case 1. (b) Case 2.

Figure 12.17: The extreme cases considered for the resolution in the DUT by the telescope given by the proportionality parameter $p1$. In (a), the tilting by an angle θ of the DUT makes the parameter $p1$ larger. In (b), the tilting of the telescope planes by an angle θ makes the parameter $p1$ smaller.

101.5 row/cm.

$$p1_{col,x} \cong \frac{1\,\text{col}}{150\,\mu\text{m} \cdot \cos(\theta_x)} \tag{12.9a}$$

$$p1_{row,y} \cong \frac{1\,\text{row}}{100\,\mu\text{m} \cdot \cos(\theta_y)} \tag{12.9b}$$

$$p1_{col,x} \cong \frac{1\,\text{col} \cdot \cos(\theta_x)}{150\,\mu\text{m}} \tag{12.10a}$$

$$p1_{row,y} \cong \frac{1\,\text{row} \cdot \cos(\theta_y)}{100\,\mu\text{m}} \tag{12.10b}$$

As mentioned in section 10.2, multiple scattering would deviate the trajectories of the incident particles from their predicted hit position. Consequently, the spread of these deviations was measured in each DUT. Figure 12.18 shows the spread in the X direction for a predicted hit column in DUT plane 6.

The bell-like distribution for the spread in each of the variables was taken into account to mask an elliptical region of 3 standard deviations in the X and the Y directions, to mask up to

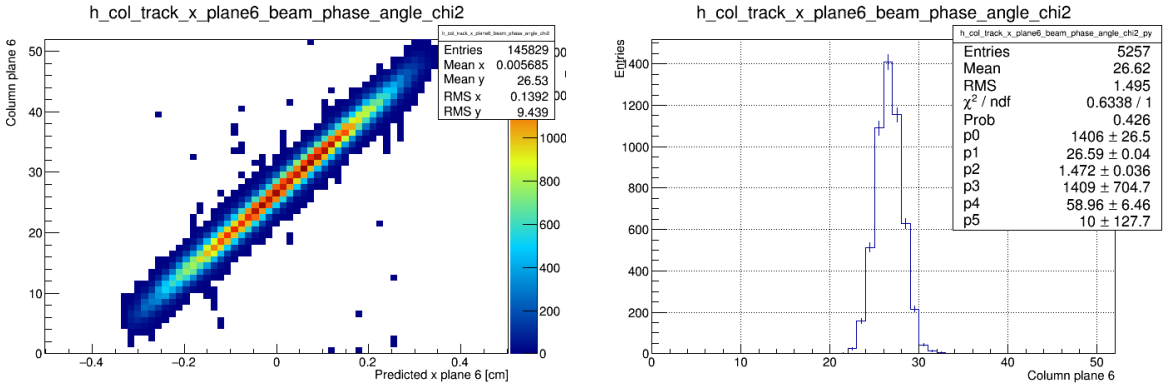

(a) Hit column vs. predicted x position.

(b) Projection of (a) along x=0.

Figure 12.18: Distribution of hit columns for a given predicted hit position in x. The σ of the bell-like distribution in (b) was found to be 1.5 columns (parameter p2 in the statistics box).

99 % of the tracks that would pass through the masked pixels. Figure 12.19 shows the occupancy before and after masking the regions around the masked pixels, shown in Figure 12.15. In the following sections, this cut will be referred to as *"mask"*.

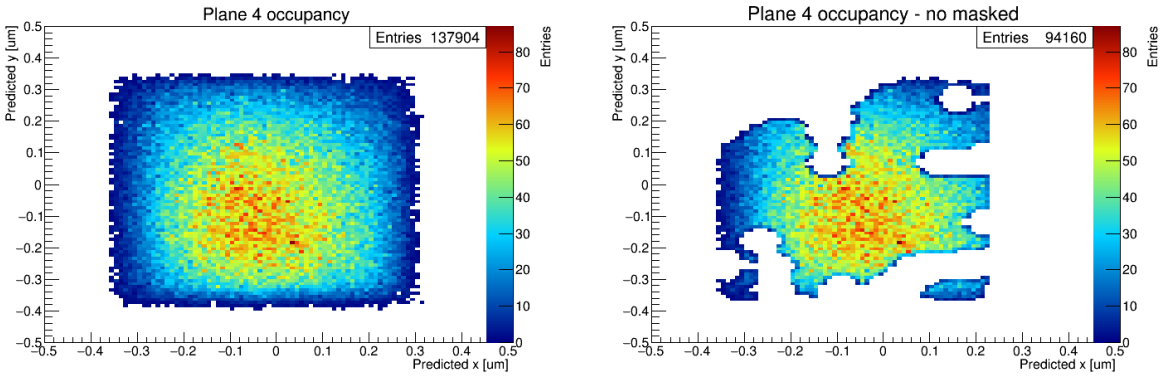

(a) Trajectories incidence before masking.

(b) Trajectories incidence after masking.

Figure 12.19: Incidence of the tracks before and after masking the regions around the unresponsive and noisy pixels shown in Figure 12.15.

12.5.6 Fiducial Region

Another measure that was taken into account to avoid the inclusion of particles that hit outside the detector or regions that were known to have problems, such as the ones damaged during the fabrication process, was to establish a fiducial region. These regions were set to be at least three pixels away from the borders in most cases. In the case of the sample CMS04, the regions that were affected by mistakes during the fabrication process were identified, and a fiducial region three pixels away from the affected areas was chosen (see Figure 12.20).

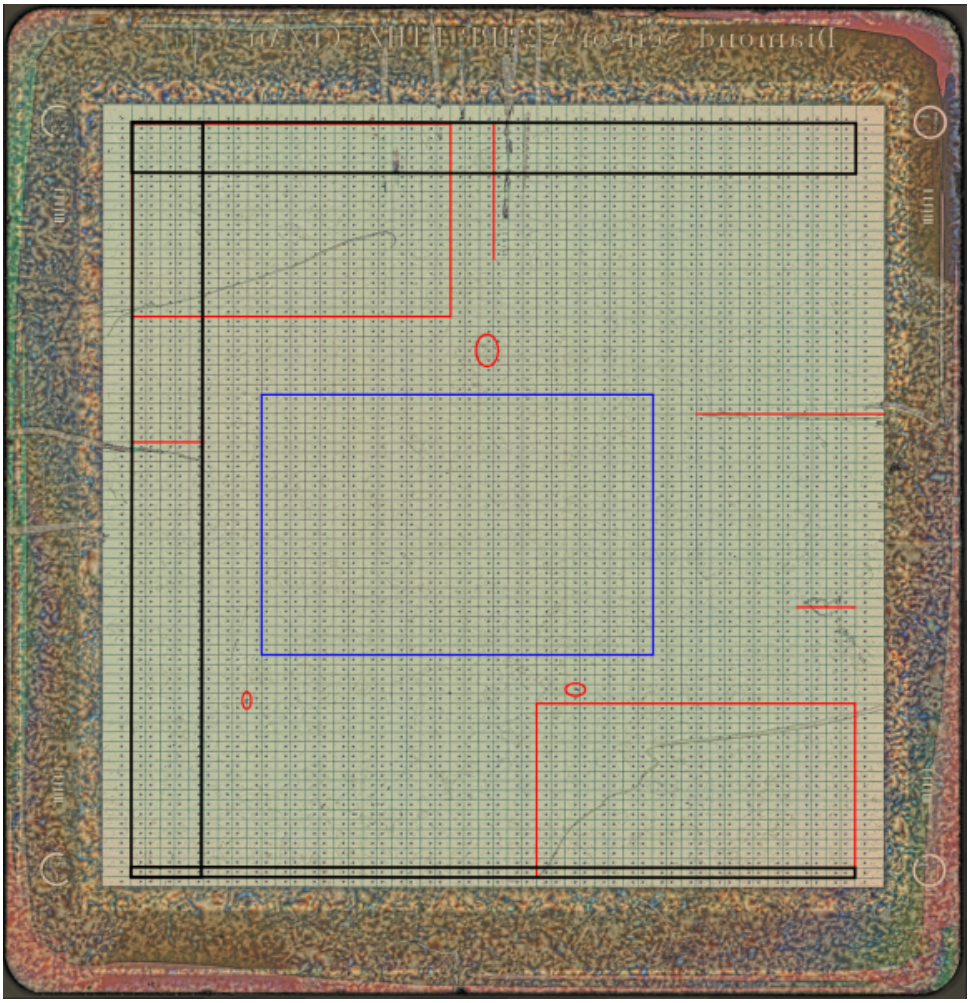

Figure 12.20: Regions showing the fabrication defects that were identified visually before the bump-bonding of sample CMS04. The regions in red enclose the affected regions. The blue rectangle, which is at least three pixels away from the affected areas, was chosen as the planned fiducial region for the studies made on this sample.

12.5.7 Hit Distance

Only events whose predicted hit position was close to the cluster position in the DUT were taken into account to get accurate maps for the charge collected by the detector. In other words, their event residuals in the DUT (X_{res}, Y_{res}) had to be within 2.5 standard deviations of the distributions of the residuals in X and Y for all the events. This measure included 95 % of the events whose predicted hit positions were closest to the actual cluster position in the DUT. Equation 12.11 shows the selection criteria described above, where $X_{res}(i)$ and $Y_{res}(i)$ are the residuals for an event i, and $\sigma_{x_{res}}$ and $\sigma_{y_{res}}$ are the standard deviations of the residuals in X and Y, respectively in the DUT. This cut will be referred to as *"rhit"*.

$$\left(\frac{dx(i)}{2.5\cdot\sigma_{dX}}\right)^2+\left(\frac{dy(i)}{2.5\cdot\sigma_{dY}}\right)^2\leq 1 \tag{12.11}$$

12.6 Pulse Height In ADC Units Vs. Charge In Vcal Units

For each event, the measured pulse height in ADC units was transformed into collected charges in Vcal units using the pulse height calibration done before the data taking during the configuration of the planes. In general, the relationship between the pulse height in ADC units and the collected charge in Vcal units has the shape of a sigmoid curve. Three different curves were tested to fit the calibration data: The error function (*erf*), the hyperbolic tangent function (*tanh*), and the CDF of a Weibull distribution (*weibull*). The parametrized functions used to fit the calibration data are shown in Equations 12.12.

$$\text{erf}: p3 \cdot \left(\text{erf}\left(\frac{x-p0}{p1}+p2\right)\right) \tag{12.12a}$$

$$\tanh: p3 \cdot \left(\tanh\left(\frac{x-p0}{p1}+p2\right)\right) \tag{12.12b}$$

$$\text{weibull}: p3 \cdot \left(p2-\exp\left(-\left(\frac{x}{p0}\right)^{p1}\right)\right) \tag{12.12c}$$

Michael Reichmann made a test by injecting charges through the Vcal DAC, ranging from 40 Vcal to 200 Vcal and reading the pulse height corresponding to the injected charges. The read pulse heights were then converted to charge calibers in terms of Vcal units using the pulse height calibration. This procedure resulted in a distribution of the measured charges in Vcal units. He found that the standard deviation of the curve for the converted charges was 7 Vcal when charges corresponding to 40 Vcal were injected and 5.6 Vcal when charges corresponding to 200 Vcal were injected[148]. Based on these findings, a fixed uncertainty of 6 Vcal for the injected calibration charges was assumed. Tests were made with different uncertainties ranging from 5 Vcal to 8 Vcal without changing the conclusions obtained with the assumption of an uncertainty of 6 Vcal.

As for the readout values of the pulse height in ADC units, only the average of the measured pulse height in ADC units for a specific injected calibration charge was retrieved from the calibration, making it impossible to find the uncertainty of the readout values. Consequently, the uncertainty values for the readout pulse heights in ADC units were increased until the obtained χ^2 values from fitting the pulse height calibration data with the functions mentioned above (i.e., erf, tanh, and weibull) were of the same order of magnitude as the degrees of freedom for all the pulse height calibrations. This value was found to be 3 ADC.

During a test beam in 2019, a pulse height calibration using 255 different calibration charges was made on the device CMS04. The data were fitted with the functions shown in Equation 12.12 to determine which function better described the calibration data. The χ^2 of the fitted curves for all the pixels in the ROC was used as the goodness of fit. For the fits, the pulse heights which reached saturation (i.e., 255 ADC) were given an upper uncertainty of 100 ADC to account for the fact that the value was saturated. Values below the trimmed value, which gave a pulse height of 0 ADC, were excluded from the fit. An example of the obtained fits and the distribution of the χ^2 for all the pixels can be seen in Figure 12.21. The results of the mean of the χ^2 are summarized in Table 12.2. As a result, the Weibull CDF function was used to interpolate the measured pulse height in ADC units into charges in Vcal units for the results shown in this work.

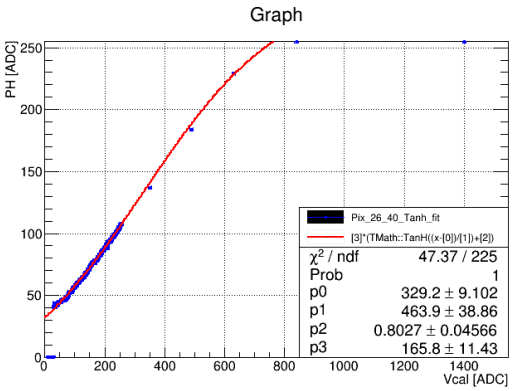

(a) Pixel data fitted with tanh.

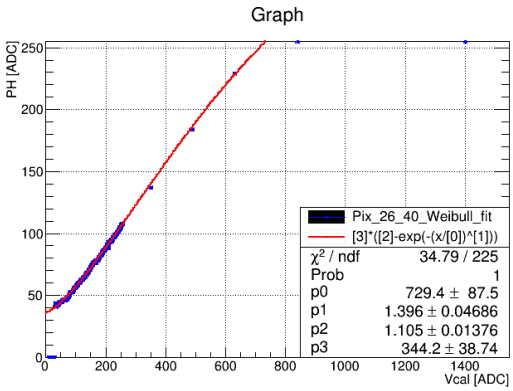

(b) Pixel data fitted with weibull.

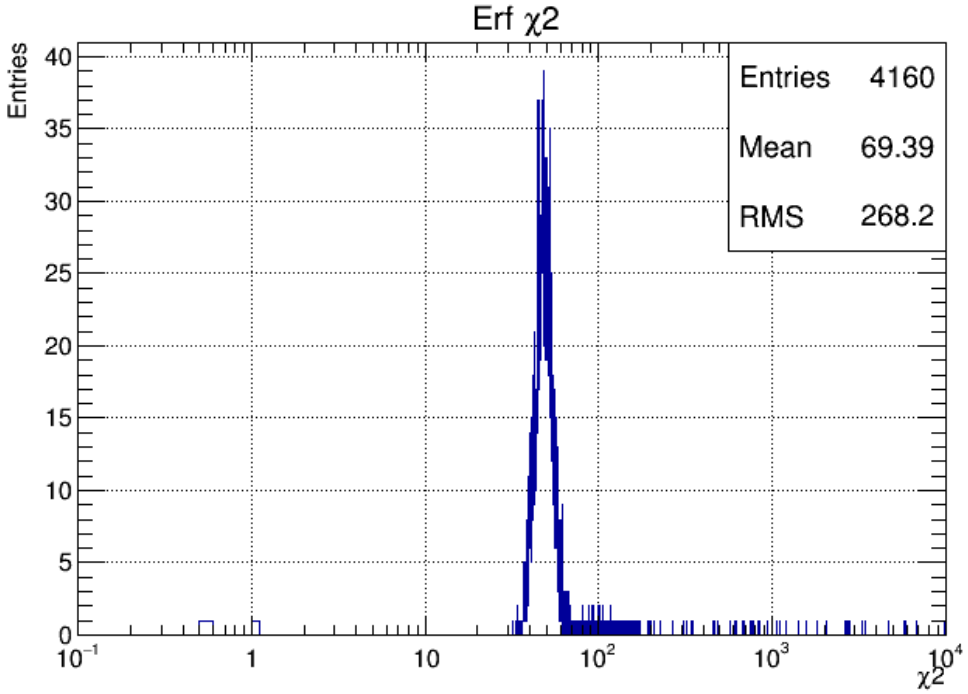

(c) Distribution of all χ^2 for erf fits.

Figure 12.21: Different fits with different functions for the data with 255 calibration values. (a) shows the data fitted with the function *tanh*, (b) shows the case for function *weibull* and (c) shows the χ^2 for all the pixels fitted with *erf*.

	erf	tanh	weibull
$\langle\chi^2\rangle$	69.4	71.4	66.0

Table 12.2: Mean value for the χ^2 distributions obtained after fitting the 4160 pixels with the functions *erf*, *tanh* and *weibull*).

12.6.1 Charge Calibration

Usually, the Vcal to electrons calibration of the ROCs is achieved by measuring the charge collected by the sensor in terms of Vcal units under different X-ray wavelengths coming from different X-ray targets. At the pixel laboratory, when the DUTs were fabricated, there were targets ranging from Zn with 8.64 keV up to Sn with 25.27 keV used for the commissioning of the pixel silicon detectors for the CMS experiment. Using these energies, it was not possible to measure the X-rays with the diamond prototypes.

The reason it was possible to calibrate silicon detectors but not diamond detectors is a combination of two factors: The low number of eh-pairs produced and collected with pCVD diamond sensors, and the low mass energy absorption coefficient of carbon[149] compared with silicon which is, in average, 17 times smaller[150] than silicon for the X-ray energies that were available in the pixel lab. Even if there had been some charge collection with some X-ray targets, the conversion between the absorbed energy and the incident energy is not trivial with pCVD diamonds as their CCE is below 100 %, and it is different for each sensor, as mentioned in section 8.1.1.

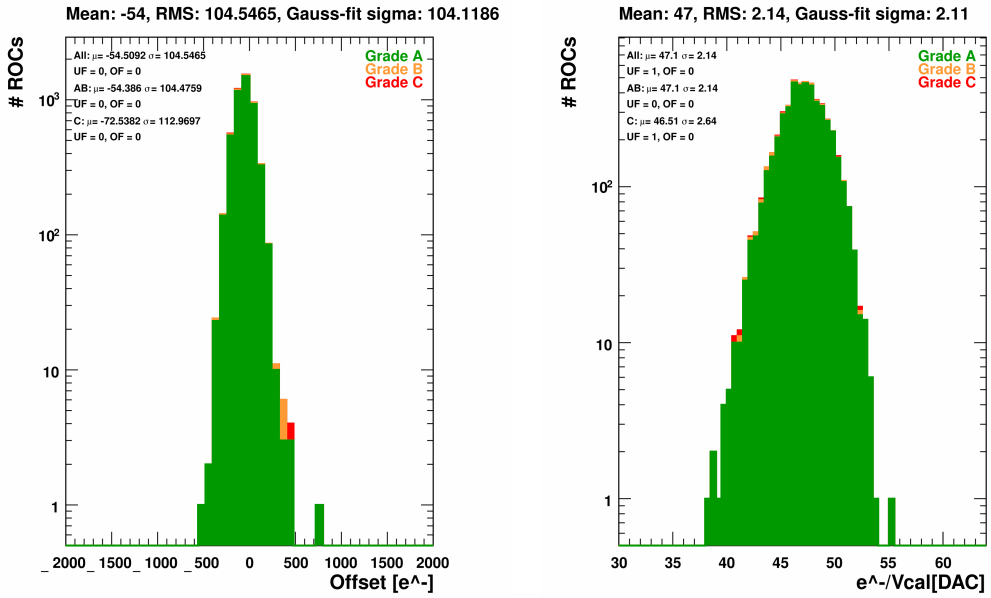

(a) Distribution of calibrated offset values.

(b) Distribution of calibrated proportional values.

Figure 12.22: Distribution obtained for the calibration of 4864 psi46digV2.1-respin ROCs with a linear regression between Vcal units and electrons.[151]

As a consequence, instead of characterizing each of the ROCs used, the average values for the linear relationship between the charge in Vcal units and the charge in electrons from the Phase 1 commissioning of the layers 2-4 pixel detectors performed at the institute for the CMS experiment were used. These results can be seen in Figure 12.22. With these results, the linear relation, with its systematic uncertainties, shown in Equation 12.13 was used to convert the

measured charges in Vcal units into electrons.

$$Q[\mathrm{e}] = -54.5(1045)\,\mathrm{e} + 47.10(214)\,\frac{\mathrm{e}}{\mathrm{Vcal}} \cdot Q[\mathrm{Vcal}] \tag{12.13}$$

12.7 Pumping And Rate Scans

As mentioned in section 10.2.2, one of the experiments made during the test beams at PSI were rate scans, where the detectors were measured with different rates of particles. The scan consisted of several up-down scans, where an up-scan refers to increasing the rate of particles between each run, while a down-scan refers to decreasing the rate of particles between each run.

During the rate scans, it was seen that in most cases, the first up-scan disagreed with the rest of the rate scan. This effect can be seen in Figure 12.23, where the first up-scan is highlighted in red. It is believed that this effect was caused by pumping, which meant that the pumping run before the rate scan was insufficient to passivate the deep traps in the sensor[152]. For this reason, the first up-scan in the rate scans was taken as part of the pumping procedure and was not included in the rate scan studies. The value for the rate was calibrated before the rate scan by adjusting the rate in the triggering planes of the telescope (i.e., planes 1 and 2 in Figure 10.5) using the beamline's collimators. An uncertainty of 10 % was assumed for the rate for every run.

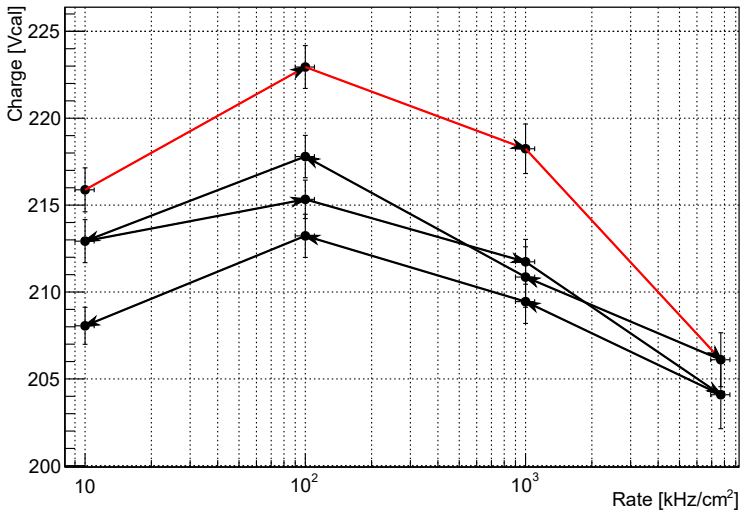

Figure 12.23: Complete rate scan for samples CMS04. The red line highlights the first up-scan which disagrees with the rest of the performed scans.

Part VII

Test Beam Results and Discussions

Chapter 13

Results Of The Fabricated Diamond Pixel Detectors Tested At PSI

In this chapter, the results from the fabricated pixel detectors described in section 3.3 with the pCVD diamonds CMS04, CMS01, CMS02, II6-93, and II6-750 that were tested at PSI test beams, as mentioned in chapter 10, will be shown. All the samples had roughly the same $\sim 1\,\text{cm} \times 1\,\text{cm}$ dimensions and a thickness of $\sim 500\,\mu\text{m}$, except for the II6-750 that had a thickness of $\sim 750\,\mu\text{m}$. As mentioned in section 10.2, all the fabricated devices were tested alongside a silicon pixel detector as a reference. As one of the main objectives of this thesis is the development of a scalable fabrication process for pixel detectors using a diamond sensor, this chapter begins with the identification of fabrication defects, followed by the selection of regions without pixel defects for the charge and efficiency studies. The effects of the different cuts will then be presented and discussed, followed by a discussion of the charge collected in electrons. During the test beam held in September 2019, there were complications with the measured data. The first problem was a missing calibration for low pulse heights of the DUTs[1], and the second was an excess of event misalignments between the DUTs and the telescope. The encountered issues and their implications in the results will be discussed. In the end, the results of the performance of the measured detectors in terms of charge collection and efficiency are discussed.

13.1 Identified Pixel Defects

As mentioned in section 12.5.5, pixels identified as defective, either from the fabrication of the sensor or from problems with the ROC, were masked following the procedure based on the predicted hit position. Table 13.1 summarizes the total percentages of masked pixels and indicates why they were masked. For the fabrication defects, the defects identified by microscopy studies are labeled in the notes of the table.

[1] Device under test

DUT	Failed PH calibration	Noisy and unresponsive	Fabrication defects (excluding bumps)	Bad bump formation	Estimated yield of good pixels after fabrication	Estimated yield of good pixels for analysis
CMS04	0.6 %	0.1 %	4.3 %$^{\$}$	0.2 %	95.5 %	94.8 %
CMS01	0 %	0.7 %	0 %	0.3 %$^{+}$	99.7 %	99.0 %
II6-93	0.2 %	0.6 %	0 %	0.1 %$^{+}$	99.9 %	99.1 %
CMS02	1.4 %	3.0 %	65.7 %$^{@}$	0.1 %$^{+}$	34.2 %	29.8 %
II6-750	0.2 %	1.8 %	14.9 %$^{@}$	0.1 %$^{+}$	85.0 %	83.0 %
Si-D8*	0.5 %	0 %	N.A.	N.A.	N.A.	99.5 %
Si-D2*	0.5 %	0.0 %	N.A.	N.A.	N.A.	99.5 %

Notes:
* Silicon reference pixel detectors.
$^{\$}$ Defects by tweezer scratches.
$^{+}$ Defective region in the photolithography mask that affected the bumps.
$^{@}$ Connected metallization after lift-off.

Table 13.1: Percentages of masked pixels according to their reasons and the expected yield of good pixels for the analysis of the DUTs tested in 2018 and 2019.

13.1.1 Pixel Defects From Fabrication

Of all the fabrication process defects, the bad bump formation was the least frequent. In each sensor, between three and 12 bumps were misshaped or wrongly placed. For four of the samples (i.e., CMS01, II6-93, CMS02, and II6-750), the reason for three misshaped bumps (the only bump problems for II6-93, CMS02, and II6-750) was identified as a problem with the photolithographic mask used before the UBM[2] deposition or before the indium deposition, as it can be seen in Figure 13.1a. Because of impurities on the mask, the indium bumps in those three pixels were wrongly formed, as seen in Figure 13.1b. This problem can be solved by cleaning and checking for impurities on the photolithography mask before each process.

For the rest of the nine bump formation defects in samples CMS04 and CMS01, the source of the problem is unknown. Figure 13.2 shows an example of these bump formation defects. Based on this, an efficiency of 99.91(2) % is estimated for fabricating well-shaped indium bumps in the correct position.

The most common issue during the fabrication of the first device (i.e., CMS04) was due to scratches caused during the fabrication process, as shown in Figure 12.20. This problem was caused by the handling of the sensors with the wrong set of tweezers (ceramic tweezers with narrow-rounded tips). It was solved by getting better tweezers for handling small samples (plastic tweezers with wide-flat tips), and as a result, no scratches were made in the following fabricated devices, CMS01, II6-93, CMS02, and II6-750.

The third fabrication defect was the interconnection of various pixels by leftover metallization

[2]Under-bump metallization

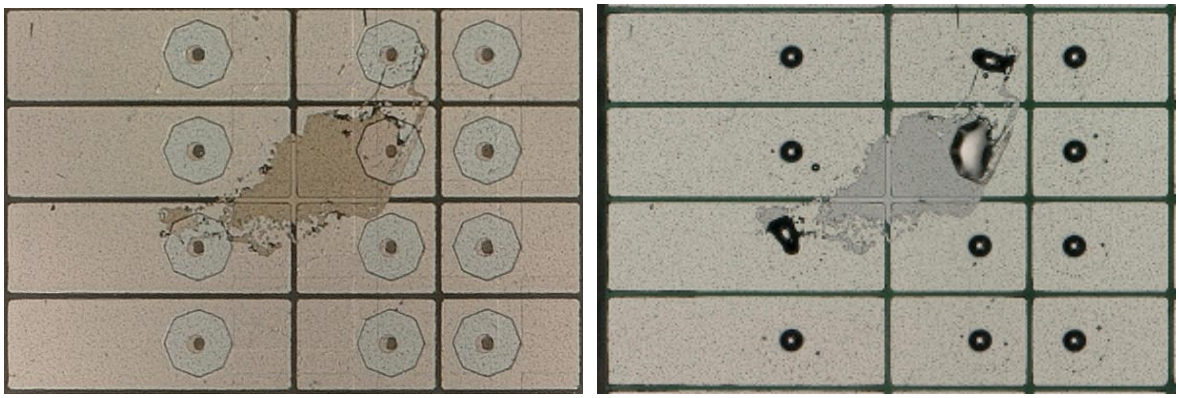

(a) After photolithography before the In evaporation. (b) After the In bump formation via reflow.

Figure 13.1: Microscope pictures of sample CMS01 after the development of the mask before the In deposition (a), and after the reflow process to form the In bumps (b).

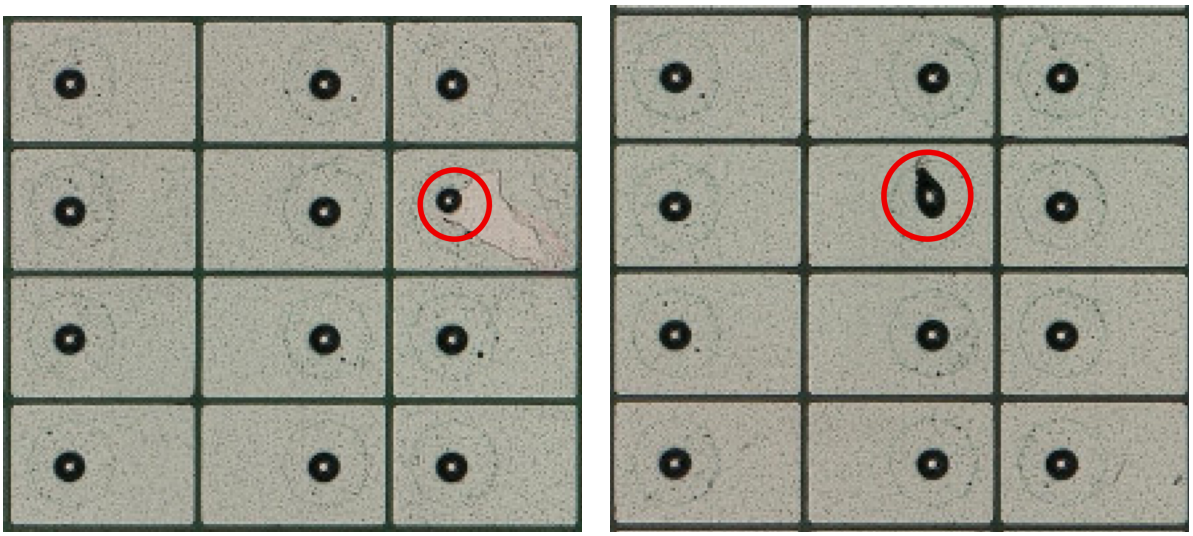

(a) Bump formed in the wrong position. (b) Bump formed with the wrong shape.

Figure 13.2: Example of the identified errors during the bump formation of the bumps on the sample CMS01. The bumps with problems are encircled in each case.

between the pixels, as seen in Figure 13.3. It is unknown if this problem happened during the photolithography before the deposition of the first metallization layer or during the lift-off of the first deposited metal. This problem could have been solved if the sample had been inspected with a microscope after the lift-off of the first metallization. If it had been identified, the metallization could have been removed, and the metallization process repeated. Unfortunately, for samples CMS02 and II6-750, due to time constraints, this was not done, and large areas of the sensor were affected by this problem. The affected areas in each of the samples were located in different regions.

The effects of these fabrication defects will be discussed in the next section in the discussion

Figure 13.3: Microscope picture of a section of the affected pixels caused by a problem with metallization in sample CMS02. The leftover metal in the corner of the pixels electrically connected them.

of the selected study regions for each device measured during the PSI test beams.

13.2 Regions Of Study

The fiducial regions selected for the silicon DUTs Si-D8 and Si-D2, that were used as reference detectors, were chosen as large as possible, leaving a clearance of at least three pixels from the borders, as seen in Figure 13.4. This was done to have the biggest area inside the DUTs as discussed in section 12.5.6.

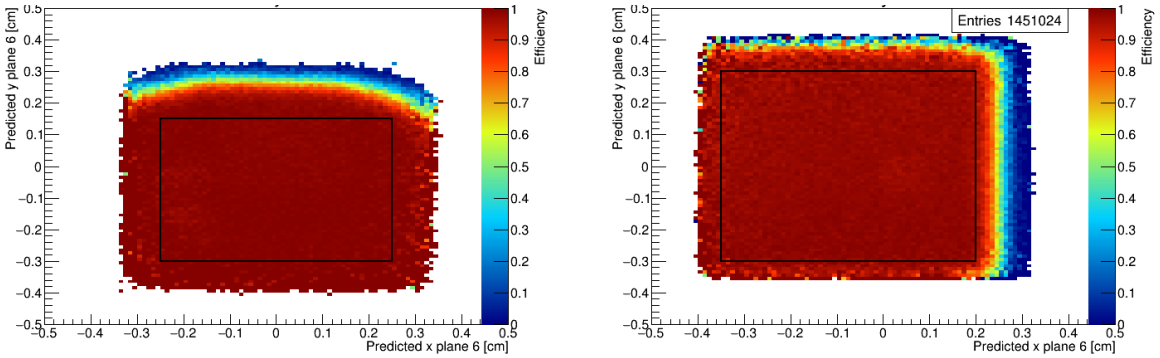

(a) Silicon DUT Si-D8.

(b) Silicon DUT Si-D2.

Figure 13.4: Detection efficiency maps of the silicon DUTs, where the black rectangles depict the selected regions for the studies.

For the pCVD diamond pixel detectors, the regions with fabrication defects presented

unresponsive pixels[3] or ineffective pixels with a diminished charge collection, as can be seen in Figure 13.5. For this reason, the fiducial region selected for the rest of the analysis was set at least three pixels away from the known defects, as mentioned in section 12.5.6. Figures 13.5 and 13.6 show the fiducial regions selected on the diamond devices for the analysis. It is worth noting that inside the region without fabrication defects in Figure 13.5b, the collected charge of the device is not uniform, which is a characteristic seen in pCVD diamond devices[153].

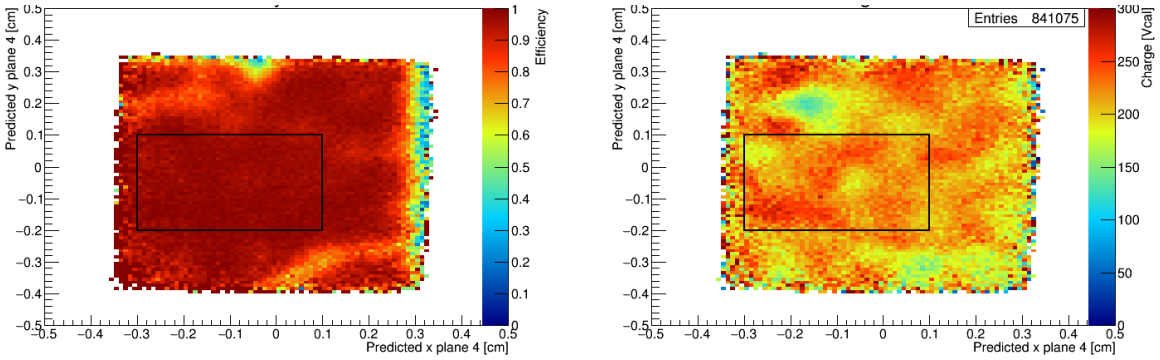

(a) Efficiency map.

(b) Cluster charge map.

Figure 13.5: Maps of the detection efficiency (a) and cluster charge (b) of CMS04 biased with $-750\,\mathrm{V}$ and a beam flux of $100\,\mathrm{kHz/cm^2}$. The black box is the selected region for analysis. The microscopy picture showing the fiducial region and the defects can be seen in Figure 12.20.

13.3 Data Selection Effects On The Efficiency And The Charge

As mentioned in section 12.5, a series of selection criteria were applied to the data for the analysis: *track, beam, phase, angle, chi2, mask, fiducial,* and *rhit*[4]. Each selection criterion is applied after applying the previous ones, so the effects of the selections are cumulative. Figure 13.7 shows the cumulative effects of these selections on the detection efficiency (efficiency for short) and the cluster collected charge (charge for short) for the DUT CMS04. A discussion regarding the reported efficiencies and their uncertainties is given in Appendix H.

The efficiency results shown in Figure 13.7a are for all the cumulative selection criteria except for *rhit*, as the effects of multiple scattering are not negligible and strongly affect the measured efficiency. The charge results shown in Figure 13.7b include the effect of *rhit* in the cumulative selection criteria to have certainty that the measured signal comes from the vicinity of the predicted hit pixel and not from noisy pixels or pixels outside the fiducial region.

[3] The pixels did not respond to injected charges from the ROC.

[4] *track* refer to reconstructed trajectory, *beam* to beam interruption, *phase* to trigger phase, *angle* to angle distribution, *chi2* to χ^2 of the linear fits, *mask* to pixel mask, *fiducial* to fiducial region, and *rhit* to hit distance (see section 11.6).

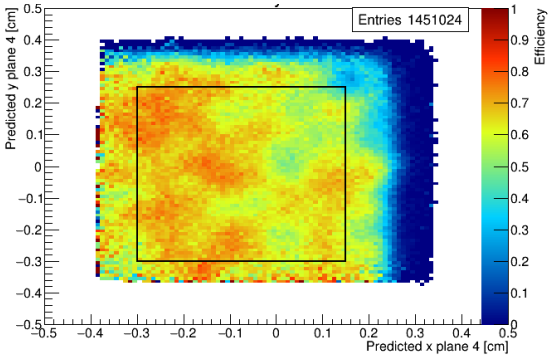

(a) CMS01

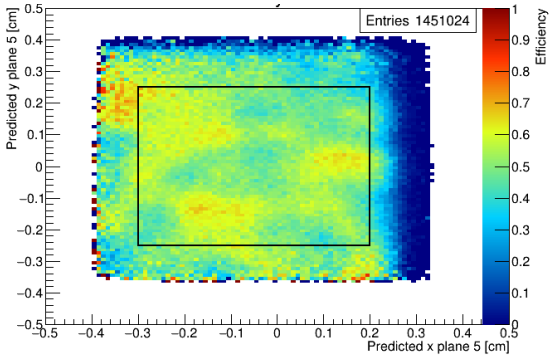

(b) II6-93

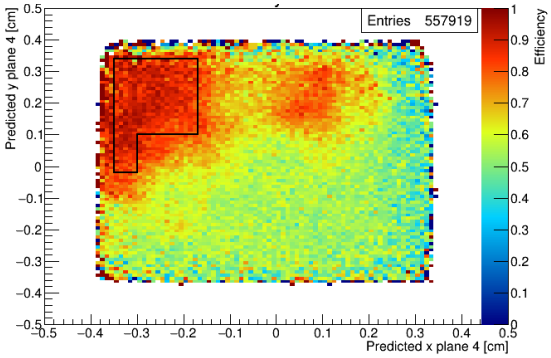

(c) CMS02

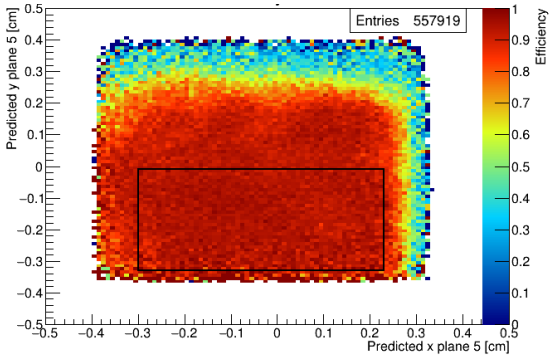

(d) II6-750

Figure 13.6: Detection efficiency maps of the diamond devices. The black polygon encloses the fiducial region chosen for each device.

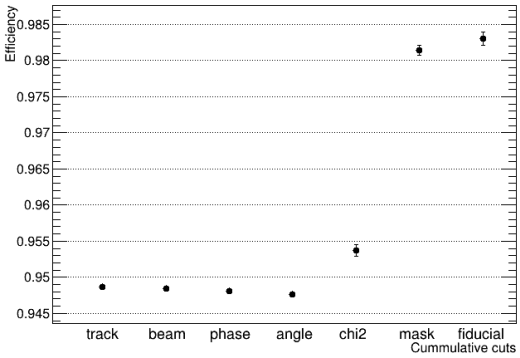

(a) Efficiency vs. cummulative cuts.

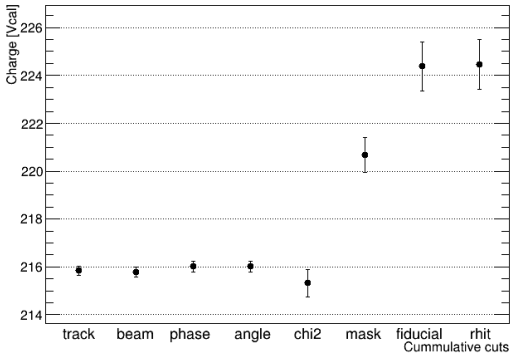

(b) Charge vs. cummulative cuts.

Figure 13.7: Effects of the cumulative cuts applied on the efficiency and the collected charge of the sample CMS04 biased with $-750\,\mathrm{V}$ at an incident particle flux of $100\,\mathrm{kHz/cm^2}$.

13.4 Charge In Electrons

The estimation of the charge in electrons has a large systematic uncertainty due to the large uncertainty in the calibration constants used, as was discussed in section 12.6.1. An example of this is shown in Figure 13.8, where the black error bars indicate the statistical uncertainty, and the red bars indicate the systematic uncertainty.

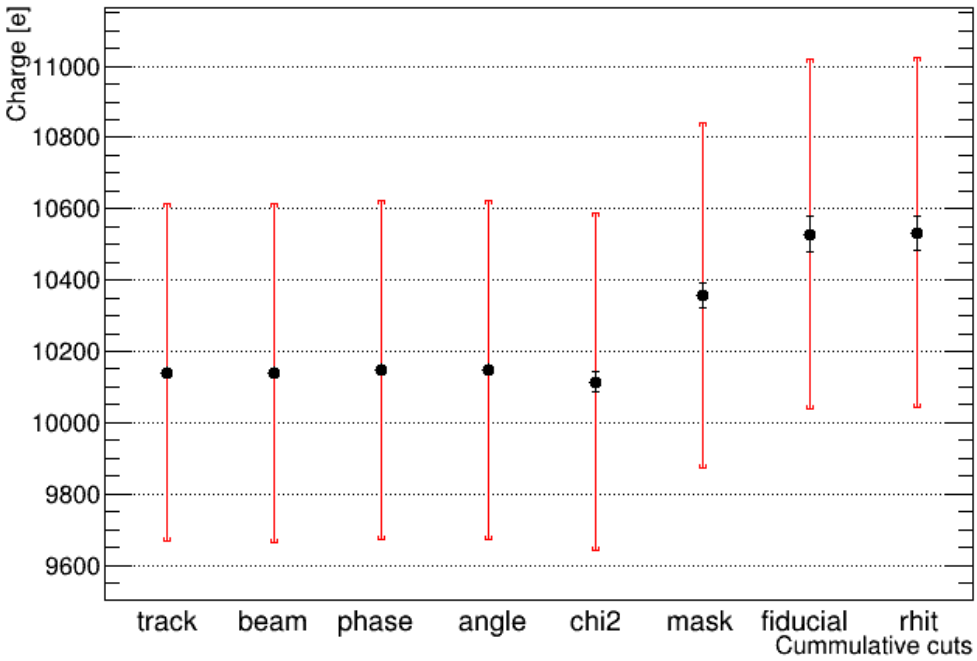

Figure 13.8: Selection effects on the collected charge shown in Figure 13.7b in electrons. The data corresponds to CMS04 biased with −750 V. The black error bars represent the statistical uncertainties, while the red error bars represent the systematic uncertainty of the Vcal-to-electron calibration.

Because all the detectors share the same calibration constant to convert charge in Vcal units into electrons, and because the systematic uncertainty from the calibration constant is much larger than the statistical uncertainty, only the plots with the charge in Vcal units are shown. Nevertheless, the results in the tables are displayed in electrons with statistical uncertainties and systematic uncertainties from the calibration constants.

13.5 Complications With The Measured Data

During the test beam carried out in September 2019, several runs were corrupted, affecting about 30 % of the analyzed data. It was unknown why the files were corrupted, but it was not possible to convert raw files. The data that suffered the most were taken at the highest incident particle rate. For this reason, the rate scans for the devices measured in 2019 (CMS01, II6-93,

CMS02, and II6-750) do not have the data point for rates corresponding to particle fluxes above 10^3 kHz/cm^2.

Besides this problem, there were two other issues during this test beam that affected the data available for analysis and the results. One of the problems was the incorrect configuration of the planes, which placed the effective threshold for the pixels above the desired value of ~ 1400 e. The other issue was an increase in event misalignments between the data recorded by the DTB handling the DUTs and the DTB handling the telescope's tracking planes.

13.5.1 Problems With The Detectors' Configuration

The wrong configuration of the planes mainly affected the data taken with the DUTs CMS01, II6-93, and the silicon Si-D2. The effect of the wrong configuration of the planes can be seen in Figure 13.9, which shows the pulse height calibration for a pixel in DUT CMS01. It can be seen that the gain of the ADC of the ROC was not optimized, which caused a low resolution of the pulse height (i.e., only 53 % of the dynamic range of the digitizer was used). Additionally, the lowest charge in Vcal units that the pixels in the ROC responded to was 100 Vcal which is about 4700 e.

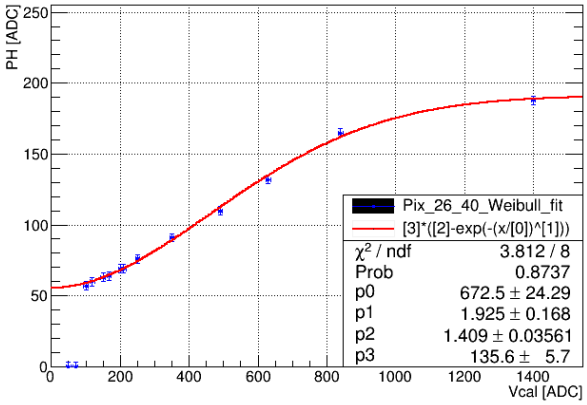

Figure 13.9: Pulse height calibration for the pixel located at column 26 and row 40 of the DUT CMS01. Around half of the available values of the ADC were not used, which suggests the amplifier gain was not set correctly, and the first injected charge, which was not read as a 0 ADC, had a value of 100 Vcal, which means the detector's threshold was around 4700 e.

A threshold of about 5000 e is too high for pCVD diamond, as seen in the charge distributions of DUT CMS04 in Figure 13.10 that did not have this problem. It can be seen that about 27 % of the read data lies below 100 Vcal for CMS04 biased with −100 V, while 20 % of the data lies below 100 Vcal when biased with −700 V.

From Figure 13.10, it can also be seen that the MPV for CMS04 changes at most 40 Vcal (~ 1800 e) for the shown voltages, while the mean of the distribution changes by about 100 Vcal (~ 4700 e). For this reason, the mean of the distribution was used to compare the charge collection performance of the detectors under different experimental conditions. Additionally, it is seen that despite the differences in the bias voltage, all the distributions have a steep rise

as the collected charges approach the configured threshold close to 50 Vcal, which suggests that the shape of the distribution in this region is determined by the configured threshold and is independent of the applied bias voltage to the detector. This would bias the mean of the distribution giving higher values for the measured average collected charge.

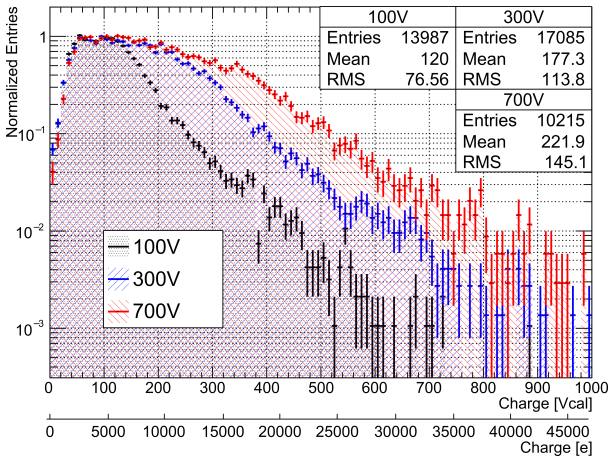

Figure 13.10: Normalized distributions to the MPV around 100 Vcal for the collected charge of DUT CMS04 for a biasing voltage of −100 V, −300 V, and −700 V.

In addition, the high threshold problem also affected the silicon plane measured together with the affected diamond samples CMS02 and II6-750, which caused the silicon planes to have a lower efficiency than expected, as the events with charges below 100 Vcal (~ 4700 e) were not registered. This can be seen in Figure 13.11, where the lower end of the charge distribution of the silicon plane Si-D8 configured correctly is compared to the affected silicon plane Si-D2 with a wrong configuration.

Although during calibration, there was no readout from any of the pixels when injected with charges below 100 Vcal as seen in Figure 13.9, during the data-taking runs, there were measured pulse heights read by the ADC which would correspond to values lower than 100 Vcal (e.g., pulse heights below 50 ADC for the pixel in Figure 13.9).

A transient effect was seen by Michael Reichmann[154], which affected the measured pulse height for a given injected charge. In his findings, up to a maximum drop of 25 % in the measured pulse height in ADC units was found in an interval of a minute. His hypothesis for this effect is that the temperature of the ROC affected the data taking, which is significant during the calibration of the ROCs, which was usually performed at room temperature. In contrast, during data taking, the ROCs warmed up, drifting the pulse heights to lower values.

This drift of the pulse height could arise from the ADC in the periphery of the ROC or the analog domain in the preamplifier or shaper in the PUCs[5]. If it were from the ADC, no effects on the efficiency would be expected. On the other hand, if it came from the analog domain, this effect would affect the efficiency as the signals would drift below the detection threshold.

[5]Pixel unit cell (see section 3.1)

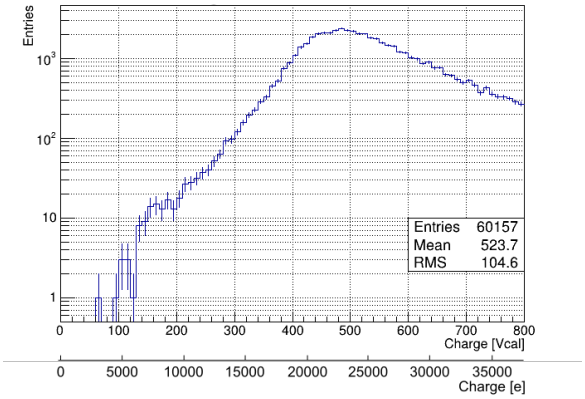

(a) Lower end of the charge collected by the silicon DUT D2.

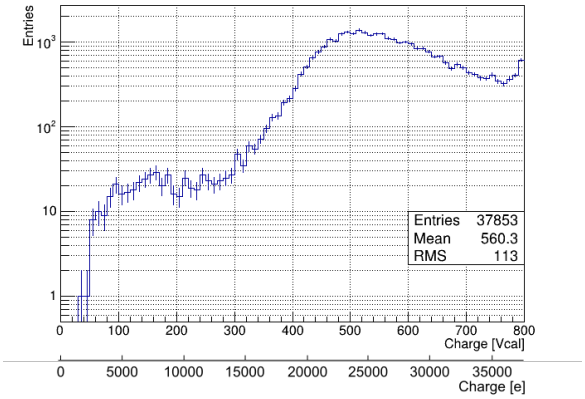

(b) Lower end of the charge collected by the silicon DUT D8.

Figure 13.11: Collected charge in the lower end of the distributions for the silicon DUTs D2 (a) and D8 (b). D2 has a lower MPV than D8 and the cutoff due to the configuration in D2 happened at a higher value (~ 100 Vcal or ~ 4700 e) than in D8 (~ 50 Vcal or ~ 2300 e).

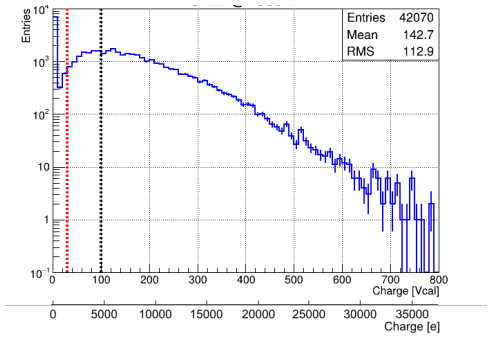

(a) Charge distribution of DUT CMS01 biased with −600 V.

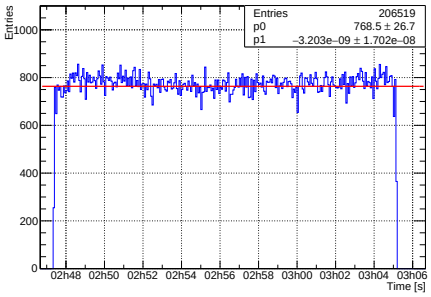

(b) Frequency of events with 0 Vcal.

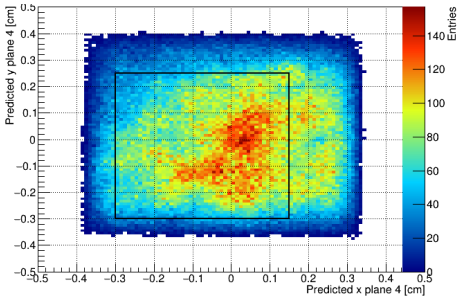

(c) Location of tracks that gave 0 Vcal.

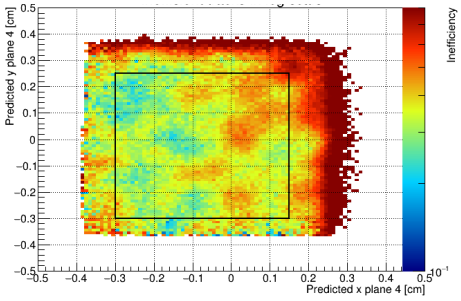

(d) Inefficient tracks in logarithmic scale.

Figure 13.12: Charge distribution for CMS01 in (a). A large peak with 0 Vcal charge is appreciated. The vertical dashed lines mark the collected charges of 30 Vcal (~ 1400 e) in red and 100 Vcal (~ 4700 e) in black. The events with extrapolated collected charge of 0 Vcal occurred at a constant rate as seen in (b), where the fitted line in red is consistent with a constant rate of 768.5 Hz. The locations of the tracks where these events happened are shown in (c) which correlate with inefficient regions which are shown in (d).

Because of the drift of the pulse height, all the runs for the DUTs CMS01 and II6-93 have a large peak at a measured charge of 0 Vcal in their charge distributions, as seen in Figure 13.12a. This affects the average charge measured with the devices; therefore, the measured charge was considered to be a lower bound on the real charge that would have been measured if the detectors had been configured correctly.

Figure 13.12b shows for a representative run that the rate of events that with an extrapolated charge of 0 Vcal was constant throughout the runs. Figures 13.12c and 13.12d show that these events happened with increased incidence in some regions, which were correlated with low-efficiency areas. These regions would correspond to the low charge collection regions of the pCVD diamond which are more affected by the high threshold.

Another piece of evidence that supports the hypothesis that the analog domain of the PUCs partly caused the pulse height drift is seen in Figure 13.13. This figure shows the efficiency of the silicon device Si-D2 during a rate scan. The silicon DUTs of the CMS experiment were designed to have efficiencies above 99 % for particle fluxes up to 120 MHz/cm^2[90]. Therefore, the initial low efficiencies of ~ 97.6 % measured in the silicon DUT Si-D2 were caused by the high threshold discussed above in section 13.5.1. Between the two measurements at a particle flux of 1000 kHz/cm^2, about an hour transpired. During this time, the efficiency in the silicon device dropped from 97.6 % to 95.7 %, as would happen if the analog domain of the PUCs partly caused the pulse height to drift to values below the detection threshold. Posterior measurements of Si-D2 with the correct configuration showed efficiencies above 99 % as expected.

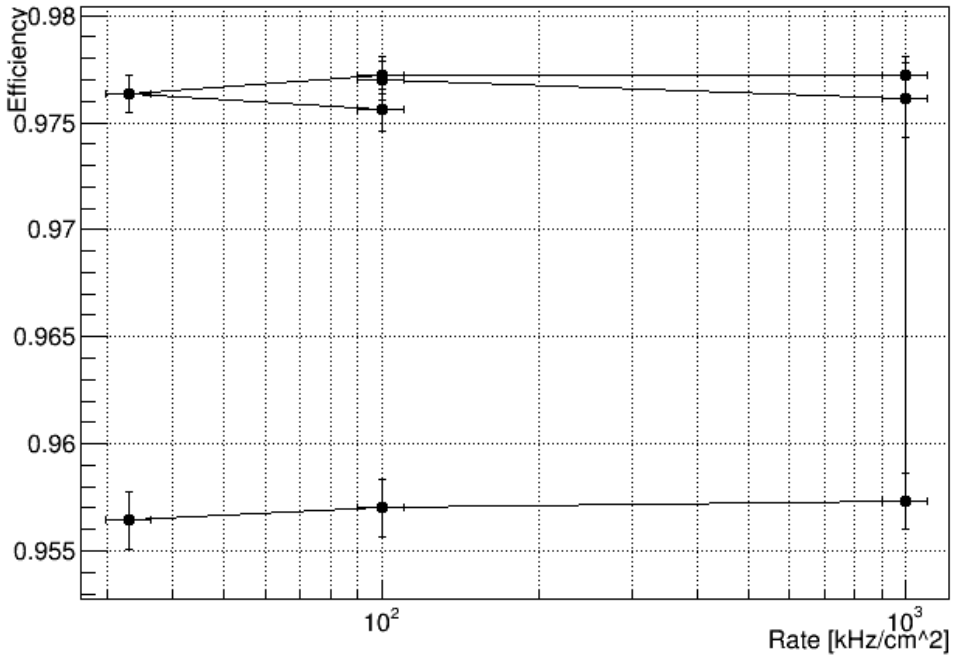

Figure 13.13: Efficiency measurements for the silicon Si-D2 during a rate scan. There is a drop in efficiency from 97.6 % to 95.7 % between two measurements at a particle flux of 1000 kHz/cm^2.

13.5.2 Problems With The Events Alignment

If there was a misalignment between the events recorded by the DUTs and the events recorded by the telescope's tracking planes, then the event of the DUTs was set by a different particle than the particle that triggered the event in the telescope's tracking planes. This causes a loss of correlation in the position of the particles between the planes. Michael Reichmann[155] developed a method implemented during the data conversion to correct the event misalignment by using the correlation coefficient between the cluster positions in one of the telescope planes and the DUTs. If no event misalignment existed, the correlation coefficient would be close to 1. Otherwise, the correlation was lost, and the coefficient would drop below a threshold set empirically to 0.4. The algorithm developed by Michael Reichmann would advance or delay the event of one of the DTBs until the correlation was recovered.

Nevertheless, some runs were severely misaligned, which means that in a short period of time, several event misalignments between the telescope's DTB and the DUT's DTB happened. As a consequence, the algorithm to correct the event misalignments was insufficient to fix all the data in these runs. The effects of one run with this issue can be seen in Figure 13.14, where the efficiency of the silicon DUT drops, and the correlation between the predicted track by the telescope and the excited column in the DUT was lost. The efficiency vs. time plot after applying all the cumulative data selections, including the *rhit*[6] criterion, helped identify the misaligned runs. The uncorrelated events between the telescope planes and the DUTs would be heavily affected by the *rhit* cut, which would cause a noticeable drop in efficiency, as shown in Figure 13.14a. The affected runs were reanalyzed using only the events before the event misalignment happened. As a result, some runs have low statistics (e.g. as low as a total of 3254 events before the data selection for the analysis of DUT CMS02).

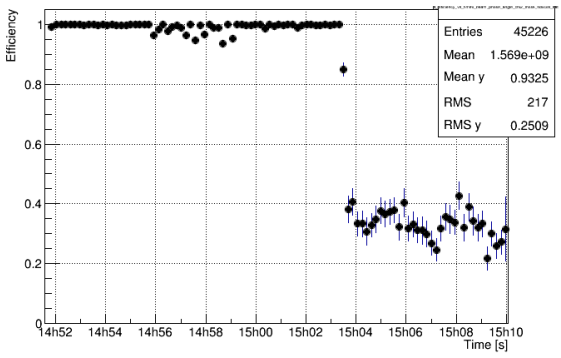

(a) Efficiency of the silicon DUT vs. time.

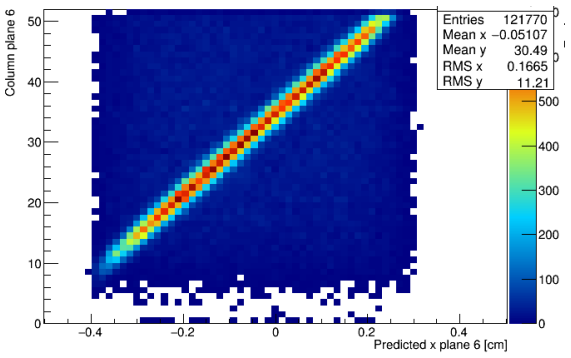

(b) Map correlating the predicted track position and the excited column in the silicon DUT.

Figure 13.14: Plots that indicate that an event misalignment beyond correction was left after the data conversion. The loss of correlation due to this effect causes a random relationship between the predicted hit position and the excited column or row in the silicon DUT. This causes the blue background seen in (b). In (a), the event misalignment causes a drop in efficiency after applying the *rhit* selection criterion.

[6] hit distance (see section 12.5)

13.6 Voltage Scans

During the voltage scan measurements, the bias voltage of each sample was increased between each run, and data was taken with a particle flux of 100 kHz/cm^2. As mentioned in section 10.2.2, this was done until the leakage current of the DUTs reached 100 nA, which was considered the maximum voltage the DUT could handle. Figure 13.15 shows the efficiency results of the tested pixel DUTs. As was expected, the efficiency of the DUTs CMS01 and II6-93, which were configured with a high threshold of 100 Vcal (~ 4700 e), was low, while the DUTs that were correctly configured reached efficiencies above 90 % for the configured thresholds of ~ 1500 e.

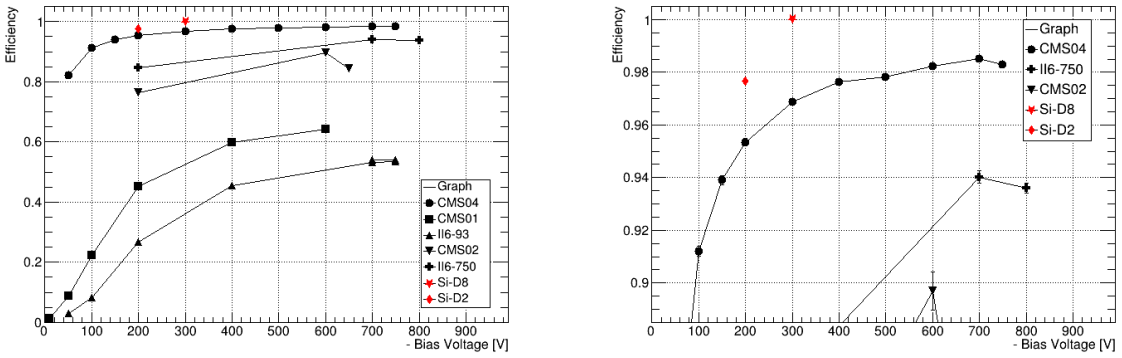

(a) Efficiencies vs. bias voltage.

(b) Zoom of (a) around efficiencies above 90 %.

Figure 13.15: Efficiencies of the pixel DUTs as a function of the bias voltage in (a). In (b), a closeup around the efficiencies above 90 % is shown. The devices that reached around 90 % efficiency were the ones that were configured correctly with a low threshold, as expected. Note that for the sample II6-750, as its thickness is 50 % larger than the other detectors, the electric field inside it is 66.7 % the electric field of the other detectors at the same bias voltage.

As shown in Figure 13.16, it seems that among the diamond DUTs, only CMS04 had reached a plateau of charge collection. As the voltage increase during the voltage scans was stopped when the leakage current, at a low particle rate (i.e., with a negligible beam-induced current), reached O(100 nA), it suggests that the limiting factor that was preventing the increase of the electric field inside the sensor were the intrinsic characteristics from the fabrication of the pCVD diamond.

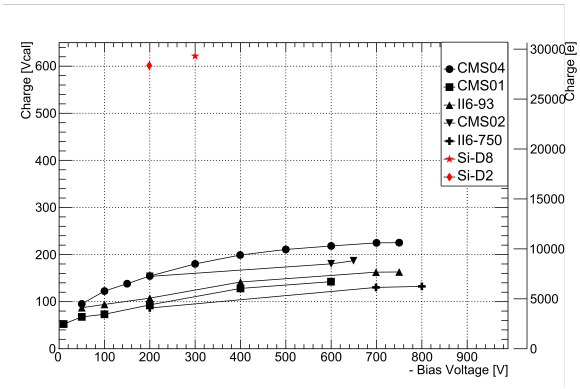

(a) Collected charge vs. bias voltage.

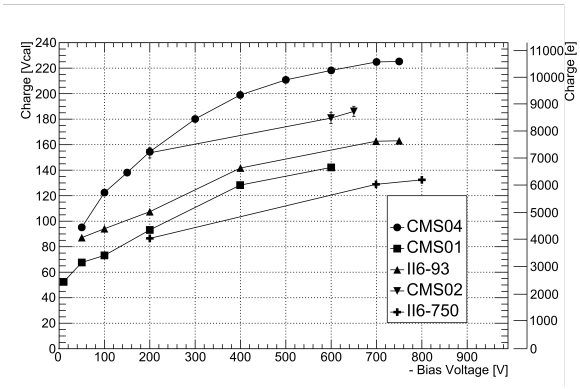

(b) Collected charge of diamonds DUTs vs. bias voltage.

Figure 13.16: Charge collection in Vcal units for different bias voltages. In (a), all the DUTs, including the silicon DUTs, are shown. In (b), only the diamond DUTs are shown. Except for CMS04 and II6-93, the other diamond DUTs seem not to have reached a plateau in their charge collection. Note that for the sample II6-750, since its thickness is ~ 50 % larger than the other detectors, the electric field inside it is ~ 66.7 % the electric field of the other detectors at the same bias voltage.

Figure 13.17 shows the voltage and current of the device II6-750 during the voltage scan. In the figures, it can be seen that as the voltage increased, the current also increased until it surpassed 100 nA and then started to become erratic[7]. It is worth noting that no breakdown current was observed in any of the samples.

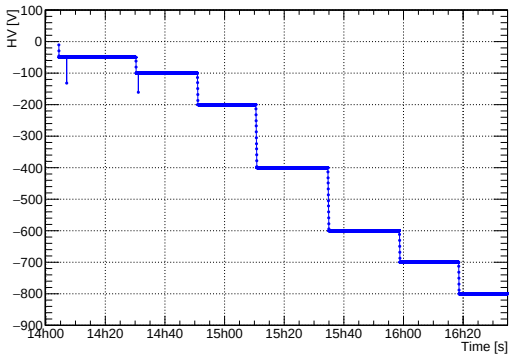

(a) HV during voltage scan.

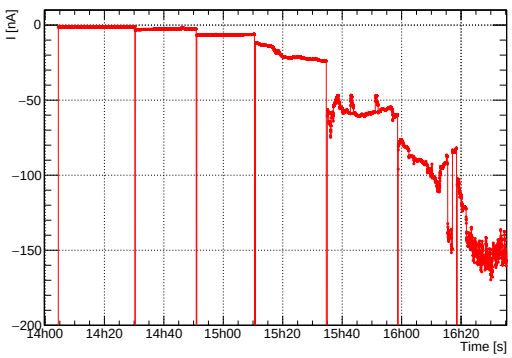

(b) Current during voltage scan.

Figure 13.17: Voltage (a) and current (b) vs. time for the voltage scan performed on the DUT II6-750. The vertical lines in the current plot are caused by the ramping of the voltage. It can be seen that the current became erratic during the last applied voltage.

The DUTs CMS01, CMS02, and CMS04 nominally have similar thicknesses and were tested

[7] In retrospect, it would have been interesting to continue taking data at higher voltages, despite the erratic currents.

with the same voltage of −600 V. Moreover, they came from the same wafer, which would give them similar characteristics compared to samples from different wafers. For these reasons, it was possible to compare the collected charge of these three DUTs under similar conditions. This comparison is shown in Figure 13.18.

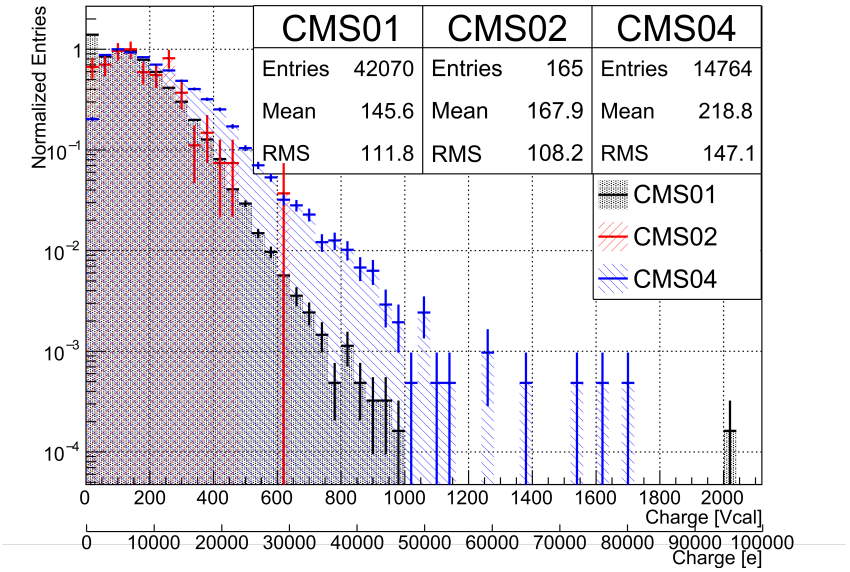

Figure 13.18: Charge collection distributions for the DUTs CMS01, CMS02, and CMS04. The distributions are normalized to the MPV around 100 Vcal (~ 4700 e). The three DUTs are biased with −600 V for this comparison.

The DUT CMS04 collected more charge than the other two devices under similar conditions. Despite the low statistics of CMS02 and the excess of collected charges extrapolated to 0 Vcal for CMS01, both DUTs are similar in their charge collection distributions above 100 Vcal (~ 4700 e). To determine if the higher charge collection of CMS04 compared with the other two DUTs was caused by the fabrication processes, which were more than a year apart[8], or by the different characteristics of the pCVD diamonds, it is necessary to compare the quantitative measurements of the CCD[9] before the fabrication steps described in this thesis.

The results for the voltage scans are summarized in Table 13.2, where the maximum efficiency and the maximum charge collection achieved by each DUT are given. The characteristics for the maximum charge collection during the voltage scan are also provided. The last column sets a lower bound to the expected average charge collection using the CCDs and thicknesses in Table 3.1. These quantities were obtained for MIPs. As the particle beam used in this thesis to measure the DUTs consisted mostly of pions with a momentum of 260 MeV/c, the measured average charge in the DUTs during the test beams was larger than the one given as a lower bound in the table.

[8]CMS04 was processed in 2017, while CMS01 and CMS02 were processed in 2019.
[9]Charge collection distance

DUT	Max. efficiency (%)	Bias (V) (Max. charge)	$\left\langle \lvert\vec{E}\rvert \right\rangle$ (V/µm) (Max. charge)	Max. measured average charge (e)	Expected average charge for MIPs (e)
CMS04	$98.50^{+0.10}_{-0.10}$	−750	1.5(2)	$10533.08 \pm 492.27(\text{sys}) \pm 48.46(\text{stat})$	8244
CMS01	$64.31^{+0.19}_{-0.19}$	−600	1.2(1)	$>6641.71 \pm 377.42(\text{sys}) \pm 24.25(\text{stat})$	7416
II6-93	$54.13^{+0.51}_{-0.52}$	−750	1.5(2)	$>7624.21 \pm 381.91(\text{sys}) \pm 27.69(\text{stat})$	8928
CMS02	$89.69^{+0.72}_{-0.76}$	−650	1.3(1)	$8754.61 \pm 420.68(\text{sys}) \pm 211.34(\text{stat})$	7236
II6-750	$94.0^{+0.25}_{-0.25}$	−750	1.0(1)	$6172.59 \pm 313.59(\text{sys}) \pm 28.58(\text{stat})$	8352
Si-D8	$100.00^{+0.00}_{-0.01}$	−300	1.1(1)	$29157.36 \pm 1331.36(\text{sys}) \pm 50.6(\text{stat})$	22800
Si-D2	$97.72^{+0.14}_{-0.15}$	−200	0.7(1)	$>28245.54 \pm 1290.39(\text{sys}) \pm 46.57(\text{stat})$	22800

Table 13.2: Voltage scan results for the tested DUTs. For the average electric field magnitude, an uncertainty of 10 % was assumed on the thickness of the sensors.

As seen in the last column of Table 13.2, it was expected that the detectors CMS01 and CMS02 would collect similar charges if configured correctly. Also, it was expected that CMS04 would collect more charge than CMS01 and CMS02. Therefore, it is possible to conclude that the differences observed in the charge collection distributions for CMS01, CMS02 and CMS04 under similar conditions were caused by the different characteristics of the pCVD diamonds and not by the fabrication process described in this thesis. It's worth noting that the charge collected by the detectors CMS04, CMS02, and Si-D8, which were configured correctly, collected more charge than if they had been tested with MIPs. Moreover, the measured average charge for CMS04 and Si-D8 was 1.3(1) times the charge collected for MIPs, and for CMS02 was 1.2(1) times the charge collected for MIPs. These factors are equivalent within the systematic uncertainties, supporting the hypothesis that the fabrication process presented in this thesis did not have a negative impact on the performance of the fabricated detectors.

13.7 Rate Scans

As mentioned in section 10.2.2, the other type of measurements performed on the DUTs were rate scans. During these measurements, the DUTs were biased with the maximum stable voltage found during the voltage scan (i.e., the maximum voltage reached in the voltage scan before the currents became erratic), and the rate of the incident particles was changed between each of the runs in a series of up-down rate scans. This was done to study the charge collection rate dependence of pCVD diamonds in the same way as was studied for scCVD diamonds[156]. The conditions used for the rate scan measurements of the DUTs are shown in Table 13.3.

DUT	Bias voltage (V)	$\langle \lvert \vec{E} \rvert \rangle$ (V/µm)
CMS04	−750	1.5(2)
CMS01	−500	1.0(1)
II6-93	−700	1.4(1)
CMS02	−600	1.2(1)
II6-750	−750	1.0(1)
Si-D8	−300	1.1(1)
Si-D2	−200	0.7(1)

Table 13.3: Bias voltages applied to the DUTs for the rate scans and their respective estimated average electric field magnitude.

All the pCVD diamond DUTs showed a small rate dependence, although no common trend was identified. DUTs CMS04, CMS01 and II6-93 presented an increase in charge collection at a flux of 100 kHz/cm^2 compared to that at O(10 kHz/cm^2). Looking at the charge distributions of CMS04 in Figure 13.19, which are normalized to the MPV, one feature distinguishes the 100 kHz/cm^2 distribution with respect to the other rates. Relative to the other two rates, the 100 kHz/cm^2 run has a larger fraction of events above the MPV peak. As for the 7.7 MHz/cm^2 run, it has a larger fraction of events at 0 Vcal below the configured threshold of ~ 1500 e. The same behavior mentioned above is seen for sample II6-93, as shown in Figure 13.20.

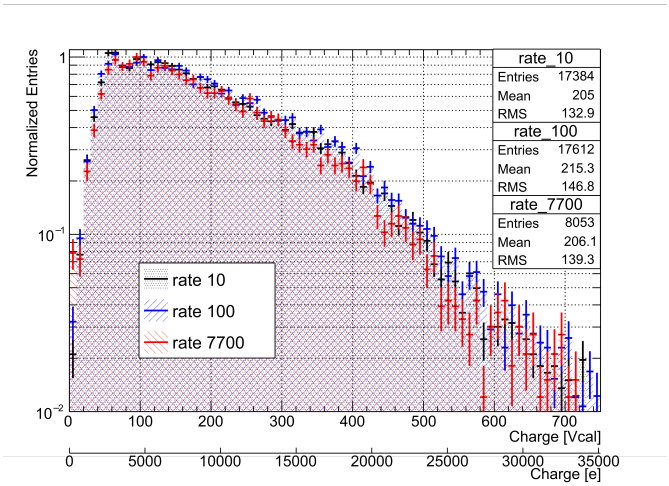

Figure 13.19: Normalized distributions to the MPV around 100 Vcal (~ 4700 e) for the collected charge of CMS04 for the particle fluxes of 10, 100 and 7700 kHz/cm^2.

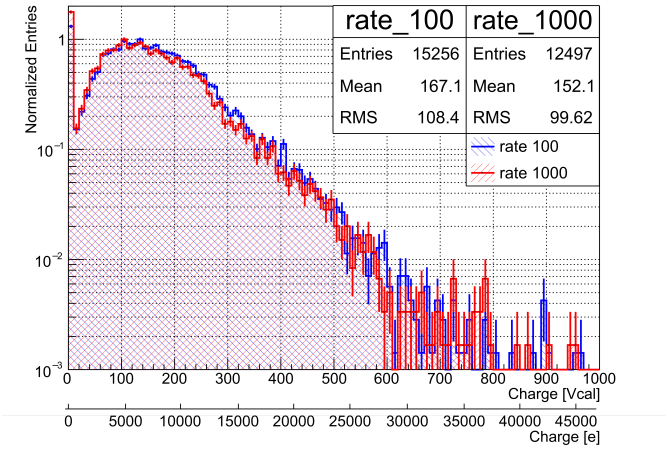

Figure 13.20: Normalized distributions to the MPV around 100 Vcal (~ 4700 e) for the collected charge of II6-93 for the rates of 100 and 1000 kHz/cm^2.

On the other hand, DUTs CMS02 and II6-750 presented a decrease in charge for a flux of 100 kHz/cm^2 and an increase in the charge collection at a particle flux of 1000 kHz/cm^2. For these samples, the runs at 1000 kHz/cm^2 had a larger fraction of events above the MPV peak, and a smaller fraction of events at 0 Vcal below the configured threshold, when compared with the runs at a flux of 100 kHz/cm^2.

The collected charges at the same beam flux were averaged for each DUT. The resulting average collected charge at each rate was then divided by the average of the collected charges for all rates. This gives a ratio of the collected charges with respect to the average as a function of the rate. As no rate dependence was found in the literature for silicon, the deviations from unity for the silicon DUTs were used to estimate a systematic uncertainty due to factors that were not controlled, such as the temperature of the ROCs. The results for the rate dependence for each

DUT are shown in Figure 13.21, where the black error bars depict the statistical uncertainty. The red boxes are the estimations of the systematic uncertainties using the silicon DUTs deviations.

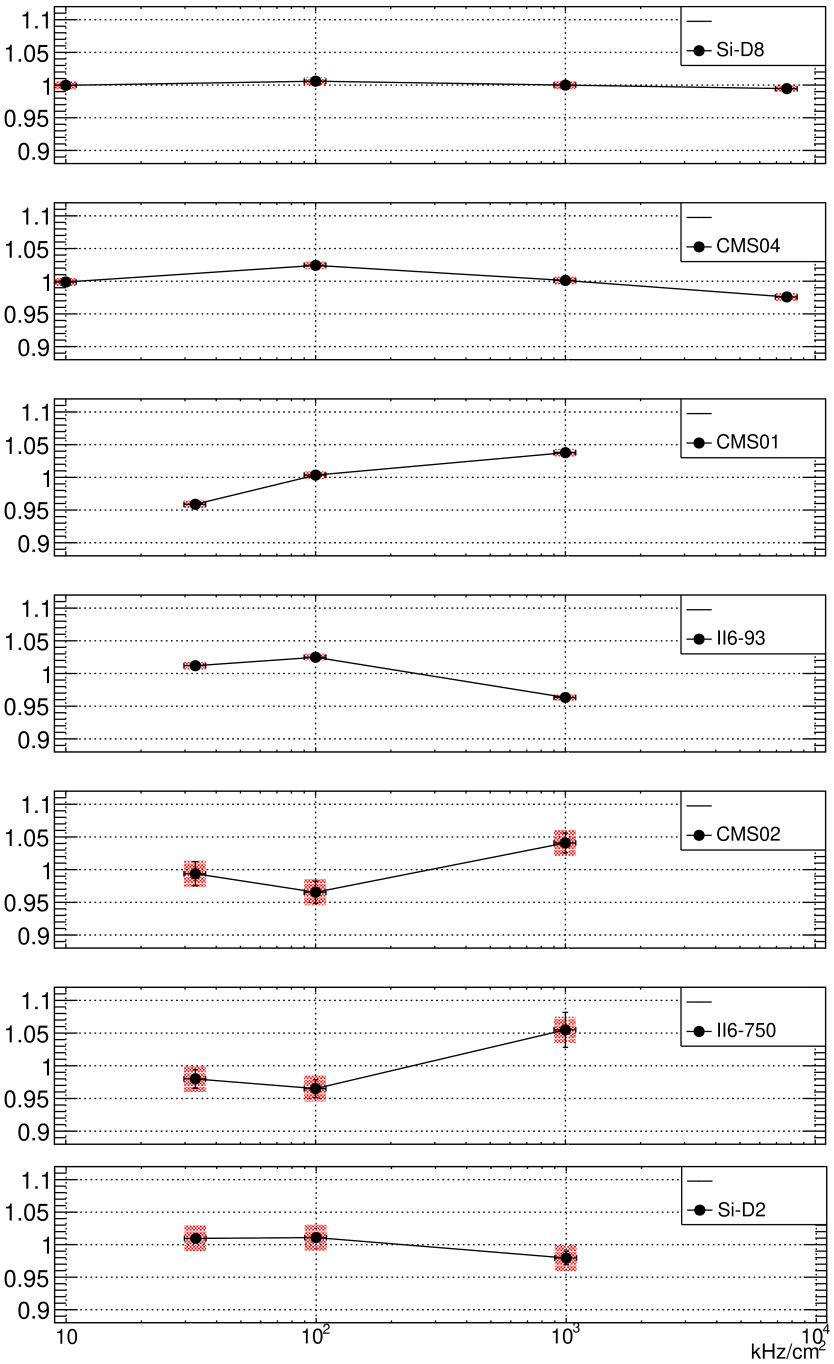

Figure 13.21: Ratios of the collected charges with respect to the average value of the data for different particle fluxes.

Overall, all the pCVD diamond DUTs showed a rate dependence below 5 % for the analyzed rates, which is within the parameters found by the RD42 collaboration with pad detectors under rate studies for pCVD diamond sensors[157]. The charge increase at a particle flux of 1000 kHz/cm^2 for DUTs CMS01, CMS02 and II6-750, and a particle flux of 100 kHz/cm^2 for DUTs CMS04 and II6-93, has the same effect as during the pumping with the beam. This could be because shallow traps with shorter lifetimes are passivated with an increasing particle rate until they reach an equilibrium. On the other hand, the drop of collected charge for CMS04 at particle fluxes above 1000 kHz/cm^2, and for II6-93 at a particle flux of 1000 kHz/cm^2 is not well understood. Polarization effects similar to the ones seen in scCVD diamonds[156] could also play a role in the rate dependence of non-irradiated pCVD diamonds. Further studies that could see the polarization inside of the diamond, such as with e-TCT, could help understand the features mentioned above.

Chapter 14

Results Of The 3D Diamond Detectors Tested At CERN

This chapter shows the results of the 3D strip detectors Poly-3D, Full-3D, Multi-3D, and Irrad-3D introduced in section 4.3. All the detectors had square 3D cells and the Multi-3D had, additionally, hexagonal and rectangular 3D cells. These detectors were tested at CERN test beams as described in chapter 9. After defining the calibration constants for the electronics attached to each sensor, the regions of interest for each of the detectors are presented. Then, the results from all the 3D strip detectors with square 3D cells are shown, followed by the performance comparison of the efficiency and charge collection of the different 3D cell geometries in the Multi-3D sample. In the end, a validation of the simulation model and the experimental data is made.

14.1 Calibration Constants And Equivalent Noise Charge

As seen in section 4.1.1, The measured noise fluctuations in each of the 128 signal outputs of the VA ASIC[1] depend on the different ENC present in each of the 128 input channels of the VA chip. Therefore, it is expected that for the VA chip's channels that were not connected to the sensor ("non-connected"), the only noise source was the VA chip's intrinsic noise given by Equation 4.1a. Non-connected channels in each experiment should have noise fluctuations equivalent to 64 e, estimated from the given values by the manufacturer[92], as discussed in section 4.1.1. The setup had a peaking time of 1.8 µs, and the manufacturer does not give the ENC for that peaking time (i.e., only the ENCs of 60 e and 80 e are given for peaking times of 2 µs and 1 µs, respectively[93]). An uncertainty of 6 % was assumed to reflect this interpolation, such that the known value of an ENC of 60 e for a rise time of 2 µs, given by the manufacturer, lies within the uncertainty from the interpolated value of 64 e.

The calibration constants used to convert the measured pulse heights in ADC units into electrons depend on the specific VA chip and the digitizer used for each measurement. For this reason, one calibration constant was calculated for each VA chip wire bonded to each detector and for each digitizer. To find the calibration constants, the fluctuations of the pedestals for the

[1] The VA ASIC is the chip used to preamplify and shape up to 128 input signals as mentioned in section 4.1.

non-connected channels were fitted with Gaussian distributions for the central 98.8 % of the data, as shown in Figure 14.1. The fitted standard deviation was taken as the noise of the channel. The differences between the standard deviations for the same VA chip but different digitizers were between 1-1.3%. For this reason, it was decided to calculate a single calibration constant from the averaged noises for non-connected channels for every detector's VA chip, as seen in Table 14.1.

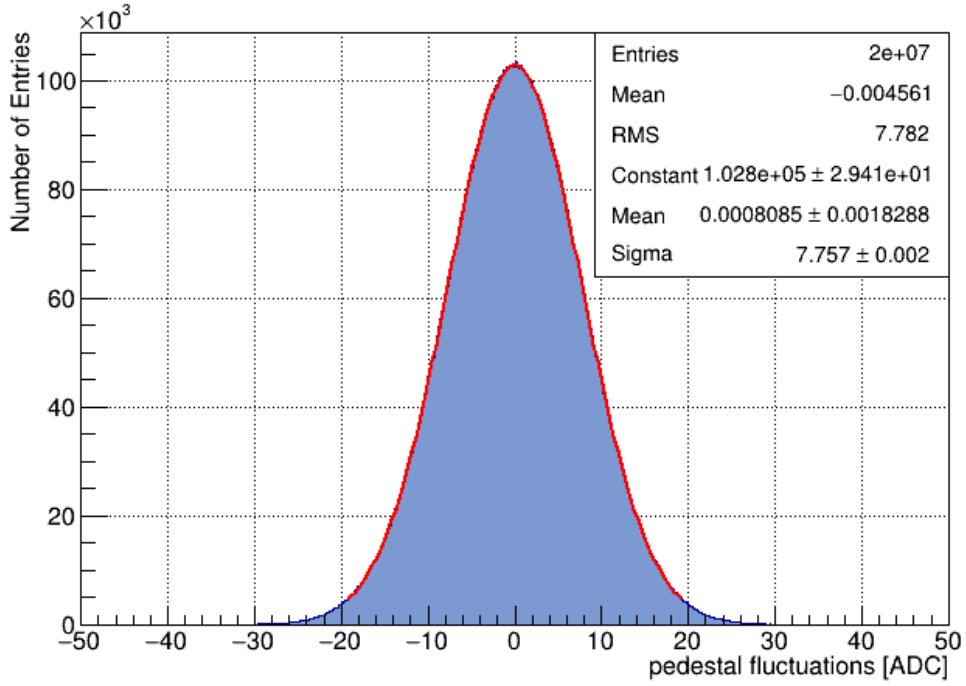

Figure 14.1: pedestal fluctuations for the non-connected channels of the VA chip for the Multi-3D device. The red curve is the fitted Gaussian distribution with $\sigma = 7.757(2)$ ADC.

Detector	Averaged Fitted Noise RMS (ADC)	Calibration constant (e/ADC)
Poly-3D	7.156(2)	9.94(55)
Full-3D	8.819(2)	9.28(58)
Multi-3D	7.814(2)	8.19(51)
Irrad-3D	6.794(1)	9.42(58)

Table 14.1: Calculated calibration constants for the non-connected channels for each detector.

Besides the non-connected channels, the noise of the connected channels to strips with 3D cells was measured to compare with the estimated values obtained by the simulations in chapter 7. For this task, the pedestal fluctuations for at least ten contiguous channels (seven for the Poly-3D that had less than 10 channels) connected to 3D cells were fitted with Gaussian distributions. It was required that the contiguous channels had roughly the same number of connected 3D cells with a tolerance of ±5 cells for the Full-3D (16 % tolerance) and the Irrad-3D (19 % tolerance)

that had many possible unconnected 3D cells. Other requirements were that selected channels be three strips away from the detector borders (except for Poly-3D and Multi-3D which had a reduced number of strips) and that the chosen runs had a leakage current below 1 nA.

The channel capacitance was obtained from the estimations in chapter 7. The number of cells and the type (i.e., squares, hexagonal, or rectangular) for each detector were chosen from the layouts shown in section 4.3. The total leakage current, which was below 1 nA for all the selected runs, was divided among the connected channels from the VA chip to the detector to estimate the leakage current of each channel. This assumes that each channel in the detector drew the same current. The biasing resistor used for the calculations was 100 MΩ. The resulting values are shown in Figure 14.2.

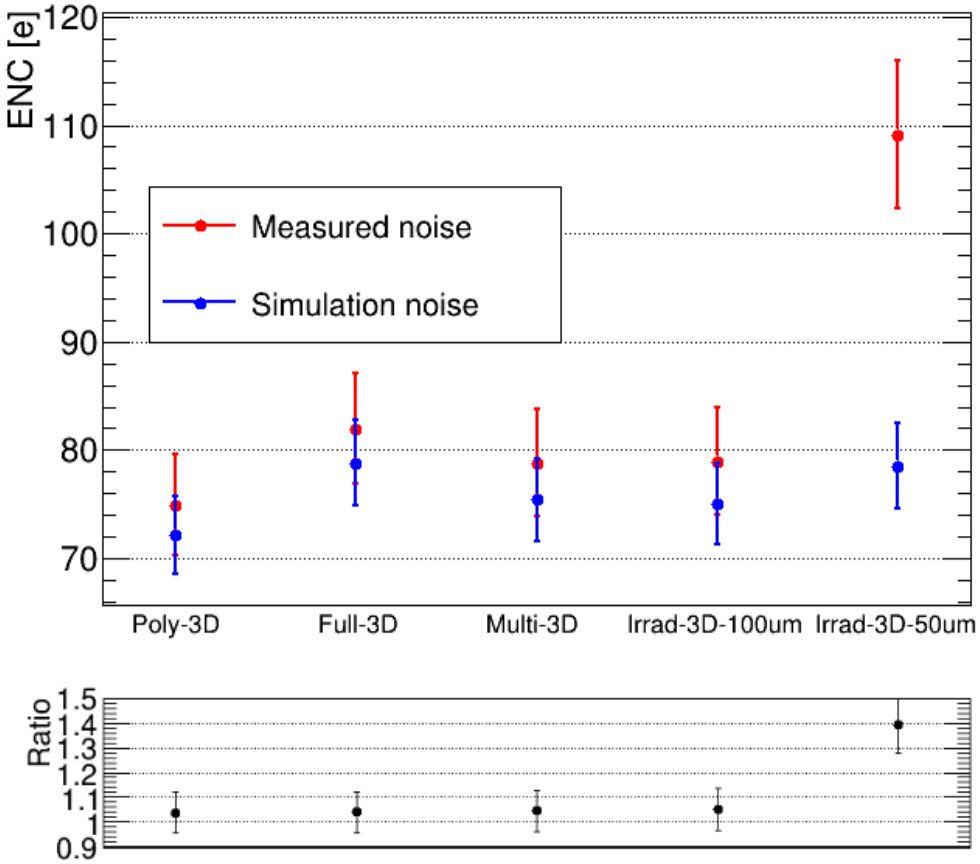

Figure 14.2: Comparison between the measured noise for each detector and the expected values from the simulations. The cell sizes of the square cells of the Poly-3D were 150 µm, and of the Full-3D and Multi-3D were 100 µm. The uncertainty for the measured noise comes from the uncertainty of the calibration constant presented in Table 14.1. The uncertainty for the expected values of the simulations originates from the variation of 5 % of the sensor's thickness used for the estimations.

The noise estimations for each detector agree within the uncertainties for the detectors Poly-3D, Full-3D, Multi-3D, and Irrad-3D-100 µm (the 100 µm cells part of the sample Irrad-3D;

see section 4.3.4). The absolute error between the measurements and the expected values for these detectors is less than 5 % and all the values lie within the uncertainties. All the noise estimations from the simulations underestimated the ENC extracted from the experimental data. This could emerge from underestimating the total capacitance in each channel, partly from stray capacitances not included in the calculations, such as the stray capacitance of the wire bonds. Additionally, the diameter of the 3D wires could have been larger than what was assumed in chapter 7. These factors would increase the capacitance in the input channels of the VA chip, which would increase the total ENC. On the other hand, it is also possible that the proportionality constant of 11.8 e/pF for the intrinsic ENC of the VA chip, discussed in section 4.1.1, could have been larger, which would increase the noise contribution from total capacitance connected to a channel in the VA chip.

For the case of the Irrad-3D-50 µm detector (the 50 µm cells part of the sample Irrad-3D), the disagreement between the measured and expected noise is 39 %. This is not well understood. The excess noise could not be attributed to the leakage current because it remained below 1 nA for the measured runs. Also, the estimated capacitance variations caused by differences in the diameter of the 3D wires fail to account for such a large discrepancy. To account for the measured noise, the capacitance should lie between [3.7-3.9]pF per strip, which would give a capacitance per cell between [138-140]fF. This value is 3.39 times the value estimated with the simulations of ~ 41 fF per cell for 50 µm square cells in section 7.2.3.

A possibility could be a local increase of the permittivity due to the fabrication of the 3D wires, which would only be significant for cell sizes of $O(50\,\mu m)$ or smaller. This increase in the permittivity would account for a larger capacitance than that estimated for diamond. Further studies of 3D detectors with cell sizes of 50 µm or smaller should be carried out to understand this result.

14.2 Regions Of Study

To assess the performance of the diamond 3D cells for each of the detectors, it was desired to select a region as large as possible without fabrication defects in order to obtain enough statistics. For the Full-3D detector, it was possible to use the photographs shown in Figure 14.3 to select the region of interest that avoided the defects observed in those photographs. An overlay of the pulse height map with the photographs of the identified crystallographic and metallization defects is shown in Figure 14.4. For the other samples, no problems were found in the metallization process.

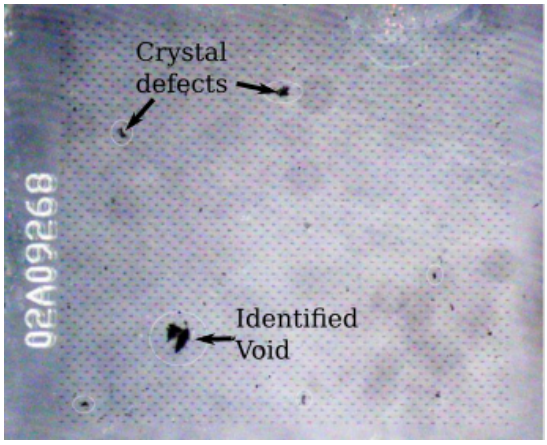

(a) Crystallographic defects observed from the substrate side of the diamond where the bias metallization was deposited[158].

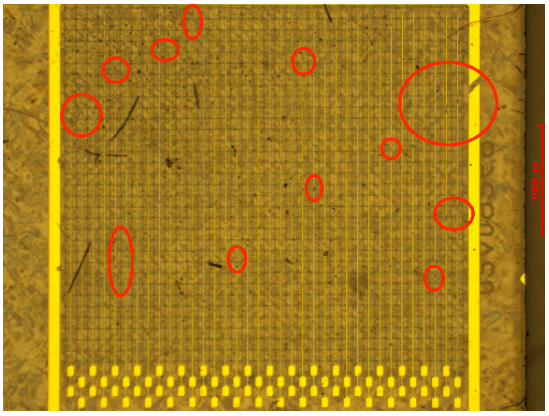

(b) Metallization defects on the growth side (i.e., opposite from growth side) of the diamond where the strip metallization for the channels was deposited.

Figure 14.3: Identified fabrication defects of the Full-3D sample. In (a), possible crystallographic defects are shown. In (b), the red circles identify possible breaks in the metallization pattern, causing multiple 3D sense wires to be disconnected in several channels.

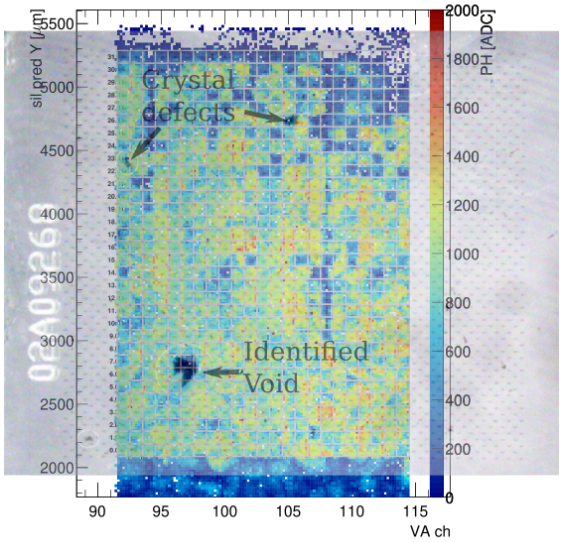

(a) Pulse height map overlaid with the identified crystallographic defects.

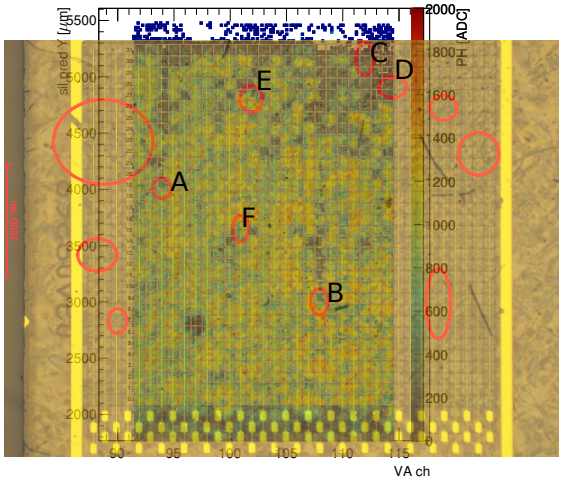

(b) Pulse height map overlaid with the identified metallization problems during fabrication.

Figure 14.4: Overlaid pictures with the pulse height maps of the Full-3D detector. In (a), The three identified crystallographic defects correspond to cells with low pulse height. In (b), the features marked with A, B, C, D, and E correspond to the identified metallization problems that cause low charge collection to the cells above each feature. The possible identified feature marked with an F did not seem to affect the charge collection of the strip.

Due to logistic issues during the Covid-19 pandemic from the laboratory at Ohio State University where the samples were kept, it was not possible to perform studies such as microscopy inspection or resistance measurements of the 3D wires to identify problematic 3D cells. Consequently, it was decided to identify possible defective cells using their collected charge.

As mentioned in section 11.10.4, cells with a problem in their 3D bias wire would exhibit an excess of negative charges for hits around the affected 3D bias wire, as shown in Figure 11.38. Issues with the readout 3D wire would manifest as a smaller charge in the cell. A threshold of five standard deviations below the average charge collected from the majority of cells was set to identify possible cells with problems in their readout 3D wire, as shown in Figure 11.41. The selected regions for the 3D detectors are shown in Figures 14.5 and 14.6.

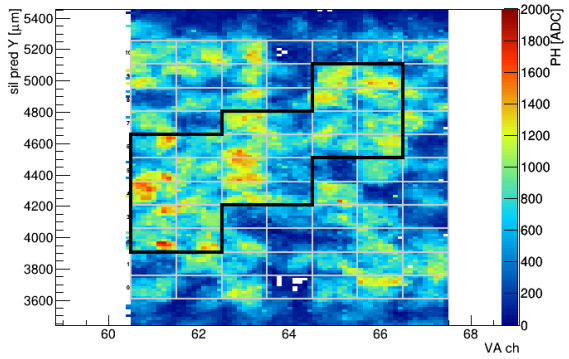

(a) Poly-3D 150 µm Squares Pulse Height Map.

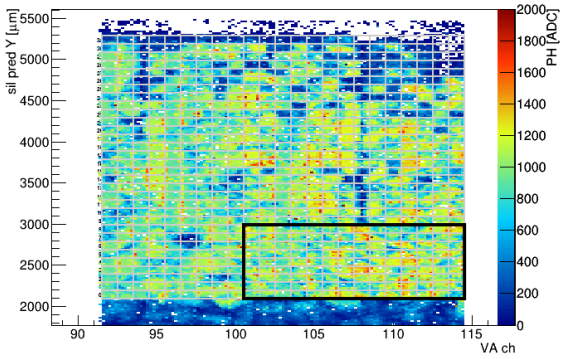

(b) Full-3D 100 µm Squares Pulse Height Map.

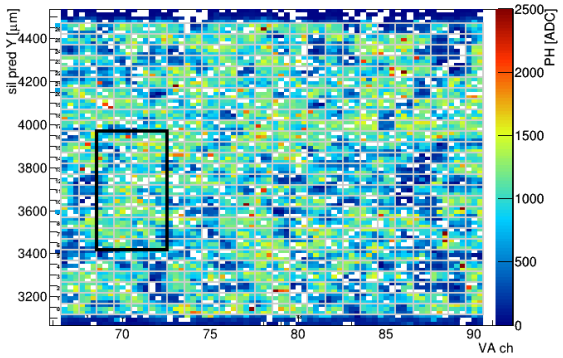

(c) Irrad-3D 50 µm Squares Pulse Height Map.

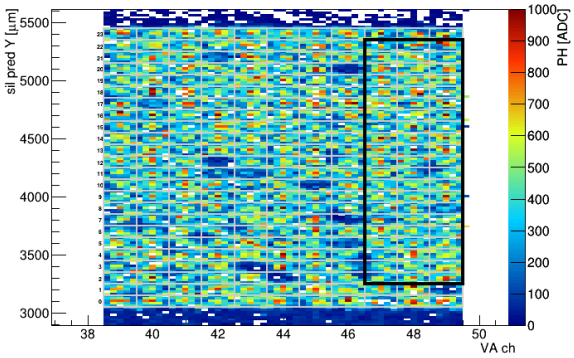

(d) Irrad-3D 100 µm Squares Pulse Height Map.

Figure 14.5: Pulse height maps and the fiducial regions enclosed with a black line for the Poly-3D (a), Full-3D (b), and Irrad-3D (c-d).

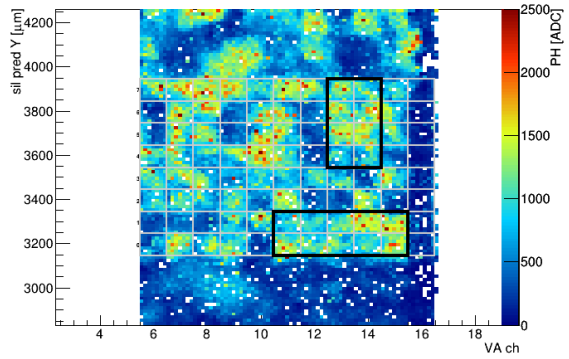

(a) Multi-3D 100 µm Squares Pulse Height Map.

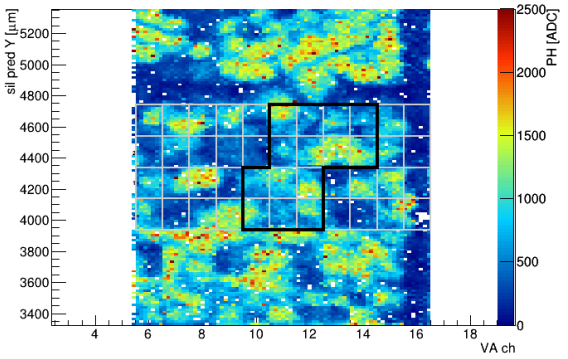

(b) Multi-3D Rectangles Pulse Height Map.

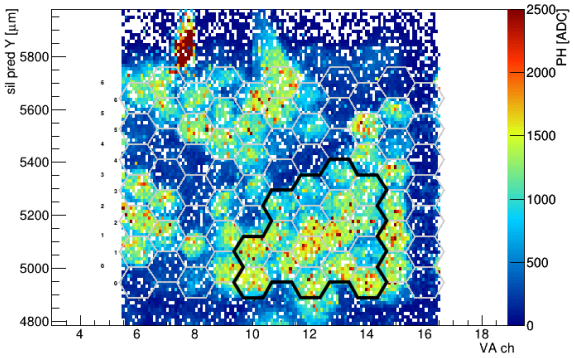

(c) Multi-3D Hexagons Pulse Height Map.

Figure 14.6: Average pulse height maps as a function of the predicted hit position and the fiducial regions enclosed with a black line for the Multi-3D detectors.

14.3 Excess Of Saturated Events In One Of The Digitizers

In section 11.1, it was discussed that the Sirocco 4 digitizer had an artificial saturation below the digitizer's real saturation, which reduced the dynamic range of the digitizer (see section 11.1). For this reason, after this revelation, the next test beams were taken with the other digitizer, Sirocco 5. Even though Sirocco 5 does not have an artificial saturation value like Sirocco 4, it was found in measurements of 3D cells biased with a positive voltage that there was an excess of real saturation events which did not happen for detectors biased with negative voltage.

The pulse height distributions of the square 3D cells in the Multi-3D detector biased with positive and negative voltages, shown in Figure 14.7, indicate a significant excess of saturated events forming a peak at ~ 2100 ADC (~ 17200 e) for the positive bias voltage. The negative bias voltage measurement does not have a noticeable peak caused by saturated events. The number of saturated events for the positive polarity was 1213, which accounts for 46 % of the events. This contrasts with the 24 saturated events (1 % of the events) measured with the negative bias polarity. The excess of saturation events raises the mean of the distribution by more than

400 ADC (~ 3300 e) for positive bias compared with the distribution for negative bias. Comparing the shape of the distributions when normalized to the MPV around 1000 ADC (~ 8200 e), it is clear that the positive polarity distribution has a deficit of events around 1500 ADC (~ 12300 e) which does not account for the total amount of saturated events around 2000 ADC (~ 16400 e).

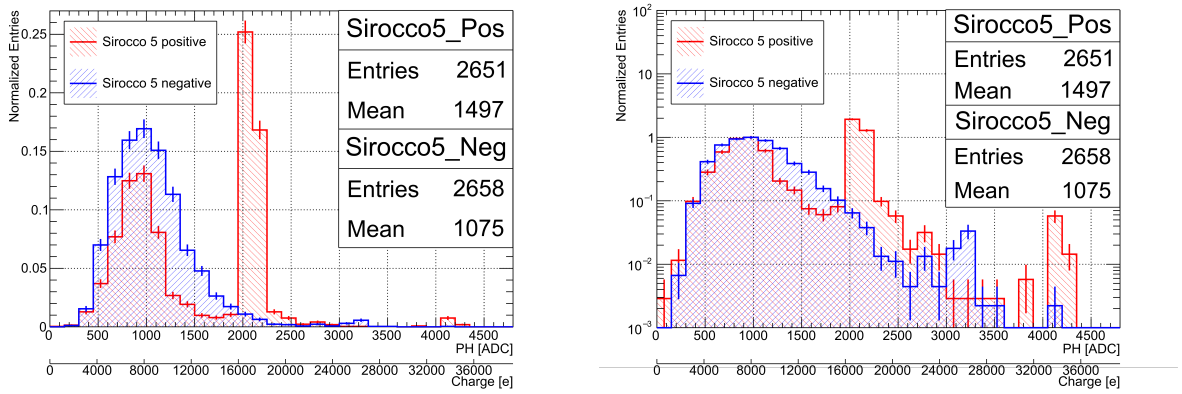

(a) Pulse height distributions normalized to the total entries.

(b) Pulse height distributions normalized to the MPV[2] around 1000 ADC.

Figure 14.7: Pulse height distributions normalized to the total entries (a) and the MPV around 1000 ADC (~ 8200 e) (b) for the 100 µm square 3D cells in the Multi-3D detector measured at the same voltage magnitude of 90 V but different polarities during the same test beam.

One hypothesis was that the excess of saturated events was a real effect caused by charge multiplication near the 3D wires and not a feature of the digitizer. To understand if this was a feature caused by the 3D wires in the 3D cells, measurements were taken using a scCVD diamond planar strip detector, and the same effect was seen as shown in Figure 14.8. The saturated events correspond to ~ 10 % of the data for the detector biased with negative bias polarity, while they correspond to more than 50 % when it is biased with positive polarity. The amount of saturated events for positive bias voltage exceeds that expected for the tail of a straggling distribution function. In contrast with the 3D detector in Figure 14.7, the distributions normalized to the MPV around 1600 ADC for the scCVD diamond planar strip detector for both polarities match, except for the number of saturated events around 2500 ADC. The significant difference in the generation of the pulse height distributions between the 3D and the planar detectors is that the transparent clusters in the 3D detectors account for at most two channels. In comparison, the planar detectors account for up to five channels. This means the charge is spread into more channels in the preamplifier in planar detectors than in 3D detectors. This suggests that part of the excess of saturated events is due to the lower dynamic range available for positive polarity than for negative polarity. Still, it is not completely understood why measuring the data with the digitizer Sirocco 5 with positive bias polarity produces a large number of saturated events compared to data generated with negative bias polarity. For this reason, it was decided to only focus on measurements made with negative bias voltages for the data taken with the digitizer Sirocco 5.

To study the agreement between the data measured with Sirocco 4 and Sirocco 5, the data

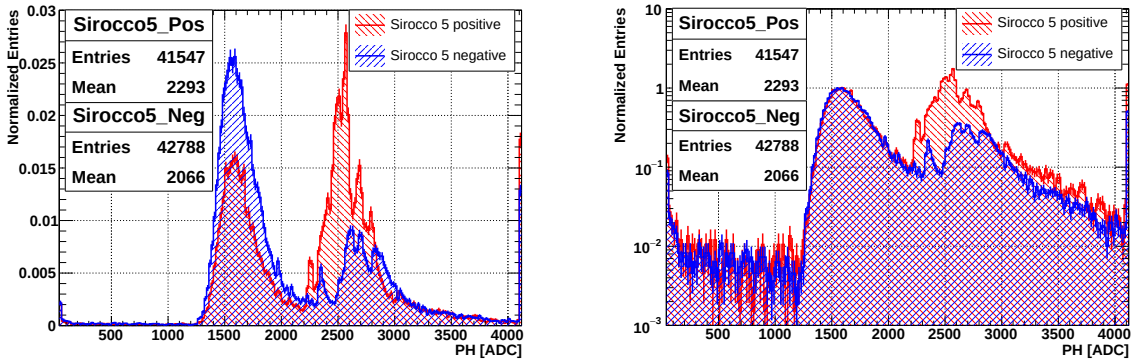

(a) Pulse height distributions normalized to the total entries.

(b) Pulse height distributions normalized to the MPV around 1600 ADC.

Figure 14.8: Pulse height distributions normalized to the total entries (a) and to the MPV around 1600 ADC (b) for a ~ 500 µm thick scCVD diamond planar strip detector measured with a voltage magnitude of 500 V with the same digitizer, Sirocco 5.

measured with both bias polarities with Sirocco 4 in 2016 and the data taken with negative polarity with Sirocco 5 in 2018 were compared. Figure 14.9 shows the comparison of the extracted pulse height distributions for the Multi-3D square cells with positive bias and digitized with Sirocco 4, negative bias and digitized with Sirocco 4, and negative bias and digitized with Sirocco 5.

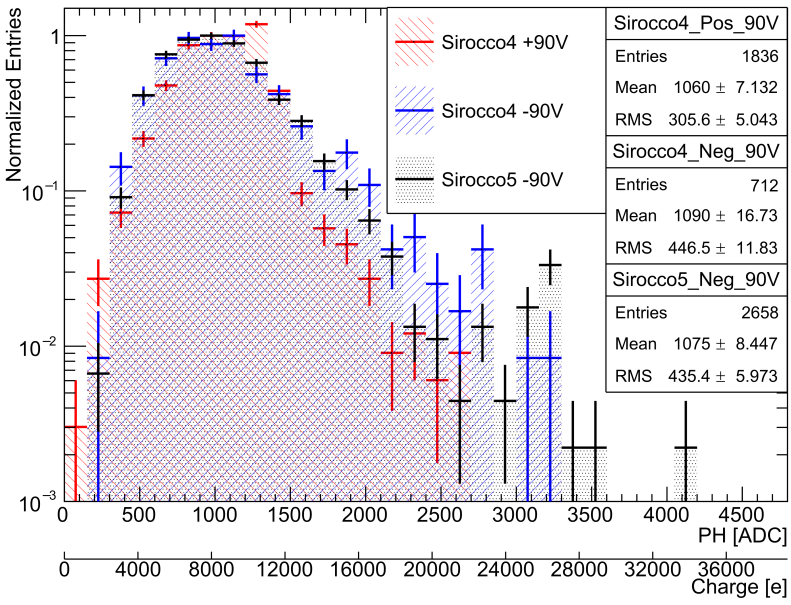

Figure 14.9: Pulse height distributions for the square cells in Multi 3D biased with a voltage of 90V with different digitizers and bias polarities.

The pulse height distributions for the same bias voltage but different polarities and digitizers are very similar. The most significant difference arises from the different dynamic ranges available to the digitizers, which causes the saturation peaks to occur at different pulse heights. Table 14.2 summarizes the comparison between the three distributions. The last two columns show the percentage difference between the data taken with different polarities and digitized with Sirocco 4, and the percentage difference between the data taken with the negative polarity and digitized with different digitizers. In Sirocco 4, the percentage difference between the data measured with positive and negative polarity is 2.8(17) %. In contrast, the percentage difference between the data measured with negative polarity and different Sirocco digitizers is 1.4(17) %, which suggests there is no difference for measurements made with the same voltage but different digitizers.

	$\langle PH_{4+} \rangle$ (ADC)	$\langle PH_{4-} \rangle$ (ADC)	$\langle PH_{5-} \rangle$ (ADC)	$\frac{\lvert PH_{4+} - PH_{4-} \rvert}{\langle PH_4 \rangle}$	$\frac{\lvert PH_{4-} - PH_{5-} \rvert}{\langle PH_- \rangle}$
Multi-3D Squares $\lvert V_{bias} \rvert = 90\,V$	1060(7)	1090(17)	1075(8)	2.8(17) %	1.4(17) %

Table 14.2: Extracted values from Figure 14.9. PH_{4+}, PH_{4-}, and PH_{5-} correspond to the pulse heights digitized by Sirrocco 4 with a positive bias, Sirocco 4 with a negative bias, and Sirocco 5 with a negative bias, respectively. The size of the squares in the Multi-3D detector was 100 µm. The last two columns show the percentage difference between the data taken with both polarities in Sirocco 4, and the percentage difference between the data taken with negative bias in Sirocco 4 and 5.

14.4 Comparing Different Geometries With Different Bias Voltages

In planar diamond detectors, the bias voltage and the thickness of the sensor are sufficient to describe the conditions of the almost uniform electric field profile generated across the sensor. This information is crucial for the transport characteristics of the generated charges as their drift velocity depends on the electric field, as mentioned in section 2.5.2. For 3D detectors, it is not enough to give the biasing voltage and the thickness of the sensor. The electric field inside a 3D cell is not uniform, and the field strength depends on various geometric parameters such as the shape of the cell, the diameter of the 3D wires, the distance between the bias 3D wires and the readout 3D wires, and the bias voltage used on the 3D bias wires.

To compare the different 3D detector geometries and detector types, it was necessary to consolidate all the parameters that would affect the general transport of the charges inside the detectors. If most of the region within a cell has a low electric field, the drift velocities of the ionized charges are, on average, low, inducing a smaller current in the readout electrodes before being trapped. If, on the other hand, most of the region within a cell has a large electric field, then the drift velocities of the ionized charges are, on average, large, inducing a larger current

in the readout electrodes before being trapped. Consequently, a cell that, on average, has a larger electric field is expected to collect, averaging over the whole cell, more charge than a cell with, on average, a smaller electric field. Following this reasoning, it was decided to compare the results as a function of the expected average electric field magnitude inside the cell. The expected average electric fields were calculated from simulations using the 3D cells' dimensions and the applied bias voltages.

Taking into account a discrepancy between the estimated value for the diameter of the 3D wires in the detectors presented in this work (2.6 µm[113]) and the estimation in the literature from similar detectors (O(2 µm)[100]), an uncertainty of 20 % was set on the diameter of the 3D wires. This uncertainty gives a maximum variation of 6 % on the calculated average electric field inside the whole cell. The estimated average electric field for the different geometries and voltages can be seen in Table 14.3.

Cell geometry	DUT	Distance between readout and bias 3D wires (µm)	Voltage (V)	Average E. Field (V/µm)
Square	Poly-3D	106.1	70	0.292(18)
Square	Full-3D	70.7	15	0.104(6)
Square	Irrad-3D	70.7	30	0.208(12)
Square	Full-3D, Irrad-3D	70.7	45	0.312(19)
Square	Full-3D, Irrad-3D	70.7	60	0.416(25)
Square	Full-3D, Multi-3D	70.7	75	0.520(31)
Square	Full-3D, Multi-3D	70.7	90	0.623(37)
Square	Multi-3D	70.7	105	0.727(44)
Square	Irrad-3D	35.4	30	0.506(30)
Square	Irrad-3D	35.4	45	0.759(46)
Square	Irrad-3D	35.4	60	1.013(61)
Rectangle	Multi-3D	111.8	75	0.346(21)
Rectangle	Multi-3D	111.8	90	0.416(25)
Rectangle	Multi-3D	111.8	105	0.485(29)
Hexagon	Multi-3D	66.6	75	0.559(34)
Hexagon	Multi-3D	66.6	90	0.671(40)
Hexagon	Multi-3D	66.6	105	0.783(47)

Table 14.3: Average electric field according to simulations for different geometries and different voltages. The 3D wires' diameter for all 3D cells is assumed to be 2.6 µm. The uncertainties in the average electric field correspond to a 6 % variation obtained from a 20 % variation on the 3D wires' diameter.

14.5 Test Beam Results For Square Cells

All the tested detectors had a region consisting of square cells. The differences between them were the different pCVD diamonds used as sensors and the geometries of the square cells. Figure 14.10 shows the efficiency map for the set threshold of 200 ADC (1856(116) e) for the Full-3D (100 µm squares) when biased with 60 V, generating an average electric field of 0.416 V/µm inside the 3D cells. This efficiency map and the efficiency maps for the other 3D strip detectors can be found in Appendix I. It can be seen that almost all the detector has efficiencies above 90 %. The selected region for the studies is highlighted by the red lines that depict the cells of the fiducial region.

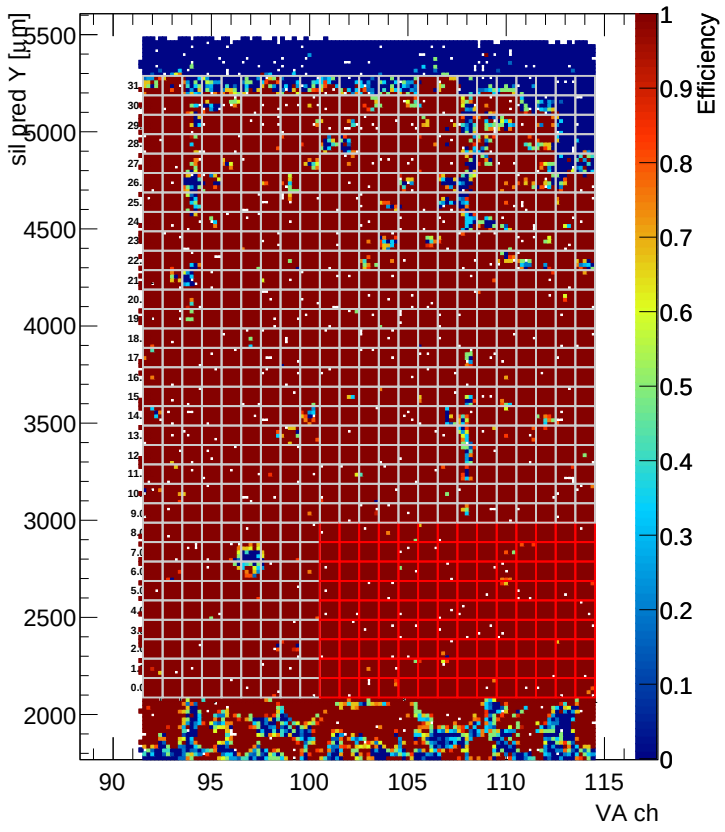

Figure 14.10: Efficiency map of the Full-3D detector biased with 60 V. The gray lines depict the location of the 3D cells, and the bright red lines highlight the 3D cells selected for the analysis.

Figure 14.11 shows the efficiency of the square 3D cells, and also of the planar strip section present in the Multi-3D device, with a threshold of a pulse height of at least 200 ADC. This threshold is larger than the ~ 1500 e threshold used for the pixel detectors' configuration, as described in section 10.2.1.

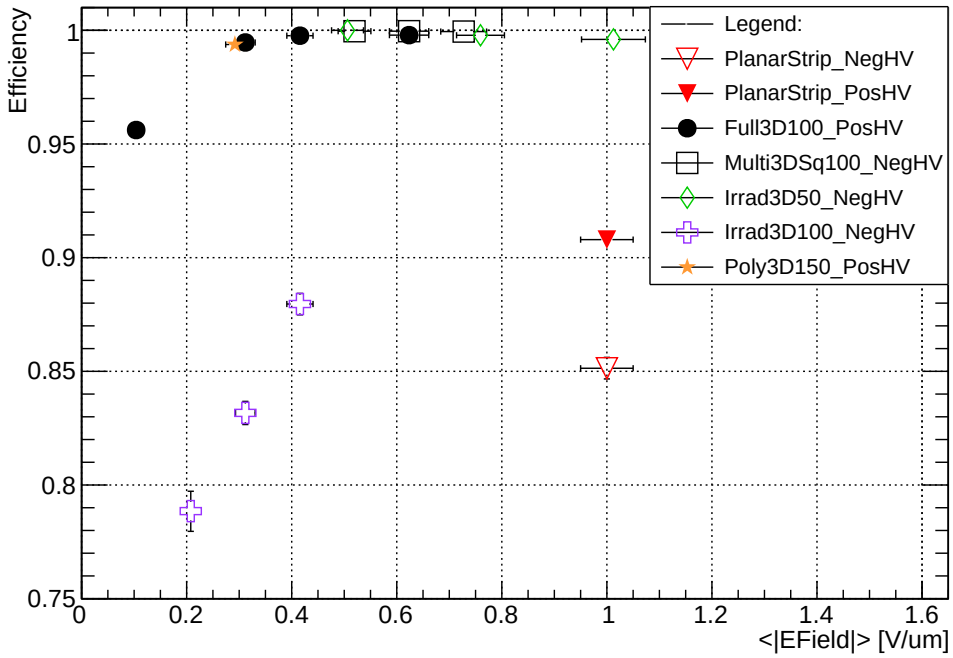

(a) Efficiencies for all the square 3D cells.

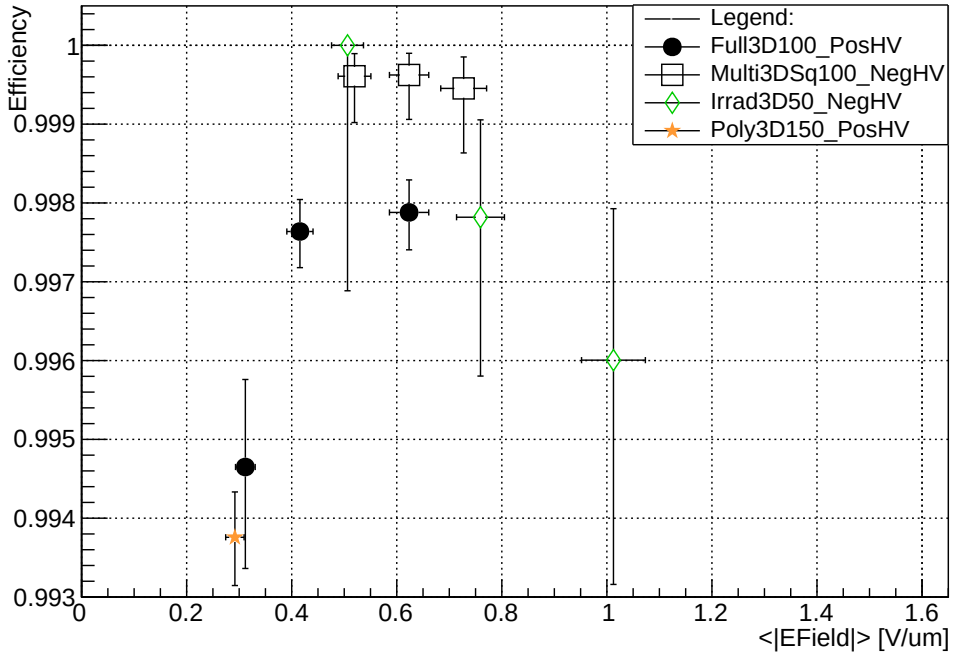

(b) Zoom into the efficiency area above 99 % for the square 3D cells.

Figure 14.11: Efficiencies of all the square 3D cells in the 3D detectors. The filled markers represent the 3D cells biased with a positive voltage, while the open markers represent the 3D cells biased with a negative voltage. Along the 3D cells, the efficiencies for the planar strip detector present in the Multi-3D sample are also presented for comparison.

The efficiency for non-irradiated diamonds plateaus above 99.5 % at average electric fields higher than 0.5 V/µm. For the Irrad-3D sample, which was irradiated to a fluence of 3.5×10^{15} p/cm^2, an average electric field of ~ 0.4 V/µm was not enough to achieve 90 % efficiency for the 100 µm cells, while for the 50 µm cells, an average electric field of 0.5 V/µm was sufficient for achieving 100 % efficiency.

All the sizes of non-irradiated square 3D cells were more efficient than the planar strip section in the Multi-3D device. This highlights the advantage of 3D over planar detectors for pCVD diamonds. For cells with efficiencies above 99 %, increasing the electric field inside the 3D cells above 0.7 V/µm decreases the efficiency. However, this might be an artifact of the small number of statistics, as suggested by the error bars.

The efficiency of a cell is related to its collected charge. The collected charge as a function of the average electric fields is seen in Figure 14.12. The vertical black error bars in the figures correspond to the statistical uncertainties, while the vertical red error bars correspond to the systematic uncertainty from the calibration constants.

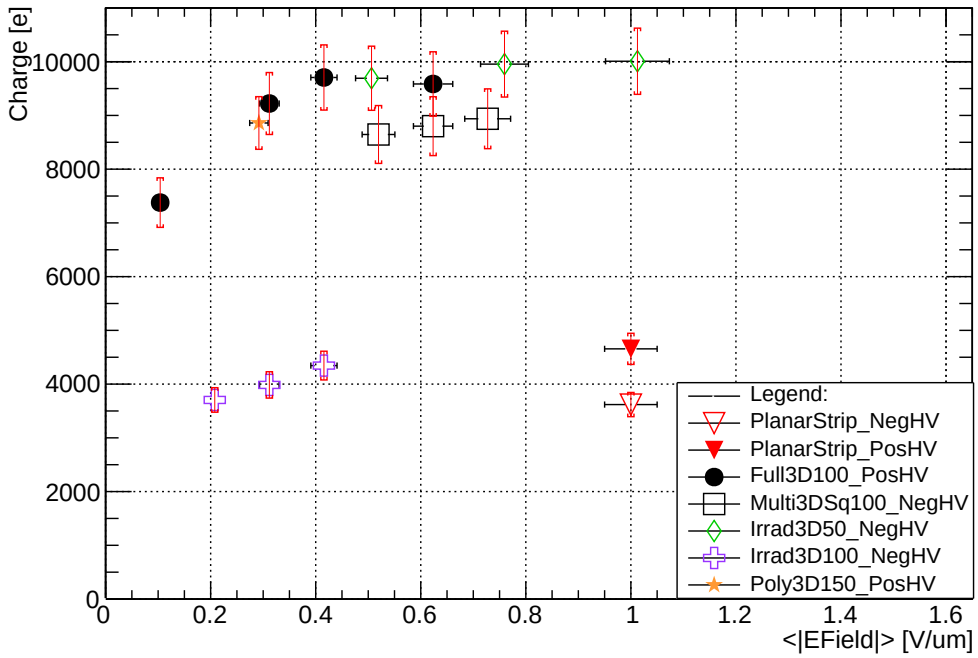

Figure 14.12: Average charge collection in the selected fiducial regions for the square 3D cells in the Poly-3D, Full-3D, Multi-3D, and Irrad-3D detectors at different bias voltages and hence different cells' average electric field. The results for the charge collection for the planar strip detector present in the Multi-3D are shown for comparison. The black error bars depict the statistical uncertainty of the mean, while the red error bars depict the systematic uncertainty from the charge calibration.

Also seen in Figure 14.12, is a comparison of the collected charge of 3D square cells with the collected charge of the planar strip section of the Multi-3D detector, which was biased with

500 V. Besides the 100 µm cells from the Irrad-3D detector, all the cells collect more charge than the planar part of the Multi-3D.

The Full-3D detector plateaus at an average electric field above 0.4 V/µm, while the Multi-3D detector, which has the same size of 100 µm for the square cells as the Full-3D, did not reach its maximum charge collection with an average electric field of 0.73 V/µm. The Poly-3D detector, which had cell sizes of 150 µm, collected a similar charge to the Full-3D detector under a similar average electric field, and a similar charge to the Multi-3D detector at a larger average electric field. These variations suggest a strong dependence on the specific pCVD diamond used as a sensor.

For the Irrad-3D, the section of the detector with 100 µm cells seemed to be under-biased and was not yet at maximum charge collection. Nevertheless, they were comparable with the planar section of the Multi-3D detector. On the other hand, the 50 µm cells of the Irrad-3D device plateaued at an average electric field of 0.76 V/µm, and despite having been irradiated with 800 MeV/c protons to a fluence of 3.5×10^{15} p/cm^2, they collected more charge than the other square 3D cells of larger sizes.

14.6 Comparison Of Different 3D Cell Geometries

The Multi-3D sample had different detector geometries, including three 3D cell geometries and a planar strip detector. The 3D cell geometries consisted of square, rectangular (nonsquare), and hexagonal cells (see section 4.3.3). The squares had a side length of 100 µm, while the rectangular cells had dimensions of 100 µm×200 µm. The hexagonal cells were regular hexagons with the same perimeter as the square cells of 400 µm. As mentioned before, the planar strip part of the sample was kept at a voltage magnitude of 500 V which generated an average electric field of 1 V/µm, while the 3D cells were measured at different bias voltages, as shown in Table 14.3. Figure 14.13 shows the pulse height distributions for the different types of detectors and geometries in the Multi-3D when the 3D cells were biased with −90 V.

Although the Multi-3D sensor in the past had a reported measurement of the CCD[3] of 245 µm (a CCE[4] of 49 %) at a bias voltage of 500 V, the measured CCD at the same bias voltage in the planar section of the Multi-3D detector during the test beams in this thesis was closer to 115 µm (a CCE of 23 %). It is unknown why the collected charge was less than 50 % of the previously reported value for the sensor.

[3]Charge collection distance
[4]Charge collection efficiency

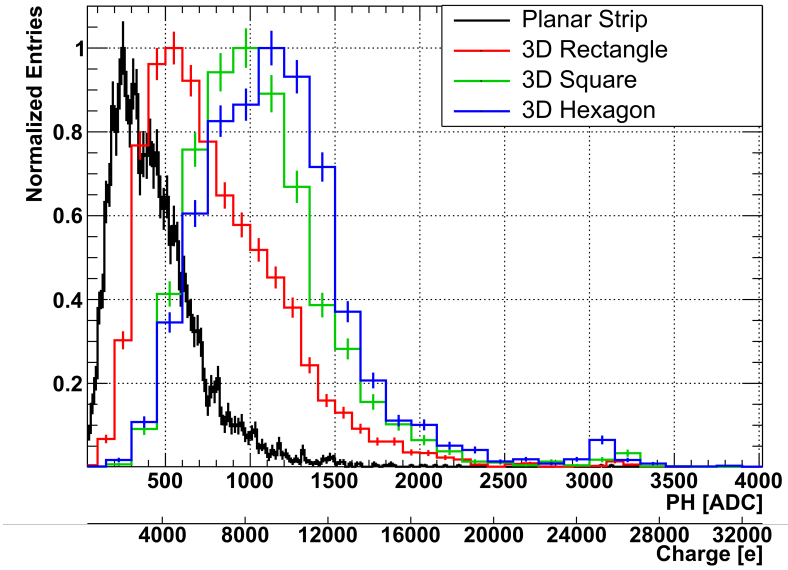

Figure 14.13: Pulse height distributions, normalized to the peak, of the 3D cells with different geometries of the Multi-3D biased with −90 V and the planar strip part of the Multi-3D with −500 V. These voltages generate an average electric field of 1 V/µm, 0.42 V/µm, 0.62 V/µm, and 0.67 V/µm for the planar strips, rectangular cells, square cells, and hexagonal cells, respectively.

In the test beam results used in this thesis, all the 3D cells collected more charge than the planar strip part of the Multi-3D detector, and the hexagons collected, on average, more charge than the other geometries. Table 14.4 shows the ratio of the average charge collection of the different 3D cell geometries with respect to the planar strip detector.

Geometry	Average E. Field (V/µm)	$\frac{\langle Q_{3D} \rangle}{\langle Q_{planar_{test\ beam}} \rangle}$	$\frac{\langle Q_{3D} \rangle}{\langle Q_{planar_{reported}} \rangle}$
Rectangle	0.416(25)	1.83(2)	0.86(1)
Square	0.623(37)	2.43(3)	1.14(1)
Hexagon	0.671(40)	2.64(3)	1.24(1)

Table 14.4: Average pulse height ratios of the 3D cells for different geometries with respect to the average pulse height of the planar strip detector. The third column is the ratio using the CCE measured during the test beams in this thesis, while the fourth column is the ratio using the previously reported CCE of the sample. The 3D cells were biased with 90 V, while the planar strip detector was biased with 500 V which gives an average electric field of 1 V/µm.

The charge collection is consistently the highest for hexagonal cells and lowest for rectangular cells, as shown in Figure 14.14, where this feature holds for the different values of average electric fields in the measured cells.

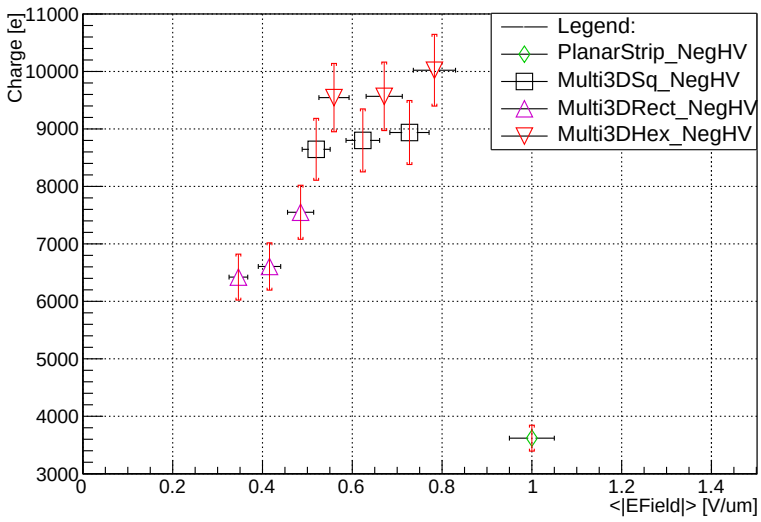

Figure 14.14: Collected charges of the different 3D cell geometries present in the Multi-3D sample, and the planar strip part of the Multi-3D.

As shown in Figure 14.15, although the hexagonal cells collect, on average, more charge than square cells, the square cells have the highest efficiency. This can be seen in the shape of the pulse height distributions in Figure 14.13, where the hexagonal cells have slightly more events for pulse heights below 500 ADC (~ 4100 e) than the square cells. Nevertheless, the efficiencies of the hexagonal and the square cells are the same within the statistical uncertainties. Both geometries show a small inefficiency.

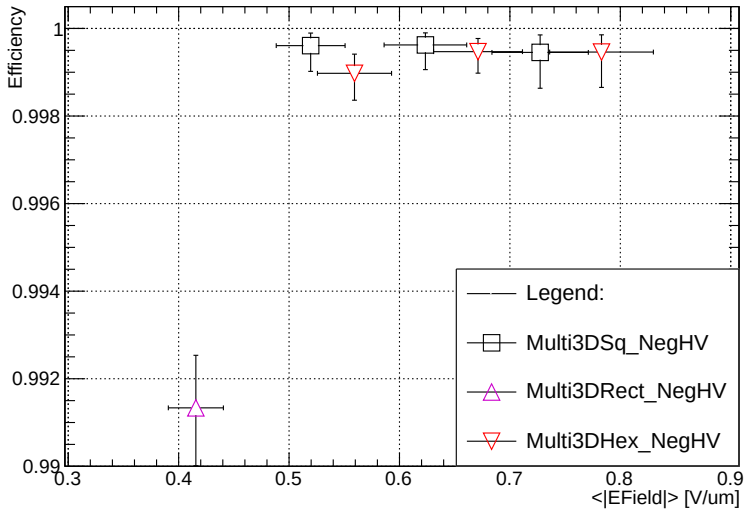

Figure 14.15: Efficiencies of the different 3D cell geometries present in the Multi-3D sample.

Figure 14.16 shows the location of the events with pulse heights below 500 ADC (~ 4100 e),

which also include the inefficient regions below the 200 ADC (~ 1600 e) threshold, in both square and hexagonal cells inside the analysis regions. It can be seen that the events with pulse heights below 500 ADC (~ 4100 e) are not a general feature of all the selected cells and that they are localized towards the edges of the cells, where the low electric field regions are located.

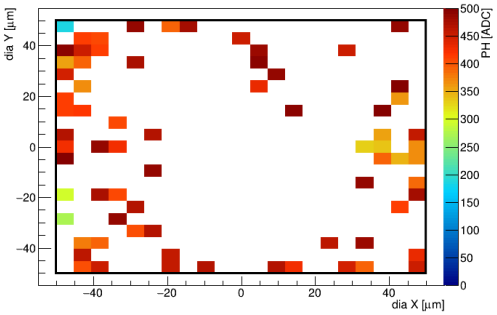

(a) Locations of the low pulse height events in the 3D square cells.

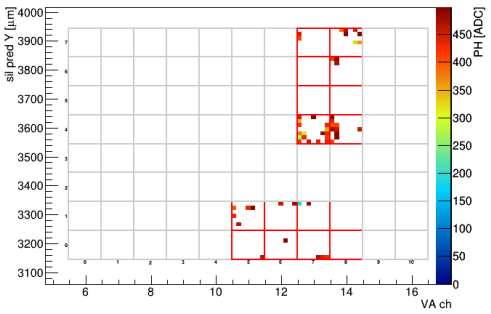

(b) Locations of the low pulse height events in the 3D square cell part of the Multi-3D detector.

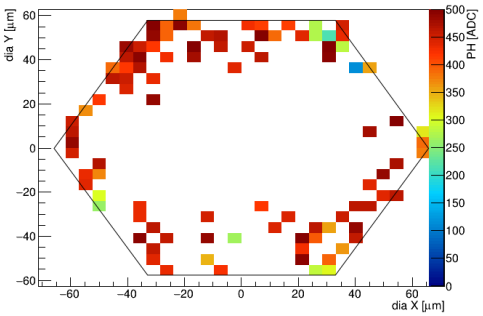

(c) Locations of the low pulse height events in the 3D hexagonal cells.

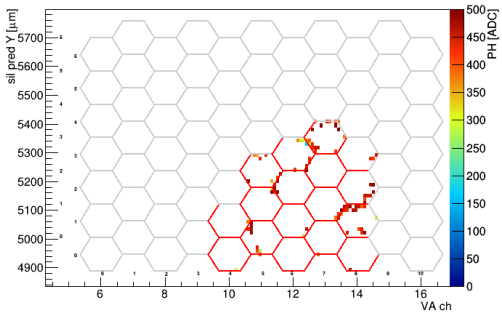

(d) Locations of the low pulse height events in the 3D hexagon cell part of the Multi-3D detector.

Figure 14.16: Localization of the pulse heights lower than 500 ADC (~ 4100 e) for square cells (a-b) and hexagonal cells (c-d). The events are localized towards the edges and are not a feature of all the cells.

14.7 Simulation Model Comparison With 3D Detectors

The simulation model, described in chapter 8, was shown in an example to be accurate in describing the charge collection and the transient currents of planar detectors. In this section, the results of the model are compared with the measured results for the collected charge from the square 3D cells. The simulated detectors described in section 8.3 are a non-irradiated pCVD 3D detector (*Poly*), an irradiated pCVD 3D detector with a fluence of $O(3 \times 10^{15}\,\mathrm{p/cm^2})$ with 800 MeV/c protons (*I-Poly*), and a highly irradiated pCVD 3D detector with a fluence of $O(10^{16}\,\mathrm{p/cm^2})$ with 800 MeV/c protons (*HI-Poly*). The I-Poly is taken to be equivalent to the Irrad-3D detector measured in this thesis. Although the Poly simulation is intended to represent

the square cells in a pCVD diamond 3D detector such as the Multi-3D detector, it is worth noting that the "life-path" parameter used for the simulation was from the expected "life-path" for a standard pCVD diamond and not the one extracted from the Multi-3D sensor. This is because of the abovementioned disagreement between the previously reported CCD on the sample used for the Multi-3D detector and the CCD measured in this thesis of the planar section of the Multi-3D detector.

As discussed in section 8.3, the variable "life-path" (λ_p) was used, which models the average distance traveled by the charge carriers by drift and diffusion before being trapped by defects. It was tuned with measurements of irradiated pCVD diamonds planar detectors performed by the RD42 collaboration[64]. This approach assumes that the MFP before trapping of the charge carriers (λ) is the same when traveling parallel to the grain boundaries in the diamond (as happens in planar detectors) as when traveling perpendicular to the grain boundaries (as happens in 3D detectors[27]).

Using the expected number of eh-pairs generated by a MIP shown in Table 2.1 (36 eh – pairs/µm), setting the thickness of the detector "Th" to the values shown in Table 4.3 and using the simulated value for the CCE[5] shown in Table 8.7, the total collected charge Q_{coll} for the simulated devices was calculated as described in Equation 14.1.

$$Q_{coll} \cong \text{Th} \cdot \text{CCE} \cdot 36\,\text{eh} - \text{pairs}/\mu\text{m} \tag{14.1}$$

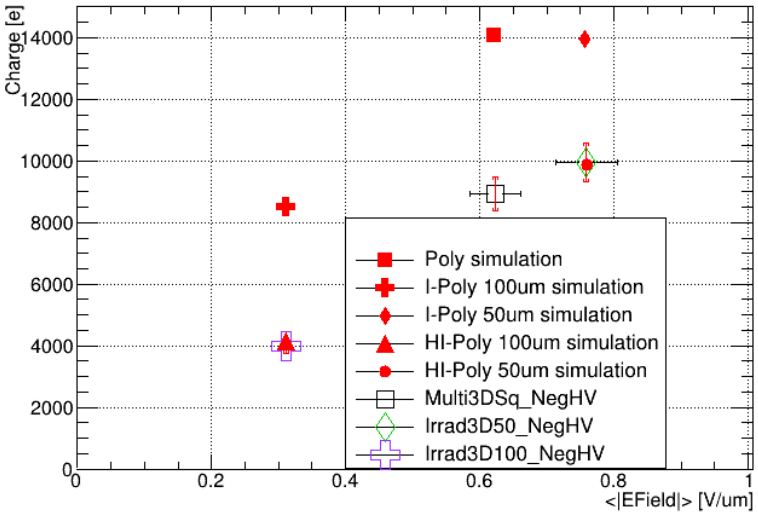

Figure 14.17: Simulated collected charges (solid red markers) and the measured collected charges for the Multi-3D (size of 100 µm) and Irrad-3D detectors (open markers). Both regions of the Irrad-3D detector, the 50um and 100um square cells, are shown. The size of the cells for the Poly simulation was 100 µm

The resulting collected charges for the simulations, compared with the measured charges for the detectors mentioned above, are shown in Figure 14.17. It can be seen that there is an

[5]Charge collection efficiency

overestimation of the collected charge by the simulation model. The I-Poly-100 µm is 113.3 % above the Irrad-3D-100 µm, the Poly is 57.5 % above the Multi-3D, and the I-Poly-50 µm is 40.3 % above the Irrad-3D-50 µm. Instead of an agreement between the simulated I-Poly with the Irrad-3D detector, there seems to be an agreement between the HI-Poly and the Irrad-3D detector. Besides the average collected charge agreement between the simulated HI-Poly and the measured Irrad-3D detector, the charge maps for the different channels in the transparent cluster also agree, as seen in Figure 14.18. In that figure, it can be seen that the ratio between the color scale for positive and negative charges is the same as for the color scale in the measured results, which indicates an agreement between the distribution of charges in the simulated model with the measured data.

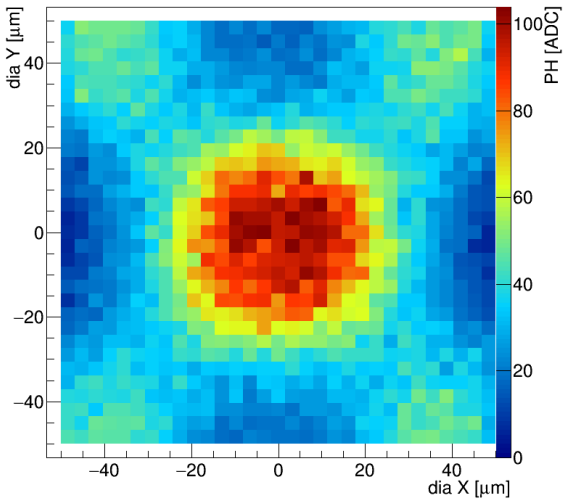

(a) Measured Irrad-3D Pulse Height of Ch0.

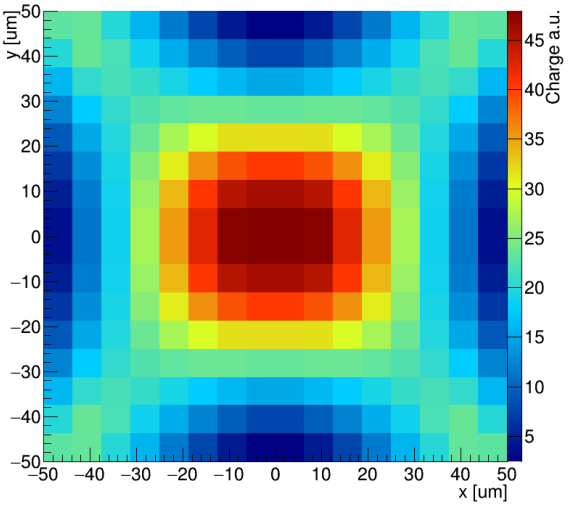

(b) Simulated HI-Poly Charge of Ch0.

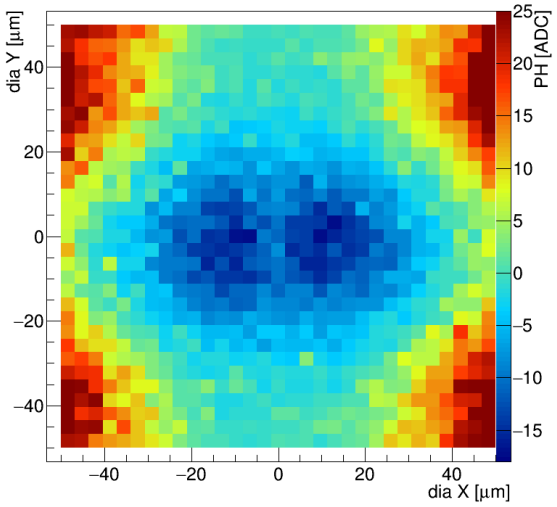

(c) Measured Irrad-3D Pulse Height of Ch1.

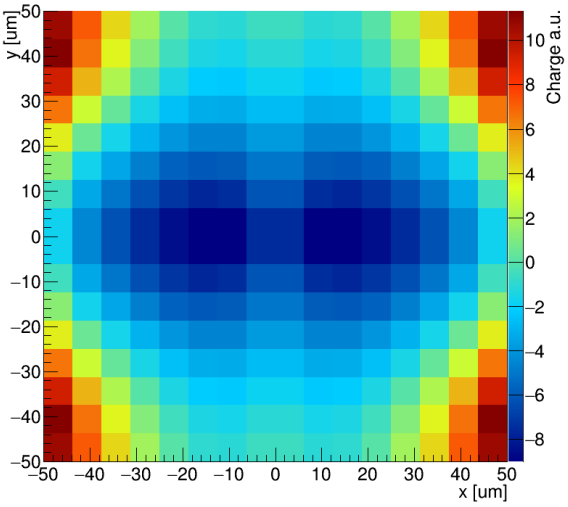

(d) Simulated HI-Poly Charge of Ch1.

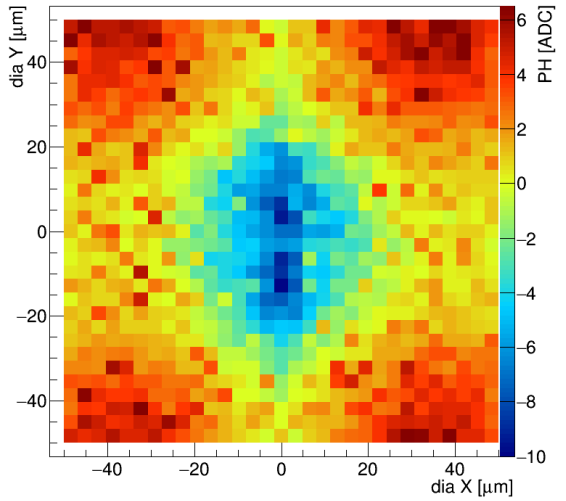

(e) Measured Irrad-3D Pulse Height of Ch2.

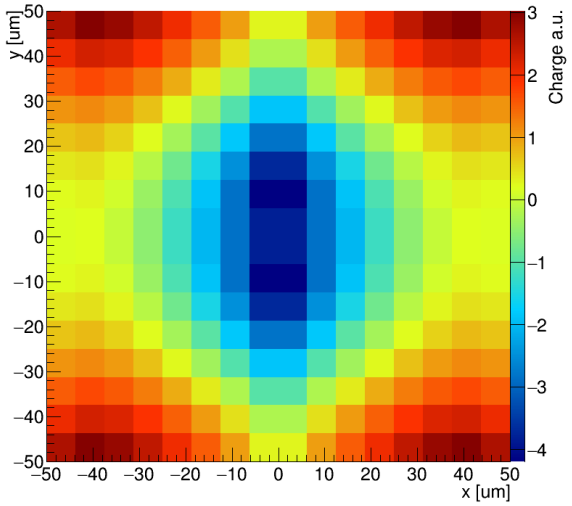

(f) Simulated HI-Poly Charge of Ch2.

Figure 14.18: Comparison between the charge collected by the 100 µm cells of the Irrad-3D sample biased with 45 V and the simulation of the HI-Poly detector biased with 45 V. The plots represent the amount of charge collected by the three channels in the transparent cluster (Ch0, Ch1, and Ch2 as defined in section 8.3.1) depending on where the ionizing particle hits the 3D cell. In (a) and (b), the charge collected by Ch0 is displayed. In (c) and (d), the charge collected by Ch1 is shown. In (e) and (f), the charge collected by Ch2 is shown.

The agreement between the simulation and the measured data suggests that the parameters used to simulate the HI-Poly detector are similar to the parameters of the Irrad-3D detector measured, and it seems that the chosen "life-path" (λ_p) to describe the HI-Poly detector gives the same result as the Irrad-3D detector. This suggests that the MFP before trapping for the charge carriers are different for charges moving along the crystal's growth direction and for charges moving across the grain boundaries. This agrees with observations made by S. Lagomarsino et al. which suggest different mean free paths for charge carriers moving across the grain boundaries[159, 160]. In the case of the measured Irrad-3D detector, the life-path of 55 µm (or a MFP $\lambda_{e,h} = 26.5\,\mu m$) for electrons and holes better describe the measured results instead of the expected life-path of 145 µm (or $\lambda_{e,h} = 69.75\,\mu m$), which describes the radiation damage for charge carriers moving parallel to the grain boundaries.

Following the model presented by S. Lagomarsino et al.[159, 160], the total MFP before trapping λ is given by two independent components: λ_0, which accounts for the natural defects and radiation damage of the sensor, and λ_g, which represents the trapping caused by the grain boundaries. The relation for the total MFP before trapping would be:

$$\frac{1}{\lambda_{\{e,h\}}} = \frac{1}{\lambda_{0_{\{e,h\}}}} + \frac{1}{\lambda_{g_{\{e,h\}}}} \tag{14.2}$$

As both formulations for the MFP before trapping and the life-path follow the same probabilistic approach (i.e., both are modeled with exponential distribution functions) and their

difference lie in whether or not the diffusion contribution is taken into account, a modeling for an effective life-path, as the one presented by S. Lagomarsino et al.[159, 160], is introduced:

$$\frac{1}{\lambda_{p_{\{e,h\}}}} = \frac{1}{\lambda_{p0_{\{e,h\}}}} + \frac{1}{\lambda_{pg_{\{e,h\}}}} \tag{14.3}$$

, where λ_p is the effective life-path, λ_{p_0} accounts for defects and radiation damage, and λ_{p_g} accounts for the trapping due to the grain boundaries.

The value for λ_{p_0} would be the previously assumed value for the life-path for the modeling with only one parameter. Using the data shown in Figure 14.18, the effective parameter λ_p is tuned with the one-parameter model, until the simulated collected charge matches the measurements. With the effective parameter λ_p and the parameter due to initial and radiation crystallographic damage λ_{p_0}, the value for λ_{p_g} can be found using Equation 14.3. The calculated λ_g and λ_{p_g} for electrons and holes for the Multi-3D and the Irrad-3D are shown in Table 14.5.

	Mean Free Path			Life-path		
Detector	$\lambda_{\{e,h\}}$	$\lambda 0_{\{e,h\}}$	$\lambda g_{\{e,h\}}$	$\lambda_{p_{\{e,h\}}}$	$\lambda_{p0_{\{e,h\}}}$	$\lambda_{pg_{\{e,h\}}}$
Multi-3D	52.7 µm	115.0 µm	97.2 µm	107 µm	350 µm	154 µm
Irrad-3D	26.5 µm	72.5 µm	41.8 µm	55 µm	145 µm	88.6 µm

Table 14.5: Calculated MFP parameters for electrons and holes for the detectors Multi-3D and Irrad-3D using the data shown in Figure 14.17 in Equations 14.2 and 14.3.

The results of the simulation using two life-path parameters (λ_{p_0} and λ_{p_g}) are shown in Figure 14.19. The simulations lie within 6 % of the measured values for the Multi-3D and the Irrad-3D detectors when modeled with two life-path parameters: one for natural and irradiation traps (λ_{p_0}) and another one for the grain boundaries (λ_{p_g}).

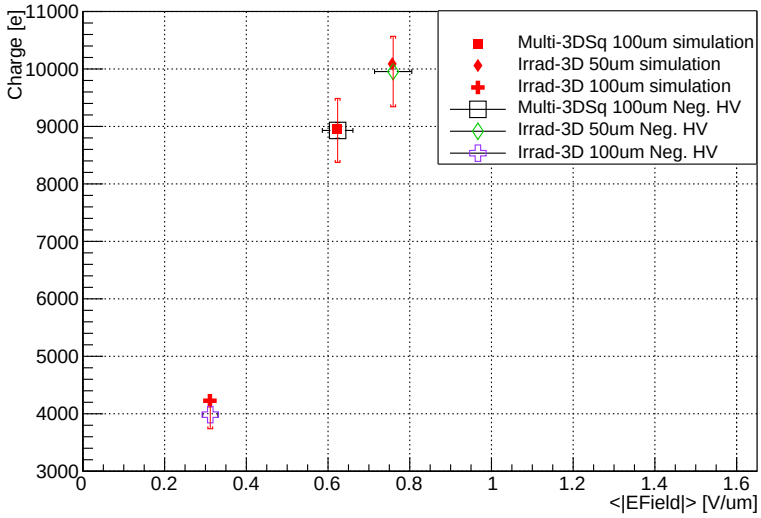

Figure 14.19: Simulated collected charges using two life-path constants (solid red markers) and the measured collected charges for the Multi-3D and Irrad-3D detectors (open markers).

Part VIII

Conclusions, Outlook And Summary

Chapter 15

Conclusions And Outlook

This thesis presents two projects in the context of diamond detector research and development. The first one focused on developing a fabrication process to produce pixel diamond detectors that could be scaled for mass production, which would be required if a tracking detector is made with diamonds in the future. It was found that using a contact metallization based on Ti/Al was as good as the traditional RD42 metallization of Cr/Au. The Ti/Al metallization was needed to correctly form the In bumps to bump-bond the sensor with the readout chip. The developed fabrication process was documented in detail, and five prototypes were fabricated following this process. Under microscope inspection, two of them were identified to have over 99.7 % yield of good pixels (samples CMS01 and II6-93), and one had a yield of 95.5 % (CMS04). The two remaining samples had a problem during the first metallization that went unnoticed. Consequently, for these samples, the yield of good pixels was 85 % for sample II6-750 and 34.2 % for sample CMS02. The identified problems in the fabrication could be avoided by spending more time between fabrication steps, checking for errors, and repeating the steps that had issues. The working pixels of the five sensors were successfully bump-bonded to the readout chips and tested at different voltages and particle rates. Under the tested conditions, the working pixels' performance was comparable to previous detectors tested by the RD42 collaboration under similar conditions, suggesting that the fabrication process was successful in producing working pixel particle detectors.

Different tools such as frames were designed to scale up the fabrication process and process a diamond sensor with the size of a full module comprised of 16 readout chips. Future work should focus on using the designed frames to process samples with the size of the complete modules, and test the resulting detector with a Sr90 source or in a test beam.

The second project focused on the research of 3D detectors fabricated by the RD42 collaboration. For this task, four samples were tested using CERN's H6A beamline. An analysis framework was developed to target individual cells in the samples. It was determined that 3D cells in the shape of hexagons collect more charge than 3D cells with rectangular or square shapes. The square and hexagonal 3D cells in the tested Multi-3D device had efficiencies above 99.9 % for thresholds similar to the ones available in current state-of-the-art readout chips used in pixel detectors (i.e. $\sim 1500\,\mathrm{e}$). Additionally, it was found that the irradiated device, Irrad-3D, up to a fluence of $3.5 \times 10^{15}\,\mathrm{p/cm^2}$ 800 MeV/c protons are above 99.6 % efficient with the same threshold mentioned before for square cells with a side length of 50 µm. The studied devices

found that the Irrad-3D devices with 50 µm cells and the non-irradiated diamonds with 100 µm cells reached charge collection efficiencies of more than 50 %.

Using the data from the test beams, a simulation framework based on first principles using COMSOL Multiphysics[112] was developed. It was possible to estimate the capacitance of the 3D strip detectors within 5 % except for the 50um cells present in the Irrad-3D detector. The estimations of the capacitance underestimated the measurements by 39 %. This large capacitance could potentially limit the applications of diamond 3D detectors. For this reason, it would be desired to understand this result.

The findings of S. Lagomarsino et al.[159, 160], in which charge carriers moving across the grains in pCVD diamonds have a shorter mean free path than if they move parallel to the grains, support the findings observed when comparing the simulation predictions with the measured data in the test beams. Implementing the modeling proposed by S. Lagomarsino et al. of introducing another mean free path constant for charge carriers moving against the grains into the simulation model, replicated the experimental data of the square cells of the Multi-3D detector and from the Irrad-3D within 6 %. It would be interesting that future studies characterize a 3D detector before and after irradiation, to see how the two mean free paths proposed by S. Lagomarsino et al. change with irradiation.

Chapter 16

Summary

The need to fabricate reliable particle detectors that can perform well detecting charged particles in high radiation environments has led to the research of different alternatives, including using diamonds as the sensing material. Two goals were set in this thesis to push forward the feasibility of using diamond sensors for future particle detectors: To develop a fabrication process that could be scaled up to mass-produce diamond planar pixel detectors and to model and understand the signal characteristics from diamond 3D detectors.

For the first objective, a fabrication process was developed using the laboratory facilities at IBM's BRNC and PSI's CMS Pixel group. The fabricated detectors were studied optically and were tested in test beams at PSI. The following findings were made:

- The developed fabrication process for diamond planar pixel detectors, based on the techniques used to fabricate silicon planar pixel detectors, successfully produced five prototypes. Four of the five prototypes were successfully tested.
- There is no significant difference in the charge collection between diamond planar detectors fabricated with the traditional Cr/Au metallization used by the RD42 collaboration and those fabricated with Ti/Al metallization.
- The fabrication process developed in this thesis gave a yield for pixels of 99.7 %.
- The average collected charge of the successfully tested prototypes fabricated in this thesis agrees with previous measurements of the charge collection performed on the diamonds before they were exposed to the fabrication processes described in this thesis.
- The measured rate dependence below 5 % of the average collected charge of the fabricated diamond planar pixel detectors in this thesis agrees with previous measurements performed by the RD42 collaboration.

A simulation framework was developed for the second goal using first principle simulations based on FEM and Monte Carlo methods in the software COMSOL Multiphysics V.6.0[112]. The simulation framework was used to understand the charge collection of diamond 3D strip detectors tested in test beams at CERN. With the simulation framework and the experimental measurements made in CERN, it was shown that:

- Although the simulation framework with one trapping mechanism of the charge carriers was able to reproduce the charge collection of diamond planar detectors, it failed to model the charge collection of pCVD diamond 3D strip detectors correctly.
- To correctly model the charge collection in pCVD diamond 3D strip detectors, it is necessary to use two independent trapping mechanisms of the charge carriers: One that models the trapping caused by intrinsic defects and irradiation defects in the diamond sample, and another that models the trapping caused for moving across the grain boundaries of the diamond. This is in agreement with the modeling proposed by S. Lagomarsino et al.[159, 160].
- Although it was possible to model the electronic noise measured in the experiments by estimating the capacitance of most of the tested diamond 3D detectors, it was not possible to model the noise measured experimentally in the 50 µm square cells in an irradiated pCVD diamond. It is unknown why this cell geometry in an irradiated sample has 1.39 times the estimated noise.
- All the tested non-irradiated pCVD diamond 3D strip detectors collect more charge than their planar counterpart.
- All the tested non-irradiated pCVD diamond 3D strip detectors with a threshold above 1500 e reached efficiencies above 99 % for charged particle detection.
- 100 µm square 3D cells in an irradiated pCVD diamond up to a fluence of 3.5×10^{15} p/cm^2 with 800 MeV/c protons are inefficient detecting charged particles with a threshold of ~ 1500 e (efficiency below 90 %). They collect as much charge as non-irradiated pCVD diamond planar strip detectors.
- 50 µm square 3D cells in an irradiated pCVD diamond up to a fluence of 3.5×10^{15} p/cm^2 with 800 MeV/c protons collect as much charge as 100 µm square 3D cells in non-irradiated pCVD diamonds. They have an efficiency above 99 % for particle detection with a threshold above 1500 e.
- Hexagonal 3D cells are the best geometry for making pCVD diamond 3D detectors as they collect the most charge, followed by square 3D cells. Rectangular (non-square) 3D cells are the worst geometry tested in this thesis in terms of charge collection and efficiency in detecting charged particles.

Part IX

Appendix

Appendix A

VA Chip Noise Calculations

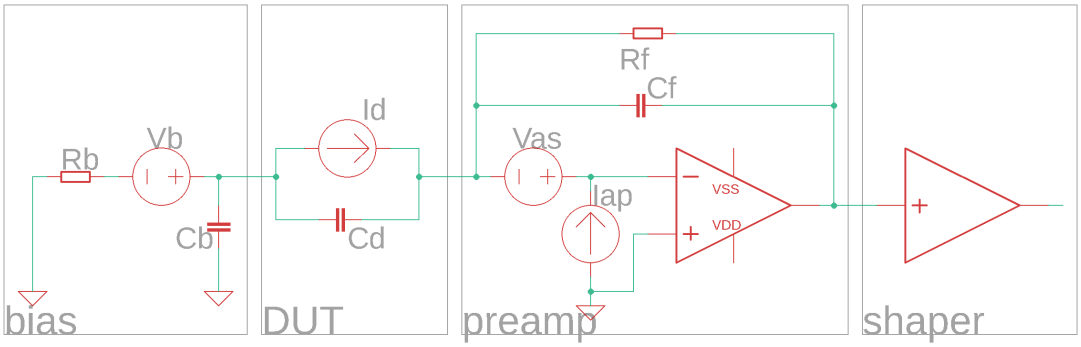

Figure A.1: Schematic circuit with the different components that affect the noise in the VA.

To calculate the ENC for the bias resistor R_b and the leakage current of the detector I_d, it is possible to consider the effects of each source independently as the assumptions are that each noise source is independent from each other and that there are no correlations between them. This means that the other noise sources different from the one being evaluated are "turned off", which means short-circuit between the terminals for voltage sources, and an open-circuit between the terminals for current sources.

These two noise sources have a "white" frequency distribution which means that the power spectrum density for every frequency is a constant. The power distribution spectrum of the detector leakage current (I_d) is referred to as shot noise, while the power distribution spectrum of the resistor (R_b) is referred to as thermal noise and they are the following[87]:

$$i_d^2 = 2qI_d \tag{A.1a}$$

$$v_b^2 = 4k_B T R_b \tag{A.1b}$$

In general, for the noise source n, the output signal from the preamplifier in the frequency domain $V_{p_n}(\omega)$ is calculated. Using the shaper's transfer function $H(s)$ (see Equation A.2a), it is

possible to calculate the total shaped integrated RMS noise V_{s_n} as follows:

$$H(s) = \frac{s\tau_0 A}{(1+s\tau_0)^2} \tag{A.2a}$$

$$|H(\omega)|^2 = \frac{\omega^2\tau_0^2 A^2}{\left(1+\omega^2\tau_0^2\right)^2} \tag{A.2b}$$

$$V_{s_n} = \sqrt{\int_0^\infty \left|H(f)\right|^2 V_{p_n}^2(f)\,\mathrm{d}f} = \sqrt{\int_0^\infty |H(\omega)|^2 V_{p_n}^2(\omega)\,\frac{\mathrm{d}\omega}{2\pi}} \tag{A.2c}$$

The resulting ENC_n for the noise source n is the ratio between the total shaped integrated RMS noise V_{s_n} with the shaped signal of a known charge, multiplied by the known charge in the input of the preamplifier. This value is usually given in terms of the electron charge q. For this reason it is useful to calculate the signal as a function of a charge of one electron. This expression is shown in equation A.3, where the total charge of 1 electron charge q gives a pulse height signal PH_{1q}, and the total shaped integrated RMS noise for the source n is V_{s_n}.

$$ENC_n = q\frac{V_{s_n}}{PH_{1q}} \tag{A.3}$$

To calculate PH_{1q} we consider the effect of a charge of q as input to the preamplfier. The preamplifier integrates the charge of one electron and gives, as a result, a step function with a voltage equal to the ratio between the electron charge q and the preamplifiers feedback capacitor C_f. The output in the s plane is therefore the multiplication of the step function with the transfer function of the shaper $H(s)$. The output signal in the time domain can then be calculated by applying the inverse Laplace transform:

$$V_{s_{1q}}(s) = \frac{q}{C_f}\cdot\frac{1}{s}\cdot H(s) \tag{A.4a}$$

$$V_{s_{1q}}(t) = \mathscr{L}^{-1}\left\{\frac{q}{C_f}\cdot\frac{1}{s}\cdot\frac{s\tau_0 A}{(1+s\tau_0)^2}\right\}(t) \tag{A.4b}$$

$$V_{s_{1q}}(t) = \frac{qAe^{-t/\tau_0}}{C_f}\left(\frac{t}{\tau_0}\right) \tag{A.4c}$$

As the signal sampled by the VA is the peak from the signal curve, searching for the maximum for this curve by differentiation gives that the peak time $T_p = \tau_0$. Therefore the peak height for the signal output for one electron charge is:

$$PH_{1q} \equiv V_{s_{1q}}(\tau_0) = \frac{q}{C_f}\cdot\frac{A}{e} \tag{A.5}$$

For the bias resistor R_b, using the thermal noise in Equation A.1, the preamplified voltage

$V_{p_{R_b}}$ and its corresponding mean squared are:

$$V_{p_{R_b}}(s) = -\frac{C_d}{C_f} \cdot \frac{v_b}{1 + sR_b(C_b + C_d)} \tag{A.6a}$$

$$\left|V_{p_{R_b}}(\omega)\right|^2 = \frac{C_d^2}{C_f^2} \cdot \frac{v_b^2}{1 + \omega^2 R_b^2 (C_b + C_d)^2} = \frac{C_d^2}{C_f^2} \cdot \frac{4k_B T R_b}{1 + \omega^2 R_b^2 (C_b + C_d)^2} \tag{A.6b}$$

In the limit, when $C_b >> C_d$, $V^2_{p_{R_b}}$ becomes:

$$\left|V_{p_{R_b}}(\omega)\right|^2 \cong \frac{C_d^2}{C_f^2} \cdot \frac{4k_B T R_b}{1 + \omega^2 R_b^2 C_b^2} \tag{A.7}$$

As for the detector's leakage current I_d, using the shot noise in Equation A.1, the preamplified voltage $V_{p_{I_d}}$ and its corresponding mean squared are:

$$V_{p_{I_d}}(s) = -\frac{i_d}{sC_f} \cdot \frac{1 + sC_b R_b}{1 + sR_b(C_b + C_d)} \tag{A.8a}$$

$$\left|V_{p_{I_d}}(\omega)\right|^2 = \frac{i_d^2}{\omega^2 C_f^2} \cdot \frac{1 + \omega^2 R_b^2 C_b^2}{1 + \omega^2 R_b^2 (C_b + C_d)^2} = \frac{2qI_d}{\omega^2 C_f^2} \cdot \frac{1 + \omega^2 R_b^2 C_b^2}{1 + \omega^2 R_b^2 (C_b + C_d)^2} \tag{A.8b}$$

Which in the limit, when $C_b >> C_d$, $V^2_{p_{I_d}}$ becomes:

$$\left|V_{p_{I_d}}(\omega)\right|^2 \cong \frac{2qI_d}{\omega^2 C_f^2} \tag{A.9}$$

Using Equations A.7 and A.9 in Equation A.2c, setting $C_b R_b >> \tau_0$, and having that $T_p \equiv \tau_0$ as mentioned above, the RMS output from the shaper due to the thermal noise from the resistor R_b, and due to the shot noise from the leakage current I_d are:

$$V_{s_{R_b}} \cong \frac{AC_d}{C_f(C_b R_b + \tau_0)} \sqrt{\frac{k_B T R_b \tau_0}{2}} \cong \frac{AC_d}{C_b C_f} \sqrt{\frac{k_B T \tau_0}{2R_b}} = \frac{AC_d}{C_b C_f} \sqrt{\frac{k_B T T_p}{2R_b}} \tag{A.10a}$$

$$V_{s_{I_d}} \cong \frac{A}{2C_f} \sqrt{qI_d \tau_0} = \frac{A}{2C_f} \sqrt{qI_d T_p} \tag{A.10b}$$

With these quantities, the ENC for the bias resistor R_b and the leakage current I_d can be calculated using Equations A.5 and A.3:

$$ENC_{R_b} \cong e \frac{C_d}{C_b} \sqrt{\frac{k_B T T_p}{2R_b}} \tag{A.11a}$$

$$ENC_{I_d} \cong \frac{e}{2} \sqrt{qI_d T_p} \tag{A.11b}$$

Appendix B

Chemical cleaning

In order for a diamond to be suitable for sensor fabrication, it was necessary that its surface was as clean as possible to prevent impurities affecting the fabrication process which could hinder the carbide formation between the diamond and the metallization which is desired form a good ohmic contact between the diamond and the metallization. The first step of the cleaning was done by using hot acids.

The following chemical cleaning recipe has been used by the RD42 collaboration as a standard to clean the diamonds before any fabrication process performed in the clean room. The acids used for this process are the following:

- Chromium(III) acid ($Cr_2O_3 \cdot H_2SO_4$ saturated solution)
- Aqua regia $(HCl : HNO_3)_{vol} = 3 : 1$
- Diluted aqua regia $(H_2O : HCl : HNO_3)_{vol} = 1 : 1 : 1$
- Nitrating acid $(HNO_3 : H_2SO_4)_{vol} = 2 : 3$
- Piranha solution 5:1 $(H_2SO_4 : H_2O_2)_{vol} = 5 : 1$
- Piranha solution 1:1 $(H_2SO_4 : H_2O_2)_{vol} = 1 : 1$

A quartz beaker was filled with 100 mL of one of the acids listed above. The diamonds were placed inside a quartz container and submerged inside the beaker with the acid. The beaker with the container was placed on top of a hotplate to bring the acid to a boil. The beaker and the container were left in each boiling acid for 10 min. Afterwards, the beaker containing the acids with the quartz container and the diamond samples were taken away from the hot plate and left outside for cooling for 5 min on top of a quartz container, which had the bottom covered with paper to avoid strong thermal shock that could break the beaker. Between each acid treatment, the samples were rinsed with deionized water. The order of the acids in the cleaning recipe was the following:

1. Chromium(III) acid
2. Aqua regia

3. Nitrating acid
4. Piranha solution 5:1
5. Diluted aqua regia
6. Nitrating acid
7. Piranha solution 1:1

Afterwards, optic inspection with a microscope was performed to assess the results from the cleaning. If any residue was left on the surface of the diamond (see Figure B.1), the cleaning steps above 1 through 7 were repeated.

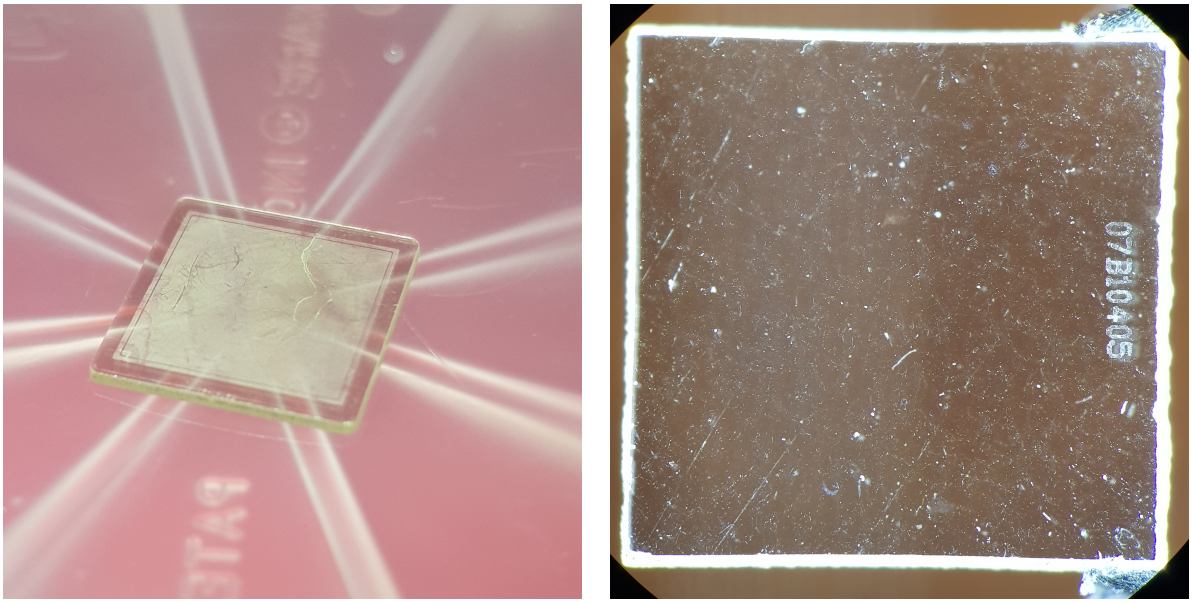

(a) sample with residue after one cleaning procedure (b) sample with a clean surface after a cleaning procedure

Figure B.1: (a) After a cleaning procedure, a gray-green residue on the surface of the diamond was present, which corresponded to a remnant of the carbide from a previous metallization. After a second cleaning procedure, the residue was gone under optical inspection. (b) Example of an optical inspection of the surface of a diamond done after a cleaning procedure. The white marks on the surface of the diamond were due to scratches during the mechanical polishing after manufacturing the sample. No residue of organic or inorganic nature was found by optical inspection on the surface of this sample.

Appendix C

ICP-RIE

Taking into account the information from Lee et al.[103] and Hausmann et al.[104] and with the help from the staff at BRNC, a recipe to etch diamond was developed. The recipe has three main stages: The first one based on sulfur hexafluoride (SF_6) and oxygen is meant to clean any organic residue left on the surface[102]. The second one is a plasma based on argon and chlorine which etches and smooths the surface of the diamond surface[103]. The last one is pure oxygen which has a higher rate of etching on diamond[104].

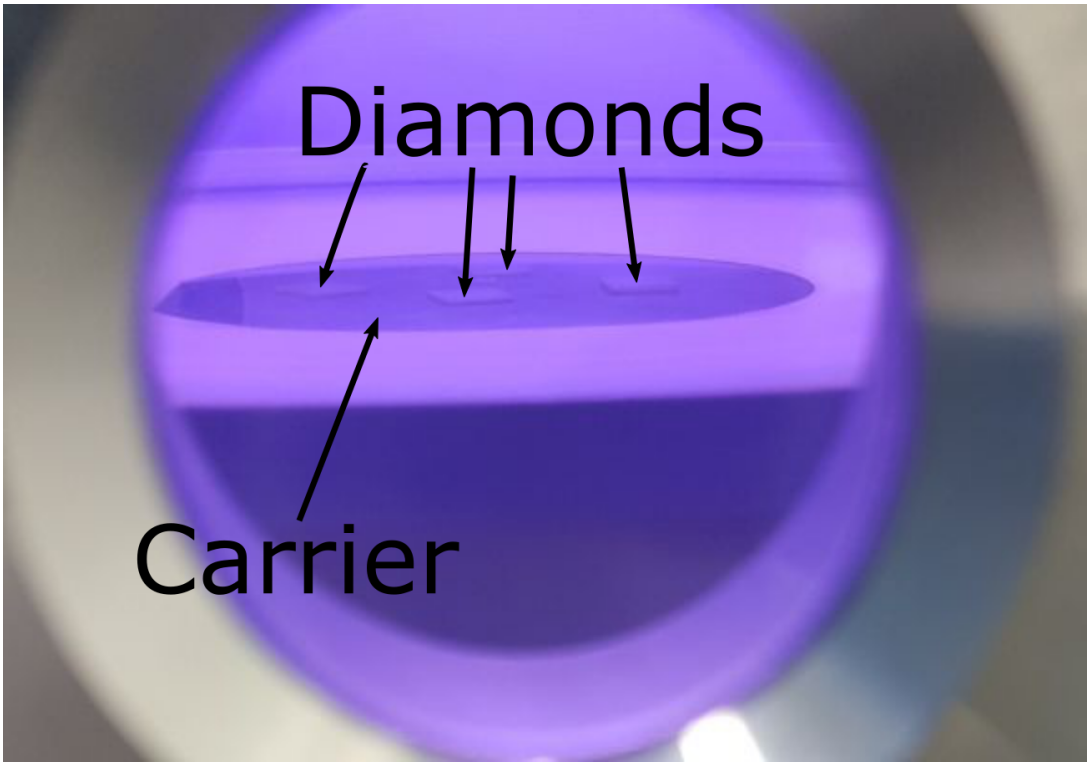

Figure C.1: Diamonds on top of a carrier inside the ICP-RIE chamber. The diamonds were being etched by Ar/Cl_2 plasma.

The following describes the whole ICP-RIE processing for each of the diamond's surfaces

after acid cleaning:

- Begin ICP-RIE process
- For 3 iterations:
  - Vacuum chamber for 2 min
  - Purge chamber with N_2 at 40 sccm
- Vacuum chamber for 2 min
- Fill chamber with O_2 at 50 sccm at a pressure of 10 mTorr for 5 min
- Gas stab pre-step: Fill chamber with 30 sccm of SF_6 and 50 sccm of O_2 at a pressure of 10 mTorr
- Plasma etch with the following conditions:
  - Gas mixture: $(SF_6{:}O_2)_{flow} = 30\,\text{sccm} : 50\,\text{sccm}$
  - RF power: 50 W
  - ICP power: 800 W
  - Pressure: 10 mTorr
  - Time: 1 min
- For 3 iterations:
  - Vacuum chamber for 2 min
  - Purge chamber with N_2 at 40 sccm
- Vacuum chamber for 2 min
- Gas stab pre-step: Fill Chamber with 25 sccm of Ar and 40 sccm of Cl_2 at a pressure of 8 mTorr
- Plasma etch with the following conditions:
  - Gas mixture: $(Ar : Cl_2)_{flow} = 25\,\text{sccm} : 40\,\text{sccm}$
  - RF power: 120 W
  - ICP power: 400 W
  - Pressure: 8 mTorr
  - Time: 10 s
- Plasma etch with the following conditions:
  - Gas mixture: $(Ar : Cl_2)_{flow} = 25\,\text{sccm} : 40\,\text{sccm}$

  - RF power: 150 W
  - ICP power: 700 W
  - Pressure: 8 mTorr
  - Time: 20 s
- Plasma etch with the following conditions:
  - Gas mixture: $(Ar : Cl_2)_{flow} = 25\,\text{sccm} : 40\,\text{sccm}$
  - RF power: 185 W
  - ICP power: 750 W
  - Pressure: 8 mTorr
  - Time: 3 min
- For 3 iterations:
  - Vacuum chamber for 2 min
  - Purge chamber with N_2 at 40 sccm
- Vacuum chamber for 2 min
- Gas stab pre-step: Fill Chamber with 50 sccm of O_2 at a pressure of 10 mTorr
- Plasma etch with the following conditions:
  - Gas mixture: $(O_2)_{flow} = 50\,\text{sccm}$
  - RF power: 200 W
  - ICP power: 1000 W
  - Pressure: 10 mTorr
  - Time: 7 min
- For 3 iterations:
  - Vacuum chamber for 2 min
  - Purge chamber with N_2 at 40 sccm
- End ICP-RIE process

Appendix D

Photolithography

Photolithography was used in two major ways for the fabrication of the diamond sensors: Patterning of metal layer with the lift-off technique, and masking before dry etching processes.

For masking before etching, one layer of positive photoresist was implemented. As for the patterning of metal layers, positive and negative photoresist were used. The first devices were fabricated using a two-layer positive photoresist, while the last ones used a one-layer negative photoresist for lift-off. The difference between positive and negative photoresist, is that when exposed to ultra violet (UV) light, positive photoresist weakens and is removed by the developing solution, while negative photoresist hardens and is not removed by the developing solution. The unexposed regions behave conversely: for positive photoresist the unexposed regions are hardened and are not washed away by the developing solution, while for negative photoresist the unexposed regions are washed away by the developing solution. Figure D.1 depicts these differences between the photoresists.

The thicknesses of the photoresist layers are control by rotational speed of the samples when they are placed in a spinner machine. The thicknesses of the layers as a function of different spinning speeds are given by the photoresist manufacturer.

The following sections list the photolithography procedures used for masking with photoresist.

D.1 Etch mask

The positive layer of photoresist used for masking before etching consisted on the photoresist AZ 6612[162] under the following process:

- HDMS sample pre-coating treatment
- Deposition of 5 mL of AZ 6612
- Spinner parameters:
  - Ramp speed: 3000 rpm/s
  - Target spin speed: 4000 rpm

  - Time: 1 min

- Soft bake:
  - Hot plate temperature: 110 °C
  - Time: 1 min
- UV exposure:
  - Type: Hard contact
  - Power: 13 mW
  - Time: 3.1 s
- Development:
  - $(\mathrm{AZ400k} : \mathrm{H_2O})_{\mathrm{Vol}} = 1 : 4$
  - Minimum volume: 50 mL
  - Time: 35 s
- Descum:
  - Plasma: O_2
  - Power: 200 W
  - Time: 1 min

D.2 Back-plane, pixel metallization and UBM lift-off masks

D.2.1 Positive photoresist

- HDMS sample pre-coating treatment
- Deposition of 5 mL of LOR 5B[162]
- Spinner parameters:
  - Ramp speed: 3000 rpm/s
  - Target spin speed: 4000 rpm
  - Time: 1 min
- Soft bake:
  - Hot plate temperature: 150 °C
  - Time: 7 min
- Deposition of 5 mL of AZ 1505[162]

- Spiner parameters:
  - Ramp speed: 2000 rpm/s
  - Target spin speed: 3000 rpm
  - Time: 1 min
- Soft bake:
  - Hot plate temperature: 110 °C
  - Time: 1 min
- UV exposure:
  - Type: Hard contact
  - Power: 13 mW
  - Time: 2 s
- Development:
  - $(\text{AZ400k} : \text{H}_2\text{O})_{\text{Vol}} = 1 : 4$
  - Minimum volume: 50 mL
  - Time: 45 s
- Descum:
  - Plasma: O_2
  - Power: 200 W
  - Time: 1 min

D.2.2 Negative photoresist

- HDMS sample pre-coating treatment
- Deposition of 5 mL of AZ nLof 2020[162]
- Spinner parameters:
  - Ramp speed: 1500 rpm/s
  - Targer spin speed: 6000 rpm
  - Time: 1 min
- Soft bake:
  - Hot plate temperature: 110 °C
  - Time: 1 min

- UV exposure:
  - Type: Hard contact
  - Power: 13 mW
  - Time: 5.4 s
- Post expose bake:
  - Hot plate temperature: 110 °C
  - Time: 1.5 min
- Development:
  - AZ726 MIF[162]
  - Minimum volume: 50 mL
  - Time: 1 min
- Descum:
  - Plasma: O_2
  - Power: 200 W
  - Time: 1 min

D.3 Indium bumps metallization lift-off mask

D.3.1 Positive photoresist

- HDMS sample pre-coating treatment
- Deposition of 5 mL of LOR 10B[162]
- Spinner parameters:
  - Ramp speed: 2000 rpm/s
  - Target spin speed: 2000 rpm
  - Time: 1 min 20 s
- Soft bake:
  - Hot plate temperature: 140 °C
  - Time: 10 min
- Deposition of 5 mL of AZ 6612[162]
- Spiner parameters:

  - Ramp speed: 2000 rpm/s
  - Target spin speed: 3000 rpm
  - Time: 1 min 20 s
- Soft bake:
  - Hot plate temperature: 110 °C
  - Time: 1 min
- UV exposure:
  - Type: Hard contact
  - Power: 13 mW
  - Time: 3.2 s
- Development:
  - $(\text{AZ400k} : \text{H}_2\text{O})_{\text{Vol}} = 1 : 4$
  - Minimum volume: 50 mL
  - Time: 45 s
- Descum:
  - Plasma: O_2
  - Power: 200 W
  - Time: 1 min

D.3.2 Negative photoresist

- HDMS sample pre-coating treatment
- Deposition of 5 mL of AZ nLof 2070[162]
- Spinner parameters:
  - Ramp speed: 2000 rpm/s
  - Targer spin speed: 5000 rpm
  - Time: 1 min
- Soft bake:
  - Hot plate temperature: 110 °C
  - Time: 2 min
- UV exposure:

  - Type: Hard contact
  - Power: 13 mW
  - Time: 14 s

- Post expose bake:
  - Hot plate temperature: 110 °C
  - Time: 1.5 min

- Development:
  - AZ726 MIF[162]
  - Minimum volume: 50 mL
  - Time: 1 min

- Descum:
  - Plasma: O_2
  - Power: 200 W
  - Time: 1 min

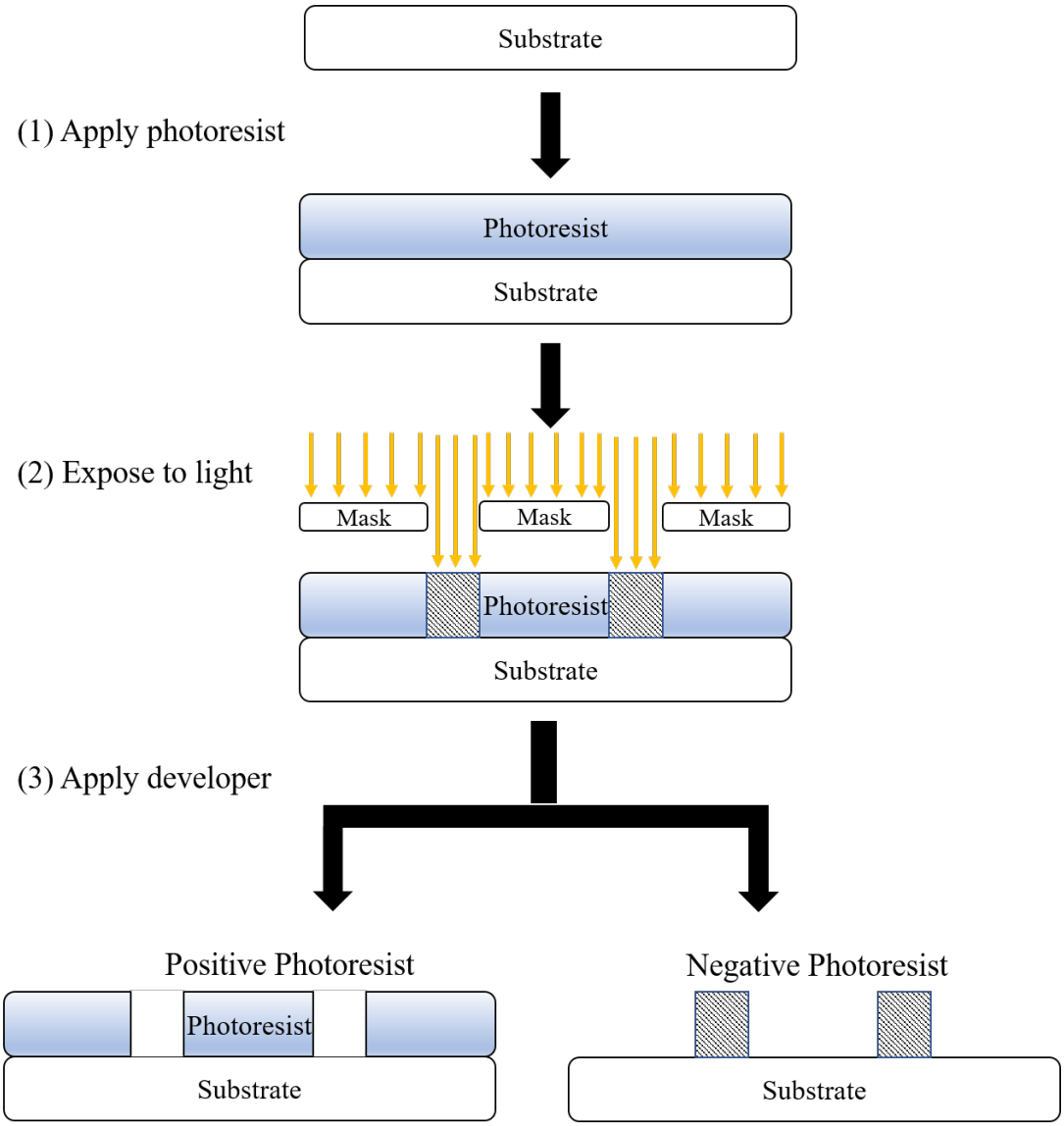

Figure D.1: Diagram showing the effects of UV light exposure on positive and negative photoresists, and the resulting pattern after development.[161]

Appendix E

PECVD SiON Recipe

The following recipe was developed to grow a passivation layer of SiO_xN_y on. The recipe was based on the study made by Mackenzie et al. on the growth of silicon based dielectrics[163].

Parameter	Value
Flow SiH_4(2%)	500 sccm
Flow NH_3	20 sccm
Flow N_2O	100 sccm
Flow N_2	80 sccm
Temperature	300 °C
Pressure	900 mTorr
RF Power	20 W
Growth rate	~ 33 nm/min
Time	18 min11 s

Table E.1: Parameters used to grow the SiO_xN_y layers.

The parameters chosen following the studies of Mackenzie et al.[163] would minimize the film stress. Figure E.1 shows the different stress characteristics that the deposited films can have. In the best case scenario, no stress in the film is desired. This prevents the formation of cracks of the passivation layer and the metallic layer underneath.

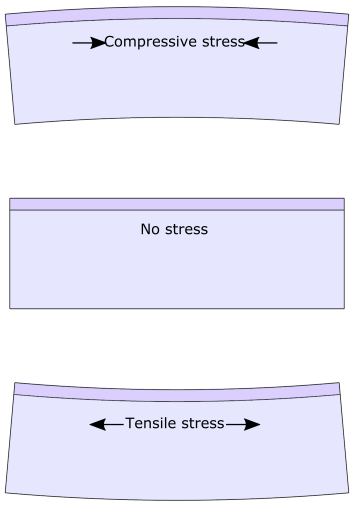

Figure E.1: Different stress of the deposited films.

The recipe was characterized by the staff at BRNC on a silicon wafer and found the results shown in Table E.2 and Figure E.2

Parameter	Value
Nonuniformity	0.98 %
Stress @ 0°	11.9 MPa - tensile
Stress @ 90°	10.6 MPa - tensile

Table E.2: Characterization of film parameters by reflectometry, ellipsometry and stress measurements.

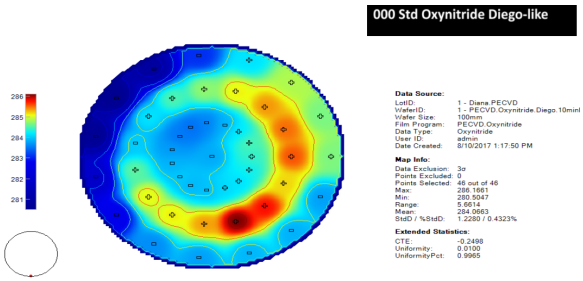

Figure E.2: Reflectometry map of the deposited thickness over the wafer.

Appendix F

RIE SiON Recipe

The following is the recipe used to etch the SiO_xN_y passivation layer deposited with PECVD. The recipe was based on Ueno et al. paper on the RIE of silicon oxynitride[164].

Parameter	Value
Flow CHF_3	50 sccm
Pressure	50 mTorr
Forward Power	100 W
Etch rate	~ 16 nm/min
Time	50 min

Table F.1: Settings used to etch SiO_xN_y passivation layer.

Appendix G

How The η Distribution Works

The distribution of the hit positions between two adjacent strips is expected to be uniform. The data sampled with this uniform distribution produces the non-uniform distribution f over the quantity η as it can be seen in Figures 11.9 and 11.10. To recover the information of the hit position it is possible to use the CDF of the distribution $f(\eta)$. This method is the reverse of the Inversion Sampling method[165] used to generate non-uniform random variables starting with a uniformly distributed samples between [0,1]. The following explanation briefly describes how the Inversion Sampling method works:

Let random variable U follow a Uniform distribution between [0, 1] and X is a random variable which follows the non-uniform distribution f.

$$U \sim \text{Unif}[0,1] \tag{G.1a}$$

$$X \sim f \tag{G.1b}$$

The CDF of f is F. By definition, it is a monotonic increasing function between [0,1]. $F(\eta)$ is the probability (Pr) of having the random variable $X \leq \eta$.

$$F(\eta) = \frac{\int_{-\infty}^{\eta} f(X)\mathrm{d}X}{\int_{-\infty}^{\infty} f(X)\mathrm{d}X} = Pr(X \leq \eta) \tag{G.2}$$

There exists a mapping G that maps random variables U into X. Its domain by definition is the interval [0,1].

$$G : U \mapsto X \mid G(U) = X \tag{G.3}$$

Starting from the definition of F in Equation G.2, one can replace the X variable in terms of the mapping G applied to U. Applying G^{-1} on both sides of the inequality, one arrives to the probability of having the random variable U is less than G^{-1} at η which is just the value of $G^{-1}(\eta)$

$$F(\eta) = Pr(X \leq \eta) = Pr(G(U) \leq \eta) = Pr(U \leq G^{-1}(\eta)) = G^{-1}(\eta) \tag{G.4}$$

Note that the relation shown at the last step in Equation G.4 can be generalized as shown in Equation G.5 if U is a random variable uniformly distributed between [0,1], the range of F is [0,1] and F is a monotonic function.

$$F(\eta) = Pr(X \leq \eta) = Pr(U \leq F(\eta)) \tag{G.5}$$

This tells us that the map G that achieves the mapping from a uniform distribution into a non-uniform distribution is the inverse of the CDF F.

$$F^{-1}(X) = G(X) \tag{G.6}$$

The reverse method to map a non-uniform sampling into a uniform one can be described as follows:

There is a mapping H from the non-uniform variable X into the uniform variable U.

$$H : X \mapsto U \mid H(X) = U \tag{G.7}$$

Starting by the definition of F in Equation G.5 and replacing U by $H(X)$, one can then apply the inverse of H at both sides of the inequality. Comparing the last step of Equation G.8a with the definition of $F(\eta)$ in either Equations G.2 or G.5, one concludes Equation G.8b.

$$F(\eta) = Pr(U \leq F(\eta)) = Pr(H(X) \leq F(\eta)) = Pr(F^{-1}(H(X)) \leq \eta) \tag{G.8a}$$

$$F^{-1}(H(X)) = X \tag{G.8b}$$

This means that the mapping H that maps the random variable X, from a non-uniform distribution into U which is uniformly distributed, is the same CDF F.

$$H(X) = F(X) \tag{G.9}$$

The above summarizes that by applying the CDF F to the random variable η, a variable uniformly distributed between [0, 1] is obtained. Scaling this by the pitch P between the strips, the predicted hit position using the η correction is obtained as it is shown in Equations G.10a.

$$F(\eta) = \frac{\int_{-\infty}^{\eta} f(\lambda)\mathrm{d}\lambda}{\int_{-\infty}^{\infty} f(\lambda)\mathrm{d}\lambda} = \frac{\int_{0}^{\eta} f(\lambda)\mathrm{d}\lambda}{\int_{0}^{1} f(\lambda)\mathrm{d}\lambda} \tag{G.10a}$$

$$x(\eta) = x_L + P \cdot F(\eta) = x_L + P \cdot \frac{\int_{0}^{\eta} f(\lambda)\mathrm{d}\lambda}{\int_{0}^{1} f(\lambda)\mathrm{d}\lambda} \tag{G.10b}$$

Appendix H

Efficiencies And Their Uncertainties

The efficiency results in this thesis follow the discussion made by Paterno[166] and Casadei[167], which follows a Bayesian approach. In their work, the measured efficiency is the most probable value of an underlying probability density function, the Beta distribution function, as shown in equation H.1.

$$f(\epsilon|k,n) = Be(\epsilon; k+1, n-k+1) \tag{H.1}$$

, where ϵ is the efficiency, $f(\epsilon|k,n)$ is the underlying distribution for the efficiency given k and n, k is the number of successes, n is the number of attempts, and $Be(x;\alpha,\beta)$ is the Beta distribution along the variable $x \in [0,1]$ with shape parameters α and β.

Figure H.1 shows an example of the underlying distribution following the mentioned approach when out of 100 attempts, there are a total of 95 successes. The depicted asymmetric error bars are calculated numerically to enclose the smallest region with 68 % probability around the distribution's MPV.

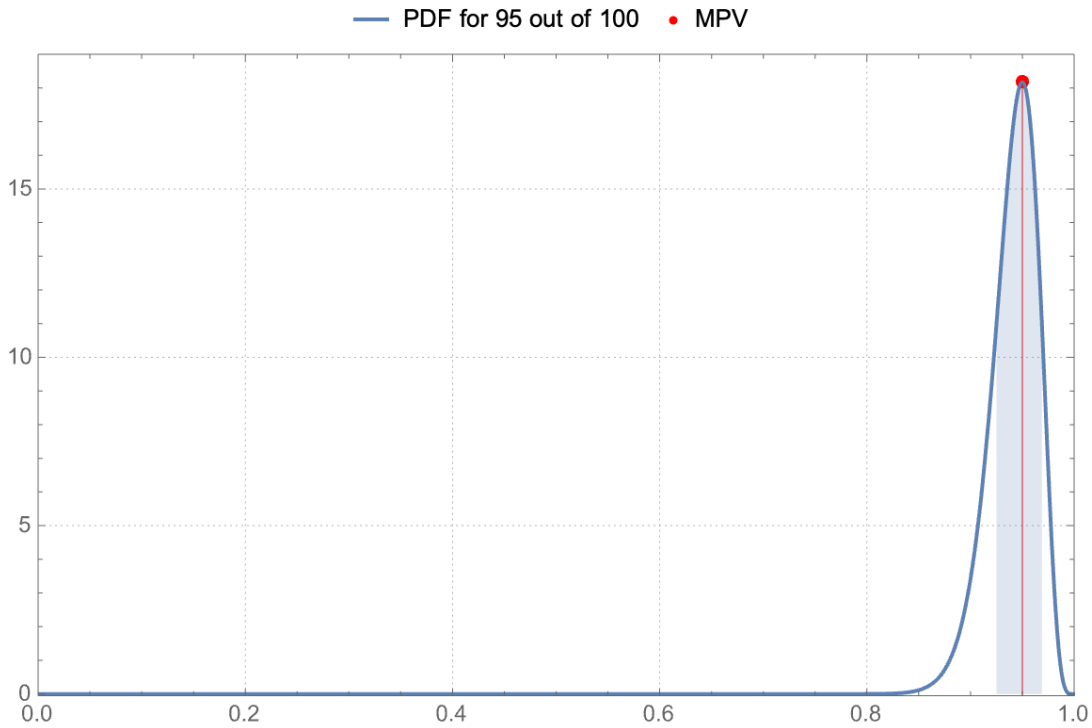

Figure H.1: Example of the PDF underlying the case of 95 successes out of 100 tries. The MPV shows the measured efficiency, and the shaded area shows the uncertainty that covers the 68 % probability.

Appendix I

Strip 3D Detectors' Efficiency Maps

The efficiency maps for the 3D detectors Poly-3D, Full-3D, Multi-3D, and Irrad-3D are shown in the following Figures I.1, I.2, I.3, I.4, I.5, I.6, and I.7.

I.1 Poly-3D

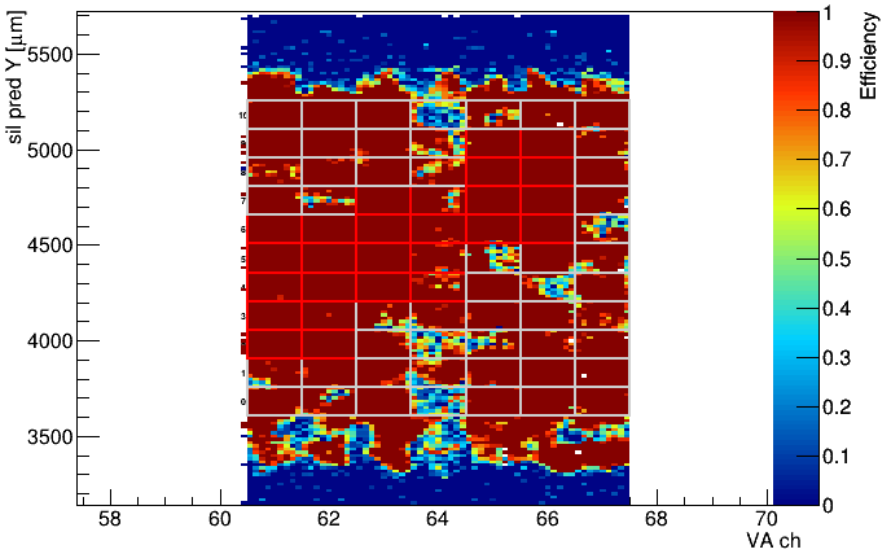

Figure I.1: Efficiency Poly-3D.

I.2 Full-3D

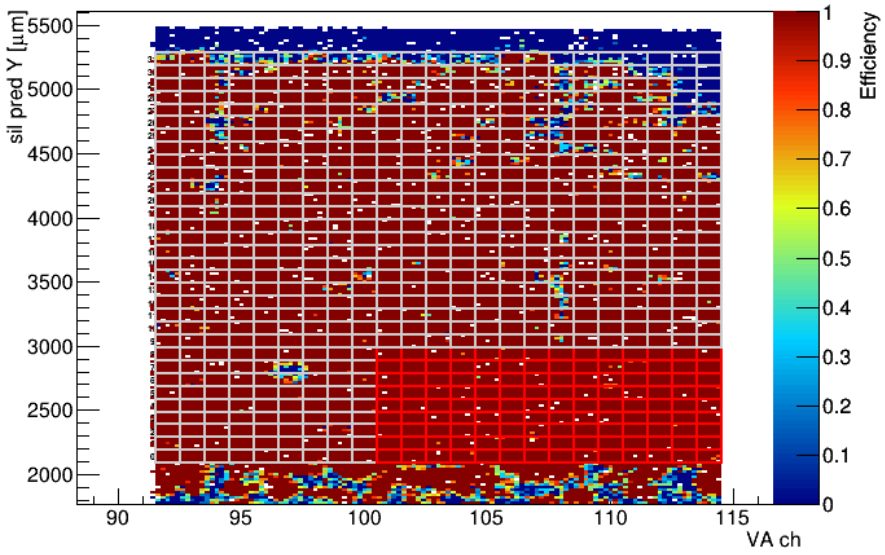

Figure I.2: Efficiency Full-3D.

I.3 Multi-3D

I.3.1 Multi-3D Squares

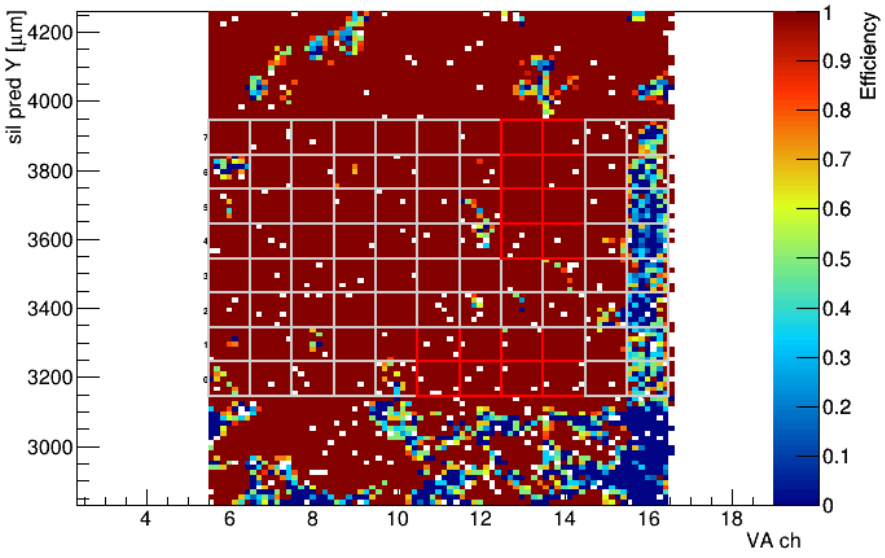

Figure I.3: Efficiency Multi-3D squares.

I.3.2 Multi-3D Rectangles

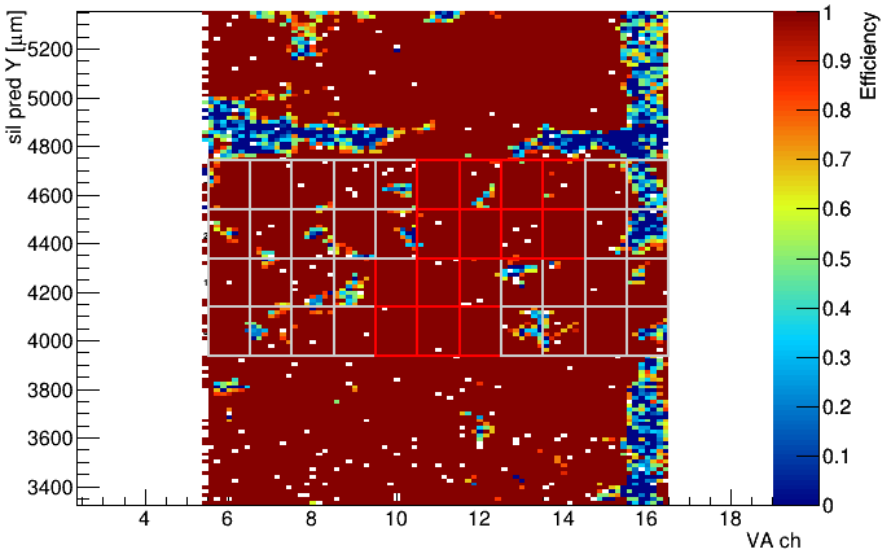

Figure I.4: Efficiency Multi-3D rectangles.

I.3.3 Multi-3D Hexagons

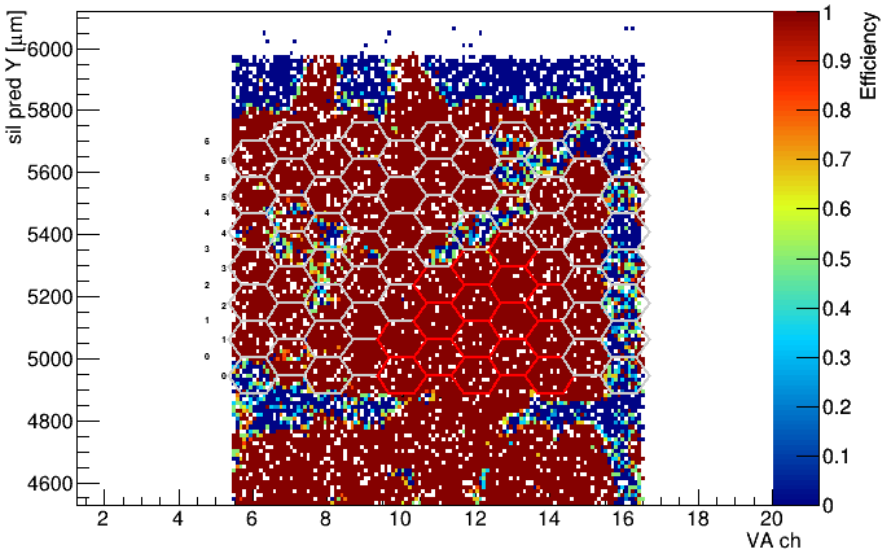

Figure I.5: Efficiency Multi-3D hexagons.

I.4 Irrad-3D

I.4.1 Irrad-3D 100 µm

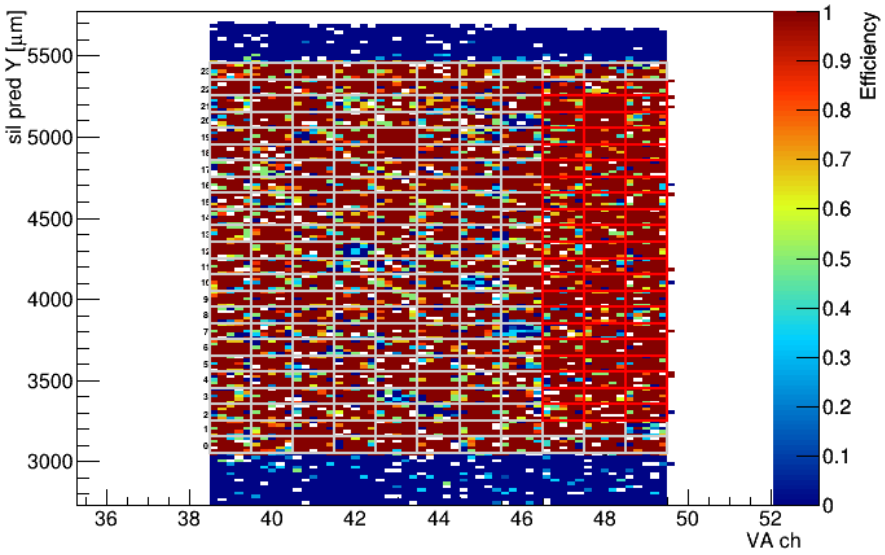

Figure I.6: Efficiency Irrad-3D 100 µm.

I.4.2 Irrad-3D 50 µm

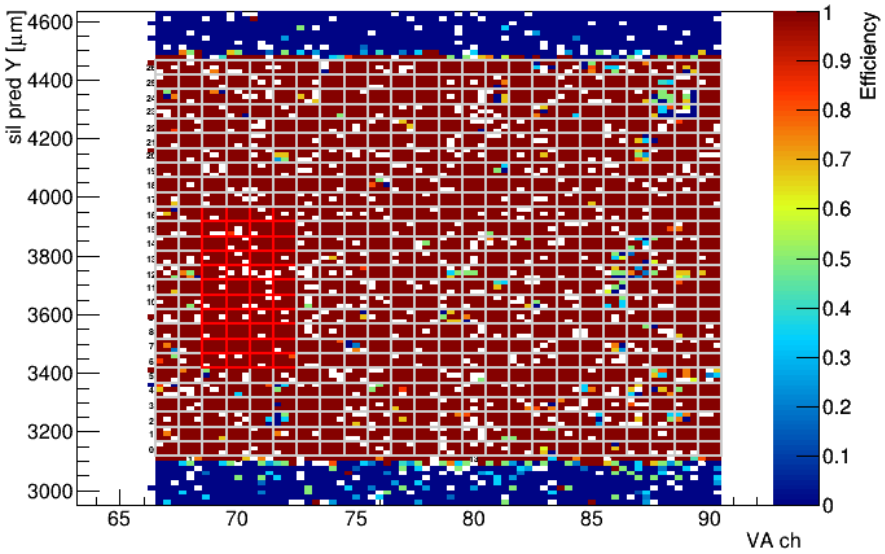

Figure I.7: Efficiency Irrad-3D 50 µm.

Appendix J

Experiments Performed During The Test Beams At CERN

Run	Events (k)	Digitizer (Sirocco)	DUT	HV (V)	I_{ini} (nA)	I_{end} (nA)	Digitizer (Sirocco)	DUT	HV (V)	I_{ini} (nA)	I_{end} (nA)	Run type
-	-	-	Poly-3D	-	-	-	-	Poly-3D-planar	-	-	-	pumping
19100	380	S4	Poly-3D	50	<1.0	-	S4	Poly-3D-planar	500	<5	-	setup
19101	480	S4	Poly-3D	50	<0.2	-	S4	Poly-3D-planar	500	<5	-	setup
19102	100	S4	Poly-3D	50	<0.2	-	S4	Poly-3D-planar	500	<5	-	setup
19103	200	S4	Poly-3D	50	<0.2	-	S4	Poly-3D-planar	500	<5	-	setup
19104	100	S4	Poly-3D	50	<0.2	-	S4	Poly-3D-planar	500	<5	-	setup
19105	2000	S4	Poly-3D	50	<0.2	-	S4	Poly-3D-planar	500	<5	-	voltage scan
19106	2000	S4	Poly-3D	60	<0.2	-	S4	Poly-3D-planar	500	<5	-	voltage scan
19107	2000	S4	Poly-3D	70	<0.2	-	S4	Poly-3D-planar	500	<5	-	voltage scan
19108	1100	S4	Poly-3D	80	<0.2	-	S4	Poly-3D-planar	500	5-10	-	voltage scan
-	-	-	Poly-3D	-	-	-	-	Poly-3D-planar	-	-	-	pumping
19110	1500	S4	Poly-3D	-60	<1.0	-	S4	Poly-3D-planar	500	<5	-	voltage scan
19111	2000	S4	Poly-3D	-70	<0.2	-	S4	Poly-3D-planar	-500	<5	-	voltage scan
19112	1500	S4	Poly-3D	-75	<0.2	-	S4	Poly-3D-planar	-500	<5	-	voltage scan

Table J.1: Relevant runs of the measurements made during the Oct. 2015 Test Beam at CERN.

Run	Events (k)	Digitizer (Sirocco)	DUT	HV (V)	I_{ini} (nA)	I_{end} (nA)	Digitizer (Sirocco)	DUT	HV (V)	I_{ini} (nA)	I_{end} (nA)	Run type
-	-	-	Full-3D	-	-	-	-	Multi-3D-planar	-	-	-	pumping
20008	400	S4	Full-3D	30	<0.1	-	S4	Multi-3D-planar	500	<5	-	voltage scan
20009	1400	S4	Full-3D	45	<0.1	-	S4	Multi-3D-planar	500	<5	-	voltage scan
20010	750	S4	Full-3D	55	<0.1	-	S4	Multi-3D-planar	500	<5	-	voltage scan
20011	100	S4	Full-3D	55	<0.1	-	S4	Multi-3D-planar	500	<5	-	setup
20012	2000	S4	Full-3D	55	<0.1	-	S4	Multi-3D-planar	500	<5	-	voltage scan
-	-	-	Full-3D	-	-	-	-	Multi-3D-planar	-	-	-	pumping
20014	400	S4	Full-3D	-30	<1	-	S4	Multi-3D-planar	-500	<5	-	voltage scan

Table J.2: Relevant runs of the measurements made during the May 2016 Test Beam at CERN.

Run	Events (k)	Digitizer (Sirocco)	DUT	HV (V)	I_{ini} (nA)	I_{end} (nA)	Digitizer (Sirocco)	DUT	HV (V)	I_{ini} (nA)	I_{end} (nA)	Run type
-	-	-	Multi-3D	-	-	-	-	Multi-3D-planar	-	-	-	pumping
22005	400	S4	Multi-3D	30	0.2	-	S4	Multi-3D-planar	500	0.9	-	voltage scan
22006	400	S4	Multi-3D	45	<1	-	S4	Multi-3D-planar	500	<1	-	voltage scan
22007	1000	S4	Multi-3D	60	0.3	-	S4	Multi-3D-planar	500	0.3	-	voltage scan
22008	1000	S4	Multi-3D	75	0.3	-	S4	Multi-3D-planar	500	0.3	-	voltage scan
22009	1000	S4	Multi-3D	90	0.6	-	S4	Multi-3D-planar	500	0.3	-	voltage scan
22010	1000	S4	Multi-3D	105	0.4	-	S4	Multi-3D-planar	500	0.3	-	voltage scan
22011	1000	S4	Multi-3D	120	0.6	-	S4	Multi-3D-planar	500	0.3	-	voltage scan
-	-	-	Multi-3D	-	-	-	-	Multi-3D-planar	-	-	-	pumping
22013	400	S4	Multi-3D	-30	0.2	-	S4	Multi-3D-planar	-500	0.4	-	voltage scan
22014	400	S4	Multi-3D	-45	0.3	-	S4	Multi-3D-planar	-500	0.3	-	voltage scan
22015	400	S4	Multi-3D	-60	0.2	-	S4	Multi-3D-planar	-500	0.3	-	voltage scan
22016	400	S4	Multi-3D	-75	0.2	-	S4	Multi-3D-planar	-500	0.2	-	voltage scan
22017	400	S4	Multi-3D	-90	0.5	-	S4	Multi-3D-planar	-500	0.3	-	voltage scan
22018	1000	S4	Multi-3D	-105	0.7	-	S4	Multi-3D-planar	-500	0.3	-	voltage scan
22019	1000	S4	Multi-3D	-120	2	-	S4	Multi-3D-planar	-500	0.3	-	voltage scan
-	-	-	Full-3D	-	-	-	-	-	-	-	-	pumping
22022	400	S4	Full-3D	30	4.4	-	-	-	-	-	-	voltage scan
22023	400	S4	Full-3D	45	4.8	-	-	-	-	-	-	voltage scan
22024	750	S4	Full-3D	60	5.9	-	-	-	-	-	-	voltage scan
22025	400	S4	Full-3D	75	8.1	-	-	-	-	-	-	voltage scan
22026	750	S4	Full-3D	90	13.5	-	-	-	-	-	-	voltage scan

Table J.3: Relevant runs of the measurements made during the Aug. 2016 Test Beam at CERN.

Run	Events (k)	Digitizer (Sirocco)	DUT	HV (V)	I_{ini} (nA)	I_{end} (nA)	Digitizer (Sirocco)	DUT	HV (V)	I_{ini} (nA)	I_{end} (nA)	Run type
-	-	-	Full-3D	-	-	-	-	-	-	-	-	pumping
25103	400	S5	Full-3D	30	<2.8	2.4	-	-	-	-	-	voltage scan
25104	400	S5	Full-3D	45	<3.8	4	-	-	-	-	-	voltage scan
25105	1000	S5	Full-3D	60	<5.7	4.5	-	-	-	-	-	voltage scan
25106	1000	S5	Full-3D	75	<5.8	5.1	-	-	-	-	-	voltage scan
25106	1000	S5	Full-3D	75	<5.8	5.1	-	-	-	-	-	voltage scan
-	-	-	Multi-3D	-	-	-	-	Multi-3D-planar	-	-	-	pumping
25108	400	S5	Multi-3D	30	0.2	0.3	S5	Multi-3D-planar	500	-	-	voltage scan
25109	400	S5	Multi-3D	45	0.2	0.2	S5	Multi-3D-planar	500	-	-	voltage scan
25110	400	S5	Multi-3D	60	0.2	0.2	S5	Multi-3D-planar	500	-	-	voltage scan
25111	1000	S5	Multi-3D	75	0.2	0.2	S5	Multi-3D-planar	500	-	-	voltage scan
25112	400	S5	Multi-3D	90	0.3	0.2	S5	Multi-3D-planar	500	-	-	voltage scan
-	-	-	Multi-3D	-	-	-	-	Multi-3D-planar	-	-	-	pumping
25113	400	S5	Multi-3D	-30	0.3	0.2	S5	Multi-3D-planar	-500	0.8	0.3	voltage scan
25114	400	S5	Multi-3D	-45	0.2	0.2	S5	Multi-3D-planar	-500	0.3	0.3	voltage scan
25115	400	S5	Multi-3D	-60	0.2	0.2	S5	Multi-3D-planar	-500	0.3	0.3	voltage scan
25116	1000	S5	Multi-3D	-75	0.3	0.3	S5	Multi-3D-planar	-500	0.3	0.3	voltage scan
25117	1000	S5	Multi-3D	-90	0.4	0.4	S5	Multi-3D-planar	-500	0.3	0.3	voltage scan
-	-	-	Full-3D	-	-	-	-	-	-	-	-	pumping
25118	400	S5	Full-3D	-15	2.6	1.6	-	-	-	-	-	voltage scan
-	-	-	Full-3D	-	-	-	-	-	-	-	-	pumping
25119	400	S5	Full-3D	15	1.2	0.5	-	-	-	-	-	voltage scan
25120	1000	S5	Full-3D	90	8.7	8.2	-	-	-	-	-	voltage scan

Table J.4: Relevant runs of the measurements made during the Sep. 2018 Test Beam at CERN.

Run	Events (k)	Digitizer (Sirocco)	DUT	HV (V)	I_{ini} (nA)	I_{end} (nA)	Digitizer (Sirocco)	DUT	HV (V)	I_{ini} (nA)	I_{end} (nA)	Run type
-	-	-	Irrad-3D	-	-	-	-	-	-	-	-	pumping
25202	400	S5	Irrad-3D	15	<0.2	0.2	-	-	-	-	-	voltage scan
25203	400	S5	Irrad-3D	30	<0.2	0.2	-	-	-	-	-	voltage scan
25204	1000	S5	Irrad-3D	45	<0.2	0.2	-	-	-	-	-	voltage scan
25205	1000	S5	Irrad-3D	45	<0.2	0.2	-	-	-	-	-	voltage scan
25206	980	S5	Irrad-3D	60	<1.5	60	-	-	-	-	-	voltage scan
-	-	-	Irrad-3D	-	-	-	-	-	-	-	-	pumping
25207	400	S5	Irrad-3D	-15	<0.2	0.1	-	-	-	-	-	voltage scan
25208	400	S5	Irrad-3D	-30	<0.2	0.1	-	-	-	-	-	voltage scan
25209	1000	S5	Irrad-3D	-45	<0.2	0.1	-	-	-	-	-	voltage scan
25210	1000	S5	Irrad-3D	-60	<0.2	40	-	-	-	-	-	voltage scan

Table J.5: Relevant runs of the measurements made during the Oct. 2018 test beam at CERN.

Appendix K

Experiments Performed During The Test Beams At PSI

K.1 PSI Test Beam 2018

Run Settings					Plane 5			Plane 4			Plane 6			
Run	Events (M)	Flux (kHz/cm^2)	FS11 [l/r]	FS11 [u/d]	DUT	HV (V)	I (nA)	DUT	HV (V)	I (nA)	DUT	HV (V)	I (nA)	Run type
125	2.0	7700	250	250	II6-A2	0	0.0	CMS04	0	0.0	Si-D8	0	0	pumping
127	8.0	7700	250	250	II6-A2	0	-0.2	CMS04	0	-0.9	Si-D8	-300	-2208	pumping
128	8.0	7700	250	250	II6-A2	0	-0.2	CMS04	0	-0.8	Si-D8	-300	-2509	pumping
129	1.5	100	77	70	II6-A2	0	-0.1	CMS04	0	-0.1	Si-D8	-300	-2783	voltage scan
130	1.5	100	77	70	II6-A2	-5	-0.1	CMS04	-50	-0.3	Si-D8	-300	-2731	voltage scan
131	1.5	100	77	70	II6-A2	-10	-0.2	CMS04	-100	-0.5	Si-D8	-300	-2768	voltage scan
132	1.5	100	77	70	II6-A2	-15	-0.2	CMS04	-150	-0.6	Si-D8	-300	-2759	voltage scan
133	1.5	100	77	70	II6-A2	-20	-0.3	CMS04	-200	-0.7	Si-D8	-300	-2735	voltage scan
134	1.5	100	77	70	II6-A2	-25	-0.3	CMS04	-300	-0.8	Si-D8	-300	-2718	voltage scan
135	1.5	100	77	70	II6-A2	-30	-0.4	CMS04	-400	-1.0	Si-D8	-300	-2700	voltage scan
136	1.0	7700	250	250	II6-A2	-30	-8.3	CMS04	-400	-35.4	Si-D8	-300	-2608	pumping
138	0.3	10	54	70	II6-A2	-30	0.2	CMS04	-400	2.0	Si-D8	-300	2500	rate scan
139	0.5	10	54	70	II6-A2	-30	-0.2	CMS04	-400	-2.0	Si-D8	-300	-2544	rate scan
140	1.2	10	54	70	II6-A2	-30	-0.2	CMS04	-400	-2.4	Si-D8	-300	-2485	rate scan
141	0.7	10	54	70	II6-A2	-30	-0.2	CMS04	-400	-2.4	Si-D8	-300	-2445	rate scan
143	1.2	100	77	70	II6-A2	-30	-0.4	CMS04	-400	-3.1	Si-D8	-300	-2550	rate scan
144	1.2	333	77	80	II6-A2	-30	-0.8	CMS04	-400	-4.5	Si-D8	-300	-2445	rate scan
145	1.2	1000	95	95	II6-A2	-30	-1.6	CMS04	-400	-8.1	Si-D8	-300	-2359	rate scan
146	1.2	3333	140	140	II6-A2	-30	-4.8	CMS04	-400	-21.9	Si-D8	-300	-2395	rate scan
147	1.2	7700	250	250	II6-A2	-30	-8.6	CMS04	-400	-37.3	Si-D8	-300	-2491	rate scan
148	1.2	3333	140	140	II6-A2	-30	-4.6	CMS04	-400	-20.9	Si-D8	-300	-2478	rate scan
149	1.2	1000	95	95	II6-A2	-30	-1.7	CMS04	-400	-7.7	Si-D8	-300	-2452	rate scan
150	1.2	333	77	80	II6-A2	-30	-0.8	CMS04	-400	-4.1	Si-D8	-300	-2539	rate scan
152	1.2	100	77	70	II6-A2	-30	-0.5	CMS04	-400	-3.3	Si-D8	-300	-2602	rate scan
153	1.2	10	54	70	II6-A2	-30	-0.3	CMS04	-400	-3.0	Si-D8	-300	-2490	rate scan
154	1.2	100	77	70	II6-A2	-40	-0.6	CMS04	-500	-4.3	Si-D8	-300	-2581	voltage scan
155	1.2	100	77	70	II6-A2	-50	-0.7	CMS04	-600	-4.3	Si-D8	-300	-2577	voltage scan
156	1.2	100	77	70	II6-A2	-60	-0.8	CMS04	-700	-5.3	Si-D8	-300	-2572	voltage scan
157	1.2	10	54	70	II6-A2	-70	-0.9	CMS04	-750	-5.3	Si-D8	-300	-2476	rate scan
158	1.2	100	77	70	II6-A2	-70	-0.7	CMS04	-750	-5.0	Si-D8	-300	-2500	rate scan
159	1.2	333	77	80	II6-A2	-70	-142.2	CMS04	-750	-6.3	Si-D8	-300	-2509	rate scan
160	1.2	1000	95	95	II6-A2	-70	-541.1	CMS04	-750	-9.9	Si-D8	-300	-2443	rate scan
161	1.2	3333	140	140	II6-A2	-70	-699.0	CMS04	-750	-61.7	Si-D8	-300	-2422	rate scan
162	1.2	7700	250	250	II6-A2	-70	-1355.5	CMS04	-750	-103.7	Si-D8	-300	-2555	rate scan
163	1.2	3333	140	140	II6-A2	-70	-1524.3	CMS04	-750	-79.5	Si-D8	-300	-2534	rate scan
164	1.2	1000	95	95	II6-A2	-70	-1484.9	CMS04	-750	-56.0	Si-D8	-300	-2489	rate scan
165	1.2	333	77	80	II6-A2	-70	-1549.1	CMS04	-750	-48.1	Si-D8	-300	-2561	rate scan
166	1.2	100	77	70	II6-A2	-70	-1658.1	CMS04	-750	-49.9	Si-D8	-300	-2653	rate scan
167	1.2	10	54	70	II6-A2	-70	-1587.5	CMS04	-750	-55.6	Si-D8	-300	-2551	rate scan
168	1.2	20	56	70	II6-A2	-70	-1473.5	CMS04	-750	-59.6	Si-D8	-300	-2581	rate scan
169	1.2	40	61	70	II6-A2	-70	-1428.1	CMS04	-750	-60.3	Si-D8	-300	-2650	rate scan
170	1.2	70	69	70	II6-A2	-70	-1404.4	CMS04	-750	-63.3	Si-D8	-300	-2631	rate scan
171	1.2	100	77	70	II6-A2	-70	-1402.0	CMS04	-750	-68.7	Si-D8	-300	-2625	rate scan
172	1.2	333	77	80	II6-A2	-70	-1328.4	CMS04	-750	-73.1	Si-D8	-300	-2552	rate scan
173	1.2	1000	95	95	II6-A2	-70	-1243.9	CMS04	-750	-82.4	Si-D8	-300	-2471	rate scan
174	1.2	3333	140	140	II6-A2	-70	-1227.7	CMS04	-750	-106.2	Si-D8	-300	-2517	rate scan
175	1.2	7700	250	250	II6-A2	-70	-1185.8	CMS04	-750	-139.9	Si-D8	-300	-2607	rate scan
176	1.2	3333	140	140	II6-A2	-70	-1196.8	CMS04	-750	-105.7	Si-D8	-300	-2625	rate scan
177	1.2	1000	95	95	II6-A2	-70	-1183.2	CMS04	-750	-66.4	Si-D8	-300	-2572	rate scan
178	1.2	333	77	80	II6-A2	-70	-1186.2	CMS04	-750	-60.0	Si-D8	-300	-2663	rate scan
179	1.2	100	77	70	II6-A2	-70	-1239.8	CMS04	-750	-56.5	Si-D8	-300	-2758	rate scan
180	1.2	70	69	70	II6-A2	-70	-1102.5	CMS04	-750	-57.1	Si-D8	-300	-2748	rate scan
181	1.2	40	61	70	II6-A2	-70	-1108.5	CMS04	-750	-57.9	Si-D8	-300	-2719	rate scan
182	1.2	20	56	70	II6-A2	-70	-1084.1	CMS04	-750	-61.0	Si-D8	-300	-2659	rate scan
183	1.2	10	54	70	II6-A2	-70	-1018.5	CMS04	-750	-63.8	Si-D8	-300	-2635	rate scan

K.2 PSI Test Beam 2019

Run Settings					Plane 4			Plane 5			Plane 6			
Run	Events (M)	Flux (kHz/cm^2)	FS13	FS11	DUT	HV (V)	I (nA)	DUT	HV (V)	I (nA)	DUT	HV (V)	I (nA)	Run type
		4800	145	450	CMS01	0		II6-93	0		Si-D2	-200		pumping
1	2.5	333	38	90	CMS01	-10	-0.2	II6-93	-50	-0.3	Si-D2	-200	-1781	voltage scan
2	2.5	333	38	90	CMS01	-50	-0.8	II6-93	-100	-1.7	Si-D2	-200	-2292	voltage scan
3	2.5	333	38	90	CMS01	-100	-1.4	II6-93	-200	-3.1	Si-D2	-200	-2241	voltage scan
4	2.5	333	38	90	CMS01	-200	-2.3	II6-93	-400	-4.8	Si-D2	-200	-2214	voltage scan
5	2.5	333	38	90	CMS01	-300	-3.1	II6-93	-600	-7.0	Si-D2	-200	-2212	voltage scan
7	2.5	333	38	90	CMS01	-400	-4.3	II6-93	-700	-9.5	Si-D2	-200	-2118	voltage scan
8	2.5	333	38	90	CMS01	-600	-6.4	II6-93	-750	-14.2	Si-D2	-200	-2195	voltage scan
9	2.5	333	28	90	CMS01	-600	-6.7	II6-93	-750	-14.1	Si-D2	-200	-2170	voltage scan
10	0.0	4800	145	450	CMS01	0	-0.7	II6-93	0	-0.6	Si-D2	-200	-2171	pumping
11	0.0	4800	145	450	CMS01	0	-0.7	II6-93	0	-0.6	Si-D2	-200	-2171	pumping
12	1.2	33	28	85	CMS01	-500	-2.3	II6-93	-700	-5.5	Si-D2	-200	-2290	rate scan
13	1.2	100	30	90	CMS01	-500	-3.1	II6-93	-700	-5.9	Si-D2	-200	-2377	rate scan
14	1.2	333	38	90	CMS01	-500	-5.2	II6-93	-700	-10.1	Si-D2	-200	-2293	rate scan
15	1.2	1000	60	125	CMS01	-500	-10.0	II6-93	-700	-18.9	Si-D2	-200	-2229	rate scan
16	1.2	3333	130	275	CMS01	-500	-28.6	II6-93	-700	-48.5	Si-D2	-200	-2228	rate scan
17	1.2	4800	145	450	CMS01	-500	-41.4	II6-93	-700	-68.8	Si-D2	-200	-5809	rate scan
18	1.2	3333	130	275	CMS01	-500	-30.0	II6-93	-700	-50.6	Si-D2	-200	-2218	rate scan
19	1.2	1000	60	125	CMS01	-500	-12.7	II6-93	-700	-22.6	Si-D2	-200	-2161	rate scan
20	1.2	333	38	90	CMS01	-500	-6.8	II6-93	-700	-12.9	Si-D2	-200	-2200	rate scan
21	1.2	100	30	90	CMS01	-500	-3.8	II6-93	-700	-6.8	Si-D2	-200	-2305	rate scan
22	1.2	100	24	90	CMS01	-500	-3.4	II6-93	-700	-5.8	Si-D2	-200	-2388	rate scan
23	1.2	33	28	85	CMS01	-500	-3.2	II6-93	-700	-5.3	Si-D2	-200	-2374	rate scan
24	1.2	100	30	90	CMS01	-500	-4.0	II6-93	-700	-7.0	Si-D2	-200	-2435	rate scan
25	1.2	333	38	90	CMS01	-500	-6.5	II6-93	-700	-11.6	Si-D2	-200	-2410	rate scan
26	1.2	1000	60	125	CMS01	-500	-12.4	II6-93	-700	-21.5	Si-D2	-200	-2240	rate scan
27	1.2	3333	130	275	CMS01	-500	-30.0	II6-93	-700	-50.4	Si-D2	-200	-2207	rate scan
29	1.2	3333	130	275	CMS01	-500	-43.0	II6-93	-700	-54.5	Si-D2	-200	-3139	rate scan
30	1.2	4800	145	450	CMS01	-500	-43.2	II6-93	-700	-72.2	Si-D2	-200	-2254	rate scan
32	2.5	1000	60	125	CMS01	-500	-18.3	II6-93	-700	-24.3	Si-D2	-200	-2267	rate scan
33	2.5	100	30	90	CMS01	-500	-7.5	II6-93	-700	-7.1	Si-D2	-200	-2499	rate scan
34	0.3	33	28	85	CMS01	-500	-5.2	II6-93	-700	-9.4	Si-D2	-200	-2503	rate scan
35	0.9	33	28	85	CMS01	-500	-5.4	II6-93	-700	-6.7	Si-D2	-200	-2478	rate scan
36	5.0	4800	145	450	CMS02	0	?	II6-750	0	?	Si-D2	-200	-2591	pumping
37	0.1	333	38	90	CMS02	-50	-32.0	II6-750	-50	-1.2	Si-D2	-200	-2975	voltage scan
38	2.5	333	38	90	CMS02	-50	-0.9	II6-750	-50	-1.2	Si-D2	-200	-3049	voltage scan
39	2.5	333	38	90	CMS02	-100	-1.5	II6-750	-100	-2.7	Si-D2	-200	-3104	voltage scan
40	2.5	333	38	90	CMS02	-200	-2.7	II6-750	-200	-6.5	Si-D2	-200	-3130	voltage scan
41	0.5	333	38	90	CMS02	-400	-5.1	II6-750	-400	-13.1	Si-D2	-200	-3095	voltage scan
42	1.8	333	38	90	CMS02	-400	-14.1	II6-750	-400	-21.7	Si-D2	-200	-3057	voltage scan
43	2.5	333	38	90	CMS02	-500	-174.2	II6-750	-600	-57.0	Si-D2	-200	-2997	voltage scan
44	2.5	333	38	90	CMS02	-600	-165.8	II6-750	-700	-95.7	Si-D2	-200	-3096	voltage scan
45	2.5	333	38	90	CMS02	-650	-233.1	II6-750	-800	-146.6	Si-D2	-200	-3087	voltage scan
46	5.0	4800	145	450	CMS02	0	-0.7	II6-750	0	-0.7	Si-D2	-200	-3087	pumping
47	1.2	33	28	85	CMS02	-600		II6-750	-750		Si-D2	-200		rate scan
48	1.2	33	28	85	CMS02	-600	-16.9	II6-750	-750	-29.4	Si-D2	-200	-3159	rate scan
49	1.2	100	30	90	CMS02	-600	-18.5	II6-750	-750	-32.1	Si-D2	-200	-3241	rate scan
50	1.2	333	38	90	CMS02	-600	-21.1	II6-750	-750	-49.8	Si-D2	-200	-3261	rate scan
51	1.2	1000	60	125	CMS02	-600	-109.8	II6-750	-750	-97.7	Si-D2	-200	-3122	rate scan
52	1.2	3333	130	275	CMS02	-600	-227.4	II6-750	-750	-194.8	Si-D2	-200	-3080	rate scan
53	1.2	4800	145	450	CMS02	-600	-364.1	II6-750	-750	-263.4	Si-D2	-200	-3047	rate scan
54	1.2	3333	130	275	CMS02	-600	-454.7	II6-750	-750	-225.0	Si-D2	-200	-3056	rate scan
55	1.2	1000	60	125	CMS02	-600	-529.7	II6-750	-750	-139.6	Si-D2	-200	-2944	rate scan
56	1.2	333	38	90	CMS02	-600	-469.9	II6-750	-750	-104.4	Si-D2	-200	-3077	rate scan
57	1.2	100	30	90	CMS02	-600	-506.2	II6-750	-750	-84.7	Si-D2	-200	-3166	rate scan
58	1.2	33	28	85	CMS02	-600	-543.8	II6-750	-750	-74.4	Si-D2	-200	-3203	rate scan
59	1.2	100	30	90	CMS02	-600	-325.2	II6-750	-750	-72.4	Si-D2	-200	-3249	rate scan
60	1.2	333	38	90	CMS02	-600	-311.2	II6-750	-750	-95.0	Si-D2	-200	-3224	rate scan
61	1.2	1000	60	125	CMS02	-600	-307.2	II6-750	-750	-129.9	Si-D2	-200	-3165	rate scan
62	1.2	3333	130	275	CMS02	-600	-305.2	II6-750	-750	-186.5	Si-D2	-200	-3056	rate scan
63	1.2	4800	145	450	CMS02	-600	-303.1	II6-750	-750	-255.5	Si-D2	-200	-3038	rate scan
64	1.2	1000	60	125	CMS02	-600	-273.0	II6-750	-750	-119.5	Si-D2	-200	-2984	rate scan
65	1.3	1000	60	125	CMS02	-600	-271.3	II6-750	-750	-120.8	Si-D2	-200	-3045	rate scan
66	2.5	100	30	90	CMS02	-600	-277.0	II6-750	-750	-75.8	Si-D2	-200	-3114	rate scan
67	1.2	33	28	85	CMS02	-600	-270.4	II6-750	-750	-80.7	Si-D2	-200	-3276	rate scan

Acronyms

ADC analog-to-digital converter. ix, xxi, xxiv, xxvii, 36, 108, 116, 118–120, 129–131, 133, 150, 157, 159, 170, 176, 177, 188, 189, 201

ALICE A Large Ion Collider Experiment. 2

ASIC Application-specific integrated circuits. vi, xix, 41, 43, 107, 118, 119, 201

ATLAS A Toroidal LHC ApparatuS. 2

BRNC Binnig and Rohrer Nanotechnology Center. 3, 56, 226, 234, 245

CCD charge collection distance. xviii, xxxii, 2, 13, 40, 47, 87, 90, 92, 195, 215, 219

CCE charge collection efficiency. xxxii, 13, 28, 102, 178, 215, 216, 219

CDF Cumulative Distribution Function. xx, 128, 129, 176, 247, 248

CERN Organization Européenne pour la Recherche. viii, ix, xix, 2, 3, 41, 46, 84, 104–109, 116, 118, 120, 122, 124, 126, 128, 130, 132, 134, 136, 138, 140, 142, 144, 146, 148, 150, 152, 154, 156, 201, 202, 204, 206, 208, 210, 212, 214, 216, 218, 220, 222, 224, 226

CMS Compact Muon Solenoid. 2, 3, 36, 67, 70, 178, 191, 226

CVD chemical vapor deposition. v, vi, xxxi, 2, 6–9, 24, 87, 88, 128

DAC digital-to-analog converters. 37, 116, 176

DAQ data acquisition. 41, 108

DI deionized. 58

DTB digital test board. xiv, xix, xxv, 37–39, 111–116, 167, 168, 188, 192

DUT devices under test. xiv, xv, xix–xxii, xxvi–xxviii, xxxii, 42, 44, 46, 47, 106–108, 111–116, 118, 120, 124–126, 130, 131, 134–140, 143–145, 147, 148, 157, 161, 162, 165, 166, 172, 173, 175, 178, 181, 182, 184, 185, 188–200, 211

e-TCT Edge transient-current technique. xviii, 90, 91, 200

eh-pair electron-hole pair. 7, 16, 19, 29, 90

ENC Equivalent Noise Charges. 42–44, 201, 204, 229, 231

FEM Finite Elements Method. 75, 226

FET field-effect transistor. 42

HFCVD Hot Filament CVD. 8

HL-LHC High Luminoisity LHC. 2, 3

HPHT High-Pressure High-Temperature. 6, 7

HV high voltage. viii, xiv, xv, xix, xxiv, 38, 39, 41–44, 46, 48–51, 54, 76, 101, 102, 152, 154

ICP-RIE inductively coupled plasma reactive ion etching. x, xxx, xxxi, 56, 58, 234–236

LHC Large Hadron Collider. 2, 3

LHCb LHC beauty. 2

MFP mean free path. xii, xxxii, 12–14, 29, 89, 92, 219, 221, 222

MIP minimum-ionizing particle. xii, 7, 18–20, 86, 115, 195–197, 219

MPV most probable vlaue. xii, xiii, xxvii–xxx, 19–21, 188–190, 195, 197, 198, 208, 209, 249, 250

MWCVD Microwave Plasma-Enhanced CVD. 8

NIEL Non-ionising energy loss. xxxi, 11, 12, 89, 105

PCB printed circuit board. xiv, xv, 37–39, 46, 47, 115

pCVD polycrystalline chemical vapor deposition. iv, xii, 8–10, 13, 36, 48, 49, 51, 86, 87, 89, 92, 97, 102, 178, 181, 184, 185, 188, 191, 193, 195, 197, 200, 212, 214, 215, 218, 219, 225, 227

PECVD plasma-enhanced chemical vapor deposition. x, xvi, 57, 64, 65, 244, 246

PH pulse height. xix, xx, xxiv, 118–120, 154, 155, 182

PSI Paul Scherrer Institute. viii, ix, xix, 3, 36, 37, 57, 62, 69, 70, 73, 110–116, 157, 158, 160, 162, 164, 166–168, 170, 172, 174, 176, 178, 179, 181, 182, 184, 186, 188, 190, 192, 194, 196, 198, 200, 226

PUC pixel unit cells. xiv, xvii, 36–38, 65, 73, 116, 189, 191

pXar Pixel eXpert Analysis & Readout. 115, 157, 159

RD42 RD of CVD Diamond Radiation Detectors. 2, 3, 12, 13, 20, 40–42, 49, 54, 60, 61, 105, 106, 200, 219, 224, 226, 232

RIE reactive ion etching. x, xvi, 54, 57, 63, 65, 66, 246

RMS root mean square. 21, 108, 115, 120, 122, 124, 141, 230, 231

ROC readout chip. viii, xiv, xvii, xxiv, xxvi, 36–38, 57, 65, 73, 94, 95, 112, 115, 116, 157–159, 170, 176, 178, 181, 185, 188, 189, 198

S&H sample and hold. 41

scCVD single-crystalline chemical vapor deposition. xx, xxii, xxix, 3, 8, 9, 13, 25, 86, 87, 102, 120, 144, 197, 200, 208, 209

Si-DUT Silicon DUT. 162

Sirocco Silicon strip read-out CAMAC controller. xix, xx, xxix, xxxii, 108, 118–120, 207–210

SNR signal-to-noise-ratio. xxii, 124–126, 144, 145

SPS Super Proton Synchrotron. 104, 105

TU trigger unit. xix, xxv, 113–116, 157, 160, 167

u.s. ultrasound. 57

UBM under-bump-metallization. x, xvi, xvii, xxxi, 57, 67–69, 182, 238, 239

USB Universal Serial Bus. 38

UV ultra violet. xxx, 237–241, 243

VLSI Very large-scale integration. 56

VME Versa Module Europa bus standard. 41, 108

Bibliography

[1] PJ van Heerden. “The crystal counter”. PhD thesis. 1945 (cit. on p. 2).

[2] L. F. Curtiss and B. W. Brown. “Diamond as a Gamma-Ray Counter”. In: *Phys. Rev.* 72 (7 Oct. 1947), pp. 643–643. DOI: 10.1103/PhysRev.72.643. URL: https://link.aps.org/doi/10.1103/PhysRev.72.643 (cit. on p. 2).

[3] W. F. Cotty. “Diamond as a Pinpoint Radiation Counter”. In: *Nature* 177.4519 (June 1956), pp. 1075–1076. ISSN: 1476-4687. DOI: 10.1038/1771075a0. URL: https://doi.org/10.1038/1771075a0 (cit. on p. 2).

[4] S. F. Kozlov et al. “Preparation and Characteristics of Natural Diamond Nuclear Radiation Detectors”. In: *IEEE Transactions on Nuclear Science* 22.1 (1975), pp. 160–170. DOI: 10.1109/TNS.1975.4327634 (cit. on p. 2).

[5] R. K. Willardson and G. C. Danielson. “Effect of Light on a Diamond Conduction Counter”. In: *Phys. Rev.* 77 (2 Jan. 1950), pp. 300–301. DOI: 10.1103/PhysRev.77.300.2. URL: https://link.aps.org/doi/10.1103/PhysRev.77.300.2 (cit. on p. 2).

[6] Seiichiro Matsumoto et al. “Growth of diamond particles from methane-hydrogen gas”. In: *Journal of Materials Science* 17.11 (Nov. 1982), pp. 3106–3112. ISSN: 1573-4803. DOI: 10.1007/BF01203472. URL: https://doi.org/10.1007/BF01203472 (cit. on p. 2).

[7] John C. Angus and Cliff C. Hayman. “Low-Pressure, Metastable Growth of Diamond and "Diamondlike" Phases”. In: *Science* 241.4868 (1988), pp. 913–921. DOI: 10.1126/science.241.4868.913. eprint: https://www.science.org/doi/pdf/10.1126/science.241.4868.913. URL: https://www.science.org/doi/abs/10.1126/science.241.4868.913 (cit. on p. 2).

[8] Walter A. Yarbrough and Russell Messier. “Current Issues and Problems in the Chemical Vapor Deposition of Diamond”. In: *Science* 247.4943 (1990), pp. 688–696. DOI: 10.1126/science.247.4943.688. eprint: https://www.science.org/doi/pdf/10.1126/science.247.4943.688. URL: https://www.science.org/doi/abs/10.1126/science.247.4943.688 (cit. on p. 2).

[9] M. A. Plano et al. “Thickness dependence of the electrical characteristics of chemical vapor deposited diamond films”. In: *Applied Physics Letters* 64.2 (1994), pp. 193–195. DOI: 10.1063/1.111501. eprint: https://doi.org/10.1063/1.111501. URL: https://doi.org/10.1063/1.111501 (cit. on p. 2).

[10] S. Schnetzer et al. “A Compact Diamond Based Detector for the SSC: An Expression of Interest for an Experiment to be Performed at the SSC”. In: (July 1990) (cit. on p. 2).

[11] M H Nazaré, B Foster, R S Gilmore, et al. *Development of diamond tracking detectors for high luminosity experiments at the LHC*. Tech. rep. Over title: R&D proposal. Geneva: CERN, 1994. URL: https://cds.cern.ch/record/293000 (cit. on p. 2).

[12] *RD42 Collaboration*. Accessed: 2022.08.13. CERN. URL: https://rd42.web.cern.ch/rd42/ (cit. on p. 2).

[13] A.J. Edwards et al. “Radiation monitoring with CVD diamonds in BaBar”. In: *IEEE Symposium Conference Record Nuclear Science 2004.* Vol. 2. 2004, 729–733 Vol. 2. DOI: 10.1109/NSSMIC.2004.1462314 (cit. on p. 2).

[14] Peter Dong et al. “Beam Condition Monitoring With Diamonds at CDF”. In: *IEEE Transactions on Nuclear Science* 55.1 (2008), pp. 328–332. DOI: 10.1109/TNS.2007.913492 (cit. on p. 2).

[15] Irena Dolenc Kittelmann. “Development of Beam Conditions Monitor for the ATLAS experiment”. Presented 18 Sep 2008. PhD thesis. 2008. URL: https://cds.cern.ch/record/1390440 (cit. on p. 2).

[16] B Macek. *Performance of the ATLAS Beam Diagnostic Systems*. Tech. rep. Geneva: CERN, 2010. URL: https://cds.cern.ch/record/1314515 (cit. on p. 2).

[17] A. E. Dabrowski et al. “The performance of the Beam Conditions and Radiation Monitoring System of CMS”. In: *2011 IEEE Nuclear Science Symposium Conference Record*. 2011, pp. 489–495. DOI: 10.1109/NSSMIC.2011.6153979 (cit. on p. 2).

[18] *CMS Experiment*. Accessed: 2022.08.13. CERN. URL: https://cms.cern (cit. on p. 2).

[19] *ATLAS Experiment*. Accessed: 2022.08.13. CERN. URL: https://atlas.cern (cit. on p. 2).

[20] *CERN Organization*. Accessed: 2022.08.13. CERN. URL: https://home.cern (cit. on p. 2).

[21] CMS Collaboration. “Observation of a new boson at a mass of 125 GeV with the CMS experiment at the LHC”. In: *Physics Letters B* 716.1 (2012), pp. 30–61. ISSN: 0370-2693. DOI: 10.1016/j.physletb.2012.08.021. URL: https://www.sciencedirect.com/science/article/pii/S0370269312008581 (cit. on p. 2).

[22] ATLAS Collaboration. “Observation of a new particle in the search for the Standard Model Higgs boson with the ATLAS detector at the LHC”. In: *Physics Letters B* 716.1 (2012), pp. 1–29. ISSN: 0370-2693. DOI: 10.1016/j.physletb.2012.08.020. URL: https://www.sciencedirect.com/science/article/pii/S037026931200857X (cit. on p. 2).

[23] *High Luminosity LHC Project*. Accessed: 2022.08.13. CERN. URL: https://hilumilhc.web.cern.ch/ (cit. on p. 2).

[24] O. Aberle, I Béjar Alonso, O Brüning, et al. *High-Luminosity Large Hadron Collider (HL-LHC): Technical design report*. CERN Yellow Reports: Monographs. Geneva: CERN, 2020. DOI: 10.23731/CYRM-2020-0010. URL: https://cds.cern.ch/record/2749422 (cit. on p. 3).

[25] D Contardo et al. *Technical Proposal for the Phase-II Upgrade of the CMS Detector*. Tech. rep. Upgrade Project Leader Deputies: Lucia Silvestris (INFN-Bari), Jeremy Mans (University of Minnesota) Additional contacts: Lucia.Silvestris@cern.ch, Jeremy.Mans@cern.ch. Geneva, 2015. DOI: 10.17181/CERN.VU8I.D59J. URL: https://cds.cern.ch/record/2020886 (cit. on p. 3).

[26] Sudhir Malik. *CMS Phase-2 Inner Tracker Upgrade*. Tech. rep. Geneva: CERN, 2021. URL: https://cds.cern.ch/record/2816244 (cit. on p. 3).

[27] Alexander Oh et al. "A novel detector with graphitic electrodes in CVD diamond". In: *Diamond and Related Materials* 38 (2013), pp. 9–13. ISSN: 0925-9635. DOI: 10.1016/j.diamond.2013.06.003. URL: https://www.sciencedirect.com/science/article/pii/S0925963513001106 (cit. on pp. 3, 219).

[28] F. Bachmair et al. "A 3D diamond detector for particle tracking". In: *Nuclear Instruments and Methods in Physics Research Section A: Accelerators, Spectrometers, Detectors and Associated Equipment* 786 (2015), pp. 97–104. ISSN: 0168-9002. DOI: 10.1016/j.nima.2015.03.033. URL: https://www.sciencedirect.com/science/article/pii/S0168900215003496 (cit. on pp. 3, 102).

[29] Markus Mathes. "Development and Characterization of Diamond and 3D-Silicon Pixel Detectors with ATLAS-Pixel Readout Electronics". Presented 18 Dec 2008. PhD thesis. 2008. URL: https://cds.cern.ch/record/1337735 (cit. on p. 3).

[30] D. Dobos and Heinz Pernegger. "Diamond pixel modules and the ATLAS beam conditions monitor". In: *Nuclear Instruments and Methods in Physics Research Section A: Accelerators, Spectrometers, Detectors and Associated Equipment* 628.1 (2011). VCI 2010, pp. 246–250. ISSN: 0168-9002. DOI: 10.1016/j.nima.2010.06.328. URL: https://www.sciencedirect.com/science/article/pii/S0168900210015184 (cit. on p. 3).

[31] *Fraunhofer Institute for Reliability and Microintegration IZM*. Accessed: 2022.08.13. Fraunhofer IZM. URL: https://www.izm.fraunhofer.de/en.html (cit. on p. 3).

[32] Michael Reichmann. "A Particle Tracker For An Extreme Radiation Environment With Strongly Changing Fluxes: pCVD Diamond". Presented 9 Sep 2022. PhD thesis. 2022. to be published (cit. on p. 3).

[33] *BRNC - Binnig and Rohrer Nanotechnology Center*. Accessed: 2022.08.13. ETHZ and IBM. URL: https://brnc.ethz.ch/ (cit. on p. 3).

[34] *Paul Scherrer Institut*. Accessed: 2022.08.13. PSI. URL: https://www.psi.ch (cit. on p. 3).

[35] Christoph Nebel Daniele Mari Luis Miguel, ed. Elsevier, Feb. 2014, p. 1806. ISBN: 9780080965284. URL: https://www.sciencedirect.com/referencework/9780080965284/comprehensive-hard-materials (cit. on pp. 5, 7, 58, 60).

[36] Don R. Kania Lawrence S. Pan, ed. Electronic Materials: Science & Technology. Springer New York, NY, pp. XIV, 472. ISBN: 978-1-4615-2257-7 (cit. on pp. 5, 7–11, 24, 55, 60).

[37] Marco A. Quiroz and Erick R. Bandala. "Types of Conducting Diamond Materials and their Properties". In: *Synthetic Diamond Films*. John Wiley & Sons, Ltd, 2011. Chap. 3, pp. 57–75. ISBN: 9781118062364. DOI: 10.1002/9781118062364.ch3. eprint: https://onlinelibrary.wiley.com/doi/pdf/10.1002/9781118062364.ch3. URL: https://onlinelibrary.wiley.com/doi/abs/10.1002/9781118062364.ch3 (cit. on pp. 6–8).

[38] H.F.-W. Sadrozinski. "Applications of silicon detectors". In: *IEEE Transactions on Nuclear Science* 48.4 (2001), pp. 933–940. DOI: 10.1109/23.958703 (cit. on pp. 5, 115).

[39] Wim de Boer et al. "Radiation hardness of diamond and silicon sensors compared". In: *physica status solidi (a)* 204.9 (2007), pp. 3004–3010. DOI: 10.1002/pssa.200776327. eprint: https://onlinelibrary.wiley.com/doi/pdf/10.1002/pssa.200776327. URL: https://onlinelibrary.wiley.com/doi/abs/10.1002/pssa.200776327 (cit. on pp. 5, 11, 12, 105).

[40] M Levinshtein, S Rumyantsev, and M Shur. *Handbook Series on Semiconductor Parameters*. WORLD SCIENTIFIC, 1996. DOI: 10.1142/2046. eprint: https://www.worldscientific.com/doi/pdf/10.1142/2046. URL: https://www.worldscientific.com/doi/abs/10.1142/2046 (cit. on p. 7).

[41] D.J. Twitchen et al. "Thermal conductivity measurements on CVD diamond". In: *Diamond and Related Materials* 10.3 (2001). 11th European Conference on Diamond, Diamond-like Materials, Carbon Nanotubes, Nitrides and Silicon Carbide, pp. 731–735. ISSN: 0925-9635. DOI: 10.1016/S0925-9635(00)00515-X. URL: https://www.sciencedirect.com/science/article/pii/S092596350000515X (cit. on p. 7).

[42] Ricardo S. Sussmann et al. "Optical and dielectric properties of CVD polycrystalline diamond plates". In: *Window and Dome Technologies and Materials IV*. Ed. by Paul Klocek. Vol. 2286. International Society for Optics and Photonics. SPIE, 1994, pp. 229–238. DOI: 10.1117/12.187344. URL: https://doi.org/10.1117/12.187344 (cit. on p. 7).

[43] Chris J.H. Wort and Richard S. Balmer. "Diamond as an electronic material". In: *Materials Today* 11.1 (2008), pp. 22–28. ISSN: 1369-7021. DOI: 10.1016/S1369-7021(07)70349-8. URL: https://www.sciencedirect.com/science/article/pii/S1369702107703498 (cit. on p. 7).

[44] H. Pernegger et al. “Charge-carrier properties in synthetic single-crystal diamond measured with the transient-current technique”. In: *Journal of Applied Physics* 97.7 (2005), p. 073704. DOI: 10.1063/1.1863417. eprint: https://doi.org/10.1063/1.1863417. URL: https://doi.org/10.1063/1.1863417 (cit. on pp. 7, 25, 86, 87).

[45] Julian Becker, Eckhart Fretwurst, and Robert Klanner. “Measurements of charge carrier mobilities and drift velocity saturation in bulk silicon of 111 and 100 crystal orientation at high electric fields”. In: *Solid-State Electronics* 56.1 (2011), pp. 104–110. ISSN: 0038-1101. DOI: 10.1016/j.sse.2010.10.009. URL: https://www.sciencedirect.com/science/article/pii/S0038110110003576 (cit. on p. 7).

[46] Alan T. Collins et al. “The Electronic and Optical Properties of Diamond; Do they Favour Device Applications?” In: *MRS Online Proceedings Library* 162.1 (Dec. 1989). ISSN: 1946-4274. URL: https://doi.org/10.1557/PROC-162-3 (cit. on p. 7).

[47] J. Koike, D. M. Parkin, and T. E. Mitchell. “Displacement threshold energy for type IIa diamond”. In: *Applied Physics Letters* 60.12 (1992), pp. 1450–1452. DOI: 10.1063/1.107267. eprint: https://doi.org/10.1063/1.107267. URL: https://doi.org/10.1063/1.107267 (cit. on p. 7).

[48] J. W. Corbett and G. D. Watkins. “Production of Divacancies and Vacancies by Electron Irradiation of Silicon”. In: *Phys. Rev.* 138 (2A Apr. 1965), A555–A560. DOI: 10.1103/PhysRev.138.A555. URL: https://link.aps.org/doi/10.1103/PhysRev.138.A555 (cit. on p. 7).

[49] J. J. Loferski and P. Rappaport. “Radiation Damage in Ge and Si Detected by Carrier Lifetime Changes: Damage Thresholds”. In: *Phys. Rev.* 111 (2 July 1958), pp. 432–439. DOI: 10.1103/PhysRev.111.432. URL: https://link.aps.org/doi/10.1103/PhysRev.111.432 (cit. on p. 7).

[50] Particle Data Group et al. “Review of Particle Physics”. In: *Progress of Theoretical and Experimental Physics* 2022.8 (Aug. 2022). 083C01. ISSN: 2050-3911. DOI: 10.1093/ptep/ptac097. eprint: https://academic.oup.com/ptep/article-pdf/2022/8/083C01/45434166/ptac097.pdf. URL: https://doi.org/10.1093/ptep/ptac097 (cit. on pp. 7, 16, 18, 20–22, 115).

[51] Jeffrey W. Keister et al. “Diamond X-ray photodiode for white and monochromatic SR beams”. In: *Nuclear Instruments and Methods in Physics Research Section A: Accelerators, Spectrometers, Detectors and Associated Equipment* 649.1 (2011). National Synchrotron Radiation Instrumentation conference in 2010, pp. 91–93. ISSN: 0168-9002. DOI: 10.1016/j.nima.2010.11.135. URL: https://www.sciencedirect.com/science/article/pii/S0168900210026823 (cit. on p. 7).

[52] Hans Bichsel. “Straggling in thin silicon detectors”. In: *Rev. Mod. Phys.* 60 (3 July 1988), pp. 663–699. DOI: 10.1103/RevModPhys.60.663. URL: https://link.aps.org/doi/10.1103/RevModPhys.60.663 (cit. on pp. 7, 20).

[53] Shulai Zhao. "Characterization of the Electrical Properties of Polycrystalline Diamond Films". Presented on 1994. PhD thesis. 1994. URL: http://rave.ohiolink.edu/etdc/view?acc_num=osu1394810346 (cit. on pp. 7, 19).

[54] F. P. BUNDY et al. "Man-Made Diamonds". In: *Nature* 176.4471 (). ISSN: 1476-4687. URL: https://doi.org/10.1038/176051a0 (cit. on p. 7).

[55] Hendrik Jansen. "Chemical Vapour Deposition Diamond - Charge Carrier Movement at Low Temperatures and Use in Time-Critical Applications". Presented 10 Dec 2013. PhD thesis. Sept. 2013. URL: http://cds.cern.ch/record/1956431 (cit. on p. 8).

[56] *The Element Six CVD Diamond Handbook*. Accessed: 2022.08.13. Element Six Technologies US Corporation. Santa Clara CA, USA, 2020. URL: https://e6cvd.com/media/wysiwyg/pdf/CVD_Diamond_Handbook_digital_01.07.20.pdf (cit. on pp. 8, 9).

[57] J. M. T. Thompson and Paul W. May. "Diamond thin films: a 21st-century material". In: *Philosophical Transactions of the Royal Society of London. Series A: Mathematical, Physical and Engineering Sciences* 358.1766 (2000), pp. 473–495. DOI: 10.1098/rsta.2000.0542. eprint: https://royalsocietypublishing.org/doi/pdf/10.1098/rsta.2000.0542. URL: https://royalsocietypublishing.org/doi/abs/10.1098/rsta.2000.0542 (cit. on p. 9).

[58] *Cross-section of a CVD diamond*. Accessed: 2022.08.13. University of Bristol. URL: http://www.chm.bris.ac.uk/pt/diamond/semflat.htm (cit. on p. 9).

[59] Jes Asmussen and D Reinhard, eds. CRC Press, Jan. 2002. ISBN: 9780429222634. URL: https://doi.org/10.1201/9780203910603 (cit. on p. 9).

[60] Carlo Bradac, Torsten Gaebel, and James R. Rabeau. "Nitrogen-Vacancy Color Centers in Diamond: Properties, Synthesis, and Applications". In: *Optical Engineering of Diamond*. John Wiley & Sons, Ltd, 2013. Chap. 5, pp. 143–175. ISBN: 9783527648603. DOI: 10.1002/9783527648603.ch5. eprint: https://onlinelibrary.wiley.com/doi/pdf/10.1002/9783527648603.ch5. URL: https://onlinelibrary.wiley.com/doi/abs/10.1002/9783527648603.ch5 (cit. on p. 10).

[61] B. Campbell and A. Mainwood. "Radiation Damage of Diamond by Electron and Gamma Irradiation". In: *physica status solidi (a)* 181.1 (2000), pp. 99–107. DOI: 10.1002/1521-396X(200009)181:1<99::AID-PSSA99>3.0.CO;2-5. eprint: https://onlinelibrary.wiley.com/doi/pdf/10.1002/1521-396X\%28200009\%29181\%3A1\%3C99\%3A\%3AAID-PSSA99\%3E3.0.CO\%3B2-5. URL: https://onlinelibrary.wiley.com/doi/abs/10.1002/1521-396X%28200009%29181%3A1%3C99%3A%3AAID-PSSA99%3E3.0.CO%3B2-5 (cit. on pp. 10, 22, 23).

[62] F. Hartjes et al. “Parameterisation of radiation effects on CVD diamond for proton irradiation”. In: *Nuclear Physics B - Proceedings Supplements* 78.1 (1999). Advanced Technology and Particle Physics, pp. 675–682. ISSN: 0920-5632. DOI: 10.1016/S0920-5632(99)00623-4. URL: https://www.sciencedirect.com/science/article/pii/S0920563299006234 (cit. on p. 12).

[63] Karl Hecht. “Zum Mechanismus des lichtelektrischen Primärstromes in isolierenden Kristallen”. In: *Zeitschrift für Physik* 77.3 (Mar. 1932), pp. 235–245. ISSN: 0044-3328. URL: https://doi.org/10.1007/BF01338917 (cit. on pp. 12, 13, 89).

[64] L Bäni et al. “A study of the radiation tolerance of poly-crystalline and single-crystalline CVD diamond to 800 MeV and 24 GeV protons”. In: *Journal of Physics D: Applied Physics* 52.46 (Aug. 2019), p. 465103. DOI: 10.1088/1361-6463/ab37c6. URL: https://doi.org/10.1088/1361-6463/ab37c6 (cit. on pp. 14, 15, 51, 140, 219).

[65] Lukas Bäni et al. “A Study of the Radiation Tolerance of CVD Diamond to 70 MeV Protons, Fast Neutrons and 200 MeV Pions”. In: *Sensors* 20.22 (2020). ISSN: 1424-8220. DOI: 10.3390/s20226648. URL: https://www.mdpi.com/1424-8220/20/22/6648 (cit. on p. 14).

[66] H. Bethe. “Bremsformel für Elektronen relativistischer Geschwindigkeit”. In: *Zeitschrift für Physik* 76.5 (May 1932), pp. 293–299. ISSN: 0044-3328. DOI: 10.1007/BF01342532. URL: https://doi.org/10.1007/BF01342532 (cit. on p. 16).

[67] W H Barkas and M J Berger. “TABLES OF ENERGY LOSSES AND RANGES OF HEAVY CHARGED PARTICLES”. In: (Jan. 1964). URL: https://www.osti.gov/biblio/4682091 (cit. on p. 17).

[68] *Atomic nuclear properties of Diamond with muons*. Accessed: 2022.08.13. Particle Data Group, 2020. URL: https://pdg.lbl.gov/2022/AtomicNuclearProperties/MUE/muE_carbon_gem_diamond.pdf (cit. on pp. 17–19).

[69] H. H. Andersen and J. F. Ziegler. *Hydrogen: Stopping Powers and Ranges in All Elements*. Vol. 3. Pergamon Press, 1977. URL: http://inis.iaea.org/search/search.aspx?orig_q=RN:09372566 (cit. on p. 18).

[70] J Lindhard. “ON THE PROPERTIES OF A GAS OF CHARGED PARTICLES”. In: *Kgl. Danske Videnskab. Selskab Mat.-fys. Medd.* 28.8 (Jan. 1954). URL: https://www.osti.gov/biblio/4405425 (cit. on p. 18).

[71] *Atomic nuclear properties of Silicon with muons*. Accessed: 2022.08.13. Particle Data Group, 2020. URL: https://pdg.lbl.gov/2022/AtomicNuclearProperties/MUE/muE_silicon_Si.pdf (cit. on p. 19).

[72] Alexander Oh. “CVD Diamant als Material für Teilchendetektoren”. Doctoral Thesis. Hamburg: Universität Hamburg, 1999 (cit. on p. 19).

[73] Michal Pomorski. “Electronic Properties of Single Crystal CVD Diamond and its Suitability for Particle Detection in Hadron Physics Experiments”. Doctoral Thesis. Frankfurt am Main: Johann Wolfgang Goethe - Universität in Frankfurt am Main, 2008 (cit. on p. 19).

[74] Hans Bichsel. "Straggling of Heavy Charged Particles: Comparison of Born Hydrogenic-Wave-Function Approximation with Free-Electron Approximation". In: *Phys. Rev. B* 1 (7 Apr. 1970), pp. 2854–2862. DOI: 10.1103/PhysRevB.1.2854. URL: https://link.aps.org/doi/10.1103/PhysRevB.1.2854 (cit. on p. 20).

[75] O. Blunck and S. Leisegang. "Zum Energieverlust schneller Elektronen in dünnen Schichten". In: *Zeitschrift für Physik* 128.4 (Aug. 1950), pp. 500–505. ISSN: 0044-3328. DOI: 10.1007/BF01330032. URL: https://doi.org/10.1007/BF01330032 (cit. on p. 20).

[76] H. A. Bethe. "Molière's Theory of Multiple Scattering". In: *Phys. Rev.* 89 (6 Mar. 1953), pp. 1256–1266. DOI: 10.1103/PhysRev.89.1256. URL: https://link.aps.org/doi/10.1103/PhysRev.89.1256 (cit. on p. 21).

[77] Hans Bichsel. "Multiple Scattering of Protons". In: *Phys. Rev.* 112 (1 Oct. 1958), pp. 182–185. DOI: 10.1103/PhysRev.112.182. URL: https://link.aps.org/doi/10.1103/PhysRev.112.182 (cit. on p. 21).

[78] G. Shen et al. "Measurement of multiple scattering at 50 to 200 GeV/c". In: *Phys. Rev. D* 20 (7 Oct. 1979), pp. 1584–1588. DOI: 10.1103/PhysRevD.20.1584. URL: https://link.aps.org/doi/10.1103/PhysRevD.20.1584 (cit. on p. 21).

[79] Gerald R. Lynch and Orin I. Dahl. "Approximations to multiple Coulomb scattering". In: *Nuclear Instruments and Methods in Physics Research Section B: Beam Interactions with Materials and Atoms* 58.1 (1991), pp. 6–10. ISSN: 0168-583X. DOI: 10.1016/0168-583X(91)95671-Y. URL: https://www.sciencedirect.com/science/article/pii/0168583X9195671Y (cit. on p. 21).

[80] Ben Streetman and Sanjay Banerjee. *Solid State Electronic Devices*. 6th ed. Pearson Education Inc., 2009. ISBN: 978-81-203-3020-7 (cit. on pp. 24, 25).

[81] D.M. Caughey and R.E. Thomas. "Carrier mobilities in silicon empirically related to doping and field". In: *Proceedings of the IEEE* 55.12 (1967), pp. 2192–2193. DOI: 10.1109/PROC.1967.6123. URL: https://ieeexplore.ieee.org/document/1448053 (cit. on p. 25).

[82] C. Dorfer et al. "Three-dimensional charge transport mapping by two-photon absorption edge transient-current technique in synthetic single-crystalline diamond". In: *Applied Physics Letters* 114.20 (2019), p. 203504. DOI: 10.1063/1.5090850. eprint: https://doi.org/10.1063/1.5090850. URL: https://doi.org/10.1063/1.5090850 (cit. on pp. 25, 86, 90).

[83] W. Shockley. "Currents to Conductors Induced by a Moving Point Charge". In: *Journal of Applied Physics* 9.10 (1938), pp. 635–636. DOI: 10.1063/1.1710367. eprint: https://doi.org/10.1063/1.1710367. URL: https://doi.org/10.1063/1.1710367 (cit. on p. 28).

[84] S. Ramo. "Currents Induced by Electron Motion". In: *Proceedings of the IRE* 27.9 (1939), pp. 584–585. DOI: 10.1109/JRPROC.1939.228757 (cit. on p. 28).

[85] C.K. Jen. "On the Induced Current and Energy Balance in Electronics". In: *Proceedings of the IRE* 29.6 (1941), pp. 345–349. DOI: 10.1109/JRPROC.1941.230316 (cit. on p. 28).

[86] G. Cavalleri et al. "Extension of Ramo's theorem as applied to induced charge in semiconductor detectors". In: *Nuclear Instruments and Methods* 92.1 (1971), pp. 137–140. ISSN: 0029-554X. DOI: 10.1016/0029-554X(71)90235-7. URL: https://www.sciencedirect.com/science/article/pii/0029554X71902357 (cit. on p. 28).

[87] Helmuth Spieler. Oxford Univ. Press, Aug. 2005, p. 512. ISBN: 9780198527848 (cit. on pp. 28, 32, 33, 42, 229).

[88] W.M.C. Sansen and Z.Y. Chang. "Limits of low noise performance of detector readout front ends in CMOS technology". In: *IEEE Transactions on Circuits and Systems* 37.11 (1990), pp. 1375–1382. DOI: 10.1109/31.62412 (cit. on p. 33).

[89] *Results from digital ROC Irradiations*. CERN. Presented at the 2013 February CMS Tracker Week, Feb. 2013 (cit. on p. 37).

[90] Jan Hendrik Hoß. "Search for Supersymmetry with Multiple Charged Leptons at sqrts = 13 TeV with CMS and Radiation Tolerance of the Readout Chip for the Phase I Upgrade of the Pixel Detector". eng. PhD thesis. 2017 (cit. on pp. 38, 191).

[91] *CVD Diamond Substrates*. Accessed: 2022.08.13. II-VI. URL: https://ii-vi.com/product/cvd-diamond-substrates/ (cit. on pp. 39, 40).

[92] *Integrated Detector Electronics AS*. Accessed: 2022.08.13. URL: https://ideas.no/ (cit. on pp. 41, 42, 107, 201).

[93] *The VA2 Specifications*. Accessed: 2022.08.13. IDEAS. URL: http://rd42.web.cern.ch/rd42/ref_articles/VA_23_DATAVA2.PDF (cit. on pp. 42, 43, 201).

[94] O. Toker et al. "VIKING, a CMOS low noise monolithic 128 channel frontend for Si-strip detector readout". In: *Nuclear Instruments and Methods in Physics Research Section A: Accelerators, Spectrometers, Detectors and Associated Equipment* 340.3 (1994), pp. 572–579. ISSN: 0168-9002. DOI: 10.1016/0168-9002(94)90140-6. URL: https://www.sciencedirect.com/science/article/pii/0168900294901406 (cit. on pp. 42, 43).

[95] RD42 meeting. *Peaking time for the used VA2.2 ASICs*. personal communication. 2016 (cit. on p. 42).

[96] S.I. Parker, C.J. Kenney, and J. Segal. "3D — A proposed new architecture for solid-state radiation detectors". In: *Nuclear Instruments and Methods in Physics Research Section A: Accelerators, Spectrometers, Detectors and Associated Equipment* 395.3 (1997). Proceedings of the Third International Workshop on Semiconductor Pixel Detectors for Particles and X-rays, pp. 328–343. ISSN: 0168-9002. DOI: 10.1016/S0168-9002(97)00694-3. URL: https://www.sciencedirect.com/science/article/pii/S0168900297006943 (cit. on p. 44).

[97] Felix Bachmair. “CVD Diamond Sensors In Detectors For High Energy Physics”. eng. PhD thesis. 2016 (cit. on pp. 47, 102, 120, 131).

[98] Lukas Baeni. “Top Quarks and Diamonds”. Presented 2017. PhD thesis. 2017. DOI: 10.3929/ethz-b-000222412. URL: https://cds.cern.ch/record/2652765 (cit. on pp. 47, 120).

[99] I. Haughton et al. “Barrier potential for laser written graphitic wires in diamond”. In: *Diamond and Related Materials* 111 (2021), p. 108164. ISSN: 0925-9635. DOI: 10.1016/j.diamond.2020.108164. URL: https://www.sciencedirect.com/science/article/pii/S0925963520307172 (cit. on pp. 54, 55, 82).

[100] M.J. Booth et al. “Study of cubic and hexagonal cell geometries of a 3D diamond detector with a proton micro-beam”. In: *Diamond and Related Materials* 77 (2017), pp. 137–145. ISSN: 0925-9635. DOI: 10.1016/j.diamond.2017.06.014. URL: https://www.sciencedirect.com/science/article/pii/S0925963517301930 (cit. on pp. 54, 102, 211).

[101] Steve Schnetzer. “Diamond Sensors for Energy Frontier Experiments”. In: *PoS* Vertex2013 (2014), p. 029. DOI: 10.22323/1.198.0029 (cit. on p. 58).

[102] Kuan-Ting Ho et al. “Fabrication of Single Crystal Diamond Membranes by Oxygen Plasma Deep Etching”. In: *Symposium Latsis 2019 on Diamond Photonics - Physics, Technologies and Applications*. Optica Publishing Group, 2019, p. 83. DOI: 10.1364/DP.2019.83. URL: http://opg.optica.org/abstract.cfm?URI=DP-2019-83 (cit. on pp. 58, 234).

[103] C.L. Lee et al. “Etching and micro-optics fabrication in diamond using chlorine-based inductively-coupled plasma”. In: *Diamond and Related Materials* 17.7 (2008). Proceedings of Diamond 2007, the 18th European Conference on Diamond, Diamond-Like Materials, Carbon Nanotubes, Nitrides and Silicon Carbide, pp. 1292–1296. ISSN: 0925-9635. DOI: 10.1016/j.diamond.2008.01.011. URL: https://www.sciencedirect.com/science/article/pii/S0925963508000174 (cit. on pp. 58, 234).

[104] Birgit J.M. Hausmann et al. “Fabrication of diamond nanowires for quantum information processing applications”. In: *Diamond and Related Materials* 19.5 (2010). Proceedings of Diamond 2009, The 20th European Conference on Diamond, Diamond-Like Materials, Carbon Nanotubes and Nitrides, Part 1, pp. 621–629. ISSN: 0925-9635. DOI: 10.1016/j.diamond.2010.01.011. URL: https://www.sciencedirect.com/science/article/pii/S0925963510000312 (cit. on pp. 58, 234).

[105] *Crystalbond 509 (Clear Color) Mounting Adhesive*. Accessed: 2022.08.13. URL: https://www.2spi.com/item/z05110/ (cit. on p. 59).

[106] T. Tachibana, B. E. Williams, and J. T. Glass. “Correlation of the electrical properties of metal contacts on diamond films with the chemical nature of the metal-diamond interface. II. Titanium contacts: A carbide-forming metal”. In: *Phys. Rev. B* 45 (20 May 1992), pp. 11975–11981. DOI: 10.1103/PhysRevB.45.11975. URL: https://link.aps.org/doi/10.1103/PhysRevB.45.11975 (cit. on p. 60).

[107] Matthias Werner. “Diamond metallization for device applications”. In: *Semiconductor Science and Technology* 18.3 (Feb. 2003), S41–S46. DOI: 10.1088/0268-1242/18/3/306. URL: https://doi.org/10.1088/0268-1242/18/3/306 (cit. on p. 60).

[108] Ching-Ting Lee and Hsiao-Wei Kao. “Long-term thermal stability of Ti/Al/Pt/Au Ohmic contacts to n-type GaN”. In: *Applied Physics Letters* 76.17 (2000), pp. 2364–2366. DOI: 10.1063/1.126347. eprint: https://doi.org/10.1063/1.126347. URL: https://doi.org/10.1063/1.126347 (cit. on p. 62).

[109] *Cividec Instrumentation*. Accessed: 2022.08.13. Cividec Instrumentation. URL: https://cividec.at (cit. on p. 62).

[110] ANANT G. SABNIS. “Chapter 7 - Multilevel Metallization Schemes”. In: *VLSI Metallization*. Ed. by Norman G. Einspruch, Simon S. Cohen, and Gennady Sh. Gildenblat. Vol. 15. VLSI Electronics Microstructure Science. Elsevier, 1987, pp. 293–343. DOI: 10.1016/B978-0-12-234115-1.50011-8. URL: https://www.sciencedirect.com/science/article/pii/B9780122341151500118 (cit. on p. 65).

[111] S. J. H. Brader A. J. Roosmalen J. A. G. Baggerman. Updates in Applied Physics and Electrical Technology. Springer New York, NY, 1991, pp. XVII, 237. ISBN: 978-1-4899-2566-4 (cit. on p. 66).

[112] *COMSOL Multiphysics v. 6.0*. Accessed: 2022.08.13. COMSOL AB, Stockholm, Sweden. URL: https://www.comsol.com (cit. on pp. 75, 86, 225, 226).

[113] RD42 meeting. *Estimated diameter for the 3D wires*. personal communication. 2017 (cit. on pp. 79, 211).

[114] H. Pernegger. “High mobility diamonds and particle detectors”. In: *physica status solidi (a)* 203.13 (2006), pp. 3299–3314. DOI: 10.1002/pssa.200671404. eprint: https://onlinelibrary.wiley.com/doi/pdf/10.1002/pssa.200671404. URL: https://onlinelibrary.wiley.com/doi/abs/10.1002/pssa.200671404 (cit. on p. 87).

[115] S. M. Hearne et al. “The role of charge trapping at grain boundaries on charge transport in polycrystalline chemical vapor deposited diamond based detectors”. In: *Journal of Applied Physics* 99.11 (2006), p. 113703. DOI: 10.1063/1.2194116. eprint: https://doi.org/10.1063/1.2194116. URL: https://doi.org/10.1063/1.2194116 (cit. on p. 87).

[116] K. Konishi et al. “Diffusion-related lifetime and quantum efficiency of excitons in diamond”. In: *Phys. Rev. B* 102 (19 Nov. 2020), p. 195204. DOI: 10.1103/PhysRevB.102.195204. URL: https://link.aps.org/doi/10.1103/PhysRevB.102.195204 (cit. on p. 87).

[117] Nobuko Naka et al. “Direct measurement via cyclotron resonance of the carrier effective masses in pristine diamond”. In: *Phys. Rev. B* 88 (3 July 2013), p. 035205. DOI: 10.1103/PhysRevB.88.035205. URL: https://link.aps.org/doi/10.1103/PhysRevB.88.035205 (cit. on p. 88).

[118] Giulio Tiziano Forcolin. "Development and simulation of 3D diamond detectors". Presented 2018. PhD thesis. 2018. URL: https://cds.cern.ch/record/2636028 (cit. on p. 89).

[119] Christian Dorfer. "Investigation of Charge Transport in CVD Diamond by Multi-Photon Absorption Edge Transient-Current Technique". eng. PhD thesis. 2020 (cit. on pp. 89–91).

[120] *Ultrafast Laser Physics*. Accessed: 2022.08.13. ETH Zurich. URL: https://ulp.ethz.ch/ (cit. on p. 90).

[121] *CERN Secondary Beams & Areas*. Accessed: 2022.08.13. CERN. URL: https://sba.web.cern.ch/sba/index.html (cit. on p. 104).

[122] Ewa Lopienska. "The CERN accelerator complex, layout in 2022. Complexe des accélérateurs du CERN en janvier 2022". In: (Feb. 2022). General Photo. URL: https://cds.cern.ch/record/2800984 (cit. on p. 104).

[123] *CERN Site and Civil Engineering*. Accessed: 2022.08.13. CERN. URL: https://gis.cern.ch/?share=87ee52bf-73bf-4607-a5f9-a3f53c39399d (cit. on p. 105).

[124] C. Colledani et al. "A submicron precision silicon telescope for beam test purposes". In: *Nuclear Instruments and Methods in Physics Research Section A: Accelerators, Spectrometers, Detectors and Associated Equipment* 372.3 (1996), pp. 379–384. ISSN: 0168-9002. DOI: 10.1016/0168-9002(95)01414-4. URL: https://www.sciencedirect.com/science/article/pii/0168900295014144 (cit. on p. 106).

[125] G. Claus, W. Dulinski, and A. Lounis. *Strip Detectors Read-Out System User's Guide*. Centre de Recherges Nucléaires. 1996. URL: https://inis.iaea.org/collection/NCLCollectionStore/_Public/28/059/28059773.pdf (cit. on pp. 108, 119).

[126] D Singh. "Developments of readout methods for silicon strip detectors; 1997 ed." 1997. URL: https://cds.cern.ch/record/383483 (cit. on p. 108).

[127] *Microware OS-9*. Accessed: 2022.08.13. Microware. URL: https://microware.com/ (cit. on p. 108).

[128] W. Adam et al. "Pulse height distribution and radiation tolerance of CVD diamond detectors". In: *Nuclear Instruments and Methods in Physics Research Section A: Accelerators, Spectrometers, Detectors and Associated Equipment* 447.1 (2000), pp. 244–250. ISSN: 0168-9002. DOI: 10.1016/S0168-9002(00)00195-9. URL: https://www.sciencedirect.com/science/article/pii/S0168900200001959 (cit. on p. 108).

[129] *PiM1 Beam Line*. Accessed: 2022.08.13. PSI. URL: https://www.psi.ch/en/sbl/pim1-beamline (cit. on p. 110).

[130] Thomas Rauber and Corina Sattler. *Secondary Beam Lines (SBL)*. Accessed: 2022.08.13. Paul Scherrer Institut. URL: https://www.psi.ch/en/sbl (cit. on p. 110).

[131] *High rate tests of CVD diamond pad detectors in PSI test beams*. CERN. Presented at the 2019 November RD42 Collaboration Meeting, Nov. 2019 (cit. on pp. 111, 113).

[132] *Measured particle fluxes for standard beam-line tune*. Accessed: 2022.08.13. Paul Scherrer Institut. URL: https://www.psi.ch/sites/default/files/import/sbl/BLPiM1EN/fig3.gif (cit. on p. 112).

[133] *Pixel DTB*. Accessed: 2022.08.13. PSI. URL: https://www.ge.infn.it/~cerchi/CMS/Rpix/RpixFlex/Documenti/PixelDTB%20_%20CMS%20_%20TWiki.pdf (cit. on p. 111).

[134] *DRS Chip Homepage*. Accessed: 2022.08.13. PSI. URL: https://www.psi.ch/en/drs (cit. on p. 112).

[135] Stefan Ritt. "Design and performance of the 6 GHz waveform digitizing chip DRS4". In: *2008 IEEE Nuclear Science Symposium Conference Record*. 2008, pp. 1512–1515. DOI: 10.1109/NSSMIC.2008.4774700 (cit. on p. 112).

[136] *Pulse height analysis of pCVD 3D diamond detectors*. CERN. Presented at the 2019 November RD42 Collaboration Meeting, Nov. 2019 (cit. on p. 114).

[137] Michael Reichmann. *Thickness of the ROCs used for the tracking planes*. personal communication. 2021 (cit. on p. 115).

[138] Simon Spannagel, Beat Meier, and Hanno Christopher Perrey. *The pxarCore Library - Technical Documentation, Reference Manual, and Sample Applications*. Tech. rep. Geneva: CERN, 2015. URL: https://cds.cern.ch/record/2137512 (cit. on p. 115).

[139] *EUDAQ Documentation*. Accessed: 2022.08.13. EUDAQ. URL: https://eudaq.github.io/doxygen/index.html (cit. on pp. 115, 160).

[140] P. Ahlburg et al. "EUDAQ—a data acquisition software framework for common beam telescopes". In: *Journal of Instrumentation* 15.01 (Jan. 2020), P01038–P01038. DOI: 10.1088/1748-0221/15/01/p01038. URL: https://doi.org/10.1088/1748-0221/15/01/p01038 (cit. on pp. 115, 160).

[141] Pirmin Berger. "Measurement of the standard model Higgs Boson decay to b-quarks in association with a vector boson decaying to leptons, and module qualification for the CMS Phase-1 barrel pixel detector". en. Doctoral Thesis. Zurich: ETH Zurich, 2021. DOI: 10.3929/ethz-b-000491182 (cit. on p. 116).

[142] J. Straver et al. "One micron spatial resolution with silicon strip detectors". In: *Nuclear Instruments and Methods in Physics Research Section A: Accelerators, Spectrometers, Detectors and Associated Equipment* 348.2 (1994), pp. 485–490. ISSN: 0168-9002. DOI: 10.1016/0168-9002(94)90785-4. URL: https://www.sciencedirect.com/science/article/pii/0168900294907854 (cit. on p. 120).

[143] D Meier. "CVD Diamond Sensors for Particle Detection and Tracking". Presented on Jan 1999. PhD thesis. 1999. URL: https://cds.cern.ch/record/456577 (cit. on p. 120).

[144] Carlo Bradac, Torsten Gaebel, and James R. Rabeau. "Nitrogen-Vacancy Color Centers in Diamond: Properties, Synthesis, and Applications". In: *Optical Engineering of Diamond*. John Wiley & Sons, Ltd, 2013. Chap. 5, pp. 143–175. ISBN: 9783527648603. DOI: 10.1002/9783527648603.ch5. eprint: https://onlinelibrary.wiley.com/doi/pdf/10.1002/9783527648603.ch5. URL: https://onlinelibrary.wiley.com/doi/abs/10.1002/9783527648603.ch5 (cit. on p. 151).

[145] Simon Spannagel, Beat Meier, and Hanno Christopher Perrey. *The pxarCore Library - Technical Documentation, Reference Manual, and Sample Applications*. Tech. rep. Geneva: CERN, Oct. 2015. URL: https://cds.cern.ch/record/2137512 (cit. on pp. 157, 159).

[146] Andrey Starodumov. "Operation of the CMS Pixel Detector". In: *PoS* Vertex 2011 (2012), p. 009. DOI: 10.22323/1.137.0009 (cit. on pp. 157, 158).

[147] Rene Brun and Fons Rademakers. "ROOT — An object oriented data analysis framework". In: *Nuclear Instruments and Methods in Physics Research Section A: Accelerators, Spectrometers, Detectors and Associated Equipment* 389.1 (1997). New Computing Techniques in Physics Research V, pp. 81–86. ISSN: 0168-9002. DOI: 10.1016/S0168-9002(97)00048-X. URL: https://www.sciencedirect.com/science/article/pii/S016890029700048X (cit. on p. 160).

[148] Michael Reichmann. *Spread of Vcals in the psi46digV2.1-respin ROC*. personal communication. 2021 (cit. on p. 176).

[149] Marco Girolami et al. "Large single-crystal diamond substrates for ionizing radiation detection". In: *physica status solidi (a)* 213.10 (2016), pp. 2634–2640. DOI: 10.1002/pssa.201600262. eprint: https://onlinelibrary.wiley.com/doi/pdf/10.1002/pssa.201600262. URL: https://onlinelibrary.wiley.com/doi/abs/10.1002/pssa.201600262 (cit. on p. 178).

[150] *X-Ray Mass Attenuation Coefficients*. Accessed: 2022.08.13. NIST. URL: https://physics.nist.gov/PhysRefData/XrayMassCoef/tab3.html (cit. on p. 178).

[151] *Total production Overview - Module test Phase 1*. Accessed: 2022.08.13. ETH Zurich. URL: https://www.cmspixel.phys.ethz.ch/MoReWeb_Phase_I/Overview/ProductionOverview/ProductionOverviewPage_Total/ProductionOverview.html#d (cit. on p. 178).

[152] RD42 meeting. *Unknown behavior of first up-scan in rate*. personal communication. 2018 (cit. on p. 179).

[153] M. Reichmann et al. "New test beam results of 3D and pad detectors constructed with poly-crystalline CVD diamond". In: *Nuclear Instruments and Methods in Physics Research Section A: Accelerators, Spectrometers, Detectors and Associated Equipment* 958 (2020). Proceedings of the Vienna Conference on Instrumentation 2019, p. 162675. ISSN: 0168-9002. DOI: 10.1016/j.nima.2019.162675. URL: https://www.

sciencedirect.com/science/article/pii/S016890021931157X (cit. on p. 185).

[154] Michael Reichmann. *Drift of pulse height in the psi46digV2.1-respin ROC*. personal communication. 2021 (cit. on p. 189).

[155] Michael Reichmann. *Analysis software for the diamond rate beam tests at PSI*. URL: https://github.com/diamondIPP/RateAnalysis (cit. on p. 192).

[156] R. Wallny. "Beam test results of the dependence of signal size on incident particle flux in diamond pixel and pad detectors". In: *Journal of Instrumentation* 10.07 (July 2015), pp. C07009–C07009. DOI: 10.1088/1748-0221/10/07/c07009. URL: https://doi.org/10.1088/1748-0221/10/07/c07009 (cit. on pp. 197, 200).

[157] RD42 Collaboration, L. Bäni, et al. "Recent Results from Polycrystalline CVD Diamond Detectors". In: (2019). DOI: 10.48550/ARXIV.1910.07621. URL: https://arxiv.org/abs/1910.07621 (cit. on p. 200).

[158] Alexander Oh. *Microscope photograph of the 3D wires in the Full-3D*. CERN, Sept. 2016 (cit. on p. 205).

[159] S. Lagomarsino et al. "Polycrystalline diamond detectors with three-dimensional electrodes". In: *Nuclear Instruments and Methods in Physics Research Section A: Accelerators, Spectrometers, Detectors and Associated Equipment* 796 (2015). Proceedings of the 10th International Conference on Radiation Effects on Semiconductor Materials Detectors and Devices, pp. 42–46. ISSN: 0168-9002. DOI: 10.1016/j.nima.2015.03.041. URL: https://www.sciencedirect.com/science/article/pii/S0168900215003575 (cit. on pp. 221, 222, 225, 227).

[160] Stefano Lagomarsino et al. "Radiation hardness of three-dimensional polycrystalline diamond detectors". In: *Applied Physics Letters* 106.19 (2015), p. 193509. DOI: 10.1063/1.4921116. eprint: https://doi.org/10.1063/1.4921116. URL: https://doi.org/10.1063/1.4921116 (cit. on pp. 221, 222, 225, 227).

[161] May Iam. *Photoresist of Photolithography*. Accessed: 2022.08.13. Wikipedia. URL: https://commons.wikimedia.org/wiki/File:Photoresist_of_Photolithography.png (cit. on p. 243).

[162] *Microchemicals Gmbh*. Accessed: 2022.08.13. Microchemicals Gmbh, Ulm, Germany. URL: https://microchemicals.com/ (cit. on pp. 237–242).

[163] *Stress control of Si-based PECVD dielectrics*. 2005, pp. 148–159. URL: https://www.researchgate.net/publication/266043105_Stress_control_of_Si-based_PECVD_dielectrics (cit. on p. 244).

[164] Kazuyoshi Ueno, Takamaro Kikkawa, and Ken Tokashiki. "Reactive ion etching of silicon oxynitride formed by plasma-enhanced chemical vapor deposition". In: *Journal of Vacuum Science & Technology B: Microelectronics and Nanometer Structures Processing, Measurement, and Phenomena* 13.4 (1995), pp. 1447–1450. DOI: 10.1116/1.588169. eprint: https://avs.scitation.org/doi/pdf/10.1116/1.588169. URL: https://avs.scitation.org/doi/abs/10.1116/1.588169 (cit. on p. 246).

[165] Luc Devroye. Springer New York, NY, pp. 27–39. ISBN: 978-1-4613-8643-8 (cit. on p. 247).

[166] Marc Paterno and /Fermilab. "Calculating efficiencies and their uncertainties". In: (Dec. 2004). DOI: 10.2172/15017262. URL: https://www.osti.gov/biblio/15017262 (cit. on p. 249).

[167] D Casadei. "Estimating the selection efficiency". In: *Journal of Instrumentation* 7.08 (Aug. 2012), P08021–P08021. DOI: 10.1088/1748-0221/7/08/p08021. URL: https://doi.org/10.1088/1748-0221/7/08/p08021 (cit. on p. 249).